DOE-ER-0313/60
Distribution
Categories
UC-423, -424

FUSION MATERIALS
SEMIANNUAL PROGRESS REPORT
FOR THE PERIOD ENDING

June 30, 2016

Prepared for
DOE Office of Fusion Energy Sciences
(AT 60 20 10 0)

DATE PUBLISHED: September 2016

Prepared by
OAK RIDGE NATIONAL LABORATORY
Oak Ridge, Tennessee 37831
Managed by
UT-Battelle, LLC
For the
U.S. DEPARTMENT OF ENERGY

FOREWORD

This is the sixtieth in a series of semiannual technical progress reports on fusion materials science activity supported by the Fusion Energy Sciences Program of the U.S. Department of Energy. It covers the period ending June 30, 2016. This report focuses on research addressing the effects on materials properties and performance of exposure to the neutronic, thermal and chemical environments anticipated in the chambers of fusion experiments and energy systems. This research is a major element of the national effort to establish the materials knowledge base for an economically and environmentally attractive fusion energy source. Research activities on issues related to the interaction of materials with plasmas are reported separately.

The results reported are the products of a national effort involving a number of national laboratories and universities. A large fraction of this work, particularly in relation to fission reactor irradiations, is carried out collaboratively with partners in Japan, Russia, and the European Union. The purpose of this series of reports is to provide a working technical record for the use of program participants, and to provide a means of communicating the efforts of fusion materials scientists to the broader fusion community, both nationally and worldwide.

This report has been compiled under the guidance of F. W. (Bill) Wiffen and Stephanie Melton, Oak Ridge National Laboratory. Their efforts, and the efforts of the many persons who made technical contributions, are gratefully acknowledged.

Daniel Clark
Research Division
Office of Fusion Energy Sciences

TABLE OF CONTENTS

1 **FERRITIC/MARTENSITIC STEEL DEVELOPMENT**

1.1 **FABRICATION OF LOW ACTIVATION FERRITIC-MARTENSITIC STEELS CONTAINING ^{54}FE ISOTOPE**—Y. Yamamoto (Oak Ridge National Laboratory) 1

1.2 **ADVANCED BAINITIC STEEL DEVELOPMENT FOR FUSION STRUCTURAL APPLICATIONS**—Y. Yamamoto (Oak Ridge National Laboratory) 6

1.3 **ON THE EFFECTS OF HE-DPA INTERACTIONS ON CAVITY EVOLUTION IN TEMPERED MARTENSITIC STEELS UNDER DUAL ION IRRADIATION**—Takuya Yamamoto, Yuan Wu, G. Robert Odette (University of California Santa Barbara), Kiyohiro Yabuuchi, Sosuke Kondo, Akihiko Kimura (Kyoto University) 12

1.4 **INFLUENCE OF ION IRRADIATION DIRECTION ON GROWTH OF NANOPRECIPITATES IN MODEL CNAs**—L. Tan (Oak Ridge National Laboratory), B.K. Kim (ORNL), G.S. Was (Univ. of Michigan) 17

2 **ODS AND NANOCOMPOSITED ALLOY DEVELOPMENT**

2.1 **Fe-Cr-Al ODS ALLOYS FOR FUSION REACTOR APPLICATIONS**—S. Dryepondt , K. A. Unocic, D. T. Hoelzer (Oak Ridge National Laboratory) 20

2.2 **X-RAY ABSORPTION SPECTROSCOPY OF EMBEDDED AND EXTRACTED NANO-OXIDES IN NANOSTRUCTURED FERRITIC ALLOY MA957**—T. Stan, G.R. Odette (University of California Santa Barbara), D. Sprouster, A. Ofran, L. Ecker (Brookhaven National Laboratory) 28

2.3 **ESTIMATES OF THE THOUGH THICKNESS RESIDUAL STRESSES IN THE AS-PROCESSED NFA-1 PLATE BASED ON NANOINDENTATION MEASUREMENTS**—S. Pal, M. E. Alam and G. R. Odette (UCSB) 35

2.4 **CHARACTERIZATION OF FE THIN FILMS ON {100} ORIENTED $Y_2Ti_2O_7$ SUBSTRATES**—T. Stan, Y. Wu, G.R. Odette (University of California Santa Barbara), and H.D. Zhou (University of Tennessee) 45

2.5 **TEM OBSERVATION OF ANNEALED AND He IMPLANTED NANOSTRUCTURED FERRITIC ALLOYS**—Y. Wu, T. Stan, T. Yamamoto, G. R. Odette (University of California Santa Barbara) 54

2.6 **THREE DIMENSIONAL ATOM PROBE TOMOGRAPHY OF 14YW AND 14YWT NEUTRON IRRADIATED AT 500ºC TO 21.2 DPA**—D.J. Edwards, K. Kruska, J. Wang, R. J. Kurtz (Pacific Northwest National Laboratory), G.R. Odette, T. Yamamoto and Y. Wu (University of California-Santa Barbara) 59

3 **CERAMIC COMPOSITE STRUCTURAL MATERIAL DEVELOPMENT**

3.1 **LOW ACTIVATION JOINING OF SiC/SiC COMPOSITES FOR FUSION APPLICATIONS: THERMOMECHANICAL MODELING OF DUAL-PHASE MICROSTRUCTURES AND DISSIMILAR MATERIAL JOINTS**—B.N. Nguyen, C.H. Henager, Jr., and R.J. Kurtz; (Pacific Northwest National Laboratory, Richland, WA, USA); M. Ferraris, (Politecnico di Torino, Torino, Italy); Y. Katoh, (Oak Ridge National Laboratory, Oak Ridge, TN, USA) 65

TABLE OF CONTENTS

3.2 **CHARACTERIZATION OF PRECIPITATES IN CUBIC SILICON CARBIDE IMPLANTED WITH $^{25}Mg^+$ IONS**—W. Jiang, S. R. Spurgeon, J. Liu, D. J. Edwards, D. K. Schreiber, C. H. Henager, Jr., R. J. Kurtz (Pacific Northwest National Laboratory), and Y. Wang (Los Alamos National Laboratory) **72**

3.3 **NEUTRON-IRRADIATION CREEP OF SILICON CARBIDE MATERIALS BEYOND THE INITIAL TRANSIENT**—T. Koyanagi, Y. Katoh (Oak Ridge National Laboratory), K. Ozawa (Japan Atomic Energy Agency), K. Shimoda, T. Hinoki (Kyoto University), L.L. Snead (Massachusetts Institute of Technology) **78**

4 **HIGH HEAT FLUX MATERIALS AND COMPONENT TESTING**

4.1 **DESIGN AND DEVELOPMENT OF NOVEL COPPER ALLOYS FOR FUSION ENERGY APPLICATIONS**—Ying Yang (Oak Ridge National Laboratory) and Steven J. Zinkle (University of Tennessee and Oak Ridge National Lab) **83**

4.2 **PRELIMINARY PROGRESS IN THE DEVELOPMENT OF DUCTILE-PHASE TOUGHENED TUNGSTEN FOR PLASMA-FACING MATERIALS: DUAL-PHASE FINITE ELEMENT DAMAGE MODELS**—C. H. Henager, Jr., B. N Nguyen, R. J. Kurtz (Pacific Northwest National Laboratory) **89**

4.3 **DUCTILE PHASE TOUGHENING OF 90-97wt% W-NiFe HEAVY METAL ALLOYS**—M.E. Alam, S. Pal, K. Field, G. R. Odette (UCSB) **93**

4.4 **FABRICATION OF FUNCTIONALLY GRADED TUNGSTEN STEEL LAMINATE**—L. M. Garrison, Y. Katoh (Oak Ridge National Laboratory), M. Norfolk (Fabrisonic LLC.), J. Wenning (Fabrisonic LLC.), J. Moon (University of Nevada-Reno) **103**

4.5 **IRRADIATION HARDENING OF PURE TUNGSTEN EXPOSED TO NEUTRON IRRADIATION**—X. Hu, T. Koyanagi, N.A.P Kiran Kumar, Y. Katoh (Oak Ridge National Laboratory), L.L. Snead (Massachusetts Institute of Technology), B.D. Wirth (University of Tennessee, Knoxville) **109**

4.6 **NEUTRON IRRADIATION EFFECTS IN TUNGSTEN**—L.M. Garrison, Y. Katoh, P. Edmondson, X. Hu, C. Parish, T. Koyanagi, M. McAlister, N.A.P. Kiran Kumar (Oak Ridge National Laboratory), M. Fukuda, T. Hwang (Tohoku University, Japan), L. L. Snead (Massachusetts Institute of Technology), T. S. Byun **125**

4.7 **NEUTRON IRRADIATION EFFECTS IN TUNGSTEN-COPPER COMPOSITES**—L. M. Garrison, Yutai Katoh (Oak Ridge National Laboratory) Jeremy Moon (University of Nevada-Reno), Joseph Willenborg (University of Tennessee-Knoxville) **130**

4.8 **HIGH-HEAT FLUX TESTING OF LOW-LEVEL IRRADIATED MATERIALS USING PLASMA ARC LAMPS**—A.S. Sabau, Y. Katoh (Oak Ridge National Laboratory) and K. Ibano (Osaka University) **134**

5 **MAGNETIC AND DIAGNOSTIC SYSTEM MATERIALS**
No contributions this reporting period.

6 **FUSION CORROSION AND COMPATIBILITY SCIENCE**

TABLE OF CONTENTS

6.1 **COMPATIBILITY OF FeCrAl IN FLOWING Pb-LI AT 550°-600°C**– B. A. Pint and S. J. Pawel (Oak Ridge National Laboratory, USA) **137**

7 **MECHANISMS AND ANALYSIS**

7.1 **QUALITATIVE ANALYSIS OF COMMERCIAL $M_{n+1}AX_n$ PHASES UNDER NEUTRON IRRADIATION**—C. Ang*, C. Shih, S.J. Zinkle, C. Silva, C. Parish, N. Cetiner, P. Edmondson, and Y. Katoh (Oak Ridge National Laboratory, USA) **141**

7.2 **DAMAGE MECHANISM INTERACTIONS AT THE PLASMA-MATERIALS INTERFACE (Early Career Award)**—C. M. Parish, K. Wang (Oak Ridge National Laboratory) **146**

7.3 **THERMOMECHANICS OF RESILIENT MICRO-ENGINEERED PLASMA FACING MATERIALS**—David Rivera, Richard Wirz, Nasr M. Ghoniem (University of California, Los Angeles) **152**

7.4 **A VARIATIONAL FORMULATION OF THE VOLTERRA DISLOCATION RECONSTRUCTION OF 3-D MOVING CRACKS**—A. Sheng, G. Po, N.M. Ghoniem (University of California, Los Angeles) **156**

7.5 **LOADING CONTROLLED TRANSITION OF PLASTIC FLOW FROM DISLOCATION AVALANCHE TO QUASI-PERIODIC STRAIN BURST BEHAVIOR**—Y.N. Cui, G. Po, N.M. Ghoniem (University of California, Los Angeles) **163**

8 **MODELING PROCESSES IN FUSION SYSTEM MATERIALS**

8.1 **DEVELOPMENT OF INTERATOMIC POTENTIALS IN TUNGSTEN-RHENIUM SYSTEMS**—W. Setyawan, G. Nandipati, and R. J. Kurtz (Pacific Northwest National Laboratory) **165**

8.2 **STRUCTURE AND MOBILITIES OF TUNGSTEN GRAIN BOUNDARIES CALCULATED FROM ATOMISTIC SIMULATIONS**—Timofey Frolov and Robert E. Rudd (Lawrence Livermore National Laboratory) **172**

8.3 **OBJECT KINETIC MONTE CARLO SIMULATIONS OF RADIATION DAMAGE ACCUMULATION IN TUNGSTEN**—G. Nandipati, W. Setyawan, K. J. Roche, R. J. Kurtz (Pacific Northwest National Laboratory) and B. D. Wirth (University of Tennessee) **178**

8.4 **INTERACTION OF INTERSTITIAL CLUSTERS WITH RHENIUM, OSMIUM, AND TANTALUM IN TUNGSTEN**—W. Setyawan, G. Nandipati, and R. J. Kurtz (Pacific Northwest National Laboratory) **183**

9 **FUSION SYSTEM DESIGN**

9.1 **MULTI-PHYSICS DESIGN OF THE FIRST WALL AND BLANKET SYSTEM IN THE FUSION NUCLEAR SCIENCE FACILITY (FNSF)**—Yue Huang, Nasr Ghoniem, Mark Tillack, Jake Blanchard, Laila El-Guebaly, Chuck Kessel **188**

10 **IRRADIATION METHODS, EXPERIMENTS AND SCHEDULES**

TABLE OF CONTENTS

10.1	**MINIATURE MECHANICAL TEST DEVELOPMENT FOR TUNGSTEN-BASED MATERIALS**—L. M. Garrison (Oak Ridge National Laboratory), Jeremy Moon (University of Nevada-Reno), Joseph Willenborg (University of Tennessee-Knoxville)	**195**
10.2	**DEVELOPMENT OF A NON-CONTACT STRAIN MEASUREMENT SYSTEM FOR POST IRRADIATED TENSILE TESTS AT HIGH TEMPERATURES**—H. Sakasegawa, T. Kato, H. Tanigawa (National Institutes for Quantum and Radiological Science and Technology), and Y. Katoh (Oak Ridge National Laboratory)	**201**
10.3	**HFIR-MFE-RB-19J THERMAL AND NEUTRONIC DESIGN**—J.L. McDuffee, C.R. Daily, N.O. Cetiner, C.M. Petrie, J.W Geringer (Oak Ridge National Laboratory)	**205**
10.4	**HFIR-MFE-RB-19J SPECIMEN LOADING LISTING**—J.W. Geringer, J.L. McDuffee, C.M. Petrie, L.M. Garrison, R.H. Howard, N.O. Cetiner, D.A. Stringfield, R.G. Sitterson (Oak Ridge National Laboratory)	**215**
10.5	**HFIR IRRADIATION EXPERIMENTS**—J.P. Robertson, Y. Katoh and J. McDuffee (Oak Ridge National Laboratory)	**234**

TABLE OF CONTENTS

1 FERRITIC/MARTENSITIC STEEL DEVELOPMENT

1.1 **FABRICATION OF LOW ACTIVATION FERRITIC-MARTENSITIC STEELS CONTAINING ^{54}FE ISOTOPE**—Y. Yamamoto (Oak Ridge National Laboratory) 1

Four trial EUROFER97 steel plates were successfully fabricated by arc-melting with natural Fe and hot-rolling with a steel guide. The arc-melting was conducted to measure the yield of each alloying element during the melt process, and the trial hot-rolling with a steel guide was performed to produce steel plates without barreling. Based on the process parameter of the trial heats, two RAFM steel plates (targeted to be EUROFER97 and CNA) made of ^{54}Fe isotope powder, with size ~0.25 x 1.4 x 2.5 inches, were successfully fabricated. The detailed planning of the machining of SS-J3 tensile specimens and M4 bend bar specimens, as well as developing an irradiation test plan for HFIR, is currently in progress.

1.2 **ADVANCED BAINITIC STEEL DEVELOPMENT FOR FUSION STRUCTURAL APPLICATIONS**—Y. Yamamoto (Oak Ridge National Laboratory) 6

A new alloy design strategy for PWHT-free bainitic steel has been proposed; reducing the as-normalized hardness without losing high hardenability, in order to reduce potential property inhomogeneity across the weldment. Four new heats of 3Cr-3WVTa base bainitic steels with low carbon combined with high Mn and Si were prepared with guidance from computational thermodynamics. The steel with the combination of 0.05C and 2 or 3Mn additions successfully showed fully bainitic microstructure together with less hardness difference between as-normalized and tempered conditions, which will reduce the potential property inhomogeneity in the weldments. High temperature tensile properties also supported potential improvement of mechanical properties at elevated temperatures. Preparation for creep-rupture testing is currently underway.

1.3 **ON THE EFFECTS OF HE-DPA INTERACTIONS ON CAVITY EVOLUTION IN TEMPERED MARTENSITIC STEELS UNDER DUAL ION IRRADIATION**—Takuya Yamamoto, Yuan Wu, G. Robert Odette (University of California Santa Barbara), Kiyohiro Yabuuchi, Sosuke Kondo, Akihiko Kimura (Kyoto University) 12

We filled some gaps in our cavity evolution database on normalized and tempered 9Cr martensitic steels (TMS) F82H under Fe^{3+} plus He^{+} dual ion beam irradiation (DII) at 500°C. New experiments were conducted at ≈ 30 appm He/dpa at relatively low nominal damage rate of 6.5x10^{-4} dpa/s. The cavity evolution database at 500°C now includes 321 material-dpa-He-dpa rate DII conditions. Two distinct trends of higher and lower swelling rates versus dpa are observed. Here we compare the detailed evolution of the cavity size distributions with increasing dpa and He to seek clues about the reasons for these differences in behavior. The higher swelling rate case was generally associated with higher dpa rates, fewer cavities and stronger bi-modality, compared to the lower swelling rate case.

TABLE OF CONTENTS

1.4 INFLUENCE OF ION IRRADIATION DIRECTION ON GROWTH OF NANOPRECIPITATES IN MODEL CNAs—L. Tan (Oak Ridge National Laboratory), B.K. Kim (ORNL), G.S. Was (Univ. of Michigan) **17**

Transmission electron microscopy of irradiated CNA alloys and statistical quantitative analysis of the ultrafine particles after heavy ion irradiation indicates that these experiments may not represent the precipitate stability under neutron irradiation. The dependence of nanoprecipitate evolution on ion beam direction is one process that may be unique to ion irradiation.

2 ODS AND NANOCOMPOSITED ALLOY DEVELOPMENT

2.1 Fe-Cr-Al ODS ALLOYS FOR FUSION REACTOR APPLICATIONS—S. Dryepondt , K. A. Unocic, D. T. Hoelzer (Oak Ridge National Laboratory) **20**

Several ODS FeCrAl alloys were fabricated by ball milling Fe-12Cr-5Al gas atomized powder with Y_2O_3 powder and ZrO_2, HfO_2, or TiO_2 powder. The Zr-containing alloy (125YZ) exhibited excellent creep properties at 700-800ºC in air, and good compatibility with Pb-17Li at 700ºC, with the formation of a thin $LiAlO_2$ layer. Extensive TEM characterization of the 125YZ revealed the presence of $Y_3Al_5O_{12}$ (YAG), Al_2O_3 and Zr(C,N) nano precipitates. A second generation of ODS FeCrAl alloys was fabricated by ball-milling Zr or Hf-containing Fe-12Cr-5.5Al powder with Y_2O_3 powder. Initial characterization of these 2nd generation alloys showed that the alloy tensile properties are very dependent on the extrusion conditions.

2.2 X-RAY ABSORPTION SPECTROSCOPY OF EMBEDDED AND EXTRACTED NANO-OXIDES IN NANOSTRUCTURED FERRITIC ALLOY MA957—T. Stan, G.R. Odette (University of California Santa Barbara), D. Sprouster, A. Ofran, L. Ecker (Brookhaven National Laboratory) **28**

The chemistries and structures of both embedded and extracted Y-Ti-O nanometer-scale oxides in nanostructured ferritic alloy (NFA) MA957 were characterized by x-ray absorption spectroscopy (XAS). $Y_2Ti_2O_7$ is the primary embedded phase, while the slightly larger extracted oxides are primarily Y_2TiO_5. Analysis of the embedded nano-oxides in MA957 is difficult partly due to the multiple Ti environments associated with different oxides and those still residing in matrix lattice sites. Thus, bulk extraction followed by selective filtration was used to isolate the larger Y_2TiO_5 oxides for XAS. The smaller $Y_2Ti_2O_7$ oxides passed through the filters but were the predominant embedded phase.

TABLE OF CONTENTS

2.3 ESTIMATES OF THE THOUGH THICKNESS RESIDUAL STRESSES IN THE AS-PROCESSED NFA-1 PLATE BASED ON NANOINDENTATION MEASUREMENTS—S. Pal, M. E. Alam and G. R. Odette (UCSB) **35**

Hardness and modulus of the as processed NFA-1 alloy plate have been measured using nanoindentations, including to probe the nature and magnitude of the residual stresses generated by thermo-mechanical processing. The residual stresses were quantified from the nanoindentation load-penetration curves. The plate surfaces (and adjoining mild steel can) are in compression, while the middle of the plate is in tension. The magnitude of the maximum tensile residual stress is ≈ +500 MPa, decreasing to ≈ +75 MPa near to the plate surface; and ≈ -30 MPa at the surface of the can. A microcrack population area density, lying perpendicular to the short thickness direction of the plate, tracks the residual tensile stress profile. The surface residual stresses were further quantified using a conventional $\sin_2\psi$ x-ray diffraction (XRD) method that yielded a value similar to the nanoindentation estimate.

2.4 CHARACTERIZATION OF FE THIN FILMS ON {100} ORIENTED $Y_2Ti_2O_7$ SUBSTRATES—T. Stan, Y. Wu, G.R. Odette (University of California Santa Barbara), and H.D. Zhou (University of Tennessee) **45**

Nanostructured Ferritic Alloys (NFAs), a variant of oxide dispersion strengthened steels, contain a high density (≈ $5x10^{23}/m^2$) of ≈ 2.5 nm average diameter Y-Ti-O nano-oxides (NOs) which help impede dislocation climb and glide, stabilize dislocation and grain structures, and trap He in fine-scale bubbles at matrix-NO interfaces. To complement other studies of the NOs themselves, mesoscopic-scale bilayer interfaces were fabricated by electron beam deposition of a thin Fe film on a {100} $Y_2Ti_2O_7$ (YTO) bulk single crystal substrate. These bilayers were prepared for He implantation and charged particle irradiations to experimentally observe defect interface interactions and the partitioning of He between the Fe, YTO, and the associated interface. We report, for the first time, the dominant epitaxial orientation relationship (OR) for a polycrystalline Fe film on {100} YTO: $\{110\}_{Fe}\backslash\backslash\{100\}_{YTO}$ and $<100>_{Fe}\backslash\backslash<110>_{YTO}$. One large grain region had an OR that is also found in embedded NOs: $\{100\}_{Fe}\backslash\backslash\{100\}_{YTO}$ and $<100>_{Fe}\backslash\backslash<110>_{YTO}$. HRTEM studies show clean semicoherent interfaces, with misfit dislocation spacings consistent with the calculated near coincidence site lattices.

2.5 TEM OBSERVATION OF ANNEALED AND He IMPLANTED NANOSTRUCTURED FERRITIC ALLOYS—Y. Wu, T. Stan, T. Yamamoto, G. R. Odette (University of California Santa Barbara) **54**

Transmission electron microscopy (TEM) studies were carried out on two 700°C He implanted NFAs that had been previously annealed to coarsen their initially ultra-high density of nano-scale oxides (NOs). All the coarsened Y-Ti-O oxides were found to be associated with at least one, and in many cases more than one, interface helium bubble.

TABLE OF CONTENTS

2.6 THREE DIMENSIONAL ATOM PROBE TOMOGRAPHY OF 14YW AND 14YWT NEUTRON IRRADIATED AT 500ºC TO 21.2 DPA—D.J. Edwards, K. Kruska, J. Wang, R. J. Kurtz (Pacific Northwest National Laboratory), G.R. Odette, T. Yamamoto and Y. Wu (University of California-Santa Barbara) **59**

Work has progressed on the characterization of two ferritic alloys, 14YW and 14YWT, irradiated in the JP27 experiment in the High Flux Isotope Reactor as part of the In-situ Helium Injection (ISHI) experiments. While much of the work has focused on high resolution analytical TEM of the bubble and dislocation structures formed during neutron irradiation, this TEM analysis has not been able to effectively characterize the nano-oxide particles present in 14YWT, which are usually less than 2 nm in size. To investigate microstructural features at this scale in a statistically meaningful manner, 3D-APT has been initiated to probe the oxide dispersion in the 14YWT. For comparative purposes, the 14YW alloy is also examined, however, the oxide dispersion is noticeably coarser due to the lack of titanium, and it is better characterized using TEM. APT of the 14YWT alloy revealed that significant precipitation of Mn-rich phases had occurred, as well as the formation of a Cr-rich α'-type phase at a composition that appears to contain less than the expected 85% Cr.

3 CERAMIC COMPOSITE STRUCTURAL MATERIAL DEVELOPMENT

3.1 LOW ACTIVATION JOINING OF SiC/SiC COMPOSITES FOR FUSION APPLICATIONS: THERMOMECHANICAL MODELING OF DUAL-PHASE MICROSTRUCTURES AND DISSIMILAR MATERIAL JOINTS—B.N. Nguyen, C.H. Henager, Jr., and R.J. Kurtz; (Pacific Northwest National Laboratory, Richland, WA, USA); M. Ferraris, (Politecnico di Torino, Torino, Italy); Y. Katoh, (Oak Ridge National Laboratory, Oak Ridge, TN, USA) **65**

Miniature torsion specimens were designed for joint testing and irradiation in test reactors with limited irradiation volumes since SiC and SiC-composites used in fusion environments are thought to require joining methods for component assembly. HFIR irradiation results indicated two broad types of joint damage due to irradiation at either 500˚C or 800˚C to 3 dpa or 5 dpa. One type of damage can be categorized as microcracking within multi-phase joints at the micron length scale. The other type of damage can be categorized as cracking within the miniature torsion sample and within the joint where the cracks are now on the scale of the joint thickness and are not considered to be microcracks. This report expands the methods developed and discussed in our previous report to model both types of cracking due to thermal stresses caused by the mismatch of thermoelastic properties (i.e., elastic properties and thermal expansion coefficients) in the constituent phases or between the joint and joint materials for a specimen uniformly heated from 28˚C to 800˚C.

TABLE OF CONTENTS

3.2 **CHARACTERIZATION OF PRECIPITATES IN CUBIC SILICON CARBIDE IMPLANTED WITH ^{25}Mg$^+$ IONS**—W. Jiang, S. R. Spurgeon, J. Liu, D. J. Edwards, D. K. Schreiber, C. H. Henager, Jr., R. J. Kurtz (Pacific Northwest National Laboratory), and Y. Wang (Los Alamos National Laboratory) **72**

This progress report presents results from high-resolution scanning transmission electron microscopy (STEM), electron energy loss spectroscopy (EELS) and atom probe tomography (APT). The APT study has been performed for cubic silicon carbide (3C-SiC) implanted to 9.6×10^{16} ^{25}Mg$^+$/cm^2 at 673 K and subsequently annealed at 1073 and 1573 K for 2, 6, and 12 h in an Ar environment. The ^{25}Mg isotope was chosen to differentiate it from $^{12}C_2$ clusters in APT. STEM and EELS characterizations have been carried out for the same 3C-SiC sample annealed at 1573 K for 12 h. The APT results show a faster Mg clustering process during isochronal annealing (12 h) at a higher temperature while growth to larger Mg clusters on the average occurs during isothermal annealing (1573 K) for a longer time. The STEM-EELS study suggests that some of the precipitates have a core (MgC_2)-shell (Mg^2Si) microstructure. The precipitate size and number density are determined to be 2-8 nm and ~10^{18}/cm^3, respectively.

3.3 **NEUTRON-IRRADIATION CREEP OF SILICON CARBIDE MATERIALS BEYOND THE INITIAL TRANSIENT**—T. Koyanagi, Y. Katoh (Oak Ridge National Laboratory), K. Ozawa (Japan Atomic Energy Agency), K. Shimoda, T. Hinoki (Kyoto University), L.L. Snead (Massachusetts Institute of Technology) **78**

Irradiation creep beyond the transient regime was investigated for various SiC materials. The materials examined included polycrystalline or monocrystalline high-purity SiC, nanopowder sintered SiC, highly crystalline and near-stoichiometric SiC fibers, and a Tyranno SA3 SiC fiber reinforced SiC matrix composite fabricated through a nano-infiltration transient eutectic phase process. Findings are 1) the stress exponent of the post-transient creep was near unity, 2) the small apparent steady-state creep rate was ~1×10^{-7} [dpa^{-1}MPa^{-1}] at ~300 to ~800°C for most polycrystalline SiC materials, and 3) the effect of material quality on the creep rate, including structure of grain boundaries and crystal orientation, increased with increasing irradiation temperature. The results have been published in J. Nucl. Mater. and a condensed version is given here.

4 **HIGH HEAT FLUX MATERIALS AND COMPONENT TESTING**

4.1 **DESIGN AND DEVELOPMENT OF NOVEL COPPER ALLOYS FOR FUSION ENERGY APPLICATIONS**—Ying Yang (Oak Ridge National Laboratory) and Steven J. Zinkle (University of Tennessee and Oak Ridge National Lab) **83**

A computation thermodynamics tool for designing and developing Cu-Cr-Nb-Zr alloys have been successfully developed. Thermodynamic modeling results based on this tool enabled a rapid development of a novel CuCrNbZr alloys with targeted microstructure using an economical, conventional ingot making method following by simple heat treatment procedures. The new alloys display uniform grain structure with bimodal distribution of precipitates.

TABLE OF CONTENTS

4.2 **PRELIMINARY PROGRESS IN THE DEVELOPMENT OF DUCTILE-PHASE TOUGHENED TUNGSTEN FOR PLASMA-FACING MATERIALS: DUAL-PHASE FINITE ELEMENT DAMAGE MODELS**—C. H. Henager, Jr., B. N Nguyen, R. J. Kurtz (Pacific Northwest National Laboratory) **89**

A promising approach to increasing fracture toughness and decreasing the ductile-brittle transition temperature (DBTT) of a W-alloy is by ductile-phase toughening (DPT) [1-3]. In this method, a ductile phase is included in a brittle matrix to prevent fracture propagation by crack bridging or crack deflection. Liquid-phase sintered W-Ni-Fe alloys and hot-pressed and sintered W-Cu composites are two examples of such materials that PNNL and UCSB are investigating. However, there is a need for improved mechanical property models of such composite systems in order to begin to optimize these structural materials with regard to strength and fracture toughness. This report describes such a model that is currently under development at PNNL.

4.3 **DUCTILE PHASE TOUGHENING OF 90-97wt% W-NiFe HEAVY METAL ALLOYS**—M.E. Alam, S. Pal, K. Field, G. R. Odette (UCSB) **93**

Ductile phase toughening (DPT) is a promising approach to improving toughness of brittle materials like tungsten (W). The fracture toughness of commercial liquid phase sintered W-based composites, containing 90, 92.5, 95 and 97 wt.% W, with the balance a 7:3 Ni:Fe ductile solid solution phase, has been characterized. Pre-cracked single edge notch bend bar fracture toughness tests were conducted at room temperature. The average maximum load initiation toughness averaged 102 ± 17 MPa√m, relatively independent of the W fraction up to 95 wt.%, but dropped to 71± 17 MPa√m for the 97%W alloy. However, crack blunting beyond the peak load (down to $P/P_{max} \approx 0.8$), prior to any significant crack growth (da), resulted in an even higher toughness of 168 ± 31 MPa√m. The toughness of the W-Ne:Fe composites compare to typical monolithic-W values of ≈ 8 MPa√m. Composite fracture occurs by stable crack growth. The enormous toughening is due to crack bridging and especially very large plastic zone deformation energy dissipation.

4.4 **FABRICATION OF FUNCTIONALLY GRADED TUNGSTEN STEEL LAMINATE**—L. M. Garrison, Y. Katoh (Oak Ridge National Laboratory), M. Norfolk (Fabrisonic LLC.), J. Wenning (Fabrisonic LLC.), J. Moon (University of Nevada-Reno) **103**

Two roll-bonded tungsten-steel composites have been fabricated. Tensile tests of the Generation 2 composite were completed and showed increasing strength and decreasing ductility with increased tungsten content. A feasibility study for ultrasonic welding tungsten to steel was completed. Thirty-four trials were completed that varied the parameters of foil thickness, interlayer material, welding force, vibration amplitude, and other welding parameters. Promising results were obtained for joining tungsten to steel and tungsten to steel with an aluminum interlayer.

TABLE OF CONTENTS

4.5 **IRRADIATION HARDENING OF PURE TUNGSTEN EXPOSED TO NEUTRON IRRADIATION**—X. Hu, T. Koyanagi, N.A.P Kiran Kumar, Y. Katoh (Oak Ridge National Laboratory), L.L. Snead (Massachusetts Institute of Technology), B.D. Wirth (University of Tennessee, Knoxville) **109**

This manuscript is in the review process for publication in the Journal of Nuclear Materials.

Pure tungsten samples have been neutron irradiated in HFIR at 90 to 850°C to damage levels of 0.03 to 2.2 dpa. A dispersed barrier hardening model informed by the available microstructure data has been employed to predict the hardness. The comparison of the model prediction and the measured Vickers hardness reveals the dominant hardening contribution at various irradiation conditions. For tungsten samples irradiated in HFIR, the results indicated that voids and dislocation loops contributed to the hardness increase in the low dose region (< 0.3 dpa), while the formation of intermetallic second phase precipitation resulting from transmutation started to dominate the radiation-induced strengthening in a relatively modest dose region (> 0.6 dpa). The precipitate contribution is most pronounced for the HFIR irradiations, whereas the radiation-induced defect cluster microstructure can rationalize the entirety of the hardness increase observed in tungsten irradiated in the fast neutron spectrum of Joyo and the mixed neutron spectrum of JMTR.

4.6 **NEUTRON IRRADIATION EFFECTS IN TUNGSTEN**—L.M. Garrison, Y. Katoh, P. Edmondson, X. Hu, C. Parish, T. Koyanagi, M. McAlister, N.A.P. Kiran Kumar (Oak Ridge National Laboratory), M. Fukuda, T. Hwang (Tohoku University, Japan), L. L. Snead (Massachusetts Institute of Technology), T. S. Byun **125**

A total of 440 samples were irradiated in HFIR at temperatures from 70 to 900°C and fast neutron fluences of 0.01 to 20 ×10^{25} n/m^2 at E>0.1 MeV as part of the TITAN project. Types of tungsten irradiated in this study were [110] single crystal tungsten, [100] single crystal tungsten, wrought tungsten foils, annealed tungsten foils, and tungsten-copper laminates. Analysis is revealing that characterizing precipitation of transmutation products in neutron irradiated tungsten is key to understanding its properties after irradiation. TEM images of higher dose samples revealed that voids tend to be near precipitates in the irradiated tungsten. Analysis of room temperature tensile test data of the single crystal samples reveals that ultimate strength decreases at less than 1 dpa. Further shipments of TITAN samples to LAMDA were completed so that the higher dose samples can be evaluated.

4.7 **NEUTRON IRRADIATION EFFECTS IN TUNGSTEN-COPPER COMPOSITES**— L. M. Garrison, Yutai Katoh (Oak Ridge National Laboratory) Jeremy Moon (University of Nevada-Reno), Joseph Willenborg (University of Tennessee-Knoxville) **130**

As part of the TITAN program, two types of tungsten-copper composites were irradiated in HFIR at temperatures from 300 to 900°C and fast neutron fluences of 0.01 to 20 ×10^{25} n/m^2 at E>0.1 MeV. One material was a tungsten-copper laminate composite composed of 0.1 mm alternating layers of tungsten and copper. Tensile tests have previously been completed on the tungsten-copper laminate and EDS and EBSD analysis of the material is underway. The other material was a tungsten-copper powder sintered composite, with 75% W and 25% Cu. Tensile tests of unirradiated and irradiated tungsten-copper sintered composite have been completed and are being analyzed.

TABLE OF CONTENTS

4.8 HIGH-HEAT FLUX TESTING OF LOW-LEVEL IRRADIATED MATERIALS USING PLASMA ARC LAMPS—A.S. Sabau, Y. Katoh (Oak Ridge National Laboratory) and K. Ibano (Osaka University) **134**

A review was conducted of relevant physical phenomena that take place during high-heat flux testing (HHFT) in order to identify areas of concentration in the ORNL program for materials characterization. Planning of activities for handling the irradiated specimens in FY17 was started in order to ensure a close coordination between the multidisciplinary efforts needed for a comprehensive material science study of irradiated effects during HHFT. Temperature-dependent physical and mechanical properties for the SiC were obtained for use as input in the numerical simulations of the HHFT to reveal insight on the temperature and stress conditions for the four W/SiC specimens. The setup of thermo-mechanical model simulations for the high-heat flux testing of W/SiC specimens was completed.

5 MAGNETIC AND DIAGNOSTIC SYSTEM MATERIALS

No contributions this reporting period.

6 FUSION CORROSION AND COMPATIBILITY SCIENCE

6.1 COMPATIBILITY OF FeCrAl IN FLOWING Pb-LI AT 550°-600°C– B. A. Pint and S. J. Pawel (Oak Ridge National Laboratory, USA) **137**

The second monometallic thermal convection loop (TCL) using Kathal FeCrAlMo alloy APMT tubing and specimens has completed 1000 h in commercial purity eutectic Pb-Li with a peak temperature of 600°C. After cleaning, the mass change data showed small mass losses for all of the specimens preoxidized at 1000°-1100°C to form an alumina scale prior to exposure in the loop. Larger mass losses were noted for specimens that were not pre-oxidized, especially at the lower temperatures. Characterization of the specimens is in progress.

7 MECHANISMS AND ANALYSIS

7.1 QUALITATIVE ANALYSIS OF COMMERCIAL $M_{n+1}AX_n$ PHASES UNDER NEUTRON IRRADIATION—C. Ang*, C. Shih, S.J. Zinkle, C. Silva, C. Parish, N. Cetiner, P. Edmondson, and Y. Katoh (Oak Ridge National Laboratory, USA) **141**

Mn+1AXn (MAX) phases are ternary nitrides and carbides. The materials studied were purchased from 3-ONE-2, LLC, and were previously characterized (see DOE/ER-0313/58). These were nominally "Ti_3SiC_2" and "Ti_2AlC" compositions irradiated to 2×10^{25} n/m^2 (E > 0.1 MeV) or ~ 2 dpa (based on the SiC displacement cross-section). After extensive characterization, weighted compositions were determined to be ~80% MAX phase. Irradiation temperatures were determined by passive dilatometry to have reached ~400, 630 and 700°C. After irradiation at ~400°C, swelling of Ti_3AlC_2-$Ti_5Al_2C_3$ material was 50% higher than Ti_3SiC_2, and this was reflected in the loss of room temperature equibiaxial fracture strength. The Si-containing MAX phase was more radiation resistant than the Al-containing material at lower temperatures. After irradiation at 630°C, electrical, thermal, and mechanical properties were unaffected. Lattice parameter swelling was mitigated at high temperature, but ~0.5-1% volumetric swelling was observed.

TABLE OF CONTENTS

7.2 DAMAGE MECHANISM INTERACTIONS AT THE PLASMA-MATERIALS INTERFACE (Early Career Award)—C. M. Parish, K. Wang (Oak Ridge National Laboratory) 146

This reporting period has emphasized experimental technique developments as the necessary foundation for all later work, continued collaborations with other institutions, and has begun exploration of defect-defect interactions within plasma-exposed and neutron-irradiated tungsten.

7.3 THERMOMECHANICS OF RESILIENT MICRO-ENGINEERED PLASMA FACING MATERIALS—David Rivera, Richard Wirz, Nasr M. Ghoniem (University of California, Los Angeles) 152

Extended abstract of a paper to be submitted to the International Journal of Plasticity in 2016.

7.4 A VARIATIONAL FORMULATION OF THE VOLTERRA DISLOCATION RECONSTRUCTION OF 3-D MOVING CRACKS—A. Sheng, G. Po, N.M. Ghoniem (University of California, Los Angeles) 156

Modeling crack growth in three-dimensional geometries poses a challenging problem especially for FEM-based techniques such as EFEM or XFEM, which display some degree of mesh dependence. Additionally, existing methods are unable to investigate the interaction between cracks and other defects present in real materials. An alternative method developed in the framework of discrete Dislocation Dynamics is presented which provides a solution to these challenges by being completely mesh-independent and capable of coupling cracking with crystal plasticity. The Discrete Crack Mechanics method is a dislocation-based fracture mechanics technique that represents cracks using arrays of Volterra dislocations. In this report, a variational formulation based on the Principle of Maximum Entropy Production rate is given of the evolution equations for cracks coupled with crystal dislocations along with examples of its implementation.

7.5 LOADING CONTROLLED TRANSITION OF PLASTIC FLOW FROM DISLOCATION AVALANCHE TO QUASI-PERIODIC STRAIN BURST BEHAVIOR—Y.N. Cui, G. Po, N.M. Ghoniem (University of California, Los Angeles) 163

Extended abstract of paper to be submitted for publication.

8 MODELING PROCESSES IN FUSION SYSTEM MATERIALS

8.1 DEVELOPMENT OF INTERATOMIC POTENTIALS IN TUNGSTEN-RHENIUM SYSTEMS—W. Setyawan, G. Nandipati, and R. J. Kurtz (Pacific Northwest National Laboratory) 165

Reference data are generated using the ab initio method to fit interatomic potentials for the W-Re system. The reference data include single phases of W and Re, strained structures, slabs, systems containing several concentrations of vacancies, systems containing various types of interstitial defects, melt structures, structures in the σ and χ phases, and structures containing several concentrations of solid solutions of Re in bcc W and W in hcp Re. Future work will start the fitting iterations.

TABLE OF CONTENTS

8.2 **STRUCTURE AND MOBILITIES OF TUNGSTEN GRAIN BOUNDARIES CALCULATED FROM ATOMISTIC SIMULATIONS**—Timofey Frolov and Robert E. Rudd (Lawrence Livermore National Laboratory) **172**

Recrystallization determines the upper extent of the operating temperature of tungsten as a divertor or first-wall material. At temperatures above the onset of recrystallization, migrating grain boundaries sweep out defects that contribute to hardening. These processes make the recrystallized material unsuitable because of its brittleness. Thermomechanical models to predict recrystallization and its effect on mechanical properties have to be informed of the mechanisms of grain boundary migration under stress and other driving forces at tokamak operating temperatures. Recent experimental and computational studies suggest that addition of impurities and elevated temperatures can trigger structural transformations at grain boundaries that result in orders of magnitude increase in mobility. Here we present preliminary results demonstrating that tungsten grain boundaries do exhibit phase transformations and calculate the mobilities needed for thermomechanical models of recrystallization.

8.3 **OBJECT KINETIC MONTE CARLO SIMULATIONS OF RADIATION DAMAGE ACCUMULATION IN TUNGSTEN**—G. Nandipati, W. Setyawan, K. J. Roche, R. J. Kurtz (Pacific Northwest National Laboratory) and B. D. Wirth (University of Tennessee) **178**

We used the lattice-based object kinetic Monte Carlo code; *KSOME* [1] to perform simulations of radiation damage accumulation in bulk tungsten at 300 K and for a dose rate of 10-4 dpa/s, up to a dose of 1.0 dpa. These are ad-hoc irradiation simulations performed using a set of cascades with the same PKA energies. In this study, eight different irradiation simulations were performed using eight sets of cascades with PKA energies of 10, 20, 30, 40, 50, 60, 75 and 100 keV. Both the number density of vacancies and vacancy clusters in the simulation box appears to saturate with increasing dose in the simulation using cascades with PKA energies of 40, 50, 60, 75, 100 keV, while the same parameters increase linearly with dose in the simulations using cascades with PKA energies of 10, 20 and 30 keV. In all simulations the average vacancy cluster size remained constant with dose. However, the vacancy cluster size increases with cascade PKA energy.

8.4 **INTERACTION OF INTERSTITIAL CLUSTERS WITH RHENIUM, OSMIUM, AND TANTALUM IN TUNGSTEN**—W. Setyawan, G. Nandipati, and R. J. Kurtz (Pacific Northwest National Laboratory) **183**

In the previous semi-annual report [1], we explored the stability of interstitial clusters in W up to size seven. In this report, we study the binding of those clusters to Re, Os, and Ta atoms. For each cluster size, the three most stable configurations are considered to average the binding property. The average binding energy to a Re decreases from 0.79 eV for a size-1 cluster (a [111] dumbbell) to 0.65 eV for a size-7 cluster. For Os, the binding decreases from 1.61 eV for a [111] dumbbell to 1.34 eV for a size-7 cluster. Tantalum is repulsive to interstitial clusters with binding energy ranges from -0.61 eV for a [111] dumbbell to -0.5 eV for a size-7 cluster.

TABLE OF CONTENTS

9 FUSION SYSTEM DESIGN

9.1 MULTI-PHYSICS DESIGN OF THE FIRST WALL AND BLANKET SYSTEM IN THE FUSION NUCLEAR SCIENCE FACILITY (FNSF)—Yue Huang, Nasr Ghoniem, Mark Tillack, Jake Blanchard, Laila El-Guebaly, Chuck Kessel **188**

The dual coolant lead-lithium (DCLL) blanket concept is based on a helium-cooled first wall and blanket structure with RAFS (Reduced Activation Ferritic Steel) and a self-cooled LiPb breeding zone. 3D finite element multiphysics modeling of the DCLL first wall and blanket has been performed using *COMSOL 5.0.* The multiphysics aspect of the design is demonstrated via coupling of fluid dynamics, conjugate heat transfer and solid mechanics modules within the COMSOL. The results of primary and thermal stress of the structure were obtained. This was followed by determination of the factors of safety along three critical paths based on the ITER Structural Design Criteria for In-vessel Components (ISDC-IC). We show that the structural design meets the design rules under both normal and off-normal operating conditions, though the safety factors under off-normal condition are marginal. Thus simple design optimization was conducted based on a parametric study on first wall dimensions to improve the design.

10 IRRADIATION METHODS, EXPERIMENTS AND SCHEDULES

10.1 MINIATURE MECHANICAL TEST DEVELOPMENT FOR TUNGSTEN-BASED MATERIALS—L. M. Garrison (Oak Ridge National Laboratory), Jeremy Moon (University of Nevada-Reno), Joseph Willenborg (University of Tennessee-Knoxville) **195**

Many tungsten based composites employ tungsten foils or tungsten fibers. Understanding the mechanical properties of the composite also requires understanding the mechanical properties of the constituent elements of the composite. While certain miniaturized mechanical tests, such as tensile testing SSJ size samples, is routinely accomplished in LAMDA, the requirements for testing foils and fibers is beyond the current capabilities in the laboratory. Three mechanical tests are being developed for the foils and fibers: a) shear punch test for foils, b) 3-point bend test for foils, and c) tensile test for fibers.

10.2 DEVELOPMENT OF A NON-CONTACT STRAIN MEASUREMENT SYSTEM FOR POST IRRADIATED TENSILE TESTS AT HIGH TEMPERATURES—H. Sakasegawa, T. Kato, H. Tanigawa (National Institutes for Quantum and Radiological Science and Technology), and Y. Katoh (Oak Ridge National Laboratory) **201**

Appropriate stress strain curves were obtained applying the non-contact strain measurement system developed in this work and the system specifications were selected. Two marks were painted on the specimen gage using a mixture of paste and fluorescent powder which can be used in high vacuum at high temperatures. UV light illuminated these two marks and clear contrast was obtained to measure the distance between marks using a video camera. This system can be used for post irradiated tensile tests at high temperatures in hot cells.

TABLE OF CONTENTS

10.3 **HFIR-MFE-RB-19J THERMAL AND NEUTRONIC DESIGN**—J.L. McDuffee, C.R. Daily, N.O. Cetiner, C.M. Petrie, J.W Geringer (Oak Ridge National Laboratory) **205**

The HFIR RB-19J irradiation experiment contains six cylindrical holders (four temperature zones) which house ~1300 tungsten and steel specimens. The capsule and shield is design to be centered about the HFIR mid-plane, but the holders are slightly shifted toward the positive axial direction from the mid-plane. The assembly of the RB19J capsule was completed in May 2016 and installed in HFIR in June 2016. The first irradiation cycle, 466, started June 14, 2016. Starting temperatures stabilized within design range for the 500°C and the 800°C holders. The 1200°C and the 300°C were lower and higher than designed by about 50°C to 100°C respectively.

10.4 **HFIR-MFE-RB-19J SPECIMEN LOADING LISTING**—J.W. Geringer, J.L. McDuffee, C.M. Petrie, L.M. Garrison, R.H. Howard, N.O. Cetiner, D.A. Stringfield, R.G. Sitterson (Oak Ridge National Laboratory) **215**

The HFIR RB-19J irradiation experiment contains six cylindrical holders (four temperature zones) which houses ~1300 tungsten and steel specimens. The capsule and shield is design to be centered about the HFIR mid-plane, but the holders are slightly shifted toward the positive axial direction from the mid-plane. The assembly of the RB19J capsule was completed in May 2016 and installed in HFIR in June 2016. The first irradiation cycle, 466, started June 14 2016. Starting temperatures stabilized within design range for the 500°C and the 800°C holders. The 1200°C and the 300°C were lower and higher than designed by about 50°C to 100°C respectively.

10.5 **HFIR IRRADIATION EXPERIMENTS**—J.P. Robertson, Y. Katoh and J. McDuffee (Oak Ridge National Laboratory) **234**

HFIR completed 2.7 cycles during the first half of 2016. Cycle 464 operated from January 1, until February 6, 2016, for 2101 MWdays. Cycle 465 started on February 23, and ran for 2093 MWdays, shutting down on March 18. Cycle 466 began on June 14, 2016.

1. FERRITIC/MARTENSITIC STEEL DEVELOPMENT

1.1 FABRICATION OF LOW ACTIVATION FERRITIC-MARTENSITIC STEELS CONTAINING ^{54}FE ISOTOPE—Y. Yamamoto (Oak Ridge National Laboratory)

OBJECTIVE

The goal of this task is to evaluate the effect on the irradiation microstructure and mechanical properties of the 9Cr base reduced activation ferritic-martensitic (RAFM) steels, such as EUROFER 97 and cast nanostructured alloys (CNA), prepared by using ^{54}Fe isotope. The ^{54}Fe was recovered from oxide powder that KIH provided. The ^{54}Fe isotope should accelerate the helium bubble formation during fast neutron exposure at HFIR, partially simulating the high dose irradiation conditions within relatively short exposure times.

SUMMARY

Four trial EUROFER97 steel plates were successfully fabricated by arc-melting with natural Fe and hot-rolling with a steel guide. The arc-melting was conducted to measure the yield of each alloying element during the melt process, and the trial hot-rolling with a steel guide was performed to produce steel plates without barreling. Based on the process parameter of the trial heats, two RAFM steel plates (targeted to be EUROFER97 and CNA) made of ^{54}Fe isotope powder, with size ~0.25 x 1.4 x 2.5 inches, were successfully fabricated. The detailed planning of the machining of SS-J3 tensile specimens and M4 bend bar specimens, as well as developing an irradiation test plan for HFIR, is currently in progress.

PROGRESS AND STATUS

Introduction

There are no test facilities available with a neutron spectrum that matches D-T fusion. Various methods are used to simulate fusion reactor conditions and evaluate irradiation effects in structural materials for fusion reactors. For reduced-activation ferritic-martensitic (RAFM) steels, alloys doped with B or Ni have been used in fission test reactors to produce helium through (n, α) reactions while the fast neutrons produce displacement damage. However, both B and Ni tend to segregate at grain boundaries, compromising the simulation of uniform irradiation damage. It has been proposed to replace all natural Fe with the isotope ^{54}Fe in selected RAFM steels to expect acceleration of the He transmutation and resulting bubble formation dispersed uniformly within relatively short period of irradiation time. This was previously attempted in the High Flux Isotope Reactor (HFIR) with ^{55}Fe by Liu et al. [1]. HFIR neutron irradiation will achieve simultaneous He and dpa production throughout the bulk of specimens in a damage evaluation study.

About 400 g of mixed oxide steel powder was delivered from Karlsruhe Institute of Technology (KIT) which consisted primarily of ^{54}Fe together with small amounts of Cr, W, and other alloying elements. The origin of the powder material was a trial heat of EUROFER 97 with ^{54}Fe made at KIT. However, the heat was accidentally contaminated with high amount of B and C so that the material was fully dissolved in an acid and turned into oxide powders during the recovery process [2]. Reduction of the oxide powders was used at ORNL, in order to extract the ^{54}Fe with reasonably low oxygen content. Total ~220 g of ^{54}Fe powder containing small amounts (~1wt.%) of Cr and W and 79 wppm of oxygen was obtained in this effort in CY2015 [3].

The powder was used for fabricating two different RAFM steels; EUROFER97 and CNA steels, and two plates of the alloys were prepared. In this report, the on-going fabrication effort of the RAFM steels with ^{54}Fe, together with trial RAFM steels with natural Fe, is summarized.

Experimental Procedures

A total of four trial reference RAFM steel ingots (with compositions targeted equal to EUROFER97 steel, ~110g for each) were arc-melted with natural Fe and pure element feedstock. Commercial CrN/Cr_2N powder was used for the nitrogen source of the ingots. A new Cu mold with size 0.5 x 1.4 x 1.4 inches was machined to produce square cast ingots, as shown in Figure 1. The ingots were homogenized at 1150°C, and then hot-rolled at 1040°C, with a guide steel plate in order to fabricate plates with target geometry ~0.25 x 1.4 x 2.5 inches. The plate samples were normalized at 1040°C for 10 min and then air-cooled to room temperature. The samples were tempered at 760°C for 1.5 h, and then air-cooled to room temperature.

The chemical compositions of the trial ingots were measured by ICP-OE/IGF analyses. The results of the first two trial ingots were used to calculate the yield of each element, and the second two trial ingots were melted with the calibrated alloy compositions. After confirming the calibration results of the second cast ingots, two RAFM steels (E97-54 and CNA-54, equivalent to EURFER97 and CNA steels, respectively) were arc-melted with the ^{54}Fe powder. The cast ingots were hot-rolled and heat-treated in the same way of the trial ingots.

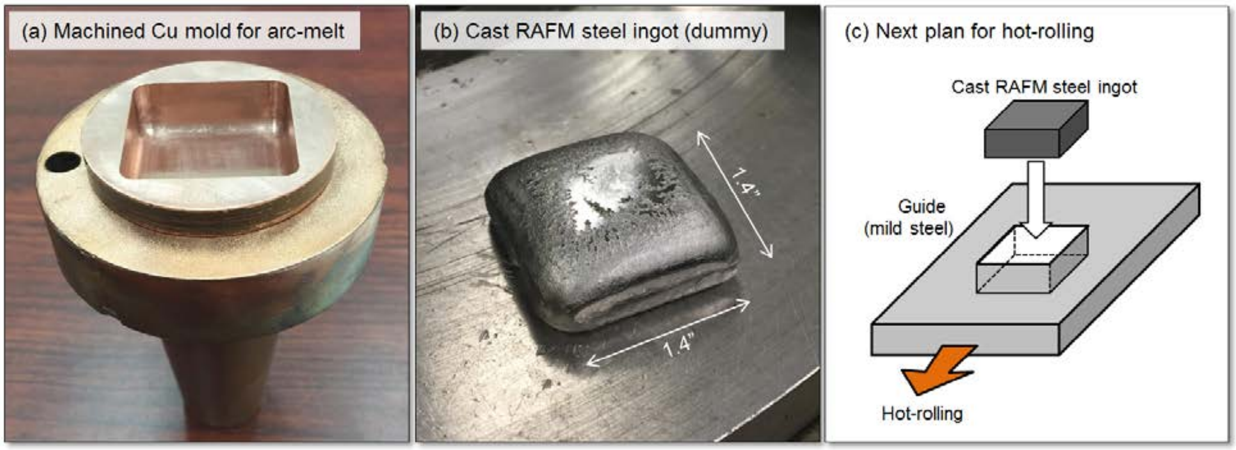

Figure 1. (a) Newly machined Cu mold, (b) a cast trial RAFM steel ingot, (c) and an illustration of the next plan (hot-rolling) to be conducted.

Results

Table 1 summarizes the analyzed chemical compositions of the trial EUROFER97 heats. The results indicated that two trial heats, E97-03 and E97-05, were out of the specification, and it was found that the W content of the heats were mistakenly selected lower than the target nominal content (1.1 wt.%). It was also found that the other elements, especially Mn, C, and N were much lower than those expected from the targets. The loss of the N content was due to the nitrogen gas bubbling during the arc-melting process, which was visually observed during the arc-melt operation. The number of arc-melting cycles (to ensure homogeneous mixing of the ingot) was also important to preserve the nitrogen content in the heat. The yields of these elements were calculated, and the calibrated amounts of the alloying additions were used for two newly arc-melted trial heats (#22 and #23). By minimizing the number of arc-melts, the resultant alloy compositions mostly met the target specification. Only the C content was higher than the target, so that re-calibration of the carbon was used for the next melt with the ^{54}Fe powder.

Table 1. Analyzed compositions of trial EUROFER97 heats melted at ORNL

Name	Composition, wt.%								Remarks
	Fe	C	Mn	Cr	V	Ta	W	N	
Target (for E97-03/05)	89.20	0.11	0.40	9.00	0.20	0.12	0.91	0.060	The target W content was incorrect
E97-03	Bal.	0.077	0.36	8.84	0.19	0.11	0.84	0.008	Arc-melted x10
E97-05	Bal.	0.077	0.37	8.83	0.18	0.11	0.87	0.014	Arc-melted x7
Target (for new heats)	88.94	0.11	0.50	9.00	0.20	0.12	1.10	0.030	Nominal (revised)
Heat #22	Bal.	0.14	0.51	8.95	0.21	0.13	1.1	0.021	Arc-melted x4
Heat #23	Bal.	0.13	0.51	8.94	0.21	0.13	1.11	0.022	Arc-melted x4

The arc-melted trial ingot with size 0.5 x 1.4 x 1.4 inches was successfully rolled into plate with size of 0.24 x 1.42 x 2.50 inches, without the formation of any edge cracks or side barreling, as shown in Figure 2. It was homogenized, hot-rolled at 1040°C, and then normalized at 1040°C for 30 min and tempered at 760°C for 90 min, with the guide steel plate. An optical micrograph of the trial EUROFER97 heat, Figure 2c, showed a uniform, full tempered martensitic microstructure without any anisotropic features (e.g. elongated grains along the rolling direction), suggesting that material fabrication process was successful.

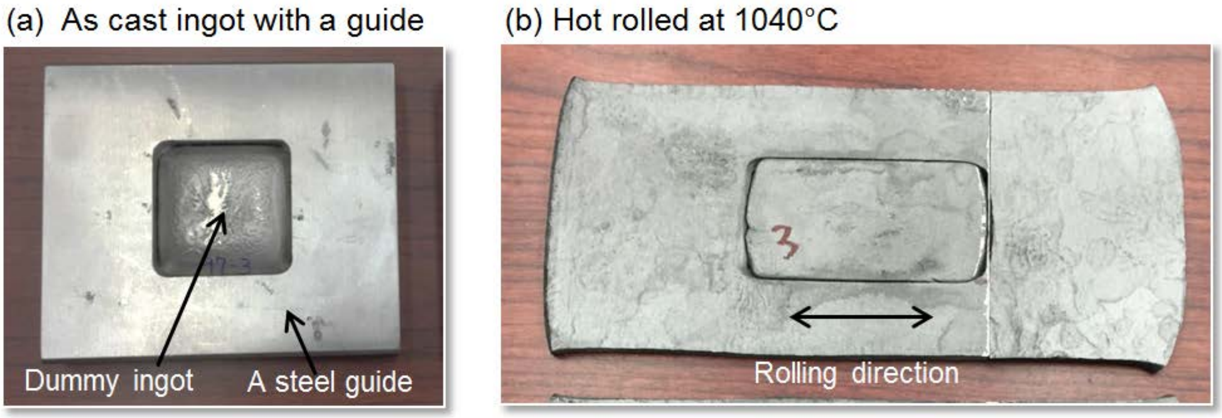

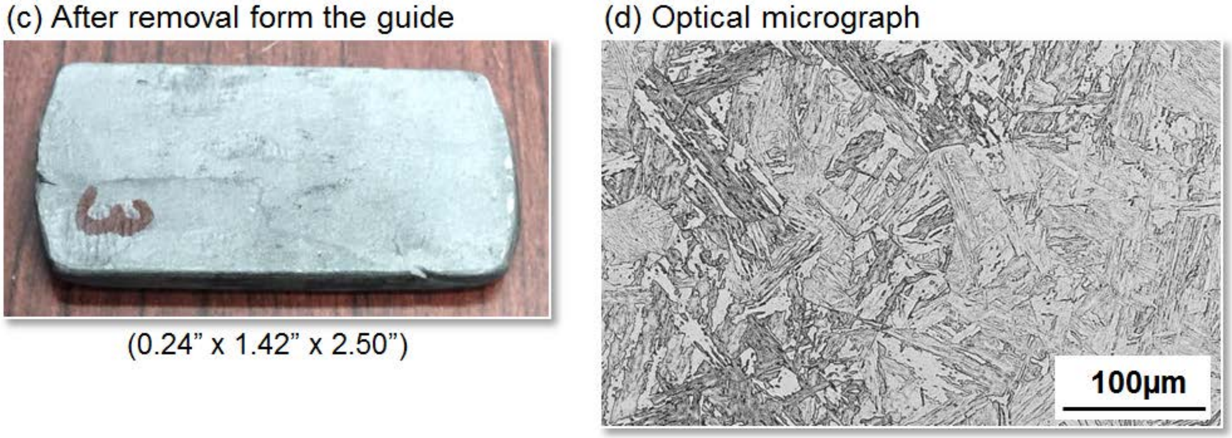

Figure 2. (a) As-cast trial ingot with a mild steel guide, (b) the rolled plate with the guide, (c) the rolled plate after removal from the guide, and (d) the microstructure after the heat treatment.

Two new heats of EUROFER97 and CNA steels were arc-melted with ^{54}Fe isotope powder. The arc-melted ingots (0.5 x 1.4 x 1.4 inches, Figure 3a) were successfully rolled to plate with size 0.24 x 1.42 x 2.50 inches, without any edge cracks or side barreling (Figure 3b). They were homogenized, hot-rolled, and then normalized and tempered. There were no edge cracks or side barreling, as with the trial EUROFER97 heat fabrication.

Discussion of the machining plan to prepare SS-J3 tensile specimens and M4 bend bar specimens is in progress. The current plan is to machine a total of 18 SS-J3 and 16 M4 bend bar specimens from each plate, as shown in Figure 4. The detailed irradiation test plans for HFIR irradiation experiments as well as the required specimen numbers will soon be finalized.

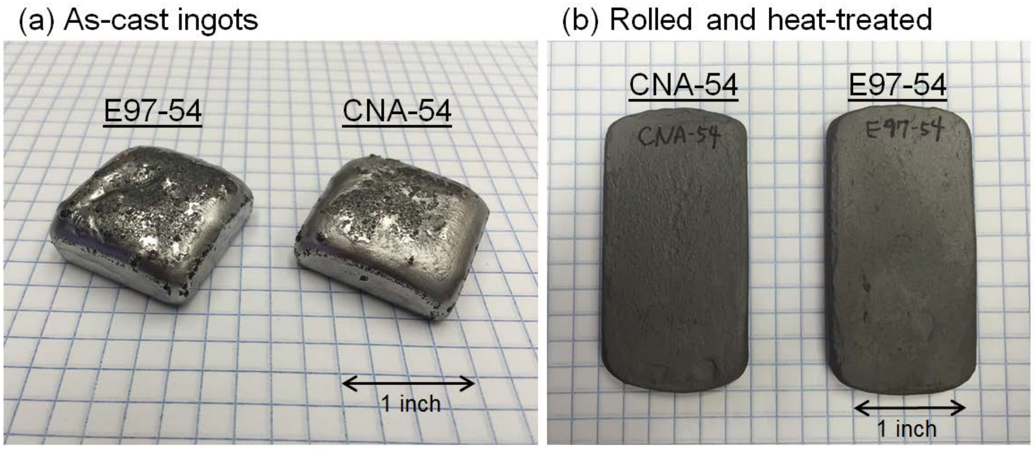
(a) As-cast ingots

(b) Rolled and heat-treated

Figure 3. (a) As-cast ingots of EUROFER97 (E97-54) and CNA (CAN-54) made with ^{54}Fe isotope, and (b) the rolled and annealed plates.

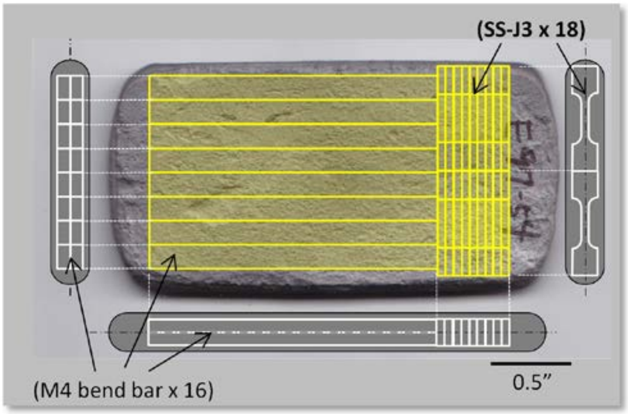

Figure 4. Machining plan for SS-J3 and M4 bend bar specimens.

References

[1] H. Liu, M. A. Abdou, L. R. Greenwood, ^{55}Fe effect on enhancing ferritic steel He/dpa ratio in fission reactor irradiations to simulate fusion conditions, Fusion Engineering and Design, 88 (2013) 2860-2864.

[2] M. Rieth et al., EUROFER-Fe54 Specimen Production and Irradiation Proposal, TW4-TTMS-001 D01,TW5-TTMS-001 D02, Karlsruhe Institute of Technology Interner Bericht, Projekt Fusion 31.40.03, Dec. 2010

[3] Y. Yamamoto et al., Fabrication of Low Activation Ferritic-Martensitic Steels Containing ^{54}Fe Isotope, poster presentation at ICFRM-17, Aachen, Germany, October 2015.

1.2 ADVANCED BAINITIC STEEL DEVELOPMENT FOR FUSION STRUCTURAL APPLICATIONS—Y. Yamamoto (Oak Ridge National Laboratory)

OBJECTIVE

This task aims to develop new bainitic steel, based on 3Cr-3WV(Ta) steels originally developed at ORNL, with mechanical properties of both base metal and weldments superior to those of existing commercial bainitic steels or ferritic-martensitic (F-M) steels, together with no requirement for post-weld heat treatment (PWHT). The target applications are high temperature structural components in fusion reactors such as vacuum vessel, structural ring which supports the blanket modules, and magnet shields, to be used at or above the 400-500ºC range. Improvement of long-term creep properties by introducing additional fine, stable second-phase dispersions, as well as maintaining good weldability, is targeted via optimization of alloy composition and thermo-mechanical heat treatment.

SUMMARY

A new alloy design strategy for PWHT-free bainitic steel has been proposed; reducing the as-normalized hardness without losing high hardenability, in order to reduce potential property inhomogeneity across the weldment. Four new heats of 3Cr-3WVTa base bainitic steels with low carbon combined with high Mn and Si were prepared with guidance from computational thermodynamics. The steel with the combination of 0.05C and 2 or 3Mn additions successfully showed fully bainitic microstructure together with less hardness difference between as-normalized and tempered conditions, which will reduce the potential property inhomogeneity in the weldments. High temperature tensile properties also supported potential improvement of mechanical properties at elevated temperatures. Preparation for creep-rupture testing is currently underway.

PROGRESS AND STATUS

Introduction

Development of new bainitic steels was initiated as part of the Fusion Energy Materials Program in FY2014, as a modification of the original 3Cr-3WV(Ta) steels developed at ORNL[1,2]. The alloy design strategy is to improve creep performance through minor alloying additions of Mn, Si, and N ("Gen I" steels). Computational thermodynamics tools were used to predict optimized minor alloying additions to promote the formation of stable MN (M: mainly V) in a wide temperature range below ~1100ºC and increase the stability of $M_{23}C_6$ (M: mainly Cr) relative to M_7C_3 (M: mainly Cr). Improved oxidation resistance was also expected through the Si addition [3]. The calculated continuous-cooling-transformation (CCT) diagram predicted a wider austenite stable region (retarding the transformation to ferrite or pearlite, $\mathbf{F}_s$ or $\mathbf{P}_s$) with lower bainitic transformation start temperature ($\mathbf{B}_s$) compared to the base steels, indicating that the transformation would occur in a relatively lower temperature range even with air cooling, equivalent to the lower bainite formation during isothermal annealing in the TTT diagram (see **Fig. 1**). The experimentally measured CCT diagrams of the developed steels exhibited lower $\mathbf{B}_s$ temperature, and improvement in the creep performance of the steels was observed, as expected, especially in relatively lower creep-stress testing [4]. However, it was also found that the hardness of the as-normalized material was extremely high compared to the original 3Cr-3WV(Ta) steels, whereas the hardness after tempering was smaller than the original, indicating that the variation of the properties across the welded material (in as-weld condition) could be significant compared to the original 3Cr-3WVa(Ta) steels. This suggests that the alloy design strategy of the Gen I steels failed to meet the PWHT-free requirement.

Based on the results of Gen I steels, it was suggested that reduced hardness in the normalized conditions could be a key for the PWHT-free material design strategy, since it could potentially reduce the cross-weld property inhomogeneity compared to that of the base steels. In order to decrease the hardness in the normalized condition without losing high "hardenability" to promote the carbide-free acicular bainite ferrite formation, a new alloy strategy with lower carbon and higher Mn, together with Si for improved oxidation resistance, was proposed for “Gen II” steels. In this report, the suitability of the new alloy strategy and selection of the alloy compositions is discussed. Initial microstructure characterization results are also shown.

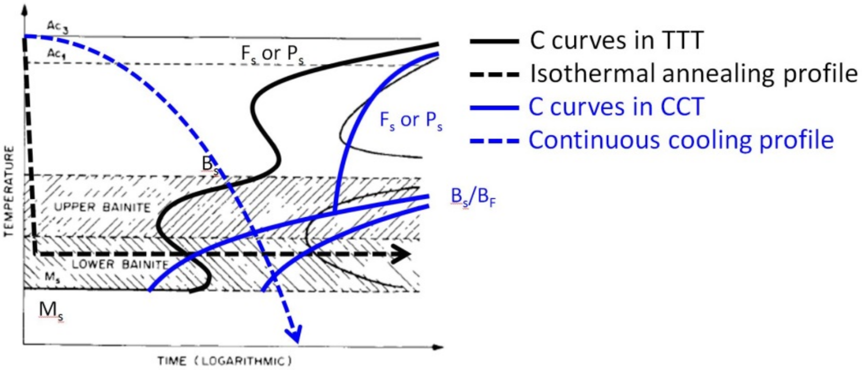

Figure 1. Schematic illustration of TTT and CCT curves for a bainitic steel

Experimental Procedure

The alloy compositions of the base and newly selected steels are listed in Table 1. The phase equilibrium and the CCT diagrams were calculated by JMatPro version 9 with Fe database. The compositions were selected based on the new alloy design strategy to produce low hardness (via 0.05C) and high hardenability (high Mn additions), as well as supplemental oxidation resistance (1Si). The ~400 g steel ingots were arc-melted and drop cast into a Cu mold with size 13 mm x 25 mm x 125 mm. The ingots were homogenized at 1200ºC for 2 h, and then water-quenched. The ingots were then hot-forged and -rolled at 1100°C to produce plate with 6 mm thickness, and then air-cooled to room temperature. Normalization at 1100°C for 30 min, followed by air-cooling, was applied to all plates. The plates were sectioned, tempering at 700°C for 1 h, followed by air cooling. Cross-sectional microstructure characterization used optical metallography, OM, and the Vickers hardness was measured with 300 g load. Tensile tests were conducted in a temperature range from room temperature to 600°C in laboratory air. Sub-sized sheet tensile specimens with gage section 0.76 mm thickness x 1.5 mm width x 7.6 mm length were used. The tests were performed with cross-head control at a constant strain rate of 10^{-3}/s.

Table 1. Nominal compositions in weight percent, balanced Fe

Heat	Composition, wt.%							Remarks
	C	Mn	Si	Cr	V	W	Ta	
Base	0.10	0.40	0.16	3.0	0.2	3	0.1	3WVTa
LC	0.05	0.40	0.16	3.0	0.2	3	0.1	Low C
MSLC1	0.05	1.00	0.5	3.0	0.2	3	0.1	Low C + 1Mn
MSLC2	0.05	2.00	0.5	3.0	0.2	3	0.1	Low C + 2Mn
MSLC3	0.05	3.00	0.5	3.0	0.2	3	0.1	Low C + 3Mn

Results

The calculated phase equilibrium of the base 3Cr-3WVTa steel and two new steels with lower C steel (LC), and Mn+Si+lower C steel (MSLC2) are shown in Figure 2. The three steels show similar matrices and second-phases, although there were two major changes produced by the alloy modifications: the A_{e1} temperature (austenite to ferrite transformation) and the amounts of the second-phases. The A_{e1}

temperature was slightly increased by lowering the carbon content, whereas the further addition of Mn (+Si) resulted in extending the austenite phase region compared to that of the base steel. This indicates that low C + high Mn would improve the phase stability of austenite relative to ferrite, so that the increased hardenability is expected to promote the formation of carbide-free acicular bainite ferrite. On the other hand, the amounts of the second phase carbides such as MC and M_6C (and M_7C_3) decreased significantly due to lower C addition, so that less hardness compared to the base steel is expected.

Figure 3 shows the calculated CCT curves of the base, LC, and MSLC2 steels. LC steel showed almost no changes in the $\mathbf{B}_s$ temperature compared to the base steel, and the ferrite formation ($\mathbf{F}_s$) was slightly promoted, consistent with what can be expected from the calculated phase equilibrium in Figure 2. On the other hand, the Mn addition in MSLC2 steel lowered the $\mathbf{B}_s$ temperature and retarded the $\mathbf{F}_s$ and $\mathbf{P}_s$ curves, indicating that improved hardenability is expected.

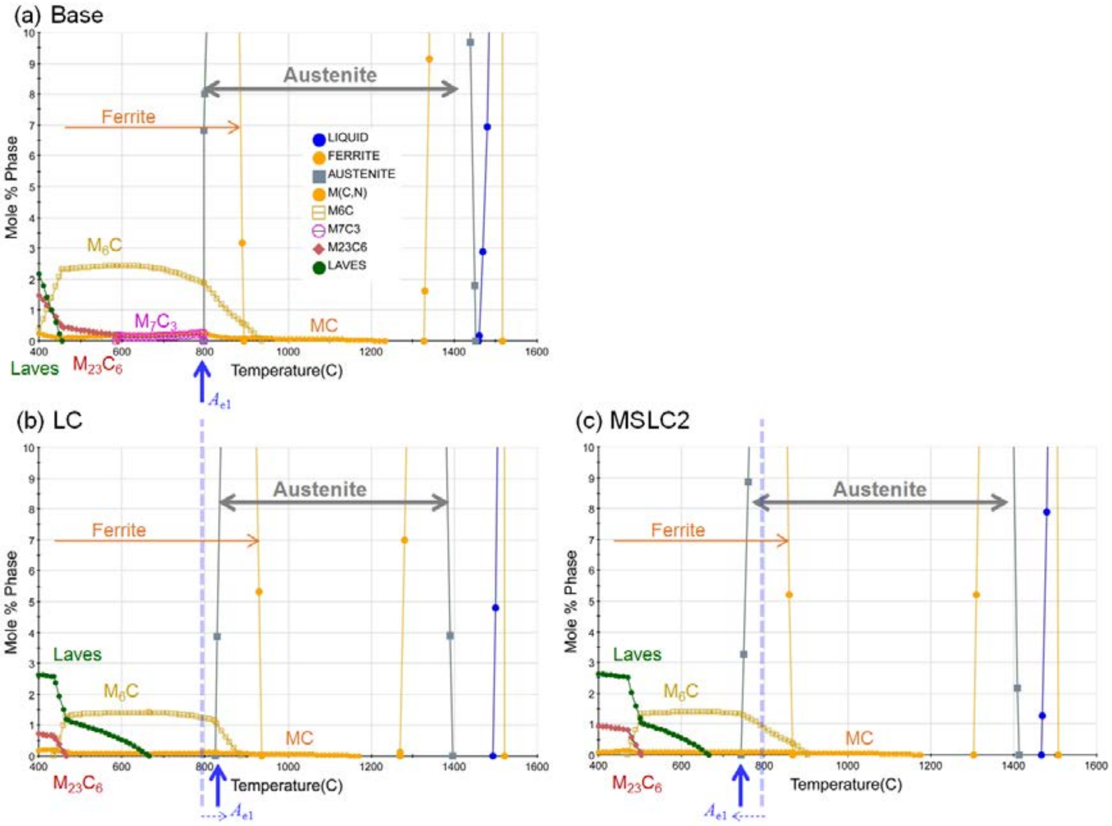

Figure 2. Calculated phase equilibrium of (a) Base, (b) LC, and (c) MSLC2 steels.

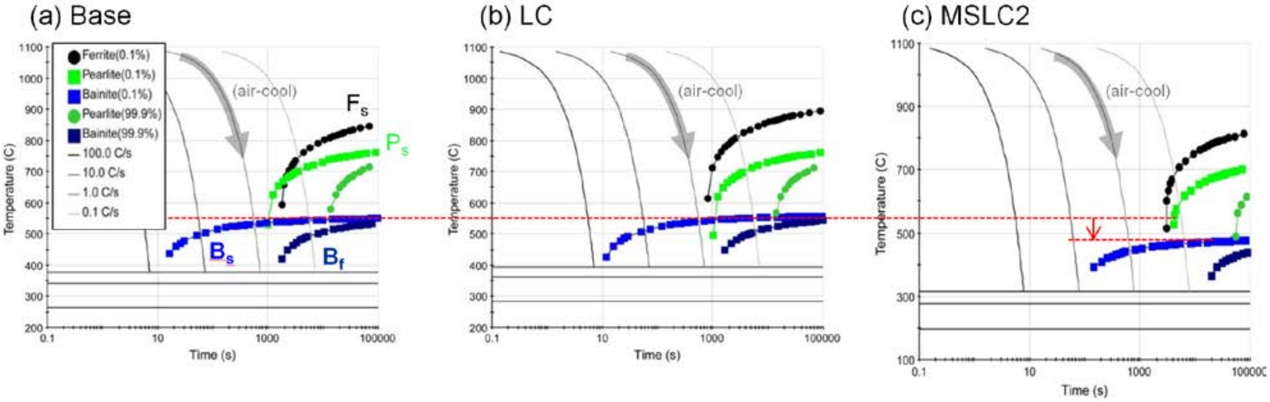

Figure 3. Calculated continuous cooling transformation diagrams of (a) Base, (b) LC, and (c) MSLC2 steels.

Optical micrographs of the as-normalized and tempered steels are shown in Figure 4. Micro-Vickers hardness of the material is also given on each micrograph. In the as-normalized condition, lowering the carbon content (LC) resulted in forming a small amount of ferrite grains and decreasing the hardness significantly. After tempering, the hardness of the base steel became ~290HV, whereas that of LC steel did not show a significant changes from as-normalized material and stayed low. On the other hand, as-normalized MSLC2 steel showed similar bainitic microstructure to the base steel, and the hardness was slightly lower than the base. The tempering resulted in similar hardness to the base steel. This result indicated that only lowering the carbon content would result in dropping the hardness at any conditions, but a careful control of the hardenability though Mn addition would allow comparable hardness of the tempered materials to that of the base steel, even with low C content.

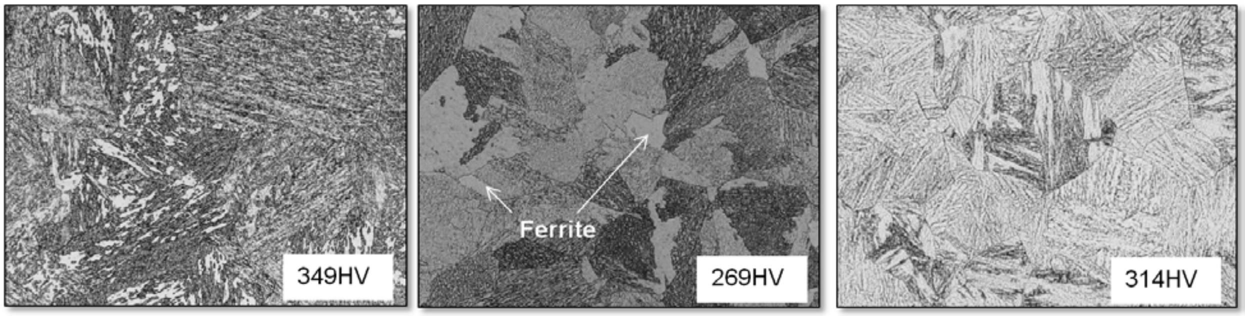
(a) Base-normalized (b) LC-normalized (c) MSLC2-normalized

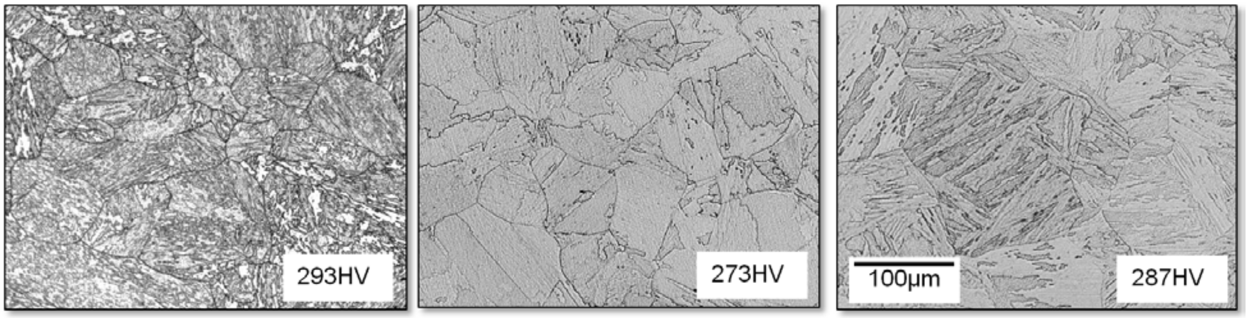
(d) Base-tempered (e) LC-tempered (f) MSLC2-tempered

Figure 4. Optical micrographs of the 3Cr-3WVTa base steels after normalization and tempering; (a) Base-normalized, (b) LC-normalized, and (c) MSLC2-normalized, (d) Base-tempered, (e) LC-tempered, and (f) MSLC2-tempered.

Figure 5 summarizes the hardness test results of as-normalized and tempered conditions of all new steels compared with the base and Gen I steels. In order to reduce the inhomogeneous properties across the welded materials, it was considered that the smaller hardness gap between the as-normalized and tempered steels was better for PWHT-free alloy design. It should be noted that the as-normalized hardness was expected to be close to that of the as-welded fusion material since the fusion material passed through the same transformation pathway as the normalization during the weld procedure. Gen I steel showed the increased hardness in the normalized condition and the lower hardness in tempered conditions compared to those of the base steel, indicating that the hardness characteristics was opposite to the current alloy design strategy. LC and MSLC1 steels showed almost no changes in the hardness before and after tempering, which might reduce the variation of cross-weld properties. However, the lower hardness of the tempered materials compared to the base steel would result in weaker mechanical properties such as poor creep deformation resistance. High Mn additions (MSLC2 and MSLC3 steels) resulted in lowering the as-normalized hardness whereas the tempered hardness was comparable to that of the base metal.

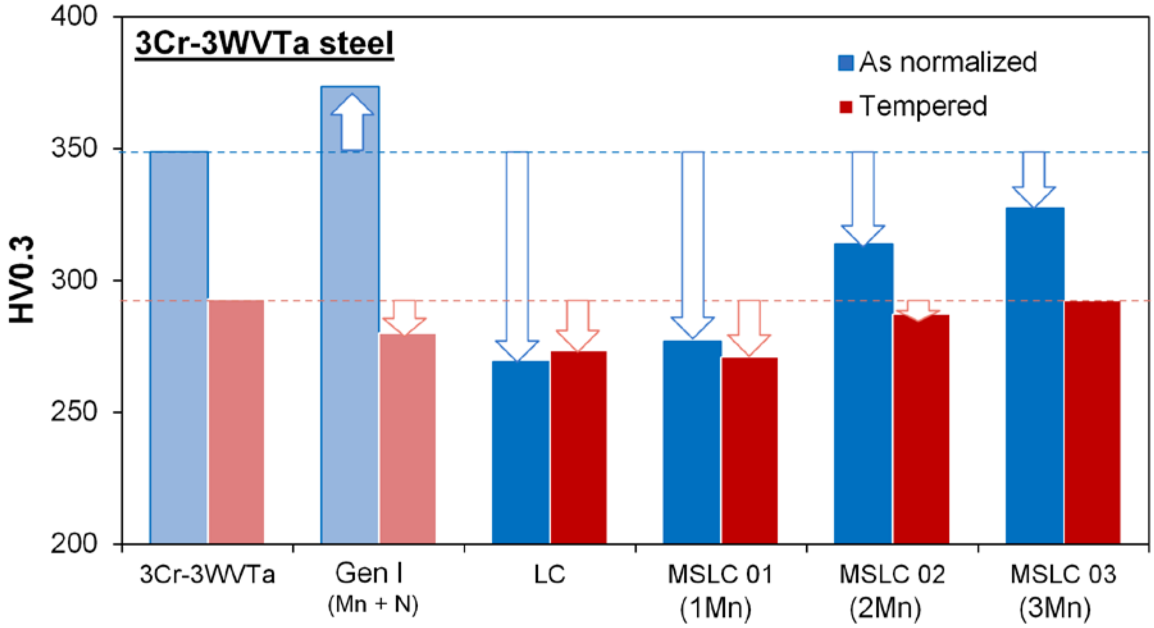

Figure 5. Micro-Vickers hardness of the bainitic steels after normalization and tempering.

Tensile properties of Gen II steels were evaluated. Figure 6 illustrates the test results of the modified steels, LC and MSLC2, as a function of test temperature. For comparison, the properties of base 3Cr-3WVTa steel reported by Jawad [5] are also shown. Although the tempering temperature of the modified steels was slightly lower than the reference material (700°C vs. 730°C) which typically made the strengths higher, the results showed obvious improvement of the yield and the ultimate tensile strengths, YS and UTS, in Mn modified alloys (MSLC2) at both RT and temperatures up to 600°C. The results indicate that the alloy design strategy for the Gen II steels (the improvement of hardenability to promote the formation of carbide-free acicular bainite ferrite) is appropriate in terms of high-temperature tensile properties. Preparation for creep-rupture testing of the materials is in progress, with testing to be initiated by the end of FY2016.

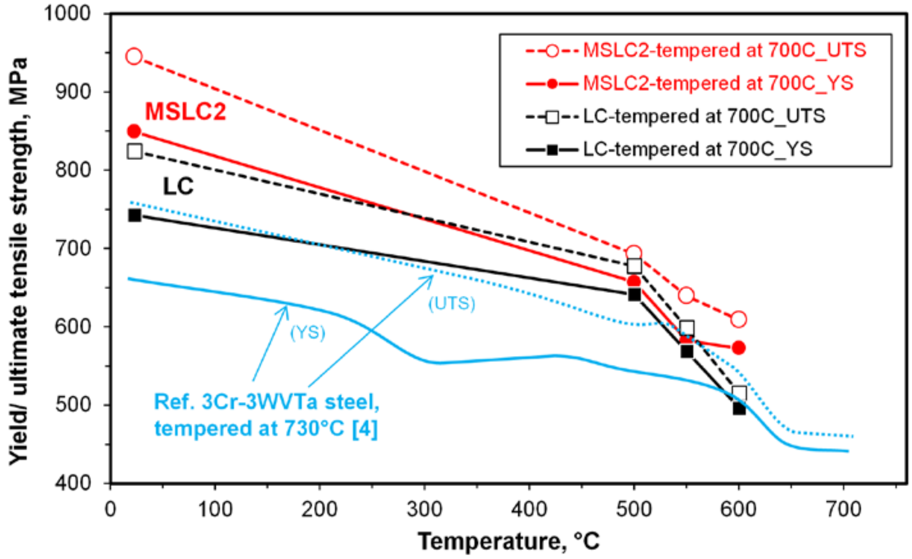

Figure 6. Tensile properties of 3Cr-3WVTa base steels (LC and MSLC2) as a function of test time, together with those of original 3Cr-3WVTa steels reported by Jawad [4].

References

[1] R.L. Klueh, Elevated-Temperature Ferritic and Martensitic Steels and Their Application to Future Nuclear Reactors, ORNL/TM-2004/176, November 2004.

[2] R.L. Klueh, N.D. Evans, P.J. Maziasz, V.K. Sikka, Creep-rupture behavior of 3Cr-3W-V bainitic steels, International Journal of Pressure Vessels and Piping, 84 (2007) 29-36.

[3] T. Ishitsuka et al., Effect of Silicon on the Steam Oxidation Resistance of a 9%Cr Heat Resistant Steel, Oxidation of Metals v.61(1-2) p125 (2004).

[4] Y. Yamamoto et al., Development of Advanced 3Cr-3WV(Ta) Bainitic Steels for Fusion Structural Applications, Presentation at ICFRM-17, Aachen, Germany, October 2015.

[5] M. Jawad, V.K. Sikka, Development of a New Class of Fe-3Cr-W(V) Ferritic Steels for Industrial Process Applications, ORNL/TM-2005/82, 2005, Oak Ridge National Laboratory.

1.3 ON THE EFFECTS OF HE-DPA INTERACTIONS ON CAVITY EVOLUTION IN TEMPERED MARTENSITIC STEELS UNDER DUAL ION IRRADIATION

—Takuya Yamamoto, Yuan Wu, G. Robert Odette (University of California Santa Barbara), Kiyohiro Yabuuchi, Sosuke Kondo, Akihiko Kimura (Kyoto University)

OBJECTIVE

The objective of this research is to characterize cavity evolution in irradiated 9Cr tempered martensitic steels (TMS) and how this is affected by the starting microstructure and irradiation variables.

SUMMARY

We filled some gaps in our cavity evolution database on normalized and tempered 9Cr martensitic steels (TMS) F82H under Fe^{3+} plus He^{+} dual ion beam irradiation (DII) at 500°C. New experiments were conducted at ≈ 30 appm He/dpa at relatively low nominal damage rate of 6.5×10^{-4} dpa/s. The cavity evolution database at 500°C now includes 321 material-dpa-He-dpa rate DII conditions. Two distinct trends of higher and lower swelling rates versus dpa are observed. Here we compare the detailed evolution of the cavity size distributions with increasing dpa and He to seek clues about the reasons for these differences in behavior. The higher swelling rate case was generally associated with higher dpa rates, fewer cavities and stronger bi-modality, compared to the lower swelling rate case.

BACKGROUND

As reported previously [1-6], we have been carrying out systematic 500°C DII studies in the DuET facility at Kyoto University (Japan) at various nominal He/dpa ratios and dpa rates, that are nominally defined at the depth of 600 nm. Here we update the DII database and report an analyses of cavity evolution (and swelling) trends in TMS F82H Mod.3 (F82HM3) for a very wide range of DII dpa, He and He/dpa.

PROGRESS AND STATUS

Experimental Procedure

Details of alloys and DII experiments can be found in [4]. Table 1 summarizes nominal He and dpa irradiation conditions at two reference depths in F82HM3 analyzed in this report at a reference depth of ≈ 600 nm. The irradiations targeted two *nominal* dpa, three He/dpa ratios and two dpa rate conditions. However, taking advantage of the varying spatial distributions of dpa, He and He/dpa, we actually characterized the microstructures over a much wider range irradiation conditions. The latest DII experiment aimed at achieving high dpa and He/dpa at a relatively low dpa rate, filling a major hole in our database at 500°C. Through focus series bright field TEM was used to characterize the cavities (bubbles and voids) in a series of 100 nm slices from near the surface to beyond the end of the range of the 6.4 MeV Fe^{3+} ions. The location specific cavity volume fractions were used to analyze void swelling trends as a function of dpa and He/dpa ratio. The dpa are based on SRIM calculations using the Kinchin-Pease model, with Fe displacement energy of 40 eV [7,8]. We analyzed size distribution evolution at two He/dpa ratio conditions (≈ 30 and 50 appm/dpa) with an emphasis on studing the He bubble to void transition.

Results

Cavity evolution trends

Here cavity evolution trends as a function of dpa and He/dpa are quantified in terms of the bubble and void volume fraction, f, and size (diameter, d) distributions. Earlier analyses showed that variations in the average void diameter, $<d_v>$, and number density, N_v, are less sensitive to local microstructure variations than f; and that the total $f \approx f_v$. We separate voids from bubbles by assuming a (≈ critical) threshold diameter of 4 nm for the latter. This threshold is not fixed or rigorous, but corresponds to a dip that is often observed between the two bubble and void peaks in the cavity size distribution. We have also previously noted that there are two distinct groups showing higher and lower swelling rates. Figure 1 summarize these two trends including the new data that falls in the low swelling group. The larger swelling rates, that was also identified in F82H IEA [1] (not included in this report), are commonly observed only at the highest nominal dpa rate of 1.3 - 1.5 x 10^{-3} dpa/s. However, there is one case in F82HM3 at the high dpa rate that showed a low swelling rate trend. Since the F82H IEA with a higher swelrate and the one F82HM3 showing a lower swelling rate were DII side-by-side, the differences are not due to an unexpectedly high temperature or large variations in dpa and He/dpa. Thus the varied swelling rates are more likely due to starting microstructural differences between the two F82H heats.

Table 1. Irradiation conditions analyzed in this report

T (^{o}C)	Nominal Condition (@550-650nm)				Peak He (@1000-1100nm)		
	dpa	He (appm)	He/dpa	dpa/s	dpa	He (appm)	He/dpa
500	26	1210	47	5.0 x 10^{-4}	45	2100	47
500	9.9	457	46	5.2 x 10^{-4}	17	795	46
500	10	480	47	5.1 x 10^{-4}	18	840	47
500	26	390	15	5.1 x 10^{-4}	44	670	15
500	30	848	29	1.5 x 10^{-3}	51	1467	29
500	30	1200	47	1.3 x 10^{-3}	45	2100	47
500	45	1290	28	8 x 10^{-4}	79	2230	28
500	51	1360	27	8.6 x 10^{-4}	88	2350	27
500	52	2327	45	6.5 x 10^{-4}	89	4024	45

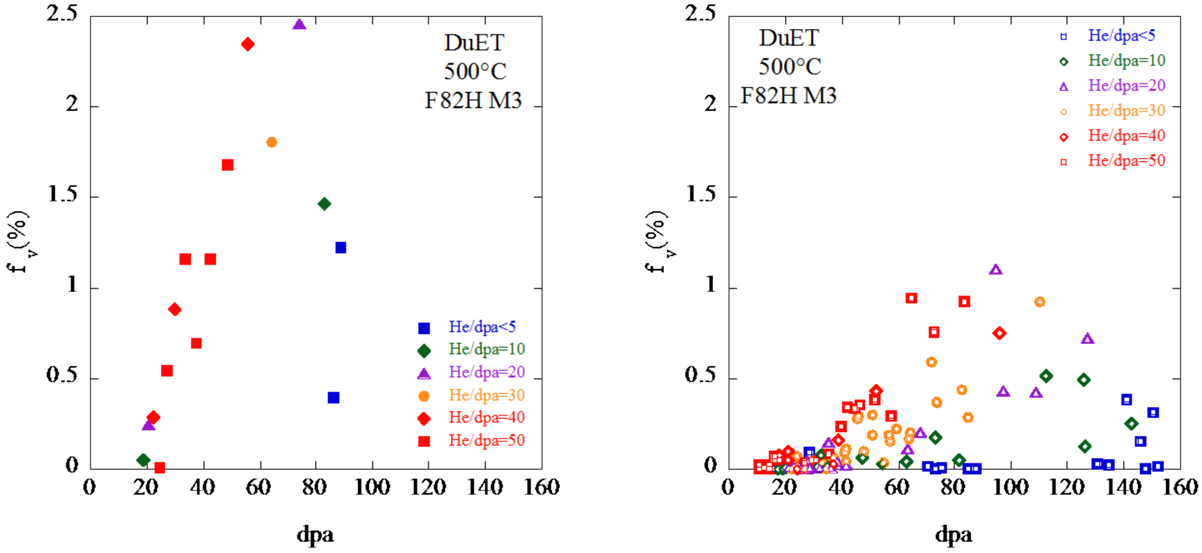

Figure 1 Void volume fraction – dpa trends at various He/dpa ratios in DII F82HM3 in two data groups respectively showing swelling rates that are: a) higher, and, b) low swelling.

Figure 2 shows size distribution evolution for (a) high and (b) low swelling groups at a He/dpa ratio of ≈ 50 ± 5 appm/dpa. The lack of fully systematic trends in individual cases reflects large specimen point-to-point variations in the cavity number densities, which are, in turn, likely mostly due to local starting microstructural variations. The number shown by the histograms are the dpa and He (appm) based on SRIM calculations. The third number in parenthesis is the amount of He estimated to be in the cavities; this will be discussed in a future report. The dashed line at 4 nm is what we assumed to be the nominal critical size for stably growing bubbles by He additions, to convert to unstably growing voids. The low swelling case in Figure 2a shows a mostly unimodal size distribution, but at higher dpa and He, the distribution gradually blends into the void category of cavities. In contrast, for the higher dpa rate case shown in Figure 2b, the cavity distributions are more bimodal, or the bubbles are almost fully transformed to voids, even relatively low dpa and He. There are also far fewer bubbles and voids in this case. That is, fewer cavities reach critical size sooner, since He is partitioned to a smaller number of bubbles that thus individually contain more He.

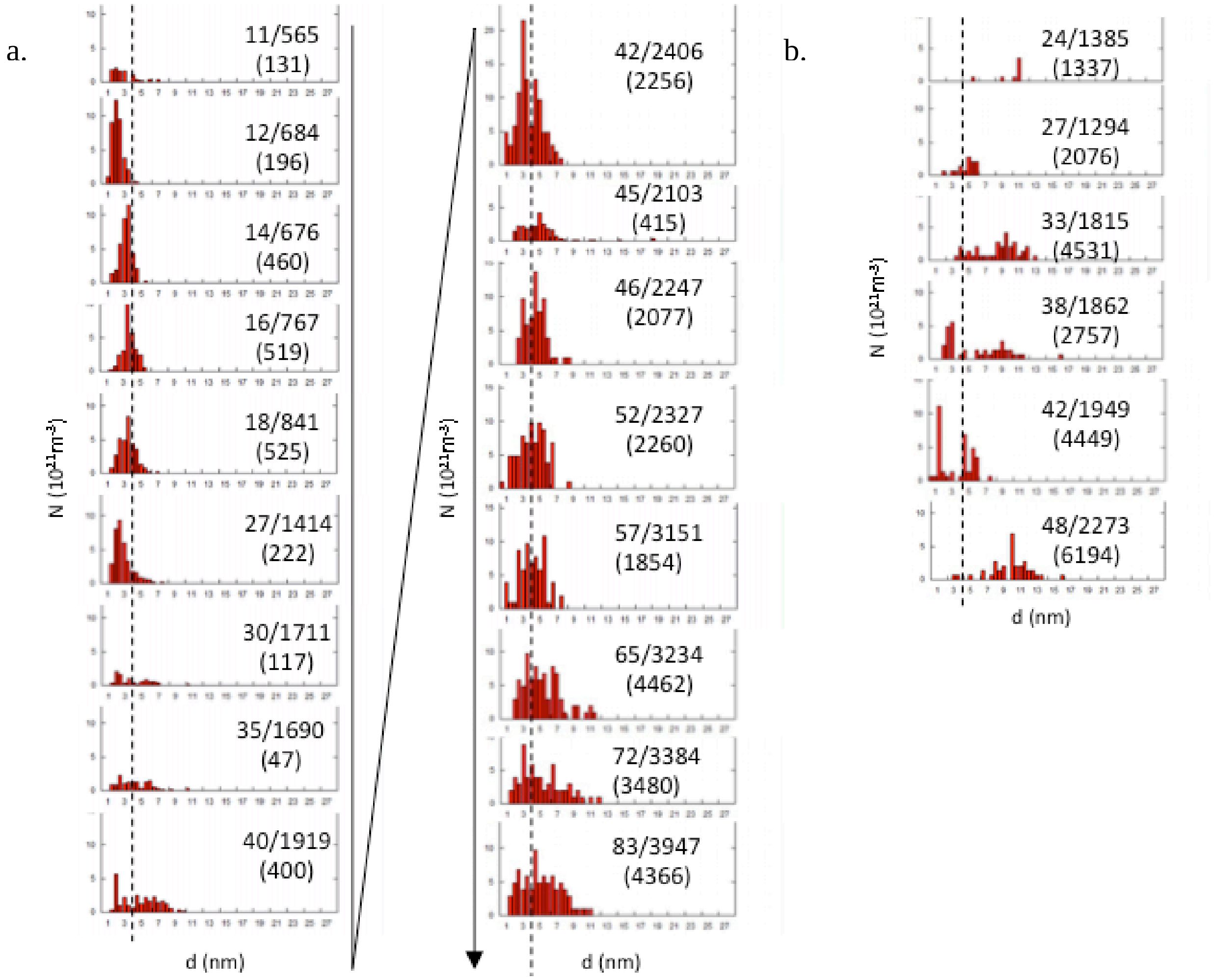

Figure 2. The cavity size distribution evolution in DII F82HM3 at ≈ 50±5 appm He/dpa for: a) a lower nominal dpa rate of ≈ 6 x 10^{-4} dpa/s (left two columns); and, b) for a higher nominal dpa rate of ≈ 1.5 x 10^{3} dpa/s.

Figure 3 shows the cavity size distribution evolutions for irradiations at 30±5 apmm He/dpa. The series of plots in Figure 3a, at low nominal dpa rates, are similar to, but somewhat more bimodal than, those in Figure 2a. The bimodal pinch-off size appears to be much smaller than 4 nm in this case. The series of size distributions in Figure 3b at high nominal dpa rates resulted in low swelling because of the small number of voids and large number of bubbles. However the distinct bimodality is consistent with the nominal d_c = 4 nm critical diameter. Notably by 64 dpa, shown in Figure 3c, all the smaller number of cavities are voids.

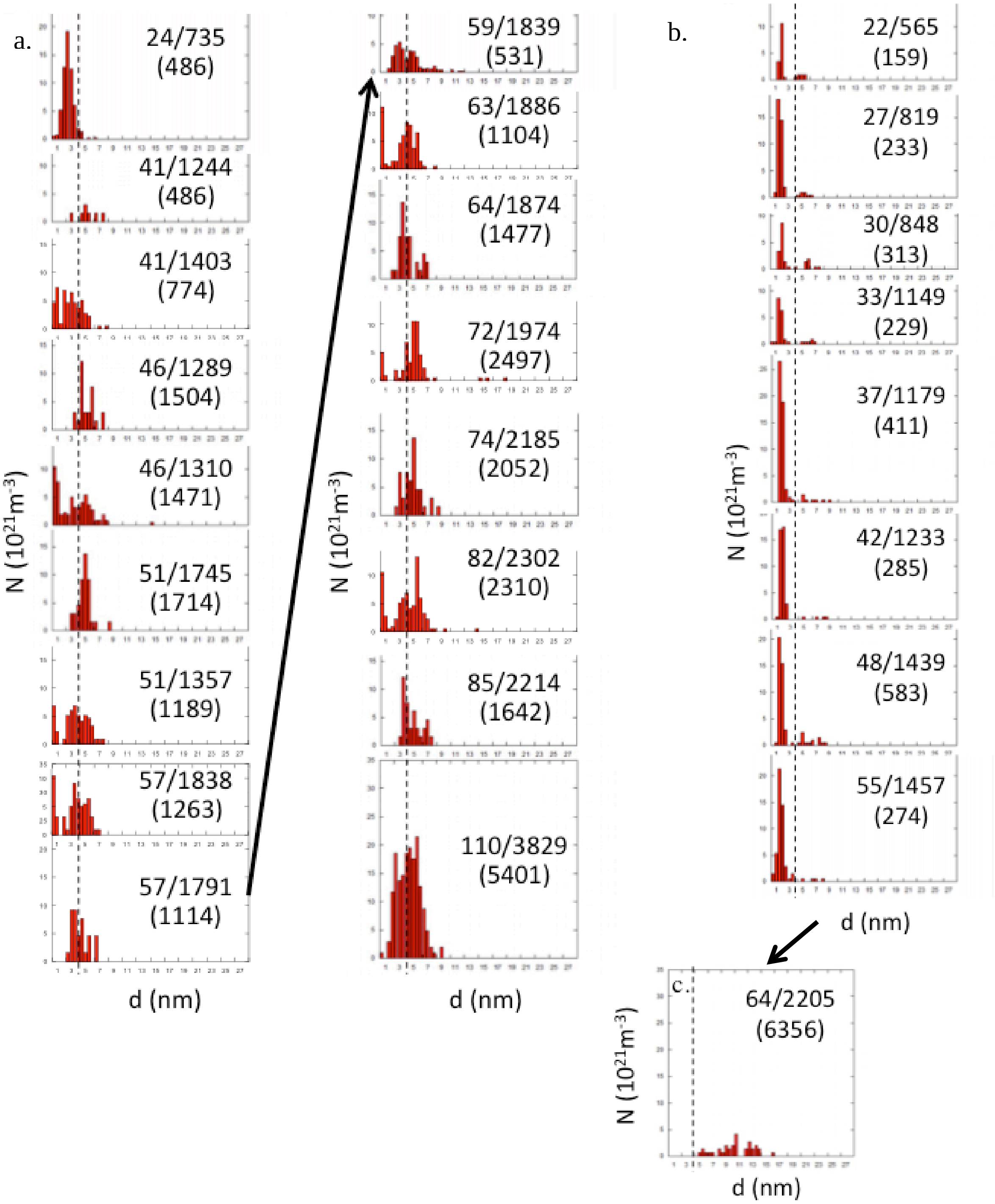

Figure 3. Size distribution evolution in DII F82HM3 at ≈ 30±5 appm He/dpa: a) at low nominal dpa rate of ≈ 6.8 x 10^{-4} dpa/s (left two columns) compared with b) high ≈ 1.5 x 10^{-3} dpa/s nominal rate to up to 55 dpa and c) to 64 dpa.

Discussion and Summary

This work in progress will be discussed in more detail in future reports and publications. In summary: a) a nominal critical size d_c = 4 nm is generally consistent to the observed cavity size distribution evolution trends; b) there is lower swelling at low dpa rates and the cavity size distributions are more unimodal; c) swelling is higher and cavity size distributions are more bimodal at high dpa rates; and, d) swelling is lower at higher dpa rates even with distinct bimodality, when more numerous bubbles may retard the bubble-to-void transition.

Acknowledgements

The dual ion-beam irradiations were conducted under the support of the “Joint Research Program on Zero-Emission Energy Research, Institute of Advanced Energy, Kyoto University (ZE28A-03, 27A-22, 26A-16, 25A-19, 24A-13 and 23B-3). The work performed at UCSB was supported by the U. S. Department of Energy, Office of Fusion Energy Sciences, under Contract DE-FG03-94ER54275. We acknowledge the contributions of the NSF sponsored UCSB Microstructure and Microanalysis Facility. We are also grateful for generous support of research materials, F82H mod.3 from Dr. K. Shiba, (JAEA, Japan).

References

[1] T. Yamamoto, Y. Wu, G.R. Odette, K. Yabuuchi, S. Kondo, A. Kimura, *Fusion Materials Semiannual Report 6/30/2015* DOE/ER-313/58 (2015) 12

[2] G.R. Odette, T. Yamamoto, Y. Wu, S. Kondo, A. Kimura, *Fusion Materials Semiannual Report 12/31/2014* DOE/ER-313/57 (2015) 8

[3] T. Yamamoto, Y. Wu, G.R. Odette, S. Kondo, A. Kimura, *Fusion Materials Semiannual Report 6/30/2014* DOE/ER-313/56 (2014) 194

[4] T. Yamamoto, Y.Wu, G.R. Odette, K. Yabuuchi, S. Kondo, A. Kimura, J. Nucl. Mater. 449 (2014) 190

[5] T. Yamamoto, Y.Wu, G.R. Odette, S. Kondo, A. Kimura, *Fusion Materials Semiannual Report 6/30/2013* DOE/ER-313/54 (2013) 6.

[6] T. Yamamoto, Y. Wu, G.R. Odette, K. Yabuchi, A. Kimura, *Fusion Materials Semiannual Report 12/31/2010* DOE/ER-313/49 (2011) 1.

[7] ASTM E521-96 (2009), ASTM

[8] R.E. Stoller, M.B. Toloczko, G.S. Was, A.G. Certain, S. Dwaraknath, F.A. Garner, Nuc Instr Mehtods Phys Res B 310 (2013) 75.

1.4 INFLUENCE OF ION IRRADIATION DIRECTION ON GROWTH OF NANOPRECIPITATES IN MODEL CNAs

—L. Tan (Oak Ridge National Laboratory), B.K. Kim (ORNL), G.S. Was (Univ. of Michigan)

OBJECTIVE

Characterize the irradiation response of CNA steel alloys.

SUMMARY

Transmission electron microscopy of irradiated CNA alloys and statistical quantitative analysis of the ultrafine particles after heavy ion irradiation indicates that these experiments may not represent the precipitate stability under neutron irradiation. The dependence of nanoprecipitate evolution on ion beam direction is one process that may be unique to ion irradiation.

PROGRESS AND STATUS

Introduction

Castable nanostructured alloys (CNAs) are being developed at Oak Ridge National Laboratory, to favor the formation of a larger amount of ultrafine precipitates in reduced-activation ferritic-martensitic steels [1]. Model CNAs were developed to explore the stability of specific types of nanoprecipitates [2], since evolution of precipitates may directly influence the mechanical properties and even corrosion-related properties of alloys. However, reports on evolution of radiation-modified precipitates in morphology, size and density are limited.

Experimental Procedure

The influence of Fe^{2+} ion irradiation on the evolution of vanadium nitride (VN) thin-lath-shaped nanoprecipitates at 500°C was investigated in a model CNA. Because of the preferential orientation of the VN nanoprecipitates in the ferritic matrix, different grains were characterized after 5 MeV Fe^{2+} irradiation. SRIM (the stopping and range of ions in matter) was used to calculate the depth-dependent profiles of irradiation dose in displacements per atom (dpa) and implanted Fe in atomic percentage (at.%) with the recommended parameters [3]. The calculated profiles in two levels of irradiation damages with peak doses up to ~49 and ~240 dpa, respectively, are shown in Figure 1. Transmission electron microscopy (TEM) was used to characterize the nanoprecipitates within 300–700 nm from irradiated-specimen surface. Examples of the nanoprecipitates at ~650 nm from irradiated-specimen surface are shown as insets of Figure 1. The relationship between the ion beam direction and the initial length direction of nanoprecipitates (ppt) is marked on each inset, indicating three orientation conditions with the angle between beam and ppt ($\angle_{\text{beam-ppt}}$) as ~12°, ~20°, and ~82°.

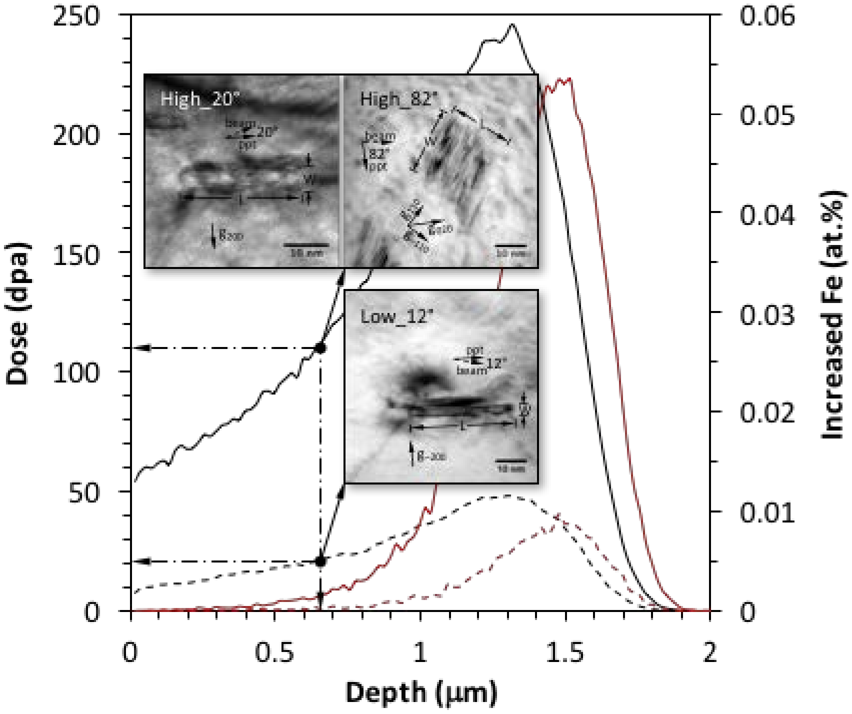

Figure 1. SRIM-calculated depth profiles of dose (black) and implanted Fe (red) after two levels of irradiation damage in dashed and solid lines, together with insets of high-resolution BF-TEM images at depth of ~650 nm from irradiated-specimen surface.

Analysis of the nanoprecipitates within 300–700 nm from irradiated-specimen surface indicates that the nanoprecipitates generally grew longer and sectioned into shorter lengths at higher dpa, resulting in higher particle densities, when the ion irradiation direction was approximately aligned with the initial nanoprecipitate length (i.e., smaller ∠beam-ppt). As ion irradiation deviated from nanoprecipitate length direction (i.e., larger ∠beam-ppt), some nanoprecipitates sectioned lengthwise and then dissolved, resulting in decreased particle densities. Surviving nanoprecipitates were transformed into parallelograms as shown in the high angle, 82°, inset of Figure 1.

The aspect ratio of the nanoprecipitates is defined as length/width (L/W as indicated in the insets of Figure 1). The aspect ratio frequency of the nanoprecipitates is shown in Figure 2, illustrating significant reductions in aspect ratio of the particles to ~2.4 in average after the high-dose irradiation compared to ~6.8 in average of the low-dose irradiated sample, both of which having small ∠(beam–ppt) angle of 20° and 12°, respectively. The larger ∠(beam–ppt) angle of 82° further decreased the aspect ratio to ~1.1 in average after the high-dose irradiation. Compared to the aspect ratio (~7.3) of the nanoprecipitates prior to irradiation, aspect ratio of the nanoprecipitates was decreased by higher doses, but more significantly by irradiation direction (∠(beam–ppt).

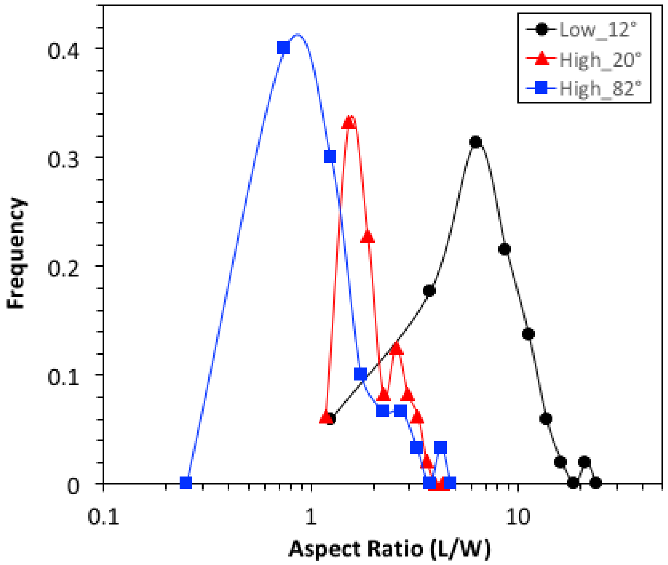

Figure 2. Aspect-ratio-dependent frequency of the particles within 300–700 nm away from irradiated-specimen surface.

Results

This study indicates that statistical quantitative analysis on the stability of ultrafine particles under heavy ion irradiation experiments may not be able to represent their stability under neutron irradiation situation. The dependence of nanoprecipitate evolution on ion beam direction is one process that may be unique to ion irradiation. Detailed information about this topic is contained in a paper submitted for journal publication.

References

[1] L. Tan, L.L. Snead, Y. Katoh, Development of new generation reduced activation ferritic-martensitic steels for advanced fusion reactors, J. Nucl. Mater. 478 (2016) 42–49.

[2] L. Tan, T.S. Byun, Y. Katoh, L.L. Snead, Stability of MX-type strengthening nanoprecipitates in ferritic steels under thermal aging, stress and ion irradiation, Acta Mater. 71 (2014) 11–19.

[3] R.E. Stoller, M.B. Toloczko, G.S. Was, A.G. Certain, S. Dwaraknath, F.A. Garner, Nucl. Instrum. Meth. Phys. Res. B 310 (2013) 75.

2. ODS AND NANOCOMPOSITED ALLOY DEVELOPMENT

2.1 Fe-Cr-Al ODS ALLOYS FOR FUSION REACTOR APPLICATIONS—S. Dryepondt , K. A. Unocic, D. T. Hoelzer (Oak Ridge National Laboratory)

OBJECTIVE

The dual coolant lead-lithium (DCLL) blanket concept requires ferritic steels with improved Pb-Li compatibility in order to demonstrate viable blanket operation in a DEMO-type fusion reactor. This project aims at developing alumina –forming oxide dispersion strengthened (ODS) FeCrAl alloy with excellent compatibility with Pb-Li and creep resistance at temperature up to 700-800ºC.

SUMMARY

Several ODS FeCrAl alloys were fabricated by ball milling Fe-12Cr-5Al gas atomized powder with Y_2O_3 powder and ZrO_2, HfO_2, or TiO_2 powder. The Zr-containing alloy (125YZ) exhibited excellent creep properties at 700-800ºC in air, and good compatibility with Pb-17Li at 700ºC, with the formation of a thin $LiAlO_2$ layer. Extensive TEM characterization of the 125YZ revealed the presence of $Y_3Al_5O_{12}$ (YAG), Al_2O_3 and Zr(C,N) nano precipitates. A second generation of ODS FeCrAl alloys was fabricated by ball-milling Zr or Hf-containing Fe-12Cr-5.5Al powder with Y_2O_3 powder. Initial characterization of these 2nd generation alloys showed that the alloy tensile properties are very dependent on the extrusion conditions.

PROGRESS AND STATUS

Introduction

The Dual Cooled Lead Lithium (DCLL) blanket concept, with Pb-Li and He as coolants, is the leading U.S. design for a test blanket module (TBM) for ITER and for a DEMO-type fusion reactor.[1] Reduced activation ferritic-martensitic (RAFM) steels are leading candidates for structural materials, but the rapid dissolution of Fe and Cr in Pb-Li limits their temperature of use to ~475ºC.[2-3]. Structural materials with enhanced creep and compatibility are required for a blanket temperature above 500ºC in a DEMO-type reactor. Nano-structured ferritic (NFA) or ODS FeCr alloys exhibit excellent radiation and creep resistance at high temperature,[4-8] but their compatibility with Pb-Li is similar to RAFM steels. [9-10].

Alumina forming Fe-Cr-Al alloys offer significantly better compatibility with Pb-Li, and only low mass losses were observed for FeCrAl alloys after isothermal compatibility tests at 800ºC.[9] A 550ºC thermal convection loop experiment also showed that only small mass changes were measured for the commercial Fe-21Cr-5Al-3Mo APMT alloy in the hot and cold legs after exposure for 1000h.[11]

ODS FeCrAl alloys are, therefore, very good candidates for structural materials with both creep and compatibility resistance, and new Fe-12Cr-5Al ODS alloys were fabricated at ORNL by ball milling Fe-12Cr-5Al gas atomized powder with Y_2O_3+FeO (125YF alloy) Y_2O_3+ZrO_2 (125YZ), Y_2O_3+HfO_2 (125YH), and Y_2O_3+TiO_2 (125YT) powders. Determination of the mechanical properties and compatibility with Pb-17Li of this first generation of ODS FeCrAl alloys has been completed,[12-16] and the characterization of a second generation of Fe-12Cr-6Al-Zr (Hf) alloys was initiated. For these alloys, Zr and Hf were directly added to the gas atomized powder to improve the homogeneity of the Zr (Hf) dispersion.

Experimental Procedure

<u>Alloy Fabrication</u>

The first generation of ODS FeCrAl alloys were fabricated by ball milling ~1 kg of Fe-12Cr-5Al gas atomized powder with Y_2O_3+FeO (125YF) Y_2O_3+ZrO_2 (alloy 125YZ), Y_2O_3+HfO_2 (alloy 125YH), and Y_2O_3+TiO_2 (alloy 125YT) powders. The powders were degassed for 24 h at 300ºC and extruded at 950ºC through a rectangular 2x1.5 inch die. Details of the alloy fabrication procedure can be found elsewhere.[12,15]. For the 2nd generation ODS FeCrAl alloys, four different gas atomized powders were purchased from ATI, with targeted compositions of Fe-12Cr-5.5Al-0.55Zr, Fe-12Cr-5.5Al-0.55Zr, Fe-12Cr-5.5Al-0.25Zr-0.13Ti and Fe-10Cr-6Al-0.3Zr. The first two powders were ball milled with Y_2O_3 and extruded the same way as for the 1rst generation ODS FeCrAl alloys (alloy 126ZY and 126ZH). The last two powders as well as a second batch of the Fe-12Cr-5.5Al-0.55Zr powder were also ball milled with Y_2O_3 for 40 h but the resulting powder was extruded at 1000ºC using a smaller extrusion can and a 7/8 inch cylindrical die (alloy 126ZY_10C, 126ZTY and 106ZY_1000ºC). Finally, a second batch of the Fe-10Cr-6Al-0.3Zr powder was extruded at 900ºC using the smaller 7/8 inch die (106ZY_900ºC). The composition of the gas atomized powders and extruded alloys are given in Table 1 and Table 2, respectively.

Table 1. Composition of the gas atomized powders provided by ATI

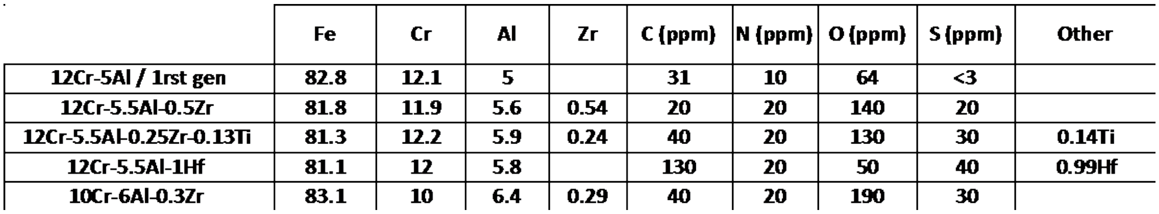

	Fe	Cr	Al	Zr	C (ppm)	N (ppm)	O (ppm)	S (ppm)	Other
12Cr-5Al / 1rst gen	82.8	12.1	5		31	10	64	<3	
12Cr-5.5Al-0.5Zr	81.8	11.9	5.6	0.54	20	20	140	20	
12Cr-5.5Al-0.25Zr-0.13Ti	81.3	12.2	5.9	0.24	40	20	130	30	0.14Ti
12Cr-5.5Al-1Hf	81.1	12	5.8		130	20	50	40	0.99Hf
10Cr-6Al-0.3Zr	83.1	10	6.4	0.29	40	20	190	30	

Table 2. Composition of some alloys measured by inductively coupled plasma analysis and combustion analysis.

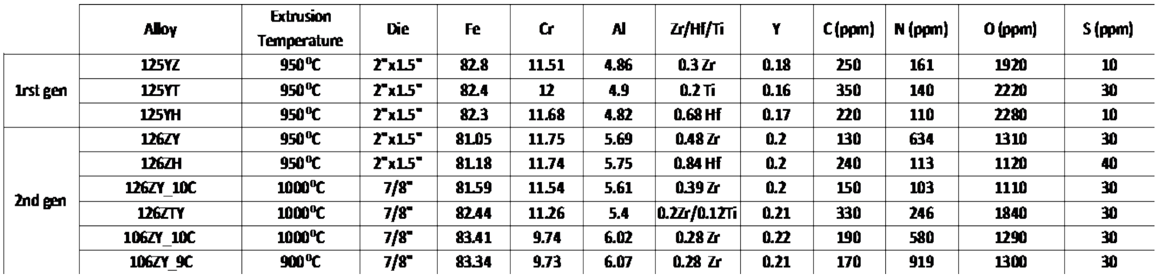

	Alloy	Extrusion Temperature	Die	Fe	Cr	Al	Zr/Hf/Ti	Y	C (ppm)	N (ppm)	O (ppm)	S (ppm)
1rst gen	125YZ	950°C	2"x1.5"	82.8	11.51	4.86	0.3 Zr	0.18	250	161	1920	10
	125YT	950°C	2"x1.5"	82.4	12	4.9	0.2 Ti	0.16	350	140	2220	30
	125YH	950°C	2"x1.5"	82.3	11.68	4.82	0.68 Hf	0.17	220	110	2280	10
2nd gen	126ZY	950°C	2"x1.5"	81.05	11.75	5.69	0.48 Zr	0.2	130	634	1310	30
	126ZH	950°C	2"x1.5"	81.18	11.74	5.75	0.84 Hf	0.2	240	113	1120	40
	126ZY_10C	1000°C	7/8"	81.59	11.54	5.61	0.39 Zr	0.2	150	103	1110	30
	126ZTY	1000°C	7/8"	82.44	11.26	5.4	0.2Zr/0.12Ti	0.21	330	246	1840	30
	106ZY_10C	1000°C	7/8"	83.41	9.74	6.02	0.28 Zr	0.22	190	580	1290	30
	106ZY_9C	900°C	7/8"	83.34	9.73	6.07	0.28 Zr	0.21	170	919	1300	30

Mechanical testing

Tensile tests were performed using SS-3 type tensile specimens (7.62 mm long and 0.762 mm thick) fabricated with the gage section parallel to the extrusion axis of the ODS FeCrAl alloys. The tensile tests were conducted in an MTS hydraulic frame at temperatures ranging from 25ºC-800ºC and a strain rate of $\sim 10^{-3}s^{-1}$.

Creep testing was performed using 25 mm long specimens parallel to the extrusion direction and with a 2 x 2 mm gauge section that was 7.6 mm long.

Compatibility tests

Static capsule tests were performed using Mo (inert to Pb-17Li) welded closed inner capsules and type 304 stainless steel (SS) outer capsules to protect the inner capsule from oxidation. The compatibility experiments were conducted at 700ºC for 1000h.[16]

Microstructure characterization

Selected specimens were mounted using conventional metallographic techniques and TEM specimens were prepared using the in situ lift-out method. A Philips model CM200 FEG-TEM/scanning TEM (STEM) with EDS and electron energy loss spectroscopy (EELS) was used for microstructural and compositional analyses. Details of the TEM characterization techniques can be found elsewhere [15-16].

Results

Alloy Characterization

Extensive TEM characterization was conducted on the 125YZ and 125YH alloys, [15] and examples of TEM images and EDS maps are shown in Figure 1 and Figure 2 for alloys 125YZ and 125YH, respectively. The nano precipitates were identified as $Y_3Al_5O_{12}$ (YAG), Al_2O_3 and Zr(C,N) for alloy 125YZ, and $Y_3Al_5O_{12}$(YAG), Al_2O_3, Hf(C,N), $Y_2Hf_2O_7$ and HfO_2 for alloy 125YH. Contrary to what was reported by Yu et al. for an Fe-16Cr-4Al-2W-0.35Y_2O_3 + Zr alloy, no $Y_2Zr_2O_7$ precipitates were observed in alloy 125YZ.[17] The presence of HfO_2 particles in alloy 125YH indicates that the 40h ball-milling step was likely insufficient to break down completely the HfO_2 powder and drive Hf into solution in the Fe matrix.

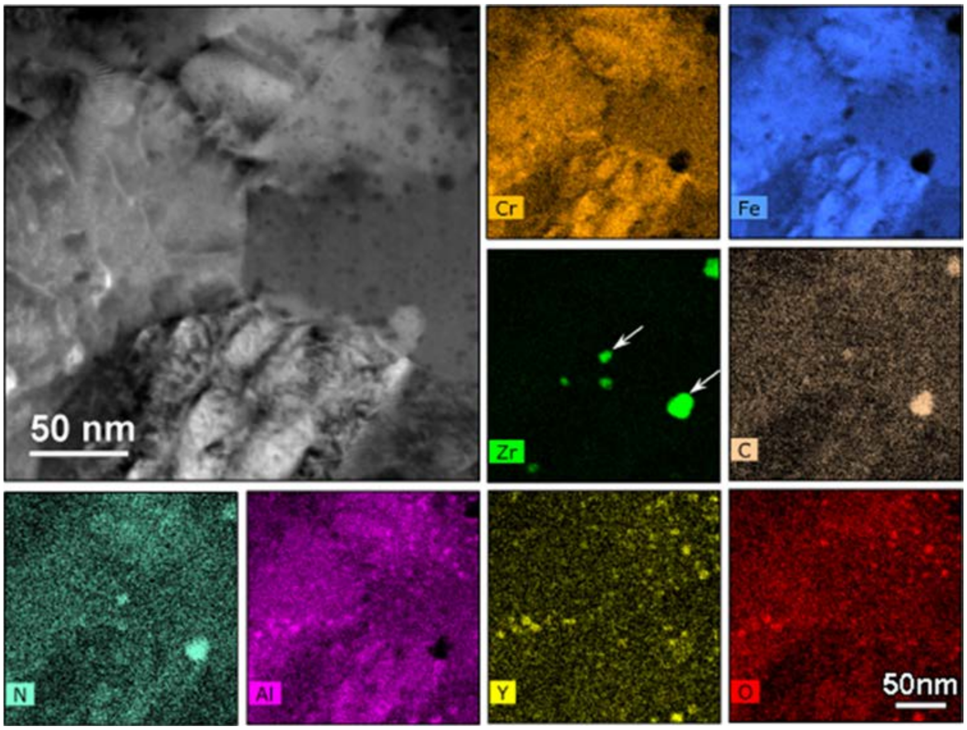

Figure 1. HAADF-STEM image of the 125YZ as-extruded (lift-out FIB) alloy with corresponding EDS elemental maps of Cr, Fe, Zr, C, N, Al, Y, and O.[15]

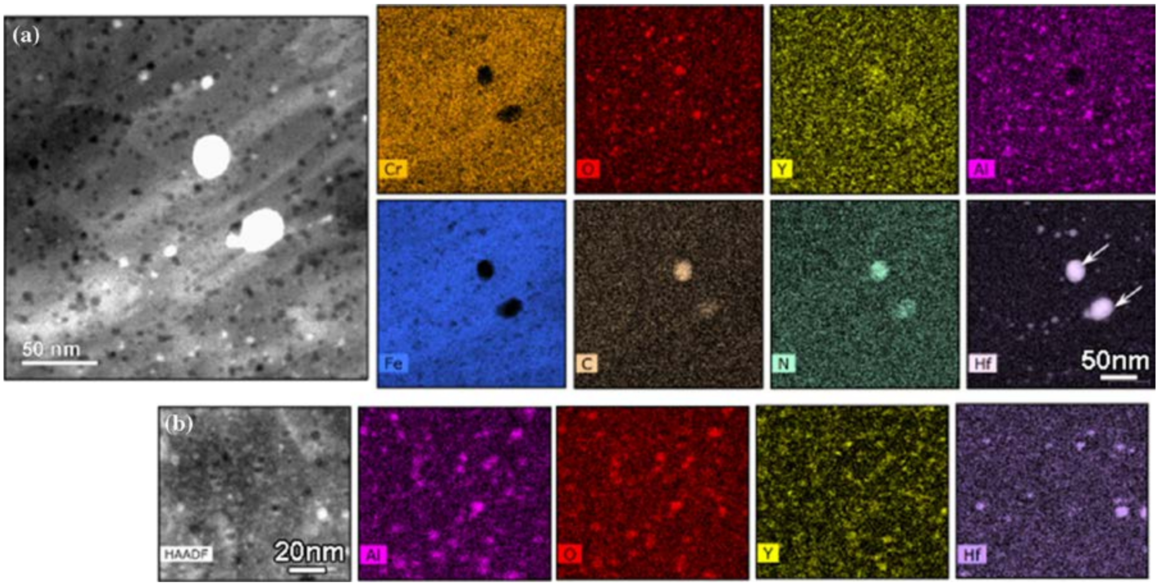

Figure 2. a) HAADF-STEM image of the as-extruded 125YH (lift-out FIB) alloy, b) corresponding EDS elemental maps of Al, O, Y, Cr, Hf, C, N, and Fe.[15]

Creep testing

Creep tests were conducted at 800ºC with an applied stress of 100 MPa, and the results for alloy 125YZ, 125YH and 125YT are summarized in Figure 3a. Alloy 125YZ performed significantly better than alloy 125YH and 12YZ, and the two 125YZ tests were interrupted before failure after respectively 1000 h and 6000 h of exposure for microstructure characterization. The microstructure of alloy 125YH was less homogeneous than the microstructure of alloy 125YZ, which might explain the early creep failures for alloy 125YH, and alloy 125YT seems less stable at temperature above 800ºC than alloy 125YZ.

Figure 3b compares the creep properties of alloy 125YZ at 700 and 800ºC with the creep properties of the former commercial alloy PM2000 and new ODS FeCrAl alloys developed in Japan.[18,19] At 800ºC, the 6000 h lifetime corresponds for alloy PM2000 to a stress of ~45 MPa, whereas alloy 125YZ did not fail after 6000 h with an applied stress of 100 MPa. At 700ºC, the best performing Japanese alloy, Fe-16Cr-4Al-2W-Y+Zr, was expected to reach the ~10,000 h lifetime limit for an applied stress of 120 MPa. The 125YZ alloy exhibited a significantly better creep behavior with one test at 700ºC, 140 MPa still running after ~16,000 h.

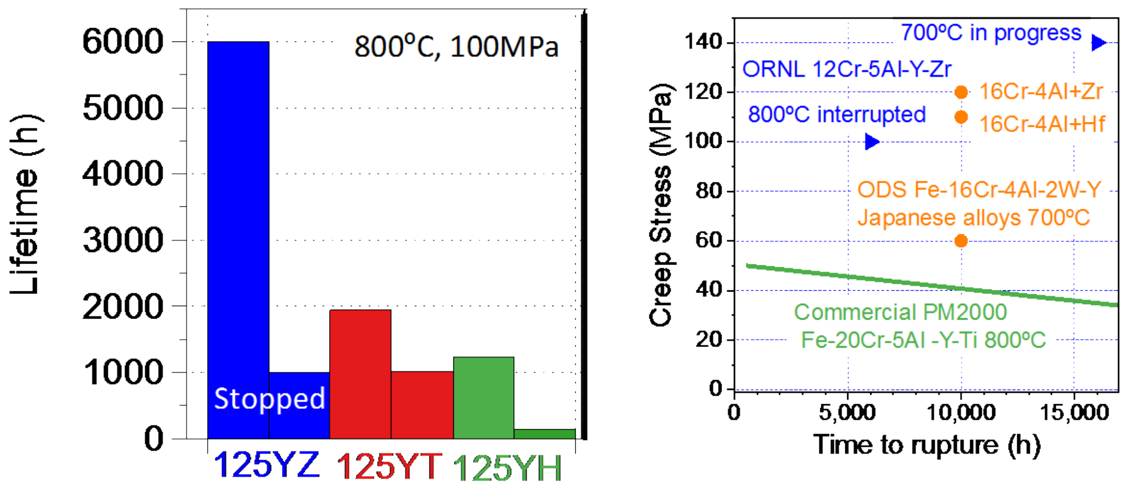

Figure 3. a) Creep lifetime at 800ºC, 100 MPa for the 125YZ, 125YT and 125YH alloys, b) comparison of the creep performance at 700-800ºC between alloy 125YZ and other ODS FeCrAl alloys.

Compatibility tests

The 125YZ, 125YH and 125YT alloys were exposed to Pb-17Li in static capsule experiments for 1000 h, and the detailed analysis of these results can be found elsewhere. [16] Very limited mass changes were measured for all the alloys with the formation after 1000 h of a thin $LiAlO_2$ layer ~0.5 to 1.5 um thick.

Example of the oxide scale TEM characterization is shown in Figure 4 for alloy 125YZ. Void formation was observed both in the scale and at the alloy/scale interface, and Zr-rich precipitates were identified in the scale. Similarly, voids formation, and Hf and Ti-rich precipitates were observed in the scale formed on alloy 125YH and 125YT, respectively.

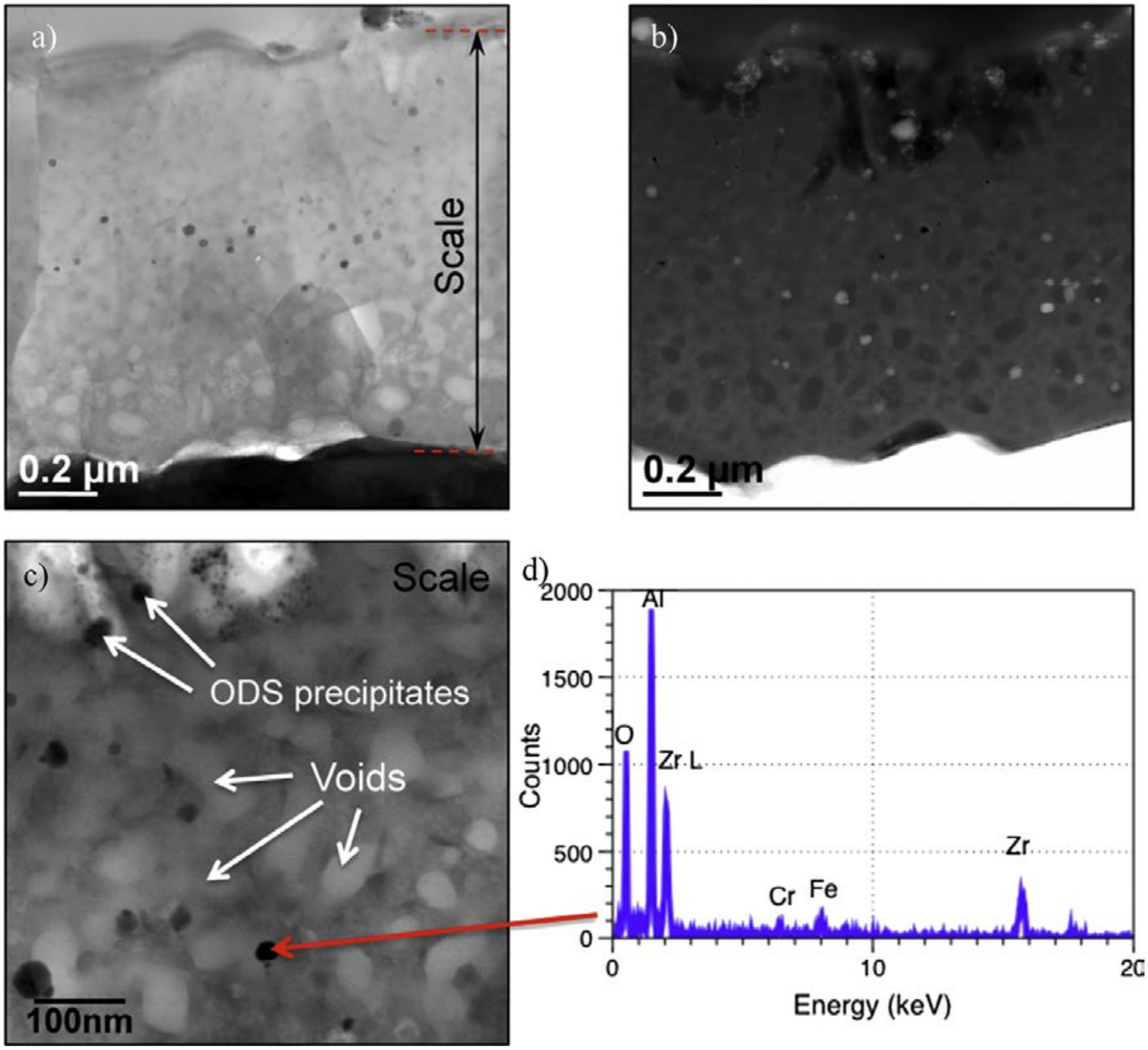

Figure 4. Cross-section of the oxide formed on 125YZ after exposure for 1000h at 700ºC in static Pb-17Li, (a,c) BF-STEM images, b) HAADF-STEM images, d) EDS point spectrum generated from a particle within the oxide.

2nd generation ODS alloys

The second generation of ODS FeCrAl alloys was fabricated by ball-milling FeCrAl+ Zr, Hf or Zr+Ti powders with Y_2O_3 powder (Tables 1 and 2). The goal was to improve the alloy homogeneity and the control of the O content in the alloy. The tensile properties of the 2nd gen 126YZ and 126YH alloys are compared in Figure 5 with the properties of the 1st generation 125YZ and 125YH alloys. At temperature below 400ºC, alloy 126YZ exhibited very high strength but no ductility, whereas the tensile strength of alloy 126HY was lower than the strength of the 1st gen ODS FeCrAl alloys.

The tensile properties of several 2nd generation alloys extruded through a smaller 7/8 inch die are again compared with the tensile properties of alloy 125YZ in Figure 6. All the 2nd generation alloys extruded at 1000ºC exhibited very similar tensile behavior, with lower tensile strength but higher ductility than alloy 125YZ. These results indicate that small variations in Zr concentration or addition of both Zr and Ti have limited effects on the alloy tensile properties. On the contrary, extrusion conditions seem to have a tremendous impact on the alloy tensile properties, with the 126ZY and 126ZY_10C alloys, fabricated with the same ball milled powder, showing very different tensile behaviors.

Finally, it is worth noting that the 106ZY_9C alloy extruded at 900ºC showed similar strength but better ductility than the 1st generation 125YZ alloy. This alloy is a promising candidate for structural applications in fusion reactors and specimens have been machined to initiate creep testing at 700 and 800ºC. Optimization of the processing conditions to enhance the creep performance and fabricability of ODS FeCrAlYZr alloys is ongoing.

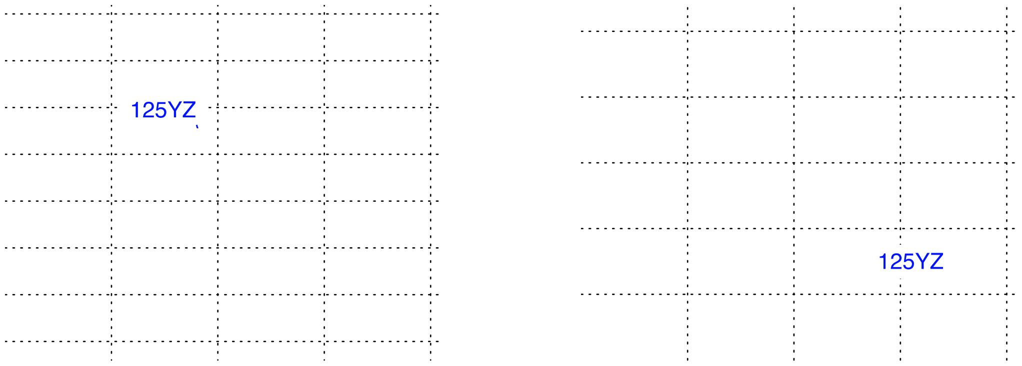

Figure 5. Tensile properties of the 1st generation 125YZ and 125YH alloys, and 2nd generation 126YZ and 126HY ODS alloys, a) Ultimate tensile strength, b) Plastic deformation.

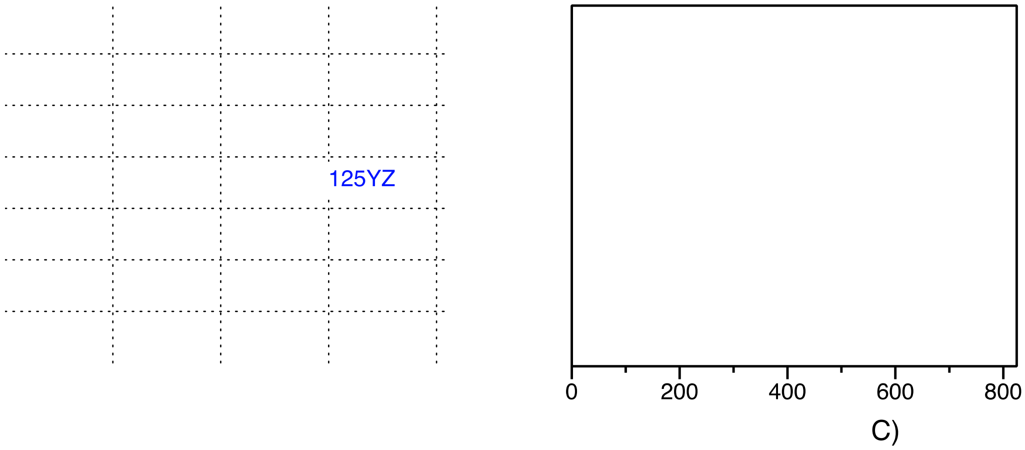

Figure 6. Tensile properties of the 1st generation 125YZ alloy, and several 2nd generation ODS FeCrAl alloys extruded at 1000ºC or 900ºC, a) Ultimate tensile strength, b) Plastic deformation.

References

[1] S. Malang, M. Tillack, C.P.C. Wong, N. Morley, S. Smolentsev, Fus. Sci. Tech., 60, (2011) 249.

[2] O. K. Chopra, D. L. Smith, P. F. Tortorelli, J. H. DeVan and D. K. Sze, Fusion Technol., 8 (1985) 1956.

[3] J. Konys, W. Krauss, J. Novotny, H. Steiner, Z. Voss and O. Wedemeyer, J. Nucl. Mater. 386-88v (2009) 678.

[4] S. Ukai and M. Fujiwara, J. Nucl. Mater. 307 (2002) 749.

[5] G. R. Romanowski, L. L. Snead, R. L. Klueh, D. T. Hoelzer, J. Nucl. Mater., 283-287 (2000) 642.

[6] R. L. Klueh, J. P Shingledecker, R. W. Swindeman, D. T. Hoelzer, J. Nucl. Mater. 341 (2005) 103.

[7] D. A. McClintock, M. A. Sokolov, D. T. Hoelzer and R. K. Nanstad, J. Nucl. Mater., 392 (2009) 353.

[8] G.R. Odette, JOM, 66 (2014)2427.

[9] B. A. Pint, L. R. Walker and K. A. Unocic, Mater. High Temp. 29 (2012) 129.

[10] B. A. Pint and K. A. Unocic, J. Nucl. Mater. 442 (2013) 572.

[11] S. J. Pawel, DOE-ER-0313/56 (2014) 178.

[12] B. A. Pint, S. Dryepondt, K. A. Unocic and D. T. Hoelzer, JOM 66 (2014) 2458.

[13] K. A. Unocic, D. T. Hoelzer and B. A. Pint, Mater. High Temp. 32 (2015) 123.

[14] B. A. Pint, K. A. Unocic, S. Dryepondt and D. T. Hoelzer DOE-ER-0313/56 (2014) 31.

[15] K. A. Unocic, B. A. Pint, and D. T. Hoelzer, J Mater Sci,51, (2016) 9190.

[16] K. A. Unocic and D. T. Hoelzer, J. Nucl. Mater, 479 (2016) 357.

[17] C.Z. Yu, H. Oka, N. Hashimoto, S. Ohnuki, J. Nucl. Mater., 417 (2011) 286.

[18] Material Data Sheet ODS-Superalloy PM 2000, Metallwerk Plansee GmbH (1993).

[19] A. Kimura, R. Kasada, N. Iwata, H. Kishimoto, C.H. Zhang, J. Isselin, P. Dou, J.H. Lee, N. Muthukumar, T. Okuda, M. Inoue, S. Ukai, S. Ohnuki, T. Fujisawa, and T.F. Abe, J. Nucl. Mater., 417 (2011) 176.

2.2 X-RAY ABSORPTION SPECTROSCOPY OF EMBEDDED AND EXTRACTED NANO-OXIDES IN NANOSTRUCTURED FERRITIC ALLOY MA957

—T. Stan, G.R. Odette (University of California Santa Barbara), D. Sprouster, A. Ofran, L. Ecker (Brookhaven National Laboratory)

OBJECTIVE

The objective of this work is to use x-ray absorption spectroscopy to characterize the Y-Ti-O nano-oxides in NFA MA957.

SUMMARY

The chemistries and structures of both embedded and extracted Y-Ti-O nanometer-scale oxides in nanostructured ferritic alloy (NFA) MA957 were characterized by x-ray absorption spectroscopy (XAS). $Y_2Ti_2O_7$ is the primary embedded phase, while the slightly larger extracted oxides are primarily Y_2TiO_5. Analysis of the embedded nano-oxides in MA957 is difficult partly due to the multiple Ti environments associated with different oxides and those still residing in matrix lattice sites. Thus, bulk extraction followed by selective filtration was used to isolate the larger Y_2TiO_5 oxides for XAS. The smaller $Y_2Ti_2O_7$ oxides passed through the filters but were the predominant embedded phase.

PROGRESS AND STATUS

Introduction

Nanostructured ferritic alloys (NFAs) are a developmental class of oxide dispersion strengthened steels (ODS) with potential applications in nuclear fission and fusion energy systems [1–4]. NFAs are thermally stable, have excellent high-temperature creep strength and are uniquely irradiation tolerant. NFAs are typically processed by ball-milling Fe–14Cr–W–Ti metallic powders with yttria (Y_2O_3) powders followed by hot consolidation leading to the precipitation of Y-Ti-O nano-oxides (NOs) that impede dislocation motion, enhance defect recombination and trap transmutation produced He in small high-pressure gas bubbles. The NO character (size, number density, composition, and structure) depends on the alloy composition and processing history. NOs have been studied using transmission electron microscopy (TEM) [5–11], atom probe tomography (APT) [12–16], as well as small angle neutron and x-ray scattering (SANS and SAXS) [8,17,18]. These studies have been interpreted to show NOs that range from solute enriched clusters with core-shell structures to various complex oxides, such as pyrochlore $Y_2Ti_2O_7$ and orthorhombic Y_2TiO_5.

A reference heat of INCO NFA MA957 with a nominal composition of 14.9Cr, 1.1Ti, 0.17Mo, 0.13Y, 0.88O, bal. Fe (at%), along with trace impurity elements such as Al, Mn, Si and C [19] was examined in this study. Previous TEM and SANS studies indicate NO averages for number densities of $N \sim 5 \times 10^{23}\ m^{-3}$, average diameters $\langle d \rangle \sim 2.5$ nm, and volume fractions of $\langle f \rangle \sim 0.4\%$ [20]. The smallest ($d < 5$ nm) NOs were found to be primarily cubic pyrochlore $Y_2Ti_2O_7$, while larger ($d > 6$ nm) NOs were primarily orthorhombic Y_2TiO_5. Larger ($d > 50$ nm) Y_2O_3, TiO_x, Mo-rich, and C-rich precipitates were also observed. Given the low fraction and ultra-small NO size, a synchrotron light source is needed to obtain reliable x-ray measurements. As a complement to x-ray diffraction (XRD) and SAXS measurements, the National Synchrotron Light Source (NSLS) was used to carry out x-ray absorption spectroscopy (XAS) studies.

One challenge to XAS on MA957 is that it contains a large amount of Ti with ≈ 2/3 of the total left in solution and only 1/3 contained in the oxides [21]. A previous XAS study by Liu et al. indicated nearly equal amounts of $Y_2Ti_2O_7$, Y_2TiO_5, and Y_2O_3 [22]. However, the remaining dissolved Ti complicated the XAS analysis. Here, we build on this work using a bulk extraction method to remove the matrix and isolate one of the NOs of interest.

Experimental

The steps involved in the bulk extraction procedure used to isolate the NOs are outlined in Fig. 1. MA957 was placed in a platinum wire mesh (Figure 1a) and submerged into a 1 L solution composed of 100 mL acetyl acetone, 10 g of tetra methyl ammonium chloride, with a balance of methanol. A 20 V potential was used to dissolve the MA957 matrix. The non-acetic solution is dark red at the end of the 24 h process (Figure 1b). A 100 nm-pore filter was then used to remove larger particles (not shown in Figure 1). The remaining liquid was drained through a polysulfone 10 nm-pore filter for 50 h. Filtering was accelerated by connecting a fume-hood vacuum under the filtration capsule (Figure 1c). The filter containing NOs was used for XAS measurements (Figure 1d). This procedure yields a roughly uniform distribution of NOs on top of the filter, which is ideal for fluorescence-mode XAS analysis.

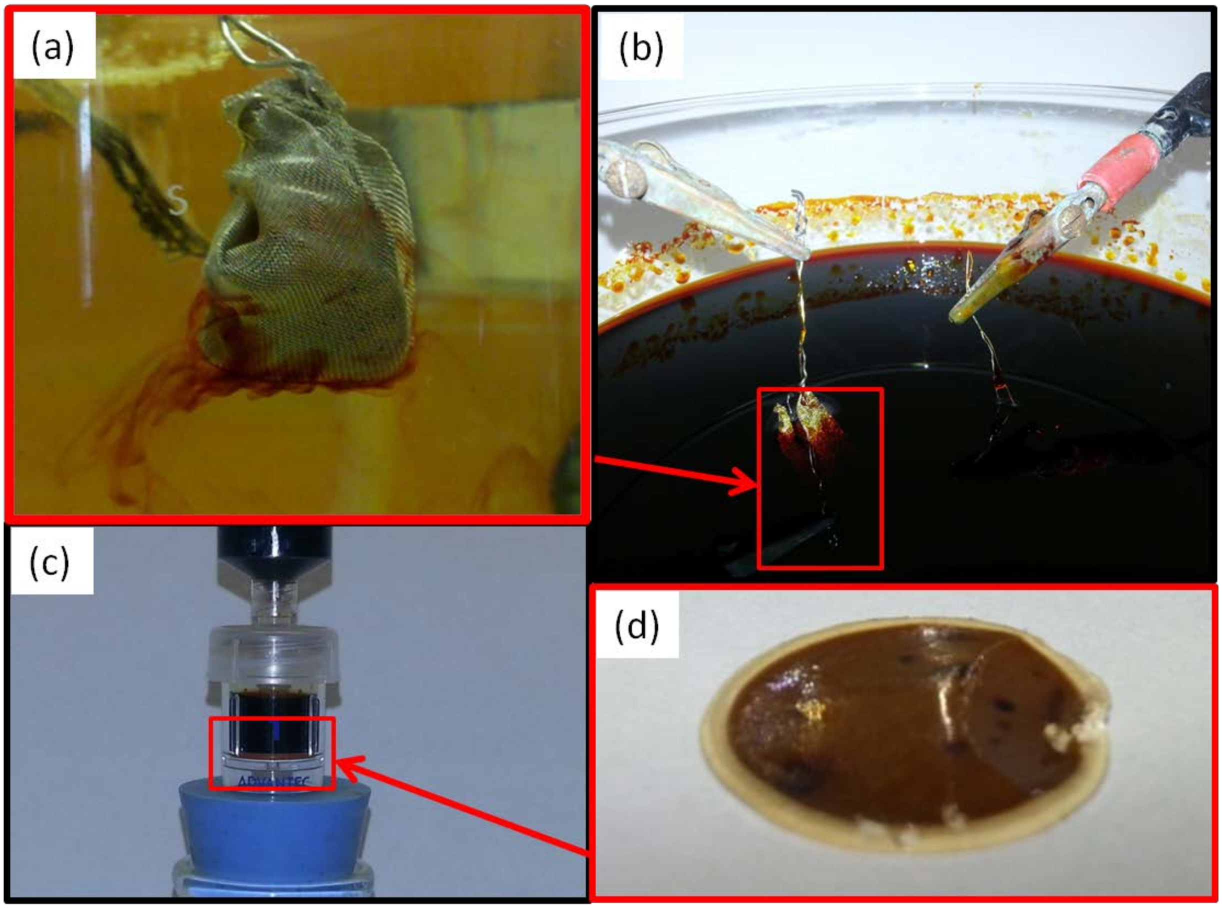

Figure 1. (a) MA957 in platinum wire mesh being dissolved; (b) The initially clear yellow liquid is dark red at the end of the process; the liquid is then pre-treated by 100 nm-pore filtration (not shown); (c) a vacuum under a 10 nm-pore filter is used to accelerate the process; and, (d) the filter containing NOs is removed and used for XAS measurements.

Both as-received MA957 alloy containing embedded NOs, and filters containing selectively extracted NOs, were studied using XAS fluorescence and transmission-mode measurements at beamline X23A2 of the NSLS at Brookhaven National Laboratory. Ambient temperature XAS spectra were measured at the Ti and Y *K*-edges (4.492 keV and 17.038 keV, respectively), at a photoelectron wavenumber (*k)* value of 13 $Å^{-1}$. Ti metal and Y_2O_3 powder were simultaneously measured in transmission mode for energy calibration. Background subtraction, spectra alignment, and normalization of the extended x-ray absorption fine structure (EXAFS) data were carried out using the ATHENA code [23]. The positions of the Ti and Y edges were determined from the reference absorption spectra using known features. Isolated EXAFS spectra were then Fourier Transformed (FT) over a *k* range of 3.0 – 11 $Å^{-1}$ and back FT over a non-phase-corrected radial distance of 0.9 – 2.4 Å to isolate the first nearest neighbor (NN) atomic shell. Structural parameters were then determined using the model-independent, or log-ratio, method [24]. The model-dependent method (using a combination of Artemis, IFEFFIT and FEFF) was found to be difficult due to the disorder and weak signals present in the samples. The changes in the coordination number (N), bond length (ΔBL), Debye – Waller factor ($\Delta\sigma^2$) and asymmetry parameter (ΔC_3), relative to the bulk standards, were allowed to vary during the fitting. Fitting of the log-ratio of amplitude and phase-difference of the isolated first shell was performed over a *k* range of ~3 – 10 $Å^{-1}$ (depending on the edge) with multiple k-weights to reduce inter-parameter correlations.

Results

The XAS spectra are plotted as absorption versus x-ray energy, and consist of an x-ray absorption near edge structure (XANES) region with a broad edge and, in some cases, a pre-edge peak at lower energy, and an extended x-ray absorption fine structure (EXAFS) oscillating region at energies beyond the edge. The Ti and Y *K*-edge XANES spectra are shown in Figure 2 for the embedded and extracted oxides, along with those for bulk standards. In Figure 2 and Figure 3, some curves have been vertically offset for clarity. The pre-edge peaks and broad features observed in the XANES spectra result from multiple-scattering resonances, and can be used to identify the crystallographic phase, symmetry and oxidation state of the metal ions [25,26]. At the Ti edge in Figure 2a, the Ti atoms in the bulk (embedded) MA957 show a complex mixture of environments, similar to metallic Ti, $Y_2Ti_2O_7$ and TiO. Note the higher intensity in the 4.99 – 5.02 keV range and subtle shifts relative to the bulk standards. In contrast, the extracted NOs show a sharp pre-edge resonance that is more characteristic of the Y_2TiO_5 phase. Additionally, the general shape and the features in the near-edge peak (~4.98 – 5.0 keV) are also most similar to the Y_2TiO_5 phase. These broad features in the XANES spectra may suggest a degree of structural disorder in the extracted NOs due to their relatively small size and complex chemistry. This observation is consistent with other NO studies, where changes in the XANES regions from structural and chemical disorder are reported [27].

The XANES spectra at the Y edge (Figure 2b) show features for the embedded NOs that are almost identical to the $Y_2Ti_2O_7$ standard. A small Y_2O_3 component may also be present in the embedded NOs as indicated by a subtle increase in intensity between 17.05 – 17.07 keV and 17.10 – 17.12 keV, where Y_2O_3 has similar XANES features. The spectra for the extracted NO again show very broad features that are more consistent with the Y_2TiO_5 phase. Further, the features observed in the XANES Y edge for the extracted NOs are consistent with the Ti edge data and a disordered atomic environment.

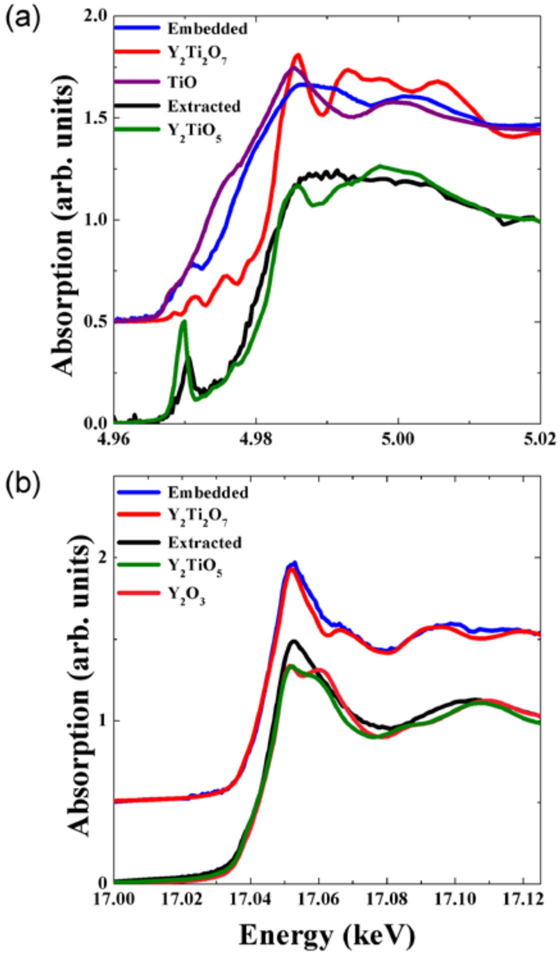

Figure 2. XANES spectra at the *K*-edge for (a) Ti and (b) Y for the embedded and extracted measurements. The TiO_2, Y_2O_3, Y_2TiO_5 and $Y_2Ti_2O_7$ bulk standards are shown for reference.

The magnitude of the Fourier Transformed EXAFS spectra, $|\chi(R)|$ ($Å^{-3}$), for the Ti and Y K-edges are shown in Figure 3a and Figure 3b, respectively. The groups of atoms that are the same radial distance from the absorbers (Ti or Y) are called a shell, and the number of atoms in the shell gives the coordination number. The Ti *K*-edge EXAFS data for the as-received MA957 (embedded) is complex, with multiple environments giving rise to the observed fine structure. For example, the first nearest neighbor at ~1.5 Å in the embedded spectra is attributed to Ti-O bonds (the large intensity is indicative of multiple environments); and the peak at ~2.5 Å is similar in position to the metallic Ti in solution. These features are consistent with previous studies where multiple environments were also observed [22]. The extracted EXAFS show significantly less structure at the Ti edge, with weak signal beyond ~2 Å. The Y *K*-edge EXAFS spectra (Figure 3b) show that atomic environments for the embedded NOs are complex with nearest neighbors shells at ~1.6, 2.4 and 3.4 Å, similar to a mixture of the $Y_2Ti_2O_7$, Y_2O_3 and Y_2TiO_5. The extracted NOs again have a different structure, more closely resembling that of the Y_2TiO_5 and Y_2O_3 phases. The heights of the nearest neighbor shells are, however, much lower in intensity compared to the standards potentially due to larger structural disorder and relatively small NO sizes.

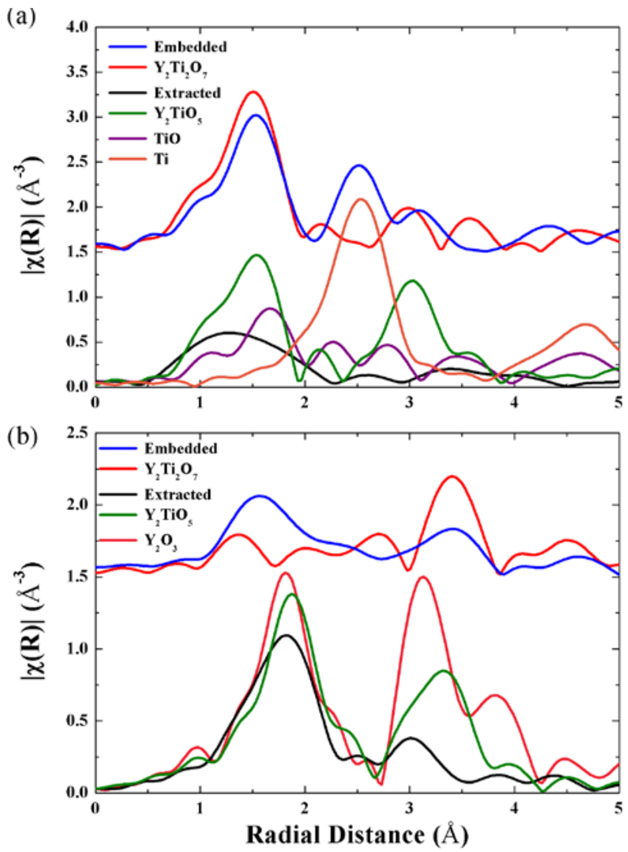

Figure 3. Fourier transform EXAFS for embedded, extracted and standards for (a) Ti *K*-edge and (b) Y *K*-edge.

The quantitative EXAFS fitting results in Table 1 show the coordination number (N), bond length (ΔBL), Debye – Waller factor ($\Delta\sigma^2$) and asymmetry parameter (ΔC_3) for the NOs as compared to standards. The relative changes in the structural parameters are also given for the different standards at both the Ti and Y *K*-edges. The Ti edge for the as-received (embedded) case has a large coordination number compared to the standards due to overlapping environments of the TiO and $Y_2Ti_2O_7$ phases. The changes in the Ti-O bond length were smaller for the $Y_2Ti_2O_7$ phase, consistent with the discussion above. The quantitative analysis at the Y edge indicates a mixture of the Y_2O_3 and $Y_2Ti_2O_7$ phases. However, the multiple overlapping environments in the embedded case (and large TiO and Y_2O_3 particles) hinder a full quantitative description of the structural parameters for both Ti and Y edges (note, this is not the ideal case for the model-independent method where an isolated first shell is needed).

The Ti *K*-edge quantitative results for the extracted NOs show a lower coordination number compared to the Y_2TiO_5 and TiO standards. An increase in the σ^2, slight bond length expansion and increase in asymmetry were also observed. The extracted NO structural parameters at the Y edge show similar trends, with a decrease in the coordination number, subtle changes in bond length and increase in σ^2. The results at both edges again indicate that the extracted NOs have a structure similar to Y_2TiO_5 phase (albeit with slightly different N, BL and σ^2). All the structural changes are consistent with the atomic environment commonly observed for NOs, where an increase in the surface-to-volume ratio results in an under-coordinated and reconstructed surface [27,28].

Table 1. Quantitative results from the EXAFS fitting indicating coordination number (N_{NO}/Ns), bond length (ΔBL), Debye – Waller factor ($\Delta\sigma^2$) and asymmetry parameter (ΔC_3). The subscripts NO and S are for Nano Oxide and Standard, respectively. *The embedded sample has multiple Ti and Y environments, and overlapping first nearest neighbor shells. The values for the embedded samples are an average of the multiple environments.

Nano Oxide	Edge	Standard	N_{NO}/N_S	($BL_{NO} - BL_S$) Å	($\sigma^2_{NO} - \sigma^2_S$) x$10^{-3}$ Å^2	($C_{3NO} - C_{3S}$) x10^{-4} Å^3
Embedded*	Ti	$Y_2Ti_2O_7$	0.96 (0.01)	0.0924 (0.001)	3.69 (0.13)	3.7 (0.3)
Embedded*	Ti	Y_2TiO_5	1.10 (0.05)	0.156 (0.001)	3.56 (0.13)	11.8 (0.2)
Embedded*	Y	Y_2TiO_5	0.64 (0.02)	0.058 (0.002)	4.74 (0.62)	34.8 (0.4)
Embedded*	Y	Y_2O_3	0.65 (0.03)	0.083 (0.001)	5.42 (0.7)	31.8 (0.3)
Extracted	Ti	Y_2TiO_5	0.55 (0.04)	0.039 (0.003)	2.93 (0.047)	15.4 (0.6)
Extracted	Ti	TiO	0.60 (0.03)	0.076 (0.002)	2.46 (0.037)	13.1 (0.4)
Extracted	Y	Y_2TiO_5	0.98 (0.07)	-0.005 (0.001)	4.82 (0.36)	2.7 (0.2)
Extracted	Y	Y_2O_3	0.87 (0.06)	0.037 (0.001)	8.05 (0.29)	2.9 (0.2)

The model-independent EXAFS analysis method is commonly used to extract atomic changes with temperature/pressure and has been used in both crystalline and amorphous materials [29]. The use of the method here, to quantify changes in nearest neighbor distances, is quite advantageous. The first atomic shell for the extracted NOs is well isolated (no multiple scattering paths overlap) and corresponds to common metal-oxygen bond. Thus, quantitative analysis yields information on the structural state of the NOs relative to the bulk standards. The combination of the qualitative XANES and quantitative EXAFS results clearly demonstrate that the extraction process is capable of isolating a minor component that is essentially overwhelmed by the large and complex environment observed when the NOs are embedded in a matrix.

The authors are aware that the extraction process may affect the character of the NOs. For example, possible segregation of Ti, O, and Cr to NO interfaces cannot be observed by XAS since the matrix is dissolved during extraction. Further, there may be some restructuring of the extracted NOs when they are released from the matrix. However, such extraction effects are not believed to be significant with respect to the core NOs, since they generally resemble those seen in TEM observations [6].

In conclusion, the chemistries and structures of NOs in NFA MA957 were characterized by XAS for both embedded and extracted precipitates. Measurements on embedded NOs in bulk MA957 are consistent with $Y_2Ti_2O_7$, while the slightly larger extracted oxides are primarily consistent with Y_2TiO_5. Analysis of the as-received MA957 was difficult due to the multiple Ti environments including $Y_2Ti_2O_7$, Y_2TiO_5, TiO, and dissolved metallic Ti. The bulk extraction and selective filtration technique successfully removed the matrix, trapped the larger Y_2TiO_5 particles, and yielded samples well suited for XAS measurements. The smaller $Y_2Ti_2O_7$ oxides passed through the filters but were the predominant embedded phase. This will be further confirmed in the future by XAS measurements on the residues in the filter effluent.

References

[1] G. R. Odette: *JOM*, 2014, vol. 66, p. 2427.
[2] G R Odette and D T Hoelzer: *JOM*, 2010, vol. 62, pp. 84–92.
[3] Steven J. Zinkle and Jeremy T. Busby: *Mater. Today*, 2009, vol. 12, pp. 12–19.
[4] N. Cunningham, Y. Wu, D. Klingensmith, et al.: *Mater. Sci. Eng. A*, 2014, vol. 613, pp. 296–305.
[5] Yuan Wu, Jim Ciston, Stephan Kräemer et al.: *Acta Mater.*, 2016, vol. 111, pp. 108–15.
[6] Y. Wu, E. M. Haney, N. J. Cunningham, et al.: *Acta Mater.*, 2012, vol. 60, pp. 3456–68.
[7] Joël Ribis, Eric Bordas, Patrick Trocellier, et al.: *J. Mater. Res.*, 2015, vol. 30, pp. 2210–21.
[8] S.Y. Zhong, J. Ribis, N. Lochet,et al.: *J. Nucl. Mater.*, 2014, vol. 455, pp. 618–23.

[9] J. Ribis and Y. De Carlan: *Acta Mater.*, 2012, vol. 60, pp. 238–52.
[10] V. Badjeck, M.G. Walls, L. Chaffron, et al.: *J. Nucl. Mater.*, 2015, vol. 456, pp. 292–301.
[11] Karl Dawson and Gordon J. Tatlock: *J. Nucl. Mater.*, 2014, vol. 444, pp. 252–60.
[12] N.J. Cunningham, Y. Wu, A. Etienne, et al.: *J. Nucl. Mater.*, 2014, vol. 444, pp. 35–38.
[13] Emmanuelle A. Marquis: *Appl. Phys. Lett.*, 2008, vol. 93, pp. 10–13.
[14] Ceri A. Williams, Paulina Unifantowicz, Nadine Baluc, et al.: *Acta Mater.*, 2013, vol. 61, pp. 2219–35.
[15] D. J. Larson, P. J. Maziasz, I-S Kim, et al.: *Scr. Mater.*, 2001, vol. 44, pp. 359–64.
[16] M.K. Miller, E.A. Kenik, K.F. Russell, et al.: *Mater. Sci. Eng. A*, 2003, vol. 353, pp. 140–45.
[17] M. Ohnuma, J. Suzuki, S. Ohtsuka, et al.: *Acta Mater.*, 2009, vol. 57, pp. 5571–81.
[18] Myriam Dumont, Lorelei Commin, Isabelle Morfin, et al.: *Mater. Charact.*, 2014, vol. 87, pp. 138–42.
[19] J.J. Fischer: Patent, Feb. 1978.
[20] N. J. Cunningham: *Thesis Univeristy Calif. St. Barbar.*, 2012.
[21] M.J. Alinger, G.R. Odette, and D.T. Hoelzer: *Acta Mater.*, 2009, vol. 57, pp. 392–406.
[22] S. Liu, G.R. Odette, and C.U. Segre: *J. Nucl. Mater.*, 2014, vol. 445, pp. 50–56.
[23] B Ravel and M Newville: *J. Synchrotron Radiat.*, 2005, vol. 12, pp. 537–41.
[24] Grant Bunker: *Nucl. Instruments Methods Phys. Res.*, 1983, vol. 207, pp. 437–44.
[25] L A Grunes: *Phys. Rev. B*, 1983, vol. 27, pp. 2111–31.
[26] Francois Farges, Gordon E Brown, and J J Rehr: *Phys. Rev. B*, 1997, vol. 56, pp. 1809–19.
[27] L L Araujo, R Giulian, D J Sprouster, et al.: *Phys. Rev. B*, 2008, vol. 78, p. 94112.
[28] Anatoly I. Frenkel, Charles W. Hills, and Ralph G. Nuzzo: *J. Phys. Chem. B*, 2001, vol. 105, pp. 12689–703.
[29] P Fornasini, S a Beccara, G Dalba, et al.: *Phys. Rev. B*, 2004, vol. 70, p. 174301.

2.3 ESTIMATES OF THE THOUGH THICKNESS RESIDUAL STRESSES IN THE AS-PROCESSED NFA-1 PLATE BASED ON NANOINDENTATION MEASUREMENTS—S. Pal, M. E. Alam and G. R. Odette (UCSB)

OBJECTIVE: The aim of the present study is to quantify the residual stresses that develop in deformation processed NFA-1 plate using a simple nanoindentation technique.

SUMMARY

Hardness and modulus of the as processed NFA-1 alloy plate have been measured using nanoindentations, including to probe the nature and magnitude of the residual stresses generated by thermo-mechanical processing. The residual stresses were quantified from the nanoindentation load-penetration curves. The plate surfaces (and adjoining mild steel can) are in compression, while the middle of the plate is in tension. The magnitude of the maximum tensile residual stress is ≈ +500 MPa, decreasing to ≈ +75 MPa near to the plate surface; and ≈ -30 MPa at the surface of the can. A microcrack population area density, lying perpendicular to the short thickness direction of the plate, tracks the residual tensile stress profile. The surface residual stresses were further quantified using a conventional $\sin^2\psi$ x-ray diffraction (XRD) method that yielded a value similar to the nanoindentation estimate.

PROGRESS AND STATUS:

Introduction

Nanostructured ferritic alloys (NFAs) are an attractive structural material for advanced nuclear fission and fusion applications due to their unique radiation tolerance, high-temperature strength, high fracture toughness and remarkably low value of the brittle to ductile transition [1,2]. However, bulk processing of NFA is extremely difficult due to a highly anisotropic α-fiber texture [3]. UCSB has collaborated with LANL and ORNL to develop a large heat NFA 14YWT variant called FCRD NFA-1. The extruded and cross rolled NFA-1 plate contains a large population of microcracks lying perpendicular to the short thickness direction, which runs in the primary deformation directions. Our previous investigation showed that during high-temperature thermo-mechanical processing, stress concentrations develop ahead of the dislocation pile-ups at {001}<110>-type low angle tilt boundaries. The tilt boundaries are composed of sessile <001> dislocations formed by reactions between two <111> dislocations gliding on {110} planes. The dislocation pile-ups lead to high-stress concentrations, and the summed Burger's vectors can directly nucleate a nano-scale crack. The {001}<110> boundary is also a low toughness brittle cleavage system for the crack nuclei. Thus residual stresses, that develop during thermo-mechanical processing, drive nano-to-micro cleavage crack propagation. The presence of residual stresses in the cracked region was previously qualitatively shown using selected area diffraction, by streaking of the diffraction spots [3]. Therefore, it is critically important to better quantify the residual stresses. Here, we use a simple nanoindentation technique to estimate the residual stresses based on a method proposed by Suresh et.al [5], as well as using a standard XRD $\sin^2\Psi$ method applied to the top surface of the canned plate. We show that the though-thickness microcrack density variation approximately tracks the residual stress profile.

Materials and Methods

A larger NFA heat, called FCRD-NFA-1, containing 14Cr-3W-0.4Ti-0.3Y and balance Fe was studied. NFA-1 was developed in a close collaboration between UCSB, LANL, and ORNL. NFA-1 was consolidated by hot extrusion at 850°C, then annealed, and hot cross-rolled at 1000°C perpendicular to the extrusion direction to a final plate plus can thickness of 12.5 mm.

The nanohardness (NH) and reduced modulus (E_r) of the as processed NFA- plate were measured using a nanoindenter (Hysitron, Tribo-indenter). Depth sensing instrumented nanoindentation provides a load versus penetration P-h curve. The P-h curve not only characterizes the NH and E_r, but can also provide information on strain hardening, creep, bi-axial residual stresses and yield strength. Here we evaluate the bi-axial residual stresses present in the as processed NFA-1 alloy following the methodology proposed by Suresh et al. [5].

Figure1 shows a typical nanoindentation P-h curve obtained, where h_f is the final plastic depth and h_{max} is the maximum depth of penetration. The method of calculating hardness and modulus of a material from the P-h curve was first proposed by Oliver and Pharr [6].

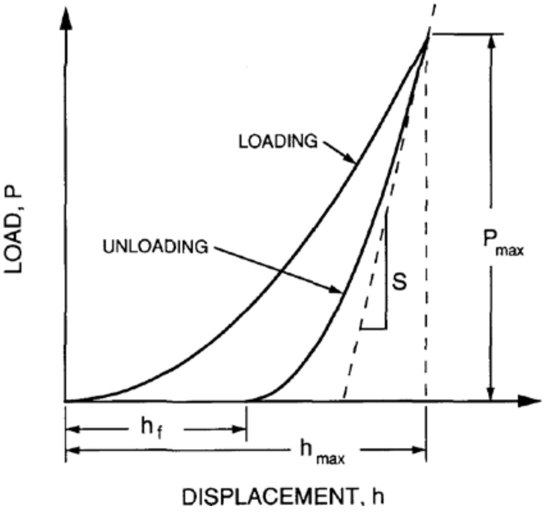

Figure 1. Schematic illustration of a typical nanoindentation load-displacement (P-h) curve.

The reduced Young modulus (E_r) of an indented substrate is related to the slope (S) of the initial unloading P-h curve and the contact area (A_r) between the indenter and the indented material as:

$$S = \frac{dP}{dh} = \frac{2}{\sqrt{\pi}} * \sqrt{A_r} * E_r \tag{1}$$

The reduced modulus, E_r, is given by,

$$\frac{1}{E_r} = \frac{1-\nu^2}{E} + \frac{1-\nu_i^2}{E_i} \tag{2}$$

Here the E and E_i are the Young moduli of the indented and indenter, and ν and ν_i are the Poisson ratios of the indented and indenter, respectively. The slope of the unloading portion of the load-displacement curve is determined by least squares fitting:

$$P = A(h - h_f)^m \tag{3}$$

Typical values of *m* fall in the range of 1.2 to 1.6, depending upon the material. Therefore, we have considered only those load-displacement curves with *m* in that range. The NH is the average contact pressure at the maximum load, defined by,

$$H = \frac{P_{\max}}{A_r} \tag{4}$$

If the indentation region is subjected to an equi-biaxial residual stress, the shape P-h curve is modified relative to a stress-free case as illustrated in Figure 2.

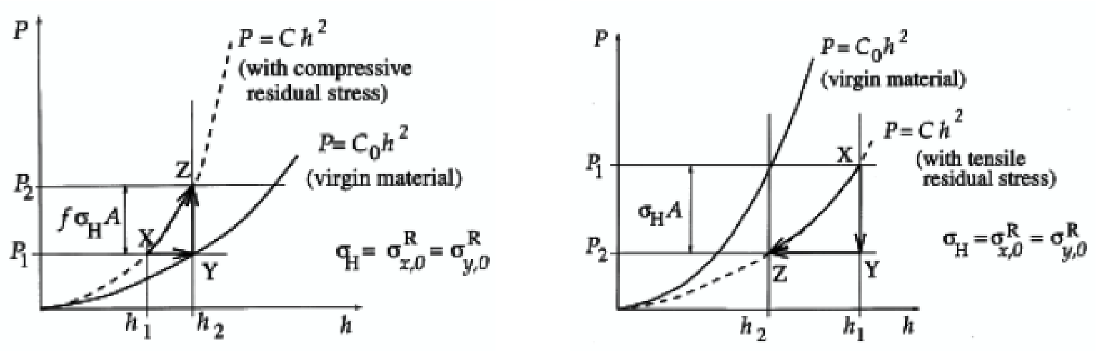

(a) **(b)**

Figure 2. Schematic illustration of the P-h curves of unstressed (virgin) material and for compressive (a) and tensile (b) residual stresses [5].

The basic physics of the modification of the P-h loading curves is easy to understand as illustrated in Figure 3. If the region is under compression it takes a higher load, P, to produce a given indentation depth, while P is lower in the case of a tensile stress. Expressions describing the effect of residual stress on the curvature of the load-displacement curve, expressed in terms of the average contact pressure and area (hardness), were derived by Suresh et. al [5].

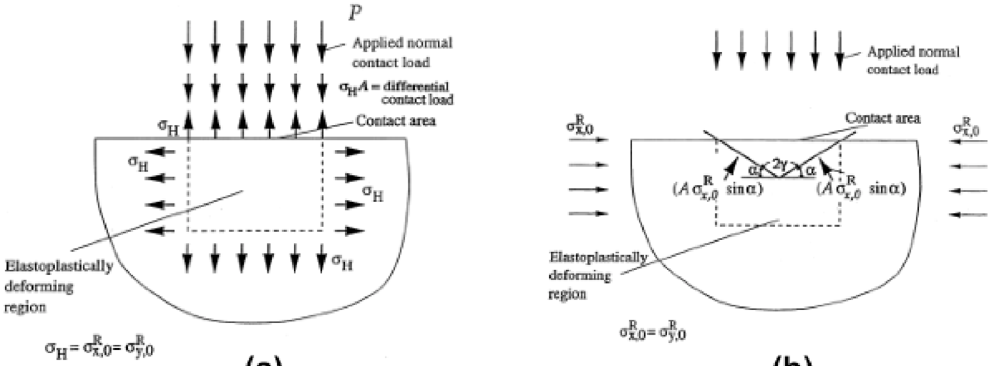

(a) **(b)**

Figure 3. Schematic illustrations of the role of elastic residual stresses at the indented surface that are: a) tensile; and, b) compressive [5].

The hardness of a material defines its ability to resist plastic deformation. For a sharp indenter, the amount of plastic strain is not affected by pre-existing elastic residual stress. However, for an elastoplastic material, the apparent contact area changes in the presence of a residual stress. For a specified indentation depth, a tensile residual stress adds a hydrostatic stress component, σ_H, to the indentation stress tensor, including a component in the loading direction. The same hydrostatic stress is subtracted in the case of constant load indentation. Similarly, compressive residual stress can either add or subtract a hydrostatic stress component, $\sigma_H \sin\alpha$, along the direction of indentation. How an elastic bi-axial residual stress on the indented surface is equivalent to either tensile or compressive hydrostatic stress component is illustrated in Figure 3. Therefore based on the equivalence of the mean contact pressure and the relation between apparent contact area, residual contact stress and mean contact pressure was established. The change in contact area due to elastic residual stress is related to mean contact pressure as:

$$\frac{A_r}{A_0} = \left(1 - \frac{\sigma_H}{P_{ave}}\right)^{-1} \quad \text{for a tensile residual stress} \qquad (5)$$

$$\frac{A_r}{A_0} = \left(1 - \frac{\sigma_H \sin\alpha}{P_{ave}}\right)^{-1} \quad \text{for a compressive residual stress} \qquad (6)$$

Here, α is the semi-apex angle of the indenter. For the sharp Berkovich indenter α = 24.8°, A_0 is the contact area between the indenter for a residual stress-free condition, and P_{ave} is the corresponding average contact pressure, or hardness [5].

Through thickness microstructural characterization of the NFA-1 plate at different plate views were carried out using FIB-SEM (Helios600, FEI), and has been reported previously [7]. Residual stress measurements using XRD were also carried out in a two-axis goniometer instrument (XPertPro, PAN-Analytical) using CuKα radiation. The (112) planes, with a peak in bcc Fe occur at 2θ = 83.219°, was chosen to measure changes in the lattice spacing, because of the higher sensitivity of the measurement at a large Bragg angles. Since the NFA-1 alloy has a strong texture, an initial θ-ω scan was performed to identify the ω angle with a maximum intensity for the (112) peak. The d-spacing measurements were performed using θ-2θ scan with a series of positive and negative ψ tilt.

Results

Figure 4 shows a schematic of the NFA-1 plate deformation directions. The residual stress profile developed in the short thickness direction of the plate was measured on a 45° cut section surface.

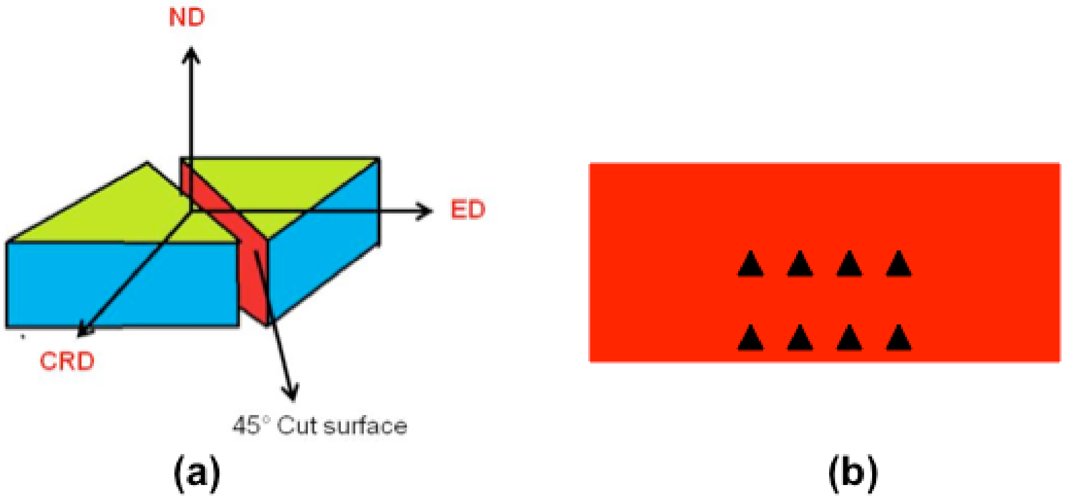

Figure 4. Schematic illustration of the: a) plate geometry and the deformation directions for the observed 45°cut plate section; and, b) the locations of nanoindentations for 45ºC surface.

Determination of the residual stress from the nanoindentation load-displacement curve requires a stress-free standard. Therefore a small rectangular specimen was cut from the thickness direction of the plate and annealed at 1000°C for 5h to relax the residual stresses present in the specimen. The standard sample was chosen from the thickness direction of the plate to maintain a microstructural and textural similarity between the stressed and standard stress-free specimens. The annealing condition was chosen in such a way that it does not change in the microstructure of the specimen. It was previously reported that even a 32.4 kh treatment of a NFA alloy at 1000°C causes only minimal change in its microstructure [1]. Figure 5 displays the measured hardness and modulus of the 45° cut surface from the as-processed plate, and, 1000°C/5h annealed specimen which is used as a residual stress-free standard for the present case. The annealed specimen has the highest hardness, whereas the modulus remains same considering standard deviation. Variation in the hardness in the plate thickness occurs due to the presence of residual stress, whereas the magnitude of the residual stress also varies along the thickness. This affect the overall hardness of the 45°cut specimen, when it is measured from the different locations.

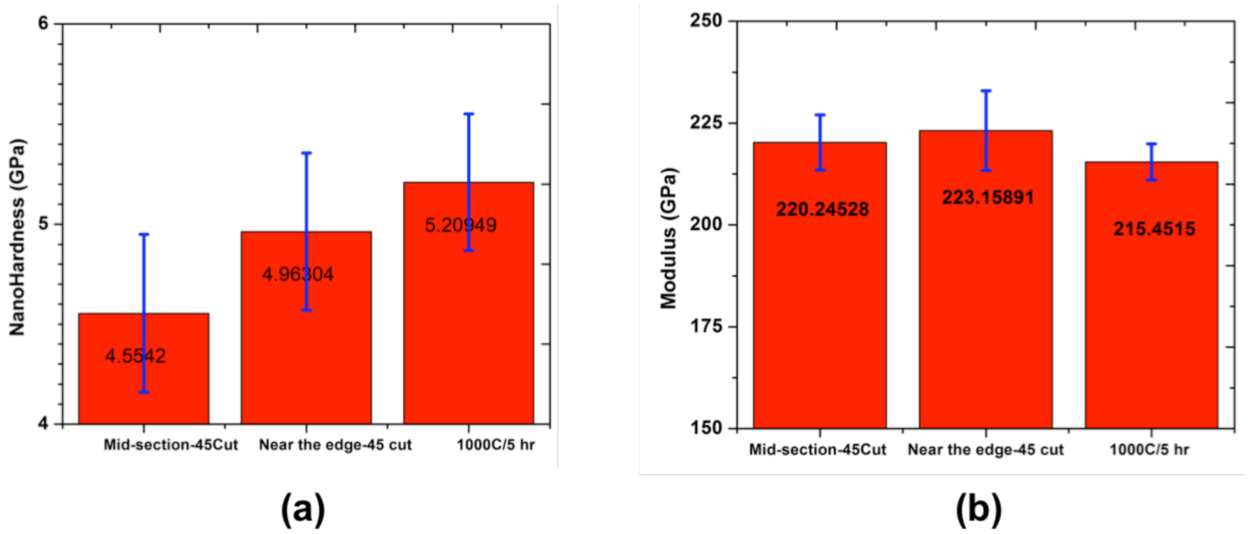

Figure 5. The NH (a) and E_r (b) for the different indent locations and specimen conditions.

Representative load-displacement curves for the three indented specimens are shown in Figure 6. The curvature of the loading portion of the load-displacement curve depends on the nature of the residual stress (compressive or tensile) in the indented region, again as described by Suresh et. al [5]. Clearly, the P-h curves are lower in the as-processed plate compared to the 1000°C/5 h heat-treated, nominally stress-free specimen. Therefore, the as-processed plate has a tensile residual stress profile in the thickness direction.

The curvatures of the loading P-h curve for the three indented specimens were least square fit using a generalized Kick's law [8], where the P is related to h as:

$$P = Ch^{n} \qquad (7)$$

Here *C* reflects the magnitude of the loading curve and n is an empirical exponent that depends on the indenter geometry. The values for C and n are given in Table 1. The best-fit n is ≈ 1.65 in all three cases, consistent with significant strain hardening [9]. Equations 5 and 6 hold for n = 1.65, and the residual stress is given by Eq. 5. The contact areas and average contact pressures, or hardness values, were evaluated from the load-displacement curves shown in Figure 7. The curvatures of the loading portions of the P-h curves, determined by the second derivative of Eq. 7 at a fixed depth of 200 nm, are also given in Table 1. The estimated magnitudes of the residual stresses ranging from ≈ 500 MPa in the middle to ≈ 75 MPa near the plate edge. Note the plate is contained inside a can so it is expected that compressive residual stresses would exist near the canned plate surface.

These residual stress estimates are very approximate, but are consistent with results in the literature, for example for cold-rolled ferritic steel in Reference [10]. The residual tensile stresses drive microcrack propagation. And, notably, the estimated stress distribution crudely tracks the through thickness variation of the microcrack density illustrated in the low magnification FIB-SEM images in Figure 8. Figure 9 shows the variation of the microcrack areal density in the plate thickness direction. The center of the plate is zero, and the distances from center of the plate to both edges are normalized by the plate thickness. The distribution is not symmetric, and peaks between the center and one of the edges of the plate. However, the middle half section of the plate has the highest crack density and the maximum residual tensile stress, whereas near to the plate edge both the crack density and the residual tensile stresses are lower.

The residual stresses in the top surface of the canned plate were also measured by the XRD $\sin^2\psi$ method [11] and found to range from ≈ -29 (compression) to +64 (tension). Details of this analysis will be reported in the future along with through-thickness measurements that are planned. The qualitative variation the residual stress is shown in Figure 10.

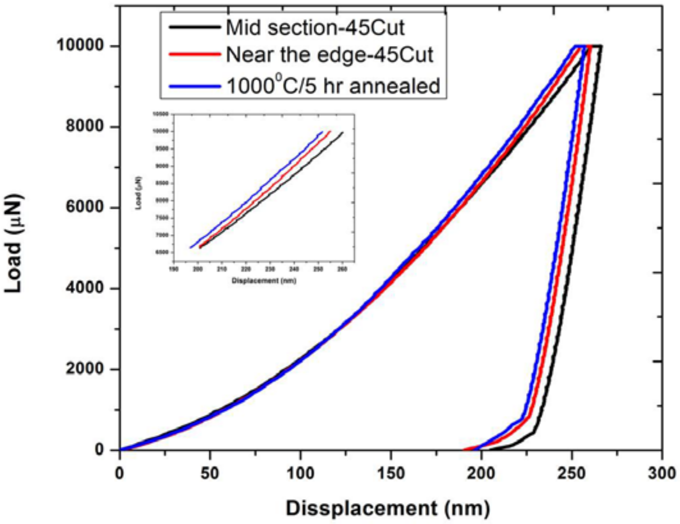

Figure 6. P-h curves obtained near the edge, and midsection of the cross-rolled plate section, as well as the 1000°C/5 h, annealed reference specimen. The inset shows a magnified view of the loading curve.

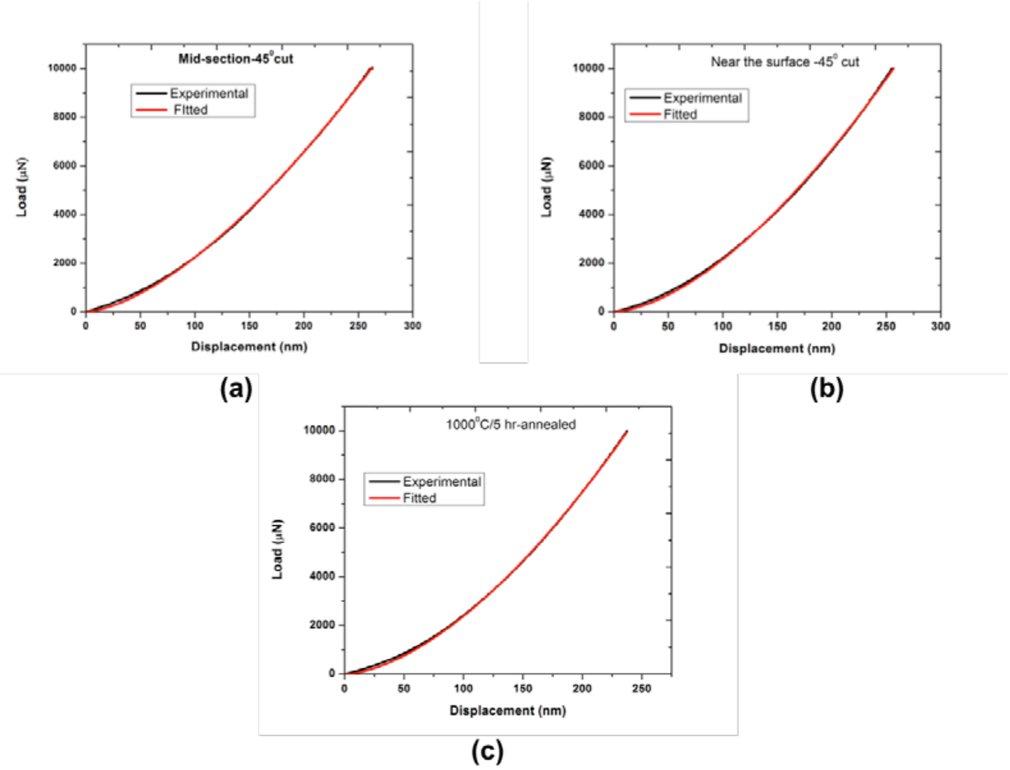

Figure 7. Least square fits to the loading indentation curves in Fig. 6: a) 1000°C/5 h; b) mid-plate; and, c) near edge.

Table 1. Least square fits of C, n, curvature of the loading portions (measured by taking double derivative of the curve at a fixed depth of 200 nm) and the corresponding estimated residual stress.

Locations /Conditions	**C**	**n**	**Curvature @200 nm**	**Residual stress (MPa)**
Mid-thickness	0.937	1.66	1.03	496
Near the edge	0.943	1.67	1.06	75
1000°C/5 hr	1.167	1.66	1.26	-

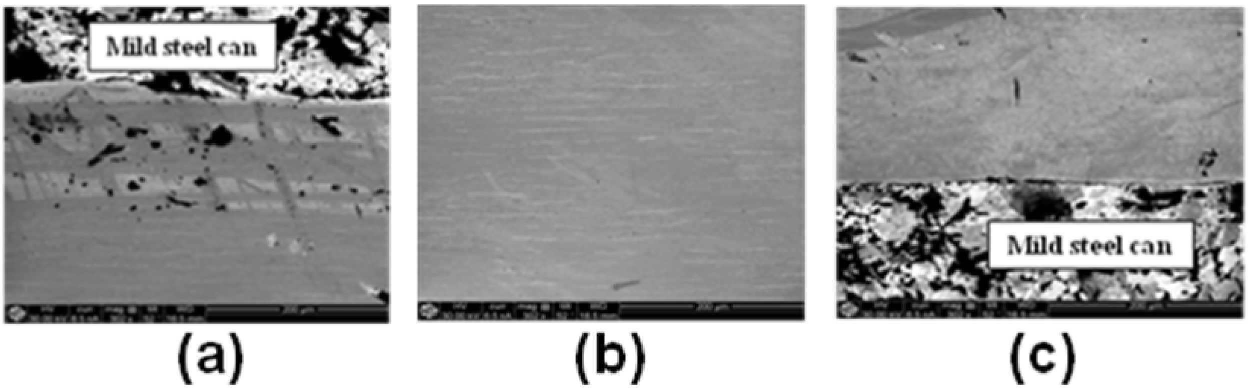

Figure 8. FIB-SEM low magnification micrographs of the of the plate thickness section: a) near the top edge; b) midsection; and, c) near the bottom edge. The mild steel can is clearly visible in the images.

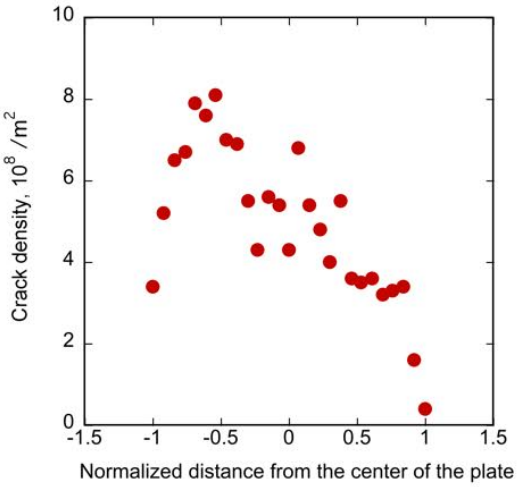

Figure 9. The crack areal density distribution profile through the plate thickness. The center of the plate is zero, and the distances from center of the plate to both edges are normalized by the plate thickness.

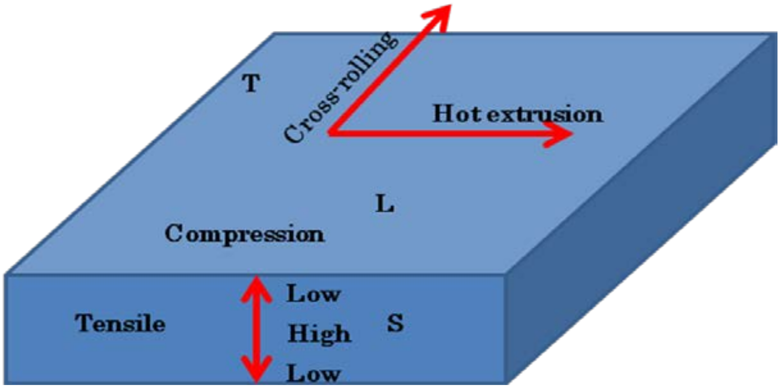

Figure 10. A schematic illustration of the NFA-1 plate showing the residual stress profiles along the different direction.

Summary and Discussion

We reported for the first estimates of the residual stress distribution in the as-processed NFA-1 plate. The results are qualitative and very approximate, but show robust trends. The mid-thickness region of the plate exhibits a very high tensile residual stress nominally ≈ +500 MPa, coincident with a very high micro-crack population area density. The residual tensile stresses near the edge of the canned plate are ≈ +75 MPa with a correspondingly low microcrack density. XRD techniques were used to characterize the stresses on the top surface of the canned plate that were also low and in one case compressive. Future residual stress measurements will be carried out at synchrotron x-ray and neutron facilities.

Acknowledgments

Acknowledge fusion, NEUP, LANL, and FCRD funding and the contributions of Hoelzer and Maloy in developing NFA-1.

References

[1] G. R. Odette, "Recent Progress in Developing and Qualifying Nanostructured Ferritic Alloys for Advanced Fission and Fusion Applications," *JOM,* vol. 66, pp. 2427-2441, 2014.

[2] M. E. Alam, N. J. Cunningham, D. Gragg, K. Fields, G. R. Odette, D. T. Hoelzer and S. A. Maloy, "Mechanical Properties Characterization of a Larger Best Practice Heat o f14YWT NFA-1," *Fusion Reactor Materials Program,* vol. 56, pp. 63-69, 30 June 2014.

[3] S. Pal, M.E. Alam, G. R. Odette, D. T. Hoelzer and S. A. Maloy (LANL) "Characterization of the Microstructure and Texture of NFA-1 for Two Deformation Processing Routes", *Fusion Reactor Materials Program*, Vol. 58, pp. 66-82, 30 June 2015.

[4] S. Pal, M.E. Alam, G. R. Odette, J. Lewandowski, D. T. Hoelzer and S. A. Maloy (LANL) "Characterization of the Microstructure and Texture of NFA-1 for Two Deformation Processing Routes", *Fusion Reactor Materials Program*, Vol. 58, pp. 29-41, 30 June 2015.

[5] S.Suresh, A.N. Giannakopoulus, "A new method of emstimating residual stress by instrumented sharp indenation", Acta Materialla, vol. 46, pp. 5755-5767, 1998.

[6] W.C.Oliver and G.M.Pharr, "An improved technique for determining the hardness and modulus using load and displacement sensing indentation experiments" J. Mater. Res., Vol. 7, 1564-1583, June 1992.

[7] M. E. Alam, S. Pal, D. Gragg, G. R. Odette, D. T. Hoelzer and S. A. Maloy, "Microstructural and Mechanical Behavior of As-Fabricated and Annealed 14YWT NFA-1 Alloy," *Fusion Reactor Materials Program,* vol. 59, December 31, 2015.

[8] F.Kick,” Das Gesetz der proportionalen Widerstände und seine Anwendung auf Sanddruck und Sprengen” Dinglers Polytechnisches Journal, vol. 250, pp.141-145, 1983.

[9] S. V. Hainsworth, H. W. Chandler, and T. F. Page, “Analysis of the nanoindentation load-displacement curve” J. Mater. Res., Vol. 11, 1987-1995, August 1996.

[10] J.M. Atienza , M.L. Martinez-Perez , J. Ruiz-Hervias, F. Mompean , M. Garcia-Hernandez , M. Elices “ Residual stress in cold drawn ferritic rods” Scripta Materialia, Vol. 52, pp. 305–309, 2005.

[11] C. Balasingh and A.K.Singh, “Residual stress and their measurements by X-ray diffraction methods” Metals, Materials and Processes, vol. 12, pp. 269-280, 2000.

2.4 CHARACTERIZATION OF FE THIN FILMS ON {100} ORIENTED $Y_2Ti_2O_7$ SUBSTRATES

—T. Stan, Y. Wu, G.R. Odette (University of California Santa Barbara), and H.D. Zhou (University of Tennessee)

OBJECTIVE

The objective of this work is to gain insight into the oxide-matrix interfaces found in Nanostructured Ferritic Alloys by studying the meso-scale Fe - {100} oriented $Y_2Ti_2O_7$ substrate bilayers.

SUMMARY

Nanostructured Ferritic Alloys (NFAs), a variant of oxide dispersion strengthened steels, contain a high density ($\approx 5x10^{23}/m^3$) of ≈ 2.5 nm average diameter Y-Ti-O nano-oxides (NOs) which help impede dislocation climb and glide, stabilize dislocation and grain structures, and trap He in fine-scale bubbles at matrix-NO interfaces. To complement other studies of the NOs themselves, mesoscopic-scale bilayer interfaces were fabricated by electron beam deposition of a thin Fe film on a {100} $Y_2Ti_2O_7$ (YTO) bulk single crystal substrate. These bilayers were prepared for He implantation and charged particle irradiations to experimentally observe defect interface interactions and the partitioning of He between the Fe, YTO, and the associated interface. We report, for the first time, the dominant epitaxial orientation relationship (OR) for a polycrystalline Fe film on {100} YTO: $\{110\}_{Fe}\backslash\backslash\{100\}_{YTO}$ and $<100>_{Fe}\backslash\backslash<110>_{YTO}$. One large grain region had an OR that is also found in embedded NOs: $\{100\}_{Fe}\backslash\backslash\{100\}_{YTO}$ and $<100>_{Fe}\backslash\backslash<110>_{YTO}$. HRTEM studies show clean semicoherent interfaces, with misfit dislocation spacings consistent with the calculated near coincidence site lattices.

PROGRESS AND STATUS

Introduction

Materials for nuclear fusion applications must reliably perform at high temperatures and accommodate high levels of helium (He) and displacement damage. Nanostructured Ferritic Alloys (NFAs) are a promising class of Fe-Cr-based stainless steels with outstanding mechanical properties, are thermally stable up to 950°C, and are remarkably irradiation tolerant [1–4]. NFAs contain a high density of $N \approx 5x10^{23}/m^2$ of YTO nano-oxides with an average diameter of $<d> \approx 2.5$ nm. The NOs impede dislocation climb and glide, stabilize dislocation and fine grain structures, and most notably, trap He in fine-scale bubbles at the matrix-NO interfaces. The high density of bubbles prevents the formation of growing voids and He accumulation at grain boundaries, which would otherwise degrade the dimensional stability, creep and fracture properties of most structural alloys, as is the case for conventional 9 Cr tempered martensitic steels. He bubbles also act as recombination sites for vacancies and self-interstitials, thus promoting radiation damage self-healing.

Research to characterize NO compositions, structures, misfit strains, core shell structures, interface characteristics, and NO-matrix orientation relationships (ORs) is continuing [5–8]. Most of the smallest NOs are the $Y_2Ti_2O_7$ (YTO) fcc pyrochlore phase [7–15]. Detailed characterization and analysis of the NO-matrix interfaces is needed to develop first principles and atomic-scale models that are part of multi-scale efforts to guide the selection of processing paths and to predict the behavior of NFAs and NOs in irradiation service environments. YTO-matrix ORs are of particular interest, because they impact the selection of compositions and processing paths, service stability, mechanical properties and irradiation tolerance of NFAs. Important interface characteristics include their structures, chemistries, defects, misfit strains, free energies and, perhaps most importantly, NO interactions with He. The embedded NOs and their interfaces are challenging to characterize, partly due to their small nm-scale size.

A comprehensive first principles study by Jiang et al. [16–18] showed that He is deeply trapped in the YTO NOs at an energy of ~1.4 eV lower than in the Fe-Cr matrix. Coupled with the ultra high NO sink strength, this ensures that the eventual fate of He is to reside in nm-scale bubbles on the oxide interfaces. The sequence of events is as follows. First He migrates to, and is deeply trapped in, the NOs. However, the He energy is even lower in sufficiently sized NO-matrix interface bubbles, that quickly nucleate and grow, thereby draining the He from the NOs. Thus characterization of the matrix-NO-interface He partitioning is critically important and is one of the major goals of the experiment described below.

To study the He transport and fate in a controlled fashion, our approach was to deposit Fe on oriented YTO single crystal substrates to create bilayers with mesoscopic-scale interfaces that facilitate detailed characterization studies. Ideally, the bilayer interfaces are the same, or similar to, those found in the embedded NOs. One such interface was found in the bilayer fabricated here, although another orientation relationship was the dominant naturally selected interface. As well as facilitating He and point defect transport and fate studies, characterization of the Fe-YTO interfaces will provide input to first principles interface modeling.

We previously reported a study of Fe deposited on {111}YTO [19]. However, {111}YTO interfaces are not usually observed in the embedded NOs. The following results are for Fe depositions on {100}YTO substrates are a significant extension of previous research. The naturally selected bilayer interfaces were characterized and compared to NOs in NFAs.

Experimental Procedure

The details of sample fabrication and characterization techniques are covered in a previous publication [19]. The feed rods for the YTO single crystal growth were prepared by solid state reactions. Appropriate mixtures of Y_2O_3 and TiO_2 were ground together, and pressed into 6 mm diameter, 60 mm long, rods under a 400 atm hydrostatic pressure, followed by calcinations in air at 1673 K (1400°C) for 24 hrs. The Czochralski growth was carried out in 5 atm oxygen in an IR-heated image furnace (NEC) at a rate of 3 mm/hr. The YTO single crystals were oriented with a {100} surface and corresponding 2 mm thick wafers were cut from the rod using a wire saw.

An Allied Multiprep was used to polish the wafers using a sequence of diamond lapping films, followed by a final 15 minute polishing step using a 0.02 µm non-crystallizing colloidal silica suspension. The substrates were then placed in an ultrasonic bath with 90% reverse osmosis water and 10% Micro-Organic soap. This was followed by an acetone ultrasonic bath for 10 minutes, and finally an isopropanol ultrasonic bath for 10 minutes.

The YTO single crystal wafer was loaded into an electron beam deposition system and heated to 1073 K (800°C) at a rate of 0.166 K/s. After outgassing for 1 h, 2 µm of Fe was deposited at a rate of ~8 nm/s (250 s total) at chamber pressure of 3 x 10^{-6} torr. After deposition the Fe-YTO bilayer was annealed in vacuum at 1073 K (800°C) for 30 min. The Fe-{100}YTO substrate bilayer was slowly cooled to room temperature prior to unloading.

Electron backscatter diffraction (EBSD) pole figures, orientation maps, and 3D representations were obtained using a FEI Quanta 400F field-emission scanning electron microscope (SEM). A FEI HELIOS Focus Ion Beam (FIB) tool was used to first deposit ~1 µm of protective platinum over areas of interest. <30 nm thick lift-outs of the Fe-YTO interface were extracted, and a low energy 2 keV 5.5 pÅ gallium beam was used for the final cleaning. Hig-resolution transmission electron microscopy (HRTEM), scanning TEM (STEM), and energy dispersive xray (EDX) observations were carried out on a 300 keV FEI Titan TEM. CrystalMaker software was used to analyze the bulk lattice matching.

Results

SEM and EBSD Characterization

The 2 µm thick Fe film had two dominant morphologies: a larger {110}Fe polycrystalline region covering ~99% of the deposit, and a smaller (100 µm x 100 µm) {100}Fe monocrystalline grain. The monocrystalline grain is of particular interest because it has an OR found in embedded NOs (as discussed below). The multipart Figure 1 and Figure 2 show Scanning Electron Microscopy (SEM) and Electron Backscatter Diffraction (EBSD) data from the two films. Note the figures are equally scaled and formatted to facilitate side-by-side comparisons.

Figure 1 shows SEM and EBSD data from the polycrystalline side. Figure 1a is a SEM image showing that the polycrystalline Fe layer is comprised of 1 – 3 µm grains. Ledges are seen on the surface of some grains. The EBSD inverse pole figure (IPF) map in Figure 1(b) shows a strong {110} out-of-plane orientation. The dark areas are locations where the electron backscattered diffraction pattern could not be indexed, often at grain boundaries. Figure 1c shows the same EBSD data as Figure 1b, but represented as an Euler pole figure (PF) map where each full crystallographic orientation is assigned a unique color. The grains all have a {110} out-of-plane orientation and four in-plane orientations represented by various colors. Comparing the SEM image in Figure 1a and the Euler map in Figure 1c, shows that the green and orange variants coalesce, as do the purple and blue grains.

Figure 1d shows three PFs (<100>, <110> and <111> reflections) for the same data as Figure 1b, colored according to the out-of-plane grain orientation (IPFZ). For clarity, only reflections from the grain centers are shown in the PFs. Spots are only seen in the center of the <110> PF, confirming the strong {110} Fe texturing. Figure 1e again shows three PFs, but colored according to the Euler orientations. The four grain variants are clearly separated into four orientations (purple, blue, green and orange). Figure 1f shows the PFs for the YTO substrate with a <100> spot close to the center reflecting the {100} YTO surface orientation.

The Fe-YTO orientation relationship (OR) was obtained by matching spots in the Fe PFs in Figure 1(e) with the accompanying YTO PFs in Figure 1f. The overlapping center spots from the <110>Fe PF and the <100>YTO PF indicate parallel surfaces. Similarly, the overlapping spots at the PF rims indicate parallel in-plane directions. Thus, the OR for the polycrystalline film is:

$\{110\}_{Fe}\backslash\backslash\{100\}_{YTO}$ and $<111>_{Fe}\backslash\backslash<110>_{YTO}$

This edge-on-cube orientation has not been observed for embedded NOs in NFAs. The 3-dimensional renderings in Figure 1g show that the four Fe grain variants have a <111> Fe direction matched with one of the two <110> YTO in-plane directions. The purple and blue grains share a common <111> Fe direction, as do the green and orange grains. The purple/blue and green/orange grain pairs have the exact same OR with the substrate, but are 90° rotated from one another to match the 2-fold symmetry of the underlying {100} YTO.

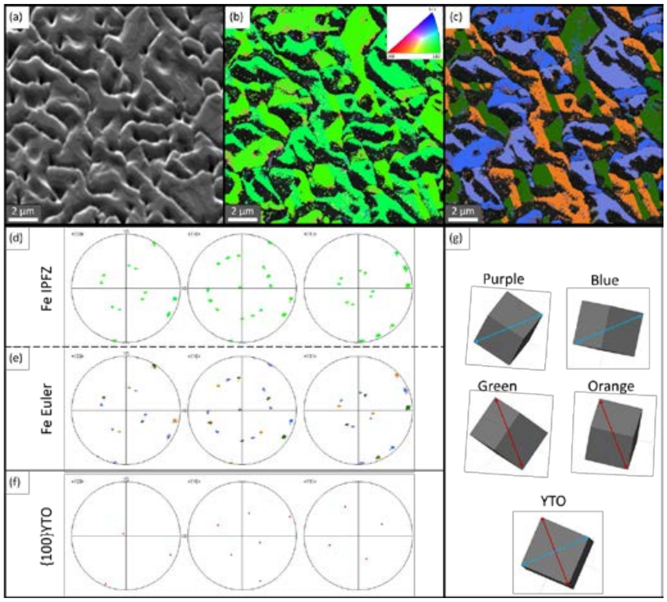

Figure 1. SEM/EBSD data from polycrystalline side showing (a) SEM image of 1 – 3 micron elongated grains, (b) IPFZ map with out-of plane {110} Fe texturing, (c) Euler map indicating four in-plane variants, (d) IPFZ pole figures, (e) Euler pole figures, (f) YTO pole figures, (g) 3D representation of {110} Fe grains and {100} YTO substrate.

Figure 2 shows SEM and EBSD data from the 100 µm x 100 µm monocrystalline grain. Figure 2a is an SEM image showing one continuous flat film with no grain boundaries. Surface ledges are seen on the film surface. Figure 2b shows an EBSD inverse pole figure (IPF) map of the same area as Figure 2a, indicating the out-of-plane {100} Fe crystallographic texturing. The black streaks coincide with ledges where the EBSD signal could not be indexed. Figure 2c represents the same EBSD data as Figure 2b but as an Euler PF map showing only one in-plane orientation.

Figure 2d shows three PFs (<100>, <110> and <111> reflections) for the same data that is in Figure 2b, with a strong, uniformly red out-of-plane {100} grain texturing. Figure 2e shows three PFs, all having same color associated with only one in-plane orientation. Figure 2f repeats the illustration in Figure 1f for easy comparison. The Fe-YTO OR for the monocrystalline film was obtained by matching spots in the Fe PFs in Figure 2e with the accompanying YTO PFs in Figure 2f. The OR for the monocrystalline crystalline film is close to:

$\{100\}_{Fe}\backslash\backslash\{100\}_{YTO}$ and $<100>_{Fe}\backslash\backslash<110>_{YTO}$

This type of edge-on-cube orientation has been observed for NOs in NFAs [8]. The 3D renderings in Figure 2g confirm that there is only one epitaxial orientation relationship between the Fe film and the underlying YTO substrate.

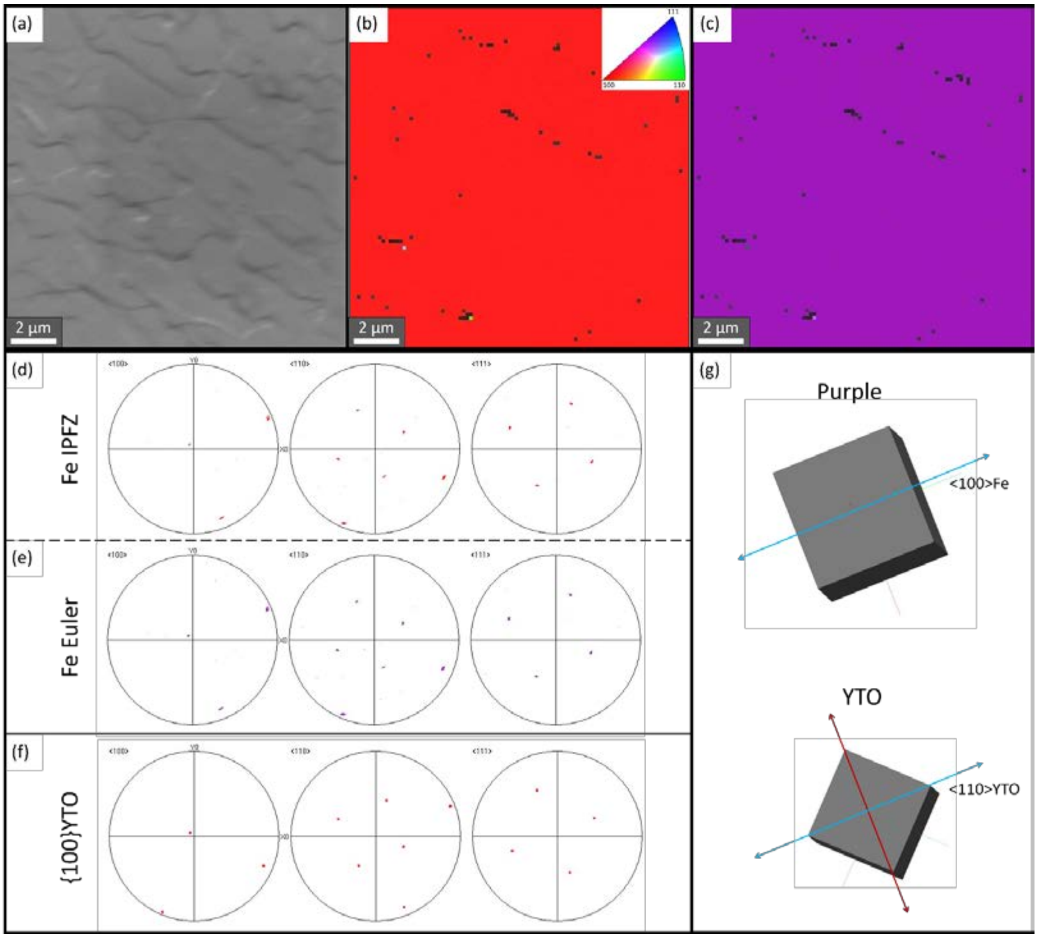

Figure 2. SEM/EBSD data from monocrystalline side showing (a) SEM scan showing a large flat area, (b) IPFZ map showing out-of plane {100} Fe texturing, (c) Euler map indicating one in-plane variant, (d) IPFZ pole figures, (e) Euler pole figures, (f) YTO pole figures, (g) 3D representation of {100} Fe film and {100} YTO substrate.

HRTEM Characterization

High Resolution Transmission Electron Microscopy (HRTEM) was used to investigate the structure of the Fe-YTO interfaces. Figure 3 shows HRTEM images from: (a) one of the {110} Fe polycrystalline grains; and, (c) the large monocrystalline grain. In both cases, the images are aligned with the <110> YTO in-plane zone axis, with the {100} YTO surface pointing up. The figures are equally scaled and formatted to facilitate side-by-side comparisons.

Figure 3a shows that the <111> Fe and <110> YTO in-plane zone axis directions are aligned and the corresponding planes are well resolved. The white arrows indicate the location of periodic interfacial misfit dislocations which are ~ 0.7 nm apart. These are more easily seen in the Fast Fourier Transform (FFT) image in Figure 3b. Energy dispersive x-ray (EDX) scans (not shown) indicate that Fe and YTO are not intermixed at the interface, and are free of detectible contaminants.

Figure 3c shows corresponding monocrystalline {100} Fe interface. There is a slight (~5^{o}) misalignment between the <100> Fe and <110> YTO zone axis thus the YTO lattice is not resolved in the image. The white arrows indicate the location of periodic misfit dislocations that are ~1.4 nm apart. Notably, this is twice the spacing found for the polycrystalline portion in Figure 3a. EDX and preliminary atom probe tomography studies (not shown) indicate clean interfaces without a contaminant interfacial layer.

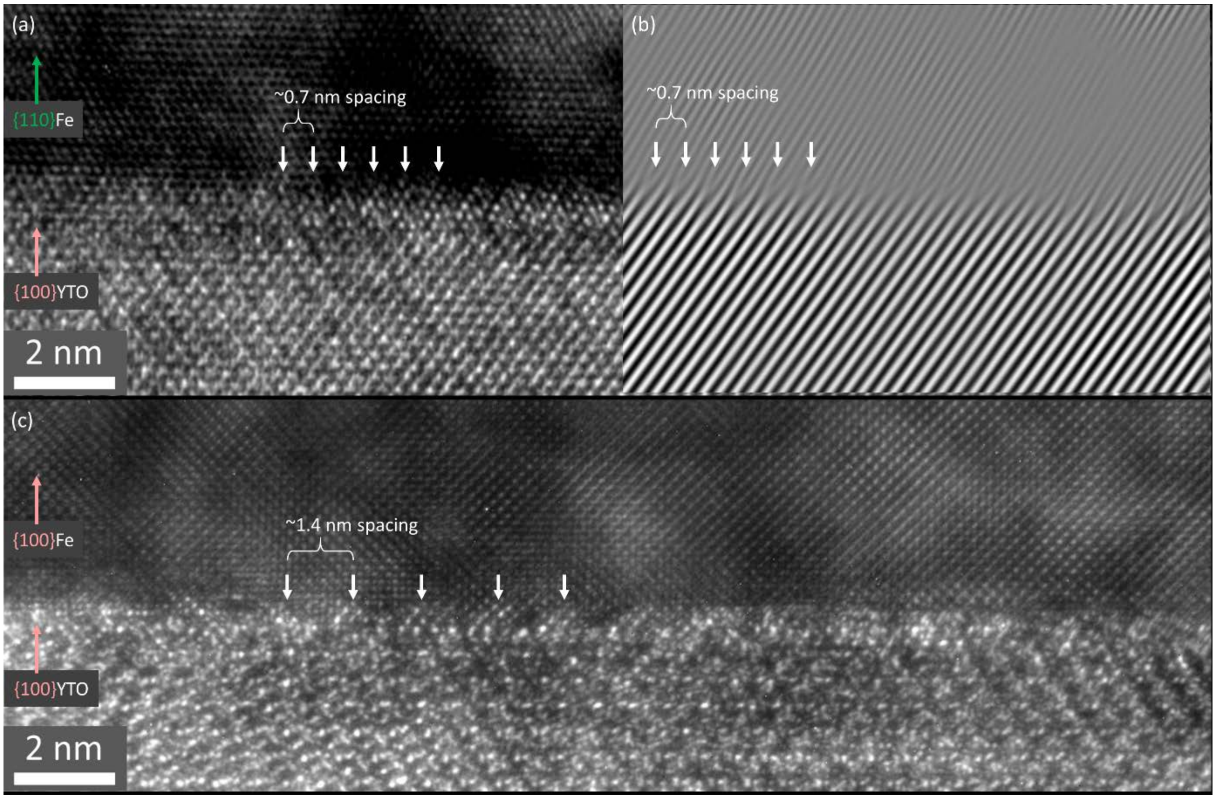

Figure 3. HRTEM image from (a) the polycrystalline side, (b) the Fast Fourier Transform, and (c) the monocrystalline side. Misfit dislocations are shown with white arrows.

For the Fe deposition conditions in this study, two epitaxial ORs were observed. The majority of the film was composed of 1 – 3 µm grains with: $\{110\}_{Fe}\backslash\backslash\{100\}_{YTO}$ and $<111>_{Fe}\backslash\backslash<110>_{YTO}$. However, a large 100 µm x 100 µm grain had an OR found in embedded NOs: $\{100\}_{Fe}\backslash\backslash\{100\}_{YTO}$ and $<100>_{Fe}\backslash\backslash<100>_{YTO}$.

CrystalMaker was used to analyze the lattice matching of the two interfaces observed in this study. Figure 4a shows a top-view of the lattice matching from the polycrystalline side. Fe atoms are orange, Y green, Ti blue, and O red. Along the $<111>_{Fe}\backslash\backslash<110>_{YTO}$ direction, every tenth d_{222} Fe plane has a coincident match with every fourth d_{440} YTO plane. The resulting misfit dislocation spacing is 0.71 nm. Along the $<112>_{Fe}\backslash\backslash<110>_{YTO}$ direction, every six d_{112} Fe plane has a coincident match with every fourth d_{440} YTO plane. The resulting misfit dislocation spacing is also 0.71 nm. The near coincidence site lattice (NCSL) is a 0.71 nm x 0.71 nm square, shown as a black dotted line in Figure 4a, that matches the HRTEM observations in Figure 3a. The small dislocation spacing indicates a higher energy semicoherent interface.

Figure 4b shows the CrystalMaker monocrystalline interface. In this case, with only in-plane $<100>_{Fe}\backslash\backslash<100>_{YTO}$ directions, every fifth d_{100} Fe plane has a coincident match with every fourth d_{440} YTO plane. This would seem to imply a misfit dislocation spacing and NCSL of 0.71 nm, the same as for the polycrystalline grain. However, analysis of the atom matching in Figure 4b shows that the 0.71 nm NCSL would not lead to a periodic lattice. Twice this distance is required, thus the actual expected misfit dislocation spacing is 1.43 nm. The resulting NCSL size is a 1.43 nm x 1.43 nm square that also matches the HRTEM observations in Figure 3b. The lower dislocation density implies a lower energy semicoherent interface.

It is not yet clear why two Fe orientations were observed. In previous studies of Fe depositions on {111} YTO [19], a dominant {110} Fe texturing was observed for grains with clean Fe-YTO interfaces. However, Fe grains had a {100} orientation when a 2 - 3 nm thick contaminant interlayer was present at the Fe-YTO interface. In the present study, neither the polycrystalline side nor the monocrystalline grain had an observable interlayer. It is possible that grain island nucleation events take place at locally contaminated or otherwise defected sites. Note that rapid, highly driven, self selection of interfaces may not always follow the minimum energy path. Local contamination or defect sites would be very difficult to detect by the HRTEM, EDX, and APT characterizations tools used in this study. However, the two {100}YTO interface variants actually present an opportunity to examine the similarities and differences in future He implantation experiments.

Even for cases with the same general OR, there are differences between the interfaces of the NOs embedded in NFAs versus the Fe-YTO bilayers in this study. The smallest NOs are likely coherent, with misfit strains partitioned between the Fe and YTO precipitate that increase with decreasing size. For example, a 2 nm x 3 nm YTO NO had ~5% coherency strain with a 5 x 7 NCSL [8]. Embedded NOs typically also have core-shell structures [5–7]. In contrast, the meso-scale bilayer interfaces are semicoherent with ORs differ from those most frequently found for embedded NOs.

We have also completed Fe depositions on {110} YTO using molecular beam epitaxy. Preliminary results show the Fe films have an axiotaxial OR that is close to: $\{100\}_{Fe}\backslash\backslash\{110\}_{YTO}$ and $<100>_{Fe}\backslash\backslash<100>_{YTO}$. However, details of this deposition and interactions with He will be the subject of a future publication. All three Fe - {100}, {110}, and {111} YTO bilayers will be subject to high temperature He implantations and charged particle irradiations of the Fe layer. The simplified bilayer model system of Fe on YTO provides the opportunities to use bulk mass spectroscopy measurements of the (Fe+YTO) and (YTO only) to observe the He partitioning. The corresponding He bubble size distributions, number densities, volume fractions, and spatial distribution will be observed using TEM. These experimental observations are critical to calibrating models that predict the behavior of NFAs and NOs in irradiation environments.

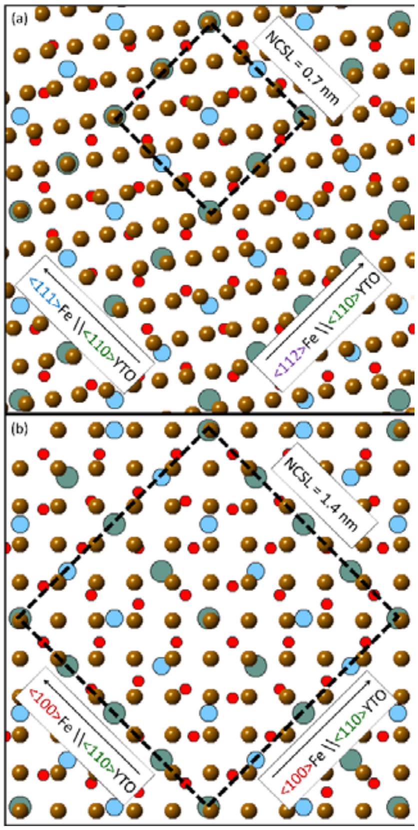

Figure 4. CrystalMaker renderings of the Fe-YTO interfaces from the (a) polycrystalline side and (b) monocrystalline side. Fe is shown in orange, Y in green, Ti in blue, and O in red. The black dotted lines show the near-coincidence site lattices.

Summary and Future Studies

Mesoscopic epitaxial Fe-YTO bilayers were successfully fabricated by electron beam Fe on {100} YTO single crystal surfaces. We report for the first time, the dominant fine grained polycrystalline OR is $\{110\}_{\mathrm{Fe}}\backslash\backslash\{100\}_{\mathrm{YTO}}$ and $<111>_{\mathrm{Fe}}\backslash\backslash<110>_{\mathrm{YTO}}$ with four variants that match the underlying substrate symmetry. HRTEM showed a semicoherent interface with misfit dislocation spacing of ~ 0.7 nm, consistent with CrystalMaker analysis. In contrast, a larger monocrystalline Fe grain had a $\{100\}_{\mathrm{Fe}}\backslash\backslash\{100\}_{\mathrm{YTO}}$ and $<100>_{\mathrm{Fe}}\backslash\backslash<110>_{\mathrm{YTO}}$ OR that is also found in embedded NOs. HRTEM showed a semicoherent monocrystalline bilayer interface with misfit dislocation spacing of ~ 1.4 nm. Unlike the monocrystalline grain, which was only observed on one bilayer sample, the polycrystalline OR is highly reproducible in electron beam deposition of Fe on {100} YTO.

Finally, we note that the bilayers were prepared for future He implantations and charged particle irradiations, with one objective being to experimentally observe the partitioning of He between the Fe, YTO, and associated interface. These studies will be used to inform multiscale models to predict NFA performance in fusion and fission reactor environments.

Acknowledgements

The authors thank D. Stave, G. Seward, P. Wells (UCSB) for help with various parts of the data acquisition and analysis. We thank Professor Y. Jiang at the Central South University in China for many helpful discussions and providing key insights on interfaces in a collaboration partially supported by NSF of China 51471189. Crystal growth was supported by NSF DMR 1350002. The characterization was done at the UCSB CNSI Microstructure and Microanalysis Facility: an NSF MRSEC, supported by NSF DMR 1121053. This work was supported by the U. S. Department of Energy, Office of Fusion Energy Sciences, under grant DE-FG03-94ER54275.

References

[1] G. R. Odette: *JOM*, 2014, vol. 66, p. 2427.
[2] G.R. Odette, M.J. Alinger, and B.D. Wirth: *Annu. Rev. Mater. Res.*, 2008, vol. 38, pp. 471–503.
[3] N. Cunningham, Y. Wu, D. Klingensmith, et al.: *Mater. Sci. Eng. A*, 2014, vol. 613, pp. 296–305.
[4] Y. Dai, G. R. Odette, and T. Yamamoto: *The Effects of Helium in Irradiated Structural Alloys*, 1st ed., Elsevier Inc., 2012.
[5] Emmanuelle A. Marquis: *Appl. Phys. Lett.*, 2008, vol. 93, pp. 10–13.
[6] S. Liu, G.R. Odette, and C.U. Segre: *J. Nucl. Mater.*, 2014, vol. 445, pp. 50–56.
[7] V. Badjeck, M.G. Walls, L. Chaffron, et al.: *J. Nucl. Mater.*, 2015, vol. 456, pp. 292–301.
[8] Yuan Wu, Jim Ciston, Stephan Kräemer, et al.: *Acta Mater.*, 2016, vol. 111, pp. 108–15.
[9] J. Ribis and Y. De Carlan: *Acta Mater.*, 2012, vol. 60, pp. 238–52.
[10] J. Ribis and S. Lozano-Perez: *J. Nucl. Mater.*, 2014, vol. 444, pp. 314–22.
[11] Karl Dawson and Gordon J. Tatlock: *J. Nucl. Mater.*, 2014, vol. 444, pp. 252–60.
[12] M. Tamura, H. Sakasegawa, K. Shiba, et al.: *Metall. Mater. Trans. A*, 2011, vol. 42, pp. 2176–88.
[13] Y. Wu, E. M. Haney, N. J. Cunningham, et al.: *Acta Mater.*, 2012, vol. 60, pp. 3456–68.
[14] A. J. London, B. K. Panigrahi, C. C. Tang, et al.: *Scr. Mater.*, 2016, vol. 110, pp. 24–27.
[15] R. Kasada, N. Toda, K. Yutani, et al.: *J. Nucl. Mater.*, 2007, vol. 367-370 A, pp. 222–28.
[16] Litong Yang, Yong Jiang, G. Robert Odette, et al.: *Acta Mater.*, 2013, vol. 61, pp. 7260–70.
[17] Litong Yang, Yong Jiang, G. Robert Odette, et al.: *J. Appl. Phys.*, 2014, vol. 115, p. 143508.
[18] Litong Yang, Yong Jiang, Yuan Wu, et al.: *Acta Mater.*, 2016, vol. 103, pp. 474–82.
[19] Tiberiu Stan, Yuan Wu, George R. Odette, et al.: *Metall. Mater. Trans. A Phys. Metall. Mater. Sci.*, 2013, vol. 44, pp. 4505–12.

2.5 TEM OBSERVATION OF ANNEALED AND He IMPLANTED NANOSTRUCTURED FERRITIC ALLOYS

—Y. Wu, T. Stan, T. Yamamoto, G. R. Odette (University of California Santa Barbara)

OBJECTIVE

The objective of this study is to characterize the details of He bubble association with Y-Ti-O oxides in nanostructured ferritic alloys (NFAs).

SUMMARY

Transmission electron microscopy (TEM) studies were carried out on two 700°C He implanted NFAs that had been previously annealed to coarsen their initially ultra-high density of nano-scale oxides (NOs). All the coarsened Y-Ti-O oxides were found to be associated with at least one, and in many cases more than one, interface helium bubble.

PROGRESS AND STATUS

Introduction

Managing helium is a grand challenge for turning the promise of C-free fusion power into a reality. Nanostructured ferritic alloys (NFAs), promising candidates for fusion applications, are dispersion strengthened by an ultrahigh density ($\approx$ 5 x 10^{23}/m^3) of Y-Ti-O nano-scale ($\approx$ 2.5 nm) oxides (NOs) with volume fractions of $\approx$ 0.5% for MA957 [1-3]. NOs trap otherwise highly damaging helium in harmless nm-scale interface bubbles [1-3], and thus they effectively manage very high concentrations of this insoluble transmutation product formed in fusion reactor materials. Hence, understanding the mechanisms of bubble formation, and bubble association with NOs, is essential to developing, qualifying and optimizing NFAs. However, when the NOs are very small, it is more difficult to characterize both the bubbles and their detailed oxide associations. Thus high temperature annealing was used to coarsen the oxides up to much larger sizes. The annealed NFAs were then implanted to a peak concentration of 4100 appm He at 700°C to form a population of bubbles on the coarsened oxides.

The ultimate objective of this study is to carry out detailed characterization of a He implanted NFA microstructure at the Lawrence Berkeley Laboratory (LBL) National Center for Electron Microscopy (NCEM), using their FEI Titan TEAM 1 and/or TEAM 0.5 aberration corrected TEMs. Here we briefly describe a preliminary scoping study carried out on the UCSB FEI Titan TEM. Four annealed and He implanted NFA MA957 FIBed lamella lift-outs were examined, and 2 lift-outs from another 14YWT NFA were characterized.

Materials

TEM studies were carried out on annealed NFA MA957 and a 14YWT developmental heat called V540H. V540H was powder processed by ball milling atomized powders to dissolve phase separated Y and consolidated by HIPing at 1150°C. Details about these alloys can be found elsewhere [4-6]. The as extruded MA957 was annealed at 1200°C for 2000 h. A calibrated coarsening model was used to estimate the average NO diameter of <d> $\approx$ 9 - 10 nm. The 14YWT sample was annealed at 1200°C for 228 hrs, with an estimated NO diameter of <d> $\approx$ 6 – 7 nm.

The annealed alloys were single He-ion (1 MeV) implanted at 700°C at the Kyoto University DuET facility in Japan at a dose rate of 1.2 x 10^{12} He/cm^2/s. A spinning degrader foil was used to spread out the He implantation profile, which is shown as a red solid curve in Figure 1. TEM examinations were carried out over the full $\approx$ 1.5 µm implanted region. The peak He concentration is 4100 appm at a depth of ~ 1.2 µm.

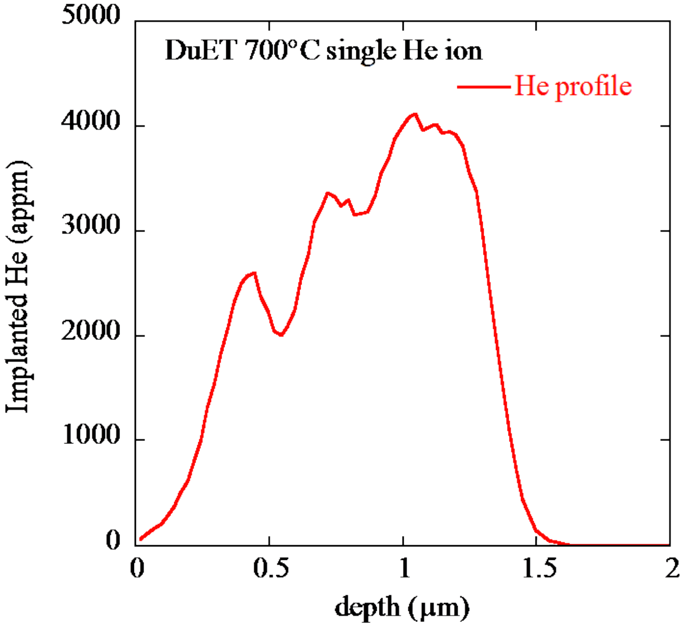

Figure 1. SRIM imulation of the He implantation profile in the MA957 and V540H NFA.

FIB lift-out electron transparent TEM lamella was prepared on a FEI Helios dual beam SEM. A finial 2 kV, 5.5 pA low energy ion beam was used to minimize gallium damage. Bright field (BF), scanning transmission electron microscopy (STEM) and high resolution electron microscopy (HRTEM) were used to observe the implanted microstructures. STEM was used to determine the number density (N), average diameter (<d>) and volume fraction (f) of the NOs and bubbles, while HRTEM Fast Forier Transform (FFT) indexing was used to study the NO crystal structure. The data was collected at 300 kV on a FEI Titan and recorded on a 2048 x 2048 pixel CCD camera. The HRTEM images were analyzed by FFT power spectrum indexing. The lattice spacings and inter-planar angles were measured using ImageJ.

Results

Previously, TEM showed that the unannealed V540H contained N_p = 6.5 x $10^{23}/m^3$, $<d_p>$ = 1.5 nm NOs with f_p = 0.18%. Small angle neutron scattering (SANS), atom probe tomography (APT) and TEM results on V540 powders annealed to simulate the HIP temperature cycle, found an average of N_p = 6.2 x $10^{23}/m^3$, $<d_p>$ = 1.7 nm NOs with f_p = 0.52%. The corresponding results of more comprehensive studies of MA957 showed that N_p = 5.0 x $10^{23}/m^3$, $<d_p>$ = 2.5 nm NOs with f_p = 0.50%.

Representative low magnification STEM images of He implanted annealed MA957 and V540H are shown in Figure 2. The oxides and cavities image in STEM as the lighter and darker features, respectively. The average coarsened NO $<d_p>$ are $\approx$ 40.4 nm in MA957 and 8.2 nm in V540H. The corresponding NO N_p are $\approx$ 5.9 x $10^{20}/m^3$ and $\approx$ 6.3 x $10^{21}/m^3$, while the corresponding f_p are $\approx$ 2.9% and 0.27%, respectively. Clearly, the NO coarsened (increased $<r_p>$ and decreased N_p) significantly after annealing in both cases. The NO f_p in V540H did not change much after annealing, while apparently the f_p increased enormously in the case of MA957.

Figure 3 shows bubbles on the NO interfaces. The cavity sides and faces are clearly faceted when not attached to NOs, while the faces that are attached to the NOs are not clearly seen in Figure 3 due to the imaging direction. In both annealed NFAs, all of the oxides are associated with at least one, and many cases more than one interface He bubble. The corresponding average bubble diameters, $<d_b>$, are $\approx$ 32.5 nm and $\approx$ 6.3 nm while the N_b are $\approx$ 6.4 x $10^{20}/m^3$ and $\approx$ 6.8 x $10^{21}/m^3$ for MA957 and V540H, respectively. The corresponding f_b are $\approx$ 2.3% and 0.10%.

Figure 4 shows a HRTEM image (a) and the corresponding FFT power spectrum (b) for a ≈ 4 x 6 nm oxide in 14YWT. After excluding multiple diffraction spots, the FFT diffraction pattern in Figure 2b has d-spacings and inter-planar angle, shown in Table 1, that are consistent with the same NO $Y_2Ti_2O_7$ pyrochlore crystal structure in the unannealed and unimplanted condition [4,6]. Further, the orientation relationship between this precipitate and ferrite matrix is cube-on-edge: [100] with a $[100]_{YTO}$ || $[010]_{Fe}$ and $[011]_{YTO}$ || $[100]_{Fe}$, as found by Dawson et al. [7], Ribis et al. [8] and Wu et al. [9].

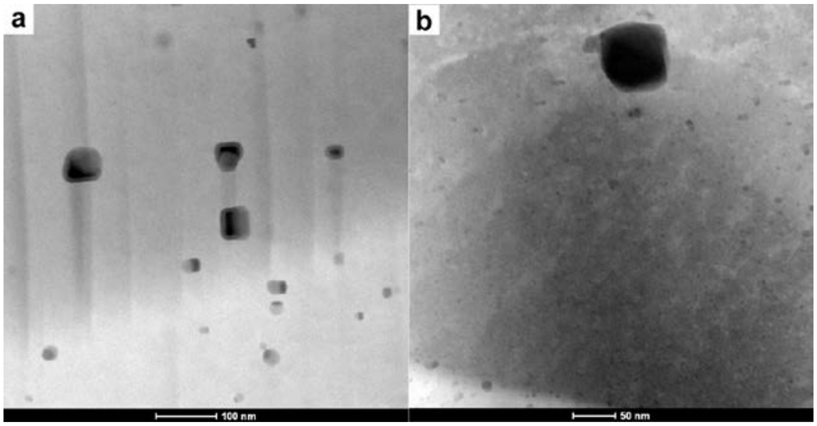

Figure 2. Low magnification STEM images of: a) annealed MA957 showing faceted cavities and coarsened oxide precipitates with a wide distribution of sizes; and, b) annealed 14YWT showing much smaller and more numerous associated bubbels and precipitates, that includes one very large cavity.

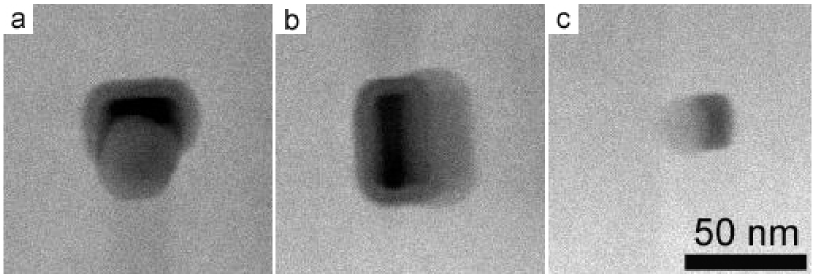

Figure 3. Higher magnification STEM images of annealed MA957, showing cavities attached to the NOs.

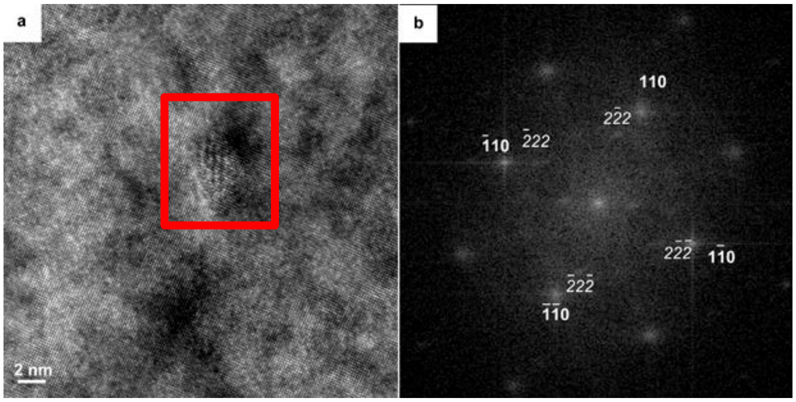

Figure 4. a) HRTEM image of a coarsened 4 nm x 6 nm NO in He implanted and annealed 14YWT; and, b) the corresponding FFT power spectrum.

Table 1. The measured d-spacings and plane angle from Fig. 2b compared to those for bulk $Y_2Ti_2O_7$.

Alloy	**d (Å)**	**d_1(2-22)**	**d_2(22-2)**	**α_{12}(°)**
V540H	Measured	2.83±0.09	2.83±0.09	72.2±0.9
	$Y_2Ti_2O_7$	2.90	2.90	70.5

Figure 5 shows a HRTEM image (a) of a large cuboidal 28 x 24 nm oxide from the annealed MA 957 and (b) corresponding FFT power spectra. In this case the d-spacings and inter-planar angle, shown in Table 2, are not consistent with $Y_2Ti_2O_7$, or any other known Y-Ti-O phase.

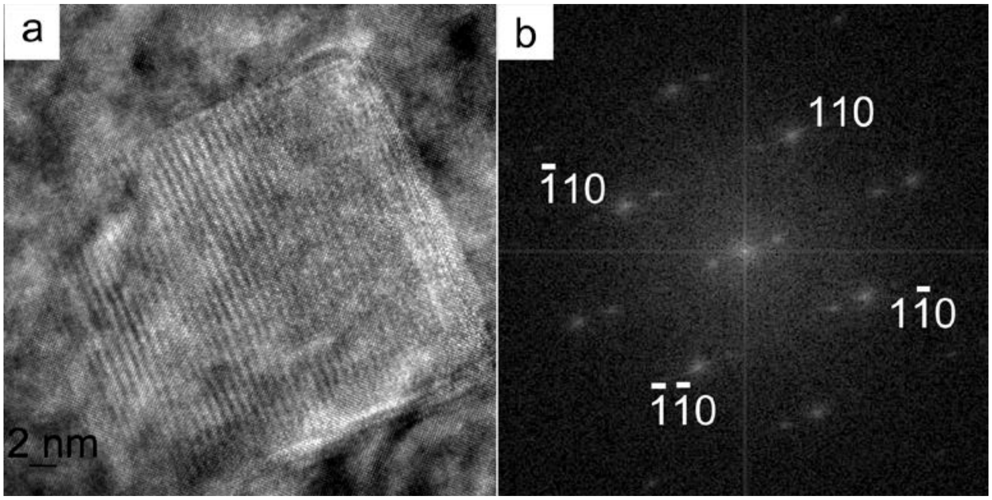

Figure 5. a) HRTEM image of a 28 x 24 nm coarsened oxide in annealed and He implanted 14YWT; and, b) the corresponding FFT power spectrum.

Table 2. The measured d-spacings and inter-planar angle in annealed MA957.

Alloy	**d (Å)**	**d_1**	**d_2**	**α_{12}(°)**
MA 957	Measured	2.45±0.09	2.45±0.09	65.0±0.9

Discussion

Detailed analysis of these results will be carried out after additional characterization at UCSB and LBL - NCEM. However, tentative preliminary conclusions include:

- Annealing coarsens the NOs in both NFA and in MA957. A large amount of additional oxide precipitation is observed.
- Even with much lower N and sink densities compared to the unannealed condition, the much larger oxides in the annealed MA957 collect a large fraction of the implanted He, which resides in very large attached interface bubbles.
- The smaller, but still coarsened, NO in annealed V540H are associated with much smaller interface bubbles.
- The NO and bubbles are similar to those in the annealed V540H, but even smaller in the unannealed MA957 and a 14YWT NFA called PM2, that is generally similar to V540H.

- In all cases (annealed and unannealed) all of the oxides are associated with one or more bubbles.

Future Work

The first set of measurements on the He implanted NFAs the LBL NCEM is scheduled for Sept. 26 – 29, based on a successful user proposal. TEM at UCSB will continue both before and after the visit.

Acknowledgements

Research at UCSB was supported by the Department of Energy Office of Fusion Energy Sciences (Grant No. DE-FG03-94ER54275) and the development of V540H was Office of Nuclear Energy (Grant No. DE-FC07-07ID14825). TEM specimen preparation and measurements were carried out in the UCSB Materials Research Laboratory Microstructure and Microanalysis Facility, supported by the Materials Research Science and Engineering Center Program of the National Science Foundation under Award No. DMR05-20415.

References

[1] G. R. Odette, M. J. Alinger, and B. D. Wirth, *Annu. Rev. Mater. Res*. 38 (2008) 471-503.
[2] G. R. Odette, *JOM* 66 (2014) 24272441.
[3] Y. Dai, G. R. Odette, and T. Yamamoto, *Comp. Nuc. Mater.* 1 - Chap 6, Elsevier 141 (2012).
[4] Y. Wu, E. Haney, N. Cunningham, G. R. Odette, *Acta Mater*. 60 (2012) 3456-3468.
[5] N. J. Cunningham, Ph.D. Thesis, University of California, Santa Barbara, Santa Barbara CA (2012).
[6] N. J. Cunningham, Y. Wu, G. R. Odette, et al. Fusion Materials Semiannual Progress Report, DOE/ER- 0313/53 (2012).
[7] K. Dawson, and G. J. Tatlock, *J. Nucl. Mater.* 444 (2014) 252-260.
[8] J. Ribis, Y. DeCarlan, et al., J. Mater. Res. 30 (2015) 2210-2221.
[9] Y. Wu, J. Ciston, S. Kraemer, et al. *Acta Mater*. 111 (2016) 108-115.

2.6 THREE DIMENSIONAL ATOM PROBE TOMOGRAPHY OF 14YW AND 14YWT NEUTRON IRRADIATED AT 500ºC TO 21.2 DPA

—D.J. Edwards, K. Kruska, J. Wang, R. J. Kurtz (Pacific Northwest National Laboratory), G.R. Odette, T. Yamamoto and Y. Wu (University of California-Santa Barbara)

OBJECTIVE

The aim of this study is to characterize the nano-oxide dispersion and precipitates in neutron irradiated ferritic alloys 14YWT and 14YW by atom probe tomography.

SUMMARY

Work has progressed on the characterization of two ferritic alloys, 14YW and 14YWT, irradiated in the JP27 experiment in the High Flux Isotope Reactor as part of the In-situ Helium Injection (ISHI) experiments. While much of the work has focused on high resolution analytical TEM of the bubble and dislocation structures formed during neutron irradiation, this TEM analysis has not been able to effectively characterize the nano-oxide particles present in 14YWT, which are usually less than 2 nm in size. To investigate microstructural features at this scale in a statistically meaningful manner, 3D-APT has been initiated to probe the oxide dispersion in the 14YWT. For comparative purposes, the 14YW alloy is also examined, however, the oxide dispersion is noticeably coarser due to the lack of titanium, and it is better characterized using TEM. APT of the 14YWT alloy revealed that significant precipitation of Mn-rich phases had occurred, as well as the formation of a Cr-rich α'-type phase at a composition that appears to contain less than the expected 85% Cr.

PROGRESS AND STATUS

Introduction

Oxide-dispersed strengthened (ODS) ferritic alloys, nanostructured ferritic alloys (NFA) and reduced activation ferritic/martensitic (RAFM) steels are currently considered the most viable candidates for structural materials for next step plasma devices]1,2]. This is due in large part to their excellent high-temperature mechanical properties and high swelling-resistance under neutron irradiation [1,2]. However, transmutation might cause significant degradation of these properties due to the large levels of helium produced during device operation. Up to 2,000 appm of helium could be produced, which is known to lead to helium bubble formation, promoting embrittlement, void swelling, and potentially enhanced irradiation creep. Understanding how helium accumulates at and interacts with various microstructural features such as grain boundaries, particle interfaces, and dislocations of various types can help to design more helium tolerant microstructures.

The following report summarizes a new set of 3D-atom probe tomography analyses conducted on two nanostructured ferritic alloys, 14YWT and 14YW, both oxide dispersion alloys based on a nominal 14Cr composition with only a few tenths of a percent of yttrium present in the form of oxide particles. The main difference between these alloys is the lack of titanium in the 14YW, the absence of which leads to a much coarser distribution of particles than is found in the 14YWT. Both of these alloys have been studied using analytical TEM, and the results of these studies have been reported in a prior semi-annual report by Jung et al [3].

Experimental Procedure

3-mm TEM discs of 14YWT and 14YW were neutron irradiated in the JP27 experiment to a dose of 21.2 dpa at 500°C in the High Flux Isotope Reactor (HFIR) at Oak Ridge National Laboratory (ORNL). The nominal compositions in the as-irradiated state as determined by EDS are provided in Table 1. While the compositions are similar to the unirradiated state, note that the tungsten experiences a significant degree of transmutation in the highly thermalized neutron environment of HFIR, leading to some of the W being transmuted into Os and Re. In addition, Fe and Cr both undergo transmutation to Mn, not only producing a few tenths weight percent of Mn, but also producing strong Mn x-rays at 5.9 and 6.5 keV via the decay of ^{55}Fe to ^{54}Mn, which needs to be accounted for in the EDS analysis from bulk samples. EDS analysis of a FIB lamella, which has virtually no detectable radioactivity because of the small volume, revealed the Mn concentration in both alloys was approximately 0.4 wt%.

A 4 µm NiAl coating used for the ISHI was applied to one side of a 3-mm TEM disc, which allows 3D-APT needles to be extracted from either side of the TEM disc to explore the impact of neutron irradiation with or without concurrent helium injection. At 21.2 dpa, the NiAl coating produces a He concentration of about 1,230 appm in the ferritic matrix extending to a depth of ~6 µm below the coating. 3D-APT needles were prepared using an FEI Quanta 3D from the neutron irradiated side of the disc. The surface of the disc was heavily oxidized, so the surface was lightly ground and then given a short electropolish using a 5% perchloric/95% methanol solution cooled to -60ºC. The electropolishing allowed the grain structure to be imaged in order to extract APT needles from the grain interiors or grain boundary regions.

The APT analysis was conducted using the LEAP® 4000 XHR instrument in the Environmental Molecular Science Laboratory User facility. Multiple needles were run at 44K using a laser wavelength of 355 nm, a pulse energy of 60 pJ, and a pulse frequency of 125-250 kHz.

Table 1. Composition of Ferritic alloys After Neutron Irradiation

Alloy	**Composition (wt.%) with Fe balance**											
	Al	**Si**	**Ti**	**Cr**	**Mn***	**Fe**	**Ni**	**Y**	**Mo**	**W**	**Re**	**Os**
14YW	1.61	0.79	0.00	13.70	~0.4	78.97	0.09	0.05	0.04	1.97	0.08	0.51
14YWT	0.82	0.22	0.41	13.76	~0.4	79.25	0.09	0.13	0.07	2.04	0.21	0.54

* *Mn levels are artificially high due to a contribution from radioactive decay, EDS analysis of a FIB lamella from each irradiated alloy showed around 0.4 wt% Mn.*

Results

The reconstruction of the APT data revealed a complicated microstructure. A thorough quantitative analysis is in progress, so only highlights will be presented here. Two needles from the 14YWT disc revealed a varying microstructure dependent on the lift-out location. One needle had relatively large Cr-O particles and smaller Ti-Cr-O particles. The 3D-APT dataset in Figure 1 shows the ion maps for the Fe, Y, CrO, TiO and Mn. This dataset revealed a number of different phases, including four large inclusions and a host of much smaller precipitates, some of which were found to be Mn-rich particles containing significant levels of Cr, Ti, Si, N and O. The compositions of the four large particles, as derived from the APT dataset, are provided in Table 2. Figure 2 shows iso-concentration surface plots for the various precipitates in the dataset, clearly demonstrating a high density of small particles interspersed among the larger particles. The Mn ion map in Figure 2(b) shows the Mn clustering, revealing both discrete particles as well as segregation around the outer surfaces of some of the larger particles. The summed composition of these clusters indicates approximately 4.4 at% Mn, 4.6 at% Ti, 22.6 at% Cr, 26 at% O, and Si and N at around 1 to 1.4 at%. Analysis of this sample also revealed clusters of Ti-Y-O of varying compositions, but requires further analysis to confirm the actual compositions. Analysis of the Cr-rich alpha prime is ongoing. Another dataset from the 14YWT disc has been acquired and will be summarized in future reports.

Recently acquired APT data from the grain interiors of irradiated 14YW show no large particles as found in the first needle for 14YWT. The Mn distribution has not yet been characterized, but the alpha prime distribution has been analyzed as shown in Figure 3 for two different needles. The alpha prime is easily visible as small clusters of Cr, and there is minor variation between the needles in terms of spatial homogeneity. The density of alpha prime, based on the 25 at% iso-concentration surface plots, varies from ~3 to 6 x 10^{23} m^{-3}, with a mean size of around ~3 ± 1 nm. The proxigrams for each needle reveal

Figure 1. An ion map shows the elemental distribution within this particular needle. Four large particles are highlighted for subsequent examination. Analysis revealed a grain boundary close to particles #2 and #3. The grain boundary only shows slight enrichment in C, but no major segregation of other alloying elements. The bulk composition of each overall particle is listed in Table 2, but a more complete analysis revealed particle #4 exhibited a Ti(Cr)N core with a Ti(Cr)O shell.

Table 2. Compositions (at%) of the Large Particles from Figure 1

	Si	N	Ti	Cr	Y	O
Particle #1	0.35	0.23	2.71	36.01	0.51	45.92
Particle #2	3.28	3.36	12.21	14.18	7.58	26.49
Particle #3	0.62	0.34	2.75	32.74	0.11	39.97
Particle #4	2.03	8.2	17.09	19.88	0.72	21.2

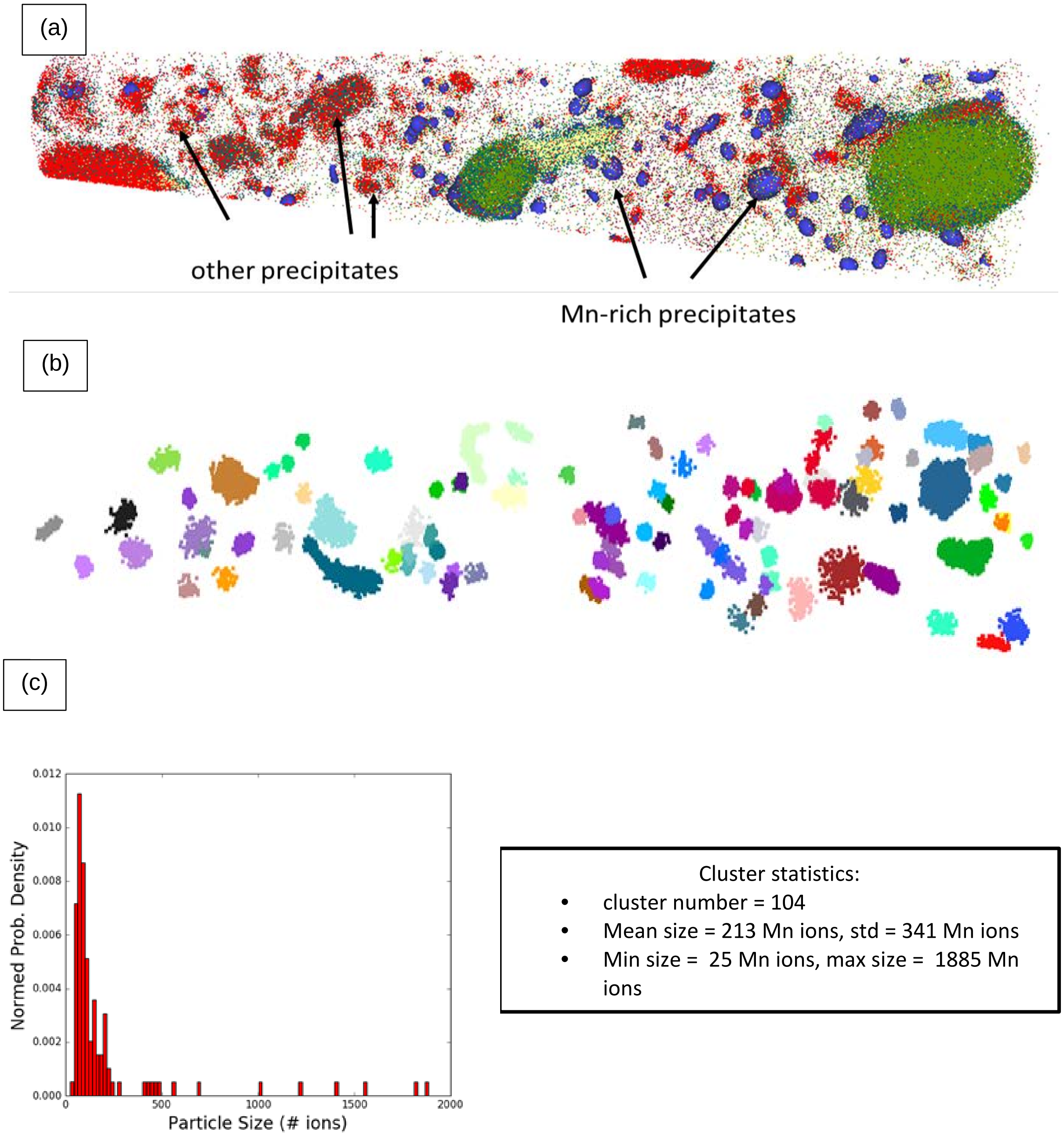

Cluster statistics:

- cluster number = 104
- Mean size = 213 Mn ions, std = 341 Mn ions
- Min size = 25 Mn ions, max size = 1885 Mn ions

Figure 2. Iso-concentration plots reveal a number of different particles of varying sizes. The blue particles in (a) were found to be Mn-rich particles with significant levels of Cr, O, Si, N and Ti. The Mn only map is provided in (b), showing that discrete Mn-rich particles are present, but there is also some association between the Mn and the outside of the larger particles identified in Figure 1. The Mn cluster size distribution shown in (c) reveals that Mn-rich clusters follow a narrow distribution and contains ~200 Mn ions in average (roughly ~2.5 nm, given the measured Mn concentration is ~3-4 at.% inside clusters), with a few precipitates extending up to nearly 10 nm. The measured statistics for the distribution are provided in the inset table.

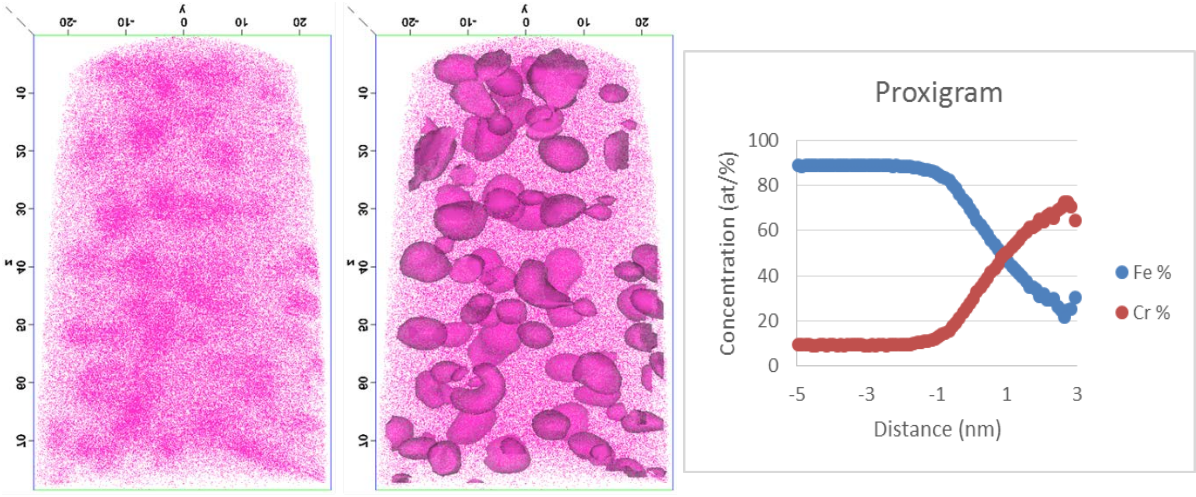

Cr Ion Map

Cr Iso-concentration surface 25at.%

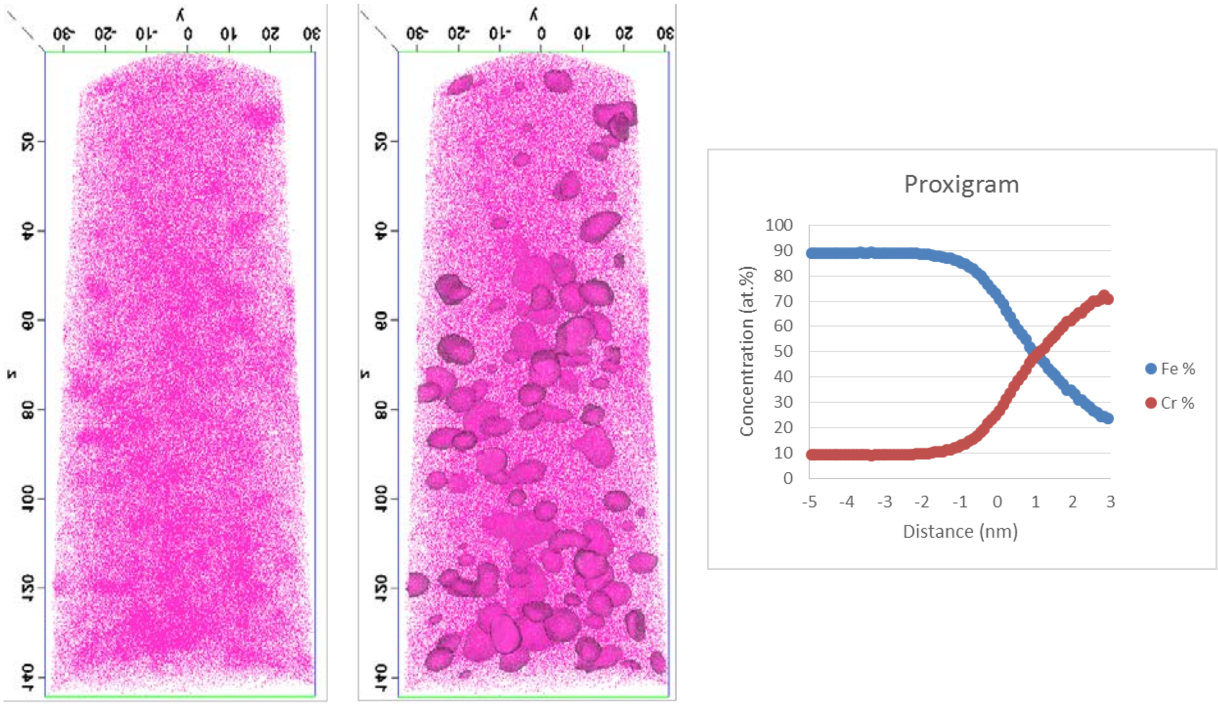

Cr Ion Map

Cr Iso-concentration surface 25at.%

Figure 3. Cr ion maps, iso-concentration plots and proxigrams are provided for two different needles, revealing a high density of alpha prime clusters in a somewhat varying spatial distribution.

the alpha prime Cr level reaches a max of around 70 at%. The nano-oxides of the 14YW are coarser than found in the 14YWT, so only a few of the smaller particles were actually captured in these two datasets. TEM analysis will be needed to more fully characterize the oxide particle distribution in this particular alloy in combination with the results of the APT analysis. In addition, further analysis will probe the clustering of other elements such as Mn to complete the picture of elemental evolution for these two alloys.

Future Work

Additional analyses are planned for the APT data to achieve a consistent comparative analysis between the microstructures of these two irradiated alloys. In addition, work is planned to explore correlative high resolution TEM/STEM on APT needles prior to an APT run. The aim will be to document the distribution of helium bubbles and cavities, dislocation structures, precipitates and elemental segregation as can be measured in the aberration corrected JEOL ARM200CF. Subsequently, these needles will be run in the LEAP 4000 with the hope to fully interrogating the microstructure over a range of length scales with two different high-resolution techniques.

Acknowledgements

This research was supported by Office of Fusion Energy Sciences, U.S. Department of Energy (DOE) under Contract DE-AC05-76RL01830. APT was performed under a general user proposal at the Environmental Molecular Sciences Laboratory (EMSL), a national scientific user facility located at PNNL.

References

[1] [1] G.R. Odette, M.J. Alinger, and B.D. Wirth, Annu. Rev. Mater. Res. 38 (2008) 471.
[2] R.J. Kurtz, A. Alamo, E. Lucon, Q. Huang, S. Jitsukawa, A. Kimura, R.L. Klueh, G.R. Odette, C. Petersen, M.A. Sokolov, P. Spätig, J.W. Rensman, J. Nucl. Mater. 386-388 (2009) 411.
[3] H.J. Jung, D. J. Edwards, B. Yao, R. J. Kurtz, G. R. Odette, T. Yamamoto , Fusion Reactor Materials Program 56 (2014) 19

3. CERAMIC COMPOSITE STRUCTURAL MATERIAL DEVELOPMENT

3.1 LOW ACTIVATION JOINING OF SiC/SiC COMPOSITES FOR FUSION APPLICATIONS: THERMOMECHANICAL MODELING OF DUAL-PHASE MICROSTRUCTURES AND DISSIMILAR MATERIAL JOINTS

—B.N. Nguyen, C.H. Henager, Jr., and R.J. Kurtz; (Pacific Northwest National Laboratory, Richland, WA, USA); M. Ferraris, (Politecnico di Torino, Torino, Italy); Y. Katoh, (Oak Ridge National Laboratory, Oak Ridge, TN, USA)

OBJECTIVE

Finite element (FE) continuum damage mechanics (CDM) models have been developed to simulate and model dual-phase joints and cracked joints for improved analysis of SiC materials in nuclear environments. This report extends the analysis from the last reporting cycle by including preliminary thermomechanical analyses of cracked joints and implementation of dual-phase damage models.

SUMMARY

Miniature torsion specimens were designed for joint testing and irradiation in test reactors with limited irradiation volumes since SiC and SiC-composites used in fusion environments are thought to require joining methods for component assembly. HFIR irradiation results indicated two broad types of joint damage due to irradiation at either 500˚C or 800˚C to 3 dpa or 5 dpa. One type of damage can be categorized as microcracking within multi-phase joints at the micron length scale. The other type of damage can be categorized as cracking within the miniature torsion sample and within the joint where the cracks are now on the scale of the joint thickness and are not considered to be microcracks. This report expands the methods developed and discussed in our previous report to model both types of cracking due to thermal stresses caused by the mismatch of thermoelastic properties (i.e., elastic properties and thermal expansion coefficients) in the constituent phases or between the joint and joint materials for a specimen uniformly heated from 28˚C to 800˚C.

PROGRESS AND STATUS

Introduction

The international fusion materials community has irradiated and is currently irradiating several joint types and compositions in the HFIR reactor at ORNL [1]. PNNL is working with Politecnico di Torino (POLITO) and ORNL using miniature torsion specimens that have been specifically designed for pre- and post-irradiation joint shear strength testing [2]. To elucidate how cracks initiate and propagate in the torsion joint specimens, FE analyses of these specimens subjected to torsion were previously performed using a CDM model developed at PNNL for elastic and elastic-plastic materials for which any nonlinearity in stress/strain response is due solely to damage and not to other irreversible processes such as plasticity [3-5]. The CDM model was implemented in the ABAQUS® finite element code via user subroutines. This CDM model [3] was also applied at the submicron scale where the OOF2[1] software package was used to create a dual-phase mesh within the joint region from an optical micrograph of a joint. The constitutive behavior of each phase in the modeling domain was described by the CDM model. Our study was conducted to explore the effects of differential material responses within the joint to external forces, such as thermal expansion, swelling, and applied loads. Although the joints survived the HFIR irradiation with reasonable properties, there was degradation observed in scanning electron microscope (SEM) images taken post-irradiation at ORNL. This report expands the methods developed and discussed in our previous reports to understand the sources for the observed cracking and subsequent joint degradation due to uniform temperature changes so that improved joints can be fabricated for fusion applications.

Model Formulation

Approach

This section provides a summary of the damage model implemented in ABAQUS® via user subroutines for the analyses of the joint specimen and of the dual-phase Ti_3SiC_2/SiC microstructural model [3-5]. The constitutive relations of the elastic damage model accounting for thermal stresses are given by:

---

[1] NIST software, see http://www.ctcms.nist.gov/oof/oof2/

$$\sigma_{ij} = C_{ijkl}(T,D)(\varepsilon_{ij}-\varepsilon_{ij}^{\mathbf{th}}) = C^{0}_{ijkl}(T)(1-D)(\varepsilon_{ij}-\varepsilon_{ij}^{\mathbf{th}}) = C^{0}_{ijkl}(T)(1-D)\varepsilon_{ij}^{\mathbf{m}} \tag{1}$$

where $C_{ijkl}(T,D)$is the material elastic stiffness tensor that varies with temperature T and is affected by the microcracking damage phenomenologically described by the damage variable, D. In Eq. (1), decoupling between the damage and thermal effects is assumed, and the elastic stiffness tensor is assumed to vary linearly with D. ε_{ij}, $\varepsilon_{ij}^{\mathbf{th}}$and $\varepsilon_{ij}^{\mathbf{m}}$are the total, mechanical and thermal strains, respectively. $\varepsilon_{ij}^{\mathbf{th}}$ is computed from the coefficients of thermal expansion (CTEs) $\alpha_{ij}(T)$and temperature change ΔT as

$$\varepsilon_{ij}^{\mathbf{th}} = \alpha_{ij}(T)\Delta T \tag{2}$$

The damage evolution law was obtained from concepts of thermodynamics of continuous media [6, 7] and a damage criterion dependent on the damage threshold function $F_{\mathrm{c}}(T,D)$ can be expressed as:

$$\mathrm{d}D = \frac{\dfrac{\partial C_{ijkl}(T,D)}{\partial D}\varepsilon_{ij}^{\mathrm{m}}\,\mathrm{d}\varepsilon_{kl}^{\mathrm{m}}}{\dfrac{\partial F_{\mathrm{c}}(T,D)}{\partial \mathrm{D}}} \tag{3}$$

This damage evolution law can describe microcracking damage caused by tensile stresses [3] or shear damage caused by shear stresses [5]. As ceramics may not suffer from microcracking under a compressive stress state, at this stage of the model development, damage is not activated under a compressive state of stress.

Identification of Temperature-dependent Thermomechanical properties

The integration of the constitutive relation requires identification of the thermomechanical properties including the damage threshold function as functions of temperature for the temperature range of interest. Measured temperature-dependent elastic modulus data from [8] and [9] were used for SiC and Ti_3SiC_2, respectively. The measured temperature-dependent thermal expansion data from [8] were used for SiC and from [10, 11] for Ti_3SiC_2. For the joint, homogenized thermoelastic properties of Ti_3SiC_2/SiC are needed for treating the joint as a continuum at the macroscopic scale. Thus, an Eshelby-Mori-Tanaka approach (EMTA) [12] was used to compute the elastic modulus and CTEs of Ti_3SiC_2/SiC using the constituent data and considering 50% volume fraction for each phase and uniform distribution of Ti_3SiC_2 in SiC. The temperature dependence of these properties is given in Figure 1.

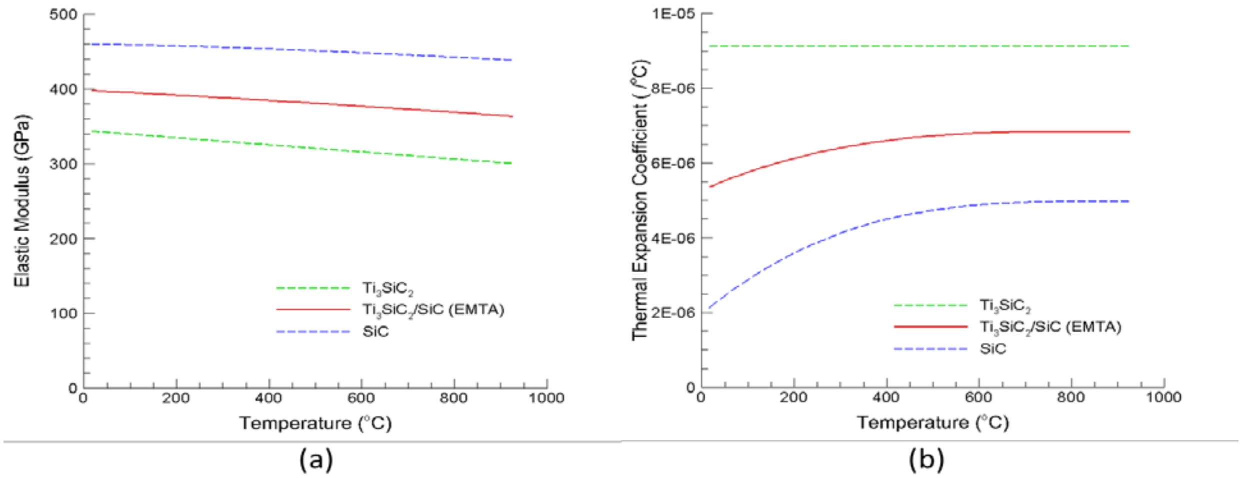

(a) (b)

Figure 1. (a) Temperature-dependent elastic modulus and (b) CTEs for Ti_3SiC_2, Ti_3SiC_2/SiC composite (EMTA prediction), and SiC from the literature [8-11].

Results

Analysis of the Joint Specimen Subjected to Uniform Temperature Increase

The joint specimen subjected to torsion analyzed in [5] and also discussed in our previous report [13] has been further analyzed during this reporting period for thermal stresses and their effect on joint integrity. To this end an unconstrained joint specimen was subjected to a uniform temperature increase from room temperature to 800˚C, which was the temperature at which the specimen underwent neutron irradiation in HFIR. Figure 2 shows the FE mesh of the joint specimen with the associated material assignments from [5]. The thermoelastic properties presented in Figure 1 were assigned to the respective materials of the joint specimen structure for the ABAQUS® analysis using the damage model.

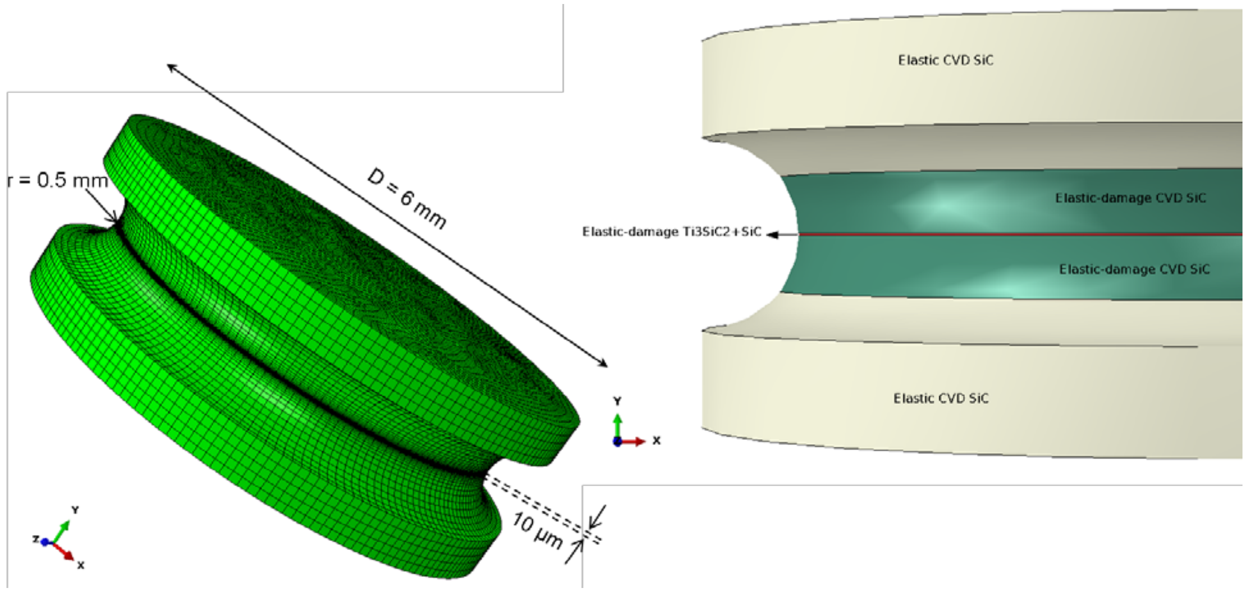

Figure 2. A FE mesh with the associated material assignments studied in [5].

Figure 3 respectively shows the uniform temperature distribution (Figure 3a) at 800˚C in the specimen, the contours of the most important stress components, σ_{rr} (Figure 3b) and σ_{tt}(Figure 3c) as well as the damage distribution in the specimen (Figure 3d) through a zoomed-in section showing the notch and the joint. Brought to 800˚C, the specimen experienced high compressive stresses in the joint but tensile stresses in the adjacent CVD-SiC region at the notch. This stress state resulted from the mismatch of CTEs between SiC and Ti_3SiC_2/SiC (Figure 1b). The CTEs of SiC are significantly lower than the values for the Ti_3SiC_2/SiC joint for the whole temperature range. The thermal expansion of the Ti_3SiC_2/SiC joint was constrained by the lesser expansion of SiC. Stress concentrations caused minor damage at the notch in the CVD-SiC along the joint/SiC interface. The damage distribution at 800˚C, presented in Figure 3c, shows very little damage at the notch. The damage variable value attained in this area was about 0.06, which was very low compared to the value at damage saturation (= 0.2). Small but confined damage at the notch and along the joint/SiC interface is evidence for the existence of some interface cracks prior to irradiation that could grow during irradiation under the right conditions. Low tensile stresses are also observed in the other areas of SiC away from the joint.

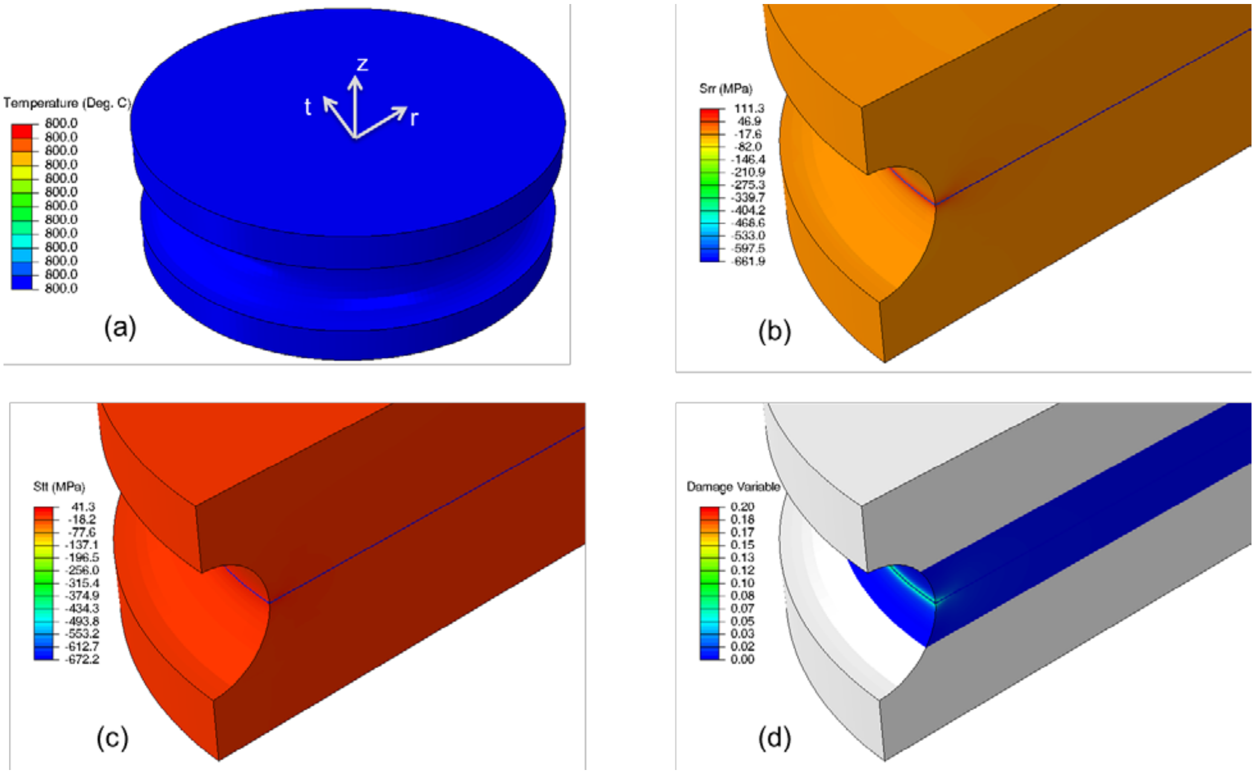

Figure 3. (a) The joint specimen uniformly brought to 800°C, (b) contour of the radial stress, σ_{rr}, (c) contour of the tangential stress, σ_{tt}, and (d) damage distribution at 800°C.

Analysis of the Ti_3SiC_2/SiC Dual Phase Microstructural Model

As discussed in Reference [1] and in our previous semiannual report [13], miniature torsion joints were irradiated in HFIR at ORNL and examined post-irradiation using SEM. Archival joints were imaged and tested pre-irradiation for comparison. Joint images showed two types of damage that is assumed to have originated from the neutron irradiation in HFIR for several of the joints. However, in view of the significant mismatches of thermoelastic properties between SiC and Ti_3SiC_2, and between SiC and the Ti_3SiC_2/SiC composite, thermal stresses caused by large temperature changes could contribute to microcracking of the joint prior to irradiation. This is the subject of our current investigation. One type of damage can be categorized as microcracking within multi-phase joints at the micron and sub-micron length scale. The other type of damage discussed in the previous section can be categorized as cracking within the miniature torsion sample and within the joint where the cracks are on the scale of the joint thickness. The present section addresses microcracking at the microstructural level.

In our previous report, a FE mesh of the joint microstructure using the OOF2 public domain software was presented. A digital image that was 14.1 µm on a side (910 x 910 pixels) was input to OOF2 and used to create a dual-phase FE mesh consisting of 230,000 nodes, containing both triangular and quadrilateral elements. This allowed a detailed discretization of the microstructure at the phase boundaries and the ability for ABAQUS® to assign individual constitutive laws to each phase. The meshed microstructure and constituent phase distribution presented in our previous report [13] are shown in Figure 4. In this report, the same microstructural model subjected to uniform temperature increase was analyzed by ABAQUS® using the damage model in order to investigate the thermal stresses that could cause microcracking.

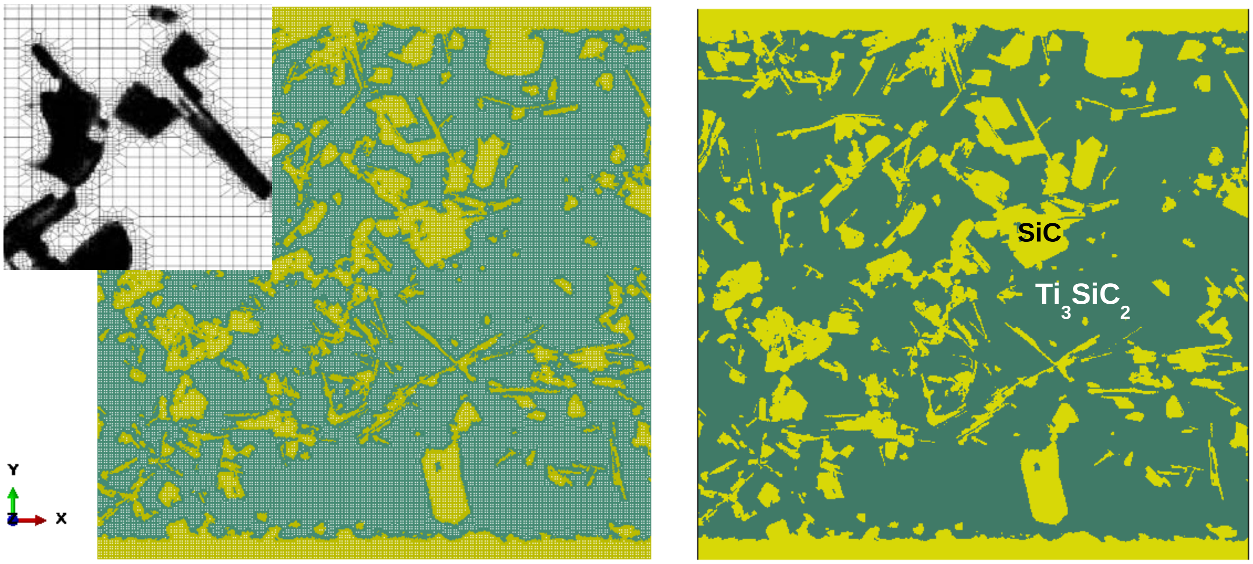

Figure 4. (a) The FE mesh is superimposed on the image of the microstructure. The insert in (a) shows the high-resolution mesh at the interfaces between the SiC (black) and the ternary MAX Ti_3SiC_2 (white) phase and (b) the same image with the two phases identified within the joint.

Figure 5 shows the uniform temperature distribution (Figure 5a) about 200°C in the specimen, the damage distribution (Figure 5b), and the contours of the principal stress components, σ_{xx} (Figure 5c) and σ_{yy} (Figure 5d). Referring to Figure 4 for the phase distribution, Figure 5b shows significant development of damage in the SiC phase. Many microcracks occurred in the SiC elements where the damage variable reached the saturation value (0.2). Microcracking of the SiC phase along the SiC/dual-phase joint interface is also observed in Figure 5b. The contours of stress distributions given in Figure 5c and Figure 5d reveal relatively high tensile stresses in all the SiC elements. The lower SiC phase region along the interface with the joint experienced high tensile stresses, σ_{xx}. Locally high tensile stresses in some SiC elements have caused failure of these elements observed in Figure 5b. The important mismatches between the thermoelastic properties of SiC and Ti_3SiC_2, in particular, the CTE mismatch were in part responsible for the stress state observed in Figure 5. There might be other mechanisms that would reduce the stresses in the SiC elements in the microstructure that will need to be investigated and potentially included in the model.

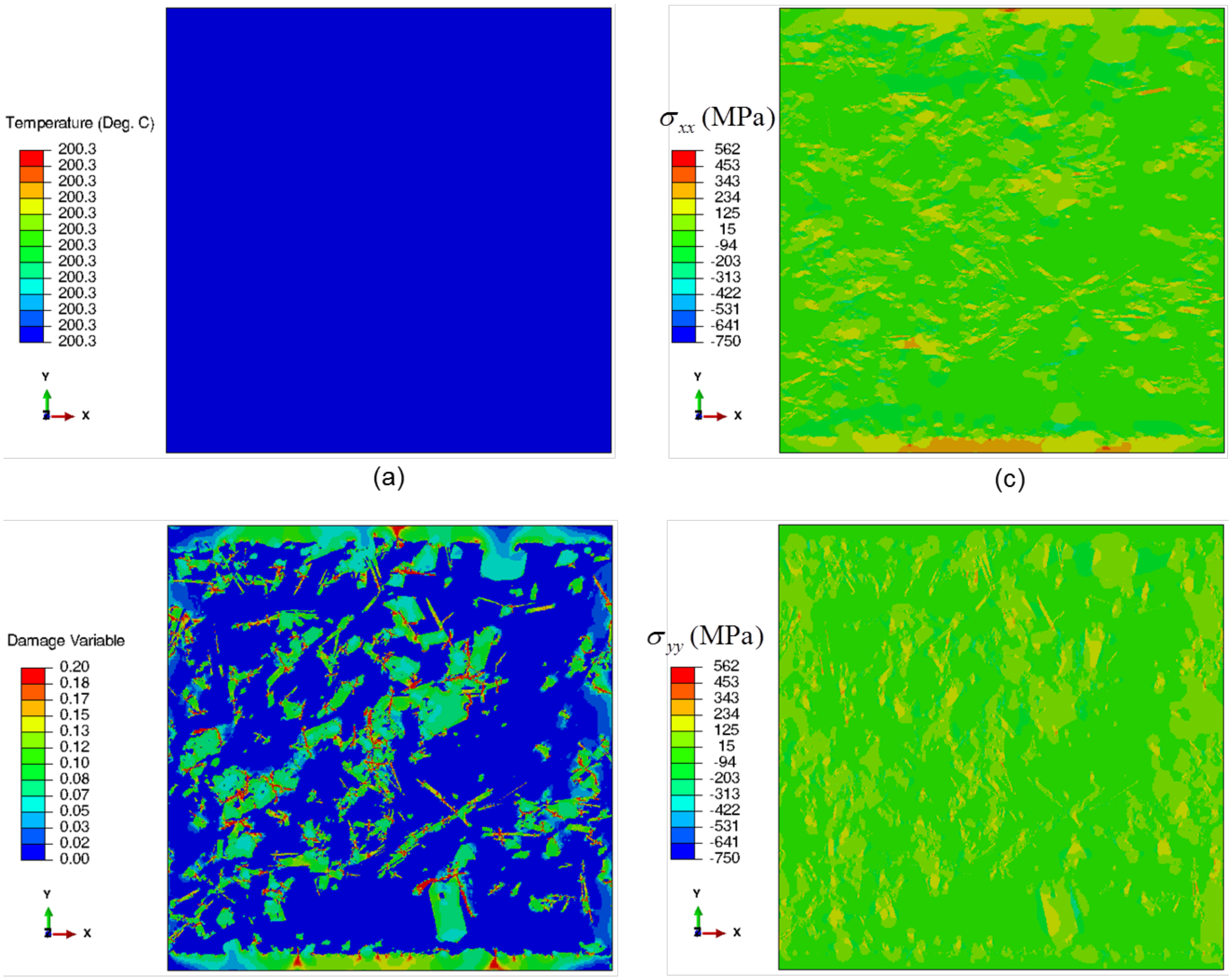

(a) (c)

(b) (d)

Figure 5. (a) Temperature reached 200.3°C during temperature increase application, (b) contour of the damage variable, (c) stress component, σ_{xx}, and (d) stress component, σ_{yy} at T=200.3°C.

Conclusion

A modification of the PNNL CDM model [4, 5] implemented in ABAQUS® to include thermal loading has been shown to provide qualitative agreement with experimental observations following SiC joint irradiations in HFIR. Both in-plane and transverse cracks are simulated and the overall damage distributions predicted appear to be in agreement with limited SEM observations of irradiated joints that indicated microcracks nucleating within the dual-phase joint region at SiC/Ti_3SiC_2 interface boundaries. At this stage, we have focused on the thermal stresses as this effect may cause microcracking in the joint or at the interface boundaries prior to irradiation solely due to temperature increases in HFIR.

Future Work

The developed FE CDM model will be modified to account for thermophysical and swelling loads consistent with the HFIR irradiation conditions.

Acknowledgements

This research was supported by Office of Fusion Energy Sciences, U.S. Department of Energy (DOE) under Contract DE-AC05-76RL01830.

References

[1] Katoh, Y., L.L. Snead, T. Cheng, C. Shih, W.D. Lewis, T. Koyanagi, T. Hinoki, C.H. Henager Jr, and M. Ferraris, J. Nucl. Mater., 2014. 448(1-3): p. 497-511.

[2] Jung, H.-C., T. Hinoki, Y. Katoh, and A. Kohyama, J. Nucl. Mater., 2011. 417(1-3): p. 383-386.

[3] Nguyen, B.N., B.J. Koeppel, S. Ahzi, M.A. Khaleel, and P. Singh, J. Am. Ceram. Soc., 2006. 89(4): p. 1358-1368.

[4] C. H. Henager, J., B.N. Nguyen, R.J. Kurtz, M. Ferraris, and Y. Katoh, in *Fusion Reactor Materials Program Semiannual Progress Reports*, Vol. 58, F. Wiffen, R. Godfrey, and B. Waddell, Editors. 2015, ORNL: Oak Ridge, TN. p. 108-118

[5] Henager, C.H., B.N. Nguyen, R.J. Kurtz, T.J. Roosendaal, B.A. Borlaug, M. Ferraris, A. Ventrella, and Y. Katoh, J. Nucl. Mater., 2015. 466: p. 253-268.

[6] Maugin, G.A., *The Thermomechanics of Plasticity and Fracture*. 1992, Cambridge, UK: Cambridge University Press.

[7] Lemaitre, J. and J.L. Chaboche, Journal de Mecanique Appliquee, 1978. 2(3): p. 317-65.

[8] Snead, L.L., T. Nozawa, Y. Katoh, B. Thak-Sang, S. Kondo, and D.A. Petti, J. Nucl. Mater., 2007. 371(1-3): p. 329-77.

[9] Barsoum, M.W., M. Radovic, A. Ganguly, T. Zhen, P. Finkel, S.R. Kalidindi, and E. Lara-Curzio, Acta Mater., 2006. 54(10): p. 2757-67.

[10] Manoun, B., S.K. Saxena, H.P. Liermann, and M.W. Barsoum, J. Am. Ceram. Soc., 2005. 88(12): p. 3489-91.

[11] Barsoum, M.W., T. El-Raghy, C.J. Rawn, W.D. Porter, H. Wang, E.A. Payzant, and C.R. Hubbard, Journal of the Physics and Chemistry of Solids, 1999. 60(4): p. 429-39.

[12] Nguyen, B.N., *EMTA User's Guide*. 2010, Pacific Northwest National Laboratory: Richland, WA.

[13] C. H. Henager, J., B.N. Nguyen, R.J. Kurtz, M. Ferraris, and Y. Katoh, in *Fusion Reactor Materials Program Semiannual Progress Reports*, Vol. 59, F. Wiffen, R. Godfrey, and B. Waddell, Editors. 2015, ORNL: Oak Ridge, TN. p. 72-78

3.2 CHARACTERIZATION OF PRECIPITATES IN CUBIC SILICON CARBIDE IMPLANTED WITH ^{25}Mg^{+} IONS

W. Jiang, S. R. Spurgeon, J. Liu, D. J. Edwards, D. K. Schreiber, C. H. Henager, Jr., R. J. Kurtz (Pacific Northwest National Laboratory), and Y. Wang (Los Alamos National Laboratory)

OBJECTIVE

The aim of this study is to characterize precipitates in Mg^{+} ion implanted and high-temperature annealed cubic silicon carbide using scanning transmission electron microscopy, electron energy loss spectroscopy and atom probe tomography.

SUMMARY

This progress report presents results from high-resolution scanning transmission electron microscopy (STEM), electron energy loss spectroscopy (EELS) and atom probe tomography (APT). The APT study has been performed for cubic silicon carbide (3C-SiC) implanted to 9.6×10^{16} ^{25}Mg^{+}/cm^{2} at 673 K and subsequently annealed at 1073 and 1573 K for 2, 6, and 12 h in an Ar environment. The ^{25}Mg isotope was chosen to differentiate it from $^{12}C_2$ clusters in APT. STEM and EELS characterizations have been carried out for the same 3C-SiC sample annealed at 1573 K for 12 h. The APT results show a faster Mg clustering process during isochronal annealing (12 h) at a higher temperature while growth to larger Mg clusters on the average occurs during isothermal annealing (1573 K) for a longer time. The STEM-EELS study suggests that some of the precipitates have a core (MgC_2)-shell (Mg_2Si) microstructure. The precipitate size and number density are determined to be 2-8 nm and ~10^{18} /cm^{3}, respectively.

PROGRESS AND STATUS

Introduction

Calculations by Sawan, *et al*. [1] have predicted significant production of transmutants in silicon carbide under high-energy neutron irradiation in a fusion environment. At 100 dpa, there are ~0.5 at.% Mg, 0.2 at.% Be and 0.15 at.% Al generated in SiC in addition to 2.2 at.% He and 0.84 at.% H. The impact on the structural stability and thermomechanical properties due to the presence of the impurities, gas species and irradiation-induced defects in SiC is currently unknown, but could potentially limit the material's service lifetime. We have initiated an experimental study to investigate the structural effects of Mg in 3C-SiC by performing a series of ion implantation experiments. Our previous study [2] suggests that precipitates of cubic Mg_2Si and tetragonal MgC_2 are likely formed in 3C-SiC implanted to 9.6×10^{16} ^{24}Mg^{+}/cm^{2} at 673 K and subsequently annealed at 1573 K for 12 h in Ar environment. Evidence for the formation of these precipitates was obtained from a fast Fourier transformation (FFT) of an atomic-level resolution high-angle annular dark field (HAADF) STEM micrograph [2]. This study focuses on confirmation and characterization of these possible precipitates in ^{25}Mg^{+} ion implanted 3C-SiC using STEM, EELS mapping and APT. Some of the recent data are presented here. More results and discussion will be reported in a full-length manuscript to be prepared for journal publication.

Experimental Procedure

As described in our previous semiannual reports [3,4], 3C-SiC was implanted 7° off the surface normal with 200 keV ^{25}Mg^{+} ions at 673 K to an ion fluence of 9.6×10^{16} ions/cm^{2}, corresponding to ~6 at.% Mg and ~53 dpa at their respective peak maxima based on SRIM simulations [5]. Utilization of ^{25}Mg^{+} ions is needed to differentiate it from $^{12}C_2$ clusters in APT using time-of-flight mass spectrometry. The implanted samples were cleaved into smaller pieces for thermal annealing under various conditions. Isothermal annealing at 1573 K was performed for 2, 6 and 12 h in an Ar environment, while isochronal annealing for 12 h was done at 1073 and 1573 K. Using a focused ion beam (FIB) secondary electron microscope (FEI Helios NanoLab), one STEM specimen was prepared for 3C-SiC implanted with ^{25}Mg ions and annealed at 1573 K for 12 h. STEM was performed using a Cs-corrected JEOL ARM 200CF TEM-STEM. Equipped with a cold field emitter, the microscope is capable of sub-Å spatial resolution under HAADF STEM imaging. The high-brightness source allows for a fast acquisition of EELS utilizing the latest Gatan Quantum 965 spectrometer. STEM and EELS were performed at both 200 and 80 kV, with the latter being used to minimize sample damage. APT examinations for a total of 5 implanted specimens prior to annealing and under the above-mentioned annealing conditions were carried out at a temperature of 44 K and a bias voltage ranging from 5.5 to 8.5 kV with a laser power of 60 – 80 pJ/pulse at a frequency of 125 kHz. The detection efficiency was 36% with an average detection rate of 0.4%. The total ions collected for each needle range from 3 to 5 M ions. The same specimen of $^{25}Mg^+$ ion implanted 3C-SiC annealed at 1573 K for 12 h was selected for study by STEM-EELS and APT for a direct comparison of results.

Results and Discussion

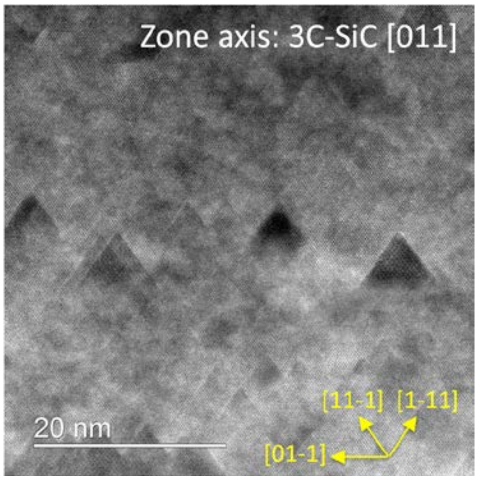

Figure 1. HAADF micrograph taken near the middle of the damage band of 3C-SiC implanted to 9.6×10^{16} $^{25}Mg/cm^2$ at 673 K and annealed at 1573 K for 12 h in Ar. Unidirectionally aligned tetrahedra appear with a number density of 1×10^{18} cm^{-3}.

The microstructure in 3C-SiC implanted to 9.6×10^{16} $^{25}Mg/cm^2$ at 673 K and annealed at 1573 K for 12 h in Ar has been examined by HAADF STEM and a typical micrograph near the damage peak is shown in Figure 1 for a general view of features along zone axis [011]. A distribution of unidirectionally aligned tetrahedra is observed with two sides of the triangular shape parallel to [1-11] and [11-1], and the other parallel to [01-1], as indicated in the figure. The size of the tetrahedra ranges from 2 to 8 nm. This microstructure confirms our previous observation [2] of 3C-SiC implanted with ^{24}Mg and annealed under the same conditions. Kondo, *et al*. [6] have reported similarly aligned tetrahedra in 3C-SiC irradiated with neutrons at 1733 K. Their report indicates that the tetrahedra in 3C-SiC are voids based on under- and over-focus imaging and the different surface energies between Si- and C-terminated polar surfaces. This is in a contrast to stacking fault tetrahedra (SFTs) that are observed in high-temperature irradiated face-centered cubic metals and alloys [7]. Faceted voids have also been observed [8] in 3C-SiC irradiated with Ag ions at room temperature and subsequently annealed at 1873 K. The material was completely amorphized after the ion irradiation and a recrystallization process occurred during a subsequent thermal annealing. In this study, irradiation was performed at 673 K, which is above the critical temperature (~550 K) for amorphization of SiC. At this temperature, self-interstitials and implanted Mg in SiC migrate and cluster to some extent, but vacancies are not mobile, leaving behind excess vacancies in the as-implanted 3C-SiC. It is also expected that the vacancy concentration is much higher than the Mg concentration (6 at.%) in this region (~53 dpa). Subsequent annealing at 1573 K could lead to formation of vacancy clusters and voids. However, this process could be mediated by Mg atoms that should precipitate at the same time and can involve Si and C atoms in the process. A full understanding of this complex process requires a computational study. We also notice that the tetrahedra in Figure 1 show different contrasts, which are related to Mg concentrations, as will be discussed below. The specimen thickness in this region was determined by EELS to be ~30 nm. The number density of the tetrahedra is estimated to be ~10^{18} cm^{-3}.

A high-resolution HAADF STEM micrograph near the damage peak is shown in Figure 2. The dark tetrahedron of ~8 nm in size in the center appears to exhibit a different lattice with a coherent interface with the 3C-SiC matrix. Dislocations or stacking faults inside or outside the tetrahedron are not observed. There is an overlap of tetrahedra due to specimen thickness. The corresponding power spectrum from the micrograph is shown in Figure 2(b), which is consistent with our previous observations [2]. Three groups of different patterns are identified for 3C-SiC, cubic Mg_2Si and tetragonal MgC_2, as shown by white, blue and red arrows in the figure, respectively. The orientation relationships are Mg_2Si(110)//3C-SiC(110) and MgC_2(110)//3C-SiC(110) with lattice mismatch of ~1% in both cases. It should be noted that as Mg_2Si and MgC_2 decompose at 873 and 1073 K, respectively, the possible precipitates should form by nucleation and growth during the cooling-down stage of the thermal annealing process at 1573 K. Magnesium in metallic form or other crystalline compound phases are not found. It should be pointed out that the two spots (red arrows) assumed to be from MgC_2 could originate from the double diffraction of Mg_2Si (001) that is forbidden for a perfect crystal.

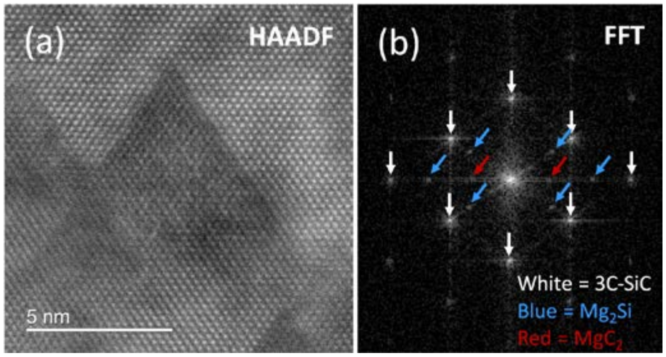

Figure 2. (a) High-resolution HAADF micrograph of 3C-SiC implanted to 9.6×10^{16} ^{25}Mg/cm^2 at 673 K and annealed at 1573 K for 12 h in Ar. (b) FFT of (a).

Figure 3(a) shows a HAADF STEM micrograph near the damage peak in 3C-SiC. A region of ~25 nm × 25 nm that contained some dark and grey tetrahedra was selected for elemental mapping using EELS. The EELS maps are shown in Figures 3(b)-(d) for C, Si and Mg, respectively. A composite image for C, Si and Mg is shown in Figure 3(e). Clearly, there is Mg enrichment with concurrent depletion of Si and C in the dark tetrahedra, indicating that the Mg-bearing precipitates are formed inside the tetrahedra. However, the greyer tetrahedra in Figure 3(a) do not show a significant Mg concentration. They could be cavities or SFTs, but the exact nature of the tetrahedra still needs further studies. An intensity scan across two overlapping tetrahedra shown in Figure 3(e) was conducted and one-dimensional concentration profiles of Si, C and Mg are plotted in Figure 3(f). The percentages of the 3 elements are normalized to 100%. While the Si concentration shows a broad valley within the tetrahedra, it is interesting to notice that C concentration shows a small peak near the center of the precipitate, which is located at the minimum intensity of the double Mg peak profile. The overall higher concentrations of Si and C may be attributed to the predominant composition in the volume of the EELS analysis due to the

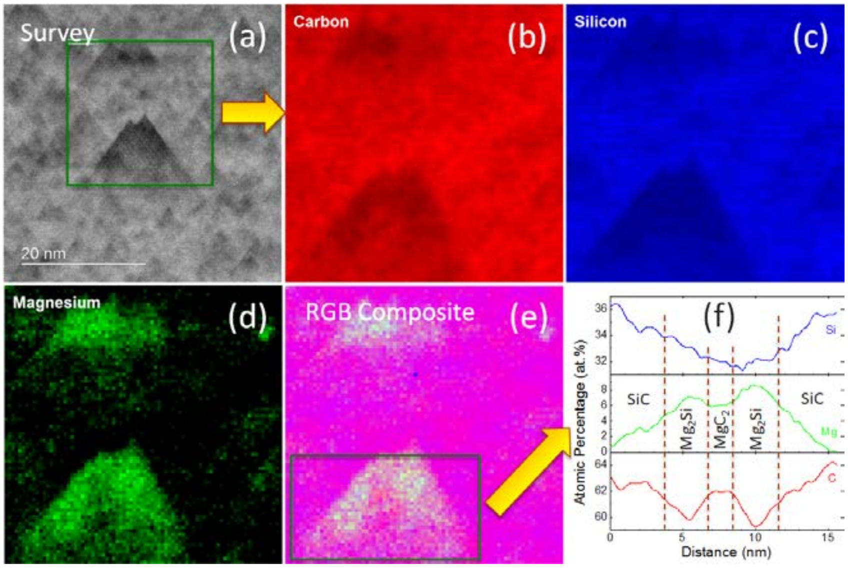

Figure 3. (a) HAADF micrograph of 3C-SiC implanted to 9.6×10^{16} ^{25}Mg/cm^2 at 673 K and annealed at 1573 K for 12 h in Ar. EELS maps of (b) carbon, (c) silicon, (d) magnesium, and (e) all the elements. (f) Elemental profiles across a tetrahedron. Maps have been denoised using principal component analysis (PCA).

film thickness. From Figure 3(f), the Mg-bearing precipitate appears to have a core-shell structure, containing compositions of SiC, Mg_2Si, MgC_2, Mg_2Si, and SiC across the precipitate volume. The data may suggest formation of possible phases of Mg_2Si and MgC_2 in proximity, which would be reasonable. The lower Mg concentration in the Mg profile would be also understandable because the Mg concentration in MgC_2 is smaller than in Mg_2Si. It should be noted that such a core-shell structure is not always the case for all Mg-containing tetrahedra. Some tetrahedra show simply a single Mg peak overlapped with Si and C valleys without fine structures. Formation of the tetrahedral shape of the Mg-bearing precipitates is not yet well understood at this time. It could be associated with vacancy agglomeration on 3C-SiC {111} planes, facilitating formation of tetrahedral voids, while Mg atoms diffuses into the volume during annealing at 1573 K. As mentioned above, the vacancy concentration is expected to be significantly higher than the Mg concentration prior to annealing. Alternatively, there might be energetically favored interfaces containing Mg and Si or C. A model calculation should help understand the mechanism for the formation of the tetrahedral precipitates.

A series of iso-concentration surfaces at 10 at.% ^{25}Mg in 3C-SiC are shown in Figure 4 as a function of annealing temperature and duration. The two-dimensional plots are generated from a 10 nm slice of material in the Mg peak region. It is seen that the degree of homogeneity of the green dots that represent Mg clusters decreases with either increasing annealing temperature or duration. This indicates that Mg atoms tend to cluster more rapidly as temperature increases during isochronal annealing for 12 h; longer duration of annealing leads to growth of larger Mg clusters on the average at 1573 K. For 1573 K and 12 h annealed 3C-SiC, the number density of the Mg-bearing precipitates is estimated to be 1.6×10^{18} cm^{-3}, which is consistent with the STEM observation shown in Figure 1. The average size (discussed below) and the number density of the precipitates should increase and decrease, respectively, with the increase of either annealing temperature or duration. It should be mentioned that the shape of the Mg-bearing precipitates are not tetrahedra that were observed from STEM. This is mainly because there is a large field evaporation difference between Mg (~21 V/nm) and SiC (>33 V/nm). Under a fixed condition, Mg evaporates at a faster rate than Si and C, leading to shape deformation of the Mg-bearing precipitates during three-dimensional atom map reconstruction. In fact, different shapes of Mg-bearing precipitates

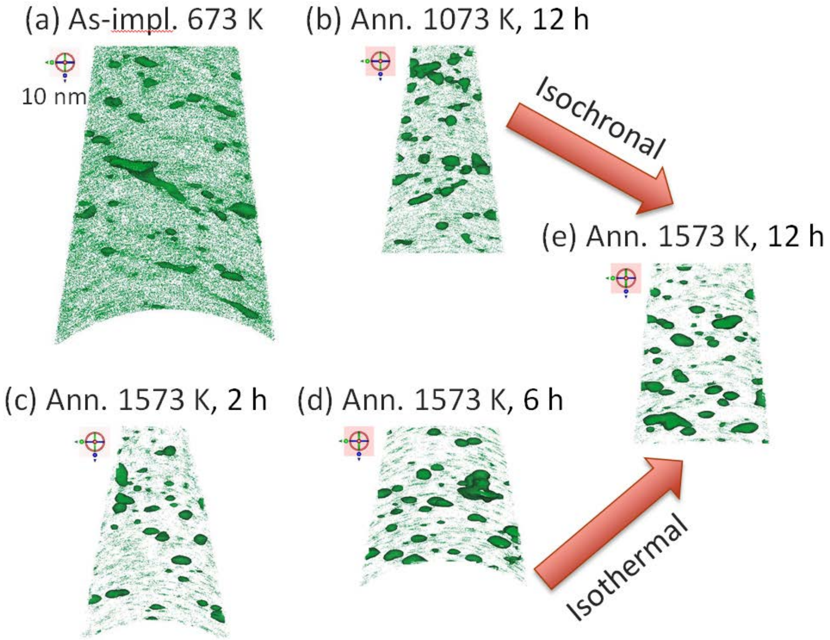

Figure 4. Iso-concentration surface at 10 at.% ^{25}Mg in 3C-SiC (a) implanted to 9.6×10^{16} ^{25}Mg/cm^2 at 673 K, and annealed at (b) 1073 K, 12 h, (c) 1573 K, 2 h, (d) 1573 K, 6 h, and (e) 1573 K, 12 h in Ar.

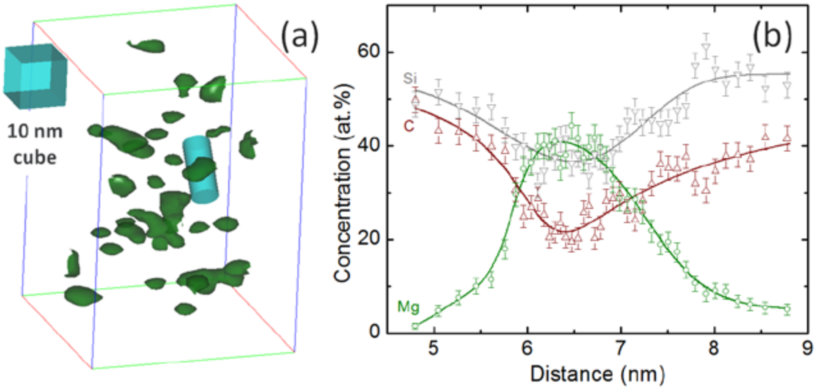

Figure 5. (a) Iso-concentration surface of ^{25}Mg at 16 at.% in 3C-SiC implanted to 9.6×10^{16} ^{25}Mg/cm^2 at 673 K and annealed at 1573 K for 12 h in Ar. (b) Concentration profiles of Si, C and Mg of the cluster scanned through a cylinder shown in (a).

are observed, including three-dimensional cluster shaped, plate-like, and curvilinear features through a series of cross sectional views of iso-concentration surfaces (data not shown).

A three-dimensional image of Mg-bearing clusters at surface concentration of 16 at.% ^{25}Mg in the implanted 3C-SiC annealed at 1573 K for 12 is shown in Figure 5(a). At this surface concentration, Mg-bearing clusters have sizes ranging from a few to over 10 nm. One-dimensional concentration profiles of Si, C and Mg from a cylinder scan across a selected precipitate indicated in Figure 5(a) are shown in Figure 5(b). The data show a distinct Mg concentration peak with a maximum of over 40 at.% Mg overlapped with depletion of both Si and C in the volume. The result is generally consistent with the EELS data (not shown) for this sample. There are also some precipitates that have the maximum concentration in excess of 80 at.% Mg [3], but diffraction spots of pure Mg metal are not observed from this sample.

An iso-concentration surface at 2.7 at.% ^{25}Mg is used in this study to define Mg precipitates for size analysis. In general, a lower surface concentration leads to a larger precipitate size because small clusters can be artificially connected into larger ones at low surface concentrations. For comparison, two definitions are used to calculate the precipitate size distribution. The first one is based on the radius of gyration R_g, which is the radius of a hypothetical body having all its mass concentration at a single distance from its center of mass, while having the same mass and the moment of inertia as the object [9]. For three dimensional precipitates, the hypothetical body is a spherical shell with a radius:

$$R_g = \sqrt{\left(R_{gx}^2 + R_{gy}^2 + R_{gz}^2\right)/3}, \tag{1}$$

where R_{gx}, R_{gy} and R_{gz} represent the radii of gyration in x, y and z directions. This value could underestimate the precipitate size [9] and is considered as the lower bound of the precipitates. The upper bound that could overestimate the precipitate size is defined as the extent dimension that accounts for the furthest Mg ions in the precipitates:

$$R_e = \sqrt{\left(R_{ex}^2 + R_{ey}^2 + R_{ez}^2\right)/3}. \tag{2}$$

Figure 6(a) shows the distributions of the total ranged Mg ions with the maximum R_g and R_e values equal to 7.7 and 19.3 nm, respectively. From the data, the mean radius is estimated to be from 0.9 to 2.2 nm, or precipitate size (diameter) from 1.8 to 4.4 nm. The second definition used in this study for estimation of the size is based on the precipitate volumes V_{Rg} and V_{Re}, representing the lower and upper bounds, respectively. The results from the analysis are plotted in Figure 6(b) with the maximum volumes V_{Rg} and

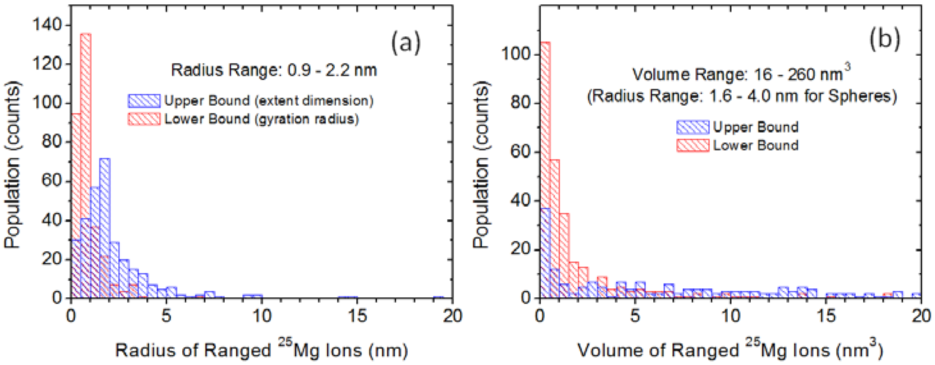

Figure 6. Size distribution as a function of (a) radius and (b) volume of ^{25}Mg-bearing precipitates, defined by iso-concentration surface at 2.7 at.% ^{25}Mg in 3C-SiC implanted to 9.6×10^{16} ^{25}Mg/cm^2 at 673 K and annealed at 1573 K for 12 h in Ar.

V_{Re} equal to 1,622 and 26,155 nm^3 that are out of the display range in the figure. The mean volumes of the precipitates are between 16 and 260 nm^3, equivalent to mean radii of 1.6 to 4.0 nm for a spherical shape. The corresponding size of the precipitates ranges from 3.2 to 8 nm, which is consistent with the STEM observation of 2-8 nm (Figure 1).

Acknowledgements

This research was supported by Office of Fusion Energy Sciences, U.S. Department of Energy (DOE) under Contract DE-AC05-76RL01830. Ion implantation was performed at the Ion Beam Materials Laboratory through partial support from the Center for Integrated Nanotechnologies (CINT), a DOE nanoscience user facility jointly operated by Los Alamos and Sandia National Laboratories. TEM and APT were performed under a general user proposal at the Environmental Molecular Sciences Laboratory (EMSL), a national scientific user facility located at PNNL. Isotope ^{25}Mg used in this research was supplied by the DOE Office of Science Isotope Program in the Office of Nuclear Physics.

References

[1] M. E. Sawan, Y. Katoh, and L. L. Snead, J. Nucl. Mater. 442 (2013) S370.
[2] W. Jiang, H. J. Jung, L. Kovarik, Z. Wang, T. J. Roosendaal, Z. Zhu, D. J. Edwards, S. Y. Hu, C. H. Henager, Jr., R. J. Kurtz, and Y. Wang, J. Nucl. Mater. 458 (2015) 146.
[3] W. Jiang, J. Liu, D. K. Schreiber, D. J. Edwards, C. H. Henager, Jr., R. J. Kurtz, and Y. Wang, Fusion Materials Semiannual Progress Report for Period Ending December 31, 2015, DOE/ER-0313/59, U.S. Department of Energy, 79.
[4] W. Jiang, J. Zhang, Z. Zhu, T. J. Roosendaal, S. Y. Hu, C. H. Henager, Jr., R. J. Kurtz, and Y. Wang, Fusion Materials Semiannual Progress Report for Period Ending June 30, 2015, DOE/ER-0313/58, U.S. Department of Energy, 119.
[5] J. F. Ziegler, J. P. Biearsack, and U. Littmark, *The stopping and Range of Ions in Solids* (Pergamon Press, New York, 1985); available from: http://www.SRIM.org/.
[6] S. Kondo, Y. Katoh, and L. L. Snead, Appl. Phys. Lett. 93 (2008) 163110.
[7] Y. N. Osetsky, D. Rodney, and D. J. Bacon, Phil. Mag. 86 (2006) 2295.
[8] R. A. Coward, C. R. Winkler, W. A. Hanson, M. L. jablonski, and M. L. Taheri, J. Nucl. Mater. 457 (2015) 298.
[9] M. K. Miller and R. G. Forbes, Atom-Probe Tomography: *The Local Electrode Atom Probe* (Srpinger, New York, 2014), p.319.

3.3 NEUTRON-IRRADIATION CREEP OF SILICON CARBIDE MATERIALS BEYOND THE INITIAL TRANSIENT

—T. Koyanagi, Y. Katoh (Oak Ridge National Laboratory), K. Ozawa (Japan Atomic Energy Agency), K. Shimoda, T. Hinoki (Kyoto University), L.L. Snead (Massachusetts Institute of Technology)

OBJECTIVE

The objective of this work is to evaluate the irradiation creep behavior of silicon carbide (SiC) materials to aid in the understanding of the performance of SiC composite as fusion reactor structural components.

SUMMARY

Irradiation creep beyond the transient regime was investigated for various SiC materials. The materials examined included polycrystalline or monocrystalline high-purity SiC, nanopowder sintered SiC, highly crystalline and near-stoichiometric SiC fibers, and a Tyranno SA3 SiC fiber reinforced SiC matrix composite fabricated through a nano-infiltration transient eutectic phase process. Findings are 1) the stress exponent of the post-transient creep was near unity, 2) the small apparent steady-state creep rate was ~1 × 10^{-7} [$\mathrm{dpa}^{-1}\mathrm{MPa}^{-1}$] at ~300 to ~800°C for most polycrystalline SiC materials, and 3) the effect of material quality on the creep rate, including structure of grain boundaries and crystal orientation, increased with increasing irradiation temperature. The results have been published in J. Nucl. Mater. [1] and a condensed version is given here.

PROGRESS AND STATUS

Introduction

Irradiation creep is an important phenomenon for nuclear materials because of its potential impact on the design stresses and service lifetimes of thermo-structural components. For SiC and SiC fiber reinforced SiC matrix (SiC/SiC) composites, irradiation creep is also known to be a key property in defining design limits. In short, and especially for materials such as SiC and its composites that possess very limited strain tolerance, irradiation creep provides an important stress mitigating function. This study shows high dose irradiation creep behavior of various SiC materials including monolithic ceramics, fibers, and a SiC/SiC composite. The experimental method can be found elsewhere [1].

Results

The creep coefficient, which is normalized creep strain with respect to stress and neutron fluence, is used to indicate creep rate and to compare the creep behavior of different materials [2]. The instantaneous creep coefficient (*K*) is defined by

$$K \cong \frac{\varepsilon_2 - \varepsilon_1}{\sigma(\gamma_2 - \gamma_1)} \ , \qquad (1)$$

where γ_1 and γ_2 ($\gamma_1 < \gamma_2$) are neutron fluences, σ is average stress during irradiation, and ε_1 and ε_2 are irradiation creep strains following irradiation to fluences of γ_1 and γ_2, respectively. Figure 1 shows the fluence dependence of the instantaneous creep coefficient of the SiC materials. The vertical error bars indicate one standard deviation. The highest and lowest horizontal error bars indicate the fluence of and for each data point, respectively. Figure 1 also shows the curves giving the creep behavior calculated by mechanistic models. The transient creep of chemical vapor deposited (CVD) SiC and sintered SiC materials is described using swelling-coupled creep and logarithmic creep, respectively [3]. The swelling-creep coupling values were expressed as products of the swelling coupling coefficient, applied stress, and swelling rate. Logarithmic creep is commonly observed in metals and ceramics in the transient stage of thermal creep. The behaviors of simultaneous transient creep (swelling coupling or logarithmic creep) and secondary creep with a constant creep coefficient of K = 1×10^{-7} or 2×10^{-7} [dpa MPa]$^{-1}$ are also shown in the graph.

The creep coefficients of CVD SiC decreased rapidly with increasing fluence in the transient creep regime up to ~1 dpa, and then the creep coefficients appeared to be constant at ~1×10^{-7} [MPa^{-1} dpa^{-1}] or to become very small, depending on the material type and irradiation temperature (Figure 1a). The swelling-creep coupling model is a good description of the initial transient creep behavior of CVD SiC materials up to ~1 dpa, as reported in [3]. However, this model cannot explain the creep behavior at higher fluence, which indicates the presence of secondary creep. Additional creep with a constant creep rate of 1×10^{-7} [MPa^{-1} dpa^{-1}] reasonably describes the overall creep behavior. The fluence dependence of the creep coefficients of the nano-powder sintered SiC (NT1 and NT2) is similar to that of CVD SiC: a significant reduction with increasing fluence up to ~1 dpa and an apparent steady state value of ~2×10^{-7} [MPa^{-1} dpa^{-1}] at higher fluence. The creep coefficients are slightly larger than for CVD SiC but are within the same order under both low- and high-dose irradiations, as shown in Figure 1b. The transient creep may be explained as logarithmic creep, as previously discussed [4]. Although the logarithmic creep cannot describe the creep behavior up to 30 dpa, simultaneous transient creep (logarithmic creep) and secondary creep at 2×10^{-7} [MPa^{-1} dpa^{-1}] reasonably fit the creep behavior up to 30 dpa. The creep coefficient of SiC fibers (HNS, SYL, SYL-iBN, and SA3) follows the trend of the nano-powder sintered materials rather than CVD SiC. No significant difference in fluence-dependent creep coefficient was observed between them. In summary, the radiation creep behavior of various SiC materials can be explained using simultaneous transient and secondary creep, and the creep coefficients are on the order of ~10^{-7} [MPa^{-1} dpa^{-1}] or less at 380–790°C above 1 dpa.

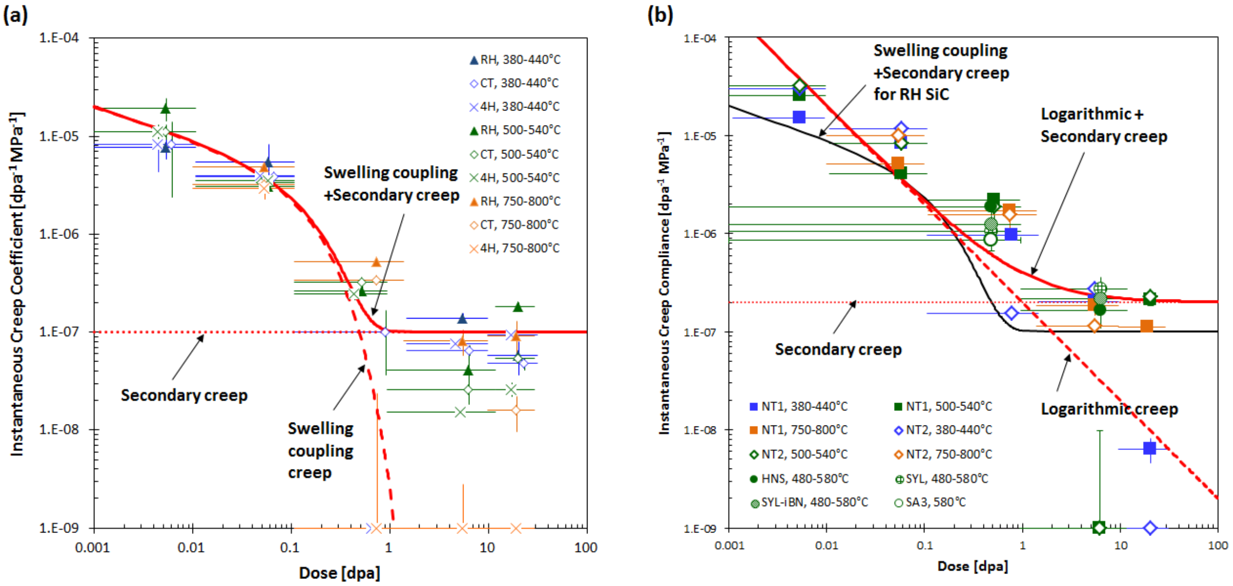

Figure 1. Neutron dose dependence of instantaneous creep coefficients of CVD SiC materials (a) and nanopowder sintered SiC and SiC fibers (b). Behavior based on creep models such as transient creep (swelling-coupled creep or logarithmic creep) and simultaneous transient and secondary creep is also shown. The data points on 1×10^{-9} [dpa MPa]$^{-1}$ in (a) are actually below that number.

The differential creep behavior among various SiC materials in Figure 1 indicates that the starting microstructure affected creep behavior in the post-transient regime. Microstructural differences among CVD SiC, sintered SiC, and SiC fibers included grain size and impurity phases located mainly between grains. Therefore, differential creep behavior is suspected to be caused by grain boundary–related mechanisms. Figure 2 shows instantaneous creep coefficients plotted against grain size for CVD SiC, sintered SiC, and SiC fibers. The grain size of single-crystal 4H SiC is assumed to be 40 mm, which is the length of the creep specimen. Irradiation temperature affected the grain-size dependence of the creep coefficient as follows. The creep was independent of grain size at ~400°C. Above this temperature, the SiC with smaller grains exhibited a larger creep coefficient, which was more significant at higher irradiation temperatures. Although the structures of grain boundaries are different depending on the material, the smaller grains led to the greater contribution of grain boundaries to irradiation creep.

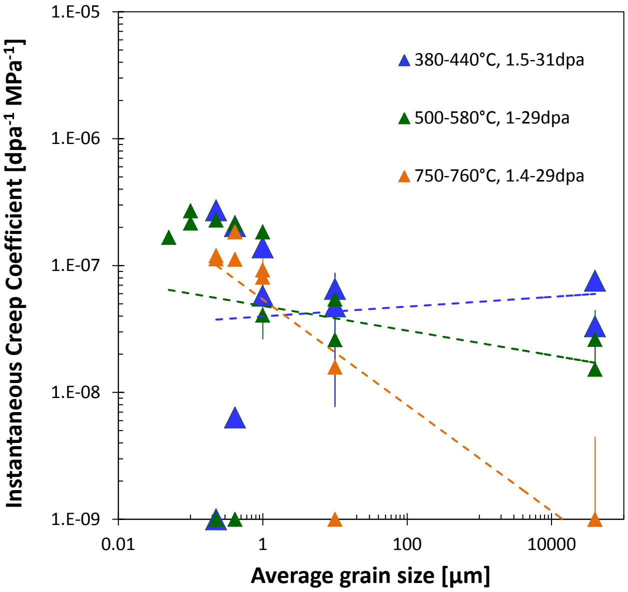

Figure 2. Grain-size dependence of instantaneous creep coefficient for various SiC materials. Trend lines fitted using a power law distribution are also shown. The data points on 1×10^{-9} [dpa MPa]$^{-1}$ are actually below that number.

We found that the instantaneous creep coefficient was ~1×10^{-7} [MPa dpa]$^{-1}$ at ~400 to ~750°C to ~1–30 dpa for all the SiC materials except for the SiC with coarse grains at ~750°C (Figure 2). That creep coefficient is compared with those of the metals in Figure 3. The post-transient irradiation creep was investigated for zirconium alloys, vanadium alloy (V-4Cr-4Ti), austenitic stainless steels including 316 and 304, oxide-dispersion-strengthened (ODS) ferritic steels (MA957 and HT9), and ferritic/martensitic steels (F82H and JLF-1). Those irradiation temperatures ranged from ~300 to ~700°C. The irradiation creep was investigated using a pressurized tube method for all the materials other than SiC. The stress exponents of those materials are reported to be between one and two. Although the test method, irradiation conditions, and stress exponents were different, the significant differences in the creep coefficient between SiC and the other materials can be discussed. The creep coefficient of the zirconium alloys was ~1×10^{-5} [MPa dpa]$^{-1}$. A slightly smaller creep coefficient of ~5 × 10^{-6} [MPa dpa]$^{-1}$ was obtained for the specific vanadium alloy. A much smaller creep coefficient of ~1×10^{-6} [MPa dpa]$^{-1}$ was typical for the austenitic stainless, ODS, and ferritic/martensitic steels. The creep coefficients of the SiC materials were approximately one order smaller than the coefficients for those steels. Therefore, the creep coefficients of the SiC materials are extremely small compared with those of the other nuclear materials. Although the smaller creep coefficient does not necessarily indicate a longer creep lifetime, it can be concluded that the smaller creep coefficient contributes to higher dimensional stability. In the case of the high-purity CVD SiC, the saturation of swelling above ~1 dpa in addition to the small creep coefficient makes the material more dimensionally stable in the irradiation environment than the metals.

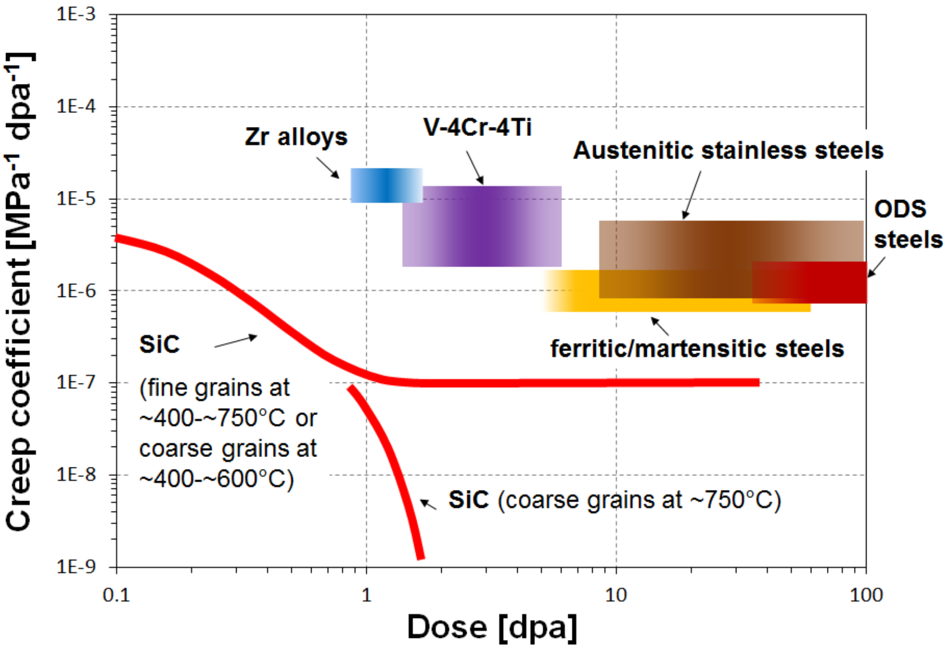

Figure 3. Comparison of typical creep coefficients among different nuclear materials. The data for the metals were reported in elsewhere [2, 5-13].

Acknowledgements

This work was supported by the Office of Fusion Energy Sciences, U.S. Department of Energy, under Contract DE-AC05-00OR22725 with UT-Battelle, LLC, and the US–Japan TITAN Collaboration on Fusion Blanket Technology and Materials. Research was supported in part by the High Flux Isotope Reactor, which is sponsored by the Office of Basic Energy Sciences, U.S. Department of Energy. The authors would like to gratefully acknowledge contributions to pre- and post-irradiation experiments from F. C. Montgomery, C. M. Silva, A. M. Williams, P. S. Tedder, C. Shih and M. R. McAlister at Oak Ridge National Laboratory, and M. Fukuda at Tohoku University.

References

[1] T. Koyanagi, Y. Katoh, K. Ozawa, K. Shimoda, T. Hinoki, L.L. Snead, Neutron-irradiation creep of silicon carbide materials beyond the initial transient, Journal of Nuclear Materials 478 (2016) 97-111.
[2] K. Ehrlich, Irradiation creep and interrelation with swelling in austenitic stainless steels, Journal of nuclear materials 100(1) (1981) 149-166.
[3] Y. Katoh, L.L. Snead, C.M. Parish, T. Hinoki, Observation and possible mechanism of irradiation induced creep in ceramics, Journal of Nuclear Materials 434(1) (2013) 141-151.
[4] T. Koyanagi, K. Shimoda, S. Kondo, T. Hinoki, K. Ozawa, Y. Katoh, Irradiation creep of nano-powder sintered silicon carbide at low neutron fluences, Journal of Nuclear Materials 455(1) (2014) 73-80.
[5] E. Ibrahim, R. Holt, Anisotropy of irradiation creep and growth of zirconium alloy pressure tubes, Journal of Nuclear Materials 91(2) (1980) 311-321.
[6] V. Fidleris, The irradiation creep and growth phenomena, Journal of Nuclear Materials 159 (1988) 22-42.
[7] F. Garner, D. Porter, Irradiation creep and swelling of AISI 316 to exposures of 130 dpa at 385–400 C, Journal of Nuclear Materials 155 (1988) 1006-1013.
[8] D. Porter, G. Hudman, F. Garner, Irradiation creep and swelling of annealed Type 304L stainless steel at~ 390° C and high neutron fluence, Journal of nuclear materials 179 (1991) 581-584.

[9] A. Kohyama, Y. Kohno, K. Asakura, M. Yoshino, C. Namba, C. Eiholzer, Irradiation creep of low-activation ferritic steels in FFTF/MOTA, Journal of nuclear materials 212 (1994) 751-754.
[10] M.B. Toloczko, D.S. Gelles, F.A. Garner, R.J. Kurtz, K. Abe, Irradiation creep and swelling from 400 to 600 C of the oxide dispersion strengthened ferritic alloy MA957, Journal of nuclear materials 329 (2004) 352-355.
[11] M. Ando, M. Li, H. Tanigawa, M. Grossbeck, S. Kim, T. Sawai, K. Shiba, Y. Kohno, A. Kohyama, Creep behavior of reduced activation ferritic/martensitic steels irradiated at 573 and 773K up to 5dpa, Journal of Nuclear Materials 367 (2007) 122-126.
[12] A. Malinge, A. Coupé, Y. Le Petitcorps, R. Pailler, Pressureless sintering of beta silicon carbide nanoparticles, Journal of the European Ceramic Society 32(16) (2012) 4393-4400.
[13] M. Li, D.T. Hoelzer, M.L. Grossbeck, A.F. Rowcliffe, S.J. Zinkle, R.J. Kurtz, Irradiation creep of the US Heat 832665 of V–4Cr–4Ti, Journal of Nuclear Materials 386 (2009) 618-621.

4. HIGH HEAT FLUX MATERIALS AND COMPONENT TESTING

4.1 DESIGN AND DEVELOPMENT OF NOVEL COPPER ALLOYS FOR FUSION ENERGY APPLICATIONS

—Ying Yang (Oak Ridge National Laboratory) and Steven J. Zinkle (University of Tennessee and Oak Ridge National Lab)

OBJECTIVE

This study aims at developing high strength, high conductivity Cu alloys with improved thermal creep strength for long pulse fusion high heat flux structures. It uses an accelerated approach of computational thermodynamics guided alloy design.

SUMMARY

A computation thermodynamics tool for designing and developing Cu-Cr-Nb-Zr alloys have been successfully developed. Thermodynamic modeling results based on this tool enabled a rapid development of a novel CuCrNbZr alloys with targeted microstructure using an economical, conventional ingot making method following by simple heat treatment procedures. The new alloys display uniform grain structure with bimodal distribution of precipitates.

PROGRESS AND STATUS

Introduction

High strength, high conductivity copper alloys are a potentially attractive option for the high heat flux structure in fusion energy systems. They are being utilized in ITER, and are under consideration for next step devices in Europe and elsewhere [1]. The conventional approach to produce high strength, high conductivity copper alloys uses fine-scale particles (either precipitates produced by solution anneal and aging, or inert dispersoids such as fine-scale oxides produced by powder metallurgy approaches). The optimized strength and conductivity near room temperature for copper alloys is typically achieved by introducing a small volume fraction ((f~1-5%) of uniformly dispersed nanoscale (diameter ~3-10 nm) precipitates or dispersoids [2]. Although impressive room temperature yield strengths of 300-1000 MPa and conductivities 200-360 W/m-K have been achieved in several Cu alloys, all current commercially available high strength, high conductivity Cu alloys suffer significant thermal creep deformation at temperatures above 300-400^{o}C [2]. Since 400^{o}C in Cu is equal to 0.5 T_M (where T_M is the melting temperature), which typically represents the onset of pronounced thermal creep in simple metals due to high atomic mobility, new Cu alloys specifically tailored for thermal creep resistance need to be designed in order to achieve improved strength near or above 400^{o}C. To date, there has been insufficient commercial incentive to develop high performance thermal creep-resistant Cu alloys since most of the current commercial applications for Cu alloys involve operating temperatures near room temperature (high field magnets, resistance spot welding electrodes, chill block molds, air- or water-cooled high heat flux apparatus, etc.)

Approach

Analysis of the thermal creep deformation mechanisms for existing Cu alloys near 400^{o}C suggests it is associated with dislocation (power law) creep and grain boundary sliding creep mechanisms [2]. For the design of improved high-performance radiation-resistant copper alloys at elevated temperatures, three key considerations (in addition to having high strength and conductivity) need to be successfully achieved: 1) thermally stable microstructure up to high temperatures; 2) specifically tailored microstructural features to inhibit the relevant thermal creep deformation mechanism (dislocation creep, grain boundary sliding, etc.) that are stable under neutron irradiation; and 3) sufficient sink strength to enable suitable radiation resistance. The physical metallurgy principles for designing high performance Cu alloys specifically tailored for resistance to thermal creep at elevated temperatures have been outlined by several authors [2-6]. Key design features include utilization of relatively large particles along grain boundaries to inhibit grain boundary movement along with a medium to high density of fine-scale matrix precipitates that provide resistance to dislocation motion. The fine-scale matrix particles also provide beneficial radiation resistance by promoting recombination of neutron irradiation-induced vacancies and interstitials [7]. For high creep strength, high thermal conductivity and radiation resistance, the optimized matrix particle distribution would consist of a volume particle concentration near f~1-5% with an average particle diameter near 10 nm [2]. The matrix and grain boundary particles must be resistant to thermal and radiation-enhanced coarsening during extended times (>1 year) at intended operating temperatures. It is also desirable (but not required) that the matrix and grain boundary particles be thermally stable during short-term exposure to joining-relevant temperatures (brazing, HIP, etc.).

The design of experimental alloy compositions and heat treatment scheme were aided by computational thermodynamics. The essence of computational thermodynamics, i.e., the CALPHAD (CALculation of PHAse Diagram) approach, was to construct phase diagrams of multicomponent systems based on well assessed thermodynamic functions of Gibbs energy of phases, through a step wise procedure such as binary$\rightarrow$ ternary $\rightarrow$ quaternary. This computational thermodynamic modeling study has been carried out for two quaternary systems, Cu-Cr-Nb-Zr and Cu-Cr-V-Zr.

Cu-Cr-Nb-Zr

The Cu-Cr-Nb-Zr system shows opportunity in forming medium-sized precipitates that pin grain boundary motion involves Cr_2Nb-type laves phase. Although Nb is not a low activation element (desirable for fusion energy applications), our initial efforts are focused on Cu-Cr-Nb-Zr alloys to examine the proof of principle of a newly designed thermal creep resistant alloy that also has good thermal and electrical conductivity and suitable neutron irradiation resistance at 300-450^{o}C.

Computational thermodynamic calculations of Cu-Cr-Nb, Cu-Cr-Zr and Cu-Cr-Nb-Zr alloys have identified several promising compositions and conventional metallurgy processing approaches that should produce a bimodal distribution of large grain boundary particles (e.g., Cu_5Zr or Cr_2Nb laves phase) and a medium to high density of matrix precipitate particles (e.g. Cr or Zr fine scale precipitates) that can be aged to provide good matrix strengthening up to 400-500^{o}C. Based on computational thermodynamic simulation, the new CuCrNbZr alloys were categorized into low Zr and high Zr alloys. Calculation results for low Zr alloys are shown here as an example.

Figure 1 provides a computational thermodynamic simulation on the isothermal phase diagram for the copper alloy within the Cu-Cr-Nb phase space for a constant 0.15 wt% level of Zr. The designed low Zr alloy alloys are located in the phase equilibria of FCC(Cu)+ Bcc(Cr)+Cu_5Zr+Laves_Cr_2(Nb,Zr).

Figure 2(a) provides the full scale plot showing the calculated amount (mole percent) of each phase as a function of temperature for the designed alloy, and Figure 2(b) shows the plot with the enlarged scale from 0 to 3 mole% , for a clear presentation of the amount of precipitate phases. Within the figure are noted the matrix FCC(Cu) phase and the precipitate phases Laves_Cr_2(Nb,Zr), BCC(Cr), Cu_5Zr and $Cu_{51}Zr_{14}$. Figure 2 provides a snapshot of the bimodal type of precipitate distribution, with Laves_Cr_2(Nb,Zr) as the large grain boundary precipitates, and BCC(Cr), Cu_5Zr and $Cu_{51}Zr_{14}$ as the matrix fine scale precipitates.

.

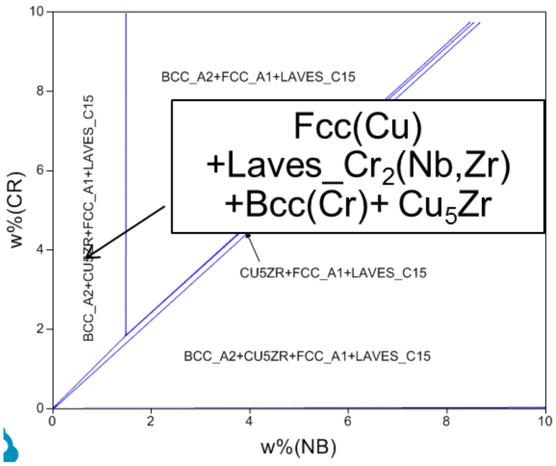

Figure 1. Isothermal section of Cu-Cr-Nb-Zr system at 600°C with a fixed Zr concentration at 0.15 wt%. The designed alloys have a microstructure with a matrix of FCC(Cu) strengthened by various types of precipitates such as Laves_Cr_2(Nb,Zr), Bcc(Cr) and Cu_5Zr.

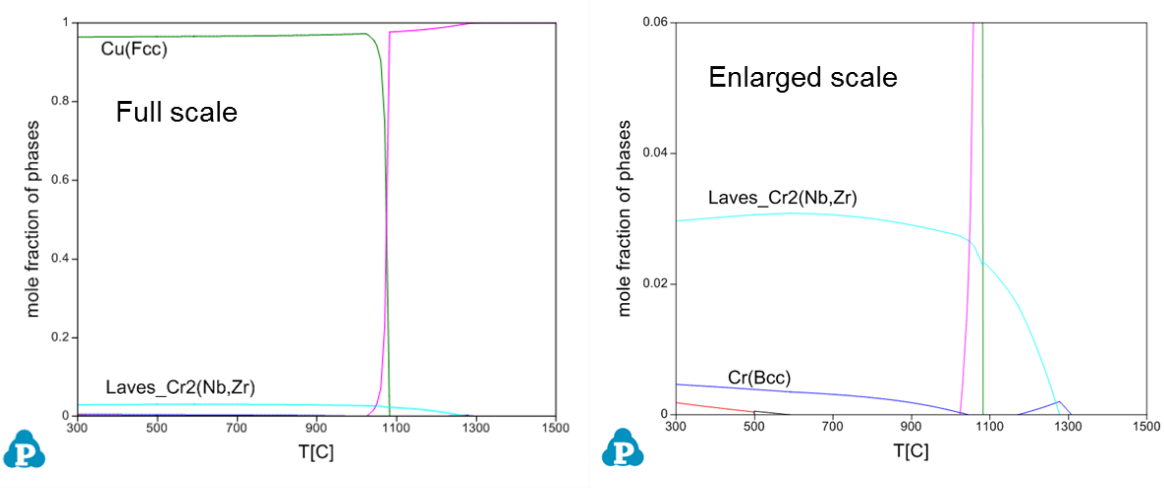

(a) (b)

Figure 2. Calculated mole fraction of phases in the designed alloy as a function of temperature in (a) full and (b) enlarged scale

<u>Cu-Cr-V-Zr</u>

V is a low activation element desirable for fusion energy applications. Therefore, the Cu-Cr-V-Zr was also thermodynamically modeled to explore the potential to form a bimodal distribution of precipitates. However, the modeling results suggested that there is no obvious advantage of V addition into the Cu-Cr-Zr alloys, in terms of precipitate distribution or amount. The same type of microstructure can be realized in the Cu-Cr-Zr ternary alloys. This is due to the lack of new precipitate phase in the Cu-Cr-V system. While in the Cu-Cr-Nb system, there exists the new precipitate Cr_2Nb. Ta and Cr can form the Cr_2Ta laves phase, therefore, Ta might be another element having similar behavior to Nb.

Experimental Procedure

A small ingot of the designed CuCrNbZr alloy was made at ORNL in an argon protected arc-melting furnace followed by drop-casting into the shape of a 0.5x0.5x10 inch rod, with an approximate mass of 100 g. The as-cast rod was then cold rolled at room temperature a total 70% and 50% reduction in thickness. The as-rolled materials were then subjected to various conventional heat treatment schemes, guided by the computational thermodynamics calculations. The optimum conditions were achieved in CCNZ5A and CCNZ5B alloys with the highest hardness, as shown in Table 1. The conditions without thermal aging are also listed in Table 1 for comparison.

Table 1. Heat treatment conditions and resulting hardness

Sample ID	**Processing (arc-melting and drop cast followed by)**	**Hardness (HV)**
CCNZ5A	Cold roll 70%, solutionized at 970C for 20m, water quench, aging at 475C for 3h, water quench	123.2±1.9
CCNZ5B	Cold roll 50%, solutionized at 970C for 20m, water quench, aging at 475C for 3h, water quench	126.2±7.7
CCNZ6A	Cold roll 70%, solutionized at 970C for 20m, water quench	60.5±3.7
CCNZ6B	Cold roll 50%, solutionized at 970C for 20m, water quench	60.6±0.7

Results

The results in Table 1 suggested that the amount of deformation had negligible effect on hardness, whereas the thermal aging at 475°C following solution quenching was very effective in increasing the alloy strength due to precipitation processes. The typical optical microstructures of samples are shown in Figures 4 (a)~(d), as observed in solution quenched and solution quenched plus aged conditions in the alloy that was initially subjected to 70% deformation. The grain structure with an average grain size of 20 µm was well developed in the thermal aged samples. Fine precipitates on the scale of 50~100 nm were found distributed along grain boundaries and dislocation lines.

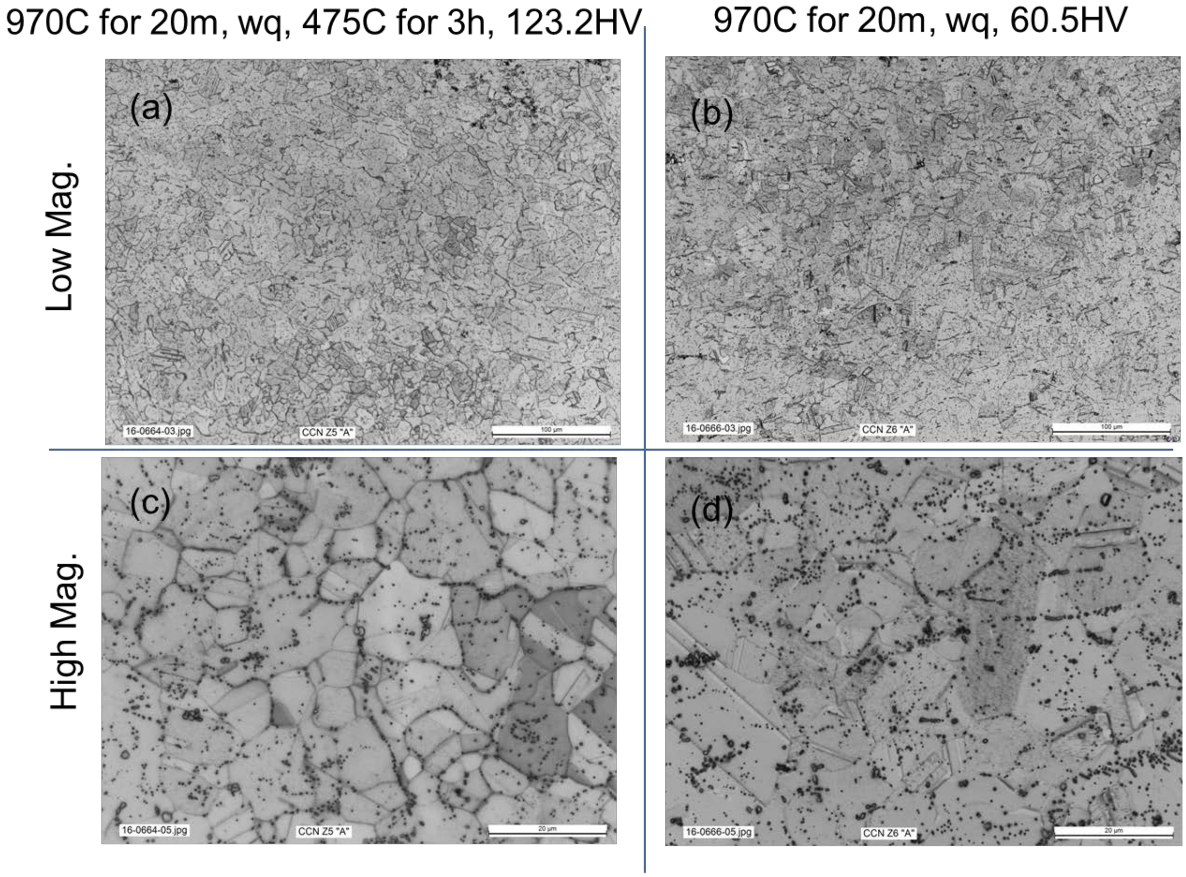

Figure 3. Typical microstructures of samples from the two conditions after 70% deformation.

High resolution of SEM (Scanning Electron Microscopy) BSE (Backscattered Electron) images of samples from CCNZ5A is shown in Figure 4 together with a high magnification optical image. The comparison of the two images in Figure 4 reveals a bimodal distribution of precipitates in the newly designed CuCrNbZr alloy: Cr_2Nb-Laves precipitates (~50-100nm diameter) are distributed at grain boundaries and matrix dislocations, and small Cr (~10nm diameter) precipitates are distributed in the matrix. These ultrafine matrixes Cr precipitates made great contribution to the overall enhancement of hardness as shown in Table 1. The TEM analysis on these ultrafine matrix precipitates is currently in progress.

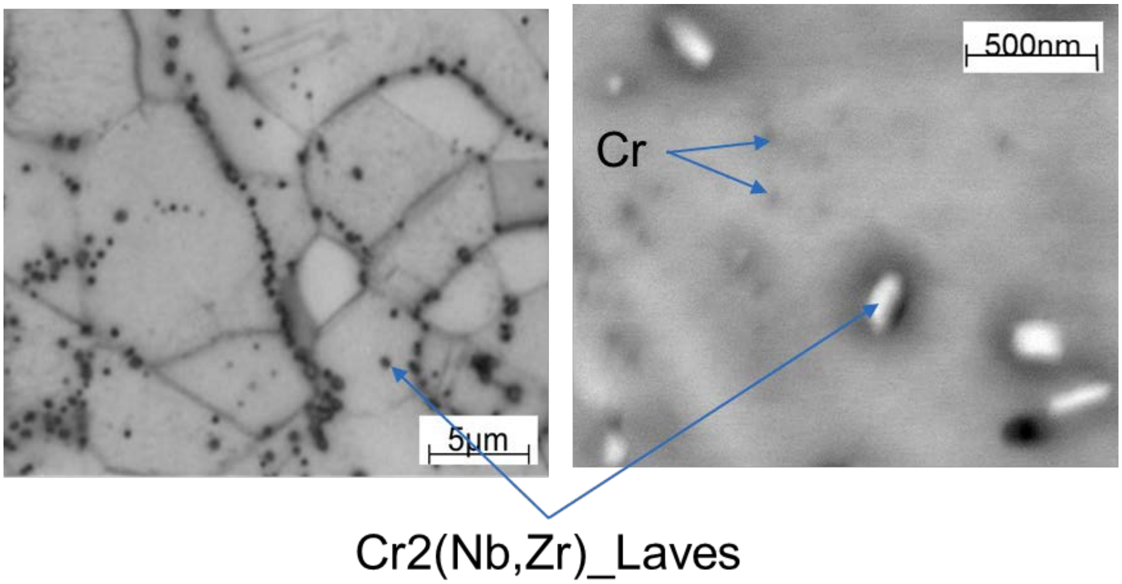

Figure 4. Comparison optical image with SEM BSE image showing a bimodal distribution of precipitates in CCNZA5 samples.

Future work

1) Complete TEM characterization of fine and ultrafine precipitates, and measure the tensile properties of the CCNZA5 and CCNZ5B samples between room temperature and 500°C.
2) Continue experimental study of the additional designed model alloys (based on insight obtained from the TEM and tensile characterization of the initial Cu alloy heats).
3) Perform thermodynamic calculations on the Cu-Cr-Ta-Zr system to explore the potential to achieve reduced activation high-performance Cu alloy for high heat flux substrates.

References

[1] D. Stork, P. Agostini, J.L. Boutard, D. Buckthorpe, E. Diegele, S.L. Dudarev, C. English, G. Federici, M.R. Gilbert, S. Gonzalez, A. Ibarra, C. Linsmeier, A. Li Puma, G. Marbach, P.F. Morris, L.W. Packer, B. Raj, M. Rieth, M.Q. Tran, D.J. Ward, S.J. Zinkle, J. Nucl. Mater., 455 (2014) 277-291.
[2] S.J. Zinkle, Phys. Scr., T167 (2016) 014004.
[3] K.R. Anderson, J.R. Groza, Metall. Mater. Trans. A 32 (2001) 1211.
[4] J.R. Groza, J.C. Gibeling, Mater. Sci. Eng. A171 (1993) 115.
[5] C. Sauer, et al., Int. J. Powder Metall. 33 (1997) 45.
[6] C. Sauer, et al., Z. Metallkunde 89 (1998) 119.
[7] S.J. Zinkle, L.L. Snead, Annu. Rev. Mater. Res. 44 (2014) 241.

4.2 PRELIMINARY PROGRESS IN THE DEVELOPMENT OF DUCTILE-PHASE TOUGHENED TUNGSTEN FOR PLASMA-FACING MATERIALS: DUAL-PHASE FINITE ELEMENT DAMAGE MODELS

C. H. Henager, Jr., B. N Nguyen, R. J. Kurtz (Pacific Northwest National Laboratory)

OBJECTIVE

The objective of this study is to develop a finite element continuum damage model suitable for modeling deformation, cracking, and crack bridging for W-Cu, W-Ni-Fe, and other ductile phase toughened W-composites, or more generally, any multi-phase composite structure where two or more phases undergo cooperative deformation in a composite system.

SUMMARY

A promising approach to increasing fracture toughness and decreasing the ductile-brittle transition temperature (DBTT) of a W-alloy is by ductile-phase toughening (DPT) [1-3]. In this method, a ductile phase is included in a brittle matrix to prevent fracture propagation by crack bridging or crack deflection. Liquid-phase sintered W-Ni-Fe alloys and hot-pressed and sintered W-Cu composites are two examples of such materials that PNNL and UCSB are investigating. However, there is a need for improved mechanical property models of such composite systems in order to begin to optimize these structural materials with regard to strength and fracture toughness. This report describes such a model that is currently under development at PNNL.

PROGRESS AND STATUS

Background

Tungsten (W) and W-alloys are the solid materials of choice for plasma-facing components (PFCs) of future fusion reactors, such as the International Thermonuclear Experimental Reactor (ITER) and Demonstration Power Plant (DEMO), due to their high melting point, strength at high temperatures, high thermal conductivity, low coefficient of thermal expansion, and low sputtering yield [4-6]. However, W and most W-alloys exhibit low fracture toughness and a high DBTT that would render them as brittle materials during reactor operations [4, 6, 7]. The DBTT for unirradiated W-alloys typically ranges from 573K to 1273K (300 to 1000˚C) and in a reactor environment radiation hardening would further elevate this range [6, 8, 9]. W-alloys toughened by engineered reinforcement architectures, such as ductile-phase toughening (DPT), are strong candidates for PFCs. In DPT, a ductile phase is included in a brittle matrix to prevent fracture propagation. The principles of DPT are illustrated in Figure 1, which shows an actual and schematic illustration of ductile bridging ligaments stretching across an open crack in a brittle matrix material, such as W [10].

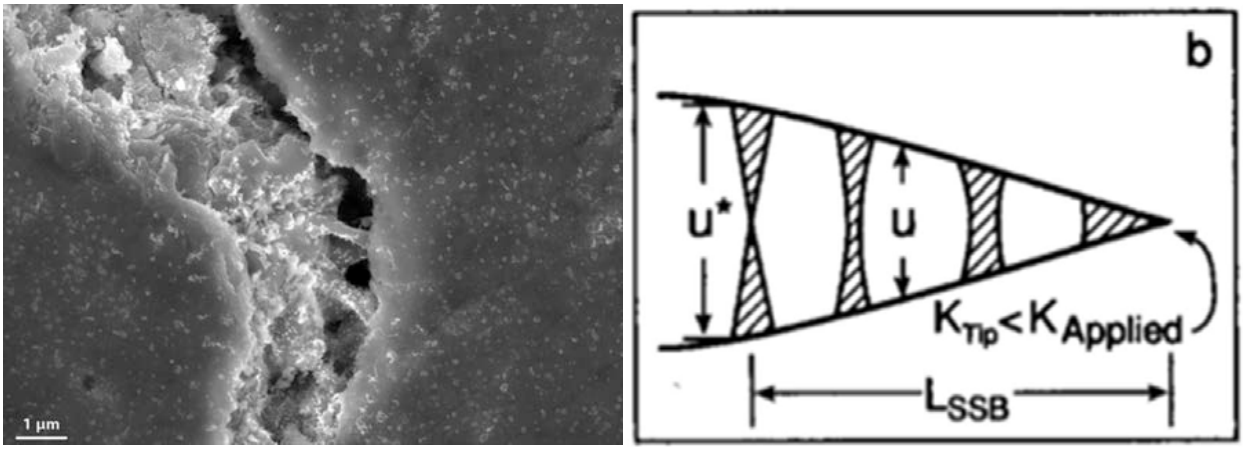

Figure 1. a) SEM image of W-Cu fracture where the ductile phase (Cu) is effectively bridging the crack. b) A steady-state bridging zone shown schematically in 2D [10].

Model Development

The specifics of the finite element continuum damage model (FE-CDM) developed at PNNL have been discussed previously [11, 12]. To understand how deformation proceeds, and how cracks initiate and propagate in DPT W-composites, finite element analyses of W-composite specimens subjected to bending are being performed using the FE-CDM model for elastic and elastic-plastic materials. The CDM is implemented in the ABAQUS® finite element code via user defined subroutines. This CDM model derived from a model developed for long-fiber thermoplastic composites [13] is now being applied at the micron and submicron scale by creating dual-phase FE mesh regions in both 2D and 3D for 3-point and 4-point bend bars for direct comparison to notched bend data. The constitutive behavior of each phase in the modeling domain is described by the CDM to explore deformation, cracking, and crack bridging in these composite materials. Comparative analyses using an elastoplastic damage model available in ABAQUS are being performed to assess the predictions by this damage model.

Summary of Approach

The FE mesh for these models is created from digital images of actual microstructures by using the public domain software OOF2[1] that creates multiple mesh domains with high-resolution elements at phase boundaries. The software allows the user to specify mechanical properties for each meshed region and outputs an input file for ABAQUS®. Figure 2 is an image of a W-Cu sample microstructure and its associated FE mesh for a notched bend bar.

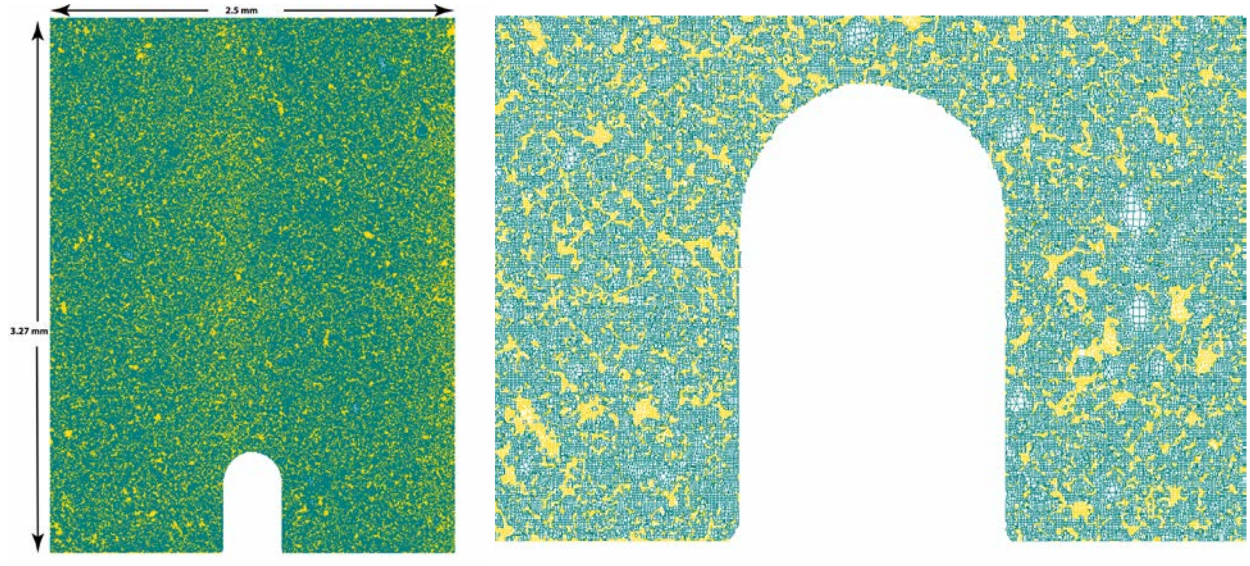

(a) (b)

Figure 2. W-Cu composite with a FE mesh shown in (a) of the entire width and a portion of the length of a 3-point single-edge-notched beam (SENB) test bar that is 3.27 x 1.60 x 16.10 mm in size with a magnified region shown in (b) with the phase regions identified by color. Dark green is tungsten and light yellow is copper. The large mesh model in (a) contains two separate meshes each with its own set of mechanical properties and consists of more than 800K finite elements both triangular and quadrilateral types.

The approach is to create homogenized, meshed regions alongside the dual-phase meshed region shown in Figure 2a to create a fully meshed model of a bend bar that corresponds to the physical dimensions of our 3-point and 4-point bend samples. Thus, homogenized regions 3.27 x 6.8 mm will be created and added to the dual-phase meshed region shown in Figure 2a to achieve a full sized FE model

---

[1] OOF2 was developed at the National Institute of Standards and Technology (NIST). See http://www.ctcms.nist.gov/oof/oof2/.

of the 3-point SENB test bar. The dual-phase meshed region at the notch is required to capture the proper cracking patterns observed in the bending test of the W-composites.

The FE model will then be deformed in 3-point bending, for the case of the W-Cu composite shown in Figure 1, and the load-displacement response will be compared to the experimental data. The FE damage model predictions would also be compared to the actual cracking observed in the bend specimens. In this way, the use of the separate constitutive relations (see Figure 3) for tungsten and copper can be validated against experiment since there are uncertainties in assuming that bulk tungsten and bulk copper constitutive relations apply to these fine-scale W-Cu composites. Larger FE models will be similarly created for the 4-point SENB test bars used to study the newer W-Ni-Fe composites.

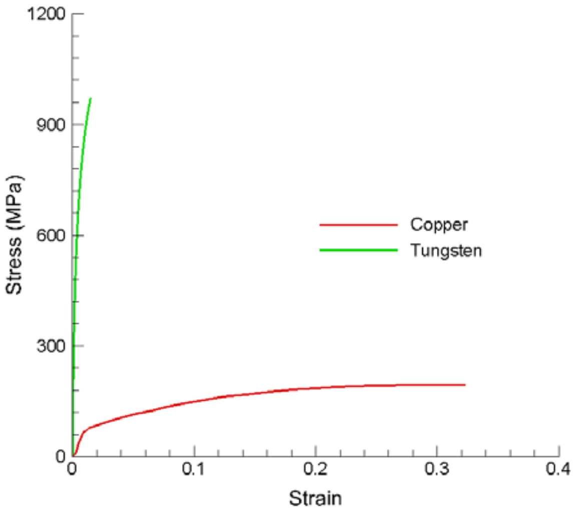

Figure 3. Constitutive relations initially assumed for each of the two phases, W and Cu, based on bulk behavior. The W phase is strong and brittle while the Cu phase is softer and much more ductile.

Discussion

This approach is anticipated to be an improvement over the dynamic bridging model previously developed and discussed to describe the amount of load sharing observed in the bend sample that increased with increasing temperature [14]. We had previously observed that multiple cracking occurs naturally in the FE-CDM model but we did not yet perform simulations as a function of temperature. We intend to show agreement with our experimental data with respect to load-displacement curves and to the distributed cracking and damage in the W-Cu composite that was one of the most significant observations made in our experimental work with this material.

Future Work

We will continue to create meshed models that correspond to actual 3D bend bar microstructures and to begin the process of model validation using SENB data.

References

[1] Deve, H.E., A.G. Evans, G.R. Odette, R. Mehrabian, M.L. Emiliani, and R.J. Hecht, Acta metallurgica et materialia, 1990. 38(8): p. 1491-502.

[2] Erdogan, F. and P.F. Joseph, J. Am. Ceram. Soc., 1989. 72(2): p. 262-270.

[3] Sigl, L.S., P.A. Mataga, B.J. Dalgleish, R.M. McMeeking, and A.G. Evans, Acta Metall., 1988. 36(4): p. 945-953.

[4] Rieth, M., J.L. Boutard, S.L. Dudarev, T. Ahlgren, S. Antusch, N. Baluc, M.F. Barthe, C.S. Becquart, L. Ciupinski, J.B. Correia, C. Domain, J. Fikar, E. Fortuna, C.C. Fu, E. Gaganidze, T.L. Galan, C.

Garcia-Rosales, B. Gludovatz, H. Greuner, K. Heinola, N. Holstein, N. Juslin, F. Koch, W. Krauss, K.J. Kurzydlowski, J. Linke, C. Linsmeier, N. Luzginova, H. Maier, M.S. Martinez, J.M. Missiaen, M. Muhammed, A. Munoz, M. Muzyk, K. Nordlund, D. Nguyen-Manh, P. Norajitra, J. Opschoor, G. Pintsuk, R. Pippan, G. Ritz, L. Romaner, D. Rupp, R. Schaublin, J. Schlosser, I. Uytdenhouwen, J.G. Van Der Laan, L. Veleva, L. Ventelon, S. Wahlberg, F. Willaime, S. Wurster, and M.A. Yar, J. Nucl. Mater., 2011. 417: p. 463-467.

[5] Pitts, R.A., A. Kukushkin, A. Loarte, A. Martin, M. Merola, C.E. Kessel, V. Komarov, and M. Shimada, Physica Scripta Volume T, 2009. 2009(T138): p. 014001 (10 pp.).

[6] Mertens, P., T. Hirai, M. Knaup, O. Neubauer, V. Philipps, J. Rapp, V. Riccardo, S. Sadakov, B. Schweer, A. Terra, I. Uytdenhouwen, and U. Samm, Fusion Eng. Des., 2009. 84(7-11): p. 1289-93.

[7] Mertens, P., V. Philipps, G. Pintsuk, V. Riccardo, U. Samm, V. Thompson, and I. Uytdenhouwen, Physica Scripta Volume T, 2009. 2009(T138): p. 014032 (5 pp.).

[8] Gludovatz, B., S. Wurster, A. Hoffmann, and R. Pippan, Int. J. Refract. Met. Hard Mater., 2010. 28(6): p. 674-8.

[9] Zinkle, S.J. and N.M. Ghoniem, Fusion Eng. Des., 2000. 51-52: p. 55-71.

[10] Odette, G.R., B.L. Chao, J.W. Sheckherd, and G.E. Lucas, Acta metallurgica et materialia, 1992. 40(9): p. 2381-9.

[11] Henager, C.H., B.N. Nguyen, R.J. Kurtz, T.J. Roosendaal, B.A. Borlaug, M. Ferraris, A. Ventrella, and Y. Katoh, J. Nucl. Mater., 2015. 466: p. 253-268.

[12] C. H. Henager, J., B.N. Nguyen, R.J. Kurtz, M. Ferraris, and Y. Katoh, in *Fusion Reactor Materials Program Semiannual Progress Reports*, Vol. 58, F. Wiffen, R. Godfrey, and B. Waddell, Editors. 2015, ORNL: Oak Ridge, TN. p. 108-118

[13] Nguyen, B.N. and V. Kunc, Int. J. Damage Mech., 2010. 19(6): p. 691-725.

[14] Cunningham, K.H., K. Fields, D. Gragg, F.W. Zok, J. C. H. Henager, R.J. Kurtz, and T. Roosendaal, in *DOE/ER-0313/54 - Volume 54, Semiannual Progress Report, June 30, 2013*, Vol. 54, F. Wiffen, R. Godfrey, and B. Waddell, Editors. 2013, US DOE: ORNL, TN. p. 95-107

4.3 DUCTILE PHASE TOUGHENING OF 90-97wt% W-NiFe HEAVY METAL ALLOYS

M.E. Alam, S. Pal, K. Field, G. R. Odette (UCSB)

OBJECTIVE

The objective of this research is to develop W-Ni:Fe and other heavy metal W alloys as ductile phase toughened composites for the fusion reactor divertor applications.

SUMMARY

Ductile phase toughening (DPT) is a promising approach to improving toughness of brittle materials like tungsten (W). The fracture toughness of commercial liquid phase sintered W-based composites, containing 90, 92.5, 95 and 97 wt.% W, with the balance a 7:3 Ni:Fe ductile solid solution phase, has been characterized. Pre-cracked single edge notch bend bar fracture toughness tests were conducted at room temperature. The average maximum load initiation toughness averaged 102 ± 17 MPa√m, relatively independent of the W fraction up to 95 wt.%, but dropped to 71± 17 MPa√m for the 97%W alloy. However, crack blunting beyond the peak load (down to $P/P_{max} \approx 0.8$), prior to any significant crack growth (da), resulted in an even higher toughness of 168 ± 31 MPa√m. The toughness of the W-Ne:Fe composites compare to typical monolithic-W values of ≈ 8 MPa√m. Composite fracture occurs by stable crack growth. The enormous toughening is due to crack bridging and especially very large plastic zone deformation energy dissipation.

PROGRESS AND STATUS

Introduction

Tungsten (W) is the leading candidate for plasma facing component of the future fusion reactor divertor applications due to its high melting temperature, good conductivity, low sputtering rates and high temperature strength [1-2]. However, an elevated brittle to ductile transition (BDT) temperature and low toughness (and ductility), which are further degraded by neutron irradiation, limit W's application as structural material. One promising approach to toughening is to include ductile phases (DP) in ta W-composite to restrict crack propagation by crack bridging and deflection mechanisms, as well as to provide energy dissipating crack tip plastic deformation processes. Both bridging and crack tip plastic deformations increase the toughness and lower the composite BDT [3]. Tungsten heavy (metal) alloys (WHAs), or composites, typically consist of 78-98 wt.% W and other ductile phase separated elements like Ni, Fe, Cu, Co, Cr. They have been studied for several decades. Most of this research has focused on processing optimization and relating the WHA microstructure to tensile properties. Surprisingly, only very few studies have been conducted on the fracture toughness of WHA's [4]. Following previous work carried out at PNNL, in collaboration with UCSB, we carried out room temperature fracture toughness tests of W-Ni:Fe WHA with 90 to 97 wt.%W. Complementary microstructural, hardness and tensile tests were also conducted.

Experimental Procedure

Four commercially available (Mi-Tech Metals, Indianapolis, In, USA) liquid-phase sintered W-Ni:Fe composites with 90, 92.5, 95 and 97 W (wt.%) and balance 7:3 Ni:Fe (see Table 1) were studied. Note it is very important to emphasize that these WHA are composed of a small volume fraction of a semi-continuous Ni:Fe fcc solid solution ductile phase, surrounding a much higher volume fraction of large W-particles. The WHA's were received in the form of 100mmx100mmx14mm plates. The specimens for the different tests were fabricated using electro-discharge machining (EDM). They were ground with to 2000 grit sand paper to remove EDM damage and residual surface stresses. Some fracture specimen sides were then polished down to 0.5µ-diamond paste, and etched in a 30% hydrogen peroxide solution for 10min to facilitate microstructural characterization. Scanning electron microscopy (SEM) with energy dispersive spectroscopy (EDS), and electron backscatter diffraction (EBSD), were used to image W particles and the surrounding Ni:Fe phase, and to identify their respective compositions.

Vickers microhardness measurements were performed on the polished surfaces at a 500g load using a LECO M-400A semi-automated hardness tester, and the reported values are based on the average of 10 to 15 indents. Nanoindentation (TriboIndenter, Hysitron Inc., MN, USA) with a Berkovich tip was used to measure the reduced elastic modulus (E_r) and the nanohardness (NH) of W and Ni:Fe phases under a 10mN loading cycle: 10s ramp loading, 10s dwell and 10s unloading. The unloading curve was used to characterize E_r. Room temperature tensile tests were performed on EDM fabricated flat dog-bone shaped sub-sized specimens with a gauge section length x width x thickness of 5.0x1.2x0.5 mm^3. The tensile specimens were sanded with 1500 grit to remove minor defects and surface residual stresses due to EDMing. The tests were carried on an 810 MTS servo-hydraulic universal load frame with a 956 controller. Tensile loading was at a crosshead speed of 0.30 mm/min, corresponding to a strain rate of $\approx 10^{-3}$/s; crosshead displacement was used to measure strain and the corresponding tensile ductility parameters.

Room temperature fracture toughness test were conducted on fatigue pre-cracked single-edged notch three-point (3PB) and four-point bend (4PB) bend specimens with nominal length x width x thickness dimensions of 16x3.3x1.65 mm^3. Pre-cracking and fracture testing were also carried out on the 810 MTS servo-hydraulic load frame. The specimens were pre-cracked to a nominal crack length (a)-to width (W) ratios, (a/W), from 0.3 to 0.5. To facilitate in-situ optical observation of the crack tip region, the fracture specimen sides were sanded with a sequence of 2000 grit, 9µ, 3µ and 1µ papers. Initially 4PB tests were conducted, in part to help control possible unstable crack growth. However, since the crack growth was found to be highly stable, subsequent fracture testing was based on a 3PB fixture. The fracture tests were carried out at a crosshead speed of 0.04mm/min. ASTM C1421 and ASTM E1921 were used to calculate the elastic and plastic components of the fracture toughness, respectively, for the 4PB tests. ASTM E1921 was used to evaluate both the elastic and plastic components of fracture toughness for the 3PB tests. The K_{Jc} were calculated at the maximum load (P_m) in the load-displacement (P-d) curve. K_{Jc} were also evaluated at loads down to ≈ 80% of P_m, since there was minimal crack growth (< 200 µm) for the displacements up to this loading point. The 4PB tests were carried out down to very low P, involving extensive crack tearing to near the back of the specimen. The 3PB tests were stopped at P/Pm of 0.77 to 0.92 to better evaluate an initiation toughness and corresponding crack tip opening displacement (CTOD). The pre-crack and crack lengths were also measured after the specimens were broken in LN_2.

Table 1. Chemical compositions (wt.%) of the W-Ni:Fe alloys

WHA	W	Ni	Fe	Ductile phase (DP) area fraction (%)	DP compositions: Ni/W/Fe
90W	90.27	6.78	2.95	21.4	51.2/28.5/20.3
92.5W	92.48	5.33	2.19	14.9	49.1/31.3/19.6
95W	95.03	3.48	1.49	12.3	49.1/32.2/18.7
97W	97.13	2.01	0.86	9.3	48.3/34.3/17.4

Results

Microstructure

SEM micrographs of the polished and etched W-N:iFe plates shown in Figure 1 reveal roughly spheroidal W particles surrounded in the interconnected skeleton of a ductile Ni:W:Fe phase. An EDX scan shows that the particles are close to 100% W, while the Ni:W:Fe phase is approximately 50%Ni, 30%W and 20%Fe. The fraction of W in the Ni:W:Fe phase increases slightly from 28.5 wt% to 34.3 wt% with increasing WHA W (Table 1). Figure 1 also shows the W–particle size increases from ≈ 18 µm for 90W-Ni-Fe alloy to ≈ 38 µm for 97W-Ni-Fe alloy (Table 2 and Figure 1). The increase in the W-particle size permits maintaining a similar Ni:W:Fe ductile phase (DP) skeleton web thickness with an increasing fraction of W. This may be an important alloy design consideration in developing WHA with more than 97% W. Of course the area fraction of the Ni:W:Fe phase decreases with higher W. Shapes of the particles are generally spheroidal up to 95W alloys, and become slightly more polyhedral at 97W. A higher W fraction lowers the Ni:W:Fe phase continuity and increases the W-W contiguity and particle bonded W-W interfaces. Note the 95W WHA contains some cracked W particles (red arrows in Figure

1c), although the reason for this is not known. Figure 2 shows the EBSD inverse pole figure (IPF) maps for the 90W alloy, indicating random orientations of the W particles. Some large particles show multiple textures in a single particle that are likely due to multiple grains or subgrains at the larger size.

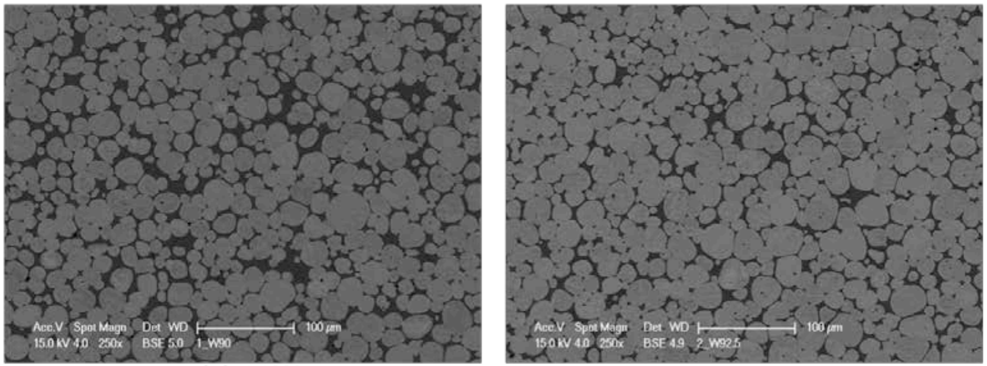

(a) 90W (b) 92.5W

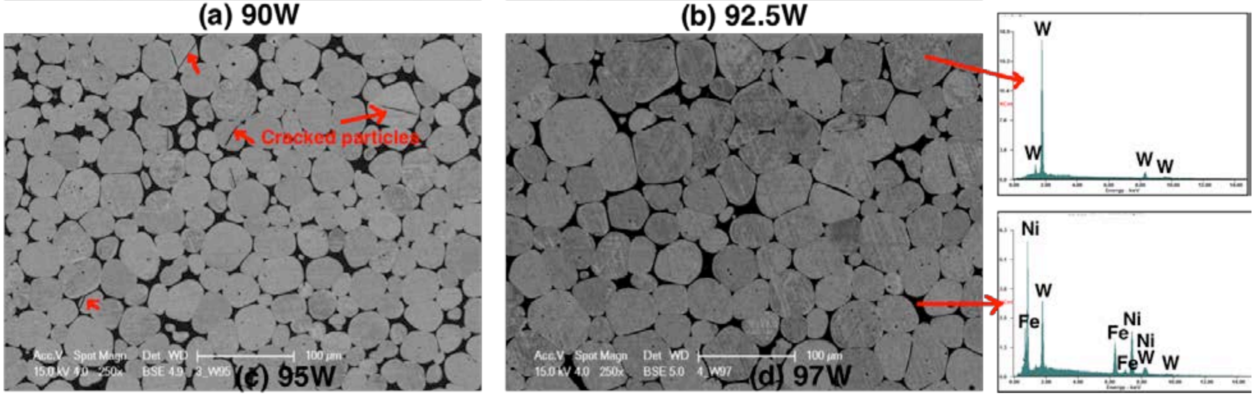

Figure 1. SEM images show the spheroidal W-particle and matrix of: (a) 90W, (b) 92.5W), (c) 95W, and (d) 97W, respectively. EDX images show the 99+% pure W particles embedded in Ni-rich Ni-W-Fe matrix.

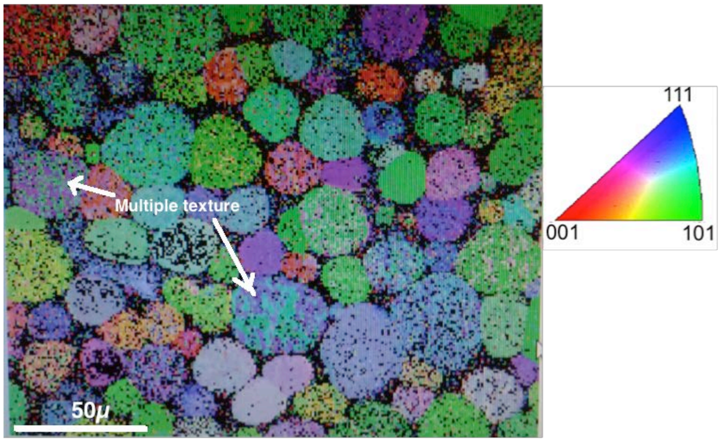

Figure 2. EBSD IPF maps show random texture, in general, with multiple textures in some large particles.

Nanoindentation and Microhardness

Table 2 shows the reduced elastic modulus (E_r) of W-particles and Ni:W:Fe phase for all four alloys. The average modulus of elasticity varies from 378 to 428 GPa for W-particles and 259 to 296 GPa for the Ni:W:Fe phase. The highest E_r is in the 95% W alloy. Nanohardness (NH) was also calculated from the indentation loading-unloading curves. The 95W alloy also shows the highest hardness of 7.2GPa, while the Ni:W:Fe phase shows the lowest hardness of ≈ 4.3 GPa. Vickers microhardness (H_v) data for the W-alloys are also summarized in Table 2. While the hardness varies between 321 (90%W) to 349 kg/mm^2 for all the W alloys, the 95W alloy again shows the highest H_v.

Table 2. Particle size, modulus of elasticity and hardness of WNiFe alloys

Code name	**Particle size (µm)**	**Er (GPa)**		**Nano-H (GPa)**		**µ-H (Hv), kg/mm^2**
		W-particle	**Matrix**	**W-particle**	**Matrix**	
90W	18 ± 7	397 ± 17	269 ± 20	7.0 ± 0.3	5.3 ± 0.2	321 ± 9
92.5W	18 ± 7	378 ± 12	268 ± 18	5.8 ± 0.2	4.8 ± 0.1	334 ± 8
95W	27 ± 11	428 ± 8	296 ± 31	7.2 ± 0.4	4.3 ± 0.2	349 ± 7
97W	38 ± 15	394 ± 29	259 ± 12	6.3 ± 0.6	4.9 ± 0.2	344 ± 9

Tensile Properties

Figure 3 shows the engineering stress-strain s(e) curves along with macroscopic fracture surface from room temperature tensile tests on the W-Ni:Fe alloys. The s(e) curves are generally similar, although the total elongation systematically decreases with increasing W. Significant strain hardening is observed in all cases. The tensile data are summarized in Table 3. The 0.2%-offset yield stress (s_y) does not vary significantly with W. However, ultimate tensile stress (s_u), uniform (e_u) and total (e_t) elongations, and reduction in area (RA) of the neck decrease with increasing W; and there is a noticeable strength and ductility drop off between 95 and 97%W. Fracture in these alloys takes place almost immediately after reaching ultimate tensile stress. Macroscopic fracture surfaces shows minimal necking, expect for 90W alloy, reflected in their lower RA value.

Table 3. Room temperature tensile properties of W-Ni:Fe alloys

Code name	**s_y (MPa)**	**s_u (MPa)**	**s_y/s_u**	**e_u (%)**	**e_t (%)**	**Hardening exponent, n**	**RA (%)**
90W	621 ± 29	891 ± 35	0.70	18 ± 4	21 ± 7	0.094	25.8
92.5W	616 ± 44	886 ± 12	0.70	13.5 ± 2.2	16 ± 4	0.099	13.1
95W	600 ± 15	818 ± 10	0.73	7.3 ± 1	8 ± 1	0.102	9.3
97W	594 ± 27	701 ± 67	0.85	3.4 ± 1	4 ± 0.7	0.071	6.2

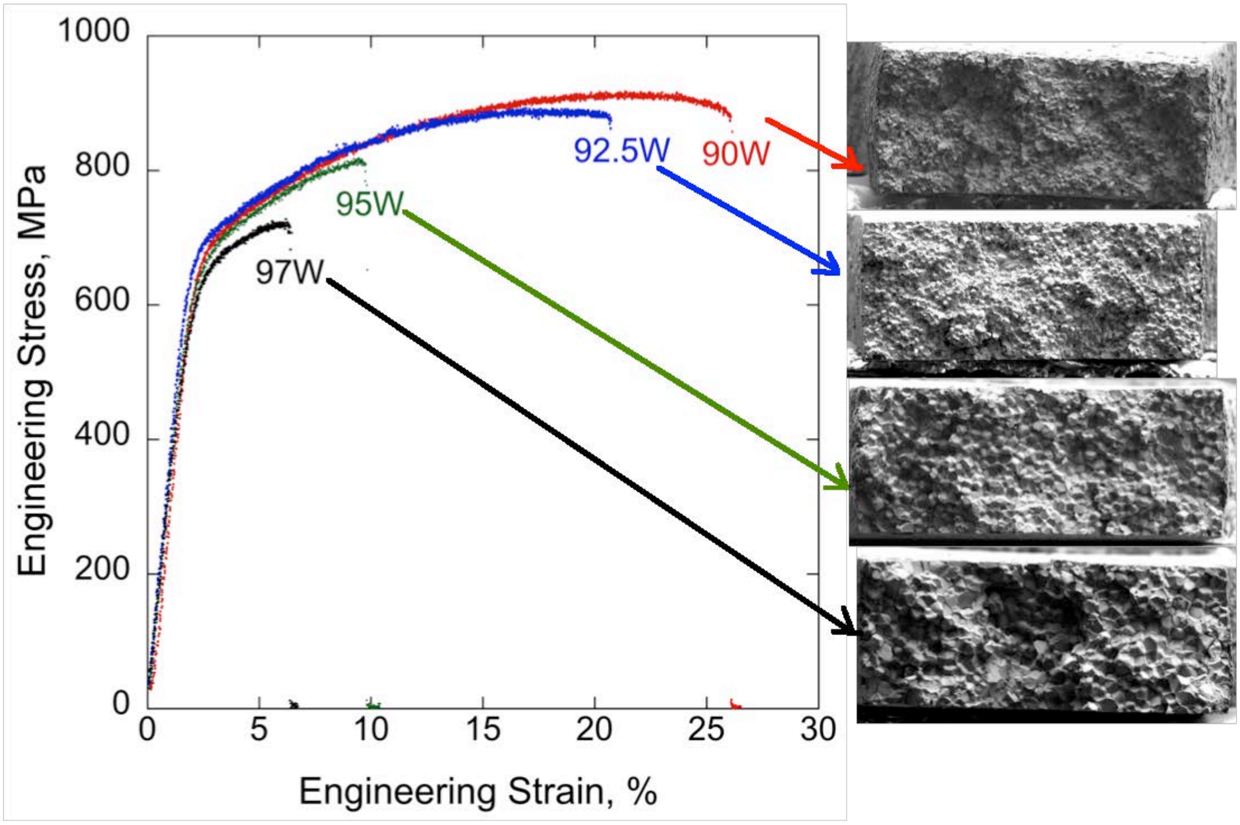

Figure 3. Room temperature engineering stress-strain curves, and their corresponding macroscopic view of fracture surface for the W-Ni:Fe alloys.

The W-Ni:Fe alloys manifest four local failure modes, namely: W-W intergranular fracture (WW), W cleavage (WC), W-Ni:W:Fe phase interfacial separation (WM), and Ni:W:Fe ductile phase rupture (MR) [4-5]. SEM micrographs of the fracture surfaces of the broken tensile specimens, shown in Figure 4, illustrate all of these failure modes. The W-W interfacial boundary is the weakest, and the W-W interfacials are increases with increasing W (see Figure1). Specimen fracture initiates by WW at the W-W particle interfaces, and continues by crack propagation though the W-Ni:W:Fe phase accompanied by W cleavage. Figure 4 shows that the fraction of WC is highest for 90W, and minimal for 97W alloys that experience more WW separation. Notably, WC appears to correlate with higher strength and ductility (see Table 3).

Fracture Toughness

Room temperature fracture toughness tests were conducted on the single-edge notched fatigue pre-cracked bend bars using both 4PB and 3PB fixtures. The fatigue crack tends to mainly propagate through the Ni:W:Fe ductile phase (white arrow, Figure 5a). The pre-cracked specimens were heat tinted at 400ºC for 1 min to mark the pre-crack front (Figure 5b). Some specimens were also speckled with graphite powders in an attempt to use *in-situ* digital image correlation (DIC) to measure the crack length during loading in the 4PB test. However, it turned out that DIC was not possible due to the large lateral contraction (Figure 5b) in the extensive crack tip plastic zone, which optically image as dark area in Figure 5c. SEM images shows that the fracture crack growth under pseudo-static loading is mainly transgranular (red arrow, Figure 5d).

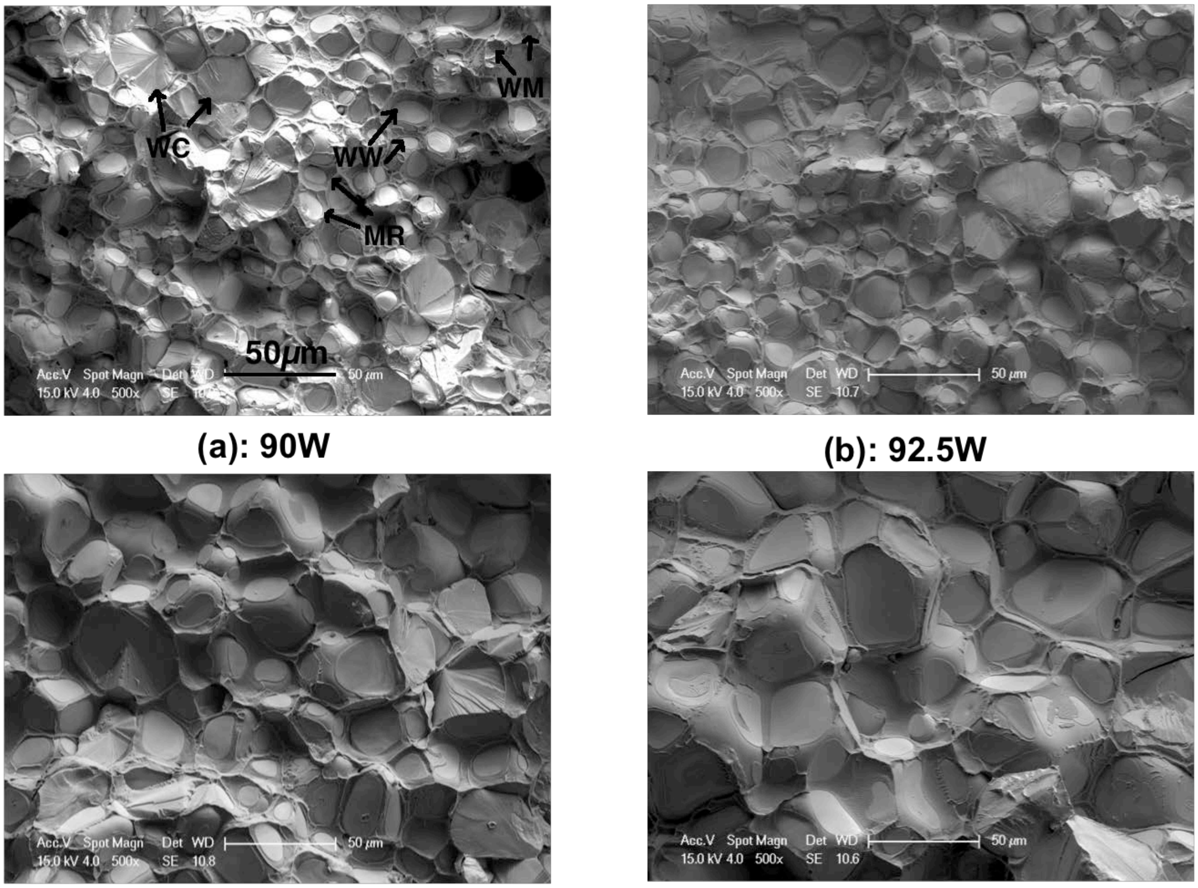

(a): 90W **(b): 92.5W**

(c): 95W **(d): 97W**

Figure 4. SEM fractographs of the room temperature tensile fracture surfaces for different WNiFe alloys.

Normalized load-displacement (P-d) curves for the W-Ni:Fe alloys, shown in Figure 6a, reveal continuous load drop after P_m with increasing d, indicating stable crack growth even at room temperature. The normalization involves adjusting the actual P-d data to a common a/W = 0.5, so that the curves can be inter compared. The peak loads are similar except for the 95% W alloy where P_m is higher. Substantial strain hardening is also observed in all alloys except for the 97W WHA (Figure 6a), consistent with the corresponding tensile s(e) curves. The shapes of the post-max P-d curves are generally similar. Since 4PB tests show massive stable crack growth, additional tests were conducted on very finely ground (down to 1µ sandpaper) specimens in the 3PB fixture, and the crack tip region was observed *in-situ* with an optical microscope. These tests were stopped at a P/P_{max} from ≈ 0.77 to 0.92 (Table 4). Unfortunately, the lateral contraction (surface dimpling), marked by the dark areas in Figure 6b, prevented imaging the crack tip. However, post-test SEM examinations show that there was very little crack growth (< 200 µm) at these P/P_m loads. Thus additional crack blunting, and the corresponding increase in the CTOD, is actually associated with the initiation toughness, rather than a classical J-da R-curve behavior. Thus the toughness versus P/P_{max} for all W alloys was calculated, showing that the toughness increases significantly with decreasing P/P_{max} (Figure 6c). Figure 6d shows the calculated K_{Jc} at P_m and P/P_m ≈ 0.8 for all 4 alloys and these results are tabulated in Table 4.

The K_{Jc} do not show a systematic trend with the W loading. K_{Jc} is highest in the 95W alloy and lowest for 97W. The slightly higher toughness of 95W might be due to the combination of: a) the presence of cracked W-particles in as-received condition; b) the higher modulus of elasticity of W-particles and the Ni:W:Fe ductile phase; and c) higher hardness of the alloy and W phase. The lower K_{Jc} in the 97W may be due to increased W-W contiguity. Most notably, however, even a minimal ductile phase content of ≈ 3 wt.% increases the room temperature initiation toughness relative to pure W between 9 and 18 times. Initiation is followed but extremely stable crack growth, and very high effective ductility. Detailed experimental and modeling studies of the toughening mechanisms illustrated in Figure 7 in the W-Ni:Fe WHA will be reported in the future.

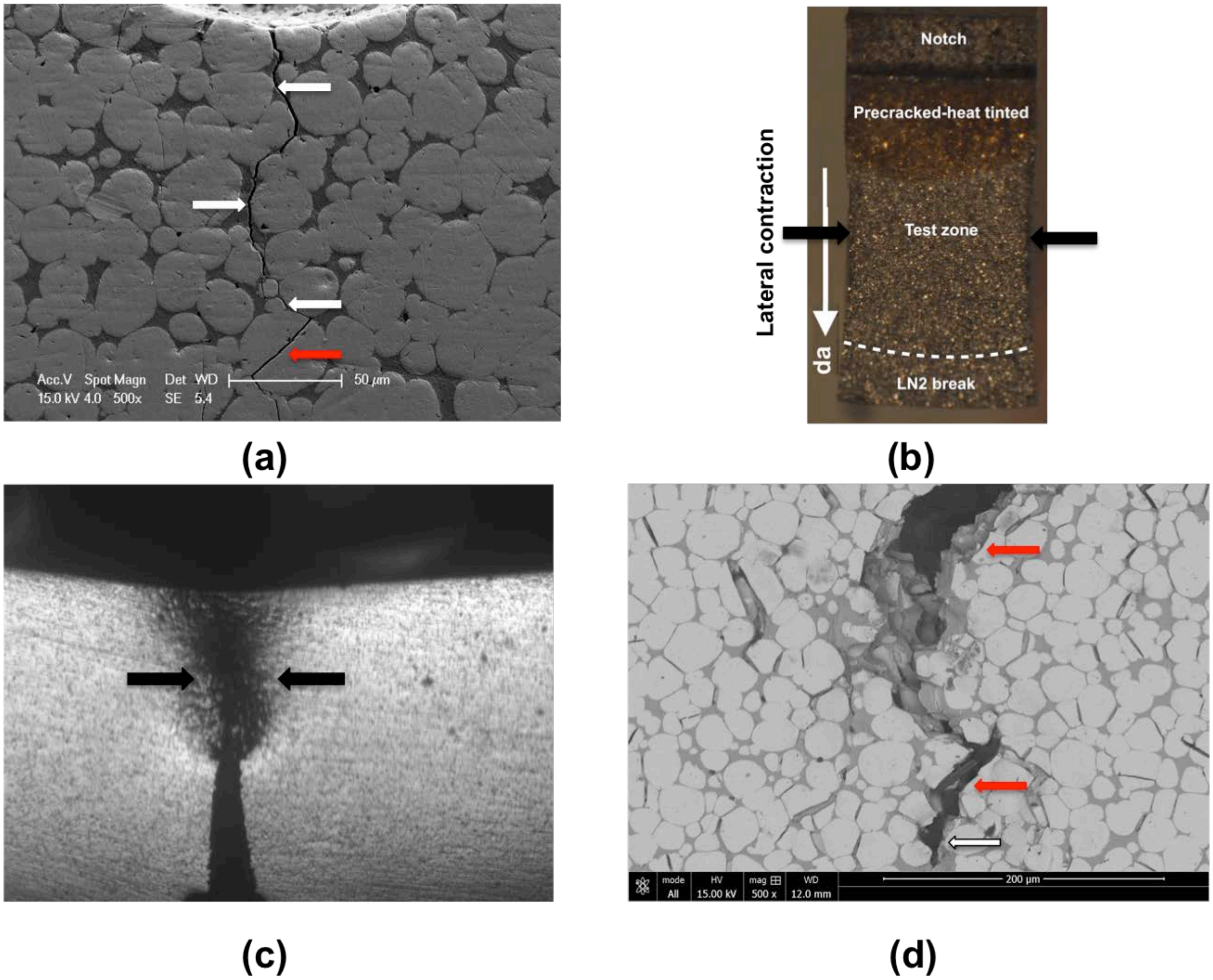

Figure 5. (a) SEM image shows the fatigue crack path mainly propagate through the matrix phase (white arrows), (b) different zones of the specimen, (c) *in-situ* optical image shows large dark area due to lateral contraction of the plastic process zone, and (d) transgranular crack propagation (red arrows) during static loading.

Table 4. Crack and toughness statistics of WNiFe alloys.

Code	Sp. ID	Crack and toughness							CTOD (µm)	Fixture
		a_i(µ)	a_i/W	**K_{Jc} (MPa√m)**	a_f(µ)	P_f/P_{max}	K_{Jf} (MPa√m)	Δa (µ)		
90W	W1-1	1291	0.389	**94.7**	2260	0.173	330.7	969	220	4PB
	W1-2	1076	0.323	**93.8**	2090	0.27	305.1	1014	310	4PB
	W1-5	1553	0.466	**125.5**	1657.4	0.818	193.4	104	46	3PB
	W1-6	1091	0.326	**78.4**	1174	0.778	158.1	83	24	3PB
	Avg:			**98 ± 20**						
92.5	W2-1	1344	0.404	**99**	2672	0.22	405	1328	243	4PB
	W2-2	1415	0.424	**94.9**	1440	0.915	135	25	16	4PB
	W2-3	1236	0.372	**101.5**	1387	0.80	154.7	67	26	3PB
	W2-6	1306	0.393	**85.2**	1368	0.802	144.6	62	34	3PB
	Avg:			**95 ± 7**						
95W	W3-1	1761	0.531	**115.6**	2501	0.281	313.4	740	209	4PB
	W3-2	1020	0.306	**121.9**	1286	0.779	227.9	266	82	4PB
	W3-3	1240	0.370	**84.4**	1410	0.816	193.4	170	22	3PB
	W3-5	1477	0.441	**126.2**	1619	0.793	192	142	56	3PB
	Avg:			**112 ± 19**						
97W	W4-1	1155	0.348	**51.2**	2781	0.209	373.61	1626	233	4PB
	W4-5	1212	0.366	**80.5**	1403	0.793	148.2	191	43	3PB
	W4-6	1271	0.383	**80.4**	1362	0.767	136.6	91	44	3PB
	Avg:			**71 ± 17**						

Note: a_i= initial crack length; a_f=final crack length; K_{Jc}= toughness at maximum load; K_{Jf}=toughness at final crack length; P_{Jf}/P_{max}= load at final crack to maximum load; Δa=crack extension, a_f-a_i; and CTOD= crack tip opening displacement.

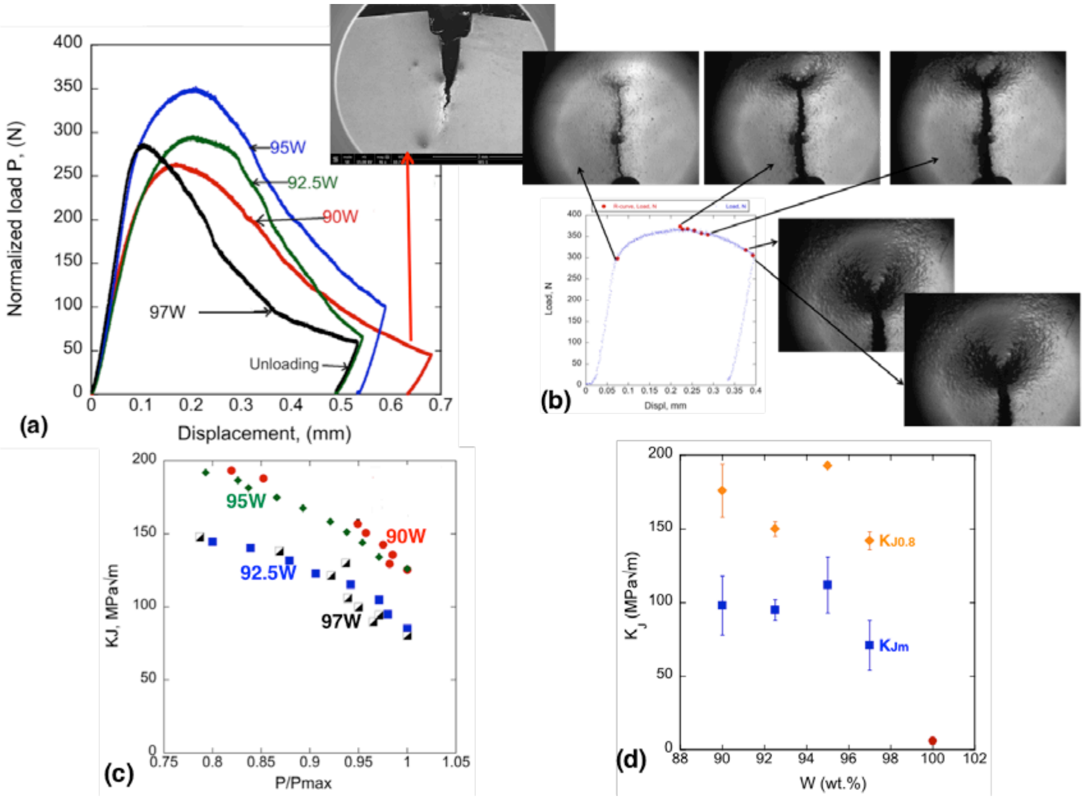

Figure 6. (a) Normalized P-D curves to a/W=0.5 tested at room temperature; insert image shows ductile tearing for 90W alloy, (b) P-D curve for a 92.5W alloy, corresponding with *in-situ* optical images, (c) K_J vs P/P_{max} of WNiFe alloys for 3PB test, and (d) average fracture toughness, K_{Jm} and $K_{J0.8m}$ of WNiFe alloys at P_{max} and P/P_m ≈0.8, respectively. Crack extension, da was less than 200μm for P/P_m ≈0.8.

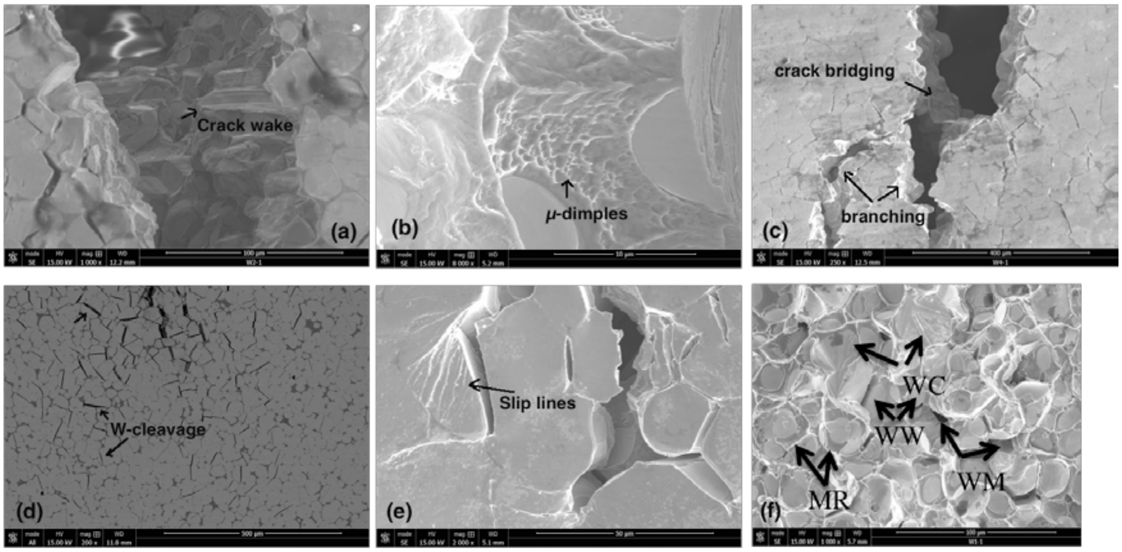

Figure 7. Series of SEM images show: (a) crack wake bridging, (b) formation of micro-dimples in NiWFe phase, (c) crack bridging and crack branching, (d) massive process zone near the crack tip plasticity and tungsten cleavage, (e) slip plane in W-particles, and (f) local fracture modes.

Room temperature fracture toughness measurements on four 90-97 wt.% W-Ni:Fe alloys showed that the initiation toughness is on the order at least 9 to 18 times that of typical the monolithic W (8 MPa√m). Extremely stable crack growth is observed for all alloys. Multiple toughening mechanisms include crack wake bridging, micro-cracking, micro-crack bridging, crack deflection, and especially extensive process zone plasticity.

In the future these initial studies will be extended to characterizing and modeling the detailed toughening mechanisms, higher and lower temperature testing, in situ XRD deformation studies and fabrication of hybrid model divertor components.

References

[1] K. H. Cunningham, K. Fields, D. Gragg, F. W. Zok, C. H. Henager, Jr, R. J. Kurtz, and T. Roosendaal, Recent Progress in the Development of Ductile-Phase Toughened Tungsten for Plasma-Facing Materials, in DOE/ER-0313/54 - Volume 54, Semiannual Progress Report, June 30, 2013. 2013, US DOE: ORNL, TN.

[2] C. H. Henager, Jr, R. J. Kurtz, T. J. Roosendaal, B. A. Borlaug, G. R. Odette, K. H. Cunningham, K. Fields, D. Gragg, and F. W. Zok, Recent Progress in the Development of Ductile-Phase Toughened Tungsten for Plasma-Facing Materials, in DOE/ER-0313/55 - Volume 55, Semiannual Progress Report, Dec. 31, 2013. 2013, US DOE: ORNL, TN.

[3] C.H. Henager, E. L. Stevens, R.J. Kurtz, T.J. Roosendaal, E.A. Nyberg, CA Lavender, GR Odette, KH Cunningham, and FW Zok, “Recent Progress in the Development of Ductile-Phase Toughened Tungsten for Plasma-Facing Materials: W-Ni-Fe Composites”, in DOE/ER-0313/58 - Volume 58, Semiannual Progress Report, June 30, 2015.

[4] KMO Zamora, JG Sevillano, MF Perez, “Fracture toughness of W heavy alloys”, Materials Science and Engineering A, 157 (1992) 151-160.

[5] ZH Zhang, FC Wang, SK Li, L Wang, “ Deformation characteristics of the 93W-4.9Ni-2.1Fe tungsten heavy alloy deformed by hydrostatic extrusion”, Mater Sci Engr A 435-436 (2006) 632-637.

4.4 FABRICATION OF FUNCTIONALLY GRADED TUNGSTEN STEEL LAMINATE

—L. M. Garrison, Y. Katoh (Oak Ridge National Laboratory), M. Norfolk (Fabrisonic LLC.), J. Wenning (Fabrisonic LLC.), J. Moon (University of Nevada-Reno)

OBJECTIVE

The objective of this project is to create a functionally graded tungsten to steel laminate composite for use in plasma facing components in fusion reactors.

SUMMARY

Two roll-bonded tungsten-steel composites have been fabricated. Tensile tests of the Generation 2 composite were completed and showed increasing strength and decreasing ductility with increased tungsten content. A feasibility study for ultrasonic welding tungsten to steel was completed. Thirty-four trials were completed that varied the parameters of foil thickness, interlayer material, welding force, vibration amplitude, and other welding parameters. Promising results were obtained for joining tungsten to steel and tungsten to steel with an aluminum interlayer.

PROGRESS AND STATUS

Introduction

For the plasma-facing components of fusion reactors, tungsten will be the interface between the plasma and the underlying structural component because tungsten has a low sputtering yield, high melting temperature, and relatively high thermal conductivity. However, because tungsten is brittle and has low fracture toughness, it is impractical to fabricate the entire plasma-facing component out of tungsten. Current divertor designs utilize various methods to bond the tungsten surface layer to the underlying structural part of the component that contains the cooling channels, but for future divertors where the operating temperature will be higher, more robust solutions are needed. Advanced steels are being developed for structural components in future fusion reactors. Unfortunately, tungsten and steel have vastly different coefficients of thermal expansion, so a direct joint would be subjected to intense thermal stresses. A tungsten-steel functionally graded material would ideally both improve the fracture toughness as compared to tungsten alone as well as reduce the thermal stresses between the tungsten and steel parts of the plasma-facing component.

Results

Roll-bonding

The Generation 1 laminate composite was fabricated by forging and hot rolling the tungsten and grade 92 steel foils within a stainless steel outer shell at 1000°C to 80% total thickness reduction overall. Tensile bars were machined from the Generation 1 composite. Because the composite has positional variations, each tensile bar must be characterized individually to count the number of layers included and the thickness of the layers. This characterization is underway and will be followed by tensile and shear punch tests.

The Generation 2 composite was fabricated using ten layers of 250 μm Grade 92 steel alternating with ten layers of 25 μm tungsten and was forged at 1000°C for only 20% thickness reduction. The goal of the Generation 2 composite is to determine if the processing parameters can be optimized to create bonding between the layers without causing fragmentation of the tungsten layers, as was seen in the Generation 1 composite.

As seen in Figure 1, in the as-fabricated state the Generation 2 laminate composite had a large outer layer of stainless steel and a small volume of composite material at the center. Tensile samples were machined from the composite with electro-discharge machining such that the tensile axis was aligned with the rolling direction of the foils. Because of the low visual contrast between the central composite and the outer stainless steel material, tensile samples could not be precisely cut from the central composite material.

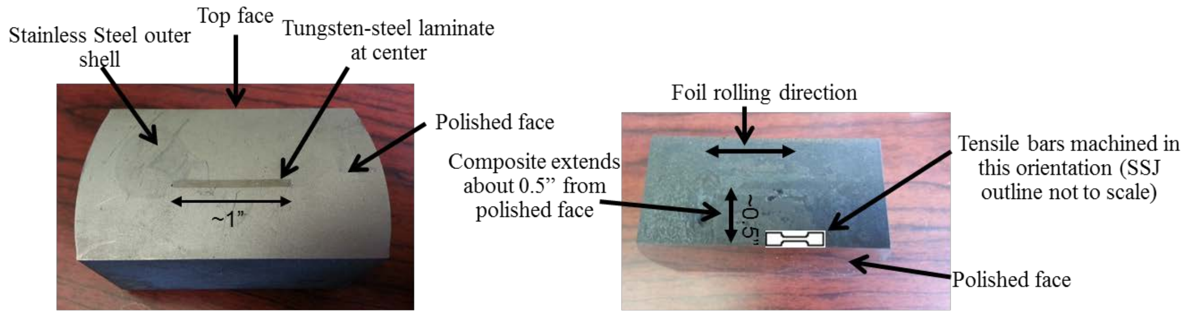

a) Front view b) Top view

Figure 1. Generation 2 laminate composite. a) front view, showing composite inside stainless steel outer shell. b) top view.

Only one of the five samples tested (Figure 2), Sample A-1-1, showed evidence of containing the expected layers of both tungsten and Grade 92 steel (Figure 3). One other sample, Sample A-2-2, appeared to have a thin layer of tungsten on the outside of one face, as evidenced by a morphological difference characterized by shallow cracking perpendicular to the axis of the tensile load. Figure 2 illustrates that Sample A-1-1 is significantly stronger and more brittle than the three samples with no evidence of the layered composite, Samples A-1-2, A-2-1, and A-2-3. It is also apparent that Sample A-2-2 was stronger and less ductile than the three homogenous-appearing samples, but less strong and more ductile than Sample A-1-1. It may be reasonable to conclude that the continuum of increasing strength and decreasing ductility can be attributed to the difference in sample composition. Samples A-1-2, A-2-1 and A-2-3 appeared to be homogenous stainless steel of the outer shell and are the least strong and most ductile. Sample A-2-2 appeared to have some limited tungsten content and is stronger and less ductile than the homogenous-appearing samples. Sample A-1-1 has the expected, high level of tungsten layer content and is the strongest and least ductile. This pattern matches what would be expected based on the current understanding of the mechanical properties of these two materials. Further tensile tests of material from the Generation 2 composite are underway.

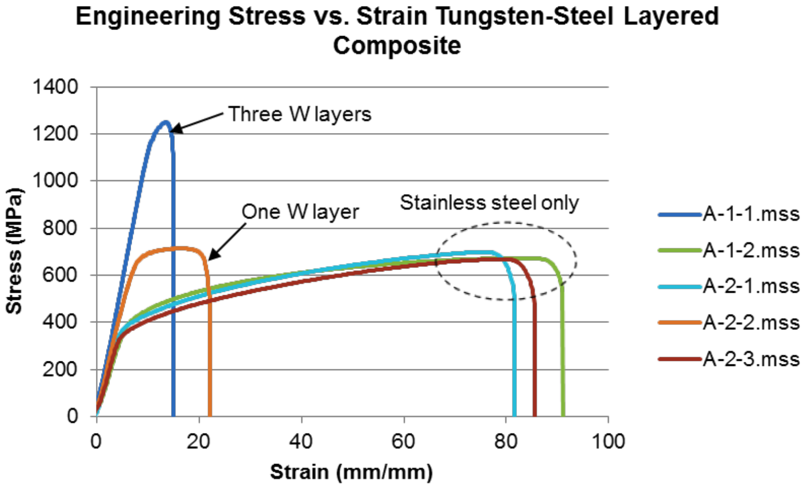

Figure 2. Stress-strain curves for composite material with three W layers, one W layer, and no W layers.

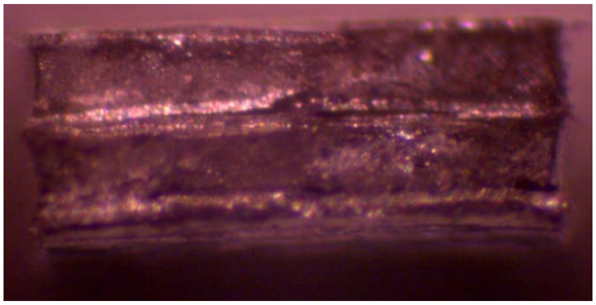

Figure 3. Fracture surface of composite Sample A-1-1 which contains three thin tungsten layers and two thicker steel layers. The height of the fracture end is approximately 0.5 mm.

Ultrasonic welding

An initial investigation of the feasibility of producing composites using ultrasonic bonding was completed with the company Fabrisonic, which specializes in ultrasonic welding of dissimilar materials. The ultrasonic welding process utilizes a sonotrode (also called a horn) that provides normal force onto the material to be bonded as well as side-to-side ultrasonic vibration (Figure 4). The combination of pressure and ultrasonic vibrations create a solid state bond between the layers. Material is built up one thin layer at a time to create a complete component. This lower temperature bonding strategy was considered for tungsten because other higher temperature bonding methods such as brazing or hot-rolling occur at temperatures where the tungsten is strong but the interlayer is usually very weak, and the different coefficients of thermal expansion of tungsten and candidate interlayers cause significantly different expansion of layers. These factors can lead to high residual stresses or non-uniform reduction in high-temperature processed tungsten composites. However, previous successful tungsten ultrasonic welds have not been reported in the literature, so this was a scoping study to evaluate the possibility of successfully welding tungsten to other candidate materials, especially steel and copper.

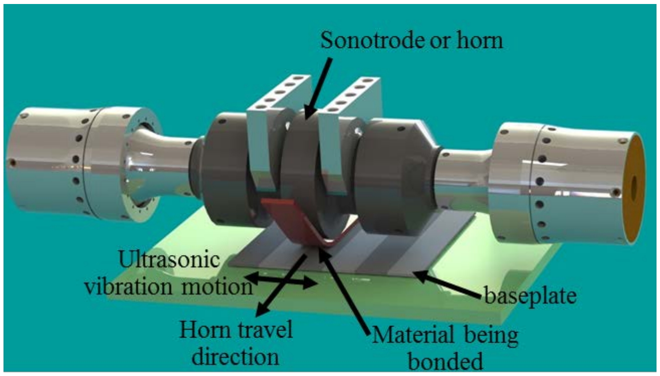

Figure 4. Image, adapted from http://fabrisonic.com/uam-overview/, shows the configuration of an ultrasonic welding device.

Two different baseplates were used in the trials, a C1020 carbon steel baseplate and an aluminum alloy 6061T6 baseplate. These two baseplates were chosen because they are frequently used at Fabrisonic and known to bond well with the trial interlayer materials of aluminum and copper. If feasibility of the tungsten ultrasonic welding could be shown, the baseplate could be replaced with a fusion specific alloy.

Three thicknesses of tungsten foils were used in the trials: 250 μm, 100 μm, and 25 μm thick. The outer dimensions of all the tungsten foils were one inch square. An important factor for the tungsten foils is their microstructure, which varies for each thickness of tungsten foil (Figure 5). The thickest foil had little grain orientation texture with somewhat elongated grains, while the thinnest foil had strong <100> texture and small grains, and the medium thickness foil had intermediate properties. The general grain shape for the 100 µm and 25 µm foils was elongated along the rolling direction and thin in the cross section of the foil. The 250 25 µm foil had slightly more equiaxied grains than the thinner foils. One of the benefits of tungsten foils is that they can have delamination rather than brittle cleavage failure at room temperature. However, this is due to the weak grain boundaries moving against each other in response to stress.

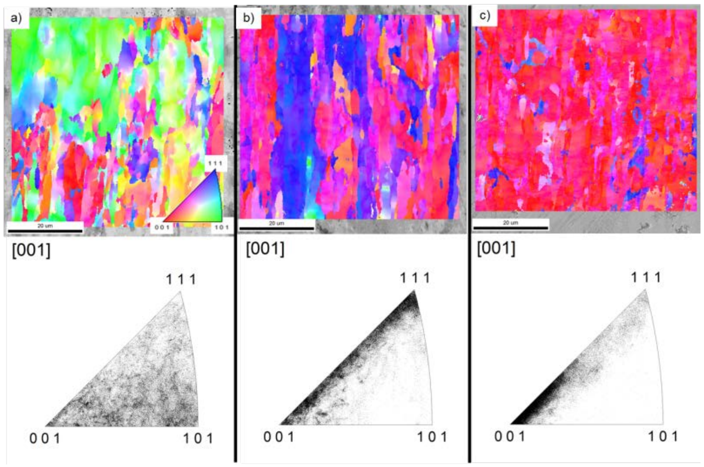

Figure 5. Electron backscatter diffraction images show the texture of tungsten foils of different thickness: a) 250 µm thick, b) 100 µm thick, and c) 50 µm thick.

The different tungsten microstructures caused the tungsten to behave differently during the ultrasonic welding. The 100 µm thick tungsten foil previously performed the best in the shear punch tests and in the hot-rolled tungsten steel composite. However, during trials of ultrasonically welding 100 µm thick tungsten foils, the foils had internal failure along the grain boundaries, which resulted in the foil delaminating into sub foils (Figure 6).

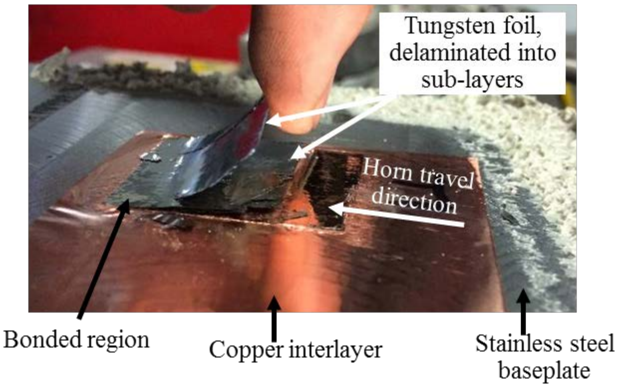

Figure 6. Welding trial of 100 µm thick tungsten foil with a 50 µm thick copper foil interlayer onto a C1020 carbon steel baseplate. The tungsten foil failed by internal delamination during the weld, but there was a bonded region at one end of the foil.

When the thinnest tungsten foil was used, it remained intact and did not fail by delamination as was seen for the 100 µm thick tungsten foil. The typical behavior for the 25 µm thick tungsten foil under various welding conditions was that the foil took on the texture of the sonotrode, showing good energy transfer and plastic deformation, but the foil did not bond to the copper interlayer. An example is shown in Figure 7 where a 25 µm thick tungsten foil lies to the side of the attempted weld region. The lack of bonding may be caused by failure to break through the surface oxide layer on the foil during welding or non-optimal welding parameters.

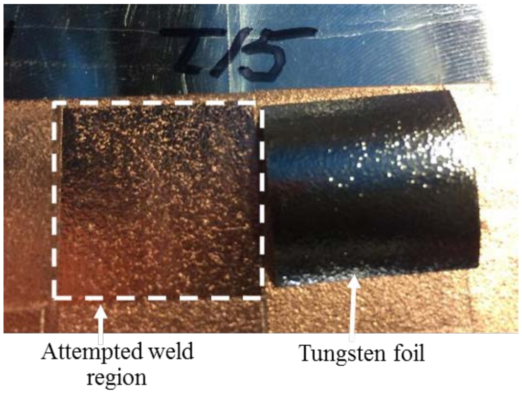

Figure 7. Weld trial using a 25 µm thick tungsten foil onto a copper interlayer on an aluminum alloy 6061T6 baseplate.

The 250 µm thick tungsten foil has less crystallographic texture than the thinner foils and in the previous shear punch test, it showed essentially no elongation. The different microstructure of the thickest tungsten foil manifested itself by shattering during many welding trials (example in Figure 8).

Figure 8. A tungsten foil, 250 µm thick cracked and shattered during a welding test with a copper interlayer and steel baseplate.

Overall, 34 trials were completed that varied the parameters of foil thickness, interlayer material, welding force, vibration amplitude, and other welding parameters. Success was achieved by lowering the normal force and adjusting the other welding parameters compared to the initial tests. Tungsten foils both 100 µm thick and 250 µm thick were able to be welded with minimal to no cracking in the tungsten layers (Figure 9). Welding parameters were developed for bonding tungsten foil to steel using an aluminum interlayer as well as separate parameters for directly bonding the tungsten foil to the steel baseplate. Further analysis will be completed on the successful weld trials including cross-sectional scanning electron microscopy to evaluate the phases and character at the bond interface. The initial investigation into ultrasonic welding of tungsten gathered important basic data on how the tungsten microstructure influences the weld and developed the general welding parameters necessary to weld tungsten to steel. The next step will be to determine if successive weld steps can be used to build a 3-D structure.

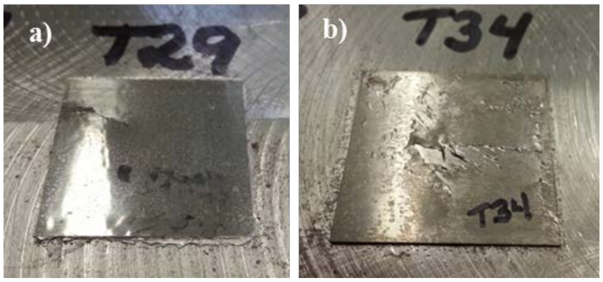

Figure 9. a) Bonding was achieved between a 100 μm thick tungsten foil, an 1100 aluminum interlayer, and a steel baseplate. b) direct bonding between a 250 μm thick tungsten foil and the steel baseplate.

Six of the trials that showed at least partial bonding success were selected for more in depth interface analysis. The welding trials were completed on large steel or aluminum base plates (Figure 10a). To prepare for interface analysis, small sub-sections of the selected trial joints were machined by electro-discharge machining, such as the example in Figure 10b. After machining, several sub-sections did not remain bonded, as in Figure 10c. The summary of which trials were selected for further analysis is in Table 1. Those that remained bonded will be examined with optical and scanning electron microscopy.

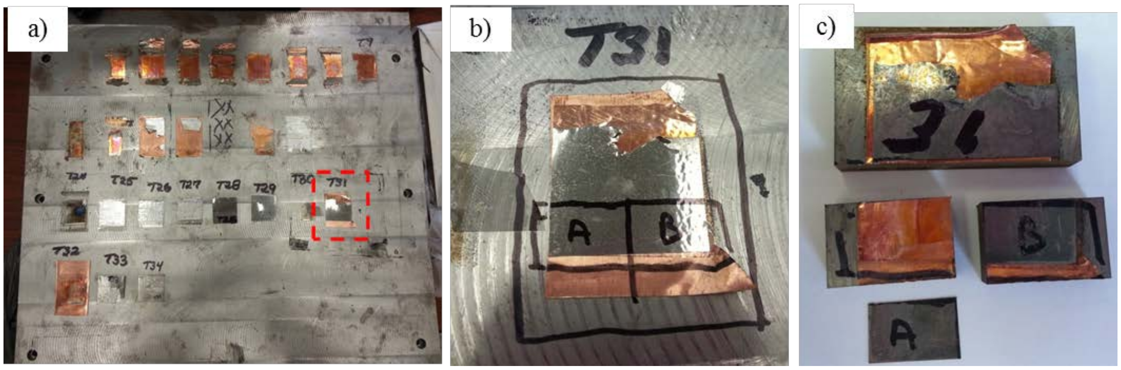

Figure 10. a) Steel baseplate with all ultrasonic weld trial locations. b) Trial 31 before sectioning. c) Trial 31 after sectioning.

Table 1. Ultrasonic welding trials selected for further interface analysis.

Trial number	W foil thickness	Interlayer	Substrate	Result after sectioning
23	0.025 mm	Cu	Al	Layers did not remain bonded
28	0.10 mm	Al	Steel	Layers remained bonded
29	0.10 mm	Al	Steel	One section remained bonded, one did not
31	0.10 mm	Cu	Steel	Layers did not remain bonded
33	0.25 mm	none	Steel	Both sections remained bonded
34	0.25 mm	none	Steel	One section remained bonded, one did not

4.5 IRRADIATION HARDENING OF PURE TUNGSTEN EXPOSED TO NEUTRON IRRADIATION

—X. Hu, T. Koyanagi, N.A.P Kiran Kumar, Y. Katoh (Oak Ridge National Laboratory), L.L. Snead (Massachusetts Institute of Technology), B.D. Wirth (University of Tennessee, Knoxville)

OBJECTIVE

The objective of this task is to understand the irradiation hardening of neutron irradiated tungsten by capturing the dependence of irradiation temperature, radiation dose, and neutron energy spectrum. The individual hardening contribution of various defects will be discussed.

SUMMARY

(This manuscript is in the review process for publication in the Journal of Nuclear Materials.)

Pure tungsten samples have been neutron irradiated in HFIR at 90 to 850°C to damage levels of 0.03 to 2.2 dpa. A dispersed barrier hardening model informed by the available microstructure data has been employed to predict the hardness. The comparison of the model prediction and the measured Vickers hardness reveals the dominant hardening contribution at various irradiation conditions. For tungsten samples irradiated in HFIR, the results indicated that voids and dislocation loops contributed to the hardness increase in the low dose region (< 0.3 dpa), while the formation of intermetallic second phase precipitation resulting from transmutation started to dominate the radiation-induced strengthening in a relatively modest dose region (> 0.6 dpa). The precipitate contribution is most pronounced for the HFIR irradiations, whereas the radiation-induced defect cluster microstructure can rationalize the entirety of the hardness increase observed in tungsten irradiated in the fast neutron spectrum of Joyo and the mixed neutron spectrum of JMTR.

PROGRESS AND STATUS

Introduction

Given its high melting temperature, high thermal conductivity, low sputtering yield, and low tritium retention in un-irradiated conditions, tungsten has been chosen as the plasma facing material for ITER, and planned for use in future Demonstration fusion nuclear power station (DEMO) and fusion reactors [1] [2]. The tungsten plasma-facing components (PFCs) of fusion reactors will experience an extreme environment characterized by high temperature, high thermal flux, intense particle fluxes (i.e., high energy neutrons, hydrogen isotope ions, helium ions), etc., the combined sum of which will impose significant challenges to tungsten performance [3, 4] [5] [6]. In particular, the 14 MeV-peak neutron irradiation produces significant displacement damage of the lattice structure creating vacancies, interstitials, and their clusters, as well as generating significant concentrations of transmutation elements (i.e. Re, Os) [7]. Severe thermo-mechanical property degradation of tungsten is expected as a result of the irradiation-induced defect accumulation [8]. In turn, the degradation of these properties could impact plasma materials interactions (PMI), such as the bulk tritium retention, temperature-dependent-mechanisms (e.g., chemical sputtering) impacted by the change of thermal conductivity.

Embrittlement is one of the most significant degradation phenomena of concern for tungsten exposed to irradiation at low to intermediate temperature, which is manifest as an increase in the ductile-to-brittle transition temperature (DBTT) that will impact the service lifetime and performance of tungsten PFCs. Hasegawa [9] [10] [11] and Fukuda [12] [13] [14] reported the neutron irradiation effects on the microstructural development of tungsten and tungsten alloys irradiated in various fission reactors, as well as the resulting hardening behavior by capturing the dependence of neutron energy spectra, irradiation temperature, and dose levels. Hu et al. [15] reported positron annihilation spectroscopy measurements and TEM observations on neutron-irradiated single crystalline tungsten irradiated in HFIR. The obtained microstructure information was then used to link to the measured hardness evolution during the isochronal annealing process. However, the underlying mechanisms governing the irradiation hardening behavior of neutron-irradiated tungsten has not been systematically reported in terms of the individual hardening contribution of different types of radiation defects present within the irradiated material, nor the dominant hardening source at various irradiation conditions. Further, there have been relatively few studies that provide quantitative correlation between the TEM-observed radiation-damaged microstructure and the measured hardness change of neutron-irradiated tungsten. In this study, we report on a systematic analysis based on implementing the available microstructural observations of neutron-irradiated tungsten within a dispersed barrier hardening model to address these issues, thereby elucidating the microstructure-property correlation of neutron-irradiated tungsten for application as fusion plasma facing material.

Materials and Neutron Irradiation

High purity single crystalline tungsten (99.999%) purchased from Goodfellow, USA, was investigated in the present study. The major impurities in the non-irradiated material are 10 ppm O, <10 ppm N, 20 ppm C, <5 ppm S, 3 ppm H, and 140 ppm Cu [15]. SS-J3 tensile test specimens [16] were machined directly from the procured tungsten rod and then exposed to neutron irradiation in the flux trap facility in the High Flux Isotope Reactor (HFIR) at ORNL, USA. The irradiation conditions are summarized in Table 2. The neutron irradiation temperature spans from 90 to 850°C and the radiation doses range from 0.03 to 2.2 dpa. In this study, we examined irradiation hardening of tungsten specifically using the Vickers microhardness testing because the tensile data cannot be used to analyze hardening due to the severe degradation in fracture toughness, preventing the determination of yield strength [17]. Vickers microhardness testing is an efficient means of assessing the mechanical properties of irradiated materials because of the small sampling volume requirement. This technique is especially appropriate for the samples with high radioactivity, like the neutron-irradiated tungsten in the present study. Following neutron irradiation, Vickers microhardness testing was performed on one tab of the tensile specimens at room temperature, with an indentation load of 1.96 N (200 gf) and a dwell time of 15 s. Microstructure characterization of the irradiated samples were conducted in the low activation materials development and analysis lab (LAMDA) at ORNL by using a JEOM JEM 2100F TEM. TEM foils were prepared using a focused ion beam system (FEI Quanta 3D Dual Beam) operated at 30 kV for initial milling and at 5 kV for final thinning. In addition, the Vickers microhardness and microstructural information of the tungsten samples irradiated in Joyo and JMTR [18] [10] [9] [12] [13] were also evaluated in this study for comparison of the impact of the neutron energy spectrum.

Irradiation hardening

Dispersed barrier hardening model

As noted in Ref. [19], two dislocation barrier hardening models have historically been used to describe radiation hardening in metals. The dispersed barrier model is based on straightforward geometrical considerations for obstacles intersecting the dislocation glide plane. It is most appropriate for strong obstacles. An alternative hardening model is developed by Friedel-Kroupa-Hirsh (FKH) [20] for weak obstacles, where the effective inter-obstacle spacing is increased compared to the dispersed hardening model due to less extensive dislocation bowing prior to obstacle breakaway. The functional dependence of yield strength increase, $\Delta\sigma_y$, on defect cluster size and density for these two limiting cases is given by the following equations, respectively:

$$\Delta\sigma_y = M\alpha\mu b(Nd)^{1/2} \tag{1}$$

$$\Delta\sigma_y = 1/8M\mu bdN^{2/3} \tag{2}$$

where μ is the shear modulus of the matrix, which is 161 GPa for tungsten, b is the magnitude of the dislocation Burgers vector, M is the Taylor factor, N is the defect number density and d is the defect diameter, α is the defect cluster barrier strength. The Taylor factor, M, is used to correlate the critical shear stress resolved on the slip plane and the yield strength in a tensile test. The value of 3.06 is recommended for non-textured BCC and FCC polycrystalline metals by Stoller and Zinkle [21]. This value was obtained by averaging the Taylor factors of all possible tensile orientations [22] in a BCC or FCC crystal. As to single crystals, Taylor factor is strongly dependent on the slip plane and the slip direction in the tensile test. Since the tungsten is brittle and even more brittle subject to neutron exposure, yield strength could not be obtained. Therefore, the information of the tensile orientation as well as the slip plane and direction are not available. Considering that {110} slip plane is somewhat preferred for BCC crystals, of which the average Taylor factor is 3.06 [22], this value will be applied here for the cases involved in single crystals.

Based on the TEM observations, to be presented in Sections 3.2 and 3.3, dislocation loops, voids, and second phase precipitates are the most commonly observed radiation damaged defect microstructure in neutron-irradiated tungsten. Voids and precipitates are considered as strong obstacles while dislocation loops are usually considered as weak obstacles, although the barrier strength factors of dislocation loop cover a large range (0.15 to 0.75) [23]. In addition, previous hardening studies of neutron-irradiated tungsten employed the dispersed hardening model [12] [18]. The use of the same model will enable a direct comparison of the barrier strength factors of various defects between the present and previous studies. Therefore, the dispersed barrier hardening model will be used to bridge the microstructure and the measured hardness in the present study. The applicability of the FKH model for the weak obstacles (i.e., dislocation loops) will be discussed in the Section 4.

In the dispersed barrier hardening model, expressed in Eq. (1), the square-root factor represents the reciprocal of the average distance between obstacles. The α factor accounts for the fact that some obstacles may be partially cut or sheared by the mobile dislocation as it bows out during the glide process. Its value can vary between zero and one, and is strongly dependent on the defect type, size, and temperature [24] [25]. In the present work, the irradiation hardening of tungsten is exclusively ascribed to the existence of irradiation induced dislocation loops, voids, and precipitates, of which the α values need to be identified. With respect to the dislocation Burgers vector, a systematic molecular dynamics study [26] of displacement cascade in tungsten revealed that the majority of the interstitial dislocation loops were ½<111> type at room temperature and 800°C. Additionally, TEM observations of self-ion irradiated tungsten [27] indicated that the dislocation loops were predominately of interstitial type and were exclusively of ½<111> type in the temperature range from 500 to 1100°C. Therefore, $\bar{b} = \frac{a}{2} < 111 >$ is used in this study with the magnitude of b set to 0.2741 nm.

Since Eqs. (1) and (2) are provided for yield strength changes and we have measured the Vickers microhardness, we must also incorporate an appropriate correlation between hardness and yield strength. Tabor [28] derived a linear correlation between the Vickers microhardness and yield strength by examining the stress loaded on the indenter tip in two dimensions (along and perpendicular to the axis of the indenter tip) during the plastic deformation process, expressed in the form of

$$H_V = k\sigma_y \tag{3}$$

with Hv and σ_y in MPa, where k is a constant and is determined as 2.74 in Tabor's theory. Busby [29] summarized the available experimental data of both irradiated austenitic and ferritic stainless steels in the open literature and concluded that the constant, k, of 3.23 and 3.20 are the most appropriate for austenitic and ferritic stainless steels, respectively. Considering that the theoretical analysis was based on an over-simplified model, the linear coefficient obtained from experimental data is used in this study. Therefore, the expression of $\Delta H_V = 3.20\sigma_y$ will be used due to the BCC lattice structure of both tungsten and the ferritic stainless steels. The final expression to bridge a specific defect and the resulting hardness increase is

$$\Delta H_V = 3.20 M\alpha\mu b(Nd)^{1/2} \tag{4}$$

In order to account for obstacles of different types, size, and number density contained within the irradiated materials, an appropriate superposition law is needed. Normally, the root-sum-square superposition law works well when obstacles have similar strengths, and the linear superposition law is better as the strengths become more dissimilar [30]. Considering there is no clear physical motivation to support these two superposition laws, the applicability of both laws will be evaluated in the present study.

Contribution of intrinsic defects to the irradiation hardening

When tungsten is subject to neutron irradiation in HFIR, its large thermal neutron capture cross section leads to the generation of Re. Much of the Re produced will, in turn, transmute to Os through subsequent nuclear transmutation reactions. With increasing radiation dose and corresponding increased Re and Os concentrations, the formation of intermetallic second phase precipitates rich in these elements is observed after the solubility limits are reached. Various TEM studies [10, 31, 32] of tungsten and its alloys irradiated in mixed neutron spectra have shown a large quantity of needle-shaped precipitates when the irradiation dose is greater than 1 dpa. The inclusion of precipitates in neutron-irradiated tungsten complicates the hardening analysis. Prior to tackle the hardening contribution from precipitates, the barrier strength of the intrinsic defects induced by irradiation, i.e., dislocation loops and vacancy clusters/voids, need to be clarified first.

In Ref. [15], we presented results from an isochronal annealing study of single crystalline tungsten exposed to low dose and low temperature neutron irradiation in HFIR. This particular sample, designated as 1W25, was irradiated to 0.03dpa at 90°C. The production of transmutation elements during this short irradiation duration is negligible. The coincidence Doppler broadening measurements of the irradiated sample following various annealing stages confirmed this hypothesis. Positron annihilation lifetime spectroscopy (PALS) was utilized to acquire the vacancy cluster population in the sample and TEM observations at selected annealing conditions provided information on the populations of dislocation loops and visible voids. In addition, Vickers microhardness following each annealing condition was obtained, thus, providing an opportunity to bridge the microstructure and the mechanical property and enabling us to focus on the hardening contribution from the intrinsic defects. Figure1 shows the measured Vickers microhardness, the number density of large vacancy cluster obtained by PALS and TEM observed dislocation loops at various annealing conditions. In the PALS analysis, three different types of vacancy clusters were quantified, namely, small (~0.31 nm), intermediate (~ 0.67nm), and large (>0.8 nm) vacancy clusters. As the barrier strength factor is size-dependent, we only consider the hardening contributions from the large vacancy clusters, assuming small and intermediate vacancy clusters have negligible effects on the hardening. TEM observations indicated that dislocation loops were only observed when annealing temperatures were lower than 1000°C, while small visible voids with a diameter of ~ 1 nm appeared when annealing temperatures were above 1000°C. Annealing hardening was observed for annealing temperatures lower than 1000°C, which we attributed to coarsening of the large, but not yet TEM visible vacancy clusters. The decreasing measured hardness in the temperature regime from 1000 to 1300°C was assumed to result from the thermally driven dissociation of the large vacancy clusters or voids.

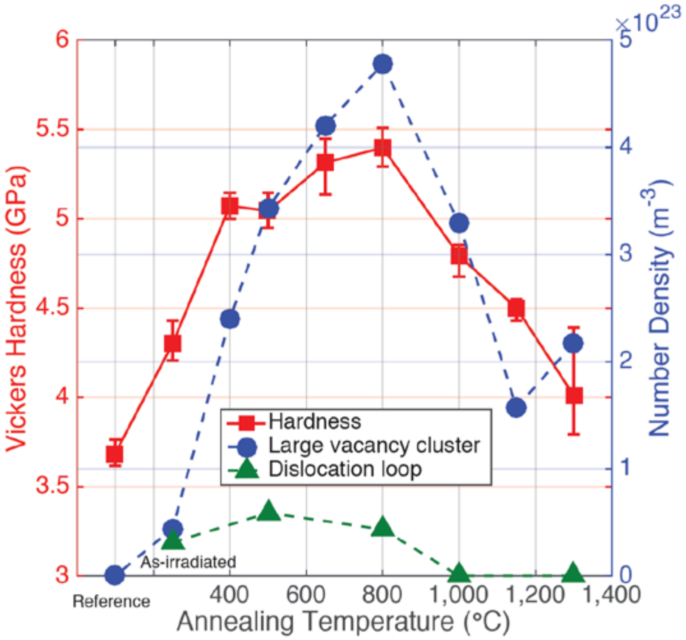

Figure 1. Measured Vickers micorhardness (Red), number density of large vacancy cluster determined by PALS (Blue), and dislocation loop observed by using TEM (Green) at various annealing conditions.

Table 1 lists the number density and size of the dislocation loops, large vacancy clusters, and voids at different annealing conditions together with the measured Vickers hardness. In order to apply the dispersed hardening model to quantitatively assess the hardening contributions, we must specify an obstacle strength factor, α, of each defect cluster type. Considering the vacancy type defects are strong obstacles to dislocation loop motion [30], the strength factor of large vacancy clusters is assigned to be 0.2, which also is used for the visible voids in TEM observations, given their similar size. Dislocation loops are considered as a slightly weaker obstacle relative to the small voids, therefore, the strength factor of dislocation loops is assumed to be 0.15 in the present work. Then substituting the available microstructural information to Eq. (1) leads to the prediction of the hardness. The determination of α values also derives from the mutual comparison of modeling prediction and the experimentally measured hardness. The assumed strength factors leads to a relatively good agreement between the modeling and the experimental data. The last three columns in Table 1 show the comparison of measured and predicted hardness data in the annealing study. The use of the root-sum-square superposition law yields a relatively good agreement with the experimental data in comparison with the linear superposition law. Therefore, this provides further confidence in our decision to use the dispersed barrier hardening model throughout the remainder of this analysis, including for the more complicated microstructures resulting in higher dose irradiation.

Table 1. Number density and size of irradiation-induced defect clusters in 1W25 (90°C, 0.03 dpa) following various annealing conditions together with the comparison of measured Vickers hardness and model-predicted hardness

Sample condition	Dislocation loop		Large vacancy cluster		Void		Measured Hardness Increase (GPa)	Modeling results – *Root-sum-square* (GPa)	Modeling results – *linear* (GPa)
	Diameter (nm)	Number density $(\times 10^{22}/m^3)$	Diameter (nm)	Number density $(\times 10^{22}/m^3)$	Diameter (nm)	Number density $(\times 10^{22}/m^3)$			
Reference	-	-	-	-	-	-	(3.69)*	-	-
As-irradiated	3.08	3.12	0.8	4.4	-	-	0.61	0.65	0.89
500°C, 1 hour	4.54	5.87		34.3	-	-	1.35	1.33	1.88
800°C, 1 hour	5.10	4.33		47.7	-	-	1.71	1.41	1.97
1000°C, 1 hour	-	-		11.9	1.0	21	1.10	1.26	1.69
1300°C, 1 hour	-	-		7.7		14	0.32	1.03	1.38

*Measured Vickers hardness of reference tungsten sample

Irradiation hardening of tungsten exposed to various neutron energy spectra

Fukuda et al. [33] summarized the irradiation hardening behavior of tungsten exposed to various neutron energy spectra that capture the neutron fluence and irradiation temperature dependence. The irradiation hardening was indicated by the difference in measured Vickers hardness before and after irradiation. As shown in Figure 2, the irradiation hardening behavior of tungsten is quite dose-dependent with very limited temperature dependence, at least for doses less than 5 dpa. For the samples irradiated in HFIR, a surprising and very significant hardness increase is observed for radiation dose higher than 0.6 dpa. The hardening behavior is very similar for the samples irradiated in JMTR, likely due to the similar neutron energy spectrum of JMTR to HFIR. Additionally, there is almost no difference in the irradiation hardening behavior below ~ 1dpa when comparing the samples irradiated in the fast reactor, Joyo, to the results of the samples subject to a mixed neutron energy spectrum (HFIR and JMTR). However, for the tungsten samples irradiated in the fast neutron spectrum of Joyo there is a suggestion of saturation in the hardness change for dose levels beyond 1 dpa. More details could be found in Ref. [33].

The number density and size of TEM observed microstructural features, i.e., dislocation loops, voids, and precipitates, in these tungsten samples following neutron irradiation in HFIR, Joyo, or JMTR are summarized in Table 2. Selected TEM images are shown in Figure 3 to demonstrate the commonly observed defect microstructures in tungsten irradiated in HFIR. Dislocation loops were observed in the samples irradiated in the low temperature regime (<500°C) at dose levels from 0.03 to 1.62 dpa. In the temperature range from 500 to 800°C, the number densities of dislocation loops are at very low levels, or even negligible, for tungsten irradiated to a dose range from 0.15 to 2.2 dpa. This observation is consistent with the high mobility of dislocation loops [26] [34] at higher temperatures that promotes recombination with vacancy clusters or annihilation at other sinks, given that the migration energy of interstitial dislocation loops are very small, 0.013eV[35]. Therefore, the temperature dependence of the dislocation loops is more significant in comparison to the dose dependence for the tungsten samples exposed to neutron irradiation in HFIR. Similar behavior can also be observed for the samples irradiated in Joyo.

In addition, voids appeared in tungsten samples irradiated in the temperature range from 724 to 800°C, covering the dose levels of 0.15 to 2.2 dpa. The large migration energy of vacancy in tungsten, spanning from1.34 to 2.44 eV according to different studies [35, 36] [37], required higher temperature to induce the interaction of vacancy clusters and thus promote void nucleation and formation. In addition to the voids and dislocation loops, large W-Re-Os precipitates were also observed in samples irradiated to higher dose levels (>1 dpa) in HFIR, presumably due to the large thermal neutron flux. The temperature dependence of precipitate generation is insignificant in comparison with its dose dependence. It is noted that the TEM-visible precipitates in HFIR samples are needle-shaped and the sizes shown in Table 2 are the measured lengths of these precipitates. Their crystal structures and coherency to the matrix are being examined and the results will be published elsewhere soon. For simplification, the length is assumed to be the characteristic size of the precipitates used in the dispersed barrier hardening model. For the samples irradiated in JMTR at 600 and 800°C to 0.15 dpa, both voids and dislocation loops were observed. No precipitation was visible in these two samples irradiated in JMTR with a mixed neutron energy spectrum, likely due to the relatively small neutron exposure. When tungsten samples were irradiated in the fast reactor, Joyo, the observed irradiation defect microstructures consisted only of dislocation loops and voids, except for the case of 750°C irradiation. It is noted that the number density of loops in these Joyo samples were low for irradiation temperatures from 580 to 760°C, consistent with the observations of the HFIR samples irradiated at high temperatures, i.e., greater than 700°C.

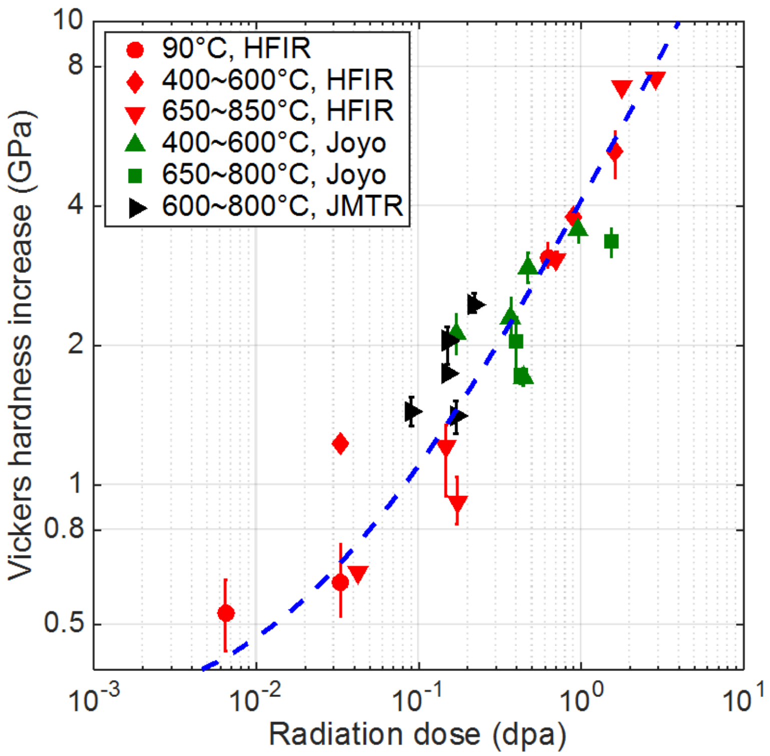

Figure 2. Dose and temperature dependence of irradiation hardening of pure tungsten irradiated in the HFIR, Joyo, and JMTR. The dashed line is plotted to guide the eye.

In order to calculate the hardness with a dispersed barrier hardening model, the obstacle strength factor, α, needs to be specified for all the TEM-visible defects contained within the neutron irradiated tungsten samples. In this study, we have assumed that these obstacle strength values are a function of defect type and size. In determining these α values, we have assumed that voids are strong obstacles to dislocation motions in comparison with dislocation loops [30] and the large TEM-observed W-Re-Os precipitates are also strong obstacles [10] [23]. Following the same methodology stated in Section 3.2, the α values of various defects are obtained and listed in Table 3. The calculated hardness values by using the two different superposition laws are shown in the last two column of Table 2.

Figure 4 shows the comparison between experimental data and the modeling predictions by using root-sum-square (Figure 4 (a)) and linear (Figure 4(b)) superposition laws, respectively. The results indicate that no obvious difference was observed for these two superposition laws in the present study while the root-sum-square law has a slightly better performance.

Based on the empirically determined barrier strength of each defect type using the linear superposition law, the individual contribution of each defect to the hardening in this case can be computed, as seen in Figure 5. Because of the nonlinear relationship of the contributions of each type of defect in the root-sum-square case, individual contributions are not shown here. Several important features of the system can be derived from Figure 5.

For the tungsten samples irradiated in HFIR, the predicted hardness has a relatively good agreement with the experimental data in the low dose (<0.1 dpa) and high dose regions (>0.6 dpa) while significant discrepancies are observed for the samples irradiated in the dose range from 0.1 to 0.6 dpa. Based on this analysis, coupled to the aforementioned TEM observations, we conclude that the irradiation hardening of neutron-irradiated tungsten in low dose regime derives from the existence of dislocation loops. The dominant hardening feature in the high radiation dose region is the large W-Re-Os precipitates. For those samples irradiated to intermediate dose, only dislocation loops and voids were TEM-visible and thus considered in the hardening model, leading to much smaller hardness predictions than measured values. This implies that a substantial volume fraction of microstructural features are invisible in TEM observations, and correspondingly, are not captured in the hardening model. The most likely cause is the formation of very small transmutation-induced W-Re-Os clusters. A recent APT study on the neutron irradiated tungsten [31] indicated that W-Re-Os clusters with a relatively large number density exist after being exposed to HFIR neutron irradiation to a dose of 0.2 dpa at 750°C.

Additionally, when applying the hardening model to the tungsten samples irradiated in JMTR, the model also underestimated the measured hardness increase. Considering JMTR has a mixed neutron spectrum, similar to HFIR, the production of transmutant elements is expected. For the two samples irradiated to 0.15 dpa in JMTR, only dislocation loops and voids were observed in TEM observations. Thus, it is tempting to conclude that, just like the tungsten samples irradiated in HFIR to the intermediate dose range, a hardening contribution from very small, TEM invisible precipitates was not captured, resulting in the underestimation of the hardness increase. Moreover, for the samples irradiated in Joyo, having a fast neutron energy spectrum, the model prediction and the experimental data have a relatively good agreement in comparison with the tungsten samples irradiated in HFIR and JMTR. When exposed to a fast neutron spectrum, the generation of transmutant elements in tungsten, and the formation of Re-Os-W precipitates are much less than those irradiated under a mixed neutron spectrum. Therefore, the hardening contribution from the W-Re-Os precipitates could be neglected while the dislocation loops and voids in irradiated tungsten are the dominant hardening sources.

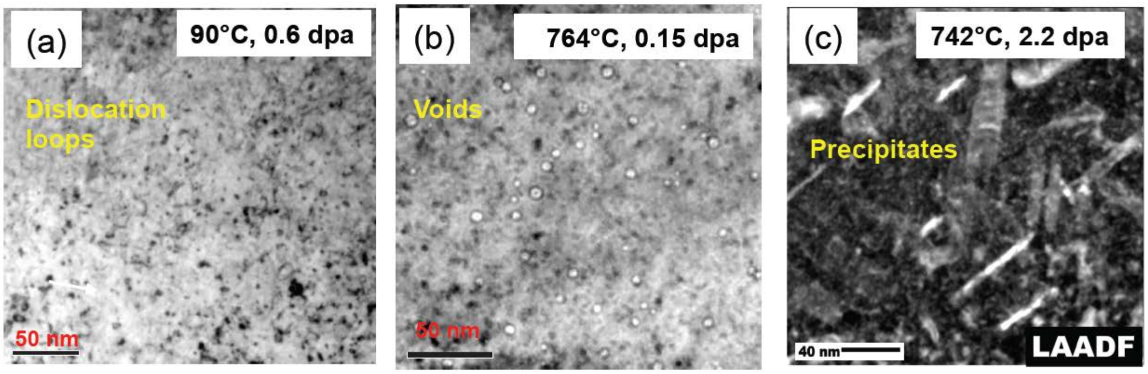

Figure 3. (a) Bright field TEM image of tungsten irradiated at 90°C to 0.6 dpa; (b) Bright field TEM image of tungsten irradiated at 764°C to 0.15 dpa; (c) LAADF TEM image of tungsten irradiated at 742°C to 2.2 dpa. All tungsten samples are single crystalline with an orientation of (110) and were irradiated in HFIR.

Table 2. Number density and size of irradiation-induced defects in tungsten subject to neutron exposure in HFIR, Joyo, and JMTR together with the comparison of measured Vickers hardness and model-predicted hardness

Reactors	Irradiation temperature (°C)	Neutron fluence (10^{25} n/m^2, E>0.1MeV)	Radiation dose (dpa)	Dislocation loop		Void		Precipitate		Measured hardness increase (GPa)	Predicted hardness increase *Root-Sum-Square* (GPa)	Predicted hardness increase *Linear* (GPa)
				Average size (nm)	Number density ($\times 10^{22}$ m^{-3})	Average size (nm)	Number density ($\times 10^{22}$ m^{-3})	Average size (nm)	Number density ($\times 10^{22}$ m^{-3})			
HFIR	90	2	0.6	4.98	4.55	-	-	-	-	3.10	0.98	0.98
	397	0.1	0.03	5.12	2.7	-	-	-	-	1.23	0.77	0.77
	467	2	0.6	5.38	3.1	-	-	-	-	3.80	0.83	0.83
	724	2	0.6	6.37	<0.01	3.03	1.22	-	-	3.07	0.79	0.84
	742	7	2.2	-	-	5.28	0.07	20	4.8	7.56	8.06	8.38
	764	0.5	0.15	6.56	<0.01	3.49	0.5	-	-	0.92	0.54	0.60
	500	5.4	1.62	2.9	3.3	-	-	5.7	8.6	5.24	5.78	6.39
	800	5.9	1.77	-	-	3.8	0.8	16.3	3.6	7.21	6.33	7.01
JMTR[38] [11]	600	0.81	0.15	7.9	4.6	1.3	6.4	-	-	2.06	1.58	2.23
	800	0.81	0.15	8.5	1.1	1.9	4.2	-	-	1.74	1.15	1.59
Joyo [39] [12]	400	1.1	0.17	2.8	2.0	1.8	19.5	-	-	2.12	2.08	2.52
	531	3.4	0.44	5.4	1.1	1.3	25.3	-	-	1.71	2.03	2.46
	538	7.8	0.96	4.7	4.7	2.1	49.0	-	-	3.56	4.28	5.13
	583	3.7	0.47	5.4	0.2	2.4	13.8	-	-	2.95	2.37	2.58
	740	2.7	0.4	12.2	0.3	2.9	12.7	-	-	2.05	2.53	2.88
	750	12	1.54	-	-	4.7	12.0	-	-	3.34	4.12	4.12
	756	3.3	0.42	5.6	0.1	2.5	12.1	-	-	1.72	2.26	2.41

Table 3. Barrier strength factor as a function of defect type and size used in the dispersed barrier hardening model

Defects	Dislocation loops	Voids				Precipitates
		1~2 nm	2~3nm	3~4nm	> 4nm	
Barrier strength factor (α)	0.15	0.25	0.30	0.35	0.40	0.60

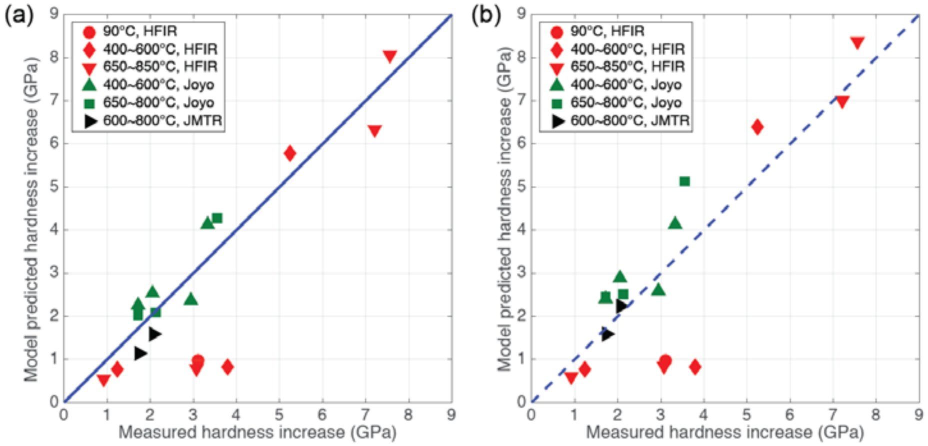

Figure 4. Comparison of experimentally measured Vickers hardness increase and hardening model predictions by using (a) root-sum-square and (b) linear superposition laws, respectively.

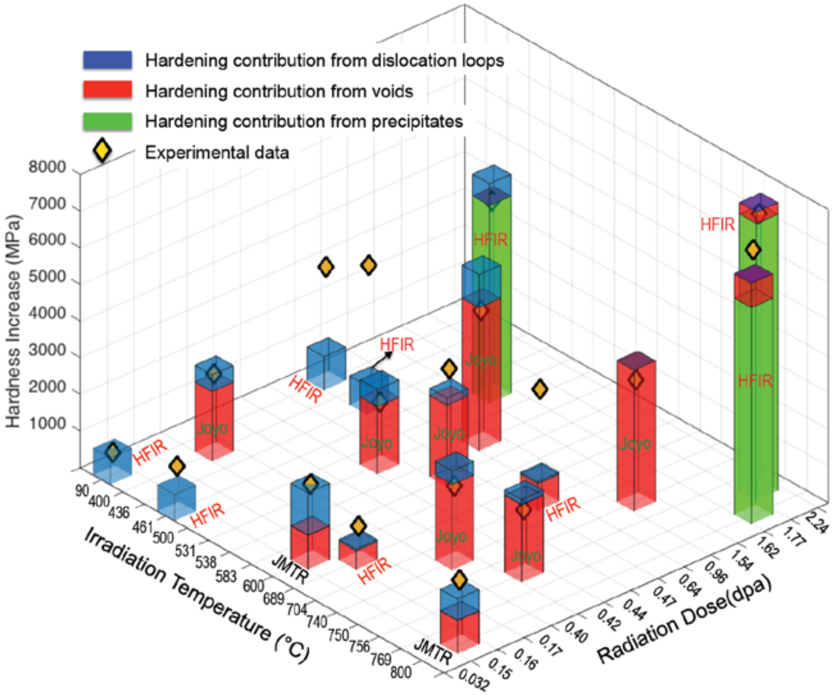

Figure 5. Radiation-induced hardening contributions due to different measured defects based on the linear superposition of the dispersed barrier hardening model for the samples listed in Table 2. The x- and y-axes are not linear scaled.

Discussions

As discussed in Section 3.1, the FKH model may be more appropriate for many radiation-induced small defect clusters which are weak obstacles to dislocation motion. According to Zinkle [19], this model is adequate for barrier strengths up to ¼ of the Orowan (impenetrable obstacle) limit, i.e., $\alpha<0.25$. The dispersed barrier model is more appropriate for barrier strengths of $0.25<\alpha<1.0$. It is commonly accepted that dislocation loops are considered as weak obstacles. Based on the barrier strength factors determined in this study, listed in Table 3, this conclusion can further be confirmed. In order to exam the applicability of FKH model, a combined model is used to predict the hardness increase of tungsten exposed to neutron irradiation, where the hardening contribution of dislocation loops is computed by using FKH model and the dispersed barrier hardening model is used for other defects' hardening contribution. The individual hardening contribution of different defects were then integrated by using the root-sum-square superposition law. The comparison of the experimentally measured Vickers microhardness and the combined model predictions is shown in Figure 6. It is evident that the application of the FKH model to the cases having dislocation loops as the dominant hardening source (hollow data points in Figure 6) significantly underestimates the hardness increase in comparison with the results obtained from the dispersed barrier hardening model as shown in Figure 4 (a). Therefore, the FKH hardening model is inappropriate in the present study on irradiation hardening of neutron-irradiated tungsten.

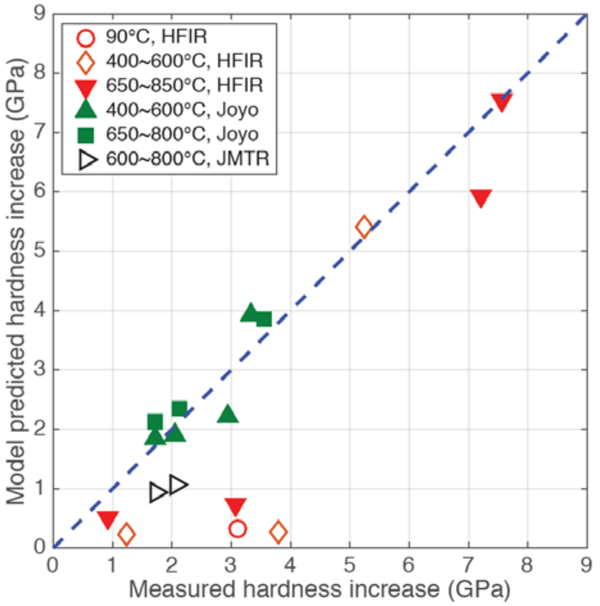

Figure 6. Comparison of experimentally measured Vickers hardness increase and the combined hardening model predictions (dispersed barrier hardening model and FKH model) by using the root-sum-square superposition law. The hollow data points indicate the cases which have significant difference compared to the same conditions shown in Figure 4 (a).

In the present study, a linear relationship between observed microstructure and the measured hardness was obtained based on the dispersed hardening model. The linear expression was also applied in previous studies on irradiation hardening of neutron irradiated tungsten and its alloys [18] [12] except that the coefficient is different, expressed in the form of

$$\Delta H_V = 6\alpha\mu b(Nd)^{1/2} \tag{4}$$

with Hv and σ_y in MPa. The equation used in these studies was originally described in Ref. [40]. When converting the critical shear stress, which is required to move dislocations through a field of obstacles, to an equivalent uniaxial tensile stress, a coefficient of 2 was used. However, Stoller and Zinkle [21] pointed out that the conversion factor of 2 is not right due to the inappropriate application of the Tresca yield criteria and concluded that the Taylor factor with a value of 3.06 is the correct parameter. Therefore, the barrier strength factors used in previous studies are overestimated by ~1.6 times the values used in the present study. In Ref. [12], the barrier strength factors of dislocation loop and void are set to be 0.2 and 0.6, respectively, without considering the size dependence. In order to obtain the same hardness predictions by using the corrected equation, Eq. (4), these values must correspondingly be modified to 0.12 and 0.38, respectively, which are close to the α values used for dislocation loops (α =0.15) and large voids (α=0.4) with a diameter greater than 4 nm in the present study. Typical experimental values of α for the TEM-visible dislocation loops in neutron irradiated BCC metals are covering a large range from 0.15 up to 0.75 [41] [42]. Tan [23] summarized that the strength factors of cavities and precipitates could be in the range of 0.01~1 and 0.2~0.6, respectively. The barrier strength factors used in the present study, listed in Table 3, fall in these ranges.

It is emphasized here that the irradiation hardening derives from all the defects contained within the materials. However, the hardening model only includes hardening contributions from the TEM-visible defects. Correspondingly, most literature studies assume that any microstructural features that are not visible in the TEM have negligible contributions to the hardening increases of materials following irradiation. This works well for most of the cases in the literature. However, as noted in the previous section, the tungsten specimens irradiated in HFIR and JMTR to an intermediate dose range from about 0.1 to 3 dpa, exhibit considerably larger hardness increases than cannot be captured by a dispersed barrier hardening model informed by a microstructure consisting only of the dislocation loops and voids observed in TEM. In this case, we believe that the dominant hardening contribution is from TEM-invisible precipitates, which form due to neutron-induced transmutation of tungsten into rhenium and osmium, and the resistance to dislocation motion of these precipitates. Actually, the generation of solid transmutant element, Re and Os, is a significant issue for neutron-irradiated tungsten. For example, in the tungsten sample irradiated in HFIR, pure tungsten is transformed to W-Re or W-Re-Os alloys as the neutron fluence increases. Greenwood and Garner's calculations [43] indicated that pure tungsten is converted to W-8%Re-15%Os alloys after 10 dpa in HFIR. Therefore, the material of interest is no longer pure tungsten. In addition to the formation of precipitates, the shear modulus will also change as the compositions of the materials change. Furthermore, even below the solubility limit, the transmutant elements may produce solid solution hardening of tungsten. Moteff and Rau [44] showed that the increase in the 1100°C creep strength of tungsten irradiated at 70°C to various radiation dose levels is a function of the Re content, following a parabolic power law. Fukuda et al. [12] measured the Vickers hardness of W-Re alloys at room temperature and found that the hardness increases as the Re content increases following an approximate linear correlation. In order to investigate the solution hardening of BCC Fe matrix, a solid solution strengthening model [45] was developed by establishing a linear correlation between the composition of the solutes in the matrix and the resultant change in yield strength. One particular observation is that interstitial solute species have a strength factor that is 2 to 3 orders of magnitude greater than that of substitutional solutes. Considering the same BCC crystalline structure of W and Fe, similar behavior could be expected for the solution hardening of tungsten irradiated in HFIR. It is likely that the solid solution is not significant when radiation dose level is low due to the low atomic fraction of the transmutant elements, compared to other hardening sources. When radiation dose is increasing, the transmutant elements are continuously generated, which also have a higher probability to be interstitials due to sever radiation damage, giving rise to the solid solution strengthening. In order to get a more accurate prediction of the irradiation hardening, the solution hardening effect should be considered in the future study. More work is needed to identify the population of the small precipitates in the tungsten samples irradiated in HFIR to intermediate doses and such information will be included in the hardening model to overcome the current gap between modeling and experimental data.

Conclusion

Irradiation hardening of tungsten exposed to various neutron energy spectra was investigated through analysis of the hardness changes using a dispersed barrier hardening model informed by the microstructures observed in irradiated tungsten using TEM. An annealing study of single crystalline tungsten following low dose and low temperature neutron irradiation was used to identify the hardening contribution of vacancy clusters and dislocation loops. The results indicated that the barrier strength factors of the large vacancy clusters and TEM-visible dislocation loops, the two major hardening sources during the isochronal annealing, were determined as 0.2 and 0.15, respectively. Vickers microhardness testing at room temperature of tungsten following various irradiation conditions showed continuously increasing hardness with increasing radiation dose level for the tungsten sample irradiated in HFIR and JMTR while the hardness increase of tungsten samples irradiated in Joyo appears to saturate for radiation doses above 1 dpa. This analysis reveals the dominant hardening source at various irradiation conditions. For the samples irradiated in HFIR, dislocation loops and voids are the major contributor to the irradiation hardening at low dose levels, while the intermetallic second phase precipitation dominate in the relatively modest dose region, leading to a tremendous hardness increase. The model fails to predict accurate hardness increase in the intermediate dose range, which we interpret result from TEM-invisible precipitates or even super-saturated solid solutions of transmutant rhenium or osmium. Future work will be dedicated to investigating the transmutant element clusters in this radiation dose range to verify the hypothesis. For the samples irradiated in Joyo and JMTR (those having detailed microstructure information), the major hardening contributors are TEM-visible dislocation loops and voids. The barrier strength factors were also determined for the observed radiation defects, which could be applied to predicting the irradiation hardening of tungsten. The strength factor of dislocation loop is determined as 0.15 while the α values for voids are a function of void size, spanning from 0.25 to 0.4. The W-Re-Os precipitates are strong obstacles to dislocation motion with α value of 0.6. Overall, this work is expected to provide insights into the underlying mechanisms controlling the embrittlement of tungsten exposed to neutron irradiation and will benefit the R&D of plasma facing materials in fusion reactors.

Acknowledgement

The work presented in this paper was partially supported by Laboratory Directed R&D funds at ORNL. The research was also sponsored by the US Department of Energy Office of Fusion Energy Science under Contract DE-AC05-00OR22725 with UT-Battelle LLC, and by the US-Japan PHENIX project under Contract NFE-13-04478, with UT-Battelle LLC.

References

[1] Rieth, M., et al., *Recent progress in research on tungsten materials for nuclear fusion applications in Europe.* Journal of Nuclear Materials, 2013. **432**(1-3): p. 482-500.

[2] Ueda, Y., K. Tobita, and Y. Katoh, *PSI issues at plasma facing surfaces of blackets in fusion reactors.* Journal of Nuclear Materials, 2003. **313-316**: p. 32-41.

[3] Zinkle, S.J., *Fusion materials science: Overview of challenges and recent progress.* Physics of Plasmas, 2005. **12**(5): p. 058101.

[4] Wirth, B.D., et al., *Fusion materials modeling: Challenges and opportunities.* MRS Bulletin, 2011. **36**(03): p. 216-222.

[5] Bloom, E.E., S.J. Zinkle, and F.W. Wiffen, *Materials to deliver the promise of fusion power – progress and challenges.* Journal of Nuclear Materials, 2004. **329-333**: p. 12-19.

[6] Wurster, S., et al., *Recent progress in R&D on tungsten alloys for divertor structural and plasma facing materials.* Journal of Nuclear Materials, 2013. **442**(1-3): p. S181-S189.

[7] Greenwood, R.L. and K.R. Smither, *SPECTER: Neutron damage calculations for materials irradiations.* 1985. **ANL/FPP/TM-197**.

[8] Fujitsuka, M., et al., *Effect of neutron irradiation on thermal diffusivity of tungsten-rhenium alloys.* Journal of Nuclear Materials, 2000. **283-287**: p. 1148-1151.

[9] Hasegawa, A., et al., *Property change mechanism in tungsten under neutron irradiation in various reactors.* Journal of Nuclear Materials, 2011. **417**(1-3): p. 491-494.

[10] Hasegawa, A., et al., *Neutron irradiation effects on tungsten materials.* Fusion Engineering and Design, 2014. **89**(7-8): p. 1568-1572.

[11] Hasegawa, A., et al., *Neutron Irradiation Behavior of Tungsten.* Materials Transactions, 2013. **54**(4): p. 466-471.

[12] Fukuda, M., et al., *Effects of Re Content and Fabrication Process on Microstructural Changes and Hardening in Neutron Irradiated Tungsten.* Materials Transactions, 2012. **53**(12): p. 2145-2150.

[13] Fukuda, M., et al., *Property change of advanced tungsten alloys due to neutron irradiation.* Journal of Nuclear Materials, 2013. **442**(1-3): p. S273-S276.

[14] Fukuda, M., et al., *Microstructural development of tungsten and tungsten–rhenium alloys due to neutron irradiation in HFIR.* Journal of Nuclear Materials, 2014. **455**(1-3): p. 460-463.

[15] Hu, X., et al., *Defect evolution in single crystalline tungsten following low temperature and low dose neutron irradiation.* Journal of Nuclear Materials, 2016. **470**: p. 278-289.

[16] Gussev, M.N., et al., *Role of Scale Factor During Tensile Testing of Small Specimens.* 2014: p. 1-19.

[17] Garrison, L.M., et al., *Irradiation Effects in Tungsten-Copper Laminate Composite.* 2015. **doe/er-0313/59**.

[18] Tanno, T., et al., *Microstructure Development in Neutron Irradiated Tungsten Alloys.* Materials Transactions, 2011. **52**(7): p. 1447-1451.

[19] Zinkle, S.J. and Y. Matsukawa, *Observation and analysis of defect cluster production and interactions with dislocations.* Journal of Nuclear Materials, 2004. **329-333**: p. 88-96.

[20] Kroupa, F. and P.B. Hirsch, *Elastic interaction between prismatic dislocation loops and straight dislocations.* Discussions of the Faraday Society, 1964. **38**: p. 49-55.

[21] Stoller, R.E. and S. Zinkle, *On the relationship between uniaxial yield strength and resolved shear stress in polycrystalline materials.* Journal of Nuclear Materials, 2000. **283-287**: p. 349-352.

[22] Kocks, U.F., *The relation between polycrystal deformation and single-crystal deformation.* Metallurgical Transactions, 1970. **1**: p. 1121-1143.

[23] Tan, L. and J.T. Busby, *Formulating the strength factor α for improved predictability of radiation hardening.* Journal of Nuclear Materials, 2015. **465**: p. 724-730.

[24] Field, K.G., et al., *Radiation tolerance of neutron-irradiated model Fe–Cr–Al alloys.* Journal of Nuclear Materials, 2015. **465**: p. 746-755.

[25] Hu, X., et al., *Modeling of irradiation hardening of iron after low-dose and low-temperature neutron irradiation.* Modelling and Simulation in Materials Science and Engineering, 2014. **22**(6): p. 065002.

[26] Setyawan, W., et al., *Displacement cascades and defects annealing in tungsten, Part I: Defect database from molecular dynamics simulations.* Journal of Nuclear Materials, 2015. **462**: p. 329-337.

[27] Ferroni, F., et al., *High temperature annealing of ion irradiated tungsten.* Acta Materialia, 2015. **90**: p. 380-393.

[28] Tabor, D., *The physical meaning of indentation and scratch hardness.* British Journal of Applied Physics 1956. **7**: p. 159.

[29] Busby, J.T., M.C. Hash, and G.S. Was, *The relationship between hardness and yield stress in irradiated austenitic and ferritic steels.* Journal of Nuclear Materials, 2005. **336**(2-3): p. 267-278.

[30] Was, G.S., *Fundamentals of radiation materials science*. 2007, New York: Springer.

[31] Edmondson, P.D., To be published, 2016.

[32] Koyanagi, T., *Microstrucrual evolution of tungsten exposed to neutron irradiation.* To be published, 2016.

[33] Fukuda, M., et al., *Neutron energy spectrum influence on irradiation hardening and microstructrual development of tungsten.* Journal of Nuclear Materials, 2016: p. submitted.

[34] Nandipati, G., et al., *Displacement cascades and defect annealing in tungsten, Part III: The sensitivity of cascade annealing in tungsten to the values of kinetic parameters.* Journal of Nuclear Materials, 2015. **462**: p. 345-353.

[35] Becquart, C.S., et al., *Microstructural evolution of irradiated tungsten: Ab initio parameterisation of an OKMC model.* Journal of Nuclear Materials, 2010. **403**(1-3): p. 75-88.

[36] Faney, T. and B.D. Wirth, *Spatially dependent cluster dynamics modeling of microstructure evolution in low energy helium irradiated tungsten.* Modelling and Simulation in Materials Science and Engineering, 2014. **22**(6): p. 065010.

[37] Marian, J. and T.L. Hoang, *Modeling fast neutron irradiation damage accumulation in tungsten.* Journal of Nuclear Materials, 2012. **429**(1-3): p. 293-297.

[38] He, J.C., et al., *Microstructural development and irradiation hardening of W and W–(3–26) wt%Re alloys after high-temperature neutron irradiation to 0.15 dpa.* Nuclear Fusion, 2006. **46**(11): p. 877-883.

[39] Tanno, T., et al., *Effects of Transmutation Elements on Neutron Irradiation Hardening of Tungsten.* Materials Transactions, 2007. **48**(9): p. 2399-2402.

[40] Moteff, J., D.J. Michel, and V.K. Sikka, *The influence of irradiation temperature on the hardening behavior of the refractory bcc metals and alloys.* Nucl. Metall., 1973. **18**: p. 198211.

[41] Rice, P.M. and S.J. Zinkle, *Temperature dependence of the radiation damage microstructure in V-4Cr-4Ti neutron irradiated to low dose.* Journal of Nuclear Materials, 1998. **258-263**: p. 1414-1419.

[42] Pokor, C., et al., *Irradiation damage in 304 and 316 stainless steels: experimental investigation and modeling. Part II: Irradiation induced hardening.* Journal of Nuclear Materials, 2004. **326**(1): p. 30-37.

[43] Greenwood, L.R. and F.A. Garner, *Transmutation of Mo, Re, W, Hf, and V in various irradiation test facilities and STARFIRE.* Journal of Nuclear Materials, 1994. **212-215**: p. 635-639.

[44] Rau, R.C. and J. Moteff, *Annealing of defect clusters in irradiated tungsten.* Radiation Effects, 1971. **8**(1-2): p. 99-105.

[45] Lu, Q., W. Xu, and S.v.d. Zwaag, *Designing new corrosion resistant ferritic heat resistant steel based on optimal solid solution strengthening and minimisation of undesirable microstructural components.* Computational Materials Science, 2014. **84**: p. 198-205.

4.6 NEUTRON IRRADIATION EFFECTS IN TUNGSTEN—L.M. Garrison, Y. Katoh, P. Edmondson, X. Hu, C. Parish, T. Koyanagi, M. McAlister, N.A.P. Kiran Kumar (Oak Ridge National Laboratory), M. Fukuda, T. Hwang (Tohoku University, Japan), L. L. Snead (Massachusetts Institute of Technology), T. S. Byun

OBJECTIVE

The objective of this work is to evaluate the effects of neutron irradiation on the mechanical properties and microstructure of tungsten-based materials to aid in developing plasma-facing materials for fusion reactors.

SUMMARY

A total of 440 samples were irradiated in HFIR at temperatures from 70 to 900°C and fast neutron fluences of 0.01 to 20 $\times 10^{25}$ n/m^2 at E>0.1 MeV as part of the TITAN project. Types of tungsten irradiated in this study were [110] single crystal tungsten, [100] single crystal tungsten, wrought tungsten foils, annealed tungsten foils, and tungsten-copper laminates. Analysis is revealing that characterizing precipitation of transmutation products in neutron irradiated tungsten is key to understanding its properties after irradiation. TEM images of higher dose samples revealed that voids tend to be near precipitates in the irradiated tungsten. Analysis of room temperature tensile test data of the single crystal samples reveals that ultimate strength decreases at less than 1 dpa. Further shipments of TITAN samples to LAMDA were completed so that the higher dose samples can be evaluated.

PROGRESS AND STATUS

Detailed microstructural analysis was completed on selected irradiated single crystal and polycrystalline tungsten samples. Irradiated tungsten transmutes to rhenium and rhenium transmutes to osmium.The rhenium and osmium precipitate out of the tungsten matrix due to irradiation induced precipitation and form needle-shaped precipitates. TEM investigation of both single crystal and polycrystalline tungsten revealed an association between the needle-shaped precipitates and voids in irradiated tungsten (Figure 1).

The last two capsules from the TITAN campaign, TB-650-4 and T9G-13, were opened and the specimens cataloged at the hot cells. The target irradiation conditions for these capsules were TB-650-4: 20×10^{25} n/m^2 at 650°C and T9G-13: 12×10^{25} n/m^2 at 300°C. The preliminary analysis of the SiC temperature monitors from capsule T9G-13 revealed the irradiation temperature was between 400 and 500°C. Based on other capsules in this campaign, the irradiation temperature of TB-650-4 is expected to be in the range of 700-800°C. The SiC temperature monitors for TB-650-4 are planned to be tested.

Radioactivity of all specimens from T9G-13 were measured and specimens packaged in several lead pigs, as noted in Table 1, for shipment to LAMDA. Pigs CCC, III, JJJ, and HHH were shipped to LAMDA, and the samples have been inspected and cleaned.

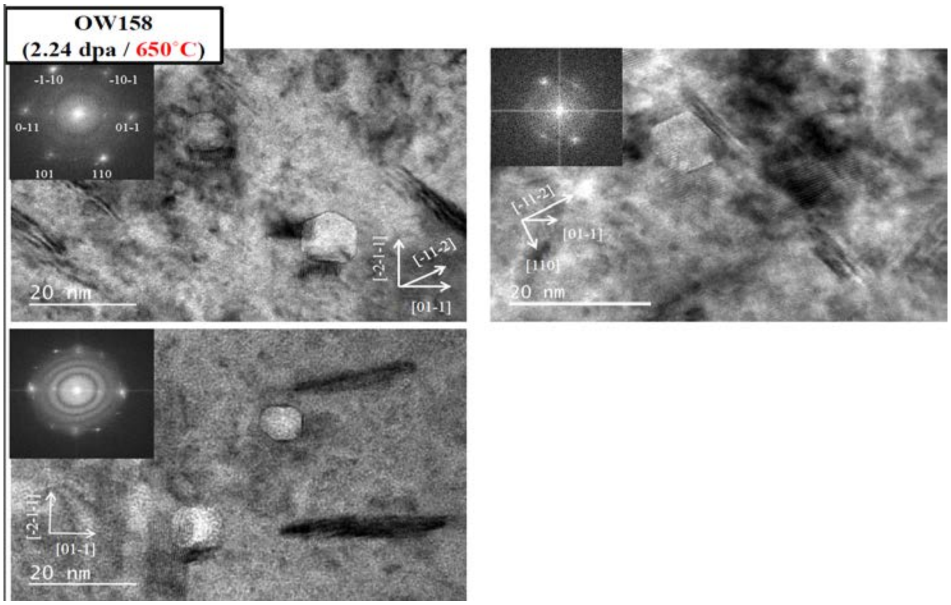

Figure 1. Polycrystalline wrought foil tungsten sample OW158 was imaged with TEM after irradiation to 2.24 dpa at an estimated 650°C irradiation temperature. The voids are faceted and appear associated with neighboring needle-shaped Re and Os rich precipitates in the tungsten matrix.

Table 1. Dose measurements for samples from rabbit capsule T9G-13

Specimen	**Open Contact**	**Closed 1 Ft DR**	**Smear #**	**Smear B/G**	**Smear Alpha**	**PIG**	DR @ a ft OT/@ 5" on side
W11	7 R/hr	7.2 mr/hr	4	6952	<Lc	FY16-CCC	128 mr/hr / 142 mr/hr
T9G-13 Foils	>10 R/hr	64 mr/hr	4	6952	<Lc	FY16-CCC	128 mr/hr / 142 mr/hr
HK40 (4X16X0.5)	>10 R/hr	187 mr/hr	4	6952	<Lc	FY16-CCC	128 mr/hr / 142 mr/hr
P13	>10 R/hr	155 mr/hr	4	6952	<Lc	FY16-EEE	110 mr/hr / 155 mr/hr
AW013 Foil	5 R/hr	10 mr/hr	4	6952	<Lc	FY16-EEE	110 mr/hr / 155 mr/hr
OW011 Foil	7.6 R/hr	9.2 mr/hr	4	6952	<Lc	FY16-DDD	105 mr/hr / 155 mr/hr
S9902	7.8 R/hr	71 mr/hr	4	6952	<Lc	FY16-DDD	105 mr/hr / 155 mr/hr
SOO02	8.7 R/hr	69 mr/hr	4	6952	<Lc	FY16-DDD	105 mr/hr / 155 mr/hr
T0015	8.5 R/hr	72 mr/hr	4	6952	<Lc	FY16-FFF	108 mr/hr / 115 mr/hr
T9915	>10 R/hr	100 mr/hr	4	6952	<Lc	FY16-FFF	108 mr/hr / 115 mr/hr
April 13th							
9BA24	>10 R/hr	130 mr/hr	4	6952	<Lc	FY16-GGG	100 mr/hr / 125 mr/hr
SW10	>10 R/hr	47 mr/hr	4	6952	<Lc	FY16-	100 mr/hr / 125

						GGG	mr/hr
1W12	>10 R/hr	6 mr/hr	4	6952	<Lc	FY16-GGG	100 mr/hr / 125 mr/hr
SW09	>10 R/hr	30 mr/hr	4	6952	<Lc	FY16-HHH	125 mr/hr / 120 mr/hr
T9G-13 Bar ID # ?	>10 R/hr	80 mr/hr	4	6952	<Lc	FY16-HHH	125 mr/hr / 120 mr/hr
OBA02	>10 R/hr	90 mr/hr	4	6952	<Lc	FY16-HHH	125 mr/hr / 120 mr/hr
Tem Monitors	55 mr/hr	1 mr/hr	4	6952	<Lc	FY16-III	95 mr/hr / 110 mr/hr
LW917	>10 R/hr	70 mr/hr	4	6952	<Lc	FY16-III	95 mr/hr / 110 mr/hr
GB05	>10 R/hr	93 mr/hr	4	6952	<Lc	FY16-III	95 mr/hr / 110 mr/hr
1W11	>10 R/hr	6.5 mr/hr	4	6952	<Lc	FY16-III	95 mr/hr / 110 mr/hr
W12	9.8 R/hr	6 mr/hr	4	6952	<Lc	FY16-JJJ	150 mr/hr / 175 mr/hr
9BA23	>10 R/hr	130 mr/hr	4	6952	<Lc	FY16-JJJ	150 mr/hr / 175 mr/hr
9BA15	>10 r/hr	130 mr/hr	4	6952	<Lc	FY16-JJJ	150 mr/hr / 175 mr/hr
A7/B2 (4X4X0.5)			4	6952	<Lc		
LW918	>10 R/hr	68 mr/hr	4	6952	<Lc	FY16-KKK	Partial
FD01			4	6952	<Lc		High Dose In Cell 6
FD02			4	6952	<Lc		High Dose In Cell 6

Previously, microhardness was measured on single crystal tungsten samples that had been irradiated up to approximately 1 dpa. The hardness was not sensitive to irradiation temperature and was increasing rapidly with increasing dose. To test if the hardness saturated, three higher dose samples were hardness tested (Figure 2). Now, it is seen that up to a dpa of 4.5 the hardness has not yet saturated.

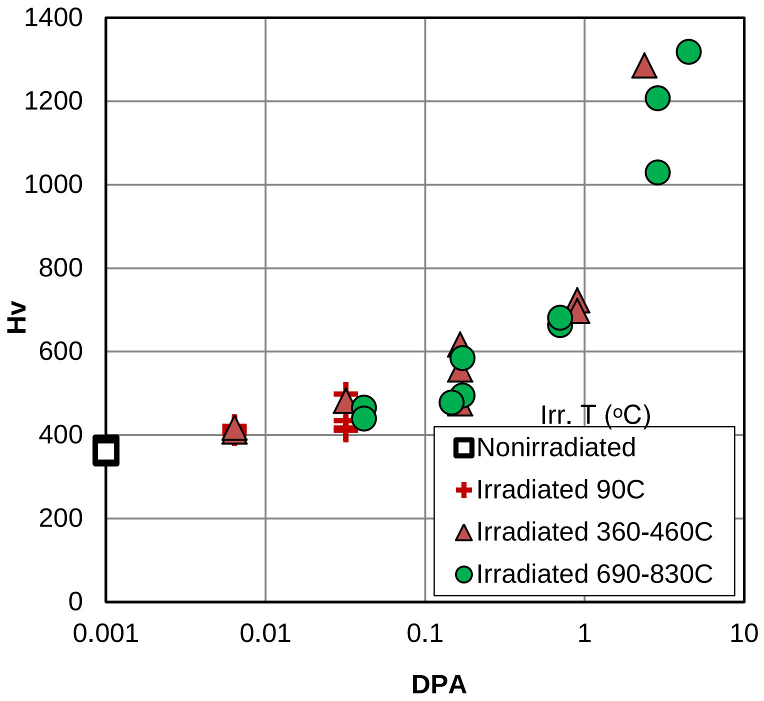

Figure 2. Microhardness on irradiated single crystal tungsten before and after HFIR irradiation.

Many of the lower dose tensile tests on the single crystal tungsten have been completed and the results are summarized in Table 2. Samples with an ID that begins with “1W” are single crystal tungsten with <110> crystal direction along the tensile direction. Those samples whose IDs begin with “W” are single crystal tungsten with <100> crystal direction along the tensile direction.

Table 2. Tensile properties of single crystal tungsten samples

ID	Irradiation T (°C)	Fast Fluence (×10^{25} n/m^2, E>0.1 MeV)	DPA	Test T (°C)	YS (MPa)	UTS (MPa)	UE (%)	TE (%)
1W24	830	0.13	0.042	650	261	278	0.96	13.7
1W02	370	0.02	0.0064	300	376	440	1.8	18.7
W02	370	0.02	0.0064	300	472	476	0.18	5.1
1W49	360	0.52	0.17	300	471	471	0.23	35.0
1W14	800	0.08	0.026	500	206	238	4.0	20.6
W25	830	0.13	0.042	650	241	286	4.4	19.7
1W18	700	2.2	0.70	500	1176	1214	0.35	0.51
1W54	800	0.46	0.15	650	407	424	1.5	21.1
1W08	430	2.82	0.90	300	brittle failure	683	0	0
1W52	690	0.54	0.17	500	518	530	0.02	12
1W01	370	0.02	0.0064	22	brittle failure	756	0	0

1W05	90	0.02	0.0064	22	654	671	0.45	0.49
1W13	800	0.08	0.026	22	brittle failure	627	0	0
1W17	700	2.2	0.70	22	brittle failure	359	0	0
1W23	830	0.13	0.042	22	brittle failure	813	0	0
1W25	90	0.1	0.032	22	674	674	0.2	0.2
1W47	460	0.1	0.032	22	brittle failure	844	0	0
1W50	360	0.52	0.17	22	brittle failure	507	0	0
1W51	690	0.54	0.17	22	brittle failure	393	0	0
1W53	800	0.46	0.15	22	brittle failure	592	0	0
W01	370	0.02	0.0064	22	brittle failure	776	0	0
W08	430	2.82	0.90	22	brittle failure	225	0	0
W13	800	0.08	0.026	22	brittle failure	460	0	0
W24	830	0.13	0.042	22	brittle failure	416	0	0
W27	800	0.46	0.15	22	brittle failure	385	0	0
W52	360	0.52	0.17	22	brittle failure	716	0	0
W54	690	0.54	0.17	22	brittle failure	286	0	0
W03	460	0.1	0.032	22	brittle failure	742	0	0
W56	N/A	N/A	N/A	22	brittle failure	322	0	0
W57	N/A	N/A	N/A	90	brittle failure	298	0	0
W58	N/A	N/A	N/A	300	222	507	3.3	3.3
W59	N/A	N/A	N/A	500	66	204	30	45
W60	N/A	N/A	N/A	650	60	188	73	94

For tungsten samples that were part of the TITAN program, the conversion of 0.32 dpa=1E25 n/m^2 (E>0.1 MeV) has been used in all reports so far. Upon recent analysis, it was determined that a lower dpa conversion rate may be more accurate for these samples, but there is not a consensus in the literature. For example, M. E. Sawan, Fusion Eng. Des., 87(5-6), 551-555 (2012) uses the conversion 0.195 dpa=1E25 n/m^2 (E>0.1 MeV), but M. Fukuda, K. Yabuuchi, S. Nogami, A. Hasegawa, and T. Tanaka, J. Nucl. Mater., 455(1-3), 460-463 (2014) uses the conversion 0.167 dpa=1E25 n/m^2 (E>0.1 MeV). This issue of calculating the dpa in tungsten in the flux trap of HFIR is being further investigated.

4.7 NEUTRON IRRADIATION EFFECTS IN TUNGSTEN-COPPER COMPOSITES

—L. M. Garrison, Yutai Katoh (Oak Ridge National Laboratory) Jeremy Moon (University of Nevada-Reno), Joseph Willenborg (University of Tennessee-Knoxville)

OBJECTIVE

The aim of this work is to evaluate tungsten-copper based composites for potential use as part of a plasma-facing component for future fusion reactors.

SUMMARY

As part of the TITAN program, two types of tungsten-copper composites were irradiated in HFIR at temperatures from 300 to 900°C and fast neutron fluences of 0.01 to 20 $\times 10^{25}$ n/m^2 at E>0.1 MeV. One material was a tungsten-copper laminate composite composed of 0.1 mm alternating layers of tungsten and copper. Tensile tests have previously been completed on the tungsten-copper laminate and EDS and EBSD analysis of the material is underway. The other material was a tungsten-copper powder sintered composite, with 75% W and 25% Cu. Tensile tests of unirradiated and irradiated tungsten-copper sintered composite have been completed and are being analyzed.

PROGRESS AND STATUS

Tungsten-copper laminates

Three tungsten-copper laminate samples that were part of the TITAN program were analyzed with scanning electron microscopy (SEM), energy dispersive spectrometry (EDS), and electron backscatter diffraction (EBSD). These three samples were previously tensile tested at room temperature. Their conditions were sample SW40 unirradiated and 15.5% total elongation, sample SW25 0.15 dpa (calculated for tungsten) at 760°C and 0.15% total elongation, and sample SW40 0.70 dpa (calculated for tungsten) at 710°C and 0% total elongation. In the unirradiated state, the tungsten foil is ductile, but has less than 2% total elongation on its own. The additional elongation comes from the copper layers of the laminate. After irradiation, it is expected that the tungsten foil becomes brittle, but the copper should remain ductile. However, in tensile testing the composite after irradiation, the copper was unable to maintain the ductility that the composite experienced before irradiation. To see if any changes were occurring in the tungsten to copper interface during irradiation that might negatively impact the composite behavior, these three samples were analyzed with the SEM.

The data is still being analyzed, but a few initial observations can be made. For one, initially the tungsten to copper interface is very distinct and clean (Figure 1). After irradiation, the interface still does not show noticeable mixing of the tungsten and copper, but voids or gaps are noticeable at the tungsten-copper interfaces (Figure 2). Also, within the three tungsten layers (top, middle, and bottom layers of the composite) horizontal striations can be seen in Figure 2. These appear to be lines of voids or gaps within each tungsten foil following the rolling direction of the tungsten foil. Although the laminate did not have any measurable elongation in the tensile test after 0.7 dpa irradiation, it can be seen that the copper layers successfully stopped many vertical cracks in the tungsten foil layers from propagating through the entire composite (Figure 2).

Although the optical images of several of the W-Cu laminate samples have yellow or orange colors on the top tungsten layer, such as in Figure 3, the EDS analysis did not measure significant oxygen, as would be present if the tungsten were oxidized. The EDS did show that Cu is on top of the W in some areas, as on the edge pictured in Figure 4. Therefore, the yellow and orange seen in the optical images is believed to be a combination of a) some Cu on the top surface from the fabrication and b) possible color enhancement from the imaging mode in the optical microscope rather than from a tungsten oxide.

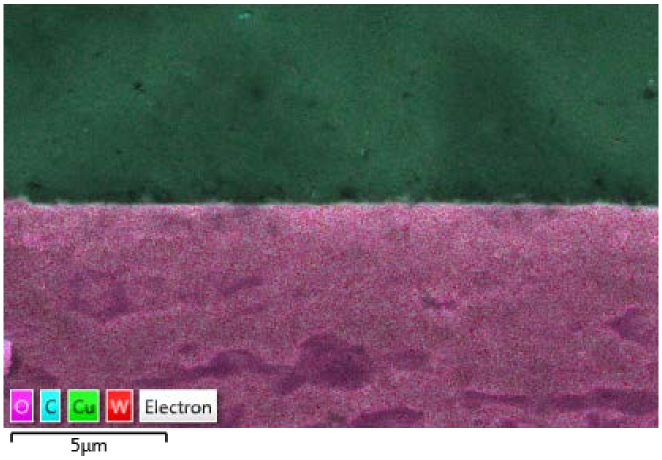

Figure 1. EDS element map of polished edge of tungsten-copper laminate sample SW40.

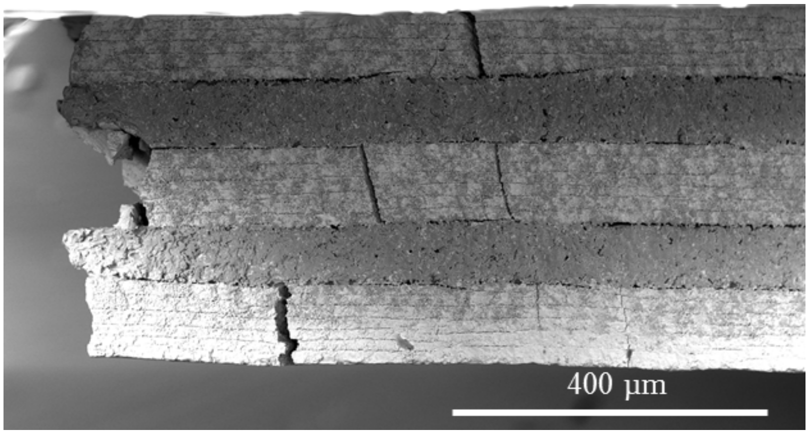

Figure 2. SEM image of the edge of the gauge section near the fracture end of SW15. The tensile direction is horizontal on the page.

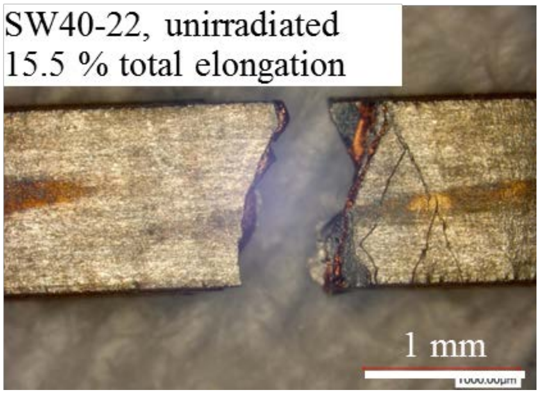

Figure 3. Optical image of SW40, unirradiated and tested at 22°C.

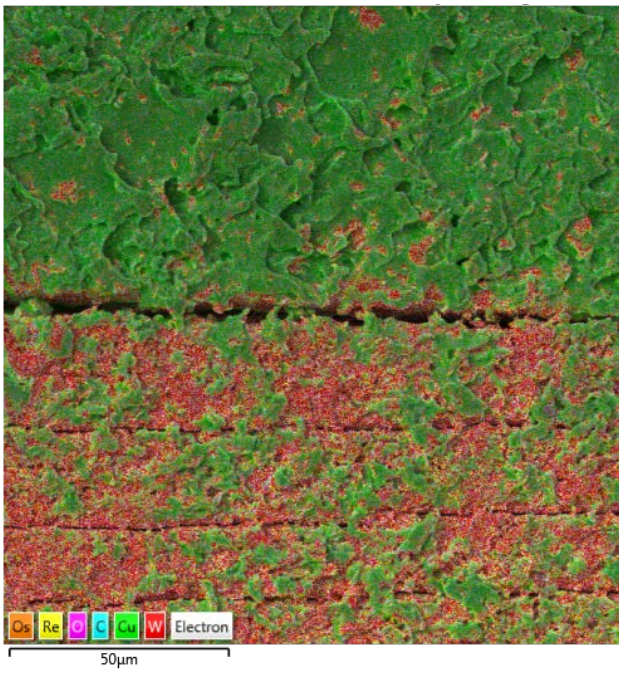

Figure 4. EDS map of unpolished edge of SW25 after irradiation. The top layer is copper and the bottom layer is tungsten, but surface deposits of copper are observed.

Tungsten-copper sintered composite

Previous analysis of the tungsten-copper laminate composites irradiated in the TITAN program showed that the laminate composites quickly loose ductility after low dose irradiation. The design space for such a continuous composite may be small because of the extreme mismatch of tensile strength in the two materials after irradiation.

As an alternative to the tungsten-copper laminate composite, a powder sintered tungsten copper composite with 75% W and 25% Cu was investigated. A polished surface of one of the tungsten copper sintered composites is shown in Figure 5. A closer examination reveals that there are sharp boundaries between the rounded W particles and the Cu. As expected, no interlayer or mixed phase formed between the elements.

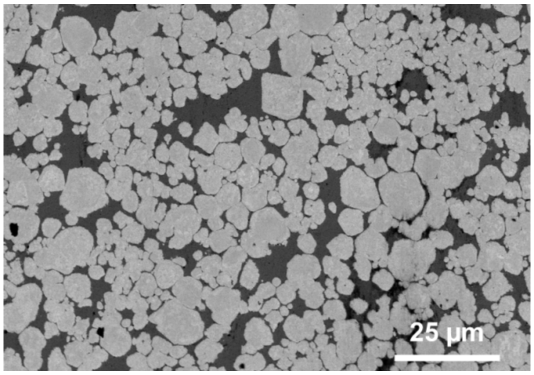

Figure 5. SEM image of the powder sintered tungsten copper composite.

Two identical tungsten-copper sintered composite samples were tensile tested at room temperature. The tensile data plotted in Figure 6 does not account for machine compliance, so the elastic region is not representative of the material properties. The material does show ductility at room temperature, which is a significant improvement as compared to traditional sintered tungsten. Examining the fracture surface of one of the samples, limited reduction in area is detected near the fracture surface, and the fracture surface itself has a bright copper-color (Figure 7).

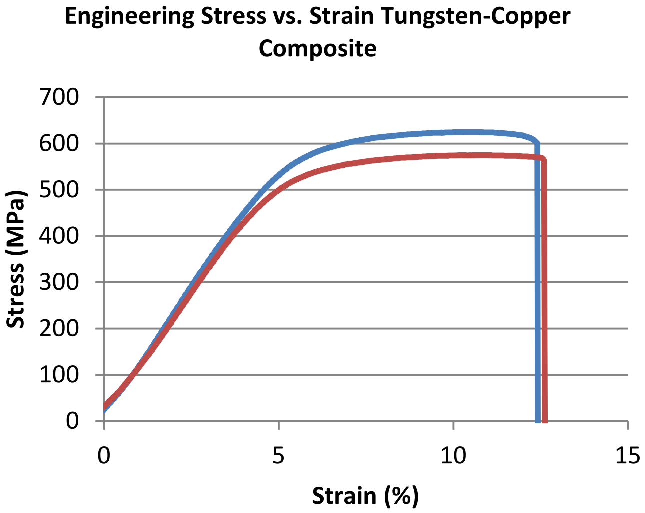

Figure 6. Tensile curves of the tungsten-copper sintered composite tested at room temperature.

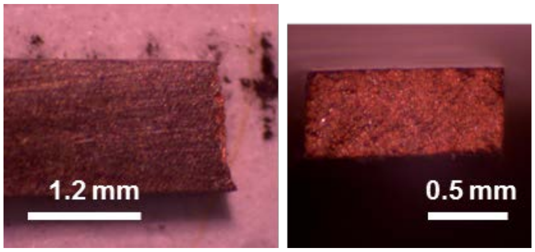

Figure 7. Fracture surface of the tungsten-copper sintered composite.

Some of the tungsten-copper sintered composite was irradiated and tensile tested as part of the TITAN program. These samples have sample IDs that begin with “KW”. The analysis of the tensile data of the irradiated material is underway and will be compared with the tungsten-copper laminate composite data.

4.8 HIGH-HEAT FLUX TESTING OF LOW-LEVEL IRRADIATED MATERIALS USING PLASMA ARC LAMPS

—A.S. Sabau, Y. Katoh (Oak Ridge National Laboratory) and K. Ibano (Osaka University)

OBJECTIVE

The objective of this work, part of the US-Japan PHENIX collaboration, is testing of irradiated materials that are candidate divertor component materials and mock-up divertor components under high-heat flux using Plasma Arc Lamps (PAL).

SUMMARY

A review was conducted of relevant physical phenomena that take place during high-heat flux testing (HHFT) in order to identify areas of concentration in the ORNL program for materials characterization. Planning of activities for handling the irradiated specimens in FY17 was started in order to ensure a close coordination between the multidisciplinary efforts needed for a comprehensive material science study of irradiated effects during HHFT. Temperature-dependent physical and mechanical properties for the SiC were obtained for use as input in the numerical simulations of the HHFT to reveal insight on the temperature and stress conditions for the four W/SiC specimens. The setup of thermo-mechanical model simulations for the high-heat flux testing of W/SiC specimens was completed.

PROGRESS AND STATUS

Effort was conducted in three main areas: (a) planning of activities for handling the irradiated specimens in FY17, (b) analysis of data acquired during HHFT of four W-SiC specimens, and (c) development of a simplified thermo-mechanical model in ABAQUS for the simulation of the state of stress and deformation during HHFT.

Planning of activities for handling the irradiated specimens in FY17 was started. A review was conducted on relevant physical phenomena that take place during HHFT in order to identify areas of concentration for specimen characterization. Based on this review, the following physical phenomena will be considered for understanding irradiation effects during HHFT of W-based materials:

1. Time to anneal irradiation defects.
2. Thermal conductivity degradation.
3. Change in mechanical properties.
4. Change in microstructure.
5. Defect evolution during HHFT.

Basic materials property information and constitutive equations for materials behavior in the harsh fusion environment will be provided based on materials science investigations. The tasks, which are needed for this materials science study, were identified to be the following:

1. Understand the temperature distribution in the specimen during HHFT.

    a. Assess accuracy of using thermocouples on the back surface of the specimen for temperature measurement.
    b. Model the temperature distribution in the specimen during HHF.

2. Understand the state of stress within the specimen.

    a. Model the specimen deformation, plastic deformation, and build-up of residual stresses during HHFT.

3. Microstructural characterization (before/after HHFT).

   a. Surface SEM.
   b. Profilometry (ORNL).

4. Defect characterization (before/after HHFT).

   a. STEM imaging.
   b. TEM imaging.
   c. Large-area high-speed STEM-X-ray mapping.

5. Property measurement (before/after HHFT).

   a. Thermal conductivity.
   b. Micro-hardness.

Fixtures which were required to clamp the specimens directly on Cu cooling module were fabricated for the PHENIX program at ORNL (Table 2).

Table 1. Clamping holders fabricated for the PHENIX project at ORNL

Sample Diameter [mm]	Sample Thickness [mm]	Clamp Material	Fabrication
10	3	Ta10W	ORNL
10	3	Ta	PHENIX/Japan
10	2	Ta10W	ORNL
10	1	Ta10W	ORNL
6	2	Ta10W	ORNL
6	1	Ta10W	ORNL

Data acquired during HHFT of W/SiC specimens (Table 1) at ORNL was analyzed. The main variables in the high-heat flux testing were the number of cycles at high heat flux and average cycle duration (Table 1). Figure 1 shows micrographs of taken from edge of the specimen S1, indicating irregular surface morphology of the SiC surface.

Table 2. Main variables for high-heat flux testing of W/SiC specimens 10 mm in diameter (SiC thickness was 1mm), PHENIX program specimens

No.	W thickness [mm]	[1]No. Cycles	[1]Average cycle time [s]	Cycle duration [s]	Max. Heat Flux [W/cm^2]	Average Heat Flux [W/cm^2]	Total heat input [MJ/cm^2]	Total time at high-heat flux [s]	Notes
1	2	122	11.1	10-15	288	264	0.361	1,356	edge melting
2	2	100	10.9	5-15	300	274	0.301	1,094	
3	1	101	11.3	10-15	288	272	0.311	1,146	edge melting
4	1	127	13	10-18	288	273	0.498	1,664	

[1] Number of cycles at heat fluxes above 210 W/cm^2 .

The setup of thermo-mechanical model simulations for the high-heat flux testing of W/SiC specimens was completed. Temperature-dependent physical and mechanical properties for the SiC were obtained for use as input in the numerical simulations of the HHFT to reveal insight on the temperature and stress conditions for the four W/SiC specimens. Numerical simulations of the HHFT will be conducted to reveal insight on the state of stress that may have lead to the surface cracking for the melting observed in the 1-st and 3-rd W/SiC specimen.

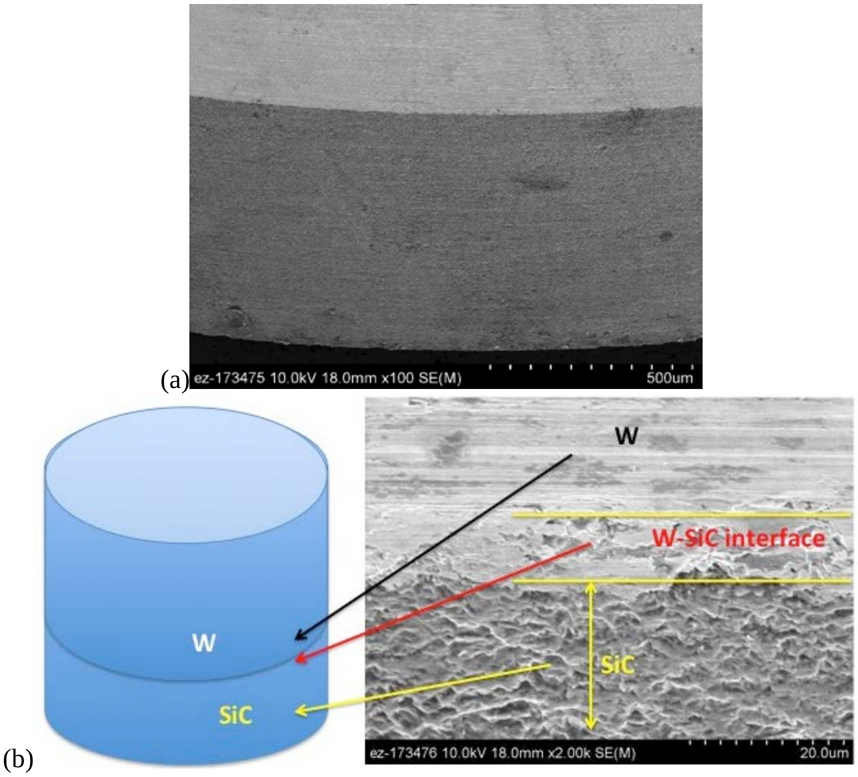

Figure 1. SEM micrographs for specimen S1 taken around the circumference: (a) low magnification, and (b) high magnification showing surface irregularities on the circumference of the SiC surface. The specimen was tilted 39^o.

5. MAGNETIC AND DIAGNOSTIC SYSTEM MATERIALS

No contributions this reporting period.

6. FUSION CORROSION AND COMPATIBILITY SCIENCE

6.1 COMPATIBILITY OF FeCrAl IN FLOWING Pb-LI AT 550°-600°C– B. A. Pint and S. J. Pawel (Oak Ridge National Laboratory, USA)

OBJECTIVE

This task is investigating the possibility of increasing the Pb-Li temperature in the dual coolant lead-lithium (DCLL) blanket concept in order to improve the overall system efficiency. Alloys based on FeCrAl are a potential candidate and monometallic thermal convection loops of a commercial FeCrAl alloy are being built and operated to establish a maximum operating temperature for operation in flowing eutectic Pb-Li.

SUMMARY

The second monometallic thermal convection loop (TCL) using Kathal FeCrAlMo alloy APMT tubing and specimens has completed 1000 h in commercial purity eutectic Pb-Li with a peak temperature of 600°C. After cleaning, the mass change data showed small mass losses for all of the specimens preoxidized at 1000°-1100°C to form an alumina scale prior to exposure in the loop. Larger mass losses were noted for specimens that were not pre-oxidized, especially at the lower temperatures. Characterization of the specimens is in progress.

PROGRESS AND STATUS

Introduction

The DCLL blanket concept (eutectic Pb-17 at.%Li and He coolants) is the leading U.S. design for a test blanket module (TBM) for ITER and for a DEMO-type fusion reactor.[1] With reduced activation ferritic-martensitic (FM) steel as the structural material, the DCLL is limited to ~475°C metal temperature because Fe and Cr readily dissolve in Pb-Li above 500°C and Eurofer 97 plugged a Pb-Li loop at 550°C.[2-3] With the addition of Al to Fe-Cr alloys, isothermal compatibility tests have shown low mass losses at up to 800°C [4-7]. Thermodynamic evaluations [8,9] indicated that Al_2O_3 should be stable in Pb-Li and inhibit dissolution by forming at the alloy surface, however, capsule studies found that a preformed α-Al_2O_3 surface layer transformed to $LiAlO_2$ during exposures at 600°-800°C [4,10]. To further evaluate the Pb-Li compatibility of FeCrAl-type, exposures in flowing Pb-Li are needed where changes in solubility with temperature can drive mass transfer [2,11]. In 2014, a monometallic thermal convection loop (TCL) was operated for 1000 h with a peak temperature of 550°C using commercial Fe-21Cr-5Al-3Mo alloy (Kanthal APMT) tubing and specimens in the hot and cold legs [12-15]. This was the first time that Pb-Li was flowed at 550°C without plugging flow and only small mass losses were noted after the exposure. The next step in the compatibility evaluation was to operate a similar TCL with a peak temperature of 600°C.

Experimental Procedure

The details of the TCL construction and operation have been previously described in detail [12-14]. The TCL was ~1 m tall and 0.5 m wide and heated on one side by resistively heated furnaces (i.e. the hot leg). The loop contained two specimen chains of 20 SS-3 type APMT specimens connected with APMT wire. One in the hot leg and one in the cold leg. Most of the specimens were heated treated for 8 h at 1050°C in air to form an α-Al_2O_3 surface layer or scale. Two specimens in each chain had no pre-oxidation treatment, preoxidation at 1000°C and preoxidation at 1100°C. Rectangular coupons of unalloyed tungsten were attached at the bottom of each specimen chain to act as a “sinker” to keep the relatively low density specimen chains from floating in the Pb-Li test fluid, and to act as “spacers” to keep the specimen chain centered within the tubing and liquid metal flow path.

Commercial purity Pb-17Li was used with impurity levels of 1200ppmw O, 240 ppmw C and <10 ppmw N (average of 6 samples) and no metallic impurities above the detection limite of ~1 ppmw. The Pb-Li was melted in the fill tank above the hot leg and the loop was evacuated prior to filling. The TCL contained six thermowells that protruded about 0.3 cm into the flow path to monitor temperature at the top, bottom and middle of each leg. The flow rate within the loop was estimated by heating a section of the tubing using a gas torch for ~15 s and then tracking the temperature spike as that heated liquid move around the loop. Following 1000 h of operation at 600°C, the Pb-Li was drained into the dump tank.at the bottom of the cold leg. After removal, specimens were soaked in cleaning solution (1:1:1 mixture of ethanol, hydrogen peroxide, and acetic acid) while within the loop (as an assembled chain) and again upon removal from the loop (as individual specimens). The cleaning solution readily dissolved residual Pb-Li rendering weight change measurements more meaningful. Following exposure to the cleaning solution, the specimens were ultrasonically cleaned in acetone followed by air drying prior to remeasuring the mass using a Mettler Toledo model XP205 balance (~0.04 mg accuracy).

Results and Discussion

Figure 1 shows the temperatures measured at the six TCL thermowells after stabilization (minor adjustments to heaters and insulation over the first 24 h or so). After operation for ~440 h, one of the hot leg furnaces failed causing a drop in all temperatures. Unfortunately, during installation of a replacement furnace, it was damaged and could not be used. There was a ~215 h delay, before a new furnace could be purchased and installed where the loop operated at a lower temperature. The experiment was completed with a cumulative 1000 h at the peak temperature of 600°C.

Figure 1 also shows that the typical temperature gradient was ~85°C during this experiment. In the previous 550°C experiment, the temperature gradient was ~115°C. During the previous experiment, the velocity was measured at ~0.4 m/min twice. This value was lower than the 0.8-0.9 m/min observed in similar ORNL sodium loops. In the 600°C TCL experiment, the velocity was measured at 0.6-0.7 m/min, more consistent with the previous work. Both the increased velocity and decreased temperature gradient, support the possibility that the chain may not have been in “single file” orientation that may have inhibited flow in the previous experiment.

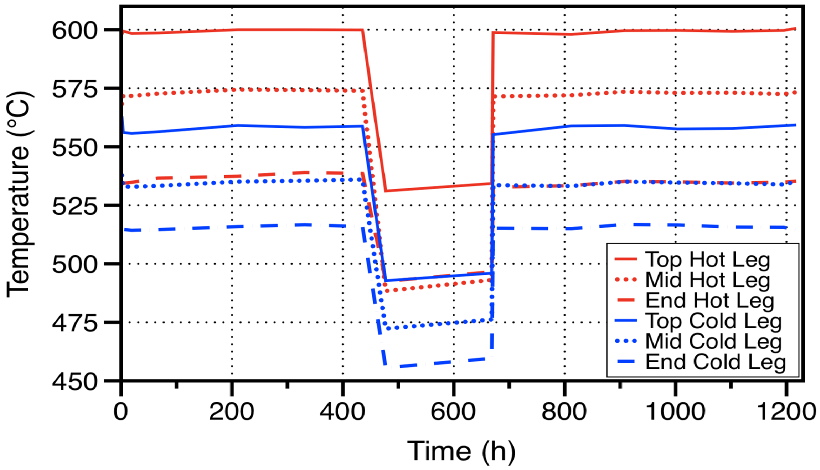

Figure 1. Thermowell temperatures measured during the experiment.

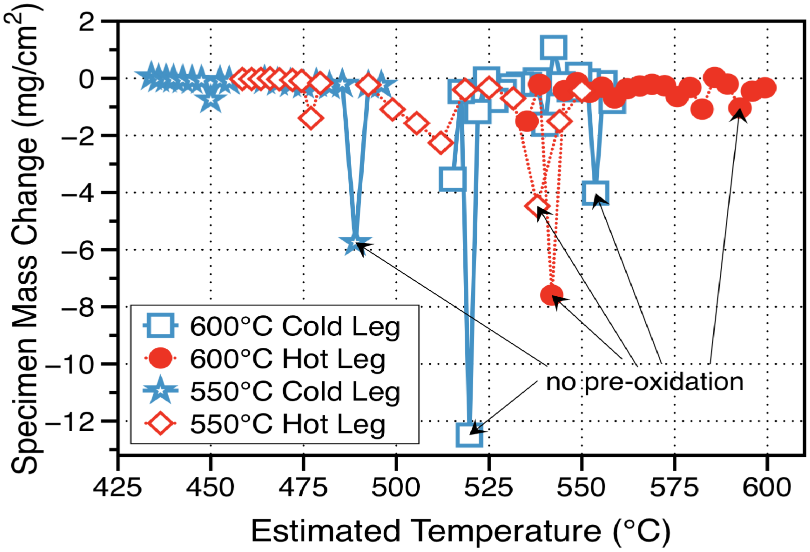

Figure 2. Specimen mass change in the hot and cold legs of the 550° and 600°C TCLs. Specimens that were not pre-oxidized are noted from both experiments.

Figure 2 shows the mass change data after cleaning for the hot and cold leg specimens from both TCLs as a function of estimated temperature in each chain of specimens. The approximate temperature of each specimen location was estimated by linear extrapolation as a function of position between thermowell locations at which the temperature was known. In the recent experiment, the mass losses were modest for the pre-oxidized specimens and comparable to the previous experiment. Varying the pre-oxidation temperature from 1000°-1100°C showed little effect on the mass loss. As observed previously, the mass losses can partially be attributed to spallation of the oxide layer, which transforms from α-Al_2O_3 to $LiAlO_2$ during the exposure. The largest mass losses were observed for the specimens that were not pre-oxidized prior to exposure. Presumably, faster dissolution occurred prior to the establishment of a protective Al-rich oxide. However, the bare specimen at the top of the hot leg did not show a large mass loss. At the higher temperature (~592°C), the oxide layer may form more quickly as Al is relatively immobile at <600°C. Figure 3 shows plan-view scanning electron microscopy images of the surface oxide morphology. Characterization of the other specimens is in progress followed by room temperature tensile testing.

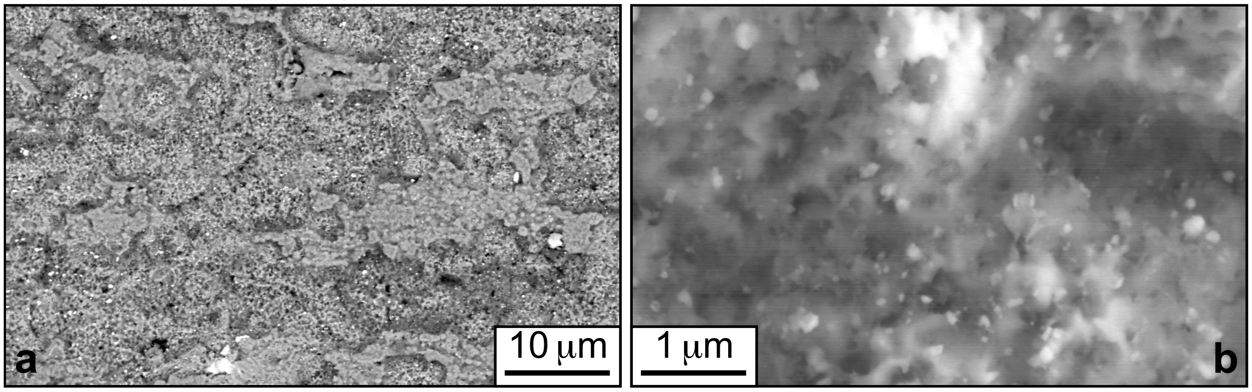

Figure 3. Scanning electron microscopy of the scale formed on an APMT specimen without pre-oxidation after exposure at ~593°C for 1000 h.

References

[1] M. Abdou, D. Sze, C. Wong, M. Sawan, A. Ying, N. B. Morley and S. Malang, Fus. Sci. Tech., 47 (2005) 475.

[2] O. K. Chopra, D. L. Smith, P. F. Tortorelli, J. H. DeVan and D. K. Sze, Fusion Technol., 8 (1985) 1956.

[3] J. Konys, W. Krauss, J. Novotny, H. Steiner, Z. Voss and O. Wedemeyer, J. Nucl. Mater. 386-88 (2009) 678.

[4] B. A. Pint, L. R. Walker and K. A. Unocic, Mater. High Temp. 29 (2012) 129.

[5] K. A. Unocic and B. A. Pint, J. Nucl. Mater. 455 (2014) 330.

[6] B. A. Pint, S. Dryepondt, K. A. Unocic and D. T. Hoelzer, JOM 66 (2014) 2458.

[7] K. A. Unocic, D. T. Hoelzer and B. A. Pint, Mater. High Temp. 32 (2015) 123.

[8] P. Hubberstey, T. Sample and A. Terlain, Fusion Technol., 28 (1995) 1194-9.

[9] P. Hubberstey, J. Nucl. Mater. 247 (1997) 208.

[10] B. A. Pint and K. L. More, J. Nucl. Mater. 376 (2008) 108.

[11] J. H. DeVan, J. Nucl. Mat., 85-86 (1979) 249.

[12] S. J. Pawel, DOE-ER-0313/56 (2014) 178.

[13] S. J. Pawel, DOE-ER-0313/57 (2014) 132.

[14] S. J. Pawel, DOE-ER-0313/58 (2015) 185.

[15] S. J. Pawel and K. A. Unocic, submitted J. Nucl. Mater.

7. MECHANISMS AND ANALYSIS

7.1 QUALITATIVE ANALYSIS OF COMMERCIAL $M_{n+1}AX_n$ PHASES UNDER NEUTRON IRRADIATION

C. Ang*, C. Shih, S.J. Zinkle, C. Silva, C. Parish, N. Cetiner, P. Edmondson, and Y. Katoh (Oak Ridge National Laboratory, USA)

OBJECTIVE

$M_{n+1}AX_n$ (MAX) phases are candidate ceramics for future nuclear applications, due to their potentially unique radiation tolerance and high fracture toughness. The report summarizes the data since DOE/ER-0313/58 and in particular, the data on mechanical feasibility, which has been the focus of the publications released in 2016.

SUMMARY

$M_{n+1}AX_n$ (MAX) phases are ternary nitrides and carbides. The materials studied were purchased from 3-ONE-2, LLC, and were previously characterized (see DOE/ER-0313/58). These were nominally "Ti_3SiC_2" and "Ti_2AlC" compositions irradiated to 2 x 10^{25} n/m^2 (E > 0.1 MeV) or ~ 2 dpa (based on the SiC displacement cross-section). After extensive characterization, weighted compositions were determined to be ~80% MAX phase. Irradiation temperatures were determined by passive dilatometry to have reached ~400, 630 and 700°C. After irradiation at ~400°C, swelling of Ti_3AlC_2-$Ti_5Al_2C_3$ material was 50% higher than Ti_3SiC_2, and this was reflected in the loss of room temperature equibiaxial fracture strength. The Si-containing MAX phase was more radiation resistant than the Al-containing material at lower temperatures. After irradiation at 630°C, electrical, thermal, and mechanical properties were unaffected. Lattice parameter swelling was mitigated at high temperature, but ~0.5-1% volumetric swelling was observed.

PROGRESS AND STATUS

Introduction

The attraction of $M_{n+1}AX_n$ (MAX) phases as engineering ceramics is due to their reversible slip-based deformation mechanism including kinking and delamination.[1] This mitigates catastrophic failure associated with brittle fracture. In these materials, the "A-layer" metal (Al or Si atoms) alternating between crystalline "MX" ceramic (TiC) unit cells results in good machinability, thermal and electrical conductivity. For radiation tolerance, the alternating layers represent a density of nanoscale interfaces that may function as natural sinks for mitigating defect accumulation that is responsible for degradation of materials under irradiation.[2] This seems to be verified by low activation energies for migration for interstitial defects and A-atom vacancies, modeled antisite accommodation of defects and the high energy barrier of migration through MX.[3,4] These layers should prevent growth in the c-axis. Specimens were irradiated at the High Flux Isotope Reactor (HFIR) in 2013 to 2, 6 and 10 dpa. After a delay of 12 months due neutron activation of Ti, investigation of mechanical properties (swelling, elastic modulus, fracture strength), morphology (microcracking, changes in interfaces) and microstructure (irradiation-induced defects, lattice expansion, phase changes) commenced on the ~2 dpa specimens in early 2015. The acquired materials were sufficient for screening of suitable MAX phases.

Experimental Procedures

Details on these experiments have been reported in DOE/ER-0313/55 and /58.

X-ray analysis

X-ray characterization of the compositions included Rietveld analysis of XRD data by GSAS™, TOPAS™ v4.2 and use of CrystalDiffract™ Suite. Crystallite size and strain were calculated by Williamson-Hall method. Both MAX phases have a HCP crystal structure. The Ti_3SiC_2 material was a ceramic composite of Ti_3SiC_2-20TiC-6$TiSi_2$. The morphology of the phases was high-aspect ratio Ti_3SiC_2 and equiaxed TiC grains, with remaining intermetallics wetting the surfaces of the grains, which indicated an excess of C and/or insufficient reaction kinetics (since the residual is ~3:Ti:Si:3C). Nappe et al used material from the same vendor, but a different batch, which suggested a systematic issue.[5-8] The Al-containing MAX phase was carbon depleted and had several other stable phases after sintering, and was calculated to be Ti_3AlC_2-$Ti_5Al_2C_3$ with ~6 wt% Ti_5Al_{11}. Irradiation temperatures were designed for 400, 700 and 1000°C but the latter capsule appeared to undergo axial heat loss, and monitors showed that it did not reach the target temperatures. Dilatometer measurement of CVD SiC passive temperature monitors yielded CTE inflections of defect annealing at ~400, 630 and 700°C for end of cycle temperatures. This mid-value of 630°C was actually serendipitous as it appeared that recovery of lattice parameter swelling occurred between these temperatures.

Swelling

As a previous paper reported, after irradiation at ~400°C the swelling of Ti_3AlC_2-$Ti_5Al_2C_3$ was anisotropic with a change in the c-axis ($\Delta c/c$) of 3% and a change in the a-axis ($\Delta a/a$) of 1% for both Al-phases.[9] Ceramics have low strain to failure, and these values are sufficient to introduce cracks in a ceramic. The volumetric swelling of larger (25 x 1.5 x 2 mm) coupons indicated a 4% increase in volume. Due to this cracking, post-irradiation fracture strength was ~10% of as-received values. At the same irradiation temperature of ~400°C, retained room temperature strength of Ti_3SiC_2 was 66% of as-received values. Figure 1 shows a photograph of the fractured materials; note that the peening depression in (a) indicates almost no compression-tension flexure took place on the outer-ring fulcrums compared to the (b) Ti_3SiC_2 material.

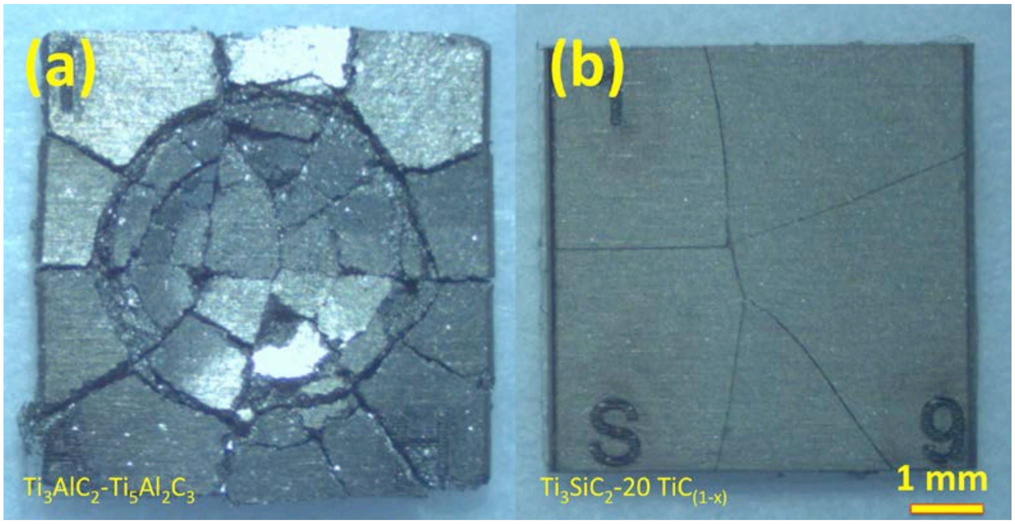

Figure 1. Low temperature irradiated (a) Ti_3AlC_2-$Ti_5Al_2C_3$ and (b) Ti_3SiC_2-20TiC after equibiaxial fracture. The measured strength in (a) was 30 MPa, or less than ~20 N applied force.

The fracture surfaces also indicated that something had occurred to negate the kinking-delamination mechanism. A smaller value of $\Delta c/c$ of 1.5% was observed for Ti_3SiC_2, and minimal a-axis shrinkage. Compared to the Al-containing MAX phase, this showed that defect accumulation was different in either microstructure or physical siting of displaced defects. The measured swelling of only ~0.7% would seem to indicate the absence of swelling from other phases. As expected, lattice parameter swelling was mitigated at high temperature, but volumetric swelling was still observed at ~0.5-1% in both materials.

Properties after irradiation

Electrical resistivity increased by 15x in Ti_3AlC_2-$Ti_5Al_2C_3$ and less than 4x in Ti_3SiC_2, which also suggested Al and Si-layer disruption, and further showed the difference between the two material compositions. Above irradiation temperatures of ~630°C, in both materials, electrical, thermal, elastic modulus and strength were unchanged compared to as-received values. Thermal diffusivity data showed that recovery of the defects responsible for thermal conduction returned more abruptly for Al- than the Si-

MAX phase. In summary, it appeared that displacement of A-layer atoms resulted in anisotropic swelling and significant detrimental effects on all desirable properties.

Equibiaxial strength and fracture surfaces

The analysis indicates an abrupt change in fracture strength and fracture surface appearance between ~400 and 630°C. The equibiaxial ring-on-ring fracture strength testing was conducted using multipurpose square coupons (Figure 1) at room temperature according to ASTM C1499. Figure 2 shows the fracture strength from three coupons at each irradiation temperature for Ti_3AlC_2-$Ti_5Al_2C_3$, and it shows an obvious difference caused by temperature. Note that the materials irradiated at ~630-700°C show minor variations, indicating that the phenomenon that affects mechanical properties changes between 400-630°C. The dotted line shows the swelling value at each irradiation temperature.

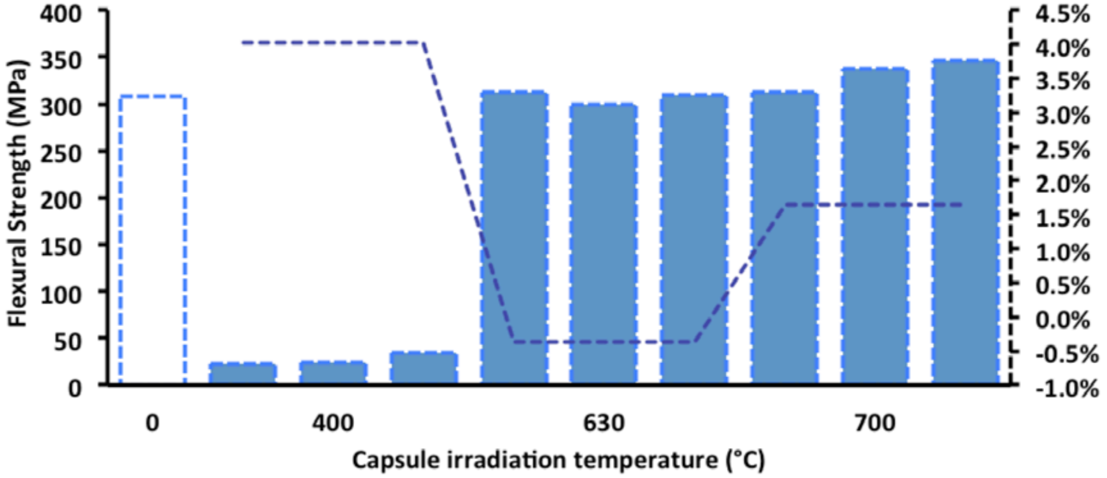

Figure 2. Equibiaxial fracture strength values of Ti_3AlC_2-$Ti_5Al_2C_3$ materials at their respective initial condition and after irradiation at selected temperatures. Swelling is shown by the dotted line from multipurpose bars irradiated in the same capsule.

Figure 3(a) shows a fracture in the unirradiated material, exhibiting a combination of delamination of kink-bands and microcracking. The kink-bands are the parallel striations in the long axis of the grain, which are observed when delamination occurs between these parallel regions. Figures 3(b) and (c) show the difference in the fracture surfaces of the samples irradiated at ~400°C and ~700°C respectively for Ti_3AlC_2-$Ti_5Al_2C_3$ material. In Figure 3(b), flat facets and transgranular cracking progressed through the morphology and explains the low strength values seen in Figure 2(a). Most of the microstructure is dominated by microcracking, shown at lower magnification than the unirradiated case of Figure 3(a). This explains why the depression in the optical micrograph in Figure 1(a) shows the morphology of a powder compact. The microcracks are so large that the samples irradiated at ~400°C had effectively no cohesion.

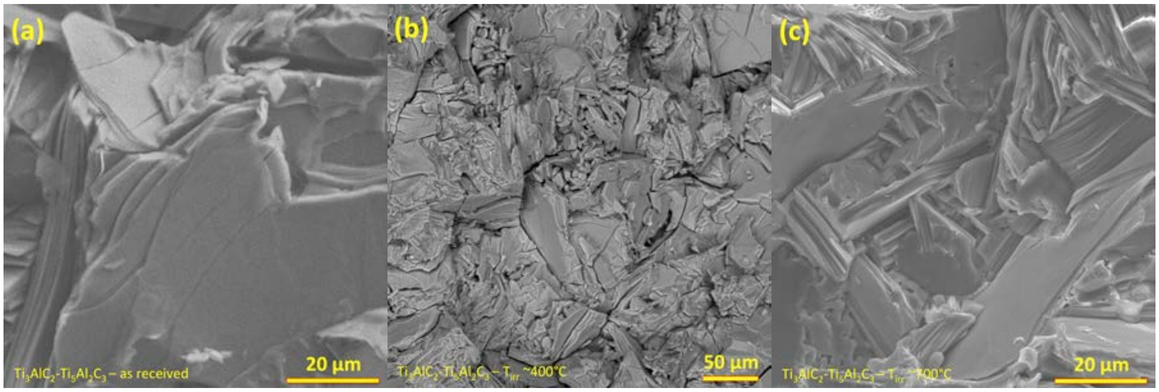

Figure 3. Ti_3AlC_2-$Ti_5Al_2C_3$ fracture surfaces (a) as-received and after being irradiated at (b) ~400°C and (c) ~700°C followed by equibiaxial test.

In Figure 3(c), the kink-bands and smaller facets are clearly obvious and appear to show a normal fracture pattern similar to Figure 3(a). As before, the facets are sub-grain size, show parallel striations with identical morphology to the kink-bands in Figure 3(a). Fracture after irradiation at ~700°C thus expends a significant amount of energy in making kinks unstable. This indicates that there is no change in fracture mechanism, which has been emphasized in recent publications.[10,11]

Results

MAX phases appear to respond under irradiation consistent with behavior of other HCP ceramics, accumulating defects that expand the c-axis. The recovery of the A-atom displacement damage appears to occur at a relatively low temperature of ~500-600°C and is thus responsible for unchanged properties. Fracture surfaces indicate that the kinking-delamination is not operational after irradiation temperatures of ~400°C. Ti_3SiC_2 performs slightly better at these temperatures. Coupled with the substantial lattice parameter and volumetric swelling, this indicates MAX phases are suitable for the higher temperature systems, and is more suitable as a fusion system material rather than for the “lower temperature” fission reactors.. Further data is required. Since the original FOA included ~6 and ~10 dpa specimens, a tentative plan exists to examine these (6 x 6 x 0.5 mm) coupons for (XRD) lattice parameter swelling to confirm saturation, morphology (SEM) and volumetric swelling. Further investigation will continue as resources are available.

Acknowledgements

The authors would like to thank Patricia Tedder, Brian Eckhart, Bill Comings, Ashli Clark, Jordan Couch, Michael McAllister and Felipe Mora for sample preparation and technical support. Particular thanks to Kenny Curtis, Jeremy McKinney and Becky Johnson for contamination control and activated materials handling. This research used equipment at the Low Activation Materials Development and Analysis (LAMDA) and the High Temperature Materials Laboratory (HTML) facility. Research was sponsored by the Office of Fusion Energy Sciences, U.S. Department of Energy, under contract DE-AC05-00OR22725 with UT-Battelle, LLC.

References

[1] M. W. Barsoum, T. Zhen, S. R. Kalidindi, M. Radovic, and A. Murugaiah. "Fully reversible, dislocation-based compressive deformation of Ti3SiC2 to 1 GPa," *Nat Mater,* **2**[2] 107-11 (2003).
[2] S. J. Zinkle and L. L. Snead. "Designing Radiation Resistance in Materials for Fusion Energy," *Annual Review of Materials Research,* **44**[1] 241-67 (2014).

[3] S. Zhao, J. Xue, Y. Wang, and Q. Huang. "Ab initio study of irradiation tolerance for different Mn+1AXn phases: Ti3SiC2 and Ti3AlC2," *J. Appl. Phys.,* **115**[2] 023503 (2014).

[4] S. C. Middleburgh, G. R. Lumpkin, and D. Riley. "Accommodation, Accumulation, and Migration of Defects in Ti3SiC2 and Ti3AlC2 MAX Phases," *J. Am. Ceram. Soc.,* **96**[10] 3196-201 (2013).

[5] J. C. Nappe, P. Grosseau, F. Audubert, B. Guilhot, M. Beauvy, M. Benabdesselam, and I. Monnet. "Damages induced by heavy ions in titanium silicon carbide: Effects of nuclear and electronic interactions at room temperature," *J. Nucl. Mater.,* **385**[2] 304-07 (2009).

[6] J. C. Nappe, C. Maurice, P. Grosseau, F. Audubert, L. Thome, B. Guilhot, M. Beauvy, and M. Benabdesselam. "Microstructural changes induced by low energy heavy ion irradiation in titanium silicon carbide," *J. Eur. Ceram. Soc.,* **31**[8] 1503-11 (2011).

[7] J. C. Nappe, I. Monnet, F. Audubert, P. Grosseau, M. Beauvy, and M. Benabdesselam. "Formation of nanosized hills on Ti_3SiC_2 oxide layer irradiated with swift heavy ions," *Nuclear Instruments & Methods in Physics Research Section B-Beam Interactions with Materials and Atoms,* **270** 36-43 (2012).

[8] J. C. Nappe, I. Monnet, P. Grosseau, F. Audubert, B. Guilhot, M. Beauvy, M. Benabdesselam, and L. Thome. "Structural changes induced by heavy ion irradiation in titanium silicon carbide," *J. Nucl. Mater.,* **409**[1] 53-61 (2011).

[9] C. Ang, C. Silva, C. Shih, T. Koyanagi, Y. Katoh, and S. J. Zinkle. "Anisotropic swelling and microcracking of neutron irradiated Ti3AlC2–Ti5Al2C3 materials," *Scr. Mater.,* **114** 74-78 (2016).

[10] C. Ang, C. Shih, C. Parish, and Y. Katoh. "Microstructure and mechanical properties of neutron irradiated titanium aluminum carbides at elevated temperatures," *submitted to Journal of the European Ceramic Society (July 27)* (2016).

[11] C. Ang, C. Shih, C. Silva, S. J. Zinkle, N. Cetiner, and Y. Katoh. "Phase stability, swelling, morphology and strength of Ti3SiC2–TiC ceramics after low dose neutron irradiation," *accepted Journal of Nuclear Materials (August 7)* (2016).

7.2 DAMAGE MECHANISM INTERACTIONS AT THE PLASMA-MATERIALS INTERFACE (Early Career Award)

—C. M. Parish, K. Wang (Oak Ridge National Laboratory)

OBJECTIVE

This work intends to develop the fundamental scientific basis for modelling and predicting the behavior of helium bubbles in refractory materials, to provide support for the science and engineering of the tokamak plasma-facing-material environment.

SUMMARY

This reporting period has emphasized experimental technique developments as the necessary foundation for all later work, continued collaborations with other institutions, and has begun exploration of defect-defect interactions within plasma-exposed and neutron-irradiated tungsten.

PROGRESS AND STATUS

Introduction

As the choice for the ITER divertor, and present leading candidate for subsequent tokamak systems, tungsten metal is the current focus for high-flux, high-fluence, high-temperature plasma-materials interactions (PMI) studies. Unfortunately, the fundamental scientific basis for explaining observed PMI behaviors (e.g., nanofuzz growth) and predicting long-term behaviors (e.g., PMI response in a nuclear environment) is lacking. In this reporting period, we have examined neutron-irradiated and plasma-exposed tungsten in order to begin building up the understanding and methods for quantitative characterization of defects in these materials.

Experimental Procedure

In this summary, data from several sets of experiments are presented. Transmission Kikuchi diffraction (tKD) was performed in a JEOL 6500F SEM using an EDAX EBSD system, with beam parameters of 20-30 keV, 3-5 nA. TEM and STEM imaging and microanalysis were performed at ORNL LAMDA lab using the FEI Talos F200X instrument.

Results

Neutron-irradiated tungsten

Eventually, in-reactor plasma-facing components (PFCs) or materials will experience high neutron loads. Developing a predictive capability for PMI behavior will require a quantitative analysis of the evolving neutron-irradiated structure. In collaboration with the ORNL PFC team, we performed STEM X-ray spectrum imaging, followed by multivariate statistical analysis (MVSA) datamining, to evaluate the structure of the neutron-irradiated polycrystalline tungsten specimens from the previous HFIR irradiation campaign. Figure 1 shows a typical dataset, in which Re-Os rich precipitates heavily penetrate a W-rich matrix. Re is seen to heavily line the irradiation-induced cavities and the grain boundaries.

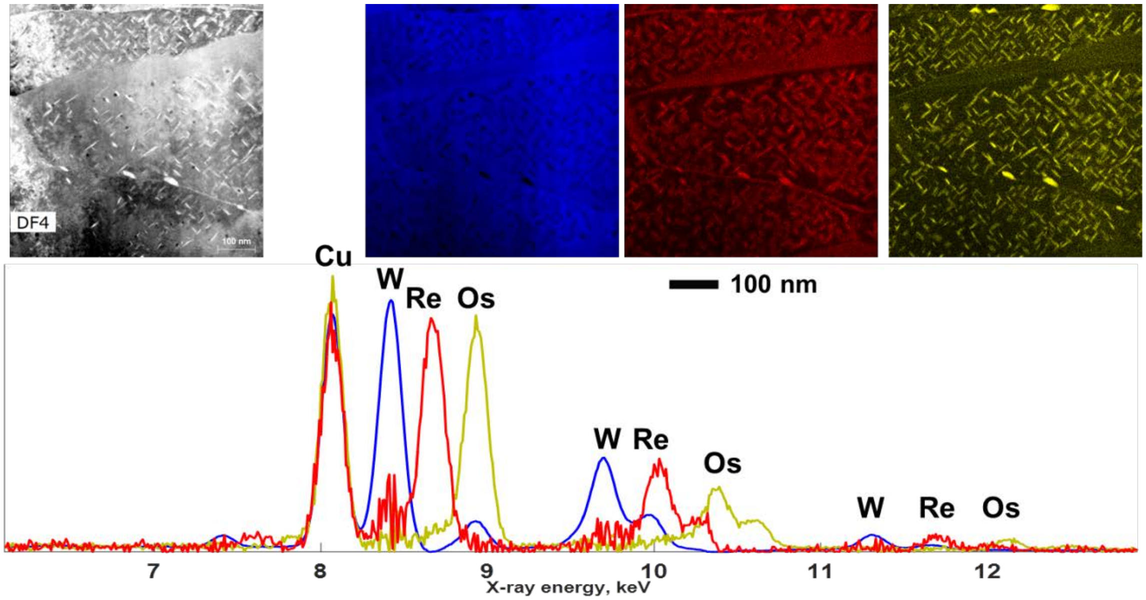

Figure 1. Medium-angle annular dark field ("DF4") image and three MVSA-derived component images. The component spectra are also shown. The W, Re, and Os components are clearly separated by datamining. Cu counts are from the sample holder. ~4 dpa, ~700°C.

Identification of the precipitates is underway. Due to highly overlapping precipitates within the foil thickness and severe irradiation damage, this is not a straightforward analysis. Figure 2 illustrates combined electron diffraction and high-resolution imaging to analyze the precipitate structures.

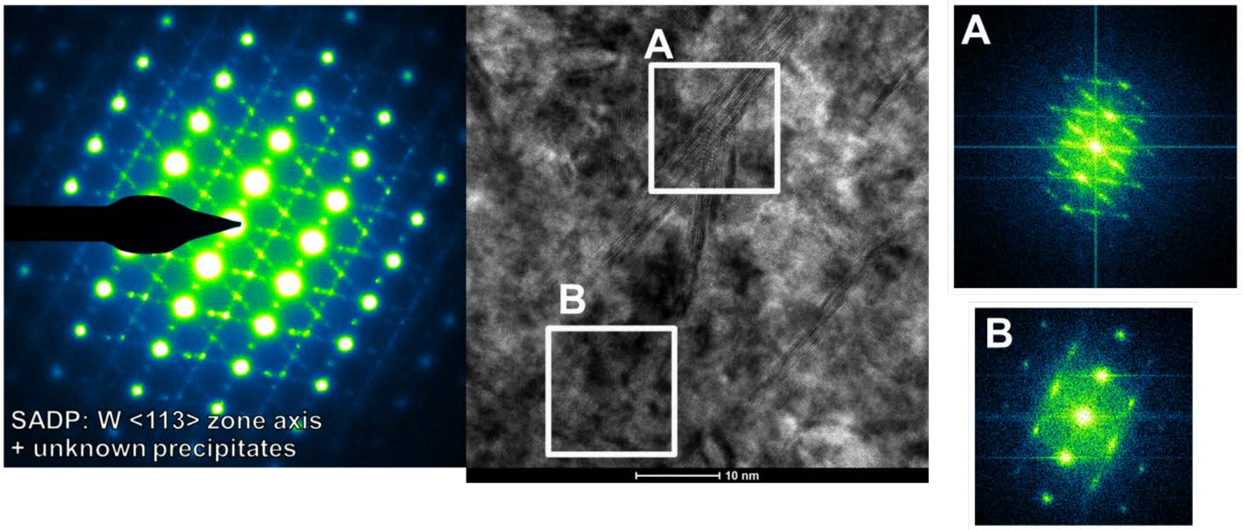

Figure 2. Electron diffraction pattern (left) and high-resolution TEM image (center). The two regions marked A and B have their Fourier transform diffractograms presented on the right. Interestingly, B appears to be matrix but shows superlattice peaks. This is under further exploration.

Several different irradiation conditions have been examined, and work is underway to quantify the microstructures.

Low-energy helium exposure of surfaces

Presently, we are addressing the question of how internal intrinsic defects (dislocations, grain boundaries, etc.) influence the disposition of helium under PMI conditions. We performed a series of helium surface exposures (80 eV, ~10^{20} He/m^2sec, 2 or 20×10^{23} He/m^2, 900°C) on two different conditions of tungsten plate (hot rolled or recrystallized).

Generally, the results indicated little difference in the near-surface regions for the hot-rolled (HR) vs. the recrystallized (RX). However, in terms of penetration of the helium deeper (>100 nm) into the microstructure, the differences became more pronounced. Figure 3 illustrates the TEM-measured bubble structure in the four conditions; note that the first panel of the image denotes relative depths. Bubbles were binned into depths 0-50 nm, 50-100 nm, and >100 nm.

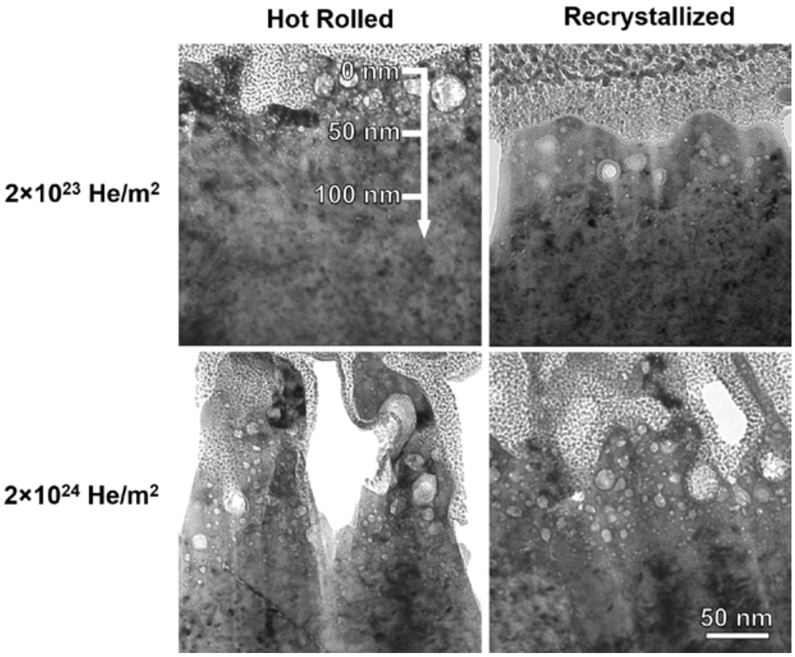

Figure 3. High-magnification TEM images showing the relative effects of microstructure and fluence. Flux ~10^{20} He/m^2sec, E=80 eV, T=900°C.

The differences in the distributions are shown in Figure 4. In short, the bubbles grew with fluence (which is unsurprising) but comparatively little difference was seen between the HR and RX conditions at a given depth and fluence, although at the deepest depth (>100 nm) the RX material did show the most penetration and significantly larger bubbles than in the HR material.

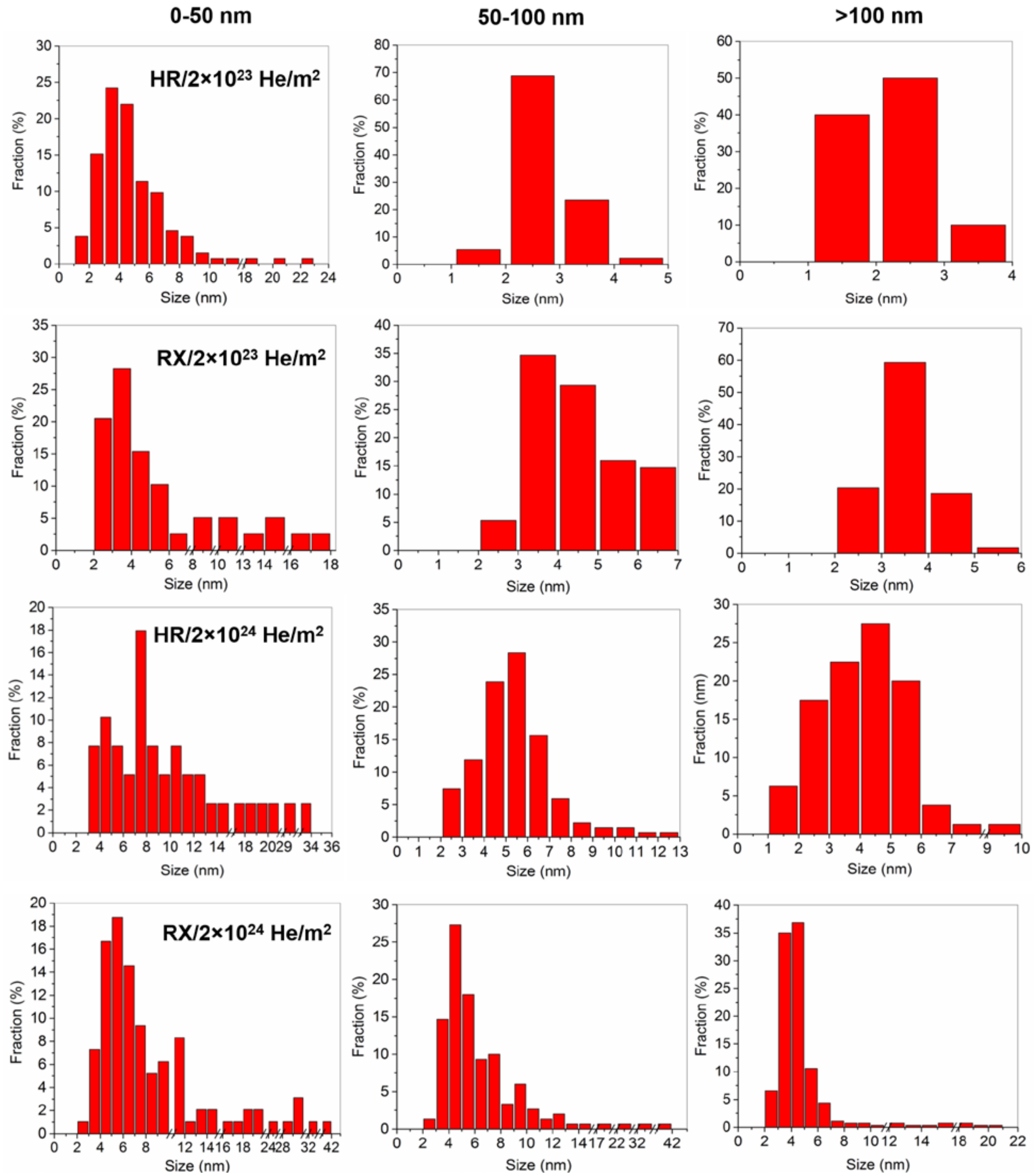

Figure 4. Size distribution of Helium cavities in various depth ranges below surface for all microstructure and fluence conditions.

Further analysis and interpretation is presently underway, but the important point to take away appears to be that at the surface, where helium concentrations will be highest, trap mutation appears to be dominant over heterogeneous nucleation on defects, which implies that materials engineering solutions at the surface to capture injected helium will require very careful consideration.

Analysis of nanotendril "fuzz"

The tKD experiments were performed on both isolated nanofuzz tendrils, and on focused ion beam (FIB) prepared specimens that contained the tendril / fuzz interface. Isolated fuzz mats or islands (Figure 5) contained small grains and many high-angle grain boundaries. Analysis of grain boundary character indicates no strong preference for any given axis/angle pair, but a slight skew toward 60° grain boundaries. Tendril grains with an obvious long axis were analyzed, and the grain long axes were also not found to have any preferred orientation.

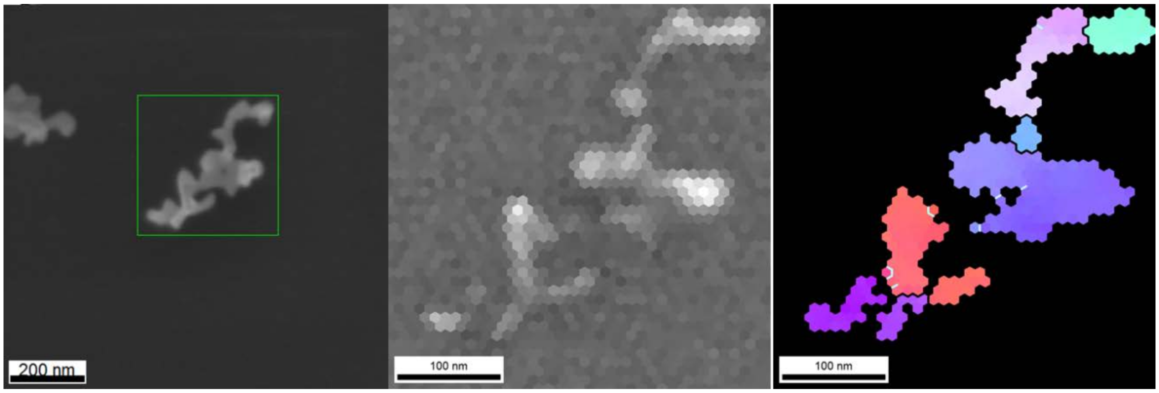

Figure 5. SEM image (left), tKD image quality map (center) and tKD grain orientation map (right) of an isolated nanotendril mat.

Examining the tendril-substrate interface is much more difficult; samples must be prepared via focused ion beam (FIB) which results in some surface damage, and more importantly, there is a slope or shank-angle to the specimens, which changes the intensity of the tKD signal and results in a concomitant baseline shift on the EBSD camera that must be accounted for; this is exacerbated at the edge of a tendril, where thickness changes rapidly. We are presently working on refining the methods, but some preliminary results have been obtained.

Figure 6 illustrates Multicharged Ion Research Facility (MIRF) exposed tungsten (HR material, 900°C, 80 eV, 20×10^{23} He/m^2), with the exact same region examined by tKD (left) and bright field TEM (right). The TEM data clearly indicates that the two tendrils are different grains than the underlying substrate; this is visible by the difference in gray scale from the substrate to the tendrils indicating a different diffracting condition. The tKD results, however, show that the rotation is actually a small angle (<15°) and therefore implies that the tendrils extending from the surface may have grown with a small rotation from the substrate, as opposed to having formed via the nucleation of an entirely new grain.

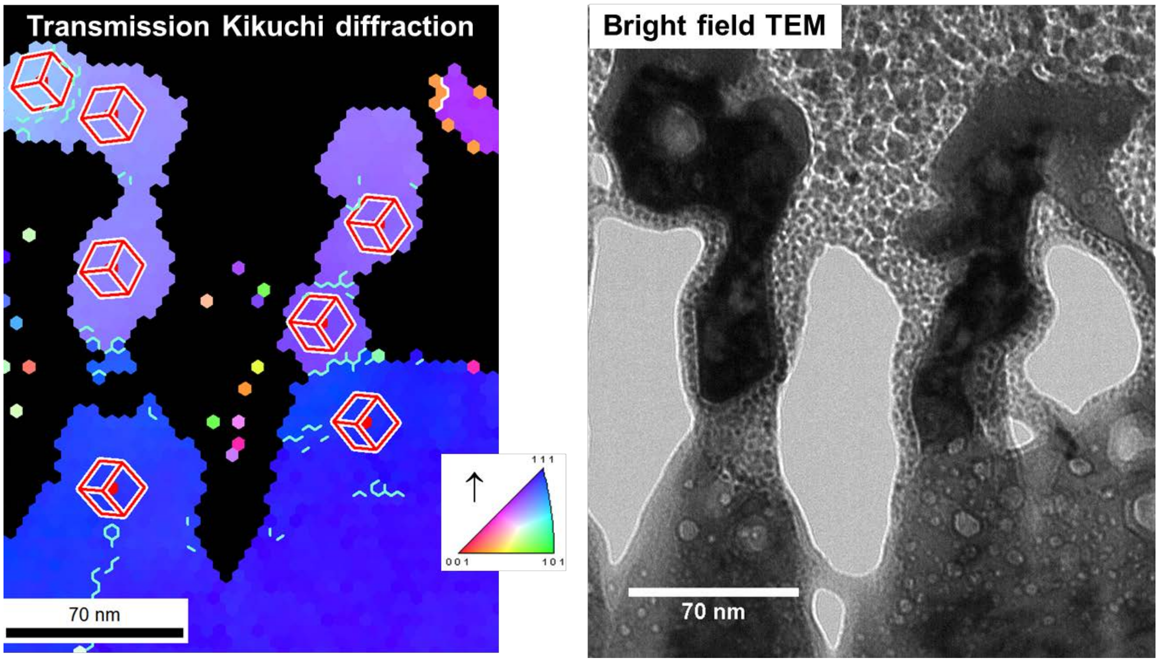

Figure 6. Left, tKD map of fuzz/substrate interface. Coloration is the IPF unit triangle projected on the vertical direction. Inset cubes are the local crystal orientation. Cyan lines are 2-15° low-angle grain boundaries. Right, BF-TEM of the same region.

Summary

We have continued to develop the necessary electron microscopy methods to examine damage mechanisms and interactions between defect types at the plasma-materials interface. We are approaching from both the near-surface plasma interactions and the neutron irradiation effects. Our goals for the next reporting period are to apply these new techniques to begin determining in detail the mechanisms underlying the specimen degradation under plasma exposure.

Acknowledgements

We thank M. Baldwin and R. Doerner, UC-San Diego, and X. Hu, F. W. Meyer and M. E. Bannister, ORNL, for collaborations. Talos F200X STEM instrument provided by the Department of Energy, Office of Nuclear Energy, Fuel Cycle R&D Program and the Nuclear Science User Facilities.

7.3 THERMOMECHANICS OF RESILIENT MICRO-ENGINEERED PLASMA FACING MATERIALS

—David Rivera, Richard Wirz, Nasr M. Ghoniem (University of California, Los Angeles)

Extended abstract of a paper to be submitted to the International Journal of Plasticity in 2016.

The need for reliable high temperature materials to facilitate the development of technologies such as fusion energy, space electric propulsion, and traditional nuclear power has led to the creation of a new materials concept making use of “microarchitected” surfaces to prevent damage due to the accumulation of detrimental plastic strains. Such surfaces are intended to be applied to engineering components in need of thermal protection in the form of a coating and are comprised of refractory metals such as tungsten and rhenium. The focus of this study is a tungsten – rhenium coating system made up of Re micro-pillars (approximately 20-25 microns in height with a diameter of 4-6 microns) coated with a light layer of W about 0.5 – 1 micron thick, an image of such a surface is shown in Figure 1. These surfaces are capable of withstanding heat fluxes in excess of 20 MW/m^2 through a distinct strain tolerant geometry capable of freely expanding or contracting to accommodate thermal strains as seen in Figure 2.

The effect of an incoming heat flux on micro-engineered surfaces was contrasted with those of conventional planar surfaces through the use of a high heat flux testing facility constructed at UCLA. Both planar and micro-engineered materials were subjected to a battery of pulsed operation high heat flux tests. Pulse duration was 6 s at 16 MW/m^2 intensity for several hundred pulses under cooled conditions. The heat flux is generated by a commercial plasma gun of arc-jet configuration. Samples are mounted using a special holder which provides cooling to the specimens while they are exposed to the plasma. This configuration prevents excessive heat buildup and premature melting or failure of the sample. During pulsing, compressive thermal stresses are generated at the sample center as a result of the constrained nature of the set-up, an illustration of the plasma beam striking the sample surface can been seen in Figure 3. This combination of high stress and high temperature leads to plastic flow as the yield stress of tungsten rapidly decreases with increasing temperature. Characterization of the exposed samples was conducted through tools such as X-ray diffraction and scanning electron microscopy.

As a result of testing, planar materials were shown to have experienced a recrystallization of their microstructure as was evidenced by the appearance of new X-ray diffraction (XRD) peaks not present in the initial unexposed profile as seen in Figure 4. Such microstructural reorganization of the material has been proven to lead to embrittlement and should be avoided [1]. In addition, analysis of the effects of heat flux on XRD peak breadth (a qualitative measure of the plastic distortion) determines that planar surfaces suffer from large plastic strains which invariably lead to fracture of the material as a result of residual stress build-up. In contrast, micro-engineered surfaces are able resist plastic distortion relative to planar surfaces as is evident from a comparison of the XRD peak broadening data as seen in Figure 5. This figure shows the decreased trend in plastic distortion as a function of accumulated energy density (no.pulses x pulse duration x pulse intensity) for micro-engineered surfaces when compared to planar material. When more quantitative XRD measures of stress are employed such as the sin^2psi method, micro-engineered material again demonstrates a marked reduction in levels of residual stress marking it as an ideal candidate for thermal protection systems. The increase in resilience when exposed to high heat flux stems from a combination of ideal material geometry (free expansion of pillars) and suitable choice of starting materials (W-Re). The W-Re alloy system has proven to be among the best choices available for elevated temperature applications [2] possessing improved ductility and flow strength over pure tungsten. The micro-engineered approach harnesses both these characteristics to pave the way towards new materials capable of safer more reliable operation of future technologies.

References

[1] Babak, A. V. "Effect of recrystallization on the fracture toughness of tungsten." *Powder Metallurgy and Metal Ceramics* 22.4 (1983): 316-318.

[2] Raffo, Peter L. "Yielding and fracture in tungsten and tungsten-rhenium alloys." *Journal of the Less Common Metals* 17.2 (1969): 133-149.

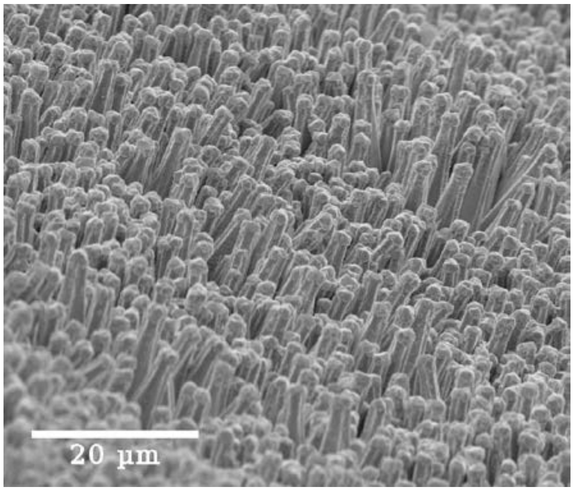

Figure 1. Micro-engineered surface consisting of W coated Re pillars.

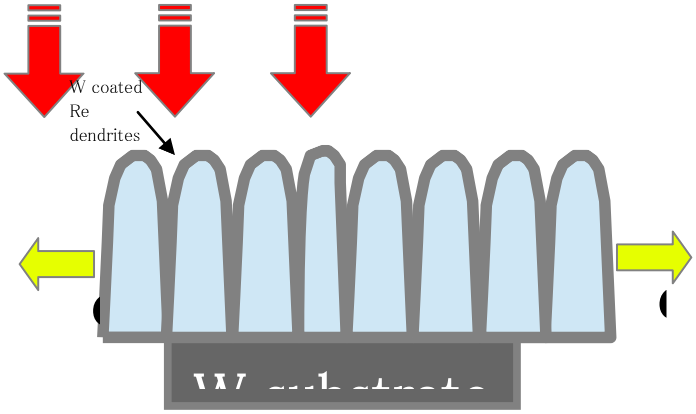

Figure 2. As a heat flux impinges on the surface pillars are able to freely expand or contract thus accommodating thermal strain and relieving stress.

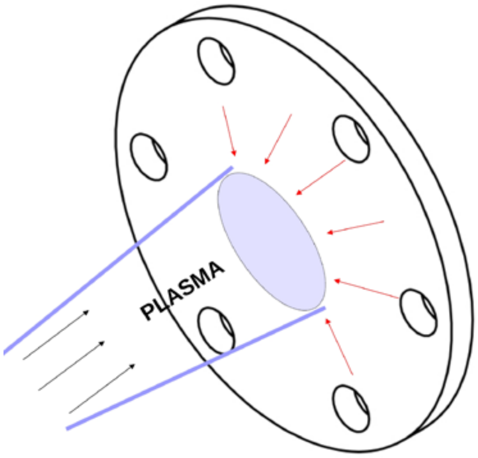

Figure 3. Illustration of a sample being struck by the plasma column during an experimental run, the small diameter of the beam relative to the sample size generates compressive stress as the hot central region of the sample is confined by the cooler unexposed material culminating in the generation of large compressive stresses at sample center.

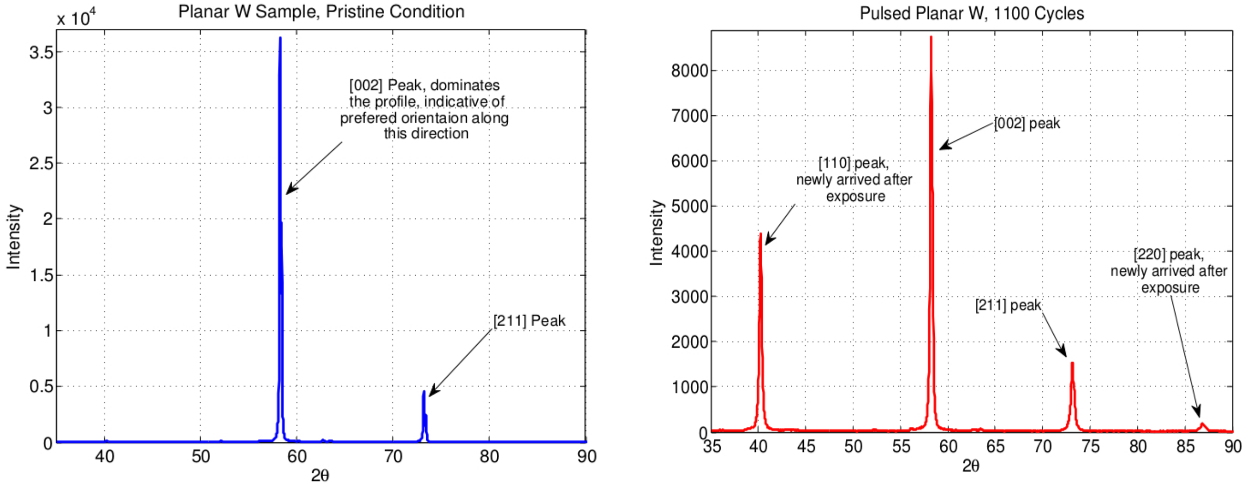

Figure 4. XRD patterns for unexposed (left) and exposed (right) planar W, emergence of new diffraction peaks in the exposed case is a result of the recrystallization of the microstructure, this type of microstructural change has been shown to lead to embrittlement of the material.

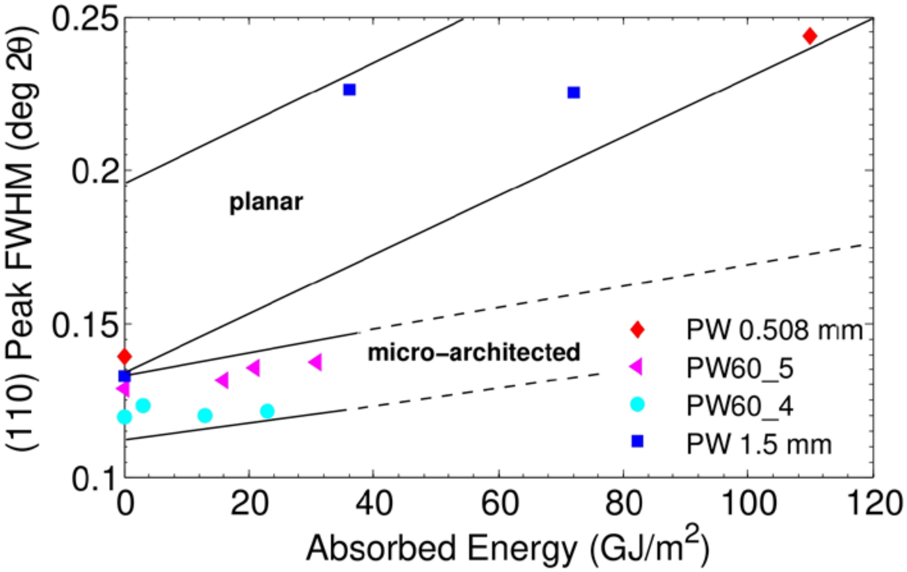

Figure 5. Peak breadth vs absorbed energy comparison between micro-engineered and planar surfaces, peak breadth can be interpreted as a qualitative measure of the level of plastic strain a material has endured, from the chart it is evident that micro-engineered surfaces exhibit less plastic deformation than their planar counterparts.

7.4 A VARIATIONAL FORMULATION OF THE VOLTERRA DISLOCATION RECONSTRUCTION OF 3-D MOVING CRACKS

—A. Sheng, G. Po, N.M. Ghoniem (University of California, Los Angeles)

OJBECTIVE

The evolution equations governing a Volterra dislocation-based reconstruction of moving 3-D cracks are formulated using a variational approach based on the Principal of Maximum Entropy Production rate (PMEP).

SUMMARY

Modeling crack growth in three-dimensional geometries poses a challenging problem especially for FEM-based techniques such as EFEM or XFEM, which display some degree of mesh dependence. Additionally, existing methods are unable to investigate the interaction between cracks and other defects present in real materials. An alternative method developed in the framework of discrete Dislocation Dynamics is presented which provides a solution to these challenges by being completely mesh-independent and capable of coupling cracking with crystal plasticity. The Discrete Crack Mechanics method is a dislocation-based fracture mechanics technique that represents cracks using arrays of Volterra dislocations. In this report, a variational formulation based on the Principle of Maximum Entropy Production rate is given of the evolution equations for cracks coupled with crystal dislocations along with examples of its implementation.

PROGRESS AND STATUS

Introduction

The resemblance between the elastic fields of cracks and dislocation arrays has long been recognized and is the foundation for the Discrete Crack Mechanics (DCM) method outlined in this report [1, 2]. In DCM, cracks are represented by arrays of discrete Volterra dislocations that are henceforth referred to as crack dislocations in order to distinguish them from crystal dislocations. DCM is an extension of the discrete Dislocation Dynamics (DD) method originally developed to investigate the evolution of crystal dislocation patterns [3, 4, 5]. In DD, dislocations are represented by parametric space curves and their interactions in 3-D are completely resolved. In DCM, crack dislocations are represented in the same manner allowing us to not only model cracks with complex shapes but also capture interactions between multiple cracks as well as between cracks and crystal dislocations.

Crack propagation occurs when the J-integral, or equivalently, the stress intensity factor *K* of a crack exceeds a critical value unique to the material. The J-integral, which can be shown to be equivalent to the unbalanced PK force on the leading dislocation in DCM, is what drives the motion of the crack tip. In this report, we present a variational formulation of the evolution equations for a system containing cracks as well as crystal dislocations. This approach utilizes the Principal of Maximum Entropy Production Rate (PMEP) to find the equations governing the motion of cracks and crystal dislocations, which are considered irreversible fluxes contributing to the internal entropy production of the system.

Dislocation-Based Fracture Mechanics

A loaded crack is completely described by a distribution of crack dislocation loops with suitable Burger's vectors ***b***. The crack tip loop, or leading dislocation, is fixed and determines the size and shape of the crack. Enclosed by this loop is a series of additional loops referred to as trailing dislocations which, as a result of the applied load, their mutual interactions, and their interactions with the crack-tip loop, experience a configurational force known as the Peach-Koehler (PK) force. When tractions are applied to an elastic body, forces cannot be transferred across crack surfaces, which remain traction-free. This condition is satisfied when the PK forces on the trailing crack dislocations are balanced. The leading dislocation however, experiences an unbalanced PK force that drives crack growth if the corresponding *K* exceeds the fracture toughness of the material K_C. The equations governing the motion of crack tips and crystal dislocations are derived in the following section.

Quasi-Static Crack Motion

The Principal of Maximum Rate of Entropy Production, or PMEP, states that generalized fluxes in an evolving system maximize the internal entropy production rate. In continuum mechanics, the expression of the second law of thermodynamics is referred to as the Clausius-Duhem statement [5]. For a body Ω with no sources of internal entropy production other than cracks and crystal dislocations, the Clausius-Duhem statement is given by:

$$-\rho_0\dot{\psi} + \sigma_{kj}v_{j,k} = \theta\pi \ \geq 0 \tag{1}$$

where ρ_0 is the mass density per unit volume, ψ the Helmholtz free energy density, σ_{jk} the Cauchy stress tensor, $v_{j,k}$ the distortion rate, θ the absolute temperature, and π the rate of internal entropy production. The distortion rate may be written in terms of the elastic distortion tensor β_{ij}^E, the plastic distortion tensor β_{ij}^P, and the crack distortion tensor β_{ij}^C by:

$$v_{i,j} = \dot{\beta}_{ij}^E + \dot{\beta}_{ij}^P + \dot{\beta}_{ij}^C \tag{2}$$

The plastic distortion tensor is given by [6]:

$$\beta_{ij}^P = \int_{S^P} b_i^P \delta(\boldsymbol{x} - \boldsymbol{x}')da_j' \tag{3}$$

where $S^P$the surface is bounded by the crystal dislocation loop and b_i^p is the crystal dislocation Burger's vector. Similarly, the crack distortion tensor is given by:

$$\beta_{ij}^C = \int_{S^C} b_i^C(\boldsymbol{x}')\delta(\boldsymbol{x} - \boldsymbol{x}')da_j' \tag{4}$$

where $S^C$the surface is bounded by the crack tip dislocation loop and $b_i^C(\boldsymbol{x}')$ is the crack dislocation Burger's vector, which is a function of the position $\boldsymbol{x}'$ on the crack plane. If the Helmholtz free energy density ψ is taken to be of the form:

$$\psi \equiv \psi(\boldsymbol{\beta^E}, \boldsymbol{\beta^P}) \tag{5}$$

then its material time derivative is given by:

$$\dot{\psi} = \frac{\partial\psi}{\partial\beta_{ij}^E}\dot{\beta}_{ij}^E + \frac{\partial\psi}{\partial\beta_{ij}^P}\dot{\beta}_{ij}^P \tag{6}$$

Substituting equations 2 and 6 into equation 1 and combining like terms gives:

$$\left(-\rho_0\frac{\partial\psi}{\partial\beta_{ij}^E} + \sigma_{ij}\right)\dot{\beta}_{ij}^E + \left(-\rho_0\frac{\partial\psi}{\partial\beta_{ij}^P} + \sigma_{ij}\right)\dot{\beta}_{ij}^P + \sigma_{ij}\dot{\beta}_{ij}^C = \theta\pi \geq 0 \tag{7}$$

Since elastic deformation is recoverable, it does not contribute to the internal entropy production rate and thus the first term in equation 7 gives the constitutive relation:

$$\sigma_{ij} = \rho_0\frac{\partial\psi}{\partial\beta_{ij}^E}\bigg|_{\beta^P} \tag{8}$$

In the second term is a stress-like quantity, $\tau_{ij} = \rho_0 \frac{\partial \psi}{\partial \beta_{ij}^P}$, represents a change in the lattice energy due to a change in local plastic deformation. Using this definition, the Clausius-Duhem statement may be rewritten as the products of generalized forces and fluxes:

$$\frac{1}{\theta}\left(\sigma_{ij} - \tau_{ij}\right)\dot{\beta}_{ij}^P + \frac{\sigma_{ij}}{\theta}\dot{\beta}_{ij}^C = \pi \geq 0 \qquad (9)$$

For convenience in the followings steps we use the following definition for the L.H.S. of equation (9), which contains all of the contributions to the internal entropy production rate:

$$\varphi \equiv \frac{1}{\theta}\left(\sigma_{ij} - \tau_{ij}\right)\dot{\beta}_{ij}^P + \frac{\sigma_{ij}}{\theta}\dot{\beta}_{ij}^C \qquad (10)$$

While equation 9 constrains π to be the product of the generalized forces and fluxes, alone it is insufficient for determining the evolution equations for the system. To obtain the evolution equations, we must combine PMEP and equation 10 to formulate a constrained functional for π using the method of Lagrange multipliers:

$$\Pi = \int_{\Omega} [\pi + \lambda(\pi - \varphi)]\, dV \qquad (11)$$

It can be shown that the value of the Lagrange multiplier λ is determined by $\lambda = n/(1-n)$ where n is the order of π in the generalized fluxes. Taking π to be a quadratic functional of the irreversible general fluxes $\boldsymbol{w}^{\boldsymbol{P}}$ and $\boldsymbol{w}^{\boldsymbol{C}}$, which are the dislocation velocity and crack tip velocity respectively, one obtains:

$$\pi[\boldsymbol{w}^{\boldsymbol{P}}, \boldsymbol{w}^{\boldsymbol{C}}] = \oint_{L^P} \delta(\boldsymbol{x} - \boldsymbol{x}') B_{ij}^P w_i^P w_j^P \, dl' + \oint_{L^C} \delta(\boldsymbol{x} - \boldsymbol{x}') B_{ij}^C w_i^C w_j^C \, dl' \qquad (12)$$

The first term corresponds to the energy dissipated by motion of the dislocation loop L^P, while the second term is associated with the energy dissipated by motion of the crack tip loop L^C during crack growth. Substituting equations 10 and 12 as well as the Lagrange multiplier value $\lambda = -2$ into equation 11 gives:

$$\Pi = \int_{\Omega} \left[\frac{2}{\theta}\left(\sigma_{ij} - \tau_{ij}\right)\dot{\beta}_{ij}^P + \frac{2\sigma_{ij}}{\theta}\dot{\beta}_{ij}^C - \oint_{L^P} \delta(\boldsymbol{x} - \boldsymbol{x}') B_{ij}^P w_i^P w_j^P \, dl' - \oint_{L^C} \delta(\boldsymbol{x} - \boldsymbol{x}') B_{ij}^C w_i^C w_j^C \, dl'\right] dV \qquad (13)$$

Taking the material time derivatives of equations 3 and 4 give the plastic and crack distortion rates to be:

$$\dot{\beta}_{ij}^P = \oint_{L^P} \delta(\boldsymbol{x} - \boldsymbol{x}') b_i^P \epsilon_{jkm} w_k^P \, dl'_m \qquad (14)$$

$$\dot{\beta}_{ij}^C = \oint_{L^C} \delta(\boldsymbol{x} - \boldsymbol{x}') b_i^C(\boldsymbol{x}') \epsilon_{jkm} w_k^C \, dl'_m + \int_{S^C} \dot{b}_i^C(\boldsymbol{x}') \delta(\boldsymbol{x} - \boldsymbol{x}') \, da'_j \qquad (15)$$

Substituting equations 14 and 15 into 13 and utilizing the sifting property of the Dirac δ function, Π may be written as a functional of the irreversible generalized fluxes $\boldsymbol{w}^{\boldsymbol{P}}$, $\boldsymbol{w}^{\boldsymbol{C}}$, and $\dot{\boldsymbol{b}}^C$ which can be thought of as a "crack opening displacement flux":

$$\begin{aligned}\Pi\left[\boldsymbol{w}^{\boldsymbol{P}}, \boldsymbol{w}^{\boldsymbol{C}}, \dot{\boldsymbol{b}}^{\boldsymbol{C}}\right] = \int_{\boldsymbol{S}^{\boldsymbol{C}}} \frac{2\sigma_{ij}}{\theta} \dot{b}_{\boldsymbol{i}}^{\boldsymbol{C}} n_j \, da + \oint_{L^C} \left[\frac{2\sigma_{ij}}{\theta}\left(b_i^C(\boldsymbol{x}') \epsilon_{jkm} w_k^C \hat{\xi}_m\right) - B_{\boldsymbol{ij}}^{\boldsymbol{C}} w_{\boldsymbol{i}}^{\boldsymbol{C}} w_{\boldsymbol{j}}^{\boldsymbol{C}}\right] dl \\ + \oint_{L^P} \left[\frac{2}{\theta}\left(\sigma_{ij} - \tau_{ij}\right) b_i^P \epsilon_{jkm} w_k^P \hat{\xi}_m - B_{ij}^P w_i^P w_j^P\right] dl \qquad (16)\end{aligned}$$

By taking the variation of Π with respect to its arguments and imposing stationarity:

$$\begin{aligned}\delta\Pi = \int_{S^C} \left(\frac{\sigma_{ij}}{\theta} n_j\right) \delta\dot{b}_i^C \, da + \oint_{L^C} \left(\frac{1}{\theta} \epsilon_{ijk} \sigma_{jm} b_m^C \hat{\xi}_k - B_{ij}^C w_j^C\right) \delta w_i^C \, dl \\ + \oint_{L^P} \left[\frac{1}{\theta} \epsilon_{ijk}\left(\sigma_{jm} - \tau_{jm}\right) b_m^P \hat{\xi}_k - B_{ij}^P w_j^P\right] \delta w_i^P \, dl = 0 \qquad (17)\end{aligned}$$

one obtains the equations of motion governing the evolution of the system. From the third term comes the celebrated Peach-Koehler force per unit dislocation length: $\epsilon_{ijk}\sigma_{jm}b_m^p\hat{\xi}_k$ and the lattice force per unit dislocation length: $\epsilon_{ijk}\tau_{jm}b_m^p\hat{\xi}_k$. The first and second terms give the governing equations for crack motion. The first term requires that the crack surface remain traction free, as discussed in the previous section:

$$\sigma_{ij}n_j = 0 \quad \text{on crack surface } S^C \tag{18}$$

The second term indicates that the crack tip velocity is proportional to the unbalanced PK force acting on it, mimicking the motion of a crystal dislocation:

$$\frac{1}{\theta}\epsilon_{ijk}\sigma_{jm}b_m^C\hat{\xi}_k = B_{ij}^C w_j^C \tag{19}$$

Implementation and Examples

The procedure for simulating crack growth is described as follows:

1. A leading dislocation loop corresponding to the shape of the crack is inserted into the body to which a prescribed load or displacement is applied.
2. Trailing dislocation loops are inserted and allowed to equilibrate according to the PK force acting on them.
3. If the *K* calculated along the leading dislocation is found to be below the fracture toughness K_C, the crack is static and the simulation is terminated.
4. If *K* at any segment along the leading crack dislocation exceeds K_C, the loop is advanced according to equation 19.
5. Steps 2-3 are repeated until *K* no longer exceeds K_C or the body is fractured completely.

Three examples in which DCM is used to model crack growth are provided below. The first example shows the growth of a penny-shaped crack in a cylinder to which a constant traction is applied as shown in Figure 1a. The second example is the growth of a penny-shaped crack in a cylinder to which a fixed displacement is applied as shown in Figure 1b.

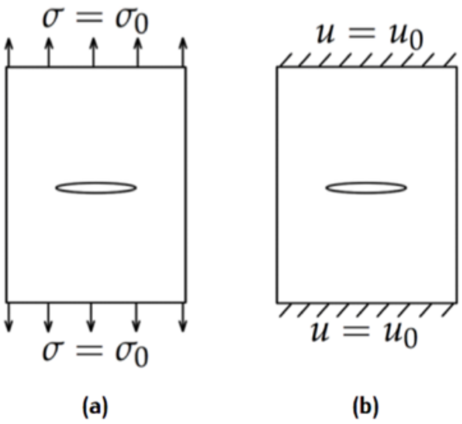

Figure 1. (a) Constant stress “dead-load” loading **(b)** Fixed displacement “fixed-grips” loading.

In the third example, a penny-shaped crack in a rectangular pillar is shown to grow preferentially towards the closest boundaries due to the increased boundary effect. The material used in all three examples has a shear modulus of *G* = 18.5 GPa, a Poisson’s ratio of *v* = 0.27, and a fracture toughness of K_C = 2.5 MPa-m$^{1/2}$.

Crack Growth Under Constant Applied Stress

In this example, a constant traction is applied to the upper and lower surfaces of a cylinder with a height of h = 8 mm and a radius of r_0 = 4 mm. The cylinder contains a penny-shaped crack with an initial radius of r = 400 μm. As shown in Figure 2, the stress intensity factor of the crack increases as the crack propagates.

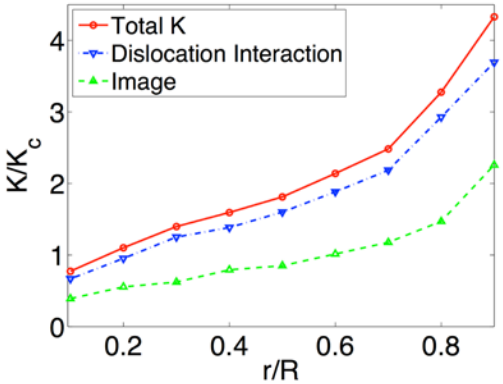

Figure 2. K/K_C vs. r/r_0 curve showing the increase in K/K_C as the crack grows under dead-load conditions.

Crack Growth Under Fixed Displacement

In the second example, a fixed displacement of 10 μm is applied to the upper and lower surfaces of a cylinder with a height of h = 8 mm and a radius of r_0 = 4 mm. A penny-shaped crack with an initial radius of r = 400 μm is placed in the center of the cylinder. Figure 3 shows that the stress intensity factor of the crack increases as the crack propagates but at a lower rate than the crack under a dead load. This is due to the fact that under fixed-grip conditions, the material relaxes and essentially becomes more compliant as the crack grows.

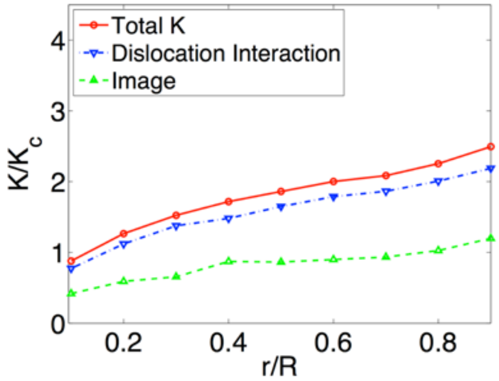

Figure 3. K/K_C vs. r/r_0 curve showing the increase in K/K_C as the crack grows under fixed-grip conditions.

Preferential Crack Growth Due to Boundary Effects

In the third example, a rectangular pillar with a height of h = 4 mm, a width of w = 2.5 mm, and a thickness of t = 1 mm contains a penny-shaped crack at its center with an initial radius of r_0 = 0.25 mm as shown in Figure 4. A constant traction of 155 MPa is applied to the top and bottom surfaces of the pillar.

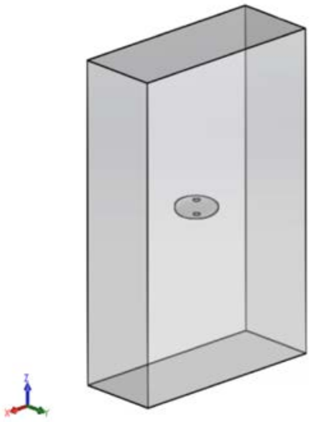

Figure 4. Rectangular pillar with a penny-shaped crack at its center.

The crack edges closest to the free boundaries of the pillar propagate at a faster rate than the edges that are further from the free boundaries as shown in Figure 5. This is because of the fact that the crack edges nearer to the free boundaries experience larger PK forces due to an increased boundary effect. The result is an elongation of the initially circular crack into an elliptical shape as it propagates. Note that the crack opening displacement also increases since more loops are required to achieve an equilibrium configuration as the crack increases in size.

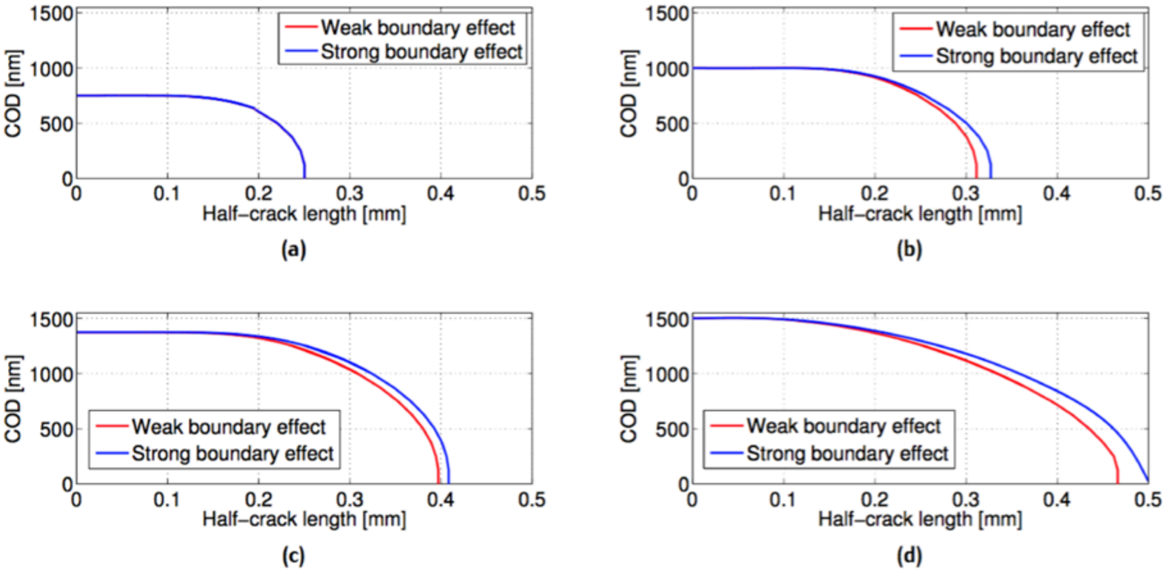

Figure 5. Crack profile along the major and minor axes of the pillar at **(a)** 822 simulation steps, **(b)** 2057 simulation steps, **(c)** 4515 simulation steps, **(d)** 4956 simulation steps (complete fracture).

References

[1] J. D. Eshelby, F. C. Frank, and F. R. N. Nabarro, *The London, Edinburgh, and Dublin Philosophical Magazine and Journal of Science*, **42 (327)** (1951), 351.
[2] J. Weertman, in Dislocation Based Fracture Mechanics, *World Scientific*, 1996, 33.
[3] N. M. Ghoniem and R. J. Amodeo, *Solid State Phenomena* **3&4** (1988)**,** 377-388.
[4] E. van der Giessen and A. Needleman, *Modelling Simul. Mater. Sci. Eng.* **3** (1995), 689.
[5] G. Po and N.M. Ghoniem, *JMPS* **66** (2014), 103.
[6] T. Mura, in Micromechanics of Defects in Solids, *Martinus Nijhoff Publishers*, 1987, 50-53.

7.5 LOADING CONTROLLED TRANSITION OF PLASTIC FLOW FROM DISLOCATION AVALANCHE TO QUASI-PERIODIC STRAIN BURST BEHAVIOR

—Y.N. Cui, G. Po, N.M. Ghoniem (University of California, Los Angeles)

Extended abstract of paper to be submitted for publication.

Numerous studies suggest that collective dislocation dynamics during plastic flow can self-organize to exhibit power law scaling avalanche behavior [1]. Here we demonstrate a dynamical regime transition toward quasi-periodic strain burst when the driving force changing rate is comparable to internal relaxation rate. Through three-dimensional discrete dislocation dynamics we can access different driving force rate of change by tuning system stiffness and directly correlate the measured intermittent plastic events with internal dislocation activities (see Figure 1). When the system stiffness is extremely soft ($\alpha=0$, pure stress control), system response is much slower than the internal relaxation, and the power law scaling avalanche behavior is reproduced (see Figure 2(a)). However, when the system stiffness is extremely high ($\alpha=\infty$, pure stress control), system response rate is comparable to internal relaxation rate, quasi-periodic strain burst is observed (see Figure 2(b)).

Careful analysis of the simulation results reveals that the dislocation mechanisms of avalanches/burst under different loading modes are significantly different. Under pure strain control, the rapid decrease of the driving force (see Figure 3(a)) inhibits the correlated dislocation activity, prevents the strain burst from continuously growing and makes it difficult to self-organize to exhibit scale free power law burst size distribution. Compared with pure strain control, finite system stiffness can promote the correlated dislocation motion. For the case of extremely soft system stiffness, each strain avalanche under pure stress control is induced by the highly correlated motion of dislocations. Multiple dislocation sources are activated correlated and simultaneously. In Figure 3(b), the autocorrelation function r_k of the dissipated energy rate is given to illustrate the apparent contrast correlation extent of dislocation motion under different loading modes.

These results are faithfully reproduced by a simple dislocation-based branching model, including the stepped or serrated burst features, and the power law scaling behavior under pure stress control. Furthermore, the branching model clearly shows as the system stiffness increases, the power law tails gradually becomes too heavy to recognize the power law scaling.

The current research presents the first systematic three-dimensional discrete dislocation dynamics investigation on the statistical properties of dislocation avalanches and strain bursts, accounting for the effects of the interaction with an external loading system. The finding raises new possibility of controlling the correlated extent of dislocation behavior and the dynamical regime transition of avalanche statistic by tuning the interaction with outer system. The importance of often-neglected interaction with outer system on intermittent plastic flow or other complex system has now come to light.

References

[1] D. M. Dimiduk, C. Woodward, R. LeSar, and M. D. Uchic, Scale-free intermittent flow in crystal plasticity, Science, 312 (2006) 1188-1190.

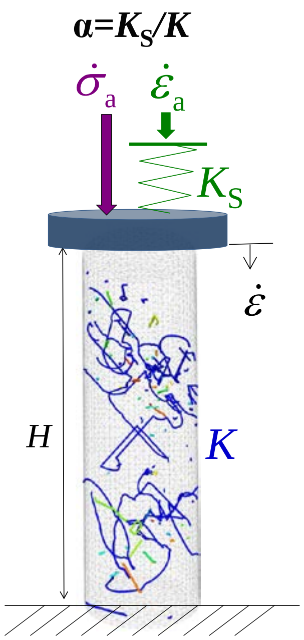

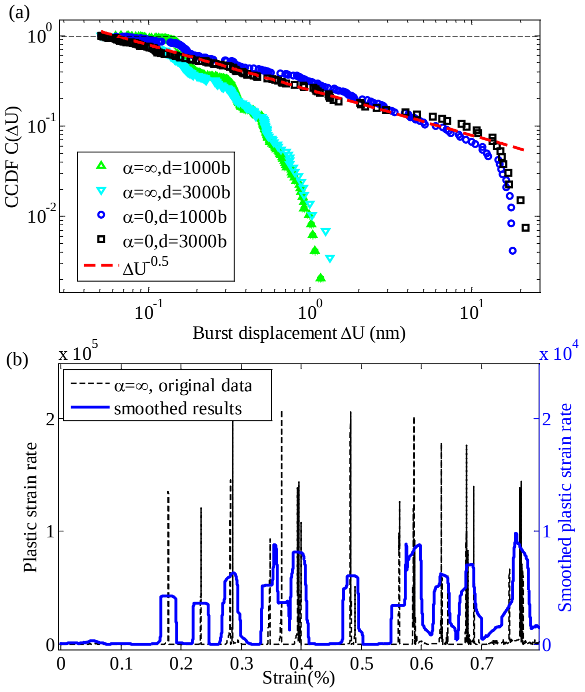

Figure 1. Simplified sketch of pillar compression with an open loop (directly applying some force) and close-loop control (connecting a spring with finite system stiffness K_s). One typical dislocation configuration in pillar with d=3000b is shown as an example.

Figure 2. (a) Statistical properties of burst displacement under pure strain and stress control for pillar with diameter d=1000 b and 3000 b, showing power-law scaling avalanche under pure stress control; (b) Typical result of the evolution of plastic strain rate and its averaged value showing quasi-periodicity strain burst under pure strain control.

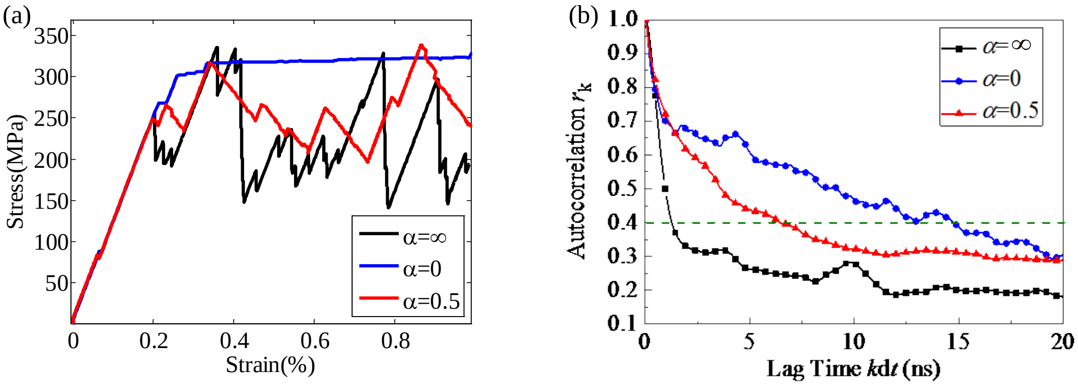

Figure 3. Typical simulation results under different loading modes for pillar with d =1000 b, (a) stress-strain curve, showing stepped or serrated burst features; (b) Autocorrelation function for dissipated energy rate showing different correlated extents of dislocation activities under different loading modes, where the dotted green lines are plotted to help visualization, which corresponds to 0.4.

8. MODELING PROCESSES IN FUSION SYSTEM MATERIALS

8.1 DEVELOPMENT OF INTERATOMIC POTENTIALS IN TUNGSTEN-RHENIUM SYSTEMS

W. Setyawan, G. Nandipati, and R. J. Kurtz (Pacific Northwest National Laboratory)

OBJECTIVE

The objective of this research is to develop interatomic potentials for exploring radiation damage in W in the presence of solid transmutant Re and radiation-induced precipitation of W-Re intermetallics.

SUMMARY

Reference data are generated using the ab initio method to fit interatomic potentials for the W-Re system. The reference data include single phases of W and Re, strained structures, slabs, systems containing several concentrations of vacancies, systems containing various types of interstitial defects, melt structures, structures in the σ and χ phases, and structures containing several concentrations of solid solutions of Re in bcc W and W in hcp Re. Future work will start the fitting iterations.

PROGRESS AND STATUS

This research is in the early stage. In this report, we present the reference structures that will be used to fit interatomic potentials. While experimental data may also be included, here we present the reference data that are calculated using VASP [1, 2] software within the density functional theory (DFT) framework. Core electrons are modeled with accurate projector-augmented-wave pseudopotentials [2]. Electrons in 6s and 5d states are treated as valence electrons. Perdew-Burke-Ernzerhof formulations [3] were employed for the exchange-correlation functionals. Plane wave cutoff energy is set at ENCUT = 300 eV. A Monkhorst-Pack [4] k-point grid is employed. Following the convergence study of k-points for the 3x3x3 bcc W (54 atoms), the energy converges to within 1 meV/atom with a 6x6x6 k-point grid, i.e. the number of atoms multiplied by the number of k-points is KPPRA = 54*6*6*6 = 11,664. Therefore, for all other systems, the k-point grid is set such that the KPPRA is approximately 12,000.

<u>Pure W</u>

Table 1 summarizes the reference data for pure W. For each system, the number of atoms (N_{atoms}) and the total energy (E_{total}) are given. In Table 1, universal strains refer to the universal linear-independent coupling strains (ULICS) [5]. In general, there are 6 ULICS strain vectors as the following (given in engineering notation):

u_1 = [1 2 3 4 5 6] * factor
u_2 = [-2 1 4 -3 6 -5] * factor
u_3 = [3 -5 -1 6 2 -4] * factor
u_4 = [-4 -6 5 1 -3 3] * factor
u_5 = [5 4 6 -2 -1 -3] * factor
u_6 = [-6 3 -2 5 -4 1] * factor

For a given strain vector u = [e_1 e_2 e_3 e_4 e_5 e_6], the corresponding strain tensor is

$$\varepsilon = \begin{bmatrix} e_1 & e_6/2 & e_5/2 \\ e_6/2 & e_2 & e_4/2 \\ e_5/2 & e_4/2 & e_3 \end{bmatrix}$$

The slab systems are constructed from a bcc conventional cell and include approximately 15 Å of vacuum space. To obtain the melt reference structures, classical molecular dynamics simulations are performed with LAMMPS [6] software using the W potential from Ref. [7]. Three melt structures are taken for the DFT simulations. In the DFT, for each melt structure, three different hydrostatic strains of -0.05, 0, and 0.2 are applied and the forces and energies are calculated.

Table 1. Reference data for pure W

System	N_{atoms}	E_{total} (eV)
bcc	54	-702.5819394
simple cubic	27	-312.636272
fcc	108	-1351.76693
hcp	48	-624.4633856
hydrostatic strain in bcc:		
-0.3	54	1097.254324
-0.25	54	379.5085514
-0.2	54	-112.8243529
-0.15	54	-420.0384223
-0.1	54	-594.0784846
-0.05	54	-676.6818088
-0.02	54	-695.6090639
-0.01	54	-698.0294595
0.01	54	-698.0363247
0.02	54	-695.9368593
0.05	54	-682.8022404
0.1	54	-644.4434419
0.15	54	-594.0470566
0.2	54	-538.4563672
0.25	54	-482.1371869
0.3	54	-427.9757802
0.4	54	-331.7395263
0.5	54	-255.0060816
universal strain u_1, factor = 0.01	54	-697.8249173
slab systems:		
{100} 9 layers	81	-1008.513982
{100} 10 layers	90	-1125.5968
{110} 8 layers	96	-1214.146302
{110} 9 layers	108	-1370.328137
{111} 15 layers	60	-749.6910502
{111} 16 layers	64	-802.0618372
vacancies in bcc:		
1	127	-1649.133084
8	120	-1534.820091
16	112	-1405.917881
32	96	-1174.650616
interstitial in bcc at site:		
octahedral	251	-3252.613316
tetrahedral	251	-3253.257761
melt structures:		

structure 1, strain = -0.05	128	-1416.5574
structure 1, strain = 0	128	-1525.7440
structure 1, strain = 0.2	128	-1291.6383
structure 2, strain = -0.05	128	-1413.6436
structure 2, strain = 0	128	-1525.1460
structure 2, strain = 0.2	128	-1293.8987
structure 3, strain = -0.05	128	-1407.0131
structure 3, strain = 0	128	-1519.3006
structure 3, strain = 0.2	128	-1292.5626

Pure Re

Table 2 summarizes the reference data for pure Re. The universal strains are applied to an hcp structure in an orthorhombic cell. In the orthorhombic cell, the x-axis is along the basal close-packed row direction, the y-axis is perpendicular to x, and the z-axis is parallel to the c-axis of the original hcp unit cell, as shown in Figure 1. Figure 2 shows interstitial sites in the hcp structure that are labeled according to Ref. [8], namely O (octahedral site), T (tetrahedral site), BO (on basal plane directly below O), BT (basal plane directly below T), BC (crowdion site in the basal close-packed row), C (midway between two atoms in the primitive hcp cell), and S (represents the position of one of the atoms in a [0001] split dumbbell). Note that Figure 2 is only for illustrating the location of the interstitial sites, while the calculations with an interstitial are performed in an hcp structure in an orthorhombic 5x3x3 supercell. The melt reference structures are generated in a similar way as in tungsten using the same ad hoc potential.

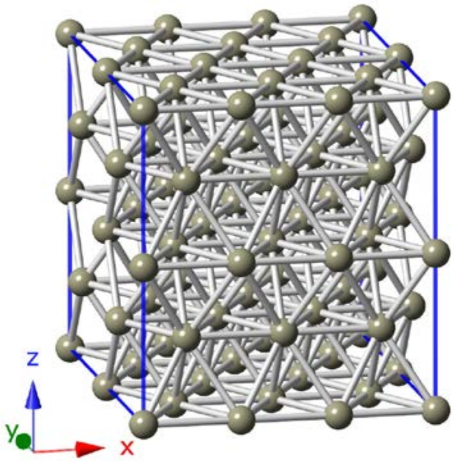

Figure 1. Hexagonal close-packed structure in an orthorhombic 3x2x2 supercell. The close-packed plane stacking is along the z axis.

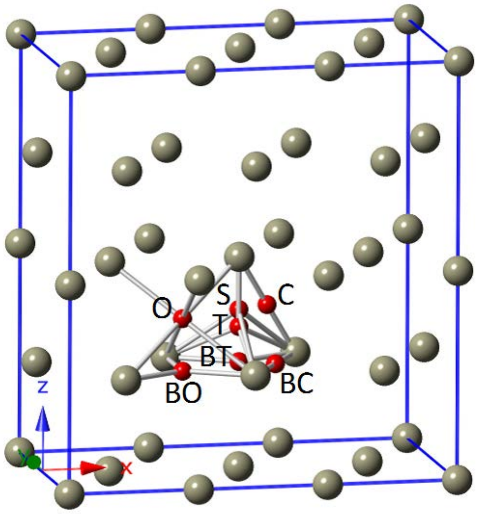

Figure 2. Schematic showing the location of interstitial sites in hcp Re.

Table 2. Reference data for pure Re

System	N_{atoms}	E_{total} (eV)
bcc	54	-650.1789284
simple cubic	27	-286.1105305
fcc	108	-1332.140438
hcp	48	-595.484282
hydrostatic strain in hcp:		
-0.3	48	1413.935322
-0.25	48	586.671512
-0.2	48	37.45553335
-0.15	48	-298.004176
-0.1	48	-484.395746
-0.05	48	-571.6722672
-0.02	48	-591.7847314
-0.01	48	-594.4713212
0.01	48	-594.9844668
0.02	48	-593.1330174
0.05	48	-580.8254842
0.1	48	-544.4645052
0.15	48	-497.0115376
0.2	48	-445.4054424
0.25	48	-394.070185
0.3	48	-345.5787228
0.4	48	-261.1465214

0.5	48	-194.5711407
universal strain u_1, factor = 0.01	48	-590.6728669
universal strain u_2, factor = 0.01	48	-591.0746809
universal strain u_3, factor = 0.01	48	-589.3892782
slab systems:		
{0001} 8 layers	96	-1165.343074
{0001} 9 layers	108	-1313.81838
{11-20} 13 layers	104	-1257.225439
{11-20} 14 layers	112	-1356.504857
{10-10} 14 layers	90	-1084.938512
{10-10} 16 layers	96	-1164.174936
vacancies in hcp:		
1	179	-2217.499345
9	171	-2095.616498
18	162	-1959.043558
36	144	-1702.973672
interstitial in hcp at site:		
O	181	-2234.04217
T	181	-2235.701694
BO	181	-2234.760093
BT	181	-2234.080058
BC	181	-2234.375194
S	181	-2235.627513
C	181	-2224.510206
melt structures:		
structure 1, strain = -0.05	144	-1473.379543
structure 1, strain = 0	144	-1636.766874
structure 1, strain = 0.2	144	-1381.390768
structure 2, strain = -0.05	144	-1469.700918
structure 2, strain = 0	144	-1635.636129
structure 2, strain = 0.2	144	-1385.244533
structure 3, strain = -0.05	144	-1488.42032
structure 3, strain = 0	144	-1646.310219
structure 3, strain = 0.2	144	-1378.614023

W-Re

Table 3 summarizes the reference data for W-Re systems. For each system, the number of W atoms (N_W) and Re atoms (N_{Re}) are presented. The crystal structure of the σ and χ phases are taken from [9]. In the σ phase, there are five unique sites labeled A, B, C, D, and E. In the χ phase, there are four sites: A, B, C, and D. In Table 3, a system in the σ phase that is labeled as WWReWRe indicates for this system the sites from A to E are occupied by W, W, Re, W, and Re, respectively.

Table 3. Reference data for W-Re systems

System	N_W	N_{Re}	N_{atoms}	N_{Re}/N_{atoms}	E_{total} (eV)
σ phase:					
dir1 WWWWW	60	0	60	0	-769.8909243
dir2 WWWWRe	44	16	60	0.266666667	-760.5954671
dir3 WWWReW	44	16	60	0.266666667	-767.0342725
dir4 WWWReRe	28	32	60	0.533333333	-757.0972315
dir5 WWReWW	44	16	60	0.266666667	-761.6438983
dir6 WWReWRe	28	32	60	0.533333333	-752.346164
dir7 WWReReW	28	32	60	0.533333333	-756.9234711
dir8 WWReReRe	12	48	60	0.8	-745.7811481
dir9 WReWWW	52	8	60	0.133333333	-763.8059406
dir10 WReWWRe	36	24	60	0.4	-755.1414963
dir11 WReWReW	36	24	60	0.4	-761.1573737
dir12 WReWReRe	20	40	60	0.666666667	-751.279495
dir13 WReReWW	36	24	60	0.4	-755.3495869
dir14 WReReWRe	20	40	60	0.666666667	-745.8949998
dir15 WReReReW	20	40	60	0.666666667	-750.2992832
dir16 WReReReRe	4	56	60	0.933333333	-739.0879598
dir17 ReWWWW	56	4	60	0.066666667	-769.2817472
dir18 ReWWWRe	40	20	60	0.333333333	-759.9939997
dir19 ReWWReW	40	20	60	0.333333333	-766.2942985
dir20 ReWWReRe	24	36	60	0.6	-755.8677306
dir21 ReWReWW	40	20	60	0.333333333	-761.1414682
dir22 ReWReWRe	24	36	60	0.6	-751.5170731
dir23 ReWReReW	24	36	60	0.6	-755.9989009
dir24 ReWReReRe	8	52	60	0.866666667	-744.1692638
dir25 ReReWWW	48	12	60	0.2	-762.9539448
dir26 ReReWWRe	32	28	60	0.466666667	-754.1006308
dir27 ReReWReW	32	28	60	0.466666667	-760.1917582
dir28 ReReWReRe	16	44	60	0.733333333	-749.7810574
dir29 ReReReWW	32	28	60	0.466666667	-754.6094754
dir30 ReReReWRe	16	44	60	0.733333333	-744.7990256
dir31 ReReReReW	16	44	60	0.733333333	-749.1253384
dir32 ReReReReRe	0	60	60	1	-737.4461744
χ phase:					
dir101 WWWW	58	0	58	0	-737.3679916
dir102 WWWRe	34	24	58	0.413793103	-735.9993855
dir103 WWReW	34	24	58	0.413793103	-731.4378711
dir104 WWReRe	10	48	58	0.827586207	-724.8259818
dir105 WReWW	50	8	58	0.137931034	-730.9013652

dir106 WReWRe	26	32	58	0.551724138	-729.1132821
dir107 WReReW	26	32	58	0.551724138	-722.8944818
dir108 WReReRe	2	56	58	0.965517241	-717.4686601
dir109 ReWWW	56	2	58	0.034482759	-735.572186
dir110 ReWWRe	32	26	58	0.448275862	-734.4248587
dir111 ReWReW	32	26	58	0.448275862	-729.3596414
dir112 ReWReRe	8	50	58	0.862068966	-723.0912448
dir113 ReReWW	48	10	58	0.172413793	-728.8281186
dir114 ReReWRe	24	34	58	0.586206897	-727.1134194
dir115 ReReReW	24	34	58	0.586206897	-720.5746825
dir116 ReReReRe	0	58	58	1	-715.5232578
Re solid solution in bcc W:					
dir201	51	3	54	0.055555556	-699.9239873
dir202	49	5	54	0.092592593	-698.2619436
dir203	40	14	54	0.259259259	-690.5199573
dir204	27	27	54	0.5	-679.4381574
dir205	14	40	54	0.740740741	-669.9094759
W solid solution in hcp Re:					
dir251	2	46	48	0.958333333	-594.7724476
dir252	5	43	48	0.895833333	-595.1800105
dir253	12	36	48	0.75	-595.7273218
dir254	24	24	48	0.5	-599.7632192
dir255	36	12	48	0.25	-614.3788765

Acknowledgement

This research has been supported by the U.S. Department of Energy, Office of Science, Office of Fusion Energy Sciences (DE-AC06-76RL0-1830).

References

[1] P. E. Blöchl, Physical Review B 50 (1994) 17953.
[2] G. Kresse and D. Joubert, Physical Review B 59 (1999) 1758.
[3] J. P. Perdew, K. Burke and M. Ernzerhof, Physical Review Letter 77 (1996) 3865.
[4] H. J. Monkhorst and J. D. Pack, Physical Review B 13 (1976) 5188.
[5] R. Yu, et al., Computer Physics Communications 181 (2010) 671.
[6] S. Plimpton, Journal of Computational Physics 117 (1995) 1.
[7] N. Juslin, B. D. Wirth, Journal of Nuclear Materials 432 (2013) 61.
[8] R. A. Johnson, J. R. Beeler, Interatomic potentials and crystalline defects, edited by J. K. Lee, AIME, New York, 1981 p. 165.
[9] J. C. Crivello, J. M. Joubert, Journal of Physics Condensed Matter 22 (2010) 035402.

8.2 STRUCTURE AND MOBILITIES OF TUNGSTEN GRAIN BOUNDARIES CALCULATED FROM ATOMISTIC SIMULATIONS—Timofey Frolov and Robert E. Rudd (Lawrence Livermore National Laboratory)

OBJECTIVE

The objective of this study is to develop a computational methodology to predict structure, energies and mobilities of tungsten grain boundaries as a function of misorientation and inclination. The energies and the mobilities are the necessary input for thermomechanical model of recrystallization being developed by the Marian Group at UCLA.

SUMMARY

Recrystallization determines the upper extent of the operating temperature of tungsten as a divertor or first-wall material. At temperatures above the onset of recrystallization, migrating grain boundaries sweep out defects that contribute to hardening. These processes make the recrystallized material unsuitable because of its brittleness. Thermomechanical models to predict recrystallization and its effect on mechanical properties have to be informed of the mechanisms of grain boundary migration under stress and other driving forces at tokamak operating temperatures. Recent experimental and computational studies suggest that addition of impurities and elevated temperatures can trigger structural transformations at grain boundaries that result in orders of magnitude increase in mobility. Here we present preliminary results demonstrating that tungsten grain boundaries do exhibit phase transformations and calculate the mobilities needed for thermomechanical models of recrystallization.

BACKGROUND

Tungsten has been identified as the divertor material in ITER and is a leading candidate for the plasma-facing components in DEMO and subsequent magnetic fusion energy systems because of its high thermal conductivity, high melting point, high mechanical strength at elevated temperature, and low sputtering yield. While tungsten has a number of favorable properties it is also intrinsically brittle even at relatively high temperatures especially after recrystallization. As metals are subjected to harsh conditions, their microstructures change leading to changes in materials properties. Defects build up in the metal, increasing its strength, but the increased mobility of grain boundaries and other defects at high temperature enables the boundaries to absorb dislocations and produce relatively pristine, recrystallized material with a different grain microstructure. Recrystallization typically sets the upper operating temperature of tungsten, affecting the performance of the fusion energy system. The need for predictive models of material behavior at first-wall and divertor conditions motivates the development of computational models and simulations that can predict mechanical and kinetic properties of tungsten grain boundaries. Recent experimental and computational studies in materials like copper demonstrated that elevated temperatures and changes in chemical composition can lead to structural transformations at grain boundaries that result in discontinuous changes in materials properties [1, 2]. Experimental studies linked this kind of transition to abnormal grain growth and embrittlement in metallic and ceramic systems [3-5]. Here we use atomistic simulations to understand the role of grain boundaries in plasticity including grain boundary mobility, which affects recrystallization, and the interaction of dislocations with the grain microstructure, which is an important part of the embrittlement problem.

PROGRESS AND STATUS

Methods

Mobilities of tungsten grain boundaries can be calculated directly from atomistic simulations of shear stress driven grain boundary motion. Shear stress applied parallel to the grain boundary plane induces grain boundary migration [6]. The deformation of a bicrystal after coupled grain boundary motion is illustrated in Figure 1a. The portion of a crystal swept by the boundary is sheared as indicated by vertical dashed line. Coupled grain boundary motion is characterized by a coupling factor, β, which is a ratio of the tangential and normal grain boundary velocities. For relatively low-angle boundaries the mechanism of coupled motion can be explained by examining the collective motion of grain boundary dislocations. When shear stress is applied to a bicrystal these dislocations move in response to the Peach-Koehler force. Figure 1b schematically illustrates grain boundary dislocations before and after coupled motion. The collective motion of grain boundary dislocations results in normal grain boundary displacement and tangential translations of the grains relative to each other. The coupling is called perfect when β is just determined by the bicrystal geometry. Based on the mechanism illustrated in Figure 1b coupling factor can be calculated as

$$\beta = 2\tan(\theta/2) \tag{1}$$

where θ is the misorientation angle across the boundary. Symmetries present in a crystal can result in multiple coupling modes, each characterized by a different coupling factor. (100) symmetrical tilt boundaries with θ closer to 0° couple in the <100> mode, while grain boundaries with θ closer to 90° couple in the <110> mode.

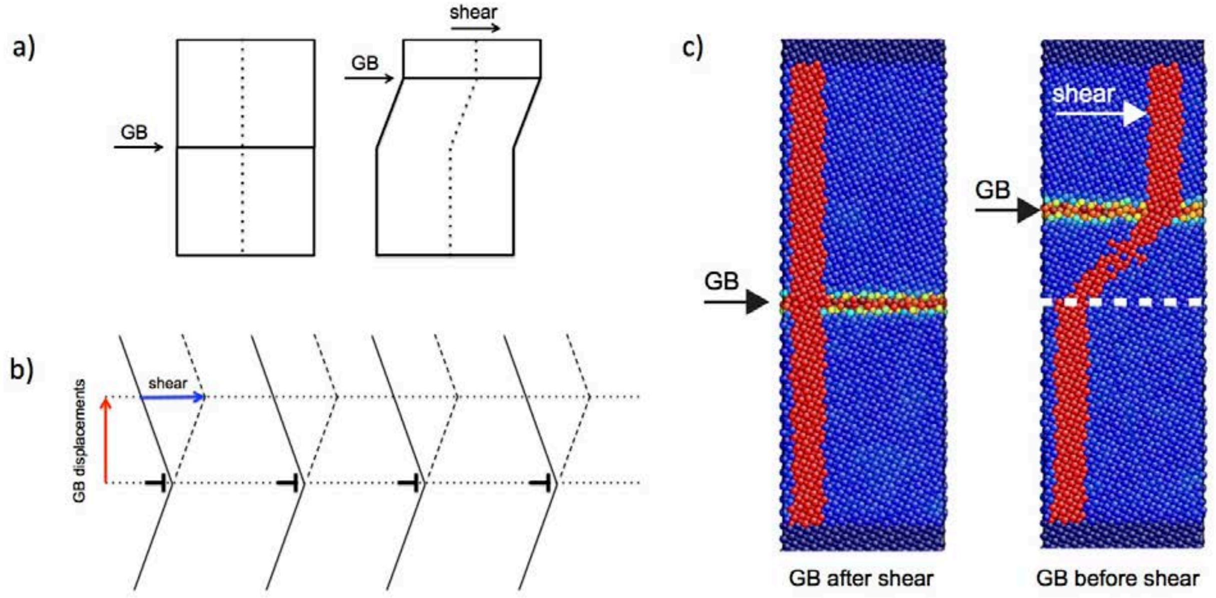

Figure 1. a) Bicrystal shear deformation produces grain boundary migration b) Mechanism of coupled motion due to the collective motion of grain boundary dislocations. c) Atomistic simulations of grain boundary coupled motion.

In the linear mobility regime relevant to recrystallization, the grain boundary velocity v_{GB} is proportional to the driving force F as $v_{GB} = MF$, where M is the grain boundary mobility. It can be shown that the driving force for coupled motion is proportional to shear stress $F=\sigma\beta$, so that the velocity is given by

$$v_{GB} = M\,\sigma\,\beta. \tag{2}$$

Grain boundary velocity, shear stress and the coupling factor can be calculated from atomistic simulations of coupled motion. Thus, Eq. (2) allows predictions of grain boundary mobility.

Molecular dynamics (MD) simulations of tungsten grain boundaries were performed using the Large-scale Atomic/Molecular Massively Parallel Simulator (LAMMPS) software package [7]. The interactions between atoms were modeled using a tungsten EAM potential [8]. We modeled high-angle Σ5(310)[001] and low-angle Σ(978)[11-2] symmetrical tilt boundaries with and without defects present. Σ5(310)[001] is a typical high angle boundary with misorientation angle of 36.87°. The dimensions of the bicrystals were 25 × 3 × 12 nm^3. The simulation block contained 60000 atoms. The low-angle boundary has a misorientation angle of 11°, with the grains rotated around the [11-2] tilt axis. The bicrystal with dimensions 10 × 10 × 30 nm^3 contained 223000 atoms. Both bicrystals had the tilt axis parallel to the *y* direction, and grain boundary planes normal to the *z* direction. Periodic boundary conditions were applied in the *x* and *y* directions, while fixed boundary conditions were used in the *z* direction to impose shear deformation.

Equilibrium boundary structures were obtained by sampling rigid translations of grains relative to each other followed by static relaxations. Figure 2a illustrates the structure of the Σ5(310)[001] boundary composed of kite-shaped structural units. The structure of the low-angle boundary is represented by a periodic array of 1/2<111> edge dislocations (Figure 3a). The bicrystals were used to perform simulations of coupled motion at temperatures ranging from 500K to 2500K. During the simulations the atoms inside the 10Å thick region at the bottom of the simulation block were kept fixed, while the 10Å thick layer of atoms at the top of the block were moved with a constant velocity of 0.1 m/s in the x direction. The atoms in the middle of the block were simulated using the canonical (NVT) ensemble with Nose-Hoover thermostat.

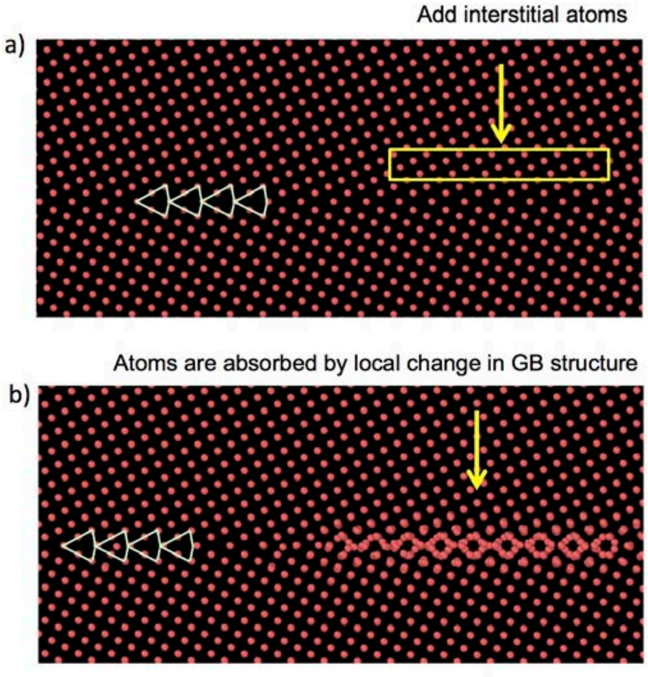

Figure 2. a) Structure of Σ5(310)[001] symmetrical tilt boundary in W composed of kite-shaped structural units. b) Grain boundary absorbs interstitial atoms by undergoing a structural transformation.

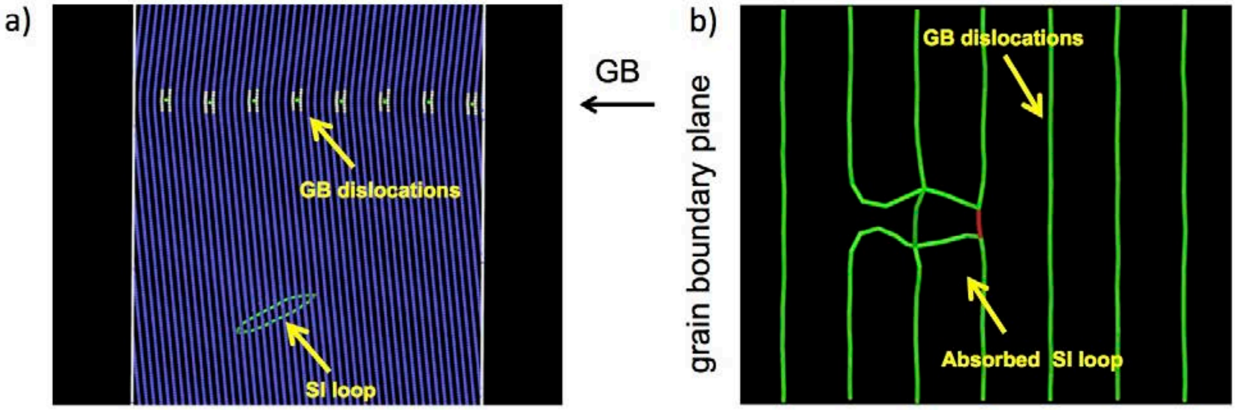

Figure 3. a) Structure of Σ (978)[11-2] symmetrical tilt boundary in W composed of 1/2<111> edge dislocations. b) Grain boundary structure after interstitial loop was absorbed.

Figure 1c illustrates a bicrystal after 30 ns of the coupled motion. The initial positions of the grain boundaries are indicated by the white dashed lines. The deformation of the bicrystal revealed by the atomistic simulations is consistent with the schematic picture in Figure 1a. The red column of marker atoms clearly demonstrates that the region swept by the boundary is sheared. The coupling factor β can be obtained directly from MD simulations by calculating the ratio of upper grain displacement and the grain boundary normal displacement. The ideal coupling factor predicted by Eq. (1) was calculated from MD simulation for both high and low-angle boundaries.

Point Defects

In the presence of high temperature, impurities and point defects, grain boundary structure and mobility can change significantly. Recent experimental studies in ceramics indicate that such transformations can change grain boundary mobility by orders of magnitude producing pronounced changes in microstructure evolution [2, 9]. To quantify the possible effect of lattice defects on grain boundary mobility, we investigate how these grain boundaries interact with interstitials and self-interstitial loops.

High-angle boundary

In the case of the high-angle boundary individual interstitial atoms were randomly injected inside a rectangular region above the boundary as indicated in Figure 2a. The bicrystal with defects was then annealed for 100ns at T=2000K. During the first several nanoseconds the interstitials diffuse to the boundary and produce noticeable reconstruction of the kite-shaped structural units. These reconstructed regions agglomerate during the later times and form a patch with a different grain boundary structure, which is illustrated in Figure 2b. Throughout the simulation the newly formed patch coexists with the original structure while atoms diffuse within the boundary. This transformation of the grain boundary structure is consistent with recent results in Cu that demonstrated multiple grain boundary states characterized by different atomic densities [10]. Atomistic simulations allow evaluation of the mobilities of the two structures, as well as the mobility of the “damaged” boundary that has two different grain boundary structures present simultaneously.

Low-angle boundary

1/2<111> interstitial loops are formed in tungsten divertors as a result of radiation damage. A single interstitial loop with diameter ranging from 10 to 50 Å was introduced inside one of the crystals in a simulation block with the 11° boundary as illustrated in Figure 3a. During subsequent isothermal annealing the loop glides towards the boundary driven by the elastic interaction and gets absorbed. The structure of the grain boundary dislocation network with the interstitial loop absorbed is illustrated in Figure 3b. The boundary is composed of 1/2<111> edge dislocations, and one segment of the loop gets annihilated upon absorption. The red segment in the figure indicates that the Burgers vector doubled. This configuration represents a boundary with a circular step and has dislocation lines that are not parallel to the tilt axis.

To evaluate the effect of loop absorption on grain boundary mobility, we performed the simulations of coupled motion of defective grain boundaries. When shear stress is applied to the bicrystal, the network of 1/2<111> dislocations at the grain boundary illustrated in Figure 3b moves in a manner consistent with perfect coupling. In other words, the absorbed interstitial loop does not change the mechanism of grain boundary motion. Figure 4 illustrates shear stress during coupled motion at 500K for one clean boundary and two boundaries with interstitial loops with diameter of 25Å and 50Å. Higher average and peak stresses are required to move the boundaries with loops, suggesting that mobility of the boundary decreased and the shear strength of the bicrystal is increased due to the loop absorption.

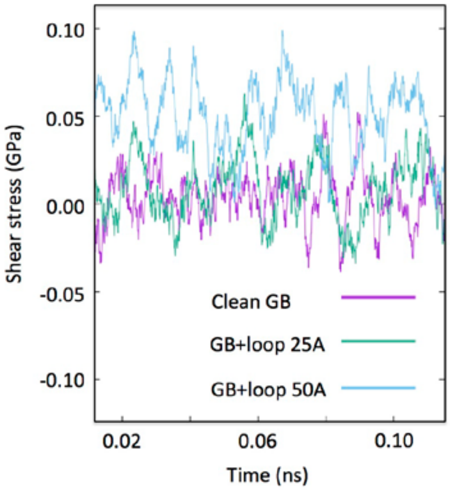

Figure 4. Shear stress during coupled motion at 500K for one clean boundary and two boundaries with interstitial loops with diameter of 25 Å and 50 Å. Higher average and peak stress is required to move the boundaries with larger loops, indicating that mobility of the boundary decreased due to the loop absorption.

Summary and future studies

In summary, we performed simulations of coupled motion of two representative high- and low-angle grain boundaries. Atomistic simulations give direct access to shear stress during grain boundary migration, predict the coupling factor β and grain boundary velocity. This information has been used to calculate grain boundary mobility. In addition to modeling of pristine or undamaged boundaries, we also investigated the effect of interstitial absorption on grain boundary structure and mobility. Low- and high-angle boundaries displayed different mechanisms of defect absorption. While the damaged low-angle boundary can be described as a network of 1/2<111> edge dislocations, high-angle boundary absorbs atoms by undergoing structural transformation. Absorption of defects has strong effect on grain boundary mobility and increases the shear strength of the material. Systematic calculation of grain boundary energies and mobilities as function of misorientation and inclination will be the subject of future work. These results will provide necessary input parameters for thermomechanical model of recrystallization under development by the Marian group at UCLA. Direct experimental measurement of the predicted high-temperature grain boundary structures and velocities is not feasible with existing technology, so we rely on comparison of the thermomechanical model with experiment for validation.

Acknowledgments

This work was performed under the auspices of the U.S. Department of Energy by Lawrence Livermore National Laboratory under Contract No. DE-AC52-07NA27344.

References

[1] T. Frolov, M. Asta, and Y. Mishin, Current Opinion in Solid State and Materials Science (2016).
[2] P. R. Cantwell, M. Tang, S. J. Dillon, J. Luo, G. S. Rohrer and M. P. Harmer, Acta Materialia 62, 1 (2014).
[3] S. J. Dillon and M. P. Harmer, Acta Materialia 55, 5247 (2007).
[4] J. Luo, H. Wang, and Y.-M. Chiang, Journal of the American Ceramic Society 82, 916 (1999).
[5] J. Luo, H. Cheng, K. M. Asl, C. J. Kiely, and M. P. Harmer, Science 333, 1730 (2011).
[6] J. W. Cahn, Y. Mishin, and A. Suzuki, Acta Materialia 54, 4953 (2006).
[7] S. Plimpton, Journal of Computational Physics 117, 1 (1995).
[8] X. W. Zhou, R. A. Johnson, and H. N. G. Wadley, Physical Review B 69, 144113 (2004).
[9] T. Frolov, Applied Physics Letters 104, (2014).
[10] T. Frolov, D. L. Olmsted, M. Asta, and Y. Mishin, Nature Communications 4, 1899 (2013).

8.3 OBJECT KINETIC MONTE CARLO SIMULATIONS OF RADIATION DAMAGE ACCUMULATION IN TUNGSTEN

—G. Nandipati, W. Setyawan, K. J. Roche, R. J. Kurtz (Pacific Northwest National Laboratory) and B. D. Wirth (University of Tennessee)

OBJECTIVE

The objective of this work is to understand the accumulation of radiation damage created by primary knock-on atoms (PKAs) of various energies, at 300 K and for a dose rate of 10^{-4} dpa/s in bulk tungsten using the object kinetic Monte Carlo (OKMC) method.

SUMMARY

We used the lattice-based object kinetic Monte Carlo code; *KSOME* [1] to perform simulations of radiation damage accumulation in bulk tungsten at 300 K and for a dose rate of 10^{-4} dpa/s, up to a dose of 1.0 dpa. These are ad-hoc irradiation simulations performed using a set of cascades with the same PKA energies. In this study, eight different irradiation simulations were performed using eight sets of cascades with PKA energies of 10, 20, 30, 40, 50, 60, 75 and 100 keV. Both the number density of vacancies and vacancy clusters in the simulation box appears to saturate with increasing dose in the simulation using cascades with PKA energies of 40, 50, 60, 75, 100 keV, while the same parameters increase linearly with dose in the simulations using cascades with PKA energies of 10, 20 and 30 keV. In all simulations the average vacancy cluster size remained constant with dose. However, the vacancy cluster size increases with cascade PKA energy.

PROGRESS AND STATUS

Simulation Details

Simulations were performed using a non-cubic box with dimensions 95.10 x 96.37 x 97.00 nm^3 (300a x 304a x 306a, where *a* is the lattice constant of tungsten), with each axis parallel to a <100> type direction. Each defect is allowed to hop to one of eight possible body-centered cubic nearest neighbor lattice sites at a distance of *a*/2 <111>, Finite periodic boundary conditions were adopted in all three directions i.e. periodic boundary conditions are applied but whenever a mobile object moved a distance larger than the average grain size, it is removed from the simulation, and it is no longer tracked. In the present simulations, we used an average grain size of 2 μm and no intragranular traps were considered.

The values of the binding energies of defects used in the present annealing simulations were taken from the *ab initio* calculations of Becquart *et al*. [3] while the migration barriers were taken from MD simulations [4] using an EAM potential for W [5]. In the present simulations, SIA clusters larger than size five were constrained to diffuse in 1D along one of four <111> directions. SIA clusters up to size five were allowed to change their direction of 1D motion via rotation and thereby perform a mixed 1D/3D motion. The activation barrier for changing direction from one <111> direction to another is 0.38 eV [6]. The direction of 1D motion was assigned randomly to the SIAs at the start of a simulation, and interstitial clusters of all sizes are assumed to be glissile (mobile). Their migration/diffusion rates decrease with increasing cluster size (n) according to $\nu_o n^{-1.0}$ ($\nu_o = 6 \times 10^{12}$ s^{-1}) while the migration barrier is taken to be independent of cluster size.

For a single vacancy, the activation barrier for diffusion is taken as 1.30 eV [4], and vacancy clusters larger than five are assumed to be immobile. But vacancy clusters of all sizes are allowed to emit mono-vacancies. All mobile vacancy clusters migrate in 3D, and their diffusion rates decrease with cluster size (n) according to $\nu_o(q^{-1})^{n-1}$ ($\nu_o = 6 \times 10^{12}$ s^{-1}, q = 1000) [3]. The vacancy (SIA) dissociation rate is given by $\Gamma_d = \nu_d\, exp((E_m + E_d)/k_B T)$, where E_d is the binding energy of a vacancy (SIA) to a vacancy (SIA) cluster, and E_m is the migration energy of a single vacancy (SIA). We have assumed that defect clusters of all sizes and types are spherical objects, and their capture radii were obtained from Reference [3].

Individual cascades are randomly selected from the database of cascades of a particular PKA energy and inserted into the simulation box at random positions based on the cascade production rate. The production rate of cascades, which is the number of cascades produced in the simulation cell per second, dose rates and the accumulated dpa (displacements per atom) are calculated based on the NRT displacements per cascade (ν_{NRT}). [7]

Results

Cascades were created using MD simulations as described in Ref. [2] Simulations were performed at 300 K and for the dose rate of 10^{-4} dpa/s. Since no intragranular traps are considered in the present simulation, interstitial clusters, which diffuse very fast, are very quickly either absorbed at grain boundaries or recombine. Therefore, only the data on vacancy type defects are presented in this report.

Figures 1(a-c) shows plots of the density of vacancies and vacancy clusters, and average vacancy cluster sizes as a function of dose for the irradiation simulations performed using cascades of various PKA energies. In the irradiation simulations using 10 keV cascades, both the density of vacancies and vacancy clusters increases linearly from very low doses all the way up to a dose of 1.0 dpa. In case of 20 and 30 keV simulations densities increase linearly with dose above 0.1 dpa. The rate of growth of these parameters with dose decreases with increasing PKA energy (Figures 1(a-b)). While in the case of simulations performed using 30, 40, 50, 60, 75 and 100 keV cascades, the density of both vacancy clusters and vacancies appears to saturate or to closely approach saturation with dose (Figures 1(a-b)). Note that for the same irradiation dose, the retained irradiation damage decreases with PKA energy from 10 to 30 keV, while it increases for PKA energies greater than 30 keV. This behavior suggests that retained damage saturates at a much lower dose in case of a radiation source with higher PKA energies

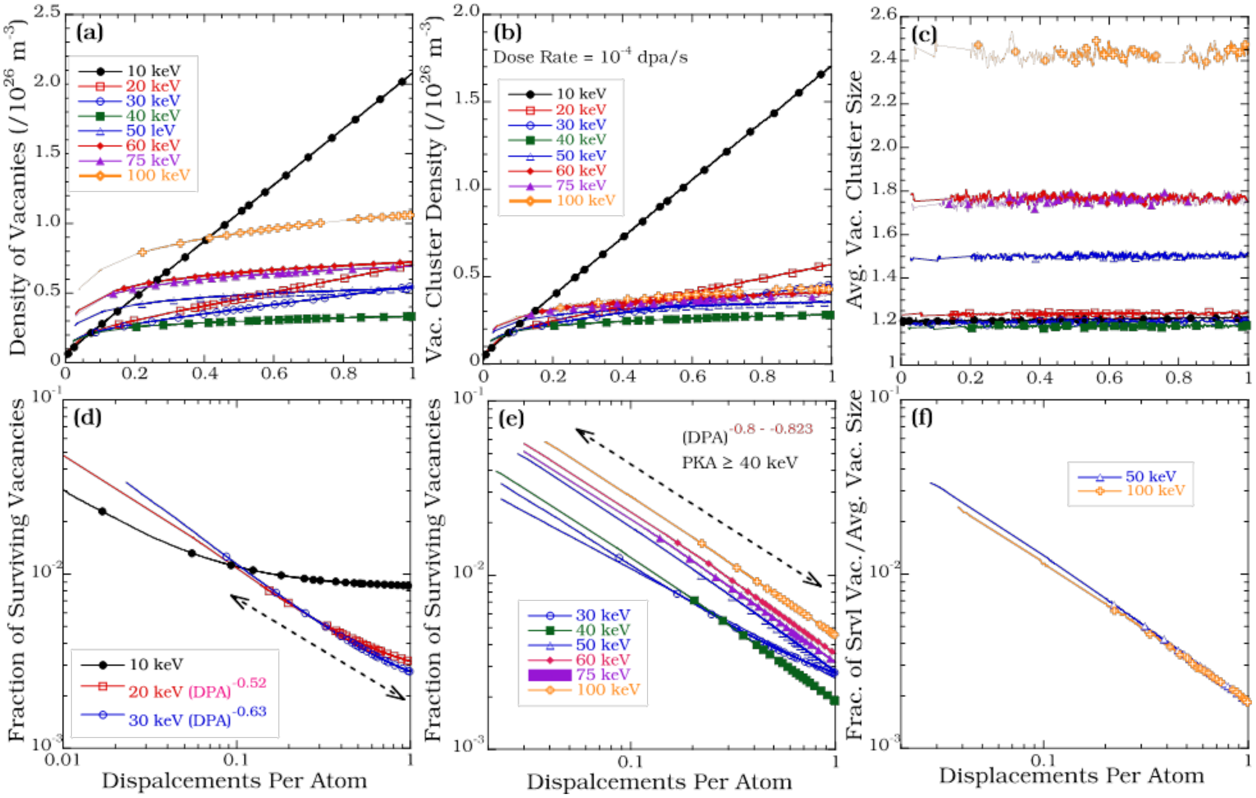

Figure 1. Comparison of damage accumulation in tungsten at 300 K as a function of dose for various PKA energies (a) Vacancy cluster density (b) density of vacancies (c) average vacancy clusters size (unit: number of vacancies), fraction of surviving vacancies (d) 10, 20, 30 keV (e) 40, 50, 60, 75, 100 keV (f) ratio of surviving vacancies and average vacancy cluster size for 50, 100 keV simulations.

than in the case of a radiation source with lower PKA energies. More importantly, the shift in the behaviorof retained damage with PKA energy occurs at a PKA energy of 40 keV, which also corresponds to a significant change in the defect cluster size distribution obtained from the MD cascades. In all cases, the average vacancy cluster size remained constant with dose but it increased with cascade PKA energy (Figures 1(c)).

Figures 1(d-e) shows plots of the fraction of surviving vacancies, while Figure 1(f) shows the ratio of the fraction of surviving vacancies and the average vacancy cluster size for 50 and 100 keV PKA simulations. Note that the fraction of surviving vacancies shown in Figures 1(d-e) is the ratio of surviving vacancies over the total number of vacancies from all the cascades inserted to reach a particular dose. In the case of 10 keV, although the fraction of surviving vacancies decreases with dose up to 0.1 dpa, it seems to saturate for higher doses. While the behavior is similar in the case of 20 and 30 keV, it is hard to say if it is saturated or not at the dose of 1.0 dpa. For higher PKA energies the behavior is similar in all PKA energies. The surviving fraction exhibits power-law decay with increasing dose with an exponent in the range 0.8-0.823 (Figure 1(e)). However, the fraction of surviving vacancies for all the PKA energies will collapse into a single curve (Figure 1(f)) when scaled with average vacancy cluster size from Figure 1(c). Note that the surviving fraction of vacancies in the case of 20 and 30 keV also exhibits power-law decay with exponents of 0.52 and 0.63, respectively.

Figures 2 and 3 shows snapshots of the vacancy distributions in the simulation box at a dose of 1.0 dpa for various PKA energies. The color scale in Figures 2 and 3 goes from a minimum of one vacancy to a maximum of 5-vacancies per cluster. From Figures 3 and 4, one can see that the spatial distribution of vacancy clusters is random and based on the average cluster size from Figure 1(c), a significant fraction of vacancy clusters are mono-vacancies. Even though the average cluster size increases with PKA energy, a significant fraction of vacancy clusters are mono-vacancies even at higher PKA energies, and the largest vacancy cluster is of size 5 for the 100 keV simulation. As expected, this behavior is due to lack of mono-vacancy diffusion and dissociation of small vacancy clusters at 300 K. Interestingly, a closer look reveals what looks like the ordering of vacancy clusters, which appear as bands. These bands are more obvious in Figure 2(b), which is the microstructure at 1.0 dpa for the irradiation simulation using 20 keV cascades. However, the bands seen in Figure 2(b) appear and disappear randomly with dose.

Future Work

Further simulations are being carried out to understand defect accumulation at various dose rates, PKA energies, temperatures, simulation cell and grain size.

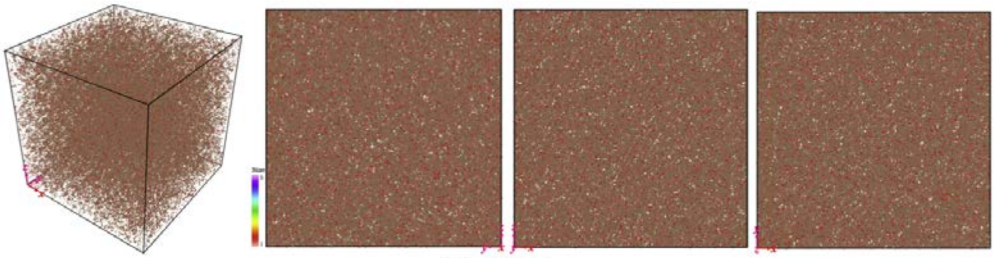

(a) 10 keV

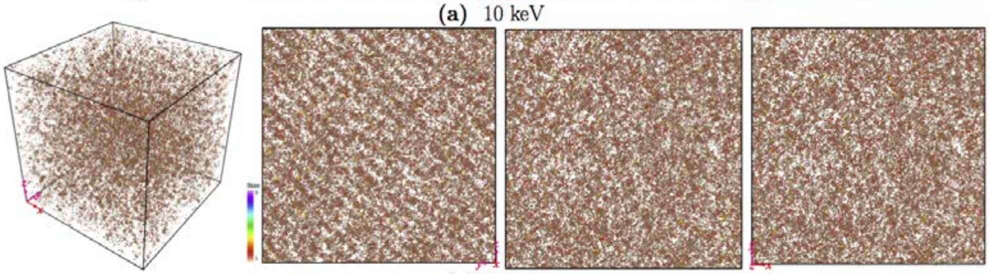

(b) 20 keV

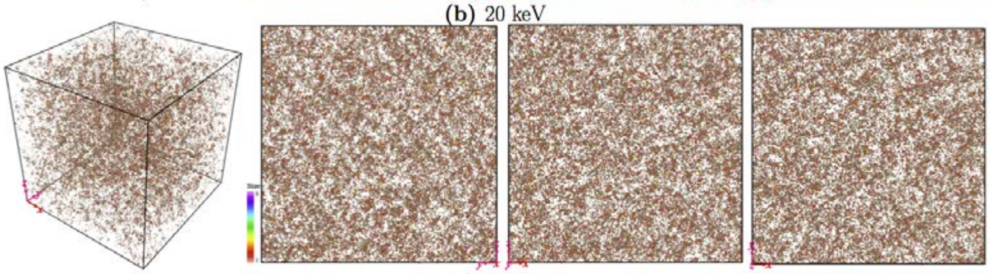

(c) 30 keV

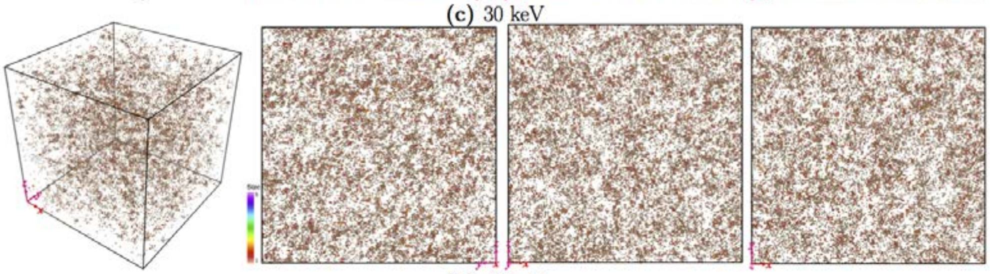

(d) 40 keV

Figure 2. Snap shots of vacancy clusters in the simulation box at 1.0 dpa (a) 10 keV (b) 20 keV (c) 30 keV (d) 40 keV.

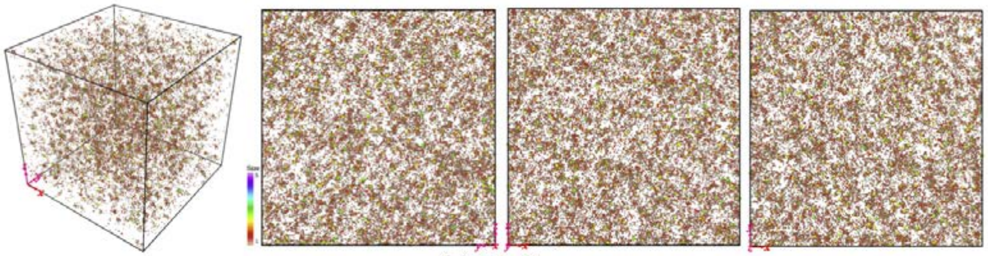

(a) 50 keV

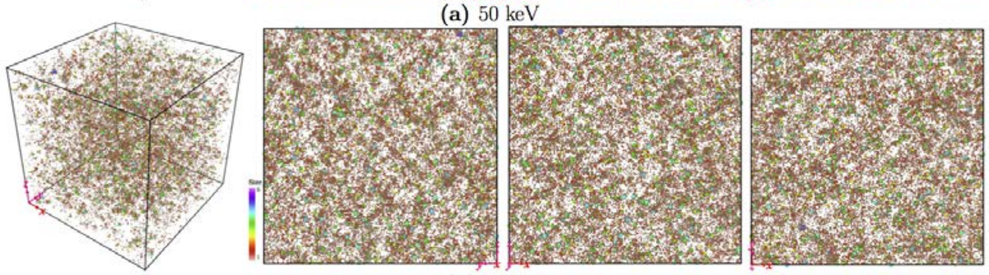

(b) 60 keV

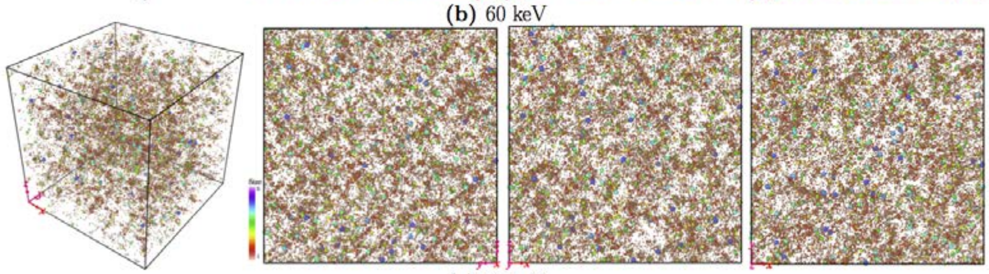

(c) 75 keV

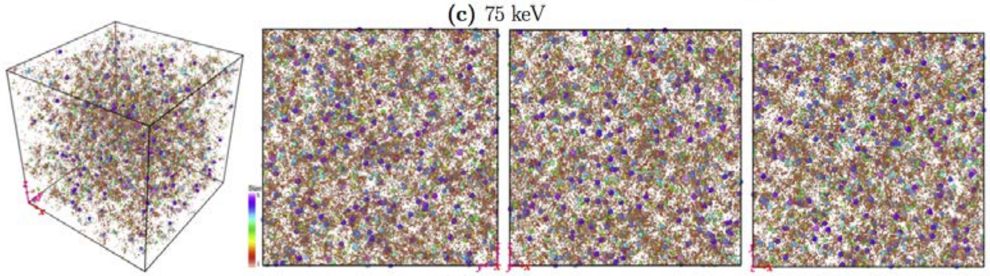

(d) 100 keV

Figure 3. Snap shots of vacancy clusters in the simulation box at 1.0 dpa (a) 50 keV (b) 60 keV (c) 75 keV (d) 100 keV.

Acknowledgement

These simulations were performed on CARVER and HOPPER at National Energy Research Scientific Computing Center (NERSC), Argonne National Lab, MCS Workstations and PNNL's PIC systems.

References

[1] G. Nandipati *et al* Semiannual Progress Report DOE/ER-0313/54, June 2013, 179-183
[2] W. Setyawan *et al* Semiannual Progress Report DOE/ER-0313/54, June 2013, 200-204
[3] C. S. Becquart *et al.* J. Nucl. Mater. 403 (2010) 75
[4] T.Faney, N.Juslin, B.D.Wirth,(*private communication)*.
[5] N.Juslin, B.D.Wirth, J. Nucl. Mater. 432(2013)61.
[6] D. A. Trentyev, L. Malerba, M. Hou, Phys. Rev. B 75 (2007) 104108.
[7] M.J. Norgett, M.T. Robinson, I.M. Torrens, Nucl. Eng. Des. 33 (1975) 50.

8.4 INTERACTION OF INTERSTITIAL CLUSTERS WITH RHENIUM, OSMIUM, AND TANTALUM IN TUNGSTEN

W. Setyawan, G. Nandipati, and R. J. Kurtz (Pacific Northwest National Laboratory)

OBJECTIVE

The objective of this research is to develop a database of binding energies of interstitial clusters in tungsten to solid transmutation products including Re, Os, and Ta. The database will be used to inform kinetic Monte Carlo simulations of damage accumulation and defect microstructure evolution in bulk tungsten under fusion neutron irradiation.

SUMMARY

In the previous semi annual report [1], we explored the stability of interstitial clusters in W up to size seven. In this report, we study the binding of those clusters to Re, Os, and Ta atoms. For each cluster size, the three most stable configurations are considered to average the binding property. The average binding energy to a Re decreases from 0.79 eV for a size-1 cluster (a [111] dumbbell) to 0.65 eV for a size-7 cluster. For Os, the binding decreases from 1.61 eV for a [111] dumbbell to 1.34 eV for a size-7 cluster. Tantalum is repulsive to interstitial clusters with binding energy ranges from -0.61 eV for a [111] dumbbell to -0.5 eV for a size-7 cluster.

PROGRESS AND STATUS

VASP [2, 3] was used to perform the quantum calculations within the density functional theory (DFT) framework. Core electrons are modeled with accurate projector-augmented-wave pseudopotentials [3]. Electrons in 6s and 5d states are treated as valence electrons. Perdew-Burke-Ernzerhof formulations [4] were employed for the exchange-correlation functionals. Defect formation energies were calculated using cubic 5x5x5 supercells of tungsten's bcc unit cell. The coordinates of atoms and box volume are optimized while maintaining cubic symmetry. In relaxed configurations, the forces are < 0.025 eV/Å and the external pressure < 0.5 kbar. At the end of the relaxations, a static calculation was performed to eliminate errors due to basis incompleteness associated with changes in the simulation cell. A convergence study of the defect formation energies of [111], [110], and [100] dumbbells was performed with respect to the energy cutoff (ENCUT) for the plane waves up to 500 eV. An energy cutoff of 250 eV was found to be sufficient to converge the formation energies to within 20 meV. Therefore, all subsequent calculations were performed with ENCUT = 250 eV.

In our previous study of self-interstitial atom (SIA) clusters, a Monkhorst-Pack [5] k-points grid of 3x3x3 was used. Since then, we perform the convergence study with respect to the k-points grid. We find that a 5x5x5 or denser grid is necessary to converge the formation energy of dumbbells to within 20 meV. Results presented in this report are obtained with the 5x5x5 grid. Table 1 shows the formation energy of [111], [110], and [100] dumbbells, mixed dumbbells, and substitutional solutes. Table 2 shows the binding energy of a size-*n* SIA cluster corresponding to an $n \rightarrow (n-1) + 1$ reaction in which the configuration for the (n-1) resultant cluster is taken to be the most stable configuration for a size-(n-1) cluster.

Table 1. Formation energies of Ta-W, W-W, Re-W, and Os-W dumbells in the [111], [110], and [100] orientations, as well as the formation energies of a substitutional Ta, Re, or Os, and a vacancy in W. All energies are in eV. Values in bold are the formation energies corresponding to the most stable orientation of these dumbbells. Note that the Ta-W [100] dumbbell instantaneously relaxes to a W-W [100] dumbbell and a substitutional Ta.

	Ta-W	W-W	Re-W	Os-W
111	**10.04**	**9.90**	9.27	9.02
110	10.46	10.16	**9.21**	**8.68**
100	11.62	11.92	11.20	10.84
Substitutional	-0.46	N/A	0.17	0.74
Vacancy	N/A	3.17	N/A	N/A

Table 2. Binding energy of a size-*n* cluster corresponding to an *n* → (*n*-1) + 1 reaction. All energies are in eV. The results for the three most stable (1st, 2nd, and 3rd) configurations are presented.

n	1st	2nd	3rd	Average
2	2.49	2.46	1.99	2.31
3	3.64	3.08	2.52	3.08
4	4.69	4.59	3.34	4.21
5	4.74	3.83	3.56	4.04
6	5.41	5.06	4.89	5.12
7	6.74	5.20	5.17	5.70

When an SIA binds to a substitutional solute positioned along its migration path, it forms a mixed dumbbell. Thus, in a mixed dumbbell, the solute atom adopts an interstitial position. Similar to the case of an SIA, when an SIA cluster binds to a substitutional solute located along its migration path, the solute adopts an interstitial site and becomes part of the dumbbell atoms. Therefore, the binding property of SIA clusters with a substitutional solute is studied by replacing one of the conjugate atoms with Re, Os, or Ta. Conjugate atoms are those initially at lattice sites but now sharing the sites with SIAs as dumbbells. Three of the most stable clusters for each cluster size are considered and their binding with a solute atom is explored. From these three clusters, the minimum, maximum, and average binding energies are calculated. The results are presented in Table 3.

Table 3. Binding energy of size-*n* SIA clusters to a substitutional solute obtained by replacing one of the dumbbell atoms with the solute. The minimum, maximum, and average values are in eV and calculated from the three most stable configurations.

n	Re			Os			Ta		
	Min	Max	Ave	Min	Max	Ave	Min	Max	Ave
1	0.79	0.79	0.79	1.61	1.61	1.61	-0.61	-0.61	-0.61
2	0.71	0.82	0.77	1.61	1.69	1.67	-0.72	-0.57	-0.62
3	0.63	0.88	0.76	1.35	1.79	1.57	-0.65	-0.49	-0.59
4	0.66	0.80	0.75	1.40	1.63	1.54	-0.64	-0.51	-0.58
5	0.53	0.77	0.71	1.11	1.59	1.45	-0.62	-0.39	-0.56
6	0.53	0.75	0.68	1.08	1.52	1.41	-0.59	-0.41	-0.53
7	0.41	0.75	0.65	0.81	1.51	1.34	-0.58	-0.35	-0.50

Further simulations to correct for the size effect of the cell are currently in progress. Final results will be presented in Ref [6].

In the meantime, we analyze the interpolation of the binding energy data towards larger clusters. The interpolation is based on the analytical expression of the formation energy $E_f(n)$ of a size-*n* dislocation loop [7, 8]:

$$E_f(n) = a\sqrt{n} + b\sqrt{n}\ln(n) \tag{1}$$

This leads to the binding energy formula:

$$E_b(n) \equiv E_f(1) + E_f(n-1) - E_f(n) \tag{2}$$

$$E_b(n) = E_f(1) - a\left(\sqrt{n} - \sqrt{n-1}\right) - b(\sqrt{n}\ln(n) - \sqrt{n-1}\ln(n-1)) \tag{3}$$

Setting $n = 1$ in Equation (1) yields $a = E_f(1)$, and using $n = 2$ in Equation (3) to solve for *b* leads to the following equations:

$$b = \frac{(2-\sqrt{2})E_f(1) - E_b(2)}{\sqrt{2}\ln(2)} \tag{4}$$

$$E_b(n) = E_f(1) - E_f(1)\left(\sqrt{n} - \sqrt{n-1}\right) - \left[\frac{(2-\sqrt{2})E_f(1) - E_b(2)}{\sqrt{2}\ln(2)}\right]\left(\sqrt{n}\ln(n) - \sqrt{n-1}\ln(n-1)\right) \tag{5}$$

where the formation energy for a [111] dumbbell is $E_f(1) = 9.90$ eV and the average binding energy for a size-2 cluster is $E_b(2) = 2.31$ eV. Figure 1 shows the minimum, maximum, and average binding energy of SIA clusters with respect to an $n \rightarrow (n\text{-}1) + 1$ reaction, as well as the interpolation model of Equation (5). For $n \rightarrow \infty$**,** the binding energy approaches the formation energy of a [111] dumbbell.

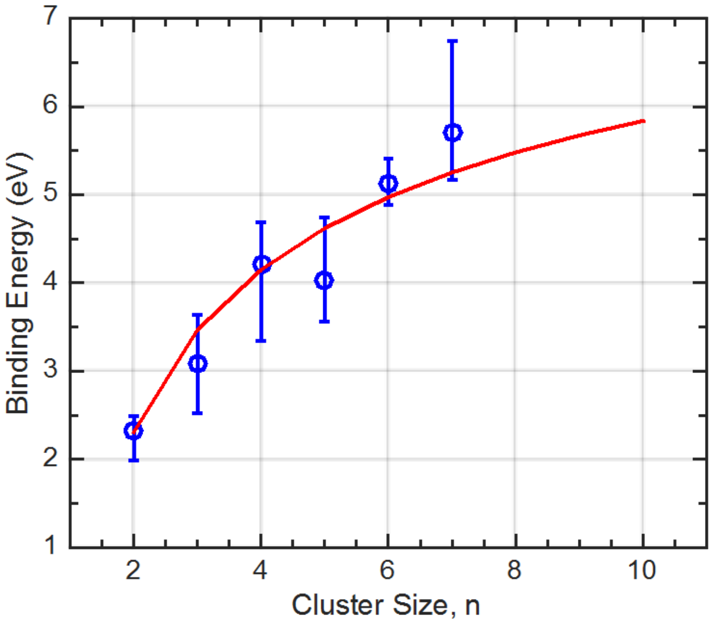

Figure 1. Binding energy of size-*n* SIA clusters with respect to an $n \rightarrow (n\text{-}1) + 1$ reaction. For this work, the average value over the three most stable clusters is plotted with the tic marks above and below the average values representing the maximum and the minimum values. Interpolation curve for large n is based on the formula $E_b(n) = 9.90 - 9.90\left(\sqrt{n} - \sqrt{n-1}\right) - \left[\frac{(2-\sqrt{2})9.90-2.31}{\sqrt{2}\ ln(2)}\right]\left(\sqrt{n}\ln(n) - \sqrt{n-1}\ln(n-1)\right)$.

To find the interpolation function for the solute's binding energy to SIA clusters ($E_{bs}(n)$), we assume that the effect of the solute in changing the charge density in the matrix is screened as a function of distance (r) from the solute similar to a screened coulomb interaction, i.e. $\sim\frac{\exp(-\alpha r)}{r}$. This implies that for an infinitely large cluster, the difference between the formation energy of an SIA cluster ($E_f(n)$) and the formation energy of an SIA cluster with a solute atom bound to it ($E_{fs}(n)$) approaches a constant value, say Δ_f. With this assumption, we may write for a loop with a radius r or size n:

$$E_f(r) - E_{fs}(r) = \Delta_f + \frac{c'\exp(-\alpha' r)}{r} \tag{6}$$

$$E_f(n) - E_{fs}(n) = \Delta_f + \frac{c\,\exp(-\alpha\sqrt{n})}{\sqrt{n}} \tag{7}$$

Then the solute's binding energy is given by

$$E_{bs}(n) = E_{sub} + E_f(n) - E_{fs}(n) = E_{sub} + \Delta_f + \frac{c\,\exp(-\alpha\sqrt{n})}{\sqrt{n}} \tag{8}$$

Where E_{sub} is the solute's substitutional formation energy. The values for Δ_f, c, and α are fitted and presented in Table 4. The solute's binding energy and the interpolation curve based on Equation (8) are shown in Figure 2.

Table 4. Fit results of the average binding energy, over the three most stable clusters, of SIAs to a substitutional solute, calculated with Equation (8), where E_{sub} is the formation energy of a substitutional solute, while Δ_f, c, and α are the fitting parameters.

	Re	Os	Ta
E_{sub} (eV)	0.17	0.74	-0.46
Δ_f (eV)	0.448	0.535	-0.021
c	0.195	0.416	-0.155
α	0.0014	0.0012	0.0011
R^2 of the fit	0.69	0.60	0.62

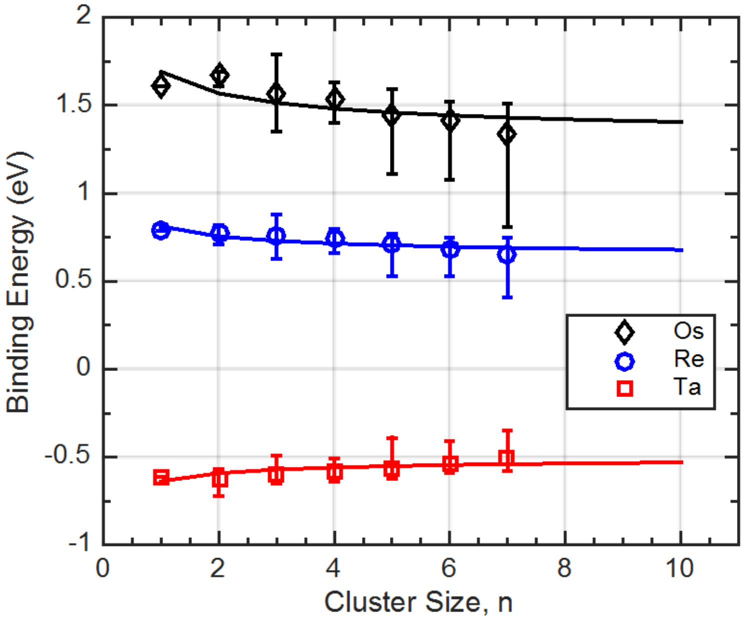

Figure 2. Binding energy of size-*n* SIA clusters to a Re, Os, or Ta atom substitutionally replacing one of the W dumbbell atoms. The data points represent the average over the three most stable clusters. The tic marks represent the maximum and minimum values. Interpolation curves for large n are based on the formula given in Equation (8) with the fitting parameters given in Table 4.

Acknowledgement

This research has been supported by the U.S. Department of Energy, Office of Science, Office of Fusion Energy Sciences (DE-AC06-76RL0-1830).

References

[1] W. Setyawan, G. Nandipati, R. J. Kurtz, Stability of small self-interstitial clusters in tungsten, in Fusion Reactor Material Program Semiannual Progress Report 59 (2015) 130.
[2] P. E. Blöchl, Physical Review B 50 (1994) 17953.
[3] G. Kresse and D. Joubert, Physical Review B 59 (1999) 1758.
[4] J. P. Perdew, K. Burke and M. Ernzerhof, Physical Review Letters 77 (1996) 3865.
[5] H. J. Monkhorst and J. D. Pack, Physical Review B 13 (1976) 5188.
[6] W. Setyawan, G. Nandipati, R. J. Kurtz, Ab initio study of interstitial cluster interaction with Re, Os, and Ta in W, Journal of Nuclear Materials, to be submitted.
[7] L. Dudarev, R. Bullough, P. M. Derlet, Physical Review Letters 100 (2008) 135503.
[8] D. J. Bacon, R. Bullough, J. R. Willis, Philosophical Magazine 22 (1970) 31.

9. FUSION SYSTEM DESIGN

9.1 MULTI-PHYSICS DESIGN OF THE FIRST WALL AND BLANKET SYSTEM IN THE FUSION NUCLEAR SCIENCE FACILITY (FNSF)—Yue Huang, Nasr Ghoniem, Mark Tillack, Jake Blanchard, Laila El-Guebaly, Chuck Kessel

SUMMARY

The dual coolant lead-lithium (DCLL) blanket concept is based on a helium-cooled first wall and blanket structure with RAFS (Reduced Activation Ferritic Steel) and a self-cooled LiPb breeding zone. 3D finite element multiphysics modeling of the DCLL first wall and blanket has been performed using *COMSOL 5.0.* The multiphysics aspect of the design is demonstrated via coupling of fluid dynamics, conjugate heat transfer and solid mechanics modules within the COMSOL. The results of primary and thermal stress of the structure were obtained. This was followed by determination of the factors of safety along three critical paths based on the ITER Structural Design Criteria for In-vessel Components (ISDC-IC). We show that the structural design meets the design rules under both normal and off-normal operating conditions, though the safety factors under off-normal condition are marginal. Thus simple design optimization was conducted based on a parametric study on first wall dimensions to improve the design.

PROGRESS AND STATUS

Approach

Three major multiphysics modules have been coupled in the current design. These are: Non-isothermal Fluid Flow, Conjugate Heat Transfer, and Solid Mechanics. The Non-isothermal Fluid module was used to simulate helium flow inside cooling channels. CFD simulations were based on k-epsilon turbulent flow model. The temperature and pressure distributions of the helium coolant can be obtained in this module. The “Conjugate Heat Transfer” module was used to compute the temperature distributions of the blanket RAFS structure. Both the surface heat flux on the FW and volumetric heating rates were considered. The “Solid Mechanics” module was used to compute the stress distributions in the structure. The primary stress is due to the pressurization of fluid flow (helium in FW, BW and stiffening plates, and PbLi in the FCI channels). Thus the pressure distribution results from CFD simulation were used as boundary condition for stress analysis. To calculate secondary (thermal) stress, it is necessary to couple heat transfer, CFD and stress analyses. The basic simulation process is shown in Fig. 1.

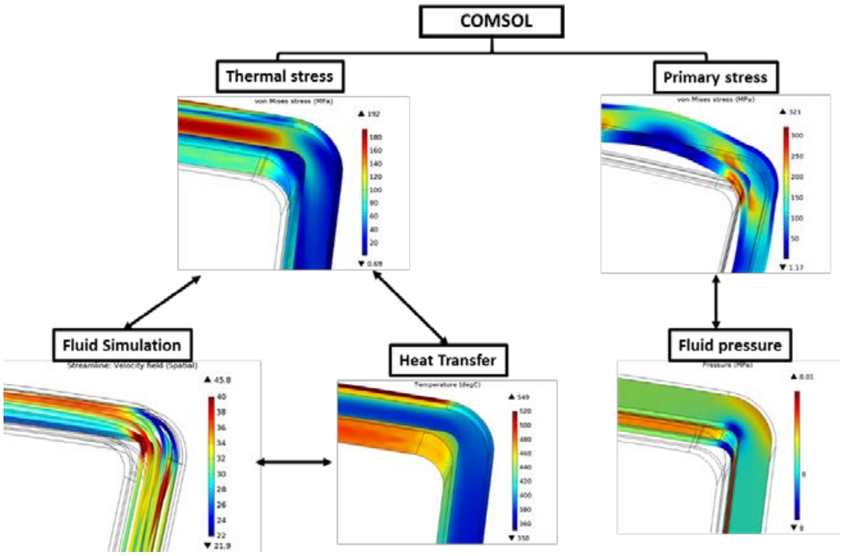

Figure 1. Summary of the multiphysics simulation process sequence.

We consider in the present design three possible scenarios; two of them are operational, and one is unlikely and requires plant interruption. These design basis scenarios are summarized in Table 1 [1]. One of the critical regions would be any breeder cell that is over-pressurized beyond the normal design basis. In the SDC-IC level A (normal operations), breeding cells would experience 1.6 MPa LiPb pressure, while an internal LOCA will lead to the off-normal condition with a pressure of helium pressure [2]. We will consider both "normal' and "upset" design conditions here.

Table 1. SDC-IC criteria levels vs. loading categories

Loading Category	**Category Conditions (Damage limits)**	**SDC-IC Criteria Level**	**Incidents**
I Operational Loading	Normal	A	Normal Condition: P_{LiPb}=1.6MPa
II Likely Loading	Upset	A	Off-normal Condition: (1) LOCA, $P_{LiPb}= P_{He}$ (2) Minor plasma disruptions
III Unlikely Loading	Emergency	C	Major plasma destruction (Inspection and repair is required)

Results

Helium Flow

As Figure 2 shows, helium flow velocity should be at least 30 m/s under 8 MPa operating pressure and 48 m/s under 5 MPa to maintain the steel structure temperature below the limit. It is clear that we need to pay for higher pumping power to reduce the operating pressure. The streamlines of helium flow with velocity magnitude are shown in Figure 3 (with pressure of 8 MPa and inlet velocity of 30 m/s).

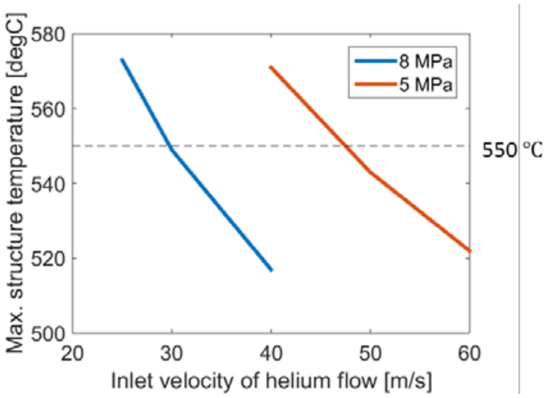

Figure 2. Max. structure temperature v.s. inlet velocity.

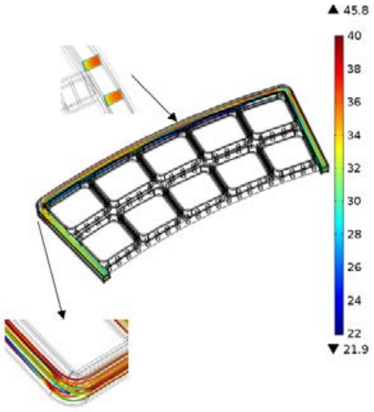

Figure 3. Streamlines of helium flow.

Temperature distribution of the solid structure

The result of the temperature distribution is shown in Figure 4. The maximum temperature of the LiPb is around 660 ℃ at the mid-plane. In the present simulations, the heat transfer coefficient was not assumed, but rather calculated as a result of the fluid flow and heat transfer simulations. Ribs and grooves need to be manufactured inside the cooling channels to enhance wall heat transfer. The side effect is that a much higher pressure drop in flow channels will occur. In the simulation, a correlation factor was introduced to account for the cooling enhancement due to the wall roughness.

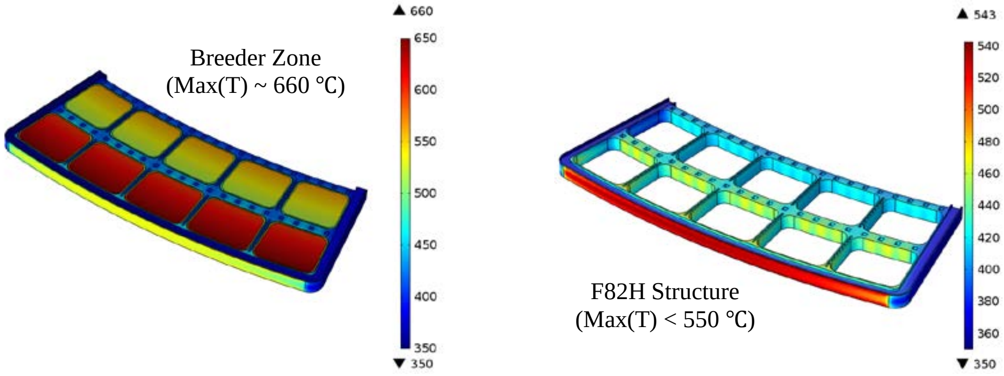

(a) Breeding zone (b) Blanket structure

Figure 4. Temperature distributions of the global FW/B structure.

By controlling the inlet velocity of the helium, the maximum temperature of steel structure can be maintained below the limit. Even with the operating pressure of 5 MPa, only 50 m/s is required. The result reveals that tubulent flow together with roughing the channel wall can lead to effective cooling.

Primary stress

The following results shown in the figures below are based on normal operating conditions with helium pressure of 8 MPa. Results of other cases (like under off-normal conditions or with a pressure of 5 MPa) are listed in Table 2-5. Figure 5 shows the global primary stress distribution of the blanket structure. There are stress concentrations at the junctions and corners. After rounding and adding fillets to junction zones, the stress concentation was reduced to about 320 MPa. Deformation of the structure resulting from the primary stress was also obtained, as shown in Figure 6.

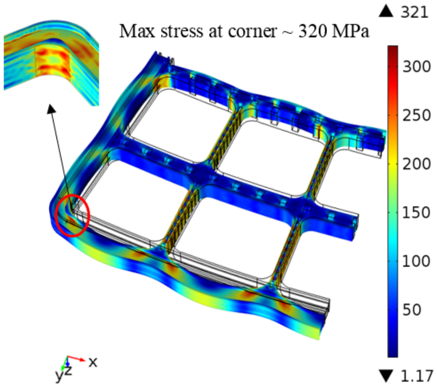

Figure 5. Primary stress distribution (Von-Mises stress).

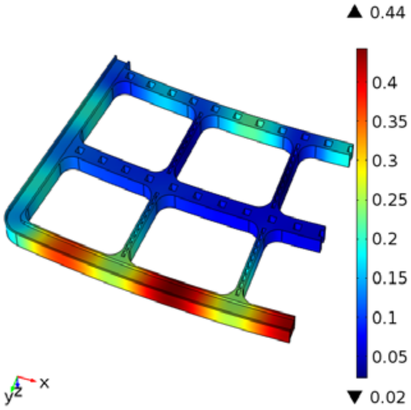

Figure 6. Displacement distribution due to the primary stress.

Thermal stress

Thermal stress was calculated based on the temperature obtained from coupled heat transfer and CFD analyses. As illustrated in Figure 7, the first wall has the largest thermal stress, although a directionally-alternating cooling channel layout has already reduced severe temperature gradients. Also, thermal expansion is shown in Figure 8, illustrating the reason why we need to leave a gap of at least 2 cm between adjacent sectors during assembly to accommodate thermal expansion.

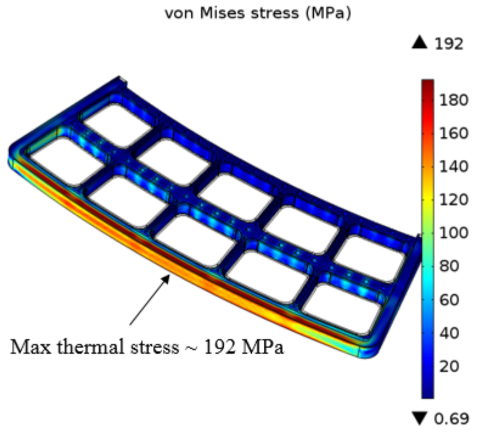

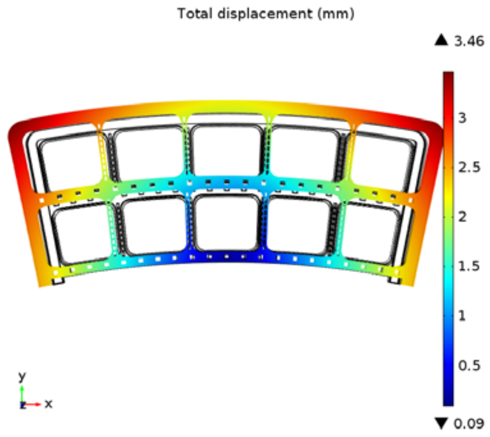

Figure 7. Thermal stress distribution.

Figure 8. Thermal expansion.

Design Factors of Safety

Line integration through the thickness of the structure is used to resolve stresses into membrane, bending and non-linear components. The membrane stress tensor has components that are equal to the mean value of stresses through the thickness. The bending stress tensor has components that vary linearly through the thickness and which, when integrated through the thickness result in equilibrium with the section moment [3]. The line along which this integration is carried out is defined as "a supporting line segment." Three supporting line segments were selected as critical paths to determine the design safety factors, as shown in Figure 9 (the result in Figure 9 is under off-normal condition).

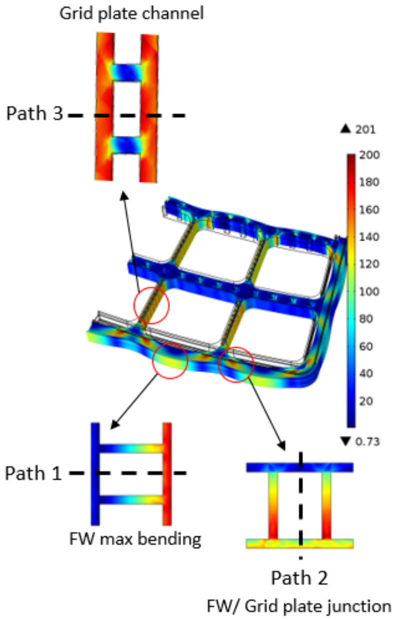

Figure 9. Critical supporting line segments.

With the results of the primary and thermal stresses, factors of safety were determined based on the three different allowable values and the low temperature design criteria. The results are shown in Table 2-5. For reference on the mechanical design procedure, including stress intensity parameters and design criteria, please see reference [4].

Table 2. Factors of safety based on necking and plastic instability limit

$\overline{P_m + P_b} \leq 1.5S_m$						
	5 MPa			8 MPa		
Path	$1.5S_m$[MPa]	Normal	Off-normal	$1.5S_m$[MPa]	Normal	Off-normal
1	205.1	4.6	1.7	203.1	4.0	**1.1**
2	206.0	4.3	1.7	204.2	3.7	**1.0**
3	228.5	5.8	2.0	228.5	5.4	**1.3**

Table 3. Factors of safety based on $3S_m$ criteria

$\overline{P + Q} \leq 3S_m$						
	5 MPa			8 MPa		
Path	$3S_m$[MPa]	Normal	Off-normal	$3S_m$[MPa]	Normal	Off-normal
1	410.1	3.4	4.7	406.2	3.8	3.1
2	411.9	2.6	2.3	408.3	2.4	2.0
3	456.9	9.2	2.6	456.9	8.3	1.6

Table 4. Factors of safety based on plastic flow localization limit

$\overline{P_m + Q} \leq S_e$						
	5 MPa			8 MPa		
Path	S_e[MPa]	Normal	Off-normal	S_e[MPa]	Normal	Off-normal
1	192.8	7.9	3.8	191.1	6.3	2.4
2	193.8	6.5	3.6	192.1	5.3	2.3
3	214.9	6.3	2.0	214.9	6.0	1.2

Table 5. Factors of safety based on ductility exhaustion limit

$\overline{P_m + P_B + Q} \leq S_d$						
	5 MPa			8 MPa		
Path	S_d[MPa]	Normal	Off-normal	S_m[MPa]	Normal	Off-normal
1	385.6	4.2	4.5	382.2	4.3	3.2
2	387.5	2.9	2.4	384.2	3.0	2.1
3	429.8	8.3	3.5	429.7	8.0	2.3

The current results indicate that structure, under normal operating conditions, meets all design criteria, while the safety factors under off-normal operating conditions are marginal. Therefore, it is recommended that further design optimization and parametric analyses be conducted.

Design optimization

To reduce the stress at critical regions, one possible solution is to add more stiffening plates. However, the design with more stiffening plates has too much steel and results in tritium breeding concerns. Thus we focused on finding a solution by adjusting the dimension or configuration of the first wall channel design. Additional to the original design, another two configurations, as Figure 10 shows, were investigated with detailed stress analyses. Configuration B retains the total thickness of the first wall panel (3.8 cm), but varies the thickness of the first wall. For configuration C, the wall thickness remains unchanged while varying the helium channel thickness.

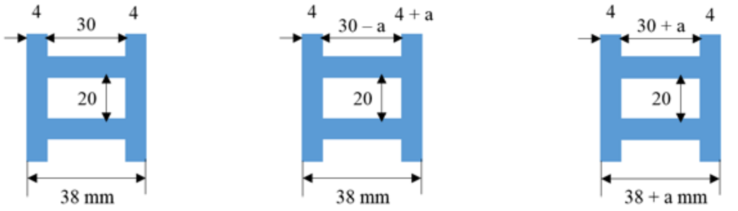

A. Reference Design B. Vary first wall thickness C. Vary He channel thickness

Figure 10. First wall configurations.

Parametric study on parameter a, which is the variation of the first wall thickness for configuration B or helium channel thickness for configuration C, was performed. The factors of safety results listed above show that the design criteria based on allowable primary membrane stress intensity S_m is the critical one. Thus only factors of safety based on the first design criteria were calculated for both configuration B and C with different values of parameter *a* to figure out the best solution. The results are shown in Figure 11. The dashed lines show the design limit. Increasing either the first wall thickness or helium channel thickness can help reduce the primary stress. It gives us the potential to optimize the first wall dimensions to accommodate more severe loading conditions.

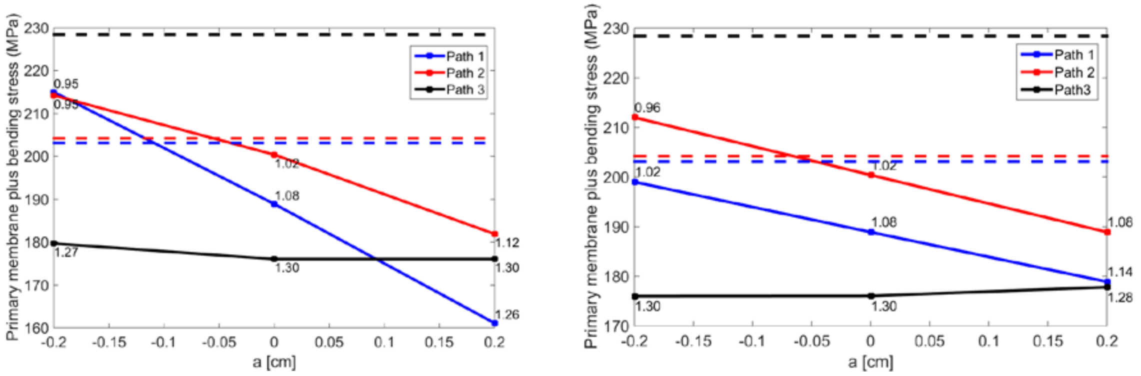

(a) Configuration B (b) Confiruation C

Figure 11. Parametric study of first wall dimensions.

Acknowledgements

This work is supported by the U.S. Department of Energy, Office of Science, Office of Fusion Energy Sciences, under Award Number DE-FG02-03ER54708. The authors would like to acknowledge the contribution of Edward Marriott and Siegfried Malang in providing basic information for the FNSF FW/Blanket system.

References

[1] ITER Structural Design Criteria for In-vessel Components, ITER Doc. G 74 MA 8 01-05-28 W0.2, 1996
[2] Wang, X. R., et al. "ARIES-ACT2 DCLL Power Core Design and Engineering."*Fusion Science and Technology* 67.1 (2015): 11.

[3] Sharafat, Shahram, Aaron T. Aoyama, and Nasr Ghoniem. "Assessment of the DCLL TBM Thermostructural Response Based on ITER Design Criteria." *Fusion Science and Technology* 60.1 (2011): 264-271.
[4] ITER Structural Design Criteria for In-vessel Components, ITER Doc. G 74 MA 8 01-05-28 W0.2, 1996

10. IRRADIATION METHODS, EXPERIMENTS AND SCHEDULES

10.1 MINIATURE MECHANICAL TEST DEVELOPMENT FOR TUNGSTEN-BASED MATERIALS—

L. M. Garrison (Oak Ridge National Laboratory), Jeremy Moon (University of Nevada-Reno), Joseph Willenborg (University of Tennessee-Knoxville)

OBJECTIVE

The aim of this work is to develop miniature mechanical test methods that can be used to evaluate neutron-irradiated tungsten and tungsten composite samples in LAMDA.

SUMMARY

Many tungsten based composites employ tungsten foils or tungsten fibers. Understanding the mechanical properties of the composite also requires understanding the mechanical properties of the constituent elements of the composite. While certain miniaturized mechanical tests, such as tensile testing SSJ size samples, is routinely accomplished in LAMDA, the requirements for testing foils and fibers is beyond the current capabilities in the laboratory. Three mechanical tests are being developed for the foils and fibers: a) shear punch test for foils, b) 3-point bend test for foils, and c) tensile test for fibers.

PROGRESS AND STATUS

Shear Punch Tests

Although a specialized clamping fixture was previously designed and fabricated for tensile testing foils, there was large scatter in the tensile data because the foils are especially sensitive to any surface defect in the gauge section and to any slight misalignment in the fixture. Shear punching is a mechanical test that is less sensitive to sample alignment or edge effects, so is well suited for the foils. Additionally, correlations can be built between the shear yield stress and the tensile yield stress. Therefore, beyond the foils, the shear punch test can be used to estimate the tensile properties of irradiated materials for which there is too small a volume available for tensile testing.

Three thicknesses of cold rolled tungsten foils and three thicknesses of grade 92 steel sheet were tested using a custom shear punch fixture with a punch diameter of 1 mm and a die diameter of 1.6 mm. The tungsten foils were 25, 100, and 250 μm thick, and the steel samples were approximately 80, 100, and 250 μm thick. Ten samples of each thickness were tested to failure at a loading rate of 0.08 mm/min.

Shear stress was calculated by Equation 1

$$\tau = \frac{F}{2\pi r t} \quad (1)$$

where τ is the shear stress, F is the force measured by the testing frame, r is the average radius of the punch and die, and t is the thickness of the sample. The x-axis in shear punch data is often represented as the normalized displacement, δ:

$$\delta = \frac{d}{t} \quad (2)$$

where d is the displacement of the punch and t is the sample thickness. The data is more accurate if the displacement can be measured independently by a linear variable differential transformer (LVDT), but for these tests the displacement is the cross-head displacement. To determine the shear yield strength, an offset of the normalized displacement of 0.01 was used. The uniform elongation (UE) and total elongation (TE) are calculated as the normalized displacement up to the ultimate shear strength (USS) and failure point, respectively.

Preliminary results indicate that, for the tungsten foils, only the 100 μm foil exhibited appreciable plastic deformation. The 25 μm samples failed with so little plastic extension that normal method of extracting the retained plastic deformation did not function properly. All thicknesses of the steel were ductile. Certain material thicknesses had a large spread in the data, and this is being investigated. Further analysis of the tests is ongoing.

Table 1. Summary of shear properties for tungsten and steel foils averaged over ten tests per material

	Thickness (µm)	YS (MPa)	USS (MPa)	UE (mm/mm)	TE (mm/mm)	
Steel	80	186	313	0.53	0.70	Average
		27	31	0.076	0.079	Std. deviation
	100	202	337	0.66	0.87	Average
		20	4.2	0.12	0.092	Std. deviation
	200	329	417	0.43	0.66	Average
		8	10	0.044	0.048	Std. deviation
W	25	463	471	0.025	0.043	Average
		14	16	0.016	0.025	Std. deviation
	100	456	645	0.69	1.16	Average
		26	39	0.14	0.14	Std. deviation
	250	624	646	0.025	0.028	Average
		19	17	0.011	0.011	Std. deviation

Although the shear punch test is useful for testing foils, it is not limited to this task. It has also thus far been used to test tungsten-steel composite samples and tungsten-copper sintered composite samples. Testing a variety of materials will allow a master curve between shear yield strength and tensile yield strength to be developed for the particular testing geometry used in LAMDA. Once this relation is obtained, it will be possible to estimate tensile properties of materials from shear-punch data.

Three-point Bend Tests

Rectangular-shaped 16 x 4 x 0.1 mm tungsten foils in the as-rolled and annealed condition were irradiated as part of the TITAN program. Tungsten foils from the same batch were also used to fabricate the tungsten-copper laminate composites. The behavior of the tungsten foils dominates the behavior of the tungsten-copper laminate composite, so it is necessary to understand changes in mechanical properties and microstructures of the foils during irradiation. Currently, the only mechanical test that can be used to evaluate the mechanical properties of the foils in LAMDA is microhardness, which gives only a limited understanding of the mechanical properties. The irradiated foils cannot be machined into tensile samples, so shear punch tests will be used to infer their tensile properties. Additionally, a suitable three-point bend test is being developed.

A three-point bend testing procedure based on ASTM E855, “Standard Test Methods for Bend Testing of Metallic Flat Materials for Spring Applications Involving Static Loading”, was developed to test small tungsten foil samples measuring 16 x 4 x 0.1 mm. To accommodate the unusually small size of the samples, the span of the test fixture was decreased from 15 mm specified by the standard for 100 µm thick samples, to 10 mm. This span will allow for a sufficient envelope of deflection to characterize plastic deformation in bending. Three-point bend testing was selected over four-point bend testing because it is expected that the unirradiated foils will be ductile, so a concentrated point load and maximum angle of bending is desired, a condition favoring the three-point bend test. Furthermore, simplicity of the fixture will reduce set-up time and thus worker dose for irradiated samples. A custom three-point bend fixture and load applicator was developed for the 10 mm span, with the remainder of the dimensions of the fixture and load applicator being in accordance with the ASTM standard (Figure 1). The fixture was fabricated from Inconel alloy so that it is suitable for testing irradiated and unirradiated samples at temperatures up to 1000 °C. The bend test fixture and load applicator are currently being machined and initial tests will be conducted when it is received.

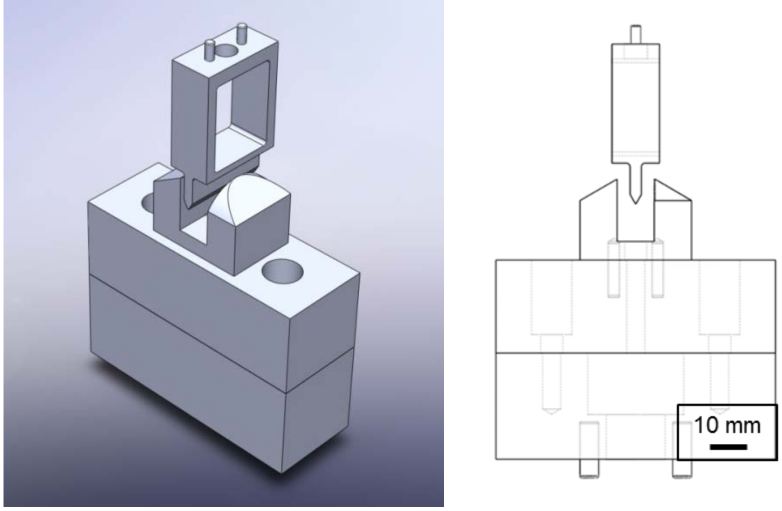

Figure 1. Design of custom three-point bend fixture for miniature tungsten foils.

Fiber Tensile Tests

Recent studies have shown that including cold worked tungsten fibers within a tungsten matrix may increase ductility and fracture toughness as compared to bulk tungsten material. Since energy dissipation in tungsten fiber-tungsten (W_f-W) composites is a purely mechanical process, additional irradiation embrittlement may not be as detrimental as for non-composite tungsten. However, understanding of W_f-W composites is limited and irradiated experiments have not been conducted. To expand the understanding of W_f-W composites, axial tensile tests of short tungsten fibers in irradiated and unirradiated conditions will be conducted. Tungsten fibers, 150 µm diameter and 36-40 mm long, are included in the PHENIX collaboration RB* 19J capsule that is currently being irradiated in HFIR.

The test methods developed here were based on the Standard Test Method for Tensile Strength and Young's Modulus of Fibers, ASTM C1557. A strain rate of 5 µm/s was chosen based on "Development of tungsten fibre-reinforced tungsten composites towards their use in DEMO—potassium doped tungsten wire" by Riesch et al. (2016) who also tested 150 µm diameter tungsten fibers. This strain rate is also in the range suggested by ASTM C1557 which recommends starting with 8 µm/s for a fiber of this length and then adjusting the rate such that the elastic region is completed within 30 s. The rate of 5 µm/s met this criteria and is thus a valid strain rate.

Two separate methods were investigated to fasten the fibers for the tensile tests. Any method used must provide enough strength for the fiber during the tensile test without putting stress concentrators on the fiber. Additionally, the method must be applicable to radioactive fibers. The first method chosen, which is suggested in ASTM C1557 was to attach each end of the 36-40 mm fiber inside a needle using Araldite A-B 5minute epoxy. The process of sample preparation included mixing epoxy in the syringe and pumping epoxy through one needle tip (Figure 2a), inserting the fiber, allowing to dry on the alignment fixture (Figure 2b), then repeating with second needle and placing in alignment fixture (Figure 2c).

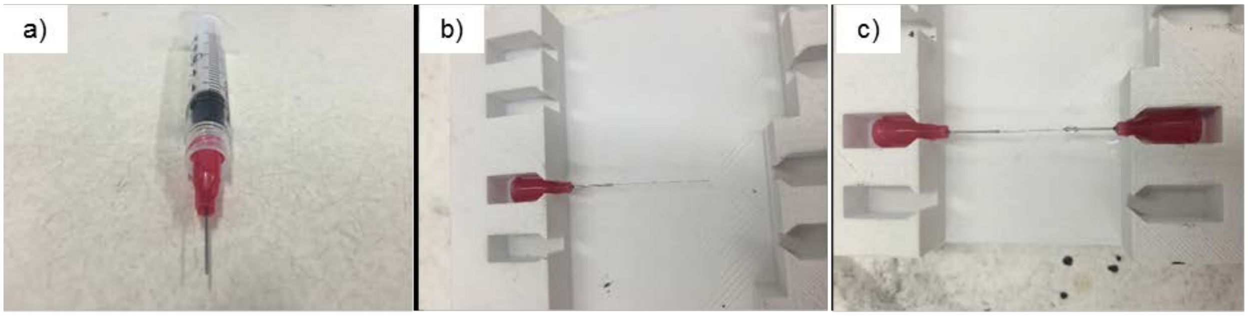

Figure 2. The procedure for preparing fibers for tensile testing. a) epoxy is pumped into a needle, b) one end of the fiber is inserted into the epoxy-filled needle and allowed to dry, c) the procedure is repeated for the other side of the fiber.

An alignment plate was designed and 3-D printed to allow for consistent production of samples that were aligned correctly and of proper length. The alignment fixture has slots for four different gauge lengths (Figure 3a). For the tensile tests, a custom fixture was also 3D printed such that the tensile force is applied to the needles which contain the fibers (Figure 3b-c).

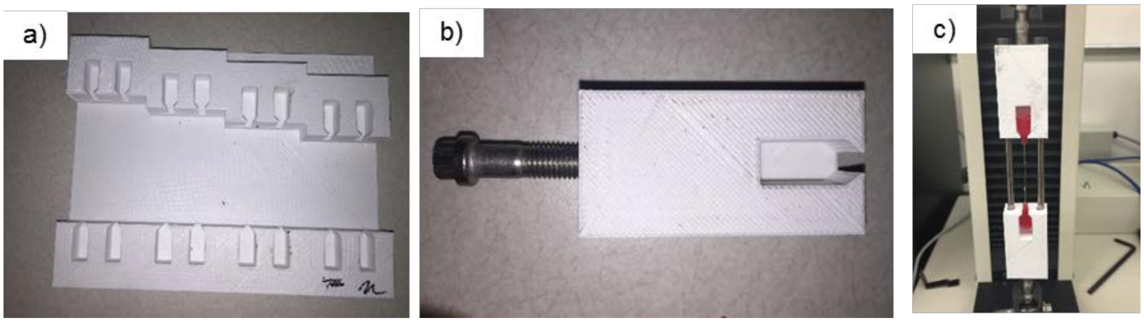

Figure 3. a) The 3D printed alignment plate b) Two brackets were 3-D printed that hold the needles in place and connect to the standard MTS tensile frame. c) W fiber in needles (red) within custom tensile fixture on tensile frame.

The advantages of this method included minimal stress, consistency in aligning the fiber, and regularity in the amount of epoxy applied to each sample. Concern about the brittleness of irradiated samples was the driving factor for selecting this method. It is assumed that the tungsten fibers will be brittle after irradiation which eliminates many methods with more direct application of force. Initial tests with the Araldite A-B 5minute epoxy proved ineffective as pullout occurred in each case after an extensive region of elastic deformation due to insufficient adhesion between the fiber and the epoxy. To combat this problem, higher Young's modulus epoxy was purchased to limit the amount of elasticity. It then became clear that the adhesive strength was the limiting factor since the fiber would slowly pull-out from the epoxy with no epoxy remaining on the fiber as determined by microscopy. As a result, a highly adhesive epoxy was then used, but was still inadequate and resulted in similar pull-out. Fiber and needle surfaces were also sanded and degreased to maximize bond strength. Unfortunately, despite many iterations of incremental improvement, it was determined that the tungsten fibers were stronger than the bond that could be formed with any of the available epoxies.

In a second method, each end of the fiber was mechanically clamped in a metal fixture (Figure 4) that had been developed at ORNL to test small SSJ shaped foil tensile samples. Although not designed for fibers, this method was attempted as a way to determine if enough force could be applied to the tungsten fibers to cause them to fail before pull-out. If successful, it would then be possible to optimize the fixture for fibers and reduce the stress concentration. To use the SSJ fixture for fibers, the fiber was placed inside the SSJ area (Figure 5a). Then, the clamps were tightened into place (Figure 5b). In this condition, the fixture can be attached to the tensile frame (Figure 5c).

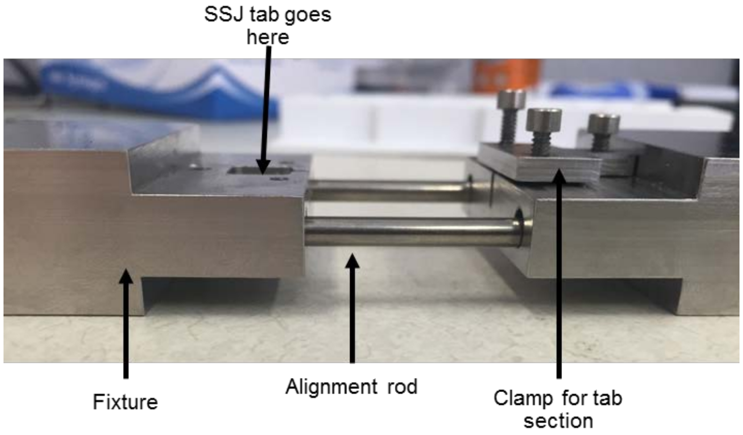

Figure 4. SSJ test fixture designed for clamping tungsten foil samples.

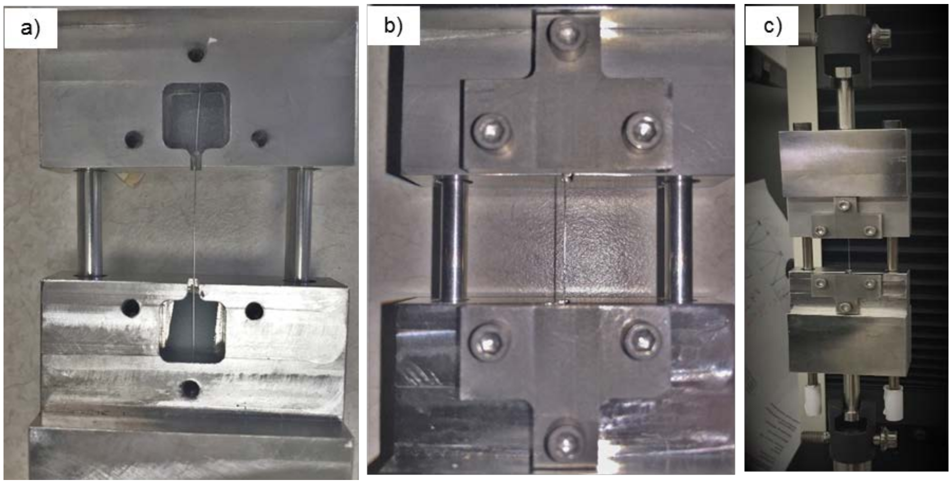

Figure 5. a) Fiber placed inside the cut-out within the fixture. b) Clamps are screwed down to hold the fiber in place. c) Fixture is placed in MTS tensile frame where tensile force is applied.

By screwing the clamp directly onto the fiber, this method was able to apply enough force to prevent the sample from pulling out of the fixture. However, some modifications of the fixture or additional material are necessary to minimize stress concentrators. So far, all trials clamped directly onto the fiber have broken near or within the clamped portion and are thus unreliable. Some improvement has been observed by inserting notecard pieces in between the fiber and fixture. However, as the tensile force is increased, at some point during testing, the fiber cuts the paper, allowing for the two metal surfaces to contact and resulting in failure. Sandpaper also shows some promise as a potential cushion layer as it does not sever like the paper does, but is also thin enough to prevent the slippage that occurred with thicker cardboard. Still, the sandpaper produces stress concentrators as one might expect and results in failure outside the gauge length. A solution to this problem may be using very fine-grit sandpaper to limit stress concentration. Combinations of sandpaper, epoxy, and paper are being experimented with to maintain proper gripping force without causing excessive stress concentrations. It is expected that the unirradiated fibers will be ductile once an acceptable method of testing is produced. Testing of irradiated samples will take place next year when the fibers return from the HFIR irradiation experiment. Conclusion of fiber testing will provide a baseline for radiation effects on tungsten fiber ductility and strength. Future testing on W_f-W composites will further the understanding of fiber and matrix contributions individually and how they interact. This knowledge will provide the basis to engineer optimal W_f-W composites.

10.2 DEVELOPMENT OF A NON-CONTACT STRAIN MEASUREMENT SYSTEM FOR POST IRRADIATED TENSILE TESTS AT HIGH TEMPERATURES

—H. Sakasegawa, T. Kato, H. Tanigawa (National Institutes for Quantum and Radiological Science and Technology), and Y. Katoh (Oak Ridge National Laboratory)

OBJECTIVE

The objective of this work is to develop a non-contact strain measurement system for post irradiated tensile tests at high temperatures. In past post irradiated tensile tests, strain was calculated from the cross head displacement and the obtained value included deformation other than specimen gage deformation, including specimen shoulder, fixture, and machine frame deformations. This is because it is hard to utilize conventional strain gages used for full size specimens due to the small specimen gage section. This work is part of the U.S. Department of Energy – Japan National Institutes for Quantum and Radiological Science and Technology fusion materials collaboration.

SUMMARY

Appropriate stress strain curves were obtained applying the non-contact strain measurement system developed in this work and the system specifications were selected. Two marks were painted on the specimen gage using a mixture of paste and fluorescent powder which can be used in high vacuum at high temperatures. UV light illuminated these two marks and clear contrast was obtained to measure the distance between marks using a video camera. This system can be used for post irradiated tensile tests at high temperatures in hot cells.

PROGRESS AND STATUS

Introduction

Post irradiated tensile testing is the most fundamental method used to evaluate mechanical properties after irradiation. In past research, changes in material strengths such as yield and ultimate tensile strength after irradiation have been measured without problems, but it has been hard to obtain accurate strain measurements. This is because specimen size is often too small to utilize the conventional strain gages used for full size specimens. Cross head displacement has alternatively been used to obtain strain. This strain calculated from cross head displacement generally includes deformation in specimen shoulders, fixtures, and tensile test machine frames in addition to the deformation in the specimen gage. In the current design activity for fusion blankets using reduced activation ferritic/martensitic steel structural material, it is desired to obtain more accurate strain. This is because significant irradiation embrittlement accompanying irradiation hardening has been observed within a few dpa at temperatures less than about 573K, which is near the lower operation temperature of the Japanese water cooled blanket design [1]. In particular, the uniform elongation of F-82H was almost zero after irradiation [2]. It is indispensable to accurately evaluate the irradiation effect on ductility for the design activity and the application of F-82H as the blanket structural material.

Experimental Procedure

In this work, we defined the specifications of a non-contact strain measurement system that can be used at room and high temperatures. The specification for room temperature was confirmed at ORNL and that for high temperatures was developed and finalized at QST in Japan.

Results

Table 1 shows the specification of the noncontact strain measurement system developed in this work. The controller, video camera, and lens specifications are the same for both room and high temperatures, but light and paint specifications are different.

Table 1. Specification of the non-contact strain measurement systems

Item	Room temperature	High temperature
Controller	Keyence CV-X292F	Keyence CV-X292F
Video camera	Keyence CA-H2100M	Keyence CA-H2100M
Lens	VST technology corp. VS-TC1-300CO	VST technology corp. VS-TC1-300CO
Light	Keyence CA-DPB2 Blue (Co-axial light)	CCS 165-SHU
Paint	General permanent maker Black (SANFORD Sharpie)	Paste for SEM at high temp. (PELCO High Performance Nickel Paste) and Fluorescence powder (Ohira Seisakusho BLP-02G)

For the room temperature tests, there were not any specific difficulties, because a clear contrast can be easily obtained using a permanent marker and a LED light which is co-axial and easily set in the lens. Figure 1 (a) shows measured pictures taken during a tensile test using the system shown in Table 1. Marks on the specimen gage were clearly seen and the distance between the outer two marks was measured during a tensile test. Figure 1 (b) shows the obtained stress-strain curves. The blue curve was obtained using the non-contact strain measurement system and the red curve was calculated from the cross head displacement (conventional measurement). The red curve tends to show larger strain than the blue curve. This means that the strain has been overestimated and it has included deformation in specimen shoulders, fixtures, and tensile test machine frames as well as the deformation in the specimen gage.

For high temperature tests, there were some difficulties. This is because marks on the specimen gage have to give appropriate contrast to be clearly observed and they have to endure high temperatures under high vacuum. We tried to use a mixture of a paste developed for SEM observation at high temperatures and fluorescent powders to be illuminated with UV light to obtain observable contrast. Since we did not have an appropriate tensile test frame to completely confirm and select the system specification at ORNL, we used tensile test frames at QST in Japan. First, we observed the endurance of the mixture of PELCO High Performance Nickel Paste and fluorescent powder, under vacuum at high temperatures, up to about 573 K and its dependence on the level of vacuum. No specific problems were found. Second, we applied the mixture to a high temperature tensile test at about ~ 523 K using a halogen spot heater in air. (We did not have a high temperature tensile test frame with a vacuum chamber with view ports to test the non-contact strain measurement system.) Figure 2 (a) shows measured pictures taken during the high temperature tensile test. Marks on the specimen gage are clearly seen and the distance between two marks was measured during the tensile test, similar to the case of the room temperature tensile test. Figure 2 (b) shows the stress-strain curves. As also shown in Figure 1, the blue curve was obtained using the non-contact strain measurement system and the red curve shows strain calculated from cross head displacement. The red curve again tends to show larger strain than the blue curve. Larger differences in strain are especially obvious at the beginning of test and this explains why a lower Young’s modulus has been obtained when using cross head displacement in past research.

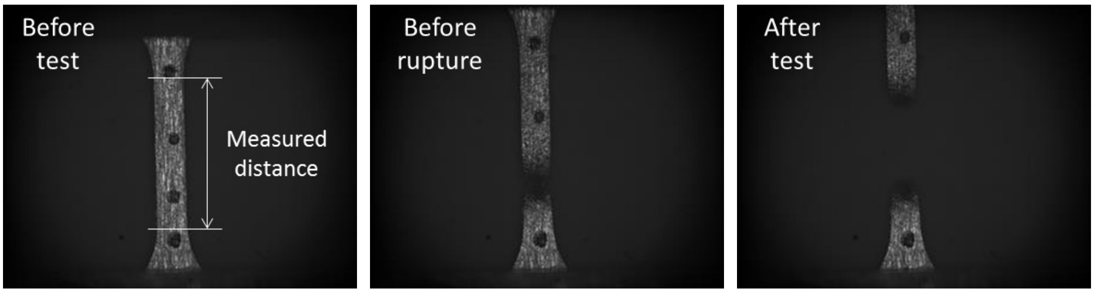

(a) Measured picture

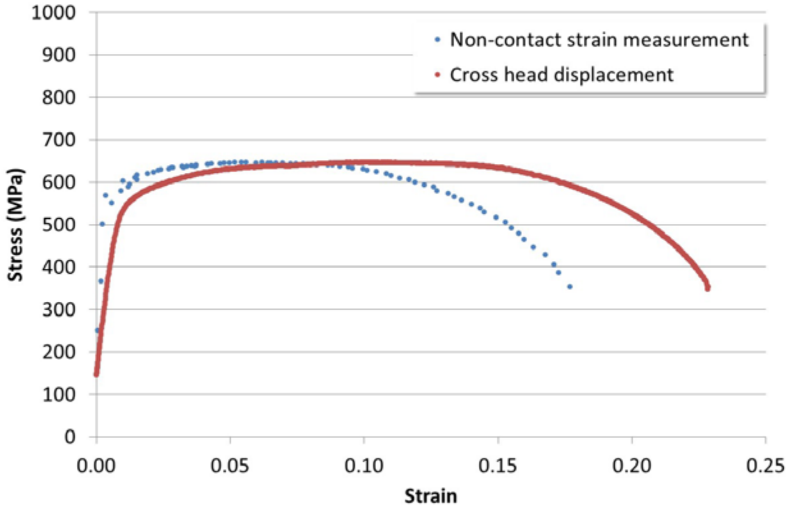

(b) Stress-strain curve

Figure 1. Room temperature tensile test result (F-82H IEA heat, SS-3 type specimen).

It should be noted that the number of points in the blue curves are less than in the red curves for both Figures 1 (b) and 2 (a). This is because the image capture rate was low, about a few seconds per image. The image capture rate depends on specifications and conditions of video camera, image resolution, and data transfer speed. In our latest tests, we obtained a 0.5 seconds per image for 2432 x 2050 image resolution (five million pixels) and it gives a number of points comparable to the conventional measurement.

Based on this work, we will finalize the specifications of a system which can be used for the high temperature tensile tests in Cell 1 in ORNL Building 3025E.

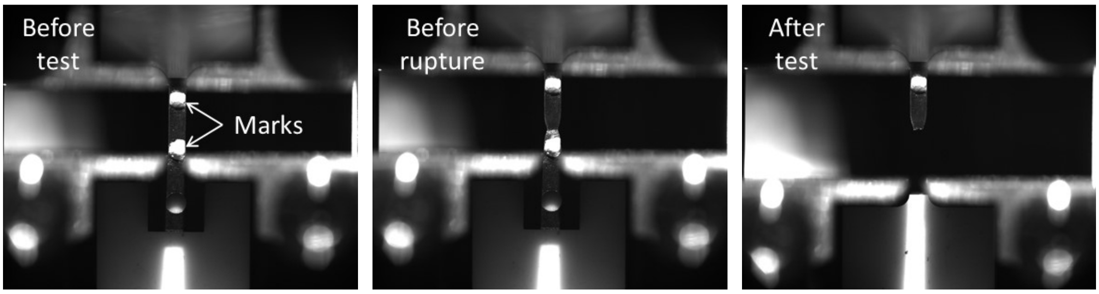

(a) Measured picture

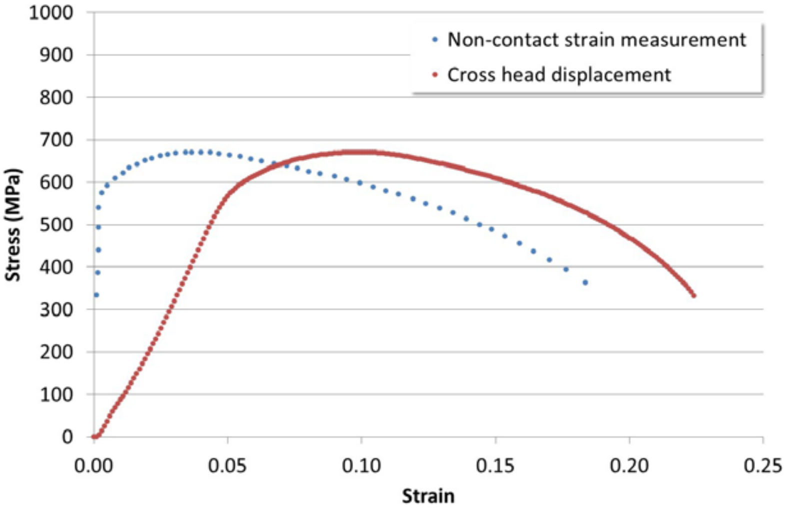

(b) Stress-strain curve

Figure 2. High temperature tensile test result (F-82H BA12 heat, SS-J3 type specimen).

Acknowledgements

This research was sponsored by the National Institutes for Quantum and Radiological Science and Technology (Japan Atomic Energy Research Institute) and the Office of Fusion Energy Sciences, U.S. Department of Energy, under contracts NFE-10-02779 and DE-AC05-00OR22725, respectively, with UT-Battelle, LLC.

References

[1] K. Tobita et al., J. Nucl. Mater. 386-388 (2009) 888-892.
[2] For example, T. Hirose et al., Fusion Materials Semi-annual Progress Report, DOE/ER-0313/46, (June 30, 2009) 72-78.

10.3 HFIR-MFE-RB-19J THERMAL AND NEUTRONIC DESIGN—J.L. McDuffee, C.R. Daily, N.O. Cetiner, C.M. Petrie, J.W Geringer, (Oak Ridge National Laboratory)

OBJECTIVE

This experiment is a collaborative effort between the US and Japan fusion programs to research tungsten as plasma facing components under divertor conditions and to evaluate blanket structural materials for DEMO Reactors.

The objective of this experiment is to irradiate tungsten and RAFM steel specimens at controlled temperatures of 300°C, 500°C, 800°C and 1200°C in the Removable Beryllium (RB) position of the High Flux Isotope Reactor (HFIR). The capsule has a gadolinium shield inside the capsule housing to reduce thermal neutron flux, and thus reduce transmutation rates in specimen materials.

This report describes the thermal and neutronic design of the RB-19J irradiation experiment.

SUMMARY

The HFIR RB-19J irradiation experiment contains six cylindrical holders (four temperature zones) which house ~1300 tungsten and steel specimens. The capsule and shield is design to be centered about the HFIR mid-plane, but the holders are slightly shifted toward the positive axial direction from the mid-plane. The assembly of the RB19J capsule was completed in May 2016 and installed in HFIR in June 2016. The first irradiation cycle, 466, started June 14, 2016. Starting temperatures stabilized within design range for the 500°C and the 800°C holders. The 1200°C and the 300°C were lower and higher than designed by about 50°C to 100°C respectively.

Capsule Description

The RB19J capsule contains six cylindrical holders located in four temperature zones 300°C, 500°C, 800°C and 1200°C as shown in Figure 1. The lower 300°C temperature zone uses a DISPAL (dispersed oxide aluminum) holder and contains only F82H steel alloy specimens, while the upper three temperature zones use a POCO graphite AXF-5Q holder and contain tungsten and tungsten alloy specimens.

The temperature regions are separated by three 20 mm Grade 5 titanium holder spacers filled with grafoil inserts. Each holder spacer also contains a flux wire dosimetry package. The three dosimetry packages 8A, 2U and 5H are located between holders 300°C & 800°C, 800°C & 1200°C and 1200°C & 500°C, respectively.

The effective total internal subcapsule length is 480 mm, with the reactor midplane crossing approximately 2 cm above the bottom of the 800°C holder. The bottom of the 300°C holder (position 3) is 217.9 mm below the midplane while the top of the 500°C holder is 261.1 mm above the midplane position.

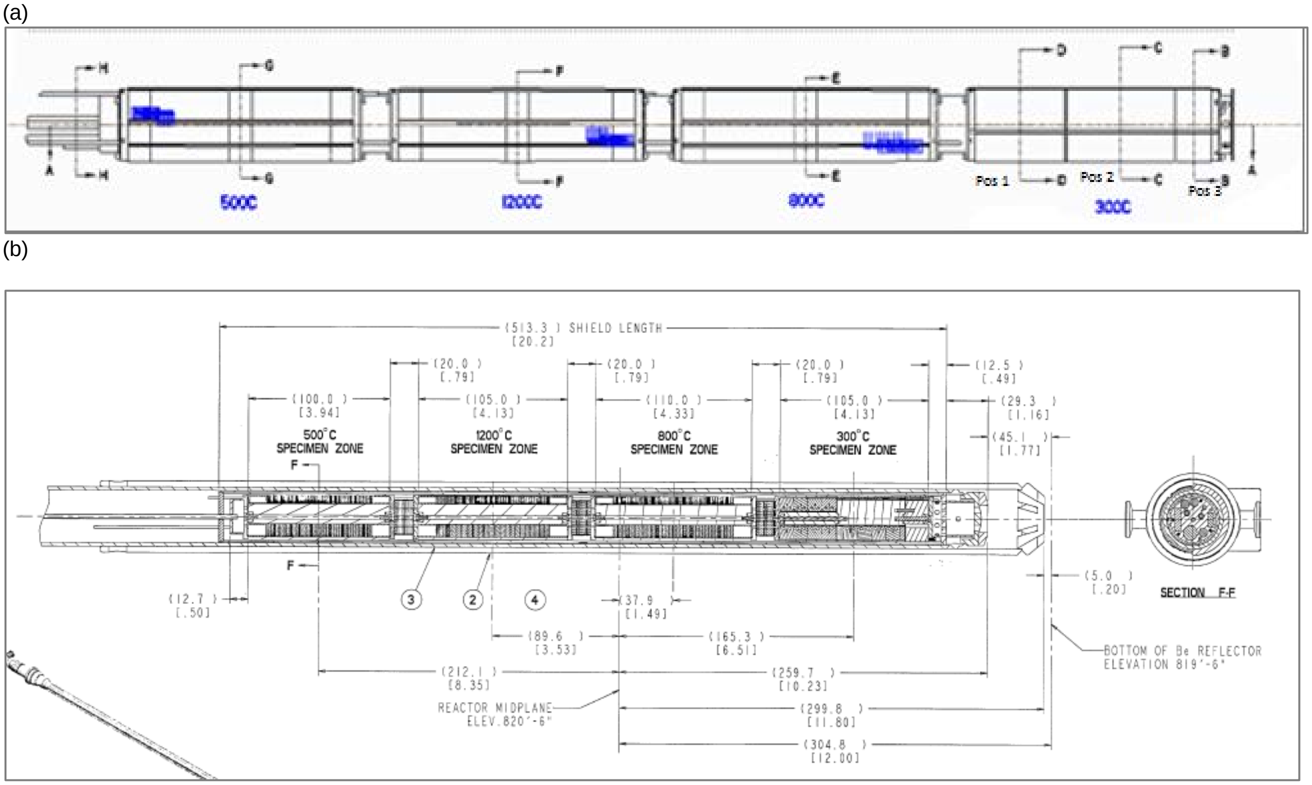

Figure 1. The layout of the RB19J Capsule Assembly – (a) Shows the internal holder positions and (b) shows the capsule dimensions; given in (mm) in parenthesis and in [inches] in brackets.

The holders are surrounded by a gadolinium shield (see next section) which serves to reduce the thermal neutron flux in the specimens. The sleeve-to-shield gap is designed to close due to differential thermal expansion. (The hotter aluminum sleeve has a much larger thermal expansion coefficient than does the gadolinium shield.)

Temperatures inside the capsule are controlled by a combination of gas gap size and gas composition. There are three gas gaps initially: holder to sleeve, sleeve to shield, and shield to housing tube. The top three holders (500°C, 1200°C, and 800°C) each have three design diameters: top, middle, and bottom. The 300°C region consists of three interlocking holders, and each holder has a top and bottom diameter. The naming convention is holder-region, so that “300°C holder middle-top” indicates the top diameter of the middle holder. Table 1 summarizes the initial (cold) diameters for the key design features. Outer surfaces are tapered between these design diameters.

Table 1. Key Design Diameters

Feature Diameter	Design Diameter (mm)
Housing tube inside	37.115±0.015
Shield outside	36.965±0.015
Shield inside	34.965±0.015
Sleeve outside	34.935±0.015
Sleeve inside	32.435±0.025
500°C holder top	32.10±0.025
500°C holder middle	32.30±0.025
500°C holder bottom	32.10±0.025
1200°C holder top	31.30±0.025
1200°C holder middle	32.00±0.025
1200°C holder bottom	31.20±0.025
800°C holder top	32.25±0.025
800°C holder middle	32.30±0.025
800°C holder bottom	31.90±0.025
300°C holder top-top	32.33±0.025
300°C holder top-bottom	32.33±0.025
300°C holder middle-top	32.33±0.025
300°C holder middle -bottom	32.33±0.025
300°C holder bottom-top	32.25±0.025
300°C holder bottom-bottom	32.20±0.025
Subcapsule end cap tabs	32.33±0.025

Every temperature region has its own gas supply line to control temperature through changing gas mixtures and flow rates. Helium gas flows through all the holders from the top to the bottom and exits at the bottom of the lowest holder. To manipulate the temperature either argon or helium gas is inserted just below and outside the specimen holder for each temperature zone to modify the effective thermal conductivity of the gas gap between the specimen holder and the outer tube.

There are two Type N Thermocouple Array Tubes (TCAT) inserted in the assembly with seven thermocouple junctions per TCAT. The TCATs extend the entire length of all the stacked holders. The thermocouple junctions from the same TCAT are in the same radial location with reference to the holders but have different axial positions so that each temperature region has at least three thermocouples. Thirteen passive SiC temperature monitors (TMs) are included in the assembly, three in each of the higher temperature holders 500°C, 800°C and 1200°C and four in the 300°C holders. There are also several SiC TMs in the 300°C holders.

Thermal Neutron Shield Design

The gadolinium shield is highly effective at reducing the thermal neutron flux. Figure 2 shows the neutron flux per unit lethargy for the beginning of the first cycle at locations outside (containment), within (shield), and internal to (holder) the gadolinium shield.

Cycle length reduction and day-by-day control rod position indicate no significant burnout of the gadolinium shield early in the first cycle of irradiation; however, more detailed multi-cycle depletion calculations will be needed to determine effects of gadolinium burnout.

Data in Figure 2 are plotted at the mid-point energy of a 44-group energy group structure. Flux spectra in Figure 2 are for a 2 cm long tally region axially centered on the core mid-plane. Because of the effectiveness of the gadolinium shield, the relative errors for the low energy groups in the tally region inside of the shield (specimen holder region) are quite large, as seen in the Table 2 data. Some of these low energy groups have not scored a single tally after 8000 kcode cycles of 100,000 histories/cycle.

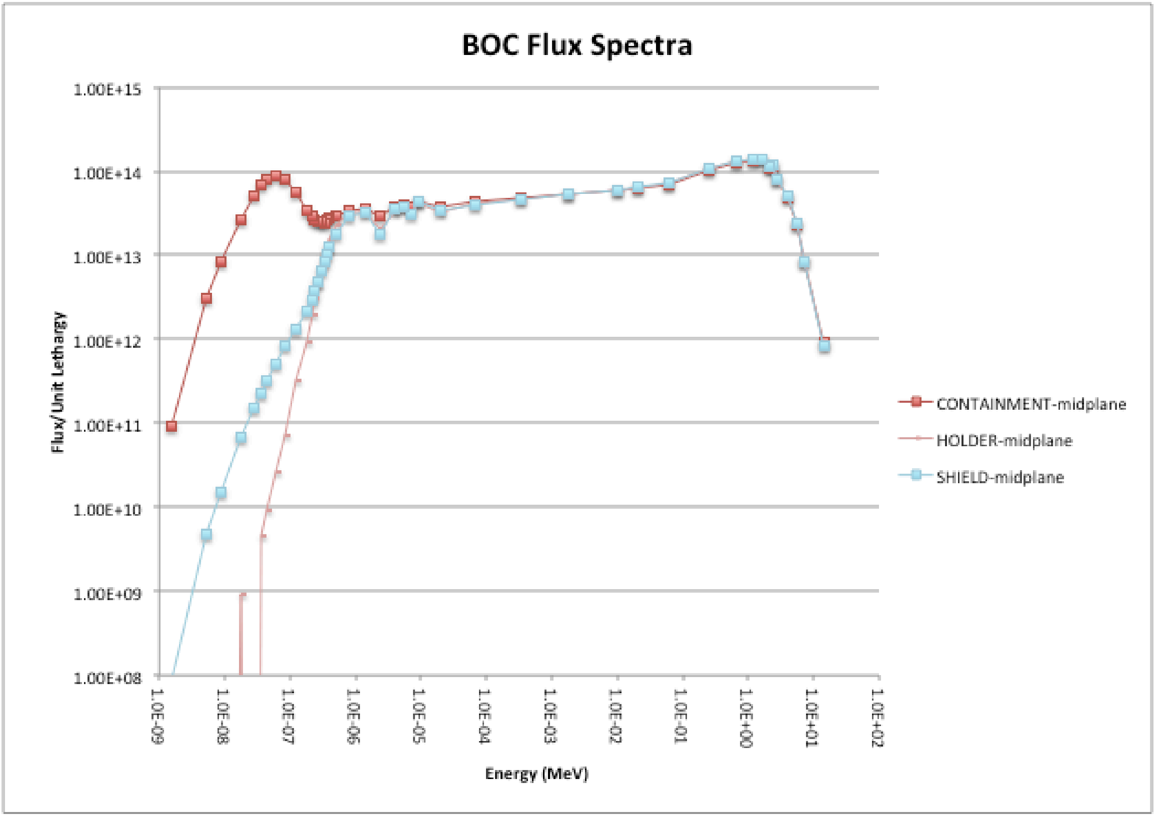

Figure 2. Beginning of Cycle (BOC) Flux Spectra for the MFE-RB-19J Experiment.

Table 2. BOC Flux Spectra Information at the Reactor Midplane for the MFE-RB-19J Experiment

E_{low} (MeV)	E_{high} (MeV)	E_{mid} (MeV)	Containment		Shield		Holder	
			Flux/ Lethargy	Relative Error	Flux/ Lethargy	Relative Error	Flux/ Lethargy	Relative Error
8.19E+00	2.00E+01	1.41E+01	9.26E+11	0.0123	8.48E+11	0.0532	8.54E+11	0.0472
6.43E+00	8.19E+00	7.31E+00	8.41E+12	0.0076	8.58E+12	0.033	9.05E+12	0.0285
4.80E+00	6.43E+00	5.62E+00	2.27E+13	0.0044	2.35E+13	0.0184	2.36E+13	0.016
3.00E+00	4.80E+00	3.90E+00	4.85E+13	0.0025	5.03E+13	0.0101	4.88E+13	0.0087
2.48E+00	3.00E+00	2.74E+00	7.84E+13	0.003	8.20E+13	0.0122	8.17E+13	0.0104
2.35E+00	2.48E+00	2.41E+00	1.13E+14	0.0045	1.18E+14	0.0189	1.16E+14	0.0163
1.85E+00	2.35E+00	2.10E+00	1.10E+14	0.0023	1.13E+14	0.0093	1.13E+14	0.0079
1.40E+00	1.85E+00	1.63E+00	1.36E+14	0.0019	1.41E+14	0.0078	1.38E+14	0.0066
9.00E-01	1.40E+00	1.15E+00	1.32E+14	0.0016	1.38E+14	0.0064	1.34E+14	0.0054
4.00E-01	9.00E-01	6.50E-01	1.28E+14	0.0013	1.32E+14	0.0049	1.30E+14	0.0041
1.00E-01	4.00E-01	2.50E-01	1.02E+14	0.0012	1.06E+14	0.0043	1.06E+14	0.0036
2.50E-02	1.00E-01	6.25E-02	7.02E+13	0.0014	7.19E+13	0.0052	7.17E+13	0.0045
1.70E-02	2.50E-02	2.10E-02	6.27E+13	0.0024	6.51E+13	0.0101	6.33E+13	0.0081
3.00E-03	1.70E-02	1.00E-02	5.80E+13	0.0013	5.96E+13	0.0052	5.91E+13	0.0045
5.50E-04	3.00E-03	1.78E-03	5.34E+13	0.0014	5.35E+13	0.0054	5.30E+13	0.0047
1.00E-04	5.50E-04	3.25E-04	4.75E+13	0.0014	4.52E+13	0.0056	4.54E+13	0.005
3.00E-05	1.00E-04	6.50E-05	4.35E+13	0.0017	4.05E+13	0.0069	4.19E+13	0.006
1.00E-05	3.00E-05	2.00E-05	3.83E+13	0.0018	3.33E+13	0.0077	3.26E+13	0.0069
8.10E-06	1.00E-05	9.05E-06	4.28E+13	0.0036	4.32E+13	0.0159	4.11E+13	0.0127
6.00E-06	8.10E-06	7.05E-06	3.70E+13	0.0032	3.12E+13	0.0145	3.23E+13	0.0121
4.75E-06	6.00E-06	5.38E-06	3.96E+13	0.0036	3.85E+13	0.0159	3.83E+13	0.0126
3.00E-06	4.75E-06	3.88E-06	3.72E+13	0.0027	3.51E+13	0.012	3.31E+13	0.01
1.77E-06	3.00E-06	2.39E-06	2.93E+13	0.0027	1.75E+13	0.0121	2.12E+13	0.0116
1.00E-06	1.77E-06	1.39E-06	3.54E+13	0.0025	3.22E+13	0.0106	3.30E+13	0.0093
6.25E-07	1.00E-06	8.13E-07	3.45E+13	0.0027	2.89E+13	0.0113	3.27E+13	0.01
4.00E-07	6.25E-07	5.13E-07	2.94E+13	0.0028	1.81E+13	0.012	2.30E+13	0.0122
3.75E-07	4.00E-07	3.88E-07	2.75E+13	0.0069	1.23E+13	0.0324	1.50E+13	0.0351
3.50E-07	3.75E-07	3.63E-07	2.68E+13	0.0067	1.02E+13	0.0327	1.20E+13	0.0378
3.25E-07	3.50E-07	3.38E-07	2.44E+13	0.0065	8.31E+12	0.0329	1.04E+13	0.0397
2.75E-07	3.25E-07	3.00E-07	2.54E+13	0.0046	6.59E+12	0.0235	7.32E+12	0.0323
2.50E-07	2.75E-07	2.63E-07	2.56E+13	0.0057	4.78E+12	0.0317	4.31E+12	0.0536
2.25E-07	2.50E-07	2.38E-07	2.62E+13	0.0053	3.75E+12	0.0304	3.02E+12	0.0616
2.00E-07	2.25E-07	2.13E-07	2.88E+13	0.0048	2.92E+12	0.0291	2.00E+12	0.0677
1.50E-07	2.00E-07	1.75E-07	3.48E+13	0.0028	2.14E+12	0.0172	9.22E+11	0.0645
1.00E-07	1.50E-07	1.25E-07	5.62E+13	0.0018	1.34E+12	0.0113	3.19E+11	0.0954
7.00E-08	1.00E-07	8.50E-08	8.09E+13	0.0015	8.38E+11	0.0095	7.27E+10	0.2047
5.00E-08	7.00E-08	6.00E-08	8.95E+13	0.0014	5.05E+11	0.009	2.66E+10	0.3879
4.00E-08	5.00E-08	4.50E-08	8.15E+13	0.0017	3.28E+11	0.0113	9.00E+09	0.7088
3.00E-08	4.00E-08	3.50E-08	6.89E+13	0.0016	2.28E+11	0.0109	4.61E+09	0.6864
2.53E-08	3.00E-08	2.77E-08	5.17E+13	0.0022	1.55E+11	0.016	0.00E+00	0
1.00E-08	2.53E-08	1.77E-08	2.61E+13	0.0015	6.70E+10	0.0096	9.17E+08	0.6006
7.50E-09	1.00E-08	8.75E-09	8.22E+12	0.0039	1.52E+10	0.0307	0.00E+00	0
3.00E-09	7.50E-09	5.25E-09	3.14E+12	0.0036	4.89E+09	0.0281	0.00E+00	0
1.00E-11	3.00E-09	1.51E-09	9.12E+10	0.0078	8.61E+07	0.0667	0.00E+00	0

Capsule Heat Generation Rates

The midplane heat generation rates in the 19J experiment at a HFIR power level of 85 MW for the materials of construction are taken from Daily[1] and summarized in Table 3.

Table 3. Design Basis Peak Heat Generation Rates (W/g) at 85 MW Reactor Power

Material	BOC	EOC	Design	Includes parts:
Steel (outside shield)	12.66	14.55	13.60	housing tube
Water	20.58	21.12	20.85	coolant
Gadolinium	22.20	25.67	23.93	shield, shield end caps
Aluminum	11.15	12.59	11.87	HFIR liner, holders
Graphite	10.30	11.17	10.74	holders, spacers
SiC	9.54	10.51	10.03	thermometry, springs
Molybdenum	14.80	16.82	15.81	gas lines
Steel (inside shield)	9.70	10.64	10.17	specimens, TCATS
Magnesium oxide	9.09	9.93	9.51	thermocouple insulation
Tungsten	18.82	22.24	20.53	specimens
Titanium	9.88	10.98	10.43	holder spacers, springs, end caps, bolts, screws

Figure 3 shows the heat generation peaking factor curves for beginning of cycle (BOC), end of cycle (EOC) and Design. The EOC peaking factor curve is used for all safety-basis calculations, which maximizes the total heat generated.

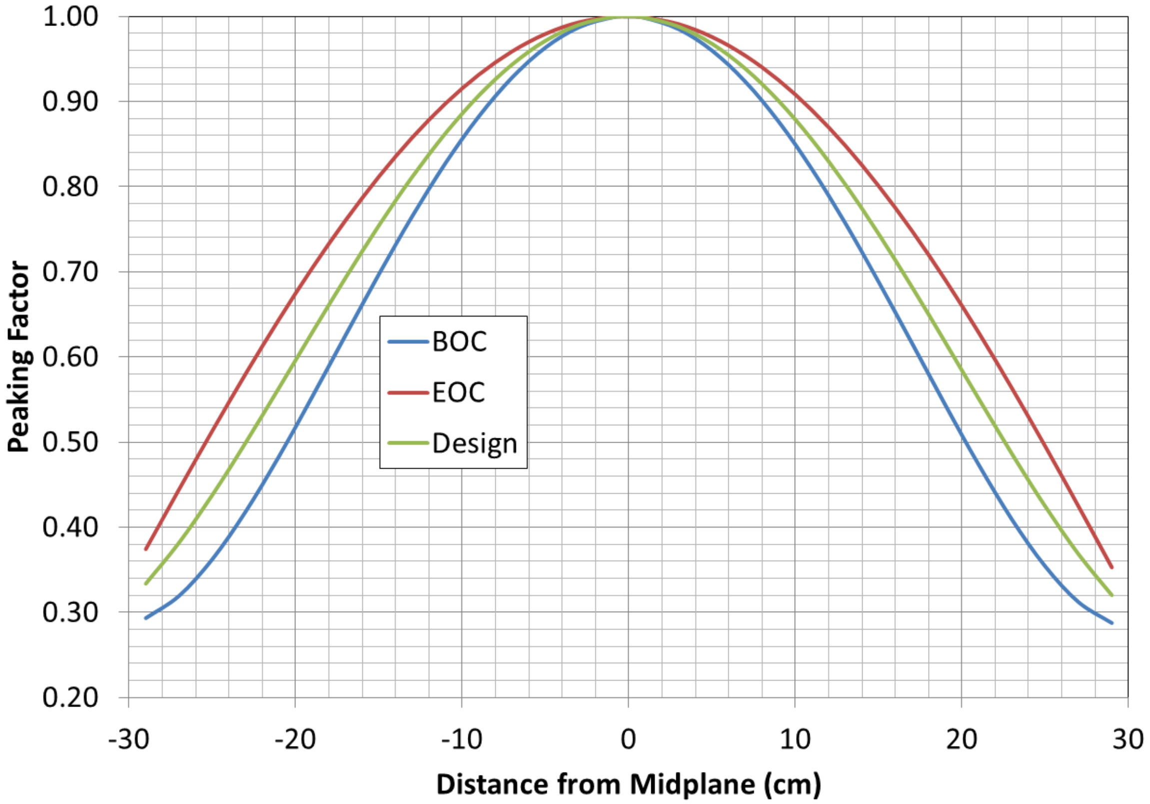

Figure 3. Heat Generation Peaking Factor Curve.

Design Basis Temperatures

Design basis temperatures are shown in Figure 4 and specimen temperatures are summarized in Table 4[2]. Contour plots for each specimen region are shown in Figure 5 through Figure 8.

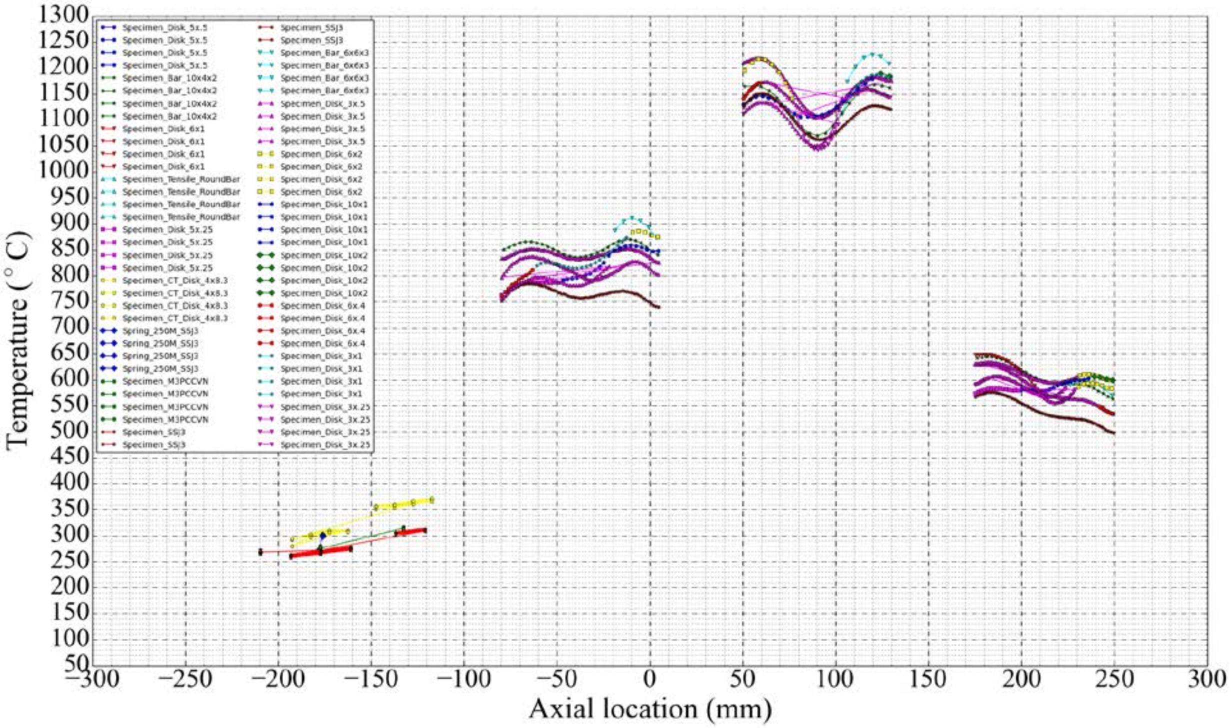

Figure 4. Design Basis Temperatures Under Nominal Reactor Conditions.

Table 4. Specimen Temperatures at Nominal Design Conditions

Specimens	Material	T_{avg}	T_{min}	T_{max}	$T_{.025}$*	$T_{.975}$*
500C	Tungsten	590	481	652	516	646
1200C	Tungsten	1144	1019	1232	1063	1222
800C	Tungsten	829	707	920	751	903
250C TOP	Steel	345	293	380	303	375
250C MID	Steel	289	253	317	260	314
250C BTM	Steel	267	262	274	264	273

**95% of the part volume is within the $T_{.025}$ and $T_{.975}$ temperature band*

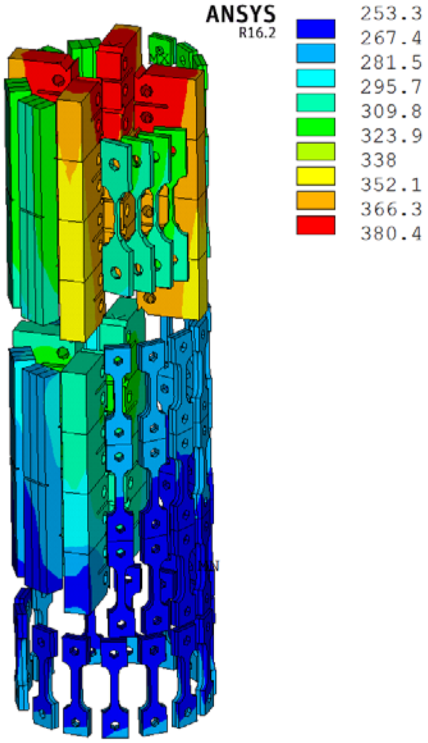

Figure 5. Design Basis Temperature Contour Plot for 300°C Specimens.

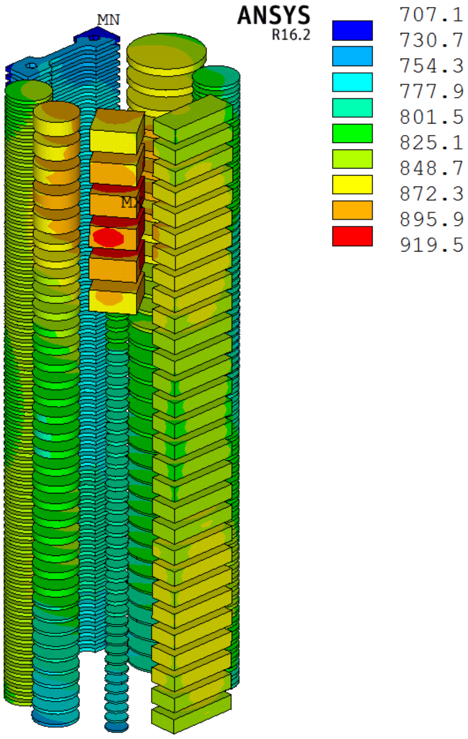

Figure 6. Plot for 800°C Specimens.

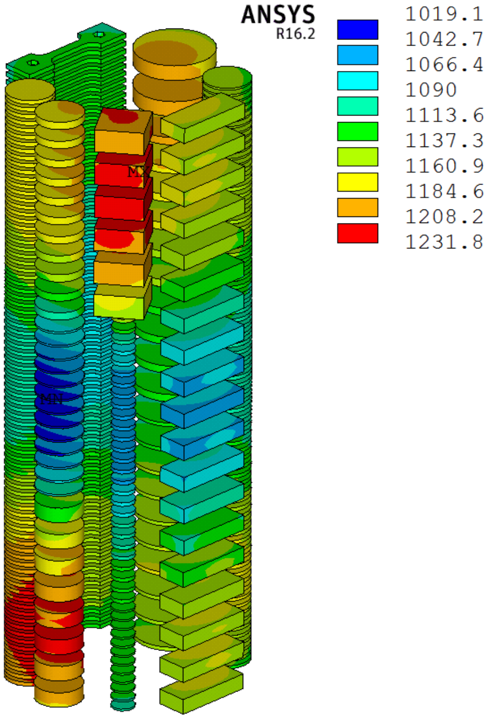

Figure 7. Design Basis Temperature Contour Plot for 1200°C Specimens.

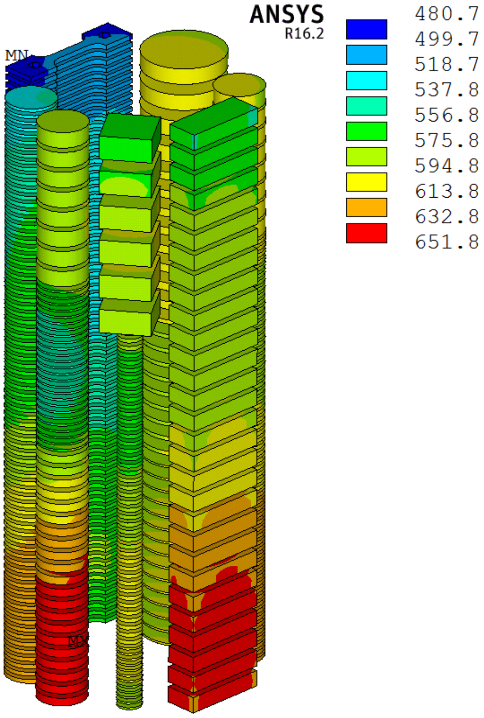

Figure 8. Design Basis Temperature Contour Plot for 500°C Specimens.

The capsule is designed such that the pure helium purge gas is introduced at the top of the capsule and is directed through the specimen region of each subcapsule until it exits at the bottom of the capsule. Control gas (60% argon and 40% helium) is introduced outside and below each subcapsule and inside the shield inner sleeve. Nominal gas concentrations in this region are shown in Table 5. The "purge" and "control" gases are what the operator will actually send to the capsule. The helium and argon concentrations result from mixing the pre-mixed control gas with the pure helium.

Table 5. Design-basis Gas Concentrations in Each Subcapsule

Subcapsule	Purge	Control	Helium	Argon
500°C	75%	25%	85%	15%
1200°C	50%	50%	70%	30%
800°C	50%	50%	70%	30%
250°C	75%	25%	85%	15%

Table 6 summarizes the coolant conditions for the design-basis case.

Table 6. Summary of Coolant Conditions for the Design-basis Condition

Subcapsule	Minimum	Maximum	Average
Bulk coolant temperature (°C)	49.0	55.9	52.5
Capsule surface temperature (°C)	54.6	81.3	68.0
Capsule surface heat flux (kW/m²)	191.4	882.9	593.0
Heat transfer coefficient (kW/m²·°C)	30.2	31.7	31.0

Conclusion

The MFE-RB-19J capsule has been designed to achieve nominal temperatures of 300°C, 800°C, 1200°C, and 500°C. The temperature of the capsule is controlled with a mixture of helium and control gas. The control gas is a mixture of 60% argon and 40% helium, which results in an effective thermal conductivity equivalent to neon.

References

[1] Daily, C., Heat Generation Rates in Gadolinium-Shielded Experiment RB19J in Position RB-5B of the HFIR Beryllium Reflector, C-HFIR-2016-010, Rev. 1, Reactor and Nuclear Systems Division, Oak Ridge National Laboratory, 2016.

[2] McDuffee, J.L., Temperature Verification, Transient Analysis, and Argon Activation for Materials Experiment MFE-RB-19J, C-HFIR-2016-007, Rev. 0, Reactor and Nuclear Systems Division, Oak Ridge National Laboratory, 2016.

10.4 HFIR-MFE-RB-19J SPECIMEN LOADING LISTING

—J.W. Geringer, J.L. McDuffee, C.M. Petrie, L.M. Garrison, R.H. Howard, N.O. Cetiner, D.A. Stringfield, R.G. Sitterson (Oak Ridge National Laboratory)

OBJECTIVE

This experiment is a collaborative effort between the US and Japan Fusion Materials programs to research tungsten for plasma facing components under divertor conditions and to evaluate blanket structural materials for DEMO and other fusion reactors.

The objective of this experiment is to irradiate tungsten and RAFM steel specimens at controlled temperatures of 300°C, 500°C, 800°C and 1200°C in the Removable Beryllium (RB) position of the High Flux Isotope Reactor (HFIR). The capsule has a gadolinium shield inside the capsule housing to reduce thermal neutron flux and thus reduce transmutation rates in specimen materials. The expected radiation damage levels for the steel and W specimens for the planned six cycles of HFIR operation are ~2.5 to 3 dpa and ~1.0 to 1.5 dpa respectively.

This report describes the specimens and specimen loading for the RB-19J irradiation experiment.

SUMMARY

The HFIR RB-19J irradiation experiment contains six cylindrical holders (four temperature zones) which houses ~1300 tungsten and steel specimens. The capsule and shield is design to be centered about the HFIR mid-plane, but the holders are slightly shifted toward the positive axial direction from the mid-plane. The assembly of the RB19J capsule was completed in May 2016 and installed in HFIR in June 2016. The first irradiation cycle, 466, started June 14 2016. Starting temperatures stabilized within design range for the 500°C and the 800°C holders. The 1200°C and the 300°C were lower and higher than designed by about 50°C to 100°C respectively.

Capsule Description

Internal Capsule Assembly Layout

The RB19J capsule contains six cylindrical holders located in four temperature zones 300°C, 500°C, 800°C and 1200°C as shown in Figure 1. Three of the six holders are Aluminum (6061-T6) and positioned in the lower 300°C temperature region. The Al holders contain only F82H steel alloy specimens. The other temperature regions have only one graphite holder each and contain tungsten and tungsten alloy specimens as well as smaller tungsten fiber holder assemblies.

The temperature regions are separated by three 20 mm Grade 5 titanium spacer assemblies. Each holder spacer contains a flux wire dosimetry package. The three packages 8A, 2U and 5H are located between holders 300°C & 800°C, 800°C & 1200°C and 1200°C & 500°C respectively.

The total effective internal subcapsule length is 480 mm. According to design it is slightly off center relative to the reactor axial midplane. The bottom of the 300°C holder (position 3) is 217.9 mm below the midplane while the top of the 500°C holder is 261.1 mm above the midplane position (see Figure 1).

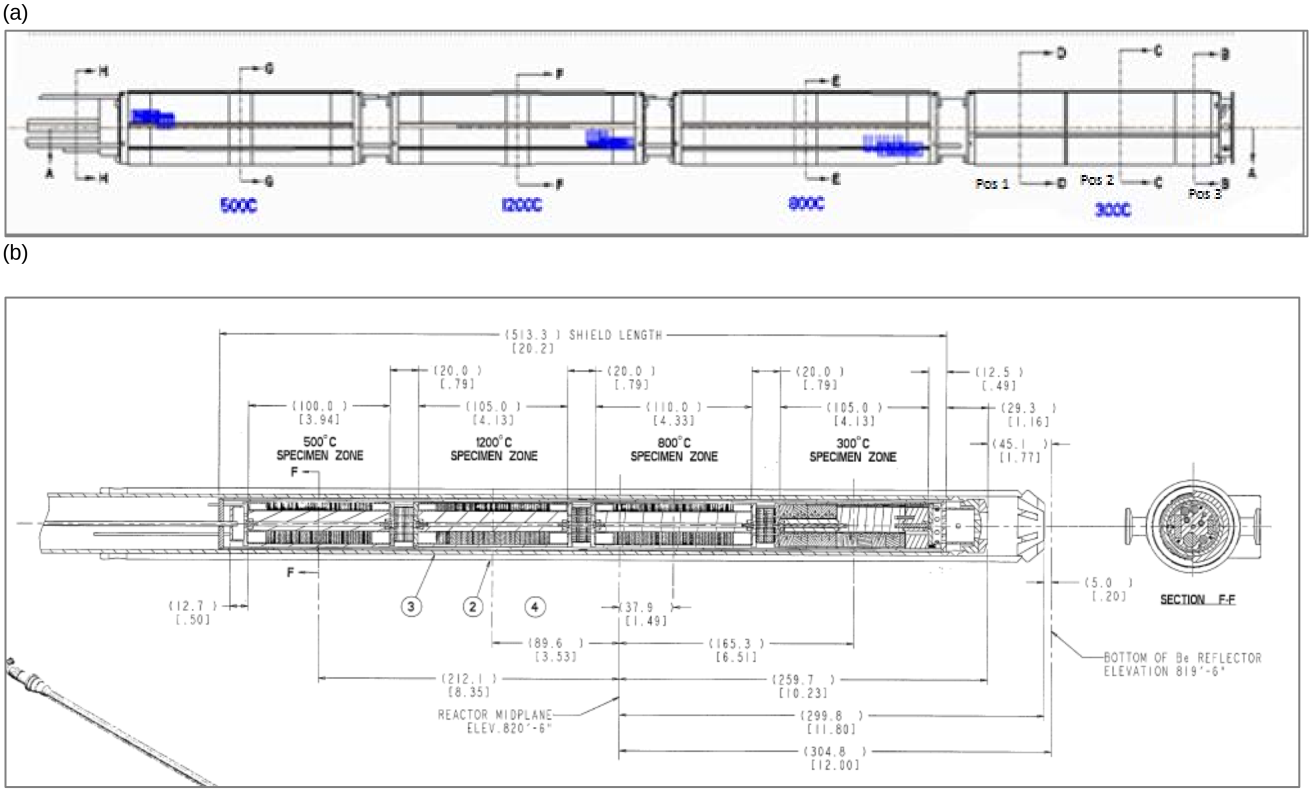

Figure 1. The layout of the RB19J Capsule Assembly – (a) Shows the internal holder positions and (b) shows the capsule dimensions in parenthesis (mm) and in brackets [inches] [D1],[D2].

The irradiation temperature control method, thermal analysis, and temperature measurement system are described in the following chapter of this progress report. The temperatures are controlled by a combination of gas gap size and gas composition. Two Type N Thermocouple Array Tubes (TCAT) inserted in the assembly with 14 junctions at different axial positions to measure temperatures. Thirteen passive SiC temperature monitors are also included in the assembly, for post irradiation determination of temperatures.

Overview of the Test Matrix and Specimens

The test matrix is divided according to materials types. The cooler 300°C capsule region contains only RAFM steel specimens (F82H) and aluminum specimen holders are used for higher thermal conductivity. The higher temperature capsule regions 500°C, 800°C and 1200°C, contain only tungsten and tungsten alloy specimens inside graphite holders which is more robust for higher temperatures environments with lower thermal conductivity.

Table 1 summarizes the specimen types and the quantities included in each holder. The F82H alloy specimens have specimen type codes assign to them to differentiate between the different preparation methods which includes notch preparation and pre-cracking. The specimen type code is associated with the specimen unique ID.

The tungsten specimens do not have specimen type code associated with their unique IDs. Fabrication and orientation characteristics are differentiated as part of the material code.

Table 1. Specimen Types included in the 300°C Aluminum holders

Specimen Type	Dim. [mm]	Type ID	Specimen Type Code	Quantity			
300°C Aluminum holders				**Pos 1**	**Pos 2**	**Pos 3**	**Total**
Tensile	16x4x0.75	SS-J3	6	12	18	9	39
Tensile –Notched type 3	16x4x0.75	SS-J3	7	0	18	9	28
Tensile - Notched type 2	16x4x0.75	SS-J3	5	0	6	10	16
Round bar	25x5x1.1	RB	3	4	0	0	4
Bend bar (a/W=0.2)	36x3.3x1.65	M3-PCCVN	1	0	6	0	6
Bend bar(a/W=0.5)	36x3.3x1.65	M3-PCCVN	2	12	6	0	18
Compact Tension	10x10x4	0.16CT	0	16	12	0	28
500°C, 800°C and 1200°C Graphite holders				**500°C**	**800°C**	**1200°C**	**Total**
TEM	D3 x t0.25	TEM	n/a	12	12	12	36
DISC 3mm	D3 x t0.5	D3TH	n/a	35	27	27	89
DISC 6mm	D6 x t0.25	D6TQ	n/a	26	24	26	76
DISC 6mm	D6 x t0.5	D6TH	n/a	142	148	146	436
DISC 6mm	D6 x t1	D6T1	n/a	21	21	11	53
DISC 6mm	D6xt2	D6T2	n/a	16	5	8	29
DISC 10mm	D10 x t0.25	D10TQ	n/a	15	15	0	30
DISC 10mm	D10 x t1	D10T1	n/a	10	8	8	26
DISC 10mm	D10 x t2	D10T2	n/a	2	0	2	4
Tensile	16x4x0.5	SS-J2	n/a	82	82	82	246
Toughness	10x4x2	NT2	n/a	29	29	19	77
Torsion	6x6x3	6SQ5D	n/a	6	6	6	18

Figures 2 to 10 show the geometry of all the specimens included in the assembly, with dimensions in millimeters.

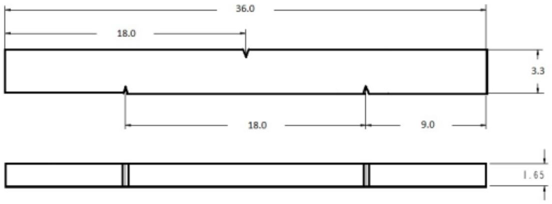

Figure 2. M3-PCCVN specimen.

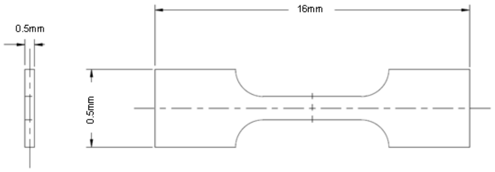

Figure 3. SSJ2 specimen.

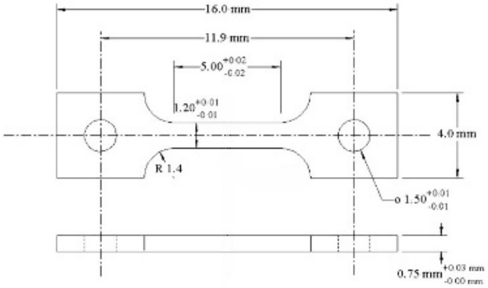

Figure 4. SSJ3 specimen without notch.

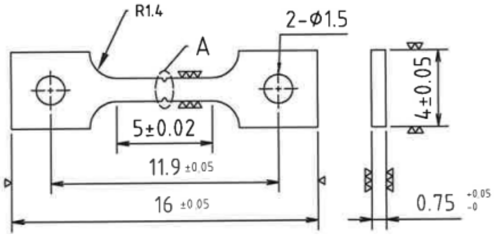

Figure 5. SSJ3 specimen with notch.

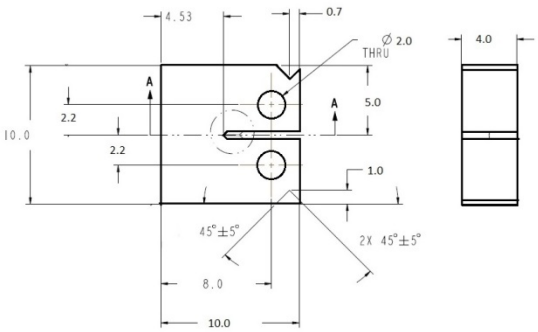

Figure 6. Compact tension (CT) specimen.

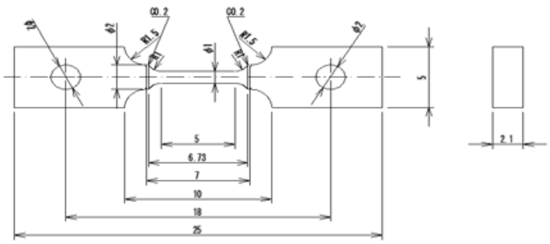

Figure 7. Round bar (RB) specimen.

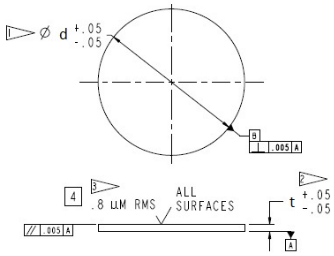

Figure 8. Disc (DdTt) specimen.

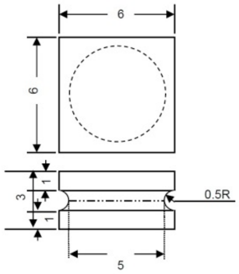

Figure 9. 6SQ5D specimen.

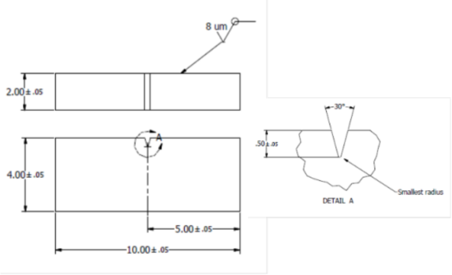

Figure 10. NT2 specimen.

Specimen Materials

The materials irradiated in this experiment are pure W, W alloys and F82H steel alloys, listed in Table 2. Each material has been given a code associated with the specimens ID number. The researchers responsible for the selected material and samples and their affiliation are also identified.

Table 2. Materials List for the RB 19J Experiment

Experimenter	Material Description	Material Code	Affiliation	Material
Buchenauer	SCW(110)	V0	US	W
Garrison	AA plate (PCW from Alfa Aeser)	FR	US	W
Garrison	AA plate tensile A (PCW from Alfa Aeser)	GE	US	W
Garrison	AA plate tensile B (PCW from Alfa Aeser)	3E	US	W
Garrison	PCW Alfa Aesar 2mm foil	EE	US	W
Garrison	PCW-0%Re (ORNL)	KE	US	W
Garrison	PCW-ITER (JP) orientation A	AT	US	W
Garrison	PCW-ITER (JP) orientation B	BT	US	W
Garrison	PCW-ITER (JP) orientation C	CT	US	W
Garrison	Rolled W foil	RE	US	W
Garrison	SCW 100 (commercial)	TE	US	W
Garrison	SCW 110 (commercial)	UE	US	W
Garrison	SCW 110 GW	GW	US	W
Garrison	SCW-100-1 tensile	HE	US	W
Garrison	SCW-100-2 tensile	JE	US	W
Garrison	W PIM	ZE	US	W
Garrison	W TiC	8E	US	W

Garrison	W-0.2%Re (ORNL)	3R	US	W
Garrison	W-3.4%Re (ORNL)	5E	US	W
Hasegawa	K-doped W (Rolled, 80%, X-direction)	60	Japan	W
Hasegawa	K-doped W-3%Re (Rolled, 80%, X-direction)	80	Japan	W
Hasegawa	K-doped W-3%Re (Rolled, 80%, X-direction, Heat treated at 1500C)	70	Japan	W
Hasegawa	Pure W (Rolled, 80%, X-direction)	P0	Japan	W
Hasegawa	Pure W (Rolled, 80%, X-direction, Heat treated at 1500C)	X0	Japan	W
Hasegawa	W-3%Re (Rolled, 80%, X-direction)	41	Japan	W
Hasegawa, Fukuda	K-doped W-Re (K-doped W-3%Re)	C0	Japan	W
Hasegawa, Fukuda	W-3Re	61	Japan	W
Hasegawa, Fukuda	W-3Re (the same as code 61)	06- -K	Japan	W
Hasegawa, Fukuda	W-3Re (the same as code 61)	06K	Japan	W
Hatano	W-5Re	71	Japan	W
Hinoki	CVD SiC/W(50um)	10	Japan	W
Hinoki	SiCf(40%)/ W(60%)	KY	Japan	W
Kasada	W(0.2mmt)-coated F82H fabricated by underwater explosive welding	11	Japan	W
Oya	Allied W	00	Japan	W
Oya	Allied W (the same as code 00)	00K	Japan	W
Oya	Allied W (the same as code 00)	10K	Japan	W
Oya	Allied W (the same as code 00)	20K	Japan	W
Oya	Allied W (the same as code 00)	30K	Japan	W
Oya	Allied W (the same as code 00)	40K	Japan	W
Oya	Allied W (the same as code 00)	50K	Japan	W
Tanigawa	F82H BA07 (8Cr-2W-0.04Ta : VIM+ESR)	SV	Japan	F82H
Tanigawa	F82H BA12 (8Cr-2W-0.08Ta : EAF+ESR)	TV	Japan	F82H
Tanigawa	F82H IEA (8Cr-2W-0.04Ta ; VIM)	0V	Japan	F82H
Ueda	ITER W (//)	40	Japan	W
Ueda	ITER W (Perpendicular)	50	Japan	W
Ueda	K-doped W-3Re (//)	90	Japan	W
Ueda	K-doped W-3Re (Perpendicular)	A0	Japan	W
Ueda	UFG-W	Y0	Japan	W
Ueda (Hinoki)	W/SiC	21	Japan	W

Not listed in the table are three types of tungsten fibers included in small fiber holders.

Type 1: W with 60 ppm K which was straightened by plastic deformation (1%) at room temperature and comes from heat lot 1151-06-13, ID 14337467 with a length of 40 mm and diameter of 150 µm.

Type 2: W with 60 ppm K which was straightened by producer at high temperature and comes from heat lot 1223-02-02, ID 22665182 with a length of 38.5 mm and diameter of 150 µm.

Type 3: W which was straightened by plastic deformation (1%) at room temperature and comes from heat lot 2618-04-14, ID 40215691 with a length of 37 mm and diameter of 150 µm.

Specimen Identification

For identification each specimen has a number assigned which consist of four or five alphanumeric characters. The specimen ID is a combined number from a few codes which have been mentioned.

The F82H steel specimens have four characters. The first two characters represent the material code, the third character represents the specimen type code and the fourth character is the specimen unique identifier. For example, the number SV72 means the specimen material is F82H BA07, it is a notched SSJ3 type 3 specimen and its unique number is 2.

Due to the number of tungsten specimens the specimen ID has a simpler code scheme, but is still represented by four or five characters. Specimens of different specimen types may share specimen IDs with other types. The typical ID scheme is defined by four characters, the first two characters represent the material code and the next two characters represent the specimen unique identifier. For example, the number EE00 refers to the material used as PCW Alfa Aesar 2 mm foil and its unique number is 00. Specimens with five characters starting with a “06-“ and ending with “-K” is an exception. This refers to W-3Re specimens which are the same as four character specimens starting with “61-“.

If the specimen has five characters, typically the first three characters represents the material and the last two characters are the unique identifier.

The typical engraving convention is shown in Figure 11.

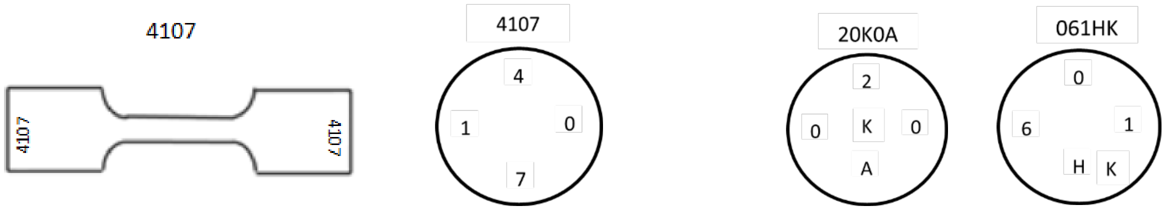

Figure 11. Specimen engraving scheme.

Holder Assemblies and Specimen Loading

The Aluminum Holders (300°C)

The layout of the 300°C holder assembly is shown in Figure 12. The three holder positions 1, 2 and 3 are indicated by numbers 2, 3 and 4 respectively. The holder dimensions are summarized in Table 3.

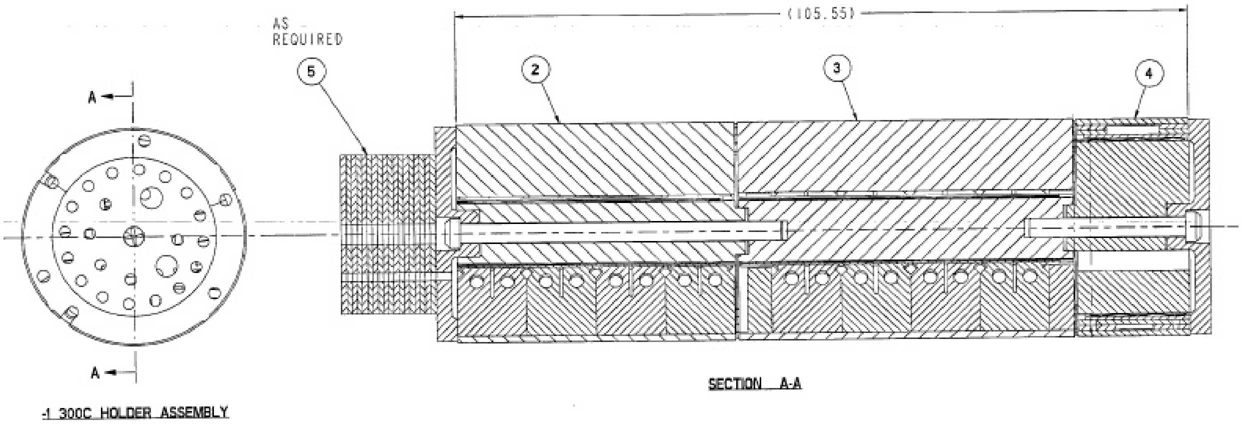

Figure 12. 300C Holders Assembly [D3].

Table 3. 300°C Holder and parts dimensions [1]

Part	Design Diameter [mm]	Design Length or Thickness [mm]
300°C holder position 1-(top & bottom)	32.33±0.025	40.0
300°C holder position 1-(top & bottom)	32.33±0.025	48.0
300°C holder position 1-(top & bottom)	32.25±0.025	16.2
Holder end caps	32.33±0.025	3.0

<u>The 300°C Position 1 Holder</u>

Figure 13 shows the holder and specimen layout of the 300°C holder position 1 and Table 4 lists the specimen loading.

SiC retainer springs provide a slight radial force to hold specimens in position and is placed next to each specimen stack. SiC temperature monitors are inserted in most of the specimen holes except for holes 6 to 9. Additional SiC temperature, C and D, are inserted in separate and dedicated holes at positions between holes 1 & 13 and holes 10 & 13 respectively (refer to no. 5 in Figure 13).

Each round bar specimen is placed in a 6061-T6 Al coffin spacer with tight tolerances around the gauge area to create a snug fit with the specimen. Graphite spacers are also used to position the specimens inside the holder. For holes 11, 12, 14 and 15 spacers with a thickness of 4.95 mm have been inserted on both the top and bottom of the specimen stack assembly. For the holes where the SS-J3 specimens are inserted, 2, 3 and 4, a 7.5mm spacer was placed only on the bottom of the specimen stack.

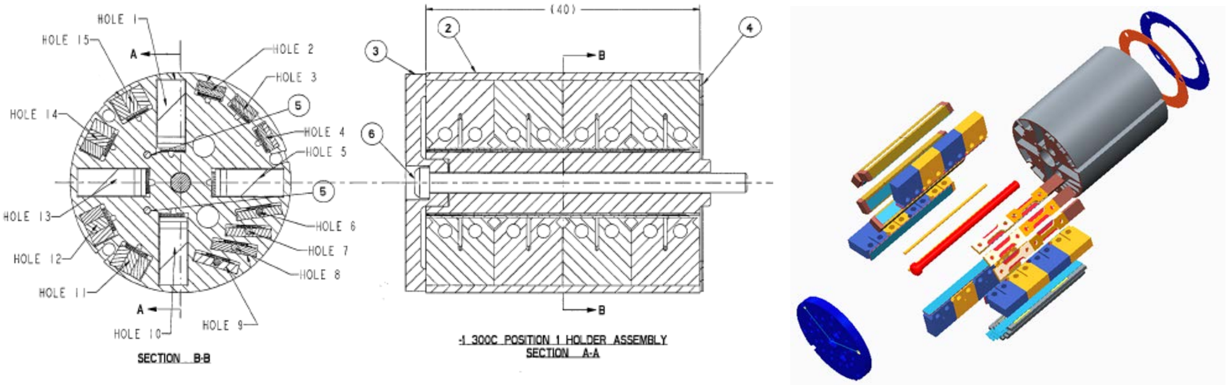

Figure 13. 300C Holders Assembly [D4].

Table 4. 300°C Holder and parts identification

Specimen Type	**0.16 CT**			
Position	**Hole 1**	**Hole 5**	**Hole 10**	**Hole 13**
Top to Bottom				
1	0V07	0V0C	SV08	SV0E
2	0V06	0V0A	SV07	SV0C
3	0V05	0V09	SV06	SV0A
4	0V04	0V08	SV05	SV09
Passive Thermometry	7-8-1	7-8-5	7-8-10	7-8-13
RETENSION SPRING	SiC	SiC	SiC	SiC
Specimen Type	**SS-J3**			
Position	**Hole 2**	**Hole 3**	**Hole 4**	
Top to Bottom				
1 (inside)	0V63	SV61	SV65	
1 (outside)	0V62	SV60	SV64	
2 (inside)	0V61	0V65	SV63	
2 (outside)	0V60	0V64	SV62	
Passive Thermometry	7-8-2	7-8-3	7-8-4	
RETENSION SPRING	SiC	SiC	SiC	
Specimen Type	**Round Bar**			
Position	**Hole 6**	**Hole 7**	**Hole 8**	**Hole 9**
1	0V30	0V31	SV30	SV31
Passive Thermometry	N/A			
Specimen Type	**M3-PCCVN**			
Position	**Hole 11**	**Hole 12**	**Hole 14**	**Hole 15**
Counter Clockwise				
1	0V26	0V29	SV26	SV29
2	0V25	0V28	SV25	SV28
3	0V24	0V27	SV24	SV27
Passive Thermometry	7-8-11	7-8-12	7-8-14	7-8-15
RETENSION SPRING	SiC	SiC	SiC	SiC

The 300°C holder, position 2

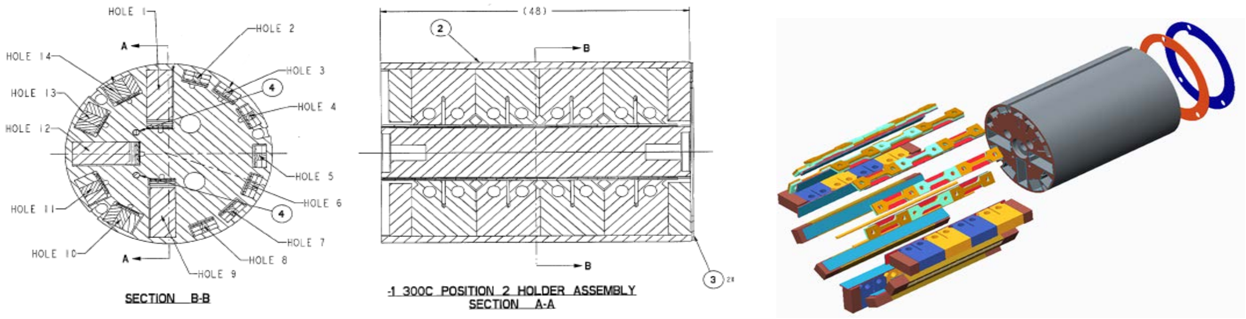

Figure 14. Specimen loading layout for the 300°C holder position 2 holder [D5].

Figure 14 shows the holder and specimen layout of the 300°C holder position 2 and Table 5 lists the specimen loading.

Similar to the previously described holder, SiC retainer springs as well as SiC temperature monitors are inserted next to each specimen stack and additional SiC temperature monitors, A and B, are inserted in separate and dedicated holes in the positions between holes 1 & 12 and holes 9 & 12 respectively (refer to 4 in Figure 14).

Graphite spacers are used to position the specimens inside the holder. For the 0.16CT specimen assemblies, spacers with a thickness of 3.5 mm have been inserted on both the top and bottom ends of the specimen stack. For the holes where the M3-PCCVN specimens are inserted, 10, 11, 13 and 14, a 5.75 mm spacer was placed on the top and bottom of the specimen stack.

Table 5. Specimen loading list for the 300°C position 2 holder

Specimen Type	**0.16 CT**						
Position	**Hole 1**	**Hole 9**	**Hole 12**				
Top to Bottom							
1	0V03	SV03	TV03				
2	0V02	SV02	TV02				
3	0V01	SV01	TV01				
4	0V00	SV00	TV00				
Passive Thermometry	9-6-15	9-6-16	9-6-12				
Retention spring	SiC	Ti	Ti				
Specimen Type	**SS-J3**						
Position	**Hole 2**	**Hole 3**	**Hole 4**	**Hole 5**	**Hole 6**	**Hole 7**	**Hole 8**
Top to Bottom							
1 (inside)	0V6C	SV6C	TV65	0V75	SV75	TV75	TV51
1 (outside)	0V6A	SV6A	TV64	0V74	SV74	TV74	TV50
2 (inside)	0V69	SV69	TV63	0V73	SV73	TV73	SV51
2 (outside)	0V68	SV68	TV62	0V72	SV72	TV72	SV50
3 (inside)	0V67	SV67	TV61	0V71	SV71	TV71	0V51
3 (outside)	0V66	SV66	TV60	0V70	SV70	TV70	0V50
Passive Thermometry	9-6-2	9-6-3	9-6-4	9-6-5	9-6-6	9-6-7	9-6-8
Retention spring	SiC	SiC	SiC	SiC	SiC	SiC	SiC
Specimen Type	**M3-PCCVN**						
Position	**Hole 10**	**Hole 11**	**Hole 13**	**Hole 14**			
Counter Clockwise							
1	0V20	SV11	TV11	TV21			
2	0V11	SV10	SV21	TV20			
3	0V10	0V21	SV20	TV12			
Passive Thermometry	9-6-10	9-6-11	9-6-13	9-6-14			
Retention spring	SiC	SiC	SiC	SiC			

The 300°C Position 3 Holder

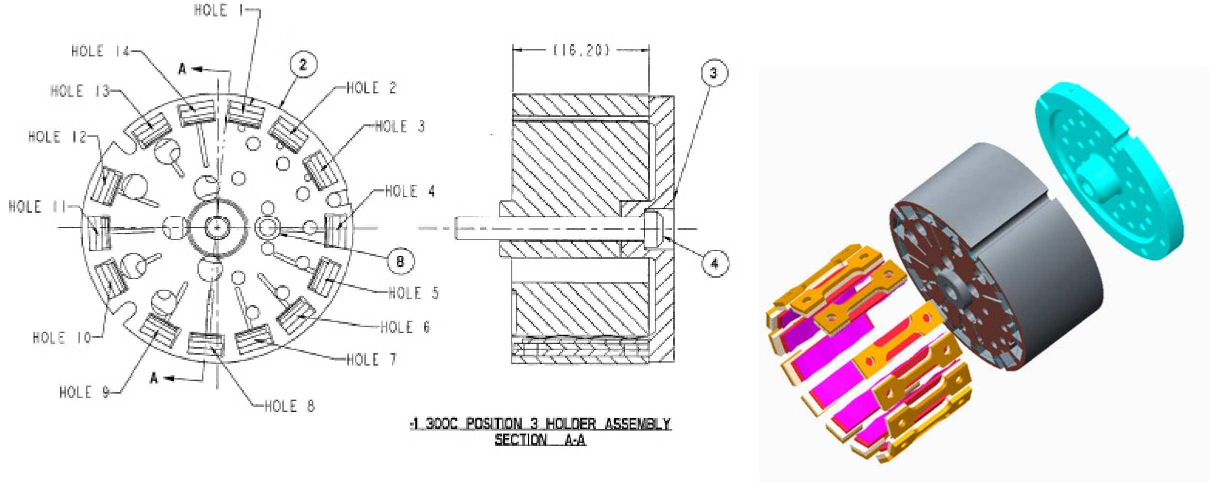

Figure15. Specimen loading layout for the 300°C holder position 3 [D6].

Figure 15 shows the holder and specimen layout of the 300°C holder position 3 and Table 6 lists the specimen loading.

Fourteen SiC temperature monitors (TMs) have been used, one placed next to each SS-J3 specimen pair on the inner radial side. The parts are kept in position with titanium retainers springs.

No temperature monitors are placed inside this holder.

Table 6. Specimen loading list for the 300°C position 3 holder

Specimen Type	**SS-J3**						
Outer to Inner	**Hole 1**	**Hole 2**	**Hole 3**	**Hole 4**	**Hole 5**	**Hole 6**	**Hole 7**
1	0V6E	0V6G	SV6F	TV66	TV68	0V77	SV76
2	0V6F	SV6E	SV6G	TV67	OV76	0V78	SV77
TM	11-6-1	11-6-2	11-6-3	11-6-4	11-6-5	11-6-6	11-6-7
Outer to Inner	**Hole 8**	**Hole 9**	**Hole 10**	**Hole 11**	**Hole 12**	**Hole 13**	**Hole 14**
1	SV78	TV77	0V52	0V54	SV52	SV54	TV53
2	TV76	TV78	0V53	0V55	SV53	SV52	TV54
TM	11-6-8	11-6-9	11-6-10	11-6-11	11-6-12	11-6-13	11-6-14

The Graphite Holder Assemblies (500°C, 800°C and 1200°C)

The graphite holder assemblies refer to the holders located in the 500°C, 800°C and 1200°C zones. There are three holders in total with varying radial as well as axial dimensions. The generic layout of each holder with specimen holes is showed in Figure 16.

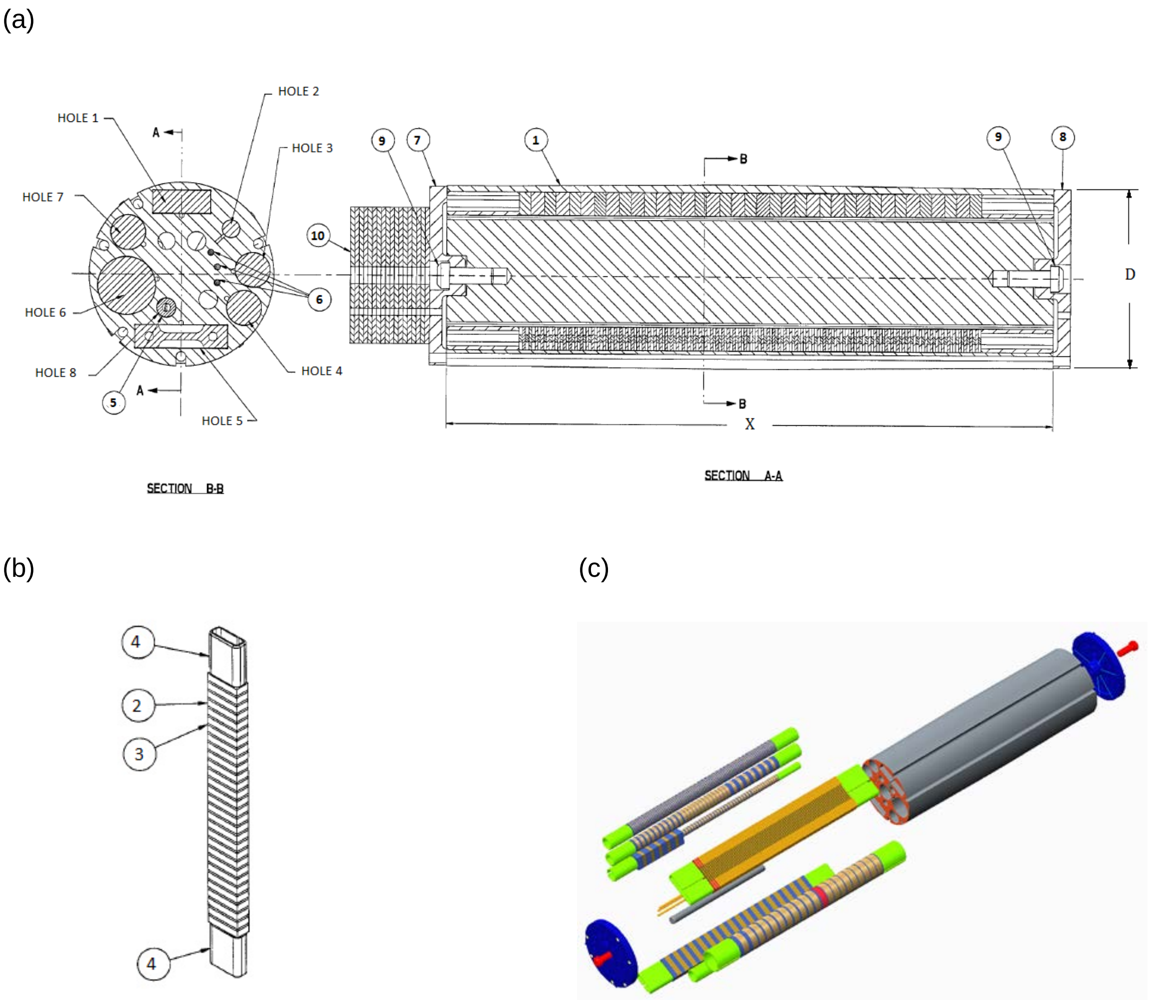

Figure 16. Specimen loading layout for a typical graphite holder (a) section drawings of the holder, (b) typical specimen stack assembly and (c) the three dimensional layout [D6].

The holders (1) have each, three design diameters for the top, middle, and bottom due to the thermal design. The dimensional ranges for the three holders are summarized in Table 7 (refer to [1], [D7], [D8], [D9] for more detail).

Table 7. Graphite holder part dimensions without tolerances

Part	Design Diameter (D) [mm]	Design Length (X) / Thickness [mm]
1200°C holder top	31.30±0.025	105.0
1200°C holder middle	32.00±0.025	105.0
1200°C holder bottom	31.20±0.025	105.0
800°C holder top	32.25±0.025	110.0
800°C holder middle	32.30±0.025	110.0
800°C holder bottom	31.90±0.025	110.0
Holder end cap tabs	32.33±0.025	3.0

Each specimen holder has seven relevant holes designed for the specimen stack assemblies. The holes from 1 to 7 are filled with NT2s, 6SQ5Ds and 3mm discs, 6mm discs, 6mm discs, SSJ2s, 10mm discs and 6mm discs respectively.

Specimens (2) are separated by graphite spacers (3) with similar shapes as the specimens but different thickness. Dimensions and quantities are given in Table 8. Each specimen assembly stack has two Ti spring pin ends (4) that keep the specimens tightly in place.

Table 8. Spacer types and thickness dimensions

Specimen Hole	**Graphite spacer type**	**800°C**		**1200°C**		**500°C**	
		Thickness on average (mm)	**Quantity**	**Thickness on average (mm)**	**Quantity**	**Thickness on average (mm)**	**Quantity**
1	NT2 (10mm x 4mm)	0.96	28	2.33	18	0.61	28
2	6SQ5D (6mm x 6mm)	1.5	5	1.5	5	1.5	5
	TEM	1.1	39	0.97	39	0.45	56
3	Disc 6mm dia.	1.43	36	1.43	31	0.57	41
4	Disc 6mm dia.	0.47	87	0.46	83	0.45	79
5	SSJ2 (16mm x 4mm)	0.54	81	0.48	81	0.42	81
6	Disc 10mm dia.	1.95	34	2.90	21	1.40	36
7	Disc 6mm dia.	0.74	73	0.62	74	0.39	69

The tungsten fiber holders are placed inside hole 8 (5) in all of the graphite specimen holders. The small fiber holders are ~3.3mm in diameter and ~50.0mm in length and are filled with three types of tungsten fibers as well as a SiC thermometer. There are also three SiC thermal couple inserts shown in position 6. See Figure 17 for the typical loading pattern of the tungsten fibers [2].

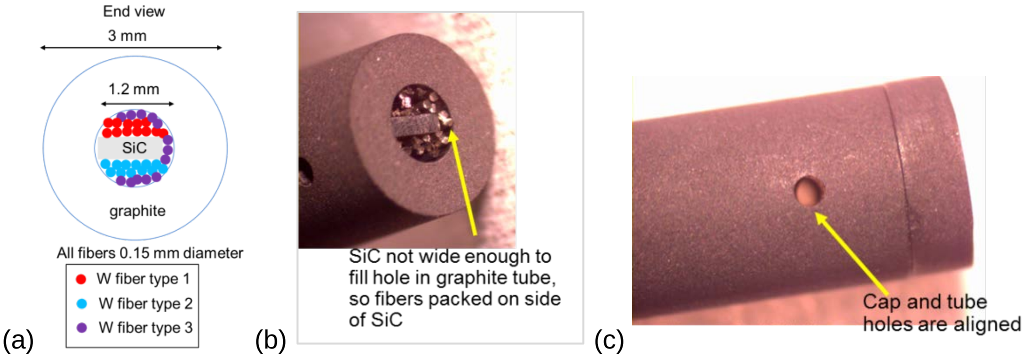

SiC not wide enough to fill hole in graphite tube, so fibers packed on side of SiC

Cap and tube holes are aligned

Figure 17. Tungsten fiber holder typical loading pattern: (a) approximate fiber loading location inside fiber holder, (b) photo after typical loading and (c) photo of tungsten fiber holder with cap.

The graphite holder is enclosed by a top and bottom cap, see positions 7 and 8 respectively, which is fastened with a Grade 5 Ti M2.5 Screw (9). The temperature zones, and therefore the holders, are separated by Ti holder spacers which are 13.95mm in length and filled with 18 Grafoil spacer fillers (10).

The 500°C Holder

The specimen loading list provided in Table 9 shows the specimen packing order from top to bottom of each of the seven specimen stacks in terms of the engraved ID’s. It also lists the specimen types as shown in Figures 2 to 10.

The tungsten fiber holder 02 contains twelve Type 1, twelve Type 2 and thirteen Type 3 tungsten fibers and one SiC thermometry (ID: 5-6-2). Three thermal couple inserts K, L and M are inserted in the small holes near to hole 2, hole 3 and holes 3 & 4 respectively.

Table 9. Specimen loading list of the 500°C holder

Top to Bottom	**Hole 1**		**Hole 2**		**Hole 3**		**Hole 4**		**Hole 5**		**Hole 6**		**Hole 7**	
	ID	**Type**	**ID**	**Type**	**ID**	**Type**	**ID**	**Type**	**ID**	**Type**	**ID**	**Type**	**ID**	**Type**
1	KY03	NT2	9	6SQ5D	9002	D6T2	10K09	D6TH	3E04	SS-J2	8E05	D10T1	V009	D6TH
2	KY02	NT2	8	6SQ5D	9001	D6T2	10K08	D6TH	3E03	SS-J2	8E04	D10T1	V008	D6TH
3	KY01	NT2	7	6SQ5D	9000	D6T2	10K07	D6TH	3E00	SS-J2	8E03	D10T1	V007	D6TH
4	KY00	NT2	6	6SQ5D	5004	D6T2	10K06	D6TH	GE04	SS-J2	8E02	D10T1	V006	D6TH
5	FR04	NT2	3	6SQ5D	5003	D6T2	10K05	D6TH	GE03	SS-J2	8E01	D10T1	V005	D6TH
6	FR03	NT2	2	6SQ5D	5002	D6T2	10K04	D6TH	GE00	SS-J2	8E00	D10T1	V004	D6TH
7	FR02	NT2	KY00	D3TH	5001	D6T2	CT01	D6TH	EE04	SS-J2	ZE03	D10T1	V003	D6TH
8	FR01	NT2	CT03	D3TH	5000	D6T2	CT00	D6TH	EE03	SS-J2	ZE02	D10T1	V002	D6TH
9	FR00	NT2	P009	D3TH	TE0A	D6T1	BT01	D6TH	EE00	SS-J2	ZE01	D10T1	V001	D6TH
10	UE01	NT2	UE02	D3TH	TE09	D6T1	BT00	D6TH	JE04	SS-J2	ZE00	D10T1	V000	D6TH
11	UE00	NT2	4100	TEM	FR00	D6T1	710C	D6TH	JE03	SS-J2	1009	D10TH	Y004	D6TH
12	BT07	NT2	AT00	D3TH	CT0J	D6T1	7109	D6TH	JE00	SS-J2	1008	D10TH	Y003	D6TH
13	BT06	NT2	CT00	D3TH	CT0H	D6T1	7108	D6TH	HE00	SS-J2	1007	D10TH	Y002	D6TH
14	BT05	NT2	CT02	D3TH	CT0G	D6T1	7106	D6TH	UE09	SS-J2	1006	D10TH	Y001	D6TH
15	BT04	NT2	BT03	D3TH	UE01	D6TH	7105	D6TH	UE08	SS-J2	1005	D10TH	Y000	D6TH
16	BT03	NT2	P001	TEM	UE00	D6TH	7104	D6TH	UE07	SS-J2	1004	D10TH	C002	D6TH
17	BT02	NT2	800A	D3TH	KE00	D6T1	7103	D6TH	UE06	SS-J2	1003	D10TH	C001	D6TH
18	BT01	NT2	6000	TEM	3R0L	D6T1	7102	D6TH	UE05	SS-J2	1002	D10TH	C000	D6TH
19	TE01	NT2	AT02	D3TH	3R0K	D6T1	7101	D6TH	UE04	SS-J2	1001	D10TH	4107	D6TH
20	TE00	NT2	EE03	D3TH	RE03	D6TQ	7100	D6TH	UE03	SS-J2	1000	D10TH	4106	D6TH
21	CT07	NT2	EE02	D3TH	RE02	D6TQ	TE01	D6TH	UE00	SS-J2	000G	D10TQ	4105	D6TH
22	CT06	NT2	8009	D3TH	RE01	D6TQ	TE00	D6TH	CT09	SS-J2	000F	D10TQ	4104	D6TH
23	CT05	NT2	8000	TEM	RE00	D6TQ	GW09	D6T1	CT08	SS-J2	000E	D10TQ	4103	D6TH
24	CT04	NT2	X000	TEM	KY0K	D6TQ	GW01	D6T1	CT07	SS-J2	000C	D10TQ	4102	D6TH
25	CT03	NT2	BT00	D3TH	KY0V	D6TQ	5E00	D6TH	CT06	SS-J2	000A	D10TQ	4101	D6TH
26	CT02	NT2	7009	D3TH	KY0J	D6TQ	3R02	D6TH	CT05	SS-J2	0008	D10TQ	4100	D6TH
27	CT01	NT2	6001	TEM	KY0W	D6TQ	3R01	D6TH	CT04	SS-J2	0007	D10TQ	20K0H	D6TH
28	CT00	NT2	P00A	D3TH	KY08	D6TQ	3R00	D6TH	CT03	SS-J2	0006	D10TQ	20K0G	D6TH
29			TE00	D3TH	KY0X	D6TQ	AT01	D6TH	CT00	SS-J2	0005	D10TQ	20K0F	D6TH
30			1103	D3TH	50K0G	D6T1	AT00	D6TH	BT06	SS-J2	0004	D10TQ	20K0E	D6TH
31			UE00	D3TH	50K0F	D6T1	7007	D6TH	BT05	SS-J2	0003	D10TQ	20K0C	D6TH
32			AT01	D3TH	50K0E	D6T1	7006	D6TH	BT04	SS-J2	0002	D10TQ	20K0A	D6TH
33			1102	D3TH	50K0C	D6T1	7005	D6TH	BT03	SS-J2	0001	D10TQ	20K09	D6TH
34			BT02	D3TH	50K0A	D6T1	7004	D6TH	BT00	SS-J2	0000	D10TQ	20K08	D6TH
35			X00A	D3TH	50K09	D6T1	7003	D6TH	AT07	SS-J2	2101	D10T2	20K07	D6TH
36			UE01	D3TH	50K08	D6T1	7002	D6TH	AT06	SS-J2	2100	D10T2	20K06	D6TH
37			EE04	D3TH	50K07	D6T1	7001	D6TH	AT05	SS-J2			20K05	D6TH
38			8001	TEM	50K06	D6T1	7000	D6TH	AT04	SS-J2			20K04	D6TH

Top to Bottom	Hole 1		Hole 2		Hole 3		Hole 4		Hole 5		Hole 6		Hole 7	
	ID	Type	ID	Type	ID	Type	ID	Type	ID	Type	ID	Type	ID	Type
39			4101	TEM	50K05	D6T1	X007	D6TH	AT03	SS-J2			20K03	D6TH
40			X009	D3TH	00K09	D6TQ	X006	D6TH	AT00	SS-J2			20K02	D6TH
41			4109	TEM	00K08	D6TQ	X005	D6TH	X006	SS-J2			20K01	D6TH
42			6009	D3TH	00K07	D6TQ	X004	D6TH	X005	SS-J2			20K00	D6TH
43			1100	D3TH	00K06	D6TQ	X003	D6TH	X004	SS-J2			10K0Z	D6TH
44			KE00	D3TH	10K01	D6TQ	X002	D6TH	X003	SS-J2			10K0Y	D6TH
45			410A	D3TH	00K04	D6TQ	X001	D6TH	X002	SS-J2			10K0X	D6TH
46			700A	D3TH	00K03	D6TQ	X000	D6TH	X001	SS-J2			10K0W	D6TH
47			1101	D3TH	00K02	D6TQ	6007	D6TH	X000	SS-J2			10K0V	D6TH
48			X001	TEM	00K01	D6TQ	6006	D6TH	7006	SS-J2			10K0U	D6TH
49			P000	TEM	00K00	D6TQ	6005	D6TH	7005	SS-J2			10K0T	D6TH
50			EE00	D3TH			6004	D6TH	7004	SS-J2			10K0R	D6TH
51			600A	D3TH			6003	D6TH	7003	SS-J2			10K0P	D6TH
52			7000	TEM			6002	D6TH	7002	SS-J2			10K0N	D6TH
53			7001	TEM			6001	D6TH	7001	SS-J2			10K0M	D6TH
54							6000	D6TH	7000	SS-J2			10K0L	D6TH
55							8007	D6TH	6006	SS-J2			10K0K	D6TH
56							8006	D6TH	6005	SS-J2			10K0J	D6TH
57							8005	D6TH	6004	SS-J2			10K0H	D6TH
58							8004	D6TH	6003	SS-J2			10K0G	D6TH
59							8003	D6TH	6002	SS-J2			10K0F	D6TH
60							8002	D6TH	6001	SS-J2			10K0E	D6TH
61							8001	D6TH	6000	SS-J2			10K0C	D6TH
62							8000	D6TH	4106	SS-J2			10K0A	D6TH
63							P007	D6TH	4105	SS-J2			A004	D6T2
64							P006	D6TH	4104	SS-J2			A003	D6T2
65							P005	D6TH	4103	SS-J2			A002	D6T2
66							P004	D6TH	4102	SS-J2			A001	D6T2
67							P003	D6TH	4101	SS-J2			A000	D6T2
68							P002	D6TH	4100	SS-J2			4002	D6T2
69							P001	D6TH	8006	SS-J2			4001	D6T2
70							P000	D6TH	8005	SS-J2			4000	D6T2
71							06K19	D6TH	8004	SS-J2				
72							06K18	D6TH	8003	SS-J2				
73							06K17	D6TH	8002	SS-J2				
74							06K16	D6TH	8001	SS-J2				
75							06K15	D6TH	8000	SS-J2				
76							06K14	D6TH	P006	SS-J2				
77							06K13	D6TH	P005	SS-J2				
78							0612K	D6TH	P004	SS-J2				
79							06K11	D6TH	P003	SS-J2				
80							06K10	D6TH	P002	SS-J2				
81									P001	SS-J2				
82									P000	SS-J2				

The 800°C Holder

The specimen loading list provided in Table 10 shows the specimen packing order from top to bottom of each of the eight specimen stacks in terms of the engraved ID’s. It also lists the specimen types as shown in Figure 16.

The tungsten fiber holder 01 contains twelve Type 1, twelve Type 2 and thirteen Type 3 tungsten fibers and on SiC thermometry (ID: 5-6-1). Three thermal couple inserts E, F and G are inserted in the small holes near to hole 2, hole 3 and holes 3 & 4 respectively.

Table 210. Specimen loading list of the 800°C holder

Top to Bottom	Hole 1		Hole 2		Hole 3		Hole 4		Hole 5		Hole 6		Hole 7	
	ID	**Type**	**ID**	**Type**	**ID**	**Type**	**ID**	**Type**	**ID**	**Type**	**ID**	**Type**	**ID**	**Type**
1	KY07	NT2	1-7	6SQ5D	710K	D6TH	3R05	D6TH	UE0K	SS-J2	8E07	D10T1	KY0H	D6TQ
2	KY06	NT2	1-6	6SQ5D	710M	D6TH	3R03	D6TH	UE0E	SS-J2	8E0A	D10T1	KY0M	D6TQ
3	KY05	NT2	1-4	6SQ5D	710R	D6TH	3R04	D6TH	UE0F	SS-J2	8E08	D10T1	KY0T	D6TQ
4	KY04	NT2	1-2	6SQ5D	710H	D6TH	600H	D6TH	UE0H	SS-J2	8E09	D10T1	KY0U	D6TQ
5	FR09	NT2	1-1	6SQ5D	710J	D6TH	X00H	D6TH	UE0J	SS-J2	8E0C	D10T1	KY0L	D6TQ
6	FR08	NT2	1-0	6SQ5D	710L	D6TH	5E01	D6TH	UE0A	SS-J2	000T	D10TQ	KY09	D6TQ
7	FR07	NT2	CT06	D3TH	710G	D6TH	700F	D6TH	UE0G	SS-J2	000X	D10TQ	V00K	D6TH
8	FR06	NT2	KE02	D3TH	710N	D6TH	700H	D6TH	UE0C	SS-J2	000P	D10TQ	V00M	D6TH
9	FR05	NT2	600E	D3TH	710P	D6TH	700E	D6TH	P00F	SS-J2	000R	D10TQ	V00H	D6TH
10	UE03	NT2	X002	TEM	710F	D6TH	700G	D6TH	P009	SS-J2	000N	D10TQ	V00L	D6TH
11	UE02	NT2	BT06	D3TH	FR01	D6T1	7009	D6TH	P00E	SS-J2	000V	D10TQ	V00C	D6TH
12	TE03	NT2	800C	D3TH	TE0E	D6T1	7005	D6TH	P008	SS-J2	000W	D10TQ	V00G	D6TH
13	TE02	NT2	4103	TEM	TE0C	D6T1	700A	D6TH	P007	SS-J2	000K	D10TQ	V00J	D6TH
14	CT0F	NT2	AT04	D3TH	UE03	D6TH	30K02	D6TH	P00C	SS-J2	000M	D10TQ	V00F	D6TH
15	CT0C	NT2	800E	D3TH	UE02	D6TH	30K04	D6TH	P00A	SS-J2	000V	D10TQ	V00A	D6TH
16	CT0A	NT2	410E	D3TH	A005	D6T2	30K03	D6TH	X00A	SS-J2	000Z	D10TQ	V00E	D6TH
17	CT09	NT2	6002	TEM	A006	D6T2	30K01	D6TH	X008	SS-J2	000J	D10TQ	RE05	D6TQ
18	CT0J	NT2	P003	TEM	5007	D6T2	30K00	D6TH	X007	SS-J2	000L	D10TQ	RE04	D6TQ
19	CT08	NT2	P00C	D3TH	5006	D6T2	06K1H	D6TH	X00F	SS-J2	000Y	D10TQ	30K09	D6TH
20	CT0G	NT2	P002	TEM	5005	D6T2	06K1M	D6TH	X009	SS-J2	100C	D10TH	30K0P	D6TH
21	CT0E	NT2	KY01	D3TH	KE01	D6T1	06K1J	D6TH	X00E	SS-J2	100E	D10TH	30K0W	D6TH
22	BT0H	NT2	CT05	D3TH	50K0L	D6T1	061GK	D6TH	X00C	SS-J2	100H	D10TH	30K08	D6TH
23	BT0F	NT2	X00C	D3TH	50K0U	D6T1	061CK	D6TH	JE07	SS-J2	100L	D10TH	30K0G	D6TH
24	BT0C	NT2	8003	TEM	50K0N	D6T1	061AK	D6TH	JE06	SS-J2	100A	D10TH	30K06	D6TH
25	BT0A	NT2	AT03	D3TH	50K0M	D6T1	06K1F	D6TH	JE05	SS-J2	100G	D10TH	30K0X	D6TH
26	BT0E	NT2	700C	D3TH	50K0P	D6T1	06K1L	D6TH	CT0H	SS-J2	100K	D10TH	30K0U	D6TH
27	BT0G	NT2	UE05	D3TH	50K0J	D6T1	06K1L	D6TH	CT0A	SS-J2	100M	D10TH	30K0T	D6TH
28	BT09	NT2	7003	TEM	50K0T	D6T1	06K1K	D6TH	CT0F	SS-J2	100J	D10TH	30K0A	D6TH
29	BT08	NT2	410C	D3TH	50K0H	D6T1	06K1E	D6TH	CT0E	SS-J2	100F	D10TH	30K0N	D6TH
30			6003	TEM	50K0K	D6T1	20K0N	D6TH	CT0C	SS-J2	ZE07	D10T1	30K0K	D6TH
31			X003	TEM	50K0R	D6T1	20K0K	D6TH	CT0G	SS-J2	ZE06	D10T1	30K07	D6TH
32			700E	D3TH	3R0M	D6T1	20K0T	D6TH	CT0J	SS-J2	ZE05	D10T1	30K0H	D6TH
33			600C	D3TH	3R0N	D6T1	20K0M	D6TH	CT0K	SS-J2			30K0F	D6TH
34			7002	TEM	CT0M	D6T1	20K0J	D6TH	7007	SS-J2			30K0M	D6TH
35			BT04	D3TH	CT0K	D6T1	20K0R	D6TH	700A	SS-J2			30K03	D6TH
36			UE04	D3TH	CT0L	D6T1	20K0Y	D6TH	700C	SS-J2			30K0R	D6TH
37			8002	TEM			20K0X	D6TH	700E	SS-J2			30K05	D6TH
38			CT04	D3TH			20K0U	D6TH	700F	SS-J2			30K0V	D6TH
39			UE03	D3TH			20K0W	D6TH	7008	SS-J2			30K0L	D6TH
40			X00E	D3TH			20K0L	D6TH	7009	SS-J2			30K0C	D6TH
41			P003	TEM			20K0Z	D6TH	EE07	SS-J2			00K0A	D6TQ
42			AT05	D3TH			20K0V	D6TH					00K0C	D6TQ
43			TE01	D3TH			20K0P	D6TH					00K0H	D6TQ
44			4102	TEM			TE03	D6TH					00K0K	D6TQ
45			BT05	D3TH			TE02	D6TH					00K0M	D6TQ

Top to Bottom	**Hole 1**		**Hole 2**		**Hole 3**		**Hole 4**		**Hole 5**		**Hole 6**		**Hole 7**	
	ID	**Type**	**ID**	**Type**	**ID**	**Type**	**ID**	**Type**	**ID**	**Type**	**ID**	**Type**	**ID**	**Type**
46							P00G	D6TH					00K0J	D6TQ
47							P00J	D6TH					00K0E	D6TQ
48							P00H	D6TH					00K0F	D6TQ
49							P00F	D6TH					00K0L	D6TQ
50							P008	D6TH					00K0G	D6TQ
51							P00E	D6TH					410F	D6TH
52							P009	D6TH					4108	D6TH
53							P00A	D6TH					410G	D6TH
54							P00G	D6TH					410E	D6TH
55							800C	D6TH					410C	D6TH
56							8009	D6TH					410J	D6TH
57							800A	D6TH					410H	D6TH
58							800F	D6TH					410A	D6TH
59							8008	D6TH					4109	D6TH
60							800H	D6TH					Y005	D6TH
61							800E	D6TH					Y009	D6TH
62							800G	D6TH					Y007	D6TH
63							800J	D6TH					Y008	D6TH
64							700C	D6TH					Y006	D6TH
65							7008	D6TH					C005	D6TH
66							600A	D6TH					C004	D6TH
67							600E	D6TH					C003	D6TH
68							6008	D6TH						
69							600G	D6TH						
70							6009	D6TH						
71							6006	D6TH						
72							600J	D6TH						
73							600F	D6TH						
74							X00F	D6TH						
75							X00A	D6TH						
76							X00J	D6TH						
77							X00E	D6TH						
78							X00C	D6TH						
79							X00G	D6TH						
80							X008	D6TH						
81							X009	D6TH						
82							CT02	D6TH						
83							CT03	D6TH						
84							BT03	D6TH						
85							BT02	D6TH						
86							AT03	D6TH						
87							AT02	D6TH						
88							GW03	D6T1						
89							GW02	D6T1						

<u>The 1200°C Holder</u>

The specimen loading list provided in Table 11 shows the specimen packing order from top to bottom of each of the seven specimen stacks in terms of the engraved ID’s. The specimen types are as identified in Figure 16.

The tungsten fiber holder 03 contains twelve Type 1, 12 Type 2 and 13 Type 3 tungsten fibers and one SiC temperature monitor (ID: 5-6-3). Temperature monitors H, I and J are inserted in the small holes near hole 2, hole 3 and holes 3 & 4 respectively.

Table 11. Specimen loading list for the 1200°C holder

Top to Bottom	**Hole 1**		**Hole 2**		**Hole 3**		**Hole 4**		**Hole 5**		**Hole 6**		**Hole 7**	
	ID	**Type**	**ID**	**Type**	**ID**	**Type**	**ID**	**Type**	**ID**	**Type**	**ID**	**Type**	**ID**	**Type**
1	TE05	NT2	2-4	6SQ5D	A00A	D6T2	50K00	D6TH	3E0A	SS-J2	2104	D10T2	410W	D6TH
2	TE04	NT2	2-3	6SQ5D	A009	D6T2	40K05	D6TH	3E09	SS-J2	2103	D10T2	410V	D6TH
3	UE05	NT2	2-2	6SQ5D	A008	D6T2	40K04	D6TH	3E08	SS-J2	8E0K	D10T1	410U	D6TH
4	UE04	NT2	2-0	6SQ5D	A007	D6T2	40K03	D6TH	GE01	SS-J2	8E0J	D10T1	410T	D6TH
5	CT0T	NT2	1-9	6SQ5D	500C	D6T2	40K02	D6TH	GE09	SS-J2	8E0H	D10T1	410R	D6TH
6	CT0R	NT2	1-8	6SQ5D	500A	D6T2	40K01	D6TH	GE08	SS-J2	8E0G	D10T1	410P	D6TH
7	CT0P	NT2	P004	TEM	5009	D6T2	40K00	D6TH	EE01	SS-J2	8E0F	D10T1	410N	D6TH
8	CT0N	NT2	P005	TEM	5008	D6T2	30K0Y	D6TH	EE09	SS-J2	ZE09	D10T1	410M	D6TH
9	CT0M	NT2	6004	TEM	FR02	D6T1	CT07	D6TH	EE08	SS-J2	ZE08	D10T1	410L	D6TH
10	CT0L	NT2	X004	TEM	CT0R	D6T1	CT06	D6TH	JE0A	SS-J2	ZE07	D10T1	410K	D6TH
11	CT0K	NT2	X005	TEM	CT0P	D6T1	CT05	D6TH	JE09	SS-J2	100Z	D10TH	C008	D6TH
12	BT0M	NT2	8004	TEM	CT0N	D6T1	CT04	D6TH	JE08	SS-J2	100Y	D10TH	C007	D6TH
13	BT0L	NT2	8005	TEM	TE0G	D6T1	BT05	D6TH	HE04	SS-J2	100X	D10TH	C006	D6TH
14	BT0K	NT2	6006	TEM	TE0F	D6T1	BT04	D6TH	UE0V	SS-J2	100W	D10TH	V00V	D6TH
15	BT0J	NT2	4104	TEM	UE05	D6TH	TE05	D6TH	UE0U	SS-J2	100V	D10TH	V00U	D6TH
16	KY0C	NT2	4105	TEM	UE06	D6TH	TE04	D6TH	UE0T	SS-J2	100U	D10TH	V00Z	D6TH
17	KY0A	NT2	7004	TEM	3R0R	D6T1	GW05	D6T1	UE0R	SS-J2	100T	D10TH	V00Y	D6TH
18	KY09	NT2	7005	TEM	3R0P	D6T1	GW04	D6T1	UE0P	SS-J2	100R	D10TH	V00X	D6TH
19	KY0E	NT2	KY02	D3TH	KE02	D6T1	5E02	D6TH	UE0N	SS-J2	100P	D10TH	V00W	D6TH
20			P00F	D3TH	00K0Z	D6TQ	3R08	D6TH	UE0M	SS-J2	100N	D10TH	V00T	D6TH
21			P00G	D3TH	00K0Y	D6TQ	3R07	D6TH	UE0L	SS-J2			V00R	D6TH
22			800F	D3TH	00K0X	D6TQ	3R06	D6TH	CT0V	SS-J2			V00P	D6TH
23			800G	D3TH	RE09	D6TQ	AT05	D6TH	CT0U	SS-J2			Y00G	D6TH
24			410F	D3TH	RE08	D6TQ	AT04	D6TH	CT0T	SS-J2			Y00F	D6TH
25			410G	D3TH	RE07	D6TQ	700W	D6TH	CT0R	SS-J2			Y00E	D6TH
26			600F	D3TH	RE06	D6TQ	700V	D6TH	CT0P	SS-J2			Y00C	D6TH
27			600G	D3TH	KY0F	D6TQ	700U	D6TH	CT0N	SS-J2			Y00A	D6TH
28			X00F	D3TH	KY0E	D6TQ	700T	D6TH	CT0M	SS-J2			40K0Z	D6TH
29			X00G	D3TH	KY0A	D6TQ	700R	D6TH	CT0L	SS-J2			40K0Y	D6TH
30			700F	D3TH	KY0G	D6TQ	700P	D6TH	BT0J	SS-J2			40K0X	D6TH
31			700G	D3TH	KY0XX	D6TQ	700N	D6TH	BT0H	SS-J2			40K0W	D6TH
32			AT06	D3TH	KY0P	D6TQ	700M	D6TH	BT0G	SS-J2			40K0V	D6TH
33			AT07	D3TH			700L	D6TH	BT0F	SS-J2			40K0U	D6TH
34			AT08	D3TH			700K	D6TH	X00J	SS-J2			40K0T	D6TH
35			KE03	D3TH			X00W	D6TH	BT0E	SS-J2			40K0R	D6TH
36			UE06	D3TH			X00V	D6TH	AT0M	SS-J2			40K0P	D6TH
37			UE07	D3TH			X00U	D6TH	AT0L	SS-J2			40K0N	D6TH
38			UE08	D3TH			X00T	D6TH	AT0K	SS-J2			40K0N	D6TH
39			TE02	D3TH			X00R	D6TH	AT0J	SS-J2			40K0M	D6TH
40			BT07	D3TH			X00P	D6TH	AT0H	SS-J2			40K0L	D6TH
41			BT08	D3TH			X00N	D6TH	AT0G	SS-J2			40K0K	D6TH
42			BT09	D3TH			X00M	D6TH	X00N	SS-J2			40K0J	D6TH
43			CT07	D3TH			X00L	D6TH	X00M	SS-J2			40K0H	D6TH
44			CT08	D3TH			X00K	D6TH	X00L	SS-J2			40K0G	D6TH
45			CT09	D3TH			600W	D6TH	X00K	SS-J2			40K0F	D6TH

Top to Bottom	**Hole 1**		**Hole 2**		**Hole 3**		**Hole 4**		**Hole 5**		**Hole 6**		**Hole 7**	
	ID	**Type**	**ID**	**Type**	**ID**	**Type**	**ID**	**Type**	**ID**	**Type**	**ID**	**Type**	**ID**	**Type**
46							600V	D6TH	X00H	SS-J2			40K0E	D6TH
47							600U	D6TH	X00G	SS-J2			40K0C	D6TH
48							600T	D6TH	700N	SS-J2			40K0A	D6TH
49							600R	D6TH	700M	SS-J2			40K09	D6TH
50							600P	D6TH	700L	SS-J2			40K08	D6TH
51							600N	D6TH	700K	SS-J2			40K07	D6TH
52							600M	D6TH	700J	SS-J2			40K06	D6TH
53							600L	D6TH	700H	SS-J2			7117	D6TH
54							600K	D6TH	700G	SS-J2			7114	D6TH
55							800W	D6TH	600N	SS-J2			7113	D6TH
56							800V	D6TH	600M	SS-J2			7112	D6TH
57							800U	D6TH	600L	SS-J2			7111	D6TH
58							800T	D6TH	600K	SS-J2			7110	D6TH
59							800R	D6TH	600J	SS-J2			710Z	D6TH
60							800P	D6TH	600H	SS-J2			710Y	D6TH
61							800N	D6TH	600G	SS-J2			710X	D6TH
62							800M	D6TH	410N	SS-J2			710W	D6TH
63							800L	D6TH	410M	SS-J2			00K0W	D6TQ
64							800K	D6TH	410L	SS-J2			00K0V	D6TQ
65							P00W	D6TH	410K	SS-J2			00K0U	D6TQ
66							P00V	D6TH	410J	SS-J2			00K0T	D6TQ
67							P00U	D6TH	410H	SS-J2			00K0R	D6TQ
68							P00T	D6TH	410G	SS-J2			00K0P	D6TQ
69							P00R	D6TH	800N	SS-J2			00K0N	D6TQ
70							P00P	D6TH	800M	SS-J2				
71							P00N	D6TH	800L	SS-J2				
72							P00M	D6TH	800K	SS-J2				
73							P00L	D6TH	800J	SS-J2				
74							P00K	D6TH	800H	SS-J2				
75							16K10	D6TH	800G	SS-J2				
76							06K1Z	D6TH	P00N	SS-J2				
77							061YK	D6TH	P00M	SS-J2				
78							06K1X	D6TH	P00L	SS-J2				
79							06K1W	D6TH	P00K	SS-J2				
80							06K1V	D6TH	P00J	SS-J2				
81							061UK	D6TH	P00H	SS-J2				
82							061TK	D6TH	P00G	SS-J2				
83							061RK	D6TH						
84							061PK	D6TH						

Conclusion

HFIR MFE-RB-19J is a complex irradiation experiment with ~1300 specimens of F82H, W and W alloy specimens. The experiment is planned for six cycle irradiation in HFIR. The experiment uses a Gd thermal neutron shield, and the expected displacement damage for F82H and W during the 6 cycles will be ~2.5 to 3 and ~1.0 to 1.5 dpa respectively.

References

[1] McDuffee, J.L., Temperature Verification, Transient Analysis, and Argon Activation for Materials Experiment MFE-RB-19J, C-HFIR-2016-007, Rev. 0, Reactor and Nuclear Systems Division, Oak Ridge National Laboratory, 2016.

[2] Garrison, J.L., “Fiber assembly in the graphite tubes for RB*19J”, March 9th 2016.

Drawings:

[D1] HFIR MFE 19J Experiment Capsule Assembly, X3E020977A663, Rev. 0, Reactor and Nuclear Systems Division, Oak Ridge National Laboratory, 2016.

[D2] HFIR 19J Experiment Specimen Holders Assembly, S15-61-RB1901, Rev. 1, Reactor and Nuclear Systems Division, Oak Ridge National Laboratory, 2016.

[D3] HFIR MFE 19J Experiment 300C Holders, S15-34-RB19J06, Rev. 0, Reactor and Nuclear Systems Division, Oak Ridge National Laboratory, 2016.

[D4] RB19J Experiment 300C Position 1 Holder Assembly, S15-35-RB19J07, Rev. 0, Reactor and Nuclear Systems Division, Oak Ridge National Laboratory, 2016.

[D5] RB19J Experiment 300C Position 2 Holder Assembly, S15-37-RB19J09, Rev. 0, Reactor and Nuclear Systems Division, Oak Ridge National Laboratory, 2016.

[D6] RB19J Experiment 300C Position 3 Holder Assembly, S15-39-RB19J11, Rev. 0, Reactor and Nuclear Systems Division, Oak Ridge National Laboratory, 2016.

[D7] RB19J Experiment 800C Holder Assembly, S15-46-RB19J17, Rev. 0, Reactor and Nuclear Systems Division, Oak Ridge National Laboratory, 2016.

[D8] RB19J Experiment 1200C Holder Assembly, S15-50-RB19J19, Rev. 0, Reactor and Nuclear Systems Division, Oak Ridge National Laboratory, 2016.

[D9] RB19J Experiment 500C Holder Assembly & Details, S15-55-RB19J23, Rev. 0, Reactor and Nuclear Systems Division, Oak Ridge National Laboratory, 2016.

10.5 HFIR IRRADIATION EXPERIMENTS—J.P. Robertson, Y. Katoh and J. McDuffee (Oak Ridge National Laboratory)

Summary of recent, current and planned Fusion Materials Program experiments.

Status of the Reactor

HFIR completed 2.7 cycles during the first half of 2016. Cycle 464 operated from January 1, until February 6, 2016, for 2101 MWdays. Cycle 465 started on February 23, and ran for 2093 MWdays, shutting down on March 18. Cycle 466 began on June 14, 2016.

Summary of Recent, Current and Planned Fusion Materials Program Experiments

Experiment Designation	Primary Materials	Specimen Types*	Irradiation Temperature (°C)	Max Exposure (dpa)	Number of Reactor Cycles	Irradiation Period (month/year)		
Beryllium reflector (RB) irradiation positions								
RB-15J	F82H	T, F, FT	300, 400	6	10	6/08	–	12/09
RB-19J	W alloys and F82H	various	250/300, 500, 800, 1200	1.5	6	6/16		6/17
Target zone full-length capsules								
JP-25	F82H	T, FT	300, 500	20	10	2/99	–	1/01
JP-26	F82H	T, FT	300,400,500	9	5	12/03	–	11/04
JP-27	F82H	T, FT	300, 400	21	13	12/03	–	1/08
JP-28	F82H	T, FT	300,400,500	80	46	4/05	–	7/13
JP-29	F82H	T, FT	300,400,500	80	46	1/05	–	7/13
12-DCT	F82H	DCT	50	1.6	1	8/11	–	8/11
JP-30	F82H	T, FT	300,400,650	20	~10	11/11	–	8/13
JP-31	F82H	T, FT	300,400,650	20	~10	11/11	–	8/13
Target zone rabbit capsules (DOE-JAEA)								
F8A1	F82H	T, FT	300	50	29	2/09	–	7/13
F8A2	"	"	"	"	"	"	–	"
F8B1	"	"	"	"	"	"	–	"
F8B2	"	"	"	"	"	"	–	"
JCR-1	SiC/SiC	Bend bars	800	30	15	10/04	–	1/09
JCR-2	"	"	"	"	"	"	–	"
JCR-3	"	"	"	"	"	"	–	"
JCR-4	"	"	"	"	"	"	–	"
JCR-5	"	"	"	>50	>25	10/04	–	2/11
JCR-6	"	"	"	"	"	"	–	"
JCR-7	"	"	"	"	"	"	–	"
JCR-8	"	"	"	"	"	"	–	"
JCR-9	"	"	500	30	15	10/04	–	1/09
JCR-10	"	"	"	"	"	"	–	"
JCR-11	"	"	"	"	"	"	–	"

Target zone rabbit capsules (DOE-JAEA) – Continued

Experiment Designation	Primary Materials	Specimen Types*	Irradiation Temperature (°C)	Max Exposure (dpa)	Number of Reactor Cycles	Irradiation Period (month/year)		
JCR-12	“	“	“	“	“	“	–	“
F11A3	F82H	T, FT	300	20	12	5/11	–	2/13
F11A4	“	“	“	“	“	“	–	“
F11B3	“	“	“	“	“	“	–	“
M4-TEN	F82H	DCT	50	1.6	1	8/11	–	8/11
JCR11-01	SiC/SiC	Bend bars	950	50	25	11/12	–	
JCR11-02	SiC/SiC	Bend bars	950	10	5	10/12	–	8/13
JCR11-03	SiC/SiC	Bend bars	950	30	15	5/13	–	8/15
JCR11-04	SiC/SiC	Bend bars	950	30	15	5/13	–	8/15
JCR11-05	SiC/SiC	Bend bars	950	50	25	10/12	–	
JCR11-06	SiC/SiC	Bend bars	950	10	5	10/12	–	7/13
JCR11-07	SiC/SiC	Bend bars	950	100	50	10/12	–	
JCR11-08	SiC/SiC	Bend bars	950	100	50	10/12	–	
JCR11-09	SiC/SiC	UDMC	950	4	2	6/13	–	11/13
JCR11-10	SiC/SiC	UDMC	950	10	8	6/13	–	8/14
JCR11-11	SiC/SiC	UDMC	950	30	15	6/13	–	8/15
JCR11-12	SiC/SiC	UDMC	950	100	50	6/13	–	
F13A5	F82H	T, FT	300	10	9	1/14	–	3/15
F13A6	F82H	T, FT	300	50	28	1/14	–	
F13B4	F82H	T, FT	300	10	9	1/14	–	3/15
F13B5	F82H	T, FT	300	20	18	1/14	–	
SCF6	SiC/SiC	Bend bars	600	10	6	11/14	–	10/15
SCF7	SiC/SiC	Bend bars	600	30	14	11/14	–	
SCF8	SiC/SiC	Bend bars	600	100	45	11/14	–	
SCF9	SiC/SiC	Bend bars	600	200	90	11/14	–	
SCF10	SiC/SiC	Bend bars	950	10	5	1/15	–	10/15
SCF11	SiC/SiC	Bend bars	950	30	14	1/15	–	
SCF12	SiC/SiC	Bend bars	950	100	45	1/15	–	
Target zone rabbit capsules (DOE-NIFS)								
T8A1	SiC	BSR	300	0.01	HT**	10/09	–	10/09
T8A2	SiC	BSR	300	0.1	HT	10/09	–	10/09
T8B1	SiC	BSR	500	0.01	HT	10/09	–	10/09
T8B2	SiC	BSR	500	0.1	HT	10/09	–	10/09
T8C1	SiC	BSR	500	~1	1	5/09	–	6/09
T8D1	SiC	BSR	800	0.1	HT	3/11	–	10/09
T8E1	SiC	BSR	800	~1	1	8/09	–	8/09
T8F1	SiC	BSR	1200	~1	1	8/09	–	8/09
T9A1	W, Ni	Discs	90	0.1	HT	1/09	–	10/09
T9A2	W, Ni	Discs	90	1.2	1	1/09	–	1/09
T9C1	Steels	T, MC	500	5.5	3	11/09	–	2/10
T9C2	Steels	T, MC	500	9.6	5	11/09	–	6/10
T9G1	Steels	T, MC	300	1.2	1	6/09	–	8/09
T9G2	Steels	T, MC	300	9.6	8	6/09	–	8/11
MTTN01	Steels	T, MC	300	4.8	4	1/12	–	8/11
300-LD-1	Steels	SSJ, MC	300	2	1	5/12	–	6/12
300-HD-1	Steels	SSJ, MC	300	12	6	5/12	–	2/13

Target zone rabbit capsules (DOE-NIFS) - Continued

Experiment Designation	Primary Materials	Specimen Types*	Irradiation Temperature (°C)	Max Exposure (dpa)	Number of Reactor Cycles	Irradiation Period (month/year)		
500-LD-1	Steels	SSJ, MC	500	2	1	5/12	–	6/12
500-HD-1	Steels	SSJ, MC	500	12	6	5/12	–	2/13
500-HD-2	Steels	SSJ, MC	500	12	6	5/12	–	2/13
500-HD-3	Steels	SSJ, MC	500	12	6	5/12	–	2/13
650-LD-1	Steels	SSJ, MC	650	2	1	5/12	–	6/12
650-LD-2	Steels	SSJ, MC	650	2	1	5/12	–	6/12
650-HD-1	Steels	SSJ, MC	650	12	6	5/12	–	2/13
650-HD-2	Steels	SSJ, MC	650	12	6	5/12	–	2/13
300-LD-2	Steels, W	SSJ, MC	300	2	2	7/12	–	8/12
300-MD-1	Steels, W	SSJ, MC	300	7	4	7/12	–	2/13
500-LD-2	Steels, W	SSJ, MC	500	2	2	1/13	–	7/13
300-LD-3	Steels, W	SSJ, MC	300	2	2	7/12	–	11/12
300-HD-2	Steels, W	SSJ, MC	300	12	8	7/12	–	2/14
500-LD-3	Steels, W	SSJ, MC	500	2	1	7/12	–	8/12
500-HD-4	Steels, W	SSJ, MC	500	12	6	7/12	–	7/13
650-LD-3	Steels, W	SSJ, MC	650	2	2	10/12	–	7/13
650-HD-3	Steels, W	SSJ, MC	650	12	8	7/12	–	11/13
PC1	Various	SSJ, MC	80/100	0.02	HT	6/12	–	6/12
PC1A	Various	SSJ, MC	80/100	0.02	HT	6/12	–	6/12
PC2	Various	SSJ, MC	80/100	0.1	HT	6/12	–	6/12
PC2A	Various	SSJ, MC	80/100	0.1	HT	6/12	–	6/12
PC3	Various	SSJ, MC	80/100	0.5	HT	6/12	–	7/12
PC3A	Various	SSJ, MC	80/100	0.5	HT	6/12	–	7/12
PC4	Various	SSJ, MC	80/100	2	1	6/12	–	7/12
PC4A	Various	SSJ, MC	80/100	2	1	6/12	–	7/12
PC5	Various	SSJ, MC	80/100	20	9	6/12	–	11/13
TB-300-1	Steels, W	SSJ, MC	300	0.02	HT	8/12	–	8/12
TB-300-2	Steels, W	SSJ, MC	300	0.1	HT	8/12	–	8/12
TB-300-3	Steels, W	SSJ, MC	300	0.5	HT	8/12	–	8/12
TB-300-4	Steels, W	SSJ, MC	300	7	5	7/12	–	6/13
TB-500-1	Steels, W	SSJ, MC	500	0.1	HT	8/12	–	8/12
TB-500-2	Steels, W	SSJ, MC	500	0.5	HT	8/12	–	8/12
TB-500-3	Steels, W	SSJ, MC	500	7	4	7/12	–	2/13
TB-650-1	Steels, W	SSJ, MC	650	0.1	HT	8/12	–	8/12
TB-650-2	Steels, W	SSJ, MC	650	0.5	HT	8/12	–	8/12
TB-650-3	Steels, W	SSJ, MC	650	7	5	7/12	–	6/13
TB-650-4	Steels, W	SSJ, MC	650	20	11	7/12	–	7/14
TTN09	SiC	Joint	500	3.4	2	8/11	–	11/11
TTN10	SiC	Joint	500	4.1	2	8/11	–	11/11
TTN11	SiC	Joint	800	4	2	3/12	–	5/12
TTN01	SiC	BSR	300	1	1	2/11	–	3/11
TTN02	SiC	BSR	300	10	6	2/11	–	12/11
TTN03	SiC	BSR	300	20	11	2/11	–	8/13
TTN04	SiC	BSR	500	10	6	5/11	–	4/12
TTN05	SiC	BSR	500	20	11	5/11	–	8/13
TTN06	SiC	BSR	800	10	6	5/11	–	4/12
TTN07	SiC	BSR	800	20	11	5/11	–	8/13
TTN08	SiC	BSR	1200	10	6	5/11	–	8/12

Target zone rabbit capsules (DOE-NIFS) - Continued

Experiment Designation	Primary Materials	Specimen Types*	Irradiation Temperature (°C)	Max Exposure (dpa)	Number of Reactor Cycles	Irradiation Period (month/year)		
TTN16	SiC	Fiber BSR	500	1	1	11/11	–	12/11
TTN17	SiC	Fiber BSR	500	10	6	8/11	–	6/12
TTN18	SiC	Fiber BSR	500	20	11	8/11	–	8/13
TTN19	SiC	Fiber BSR	1200	1	1	3/12	–	4/12
TTN20	SiC	Fiber BSR	1200	10	6	3/12	–	11/12
PXW1	W	Discs	800	2	1		–	
PXW2	W	Discs	800	2	1	1/15	–	2/15
PXW3	W	Discs	800	6	3		–	
PXW4	W	Discs	1100	2	1		–	
PXW5	W	Discs	1100	2	1	1/15	–	2/15
PXW8	W	Discs	1100	6	3		–	
Target zone rabbit capsules (US-NIFS-JAEA)								
T11-01J	V-4Cr-4Ti	BTC	425	2	1	11/12	–	12/12
T11-02J	V-4Cr-4Ti	BTC	425	6	3	1/13	–	7/13
T11-03J	V-4Cr-4Ti	BTC	425	2	1	11/12	–	12/12
T11-04J	V-4Cr-4Ti	BTC	425	6	3	1/13	–	7/13
T11-05J	SiC	BTC	600	2	1	11/12	–	12/12
T11-06J	SiC	BTC	600	6	3	1/13	–	7/13
T11-08J	SiC	BTC	600	6	3	1/13	–	7/13
T11-09J	SiC	BTC	600	2	1	11/12	–	12/12
T11-11J	SiC	BTC	600	2	1	11/12	–	12/12
T11-13J	Graphite	BTC	600	2	1	11/12	–	12/12
T11-14J	Graphite	BTC	600	6	3	1/13	–	7/13
J12-01	F82H	BTC	300	1.5	1	1/13	–	2/13
J12-02	F82H	BTC	300	6	3	5/13	–	7/13
J12-03	F82H	BTC	300	1.5	1	5/13	–	2/13
J12-04	F82H	BTC	300	6	3	1/13	–	6/13
J12-05	F82H	BTC	300	1.5	1	1/13	–	2/13
J12-06	F82H	BTC	300	6	3	5/13	–	6/13
Target zone rabbit capsules (US-IMR)								
MX-1	Ceramics	Various	400	2	1	7/13	–	8/13
MX-2	Ceramics	Various	400	6	3	7/13	–	3/14
MX-3	Ceramics	Various	400	10	6	7/13	–	7/14
MX-4	Ceramics	Various	700	2	1	7/13	–	8/13
MX-5	Ceramics	Various	700	6	3	7/13	–	2/14
MX-6	Ceramics	Various	700	10	5	7/13	–	5/14
MX-7	Ceramics	Various	1000	2	1	7/13	–	8/13
MX-8	Ceramics	Various	1000	6	3	7/13	–	3/14
MX-9	Ceramics	Various	1000	10	5	7/13	–	5/14
IMR1	Various	Various	200	2	1	6/15	–	7/15
IMR2	Various	Various	200	2	1	6/15	–	7/15
IMR3	Various	Various	200	2	1	6/15	–	7/15
IMR4	Various	Various	200	2	1	6/16	–	
IMR5	Various	Various	200	4	2	6/15	–	2/16

Target zone rabbit capsules (US-IMR) - Continued

Experiment Designation	Primary Materials	Specimen Types*	Irradiation Temperature (°C)	Max Exposure (dpa)	Number of Reactor Cycles	Irradiation Period (month/year)		
IMR6	Various	Various	600	2	1	6/16	–	
IMR7	Various	Various	600	6	3	6/16	–	
IMR8	Various	Various	600	10	5	6/16	–	
IMR9	Various	Various	1000	2	1	6/16	–	
IMR10	Various	Various	1000	6	3	6/16	–	
IMR11	Various	Various	1000	10	5	6/16	–	
Target zone rabbit capsules (US)								
SCJ2-10	Ceramics	Joint	500	3	2	5/14	–	7/14
SCJ2-11	Ceramics	Joint	500	>10	12	5/14	–	
SCJ2-12	Ceramics	Joint	500	3	2	5/14	–	7/14
SCJ2-16	Ceramics	Joint	1000	3	2	6/14	–	8/14
SCJ2-17	Ceramics	Joint	1000	3	2	6/14	–	8/14

*T = Tensile, F = Fatigue, FT = Fracture Toughness, MC = Multipurpose Coupon, BSR = Bend Stress Relaxation Creep, DCT = Disc Compact Tension, BTC: Bellows-loaded Tensile Creep, UDMC: Uni-directional Mini-composite. Most experiments also contain TEM disks, other special purpose specimens, and monitors occupying small spaces.

**Hydraulic tube – fractional cycle exposures.